Validation of OSEM algorithm for attenuation correction in cardiac SPECT studies

By

Ahmed M. Alenezi, M.Sc.

A thesis submitted for the degree of PhD
in Medical Physics and Clinical Engineering
at the Department Medical Physics and Clinical Engineering
The University of Sheffield
Sheffield, United Kingdom

Sheffield Teaching Hospitals NHS
NHS Trust

December 2004

In the Name of Allah the Most Gracious the Most Merciful

All praises and thanks are to Allah, the lord of the worlds who says which means:

"Those who believe, and whose hearts find satisfaction in the remembrance of Allah: for without doubt in the remembrance of Allah do hearts find satisfaction".

(The Holy Qur'an, Surah Al-Raad: 28).

I seek Allah to make my heart full of the remembrance of Allah (S.W.T).

I dedicate this thesis to my mother, my wife, and my kids.

Table of contents

Abstract

Photon attenuation is believed to be one of the major causes of artefacts in cardiac SPECT studies and therefore should be corrected to improve the specificity of cardiac SPECT imaging for the detection of coronary artery disease. Today, many SPECT system manufacturers provide optional hardware (CT imaging) and software (OSEM reconstruction algorithm) technology attempting to produce attenuation corrected (artefacts-free) images and more accurate quantitative cardiac SPECT studies. However, this attenuation correction (AC) technique has not received widespread acceptance in routinely clinical practice due to the less-than-optimal validations of AC using realistic data and the potential for creating new artefacts. The purpose of this study is to validate whether AC can produce quantitatively accurate cardiac SPECT images and whether it creates more additional artefacts than it has cured. **METHODS:** Multiple experiments were carried out using cardiac SPECT data and the state-of-the-art AC technology available in Sheffield Teaching Hospitals (CT/SPECT hybrid system and OSEM algorithm). Cardiac SPECT data obtained from computer-simulated models, a physical phantom (anthropomorphic phantom with cardiac insert) and one patient data were used to validate and evaluate AC technique. Qualitative and quantitative analysis was performed to compare cardiac SPECT images without and with AC. **RESULTS:** The computer-simulated phantom showed that a realistic model can be generated and was used successfully for validation purposes. The simulation results showed that the attenuation artefacts were corrected significantly in both noiseless and noisy data. Using post-filtering with high number of iterations was found to be the reasonable criteria of stopping the reconstruction. The simulated data with 1 cm misregistration error between emission and transmission images produces a significant error in AC images. Attenuation artefacts were significantly corrected in all walls of cardiac insert in physical phantom with some non-uniformity in images reconstructed with low number of iterations. These images become more uniform with high number of iterations. Patient data demonstrated that AC appears to have worked well. **CONCLUSION:** OSEM algorithm was able to correct attenuation artefacts (without scatter modelling) of cardiac SPECT images using CT attenuation map with no evidence of generating additional artefacts. If such artefacts exist they must arise either from early stopping of the OSEM algorithm or other sources e.g. scatter and misregistration. In conclusion, OSEM algorithm is recommended for AC in cardiac SPECT studies.

Acknowledgments

First of all I am indebted to my supervisor Professor David Barber whom I cannot forget his support and guidance in this period of my life.

I would like to acknowledge my friend Mr. Andrew Harris for his constant encouragement during the course of this research programme. Also, I would like to express my appreciation to Mr. Mike Avison from Medical Physics Department at Bradford Royal Infirmary Hospital for his help in using their physical phantom.

I would also like to thank all staff in medical physics department at Sheffield teaching hospitals, who have made my working time more pleasant (with apologies to anyone whose name I have accidentantly left out) Dr.Wendy Tindale, Dr. Andrew Leathard, Miss Anna Swift, Dr. Ian Scivill, Dr.Pete Metherall, Dr.Richard Walker, and Mr.Philip Hillel.

I also wish to thank Dr.Ueber Miola, Dr.Saleh Bamjboor, Dr.David Hamilton and all the staff in Medical Physics Department at Riyadh Alkarj Hospital in Saudi Arabia for their advice and encouragement.

I want to express my thanks to my mother for her full support throughout my education and to my wife for encouraging me and sharing with me the both the sadness and the joy.

My sincere thanks to my brothers Dr.Daher, Mr.Faisal, Dr.Thamer, Dr.Amer, and Engineer Omar and to my sisters Seda, Lyla, Mona, Menwa, Amina, Maha, Badrya and Jawaher and the rest of my family for their constant love and moral support. I am also extremely appreciative to my kids Mohammad and Mona for long hours from home.

Finally, I would like to thank the Medical Service Division, Ministry of Defence in Saudi Arabia for their financial support, which has led forward to this Doctorate thesis

Declaration

I declare, that the work presented in this thesis was carried out in accordance with the Regulation of the University of Sheffield. No part of this thesis has been submitted or presented to any other universities for examination purpose to obtain another qualification either in the United Kingdom or overseas.

Ahmed M. Alenezi

Abbreviations

CT	Computed Tomography
SPECT	Single Photon Emission Computed Tomography
PET	Positron Emission Tomography
ECT	Emission Computed Tomography
TCT	Transmission Computed Tomography
AC	Attenuation-corrected
UAC	Uniform attenuation correction
NUAC	Non-uniform attenuation correction
NC	No attenuation correction
CAD	Coronary Artery Disease
SC	Scatter Correction
FBP	Filtered back-projection
OSEM	Ordered-Subset Expectation Maximisation
FOV	Field of view
MLEM	Maximum Likelihood Expectation Maximisation
LAD	Left anterior descending coronary artery
RCA	Right coronary artery
LCx	Left circumflex artery
MI	Myocardial Infarction
MPI	Myocardial Perfusion Imaging
LV	Left Ventricle
ROI	Region of interest
SA	Short-axis
HLA	Horizontal long-axis
VLA	Vertical long-axis
GM	Geometric Mean
AM	Arithmetic Mean
FWHM	Full-width at half maximum
QC	Quality Control
1D	One-dimensional
2D	Two-dimensional
3D	Three-dimensional
μ	Linear attenuation coefficient
LAO	Left Anterior Oblique
GE	General Electric-Medical systems
^{99m}Tc	Technetium
^{201}Tl	Thallium
MLA	Multiple Line Array
PHA	Pulse Height analyser
MRI	Magnetic Resonance Imaging
SSCT	Single-Slice Computed Tomography
MSCT	Multiple-Slice Computed Tomography

List of Tables

List of Figures

Chapter One Introduction

1.1. Overview

Coronary Artery Disease (CAD) is a process in which the arteries of the heart (coronary arteries) become partially or completely occluded. CAD can lead to a myocardial infarction (heart attack), in which portions of the heart muscle die, or myocardial ischemia (reduced blood flow), which may result in irreversible damage to the heart. CAD is a major cause of death in almost all countries: in the UK, about 2.65 million people have CAD and in 1999, this accounted for a total cost of approximately two billion pounds[1]. If diagnosed in the early stages, improved management of CAD could be achieved, reducing mortality rates and cost.

CAD diagnosis is commonly performed by means of medical imaging techniques. A widely used technique is Single Photon Emission Computed Tomography (SPECT), which may be applied to patients with known or suspected CAD. In this imaging method the patient is injected with a radioactive imaging agent that is taken up in the heart muscle (myocardium). A gamma camera then rotates around the patient and detects the emitted gamma radiation. The detected gamma rays are converted into an image of the agent's distribution with gamma rays appearing as count intensities in the reconstructed SPECT image. The myocardial perfusion SPECT image of the blood flow of the heart is used for the visual and quantitative analysis of absent or diminished agent uptake in proportion to the blood flow-myocardial territories corresponding to infarction and ischemia respectively. In the cases of significant shortage of blood flow other medical procedures are then utilized. These include angiography and cardiac catheterisation.

---

[1] www.nice.org.uk. "National Institute for Clinical Excellence-Myocardial perfusion scintigraphy for the diagnosis and management of angina, and myocardial infarction". Technology Appraisal 73,November 2003.

It is known that the presence of tissue surrounding the heart causes attenuation of the emitted gamma rays. This leads to artificial reduction in the count intensity. The diagnostic value of the reconstructed images may therefore be diminished because of those artefacts. Clinically, attenuation artefacts appear as a local decrease in count density of the cardiac SPECT images and could be reported as a perfusion defect. This could result in an increase in the number of false positive scan interpretations. Ultimately, patients with false positive results are likely to be referred for additional investigations and/or therapy and will unnecessarily consume health care resources.

Attenuation artefacts in myocardial perfusion SPECT impose a limitation on the accuracy of the diagnosis of CAD. This attenuation artefact should be corrected and eliminated from the final reconstructed image. Correction for attenuation could eliminate unwanted false positive results and improve the confidence level of the physician interpreting the scan. Additionally it could reduce the number of patients referred for catheterisation who have an apparent perfusion defect, rather than true myocardial defect.

Due to its importance to cardiac patient investigation, attenuation compensation or correction (AC) has been an active area of research in SPECT myocardium perfusion imaging implementation. A recent study (2002) states "Although considerable progress has been made, SPECT attenuation compensation technology is still a work in progress" [1]. The main goal of this thesis is to evaluate the accuracy of attenuation correction in SPECT myocardial imaging.

Today, many SPECT systems include transmission tomography by which attenuation maps are generated and incorporated into the reconstruction process in order to correct attenuation artefacts. Advanced iterative reconstruction algorithms such as the Ordered Subset Expectation Maximisation (OSEM) are also included in many modern SPECT systems. These algorithms can easily be modified to incorporate attenuation.

A variety of transmission-based AC methods have been proposed for commercial SPECT system and these systems generally differ from one vendor to another. Differences include the hardware design, types of transmission source, as well as the acquisition/processing algorithms [1].

One of these developments is the hybrid imaging system in which two systems, namely CT and SPECT are, integrated on a single gantry. The hybrid system has been introduced recently to the commercial marketplace. One of these hybrid systems is the "Hawkeye" system, manufactured by General Electric-Medical System (GE). This system consists of a low dose CT x-ray tube and detectors mounted on a dual-head variable-angle camera. This system was initially developed to produce anatomic images in registration with emission images for oncology studies. However, this system can also provide a high quality transmission image (patient specific attenuation map) for use in attenuation correction (AC) of cardiac SPECT and other studies. The validation of attenuation corrected images using this system remains however a major issue. In this thesis, particular attention is paid to the Hawkeye GE hybrid system and OSEM algorithm in evaluating and validating the attenuation correction of cardiac SPECT.

1.2. Statement of the problem

Despite the availability of transmission/emission systems and new reconstruction algorithms in many hospitals, AC has not gained general acceptance as a useful clinical tool for SPECT myocardium perfusion. This can be attributed to a variety of factors: (1) less-than-optimal implementations of these advanced AC techniques, (2) resistance to change from a known set of image artefacts obtained with FBP to the unknown territory of iterative reconstruction with AC [2], and (3) the possibility of introducing additional artefacts in AC images [3], [4] . It is reported that "AC comes with its own considerable array of poorly understood and as yet unresolved technical challenges, including, of all things, the potential for creating new artefacts"[5] .

Published clinical validations of AC using some of the commercially available SPECT systems (with transmission imaging) have reported significant improvement in specificity[2] and sensitivity[3]. This is particularly true for high-risk patterns of CAD [6], [7]. However, Vidal [8], Hendal [9], and Banzo[10] reported improved specificity at the cost of sensitivity. Other researchers; Hendel [11] and Lee [12] reported little or no benefit, especially with intermediate pre-test likelihood of CAD.

[2] A highly specific test confirms the presence of a disease, when reporting negative answers.
[3] A highly sensitive test excludes the presence of a disease when reporting positive results.

In general, the application of attenuation correction has been shown to be positive in some studies and to be negative in others. This has lead to the view that transmission-based AC imaging is still investigational and in a development phase.

1.3. Significance of the study

The suitability of AC technology for routine clinical practice is still debatable due to the issues mentioned previously. This necessitates a detailed investigation of commercial AC packages prior to their clinical implementation. To answer the question "Does AC create additional unfamiliar artefacts", considerable research is required for the validation of attenuation correction prior to the wide application in SPECT.

Some Clinical interpreters suggest that phantom simulation is never close enough to "real" patient imaging to replace clinical testing. However for the evaluation of the effects of attenuation, which is a physics problem, it is entirely appropriate to use realistic patient simulation.

1.4. Objectives and outline of the thesis

The aims of this thesis are to provide a methodology for the evaluation of attenuation correction (AC) for routine clinical work and to answer the question "Does AC produce quantitatively accurate cardiac SPECT images and does it create additional unfamiliar artefacts".

This thesis evaluates and validates the use of AC with an OSEM reconstruction algorithm using simulation, physical phantom and clinical data. Multiple validation experiments were carried out. The specific aims of these experiments were as follows:

- To validate both the uniform and non-uniform AC with OSEM reconstruction using two-dimension simulated simplified models.
- To develop a realistic three-dimension models using an anatomical phantom and use it to validate AC.
- To optimise the parameters used in the OSEM reconstruction package for better understanding and testing prior to clinical implementation.
- To investigate the influence of adding attenuation from breasts, arms, and scanning couch upon AC on the 2D simplified models

- To assess the effectiveness of AC using noisy data and to investigate the influence of misregistration between transmission and emission scans on the AC.
- To validate and evaluate AC using hardware phantom data and some cardiac SPECT clinical data obtained from CT/SPECT Hawkeye system.

1.5. Thesis layout

The remainder of this thesis is divided as follows:

In Chapter-2 an introduction of the SPECT imaging system is given. A brief description of myocardial perfusion SPECT imaging, the effects of attenuation, and image reconstruction algorithms is also given. Chapter-3 provides a review of some commercially available configurations of non-uniform AC methods. The clinical impact of some clinical trials of AC is also presented. The results of the AC validation using 2D simplified models are presented in Chapter-4. Also, this chapter provides the results of the validation of AC with additional attenuation from breasts, arms, and scanning couch. The developments of the 3D model and validation results are presented in Chapter-5. Furthermore, the influence of noise and misregistration (between transmission and emission images) on AC is also presented in this chapter. Chapter-6 presents a qualitative evaluation applied to both physical phantom and clinical data obtained from the Hawkeye system. Finally, Chapter-7 summarizes the major findings of this work and provides avenues for future developments.

Chapter Two

Cardiac SPECT imaging

Coronary artery disease (diseases of the heart blood vessels) results in a large morbidity in western civilizations. Over the last few years, Single Photon Emission Computed Tomography (SPECT) has gained wide acceptance as a major imaging technique for evaluation of patients with Coronary Artery Diseases (CAD). It utilizes an intravenously administered radiopharmaceutical (a pharmaceutical which is labelled with a radioactive isotope) to image the abnormal distribution of blood flow in the heart muscle (myocardial perfusion) associated with CAD. Despite the high level of diagnostic accuracy for evaluation of known or suspected CAD, cardiac SPECT imaging still has several potential problems including the production of artefacts due to photon attenuation. These artefacts cause the resulting reconstructed images to be quantitatively inaccurate and diminish their diagnostic value. The attenuation effect in cardiac SPECT imaging is discussed in this chapter and the attenuation correction technique introduced.

2.1. Anatomy and blood supply of the heart

The heart is a four-chambered muscular organ located in the lower portion of the thoracic cavity between the lungs, which receives and circulates blood. The four chambers are; the right atrium, the right ventricle, the left atrium, and the left ventricle (Figure 2-1(a)). It is easiest to consider the heart as having two pumps (the right heart and left heart) operating in parallel, with no direct communication of blood between the left and right sides. The right side of the heart pumps deoxygenated blood into the lungs and left side of the heart pumps oxygenated blood throughout the rest of the body. Valves in the heart and cardiac vessels allow the blood to flow only in one direction. The Left Ventricle (LV) has to push blood throughout the whole body; therefore it has the greatest mass of myocardium and requires a large blood supply to do this (the

cardiac output at rest is about 5 litre/minute)[4] [13] The LV receives a greater proportion of the blood supply; therefore it is the most visible structure on the perfusion scan[14].

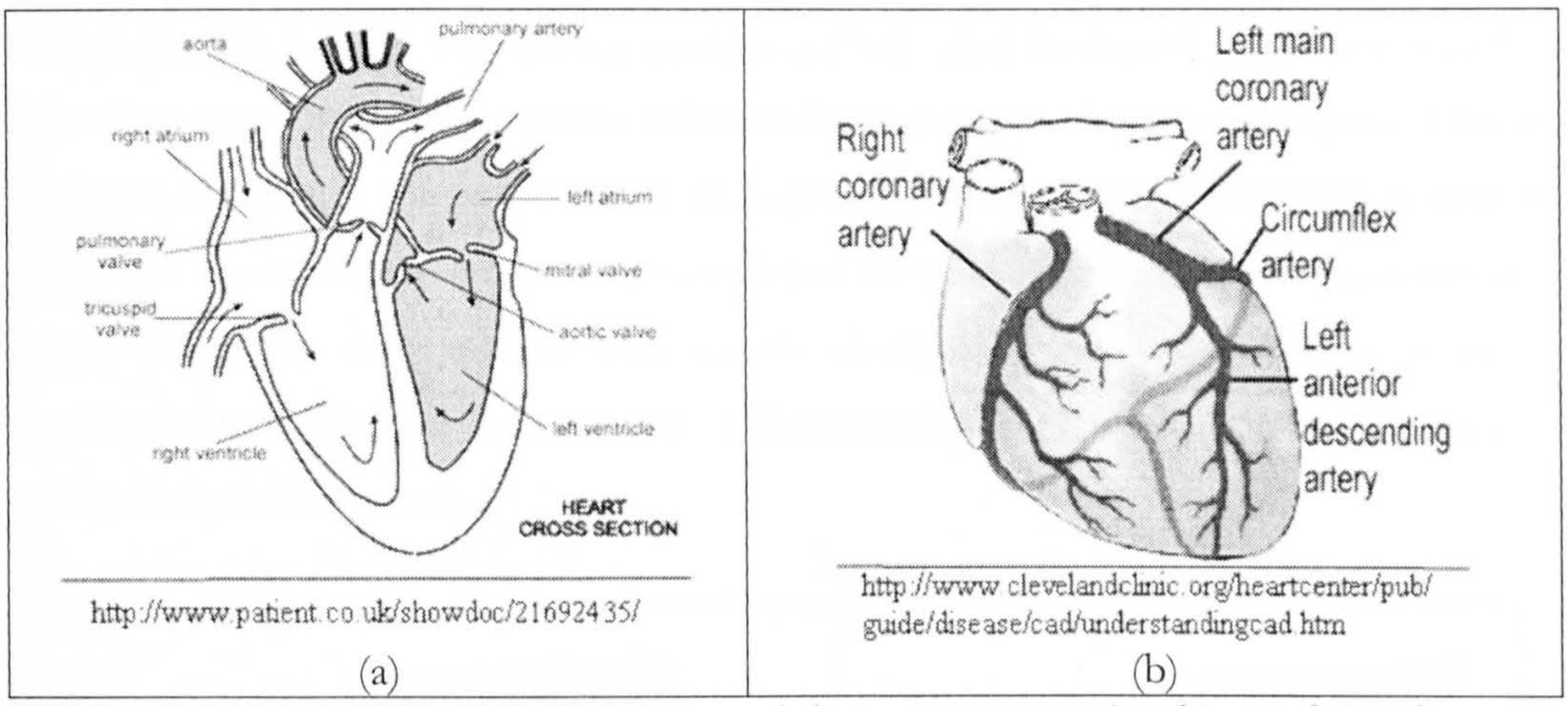

Figure 2-1 Cross-section of the heart: (a) and the coronary arteries (b) supplying the heart.

The heart, like any other organ, needs oxygenated blood to function. It has dedicated blood vessels that provide the myocardium with oxygen and nutrition. The cardiac blood vessels which wrap around the heart like a crown [15] are called "Coronary Arteries". They originate from the aorta and divide into the left and right coronary arteries. The left coronary artery further divides into the left anterior descending (LAD) and the circumflex branch (LCx) (Figure 2-1(b)). These major coronary arteries branch into smaller arteries supplying different regions of the heart with blood. The Right coronary artery (RCA) supplies blood to the inferior wall of LV. The LCx supplies blood to the lateral wall of LV. The LAD supplies the largest proportion of the myocardium; the anterior, septal, and antero-lateral regions of the LV.

2.2. Coronary artery disease

CAD is usually the result of atherosclerosis. Atherosclerosis is a change in the inner lining of the artery causing stiffening of arterial walls and narrowing (stenosis) of the internal diameter of the artery. This narrowing is a result of a focal accumulation of lipids, complex carbohydrates, and calcium deposits. Risk factors include smoking, diabetes, obesity, high cholesterol diet, high blood pressure, and sedentary lifestyle (lack of exercise).

[4] Cardiac output is the volume of blood pumped through the heart per minute

The narrowing of the coronary arteries reduces the amount of oxygenated blood that can pass through the vessel and perfuse the myocardium. As a result, the partially blocked (Figure 2-2(a)) coronary arteries can no longer meet the increased blood oxygen demand by the heart muscle during exercise (stress). This decreased blood flow and the lack of oxygen to the heart muscle (called ischemia) causes chest pain (angina). This is seen as a decrease in the uptake of the radiopharmaceutical in the myocardial perfusion scan. If a coronary artery becomes completely blocked (Figure 2-2(b)) blood can no longer reach the myocardium. This causes death of a part of the heart muscle, (myocardial infarction). This is seen as an absence of radiopharmaceutical uptake in the myocardial perfusion scan.

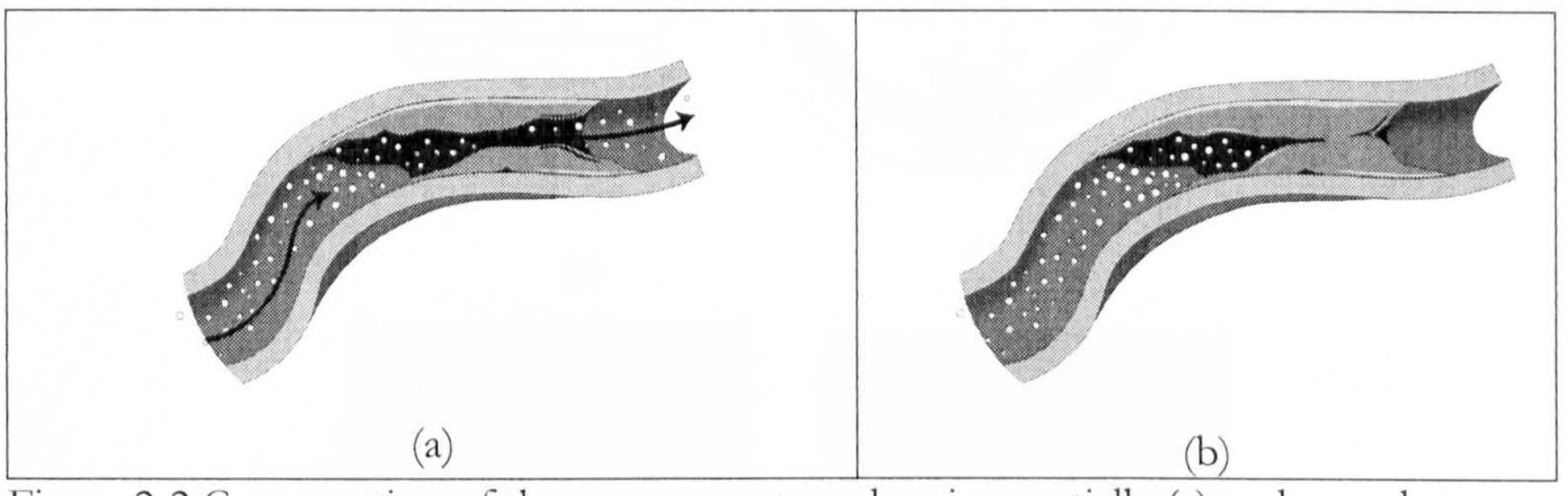

Figure 2-2 Cross-section of the coronary artery showing partially (a) and complete stenosis (b) which leads to the formation of ischemia (a) and infarction (b).

While the lack of oxygen to the heart muscle (ischemia) is temporary and reversible, the muscle damage accompanying myocardial infarction is permanent (irreversible). The infarcted myocardium turns into scar tissue when it heals. A scarred heart cannot pump blood as efficiently as a normal heart, and can lead to heart failure. If there is sufficient perfusion to keep the muscle cells alive but not to provide the energy for contraction, this is referred to as viable myocardium. There is a need for the imaging technique to differentiate between, ischemic, viable, and infarcted myocardium as each impacts differently on the patient's treatment and prognosis.

Nowadays, multiple imaging modalities for cardiac imaging are available commercially, contributing to improved accuracy in the diagnosis of CAD disease. These tomographic imaging modalities, including Transmission Computed Tomography (TCT) (Figure 2-3(b)) and Emission Computed Tomography (ECT) (Figure 2-3(a)), record two-dimensional (2D) projections of a three-dimensional (3D) object, the heart. While the TCT imaging modalities provide anatomical information about the heart (Figure 2-3(d)),

ECT techniques provide functional information (Figure 2-3(c)). ECT imaging modalities are nuclear medicine systems, in which a radiopharmaceutical is injected into the patient: by detecting the gamma rays emitted in the radioactive decay of the isotope. The distribution of the pharmaceutical can be mapped into an image.

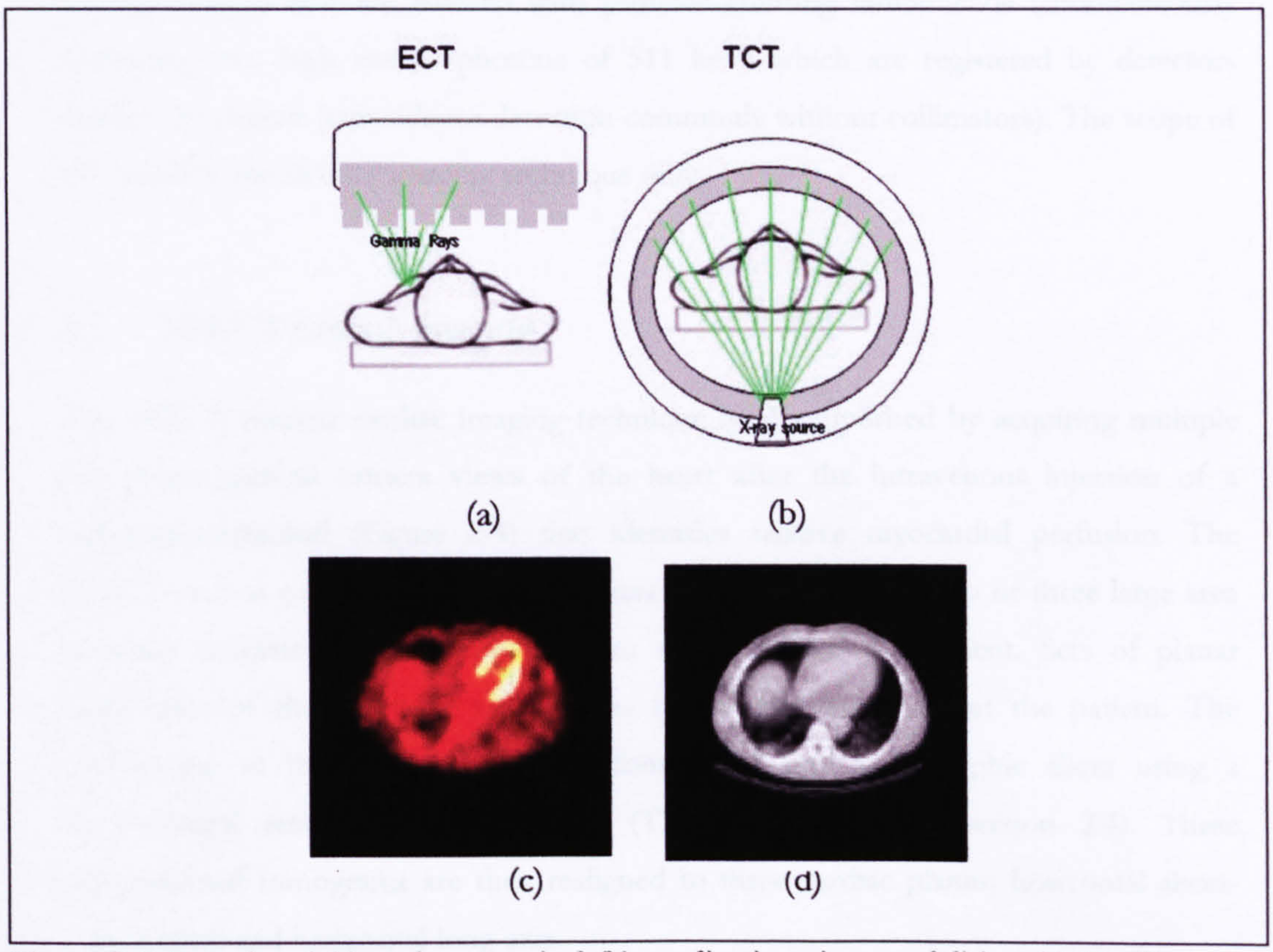

Figure 2-3 Functional (a) and anatomical (b) cardiac imaging modalities. (c) Cardiac SPECT image and (d) CT cardiac image.

While ECT and TCT are based on similar underlying computational techniques there are some important differences between them;

(1) With TCT the radiation source's location is external and known (Figure 2-3(b)), while in ECT, the source is internal and its distribution unknown (Figure 2-3(a)).

(2) In TCT images photons are transmitted through the body whereas for ECT images the photons are emitted from within the body.

(3) The TCT image depicts the attenuation coefficients whereas the ECT reconstructed image represents the radioactivity distribution.

(4) In ECT, the photon emissions are attenuated by the intervening tissues before reaching the detector, so attenuation effects must be compensated to reconstruct a quantitatively accurate image of the radioactivity distribution.

ECT may be subdivided into two imaging techniques: Positron Emission Tomography (PET) and Single Photon Emission Computed Tomography (SPECT). SPECT uses radiopharmaceuticals that emit a single photon with energy typically between 60 and 300 keV and detected by a gamma camera with a collimator, whereas PET uses pharmaceuticals that are labelled with positron-emitting radionuclide (simultaneously producing two high energy photons of 511 keV) which are registered by detectors around the patient (coincidence detection commonly without collimators). The scope of this thesis is the SPECT imaging technique only.

2.3. SPECT cardiac imaging

The SPECT nuclear cardiac imaging technique is accomplished by acquiring multiple 2D planar gamma camera views of the heart after the intravenous injection of a radiopharmaceutical (Figure 2-4) that identifies relative myocardial perfusion. The SPECT system consists of a gamma camera incorporating one, two or three large area detectors mounted on a gantry that can rotate around the patient. Sets of planar projections of the heart are collected as the gantry rotates about the patient. The information in these projections is reconstructed into tomographic slices using a mathematical reconstruction algorithm (This is discussed in section 2.4). These reconstructed tomograms are then realigned to three cardiac planes; horizontal short-axis, vertical and horizontal long-axis.

2.3.1 Myocardial perfusion agents

A myocardial perfusion agent should be readily taken up by the heart muscle cell (myocytes) in proportion to the perfusion and should be retained permanently or at least for sufficient time to allow the acquisition of the images. Many radiopharmaceuticals have been investigated for cardiac SPECT imaging over the years.

Those currently used in UK are; thallium chloride (^{201}Tl), and technetium ^{99m}Tc labelled agents (sestamibi and tetrofosmin). Thallium redistributes within a few hours, so a single injection is used for both stress and rest (redistribution) imaging. However, the energy of its predominant photon is low (80 keV) for ideal SPECT imaging, and its radiation

dosimetry severely limits the injected activity[5] and image quality. In addition, the emission of low-energy photons can leads to images with significant attenuation by soft tissue.

Technetium (^{99m}Tc) labelled radiopharmaceuticals provides certain advantages over ^{201}Tl. These include availability of ^{99m}Tc via an on-site generator when required (^{201}Tl is cyclotron generated and requires off-site delivery), more suitable photons (140 keV) for gamma camera imaging and, due to its shorter half-life (6.03 hr), reduced patient radiation dose for a higher injected activity (400 MBq) [16]. The large injection dose leads to an image with high counts density. In contrast to ^{201}Tl, the ^{99m}Tc tracer does not redistribute, and two separate injections must be given for stress and rest imaging. The higher energy photon of ^{99m}Tc (140 keV) versus ^{201}Tl (80 keV) is less attenuated by soft tissue. For these reasons, the ^{99m}Tc produces images with increased counting statistics than ^{201}Tl. This thesis will be limited to SPECT myocardial perfusion using ^{99m}Tc tracer.

2.3.2 Gamma camera

After the radiopharmaceutical is injected single photons emitted by the decaying isotope are detected with a scintillation camera (or gamma camera). A schematic picture of the gamma camera is shown in Figure 2-4. The camera consist of a lead collimator to ensure that all detected photons are propagated along parallel paths, a crystal scintillator [NaI] to convert high-energy photons to visible light, and photo-multiplier tubes (PMTs) and associated electronics to determine the position of each incident photon from the light distribution in the crystal. PMTs are arranged in a close packed array covering the entire sensitive area of the crystal. In addition to estimating the position of the scintillation event, the PMT signals are also combined to estimate the energy of the incident photon.

[5] The radiation dose is proportional to the combination of both the injected activity in MBq and the half-life of the injected radioisotope. Therefore, the relatively long half-life of ^{201}Tl (74 hr) limits the amount of administered activity used to 80 MBq, and this leads to an image with relatively low count density.

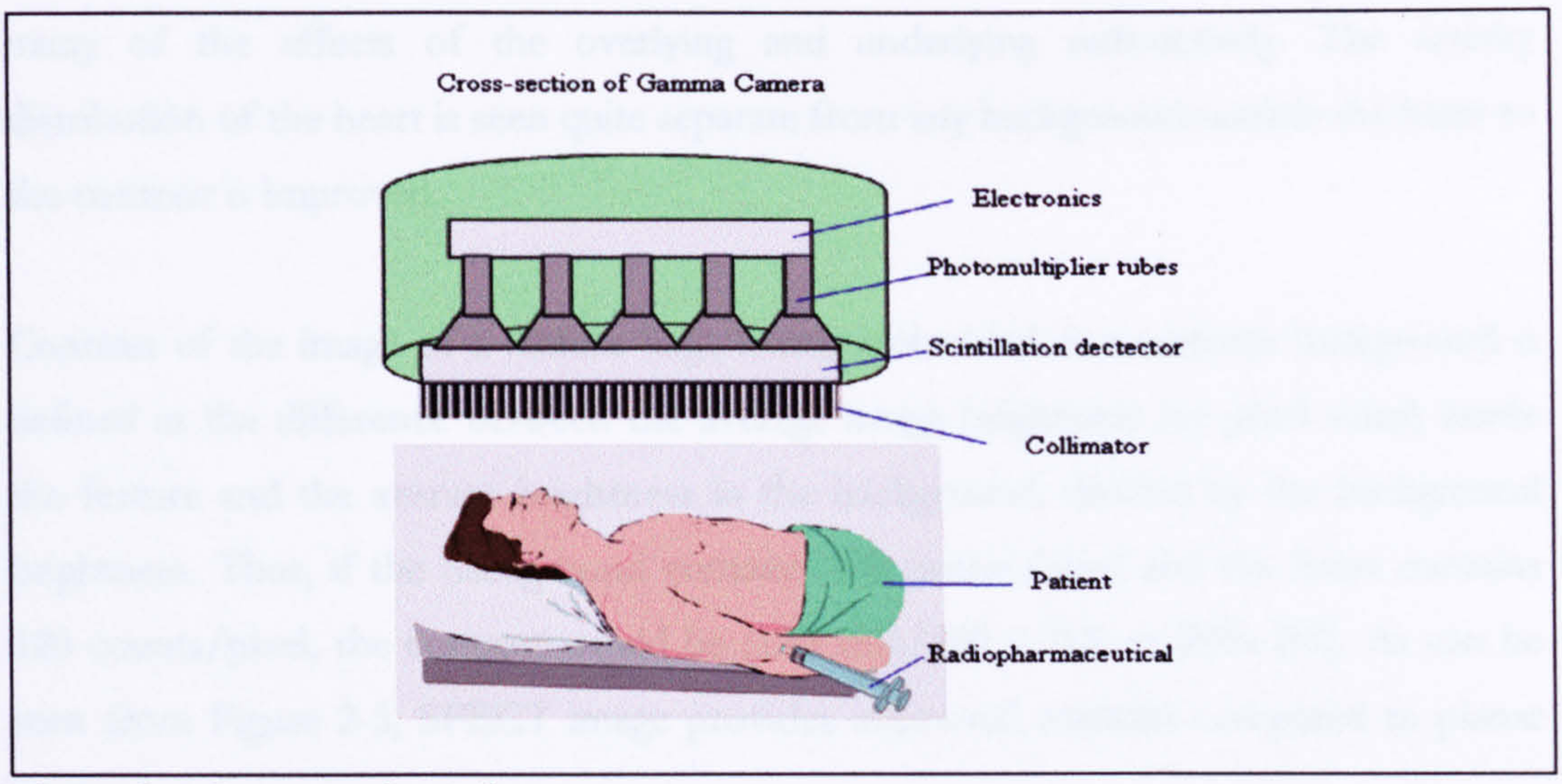

Figure 2-4 Cross-section of gamma camera.

A Pulse height analyser (PHA) is applied to the detected signals such that only un-scattered photons are included in the image, thus reducing noise and improving contrast. The 2D accumulation of these events forms a projection image of the distribution of the radiopharmaceutical. This image is a 2D digital image, or matrix of numbers representing the number of photons detected as they emanated from the patient. If the numbers are mapped to colours or shades of grey this set of numbers can be viewed as a picture.

The gamma camera is used in both planar and tomographic imaging. The basic nuclear medicine acquisition is the static planar view (or projection). In planar imaging, the camera is fixed relative to the patient, so one obtains a 2D image that reflects the projection of the 3D distribution of activity inside patient. The planar projections most commonly used for cardiac imaging are the anterior, the 45° left anterior oblique (LAO), and left lateral view. The resulting planar image has two major shortcomings. First, the images are projections, so the heart can be obscured by activity in front of or behind the heart (reducing the contrast). Second, overlying tissue can attenuate photons originating in the heart. This is a problem, for example, in scans of obese women, where attenuation by the breast tissue can be misinterpreted as a cardiac defect. As a result, these images frequently suffer from low contrast (Figure 2-5(a)) and inaccurate quantification. The overlap of normal and abnormal segments on planar images also makes detection and localization of small perfusion abnormalities difficult. Therefore, a SPECT technique is used whereby a cross-sectional image is produced which removes

many of the effects of the overlying and underlying radioactivity. The activity distribution of the heart is seen quite separate from any background outside the heart so the contrast is improved.

Contrast of the image of a feature (e.g., heart) embedded in a uniform background is defined as the difference between the average image brightness (or pixel value) inside the feature and the average brightness in the background, divided by the background brightness. Thus, if the background contains 100 counts/pixel and the heart contains 120 counts/pixel, the contrast would be (120-100)/100 = 0.2, or 20% [17]. As can be seen from Figure 2-5, SPECT image provides improved contrast compared to planar image.

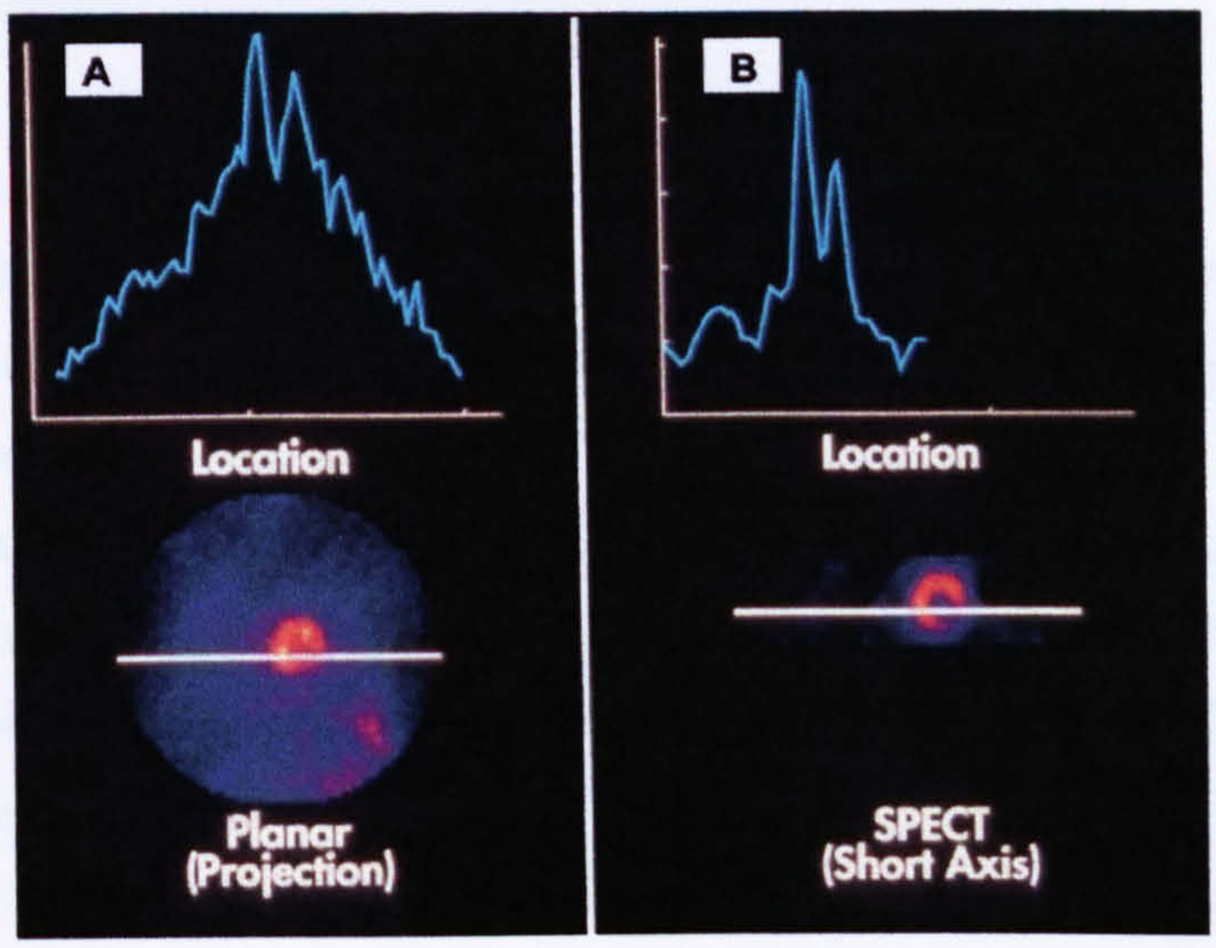

Figure 2-5 Shows the cardiac planar image (A) and how the image contrast improves with SPECT (B).

The contrast of the SPECT image is higher with tomographic reconstructed views than on planar projections. This significantly improves the image contrast (Figure 2-5(b)) and the 3D visual interpretation (high qualitative assessment) of the scan. Although SPECT significantly increases the diagnostic utility of nuclear medicine imaging, it still suffers from problems of poor quantitative accuracy. In SPECT imaging, quantitative accuracy can only be achieved if photon attenuation (or/and scatter) is taken into account and corrected in the tomographic reconstruction.

2.3.3 Collimation

A collimator is a honeycomb-like arrangement of lead. It consists of holes (square, round or hexagonal) separated by septa (lead separators between the holes are called septa), and is used to pass photons arriving from the patient in a direction normal to the crystal. Because the septa have a finite width, some photons travelling perpendicular to the detector will by absorbed by the septa. The septa dividing the individual holes of the collimator have to stop the non-perpendicular rays reaching the detector [18] (Figure 2-6(a)). The use of a collimator results in a tremendous decrease in detection sensitivity compared to the case where no collimators (intrinsic measurements) are present. Due to the limited acceptance angle of the collimation holes, the camera resolution decreases with increasing distance between the patient and collimator. Reducing the distance between the patient and collimator or using a different design of collimator can result in improved resolution.

The design parameters of a collimator are a compromise between resolution and sensitivity, which are inversely related. Sensitivity[6] refers to the fraction of emitted photons, which actually pass through the collimator holes and are registered by the detector. The ratio of the inter-septa distance and the septa length determines the acceptance angle of the collimator. Long septa or small diameter holes result in a small solid angle, so few photons are accepted (low sensitivity) but they will all originate close to the ideal projection line (good spatial resolution). The thickness of the lead septa is determined by the energy of the gamma rays that are to be detected [19]. When using more lead in the collimator this causes a reduction in the septal penetration, hereby improving resolution but at the expense of sensitivity. Increasing the hole size will improve the sensitivity but the resolution deteriorates.

The collimator types can be classified into parallel-hole and focusing collimators. A parallel-hole collimator has holes that are parallel to one another and perpendicular to the plane of the camera crystal. It is the simplest and most widely used collimator design and permits the use of a relatively simple and fast image reconstruction technique.

In most cases, a parallel-hole collimator is used for emission SPECT (and transmission studies-Chapter 3), however there are other collimators that are sometimes used for

[6] Sensitivity is a combination of the efficiency and the geometry of the detector.

both emission and transmission acquisition (to acquire a transmission scan which may used for attenuation correction purposes including; parallel-hole, fan-beam, and cone-beam collimators)[20], [21], [22] (Figure 2-6(b)).

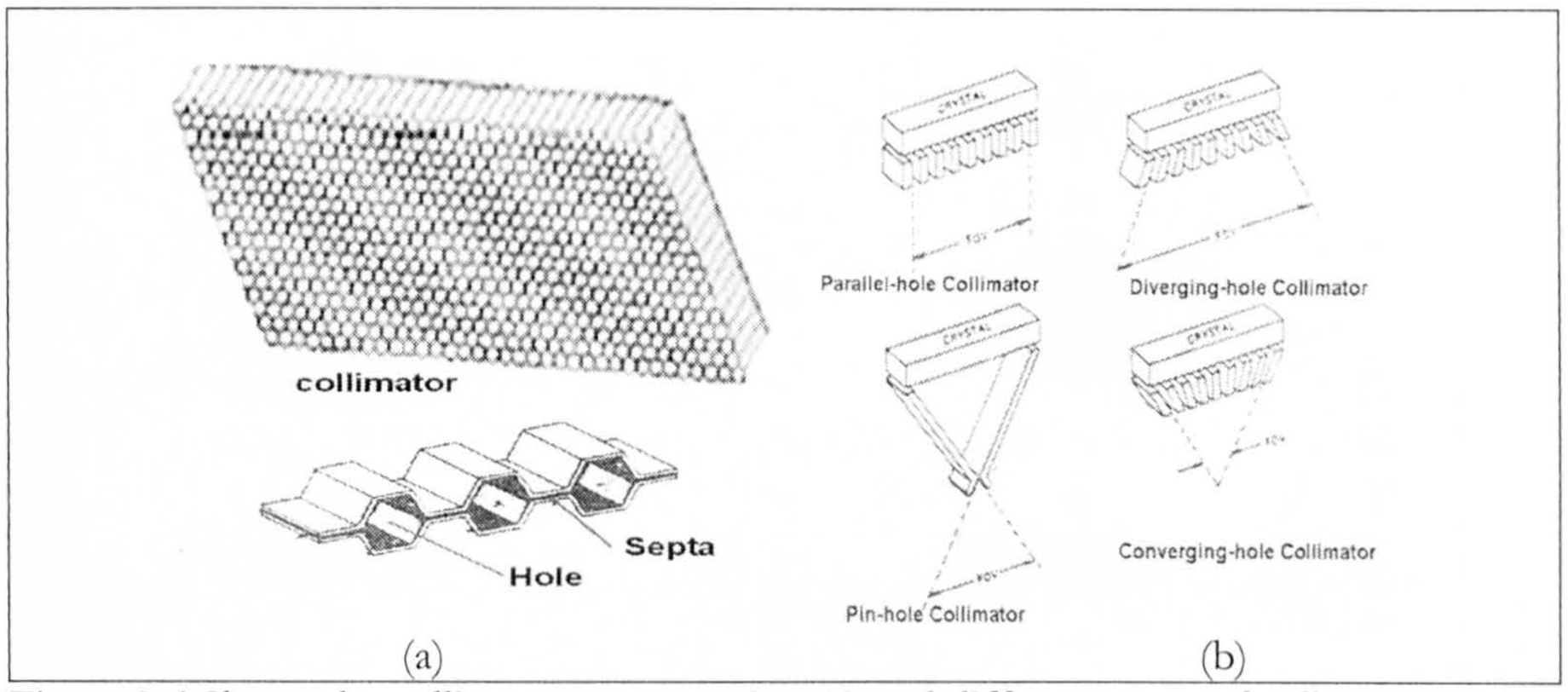

Figure 2-6 Shows the collimator cross-section (a) and different types of collimators (b) [23].

2.3.4 SPECT configurations

Modern SPECT gamma cameras are available in a number of configurations. In the past they were limited to single (head) detector gamma cameras; nowadays multi-headed (double and triple detector) gamma cameras (Figure 2-7) are available. The benefits of a single-head camera SPECT system (Figure 2-7(a)) are that it is relatively inexpensive compared with multi-head SPECT systems, and it is less claustrophobic for the patient. The disadvantages of single-head SPECT systems include relatively low sensitivity compared with multi-head systems and thus, a generally longer data acquisition time. This long acquisition time can cause significant patient discomfort and may provide inferior scans, due to increased patient movement. Using a camera with multiple detectors and a continuous method of rotation can either reduce the acquisition time or increase the number of counts acquired. This results in increased sensitivity and a potential increase in patient throughput [24]. The disadvantages of multi-head systems are that they are more expensive than single-head cameras, and the quality control (QC) procedures must ensure that adding the data from different heads can be performed without artefact. These systems also require more elaborate or automated devices to aid in changing the multiple collimators per system [25].

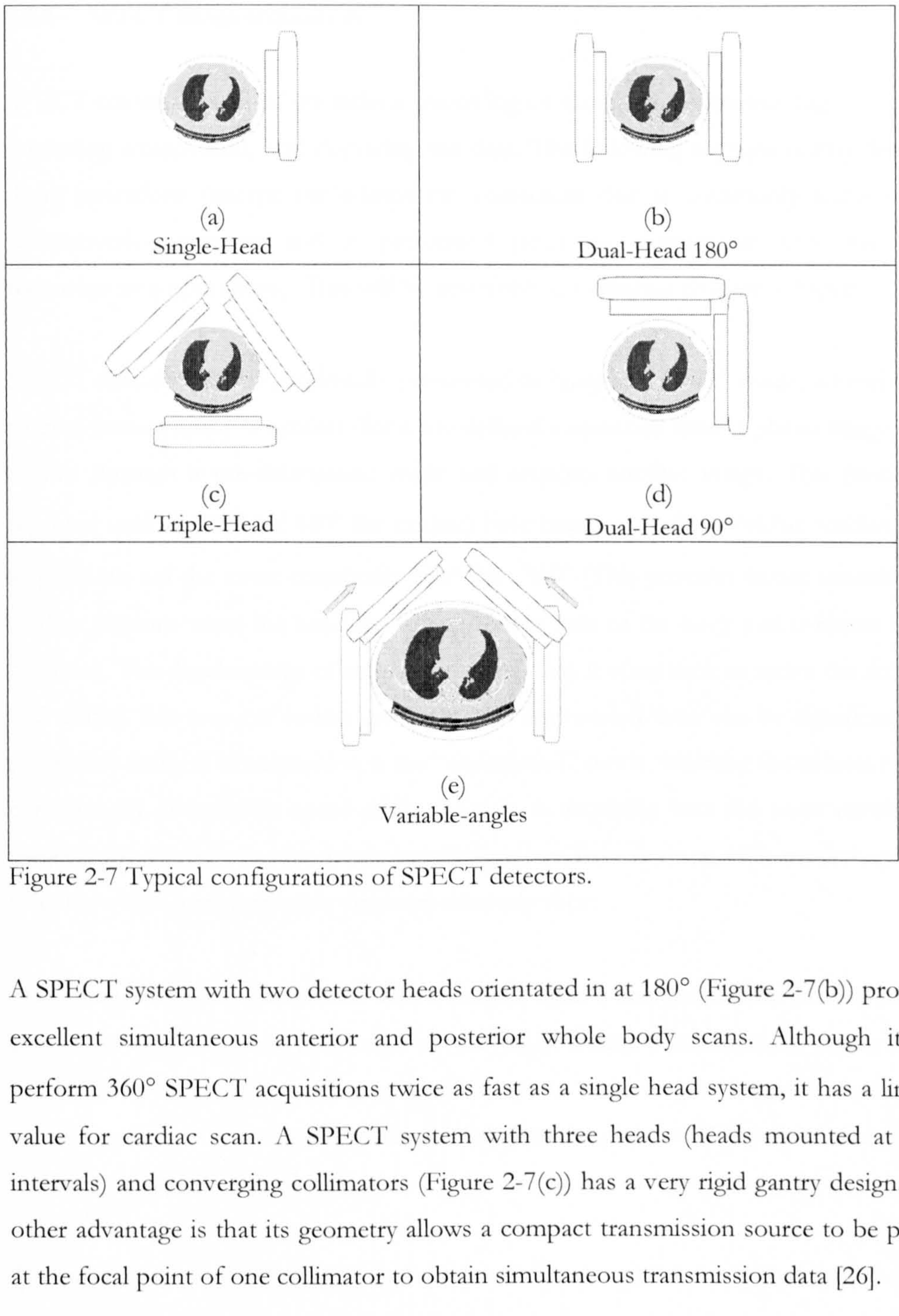

Figure 2-7 Typical configurations of SPECT detectors.

A SPECT system with two detector heads orientated in at 180° (Figure 2-7(b)) provides excellent simultaneous anterior and posterior whole body scans. Although it can perform 360° SPECT acquisitions twice as fast as a single head system, it has a limited value for cardiac scan. A SPECT system with three heads (heads mounted at 120° intervals) and converging collimators (Figure 2-7(c)) has a very rigid gantry design. The other advantage is that its geometry allows a compact transmission source to be placed at the focal point of one collimator to obtain simultaneous transmission data [26].

The most popular cameras are those that offer a selectable variable angle between two detectors (Figure 2-7(e)). These detectors are positioned at 90° from each other for the 180° orbits used in cardiac imaging, and 180° from each other for the 360° orbits used in most other applications [27]. The two-heads 90° system (Figure 2-7(d)) also offers the opportunity for simultaneous transmission and emission data acquisition.

2.3.5 SPECT image acquisition

SPECT covers a chain of operations consisting of acquiring, reconstructing, correcting (including attenuation), and displaying the data. The following sections briefly describe these operations (except for attenuation correction that is commonly included the reconstruction process and is performed prior to, during, or after the main reconstruction operations). This will be described in a separate chapter (Chapter 3).

SPECT data acquisition is normally performed in "step and shoot" mode, whereby; the gamma camera stops to acquire (for a pre-defined acquisition time) a planar image, then rotates through a pre-determined angle and acquires another image. This process is repeated until all 360° (or 180° for cardiac) have been covered. In cardiac studies, 180° acquisitions are the more commonly used than 360° (This provides better sensitivity to cardiac photons since the heart lies nearer to one side of the body and is closer to the detector). The disadvantage of step and shoot is that it takes time to move the detector and during this time no counts are recorded. The wasted time can be significant. An alternative method of acquisition is the "continuous" mode, whereby the camera rotates continuously at constant speed while the data is acquiring into the same number of projections. The continuous mode acquisitions are less common with modern gamma cameras where gantry rotation times are relatively short.

Many acquisitions are performed with a circular orbit where the camera head is rotated at a fixed distance from the centre of the body. Because resolution is better if the camera is as close to the heart as possible, some cameras are designed to rotate in elliptical orbits, which allow the camera head to be positioned closer to the patient resulting in improved resolution.

The selection of matrix size in the computer for the projection view is an essential aspect of SPECT imaging so that the resolution of the imaging system is not lost. The computer divides up the gamma camera field of view (FOV) into a matrix of pixels (typical matrix size for SPECT are 64×64 and 128×128). The choice of matrix size depends on the resolution of the system. It is recommended that 2 to 3 mm per pixel be used [28]. A "rule of thumb" in nuclear medicine physics is that one needs at least 3

pixels for every FWHM [7] (1/3 of FWHM [8]) of resolution in the image [28] [29]. For example, if the data are reconstructed to 15 mm FWHM, then one needs roughly 15 mm/3 = 5 mm/pixel. For a gamma camera with 540 mm FOV, the pixel size for a 128×128 matrix with no zoom would be 4.21 mm (540/128), whereas, a 64×64 matrix would have an 8.43 mm pixel size. Therefore, the 64×64 matrix is a typical limit for this combination of FWHM and FOV (no zoom). A slight improvement in resolution can be achieved by increasing the matrix size from 64×64 to 128×128, but this also leads to increased image processing time and disc storage space. Processing and displaying a 128×128 image will consume 4 times as much as disc space as a 64 ×64 image, with correspondingly increased processing times. However, 128×128 is normally used.

The optimal number of projections depends on matching the number of projections to the matrix size (which depends on the resolution of the system). The number of angular views (projections) over 360° should be at least equal to the projection image matrix size (e.g., 64 views for a 64×64 matrix and 128 views for 128×128 matrix). When the number of views is less than this, streak artefacts may appear in the reconstructed slices [29]. The elimination of streak artefacts and improved image quality can be obtained using an increased number of projections (this is also shown in Figure 2-9).

2.3.6 Interpretation of SPECT image

The amount of radiopharmaceutical taken up by the myocardium is proportional to the blood flow. If there is an area of reduced radiopharmaceutical uptake (defect) within the myocardium in comparison to normal surrounding tissue there is said to be perfusion abnormality (ischemia or infarcted myocardium). To distinguish between myocardial ischemia and infarction, two studies (rest and stress studies) are performed; one under normal rest conditions (rest images) and one at stress (with radiopharmaceutical injection during maximal stress; stress images). The stressing of the patient accomplished either by exercise (commonly using a treadmill) or by administration of pharmacological stressing agents. For reporting and interpretation the two studies are

[7] The width of the photopeak at half its height is used to measure energy resolution or of a line spread function to measure spatial resolution.
[8] Sampling theory states that to resolve frequencies (objects) up to a maximum frequency (smallest object), the pixel size of the sampling matrix should be consistent with the Nyquist frequency-sampling rule.

displayed as paired stress-rest images in each of the cardiac planes (Clinicians compare the two images qualitatively to detect abnormalities in distribution of blood flow within the myocardium).

Patient with ischemia will have a normal "resting" myocardial perfusion study because the coronary arteries are able to supply sufficient blood when the heart at rest. If a defect is found at stress imaging but not on rest (mismatch) it is most likely to be caused by myocardial ischemia. If there is a matching defect on both the stress and rest images it is most likely to be a myocardial infarct, an area of permanent damage. If there is no defect on stress or rest images the myocardial perfusion study is said to be normal. Myocardial perfusion defects should be characterized by their location as they relate to myocardial walls. Defect extent and severity should be evaluated by qualitative or quantitative methods (section 2.5).

2.4. Reconstruction algorithms

Tomographic reconstruction is a systematic mathematical procedure (algorithm) to put the projections of a patient together to obtain a cross-section of the patient. The image could represent the distribution of attenuation coefficients from different tissue as obtained from TCT, or radioactivity distribution resulting from the radiopharmaceutical uptake inside the patient as obtained from ECT. There are two classes of image reconstruction algorithms used in SPECT, analytical and iterative algorithms. The most commonly used analytical reconstruction algorithm is filtered back projection (FBP). The most common iterative algorithm is maximum-likelihood expectation-maximization (MLEM).

2.4.1 Filtered-backprojection algorithm

The Filtered-Back Projection (FBP) is a technique used to reconstruct a slice from a set of its projections [30]. It is based on the projection of the acquired images into images perpendicular to the axis of rotation. In SPECT the projection data measures the emission photons, which are acquired by rotating the detector (single or multiple) around the patient. From a mathematical point of view the parallel-beam tomographic reconstruction, the projection $P(t,\theta)$ approximates a line integral through the

radiopharmaceutical activity distribution *f(x,y)* at a particular angle θ and a particular distance *t* from the origin within the projection. This is known as the "Radon transform". This is schematically illustrated in Figure 2-8(a). The Radon transform states that the projection data $P(t,\theta)$ is formed by combining a set of line integrals of an unknown 2D source distribution *f(x,y)*. The projection data $P(t,\theta)$ for an angle θ is

$$P(t,\theta) = \int_{-\infty}^{\infty}\int f(x,y)\delta(x\cos\theta + y\sin\theta - t)dxdy \qquad \text{Eqn 2-1}$$

Where the δ function selects points along a line (defined by *t* and θ) passing through the object *f(x,y)*. Back-projection (*B*) can be expressed mathematically as described by Larson [31].

$$B(x,y) = \int_{-\infty}^{\infty}\int P(t,\theta)\delta(x\cos\theta + y\sin\theta - t)d\theta dt \qquad \text{Eqn 2-2}$$

Direct back-projection of all projections will create a blurred representation of the object. If only a finite number of projections are used the image will contain streak artefacts (Figure 2-9). The projections need to be filtered before backprojection.

The "Fourier slice theorem" provides a means for obtaining 2-D Fourier Transform (FT) data for an object from a series of one-dimensional FT of this object. Based on this theorem (Figure 2-8), filtered back-projection can therefore be summarised as a four-step process:

1. One-dimensional Fourier transform (1DFT) is computed of each projection.
2. Multiplying the results of step 1 by frequency filter.
3. Compute the inverse FT (F^{-1}) of each filtered FT obtained from step 2.
4. Perform back projections of the results obtained from step 3 and then summing up all filtered projections to form the image.

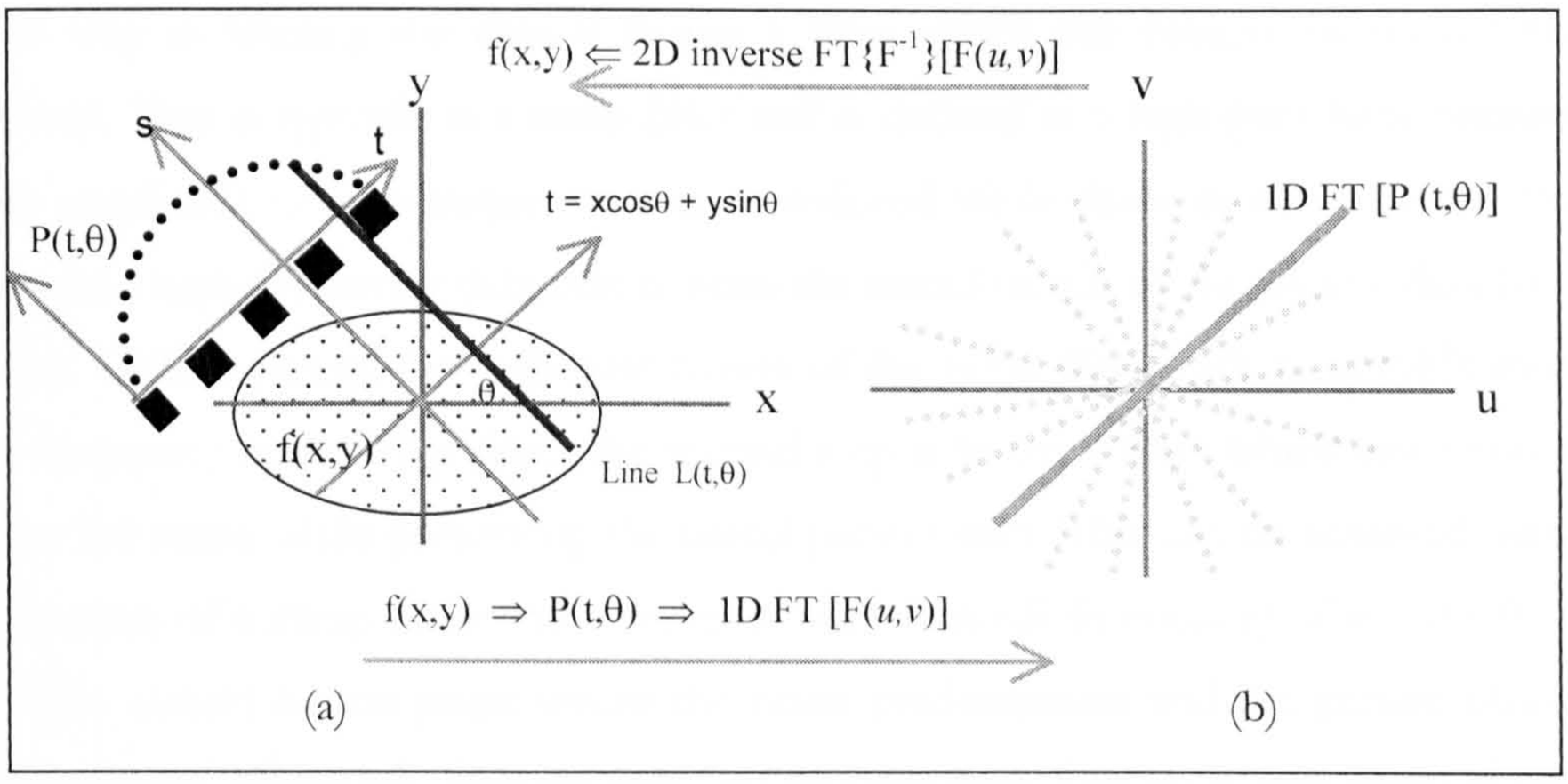

Figure 2-8 the relation of the Radon space (a) and the Fourier space (b) according to the Fourier slice theorem.

The name of FBP comes from combining the back projection and the ramp filtering. Back-projection means that all projection data are smeared back across the object space. The problem associated with this is that all projections will interact constructively in the original images, causing image blurring (star-effect blur pattern) and streak artefacts (Figure 2-9), which appear in both nuclear medicine and CT modalities. This blur pattern inherent in backprojection results in a background that reduces image contrast. To reduce these effects, and to reduce the statistical noise in the image, the mathematical technique of filtering is applied to the count profile in the projection data before backprojection is performed.

The projection data can be represented as a frequency spectrum in which the amplitude of each frequency in the data is plotted. In SPECT, this frequency spectrum has three distinct components. Background, including the data from the star effect, typically has a very low frequency and therefore dominates the low frequencies of the spectrum. Statistical fluctuations in the data (noise) generally have a high frequency and therefore dominate the high frequencies of the spectrum. True patient data lie somewhere in the middle but overlap the background and noise components of the spectrum. The main goal of filtering is to eliminate as much as background and noise from the data while preserving as many of the useful patient data as possible [32].

The first step in filtering the data is to use a filter which can remove or reduce the background. This is typically is a ramp filter and is defined as a high-pass filter because only the amplitude of low-frequency data is reduced while there is no effect on the midrange and high-frequency data that contain the useful details of the patient data (and the noise). Unfortunately, the high-pass nature of the ramp filter leads to amplification of high-frequency noise. Therefore, the second step is to use a filter which can remove or reduce the noise while preserving the useful patient data. This can be achieved using a combination of a ramp filter and a window filter (cut-off frequency). The cut off of the window should be the point where the noise predominates and the patient object data are minimal. There are different types of window filter functions with variable cut-off frequencies used in SPECT. The most common popular window filter used in SPECT imaging is the Butterworth filter [29]. In this thesis, only the Butterworth filter will be considered.

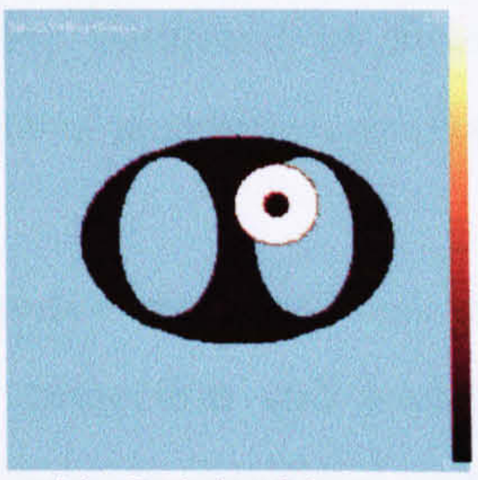

(a) Original image

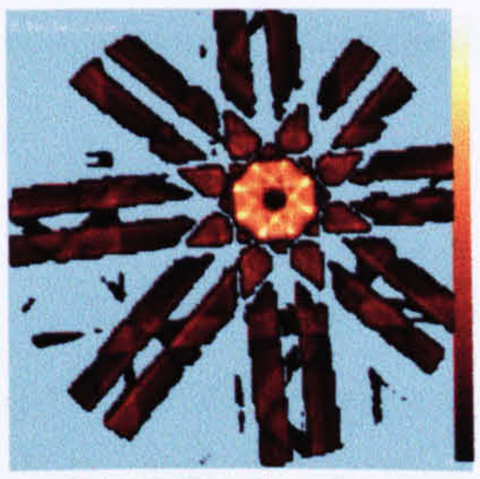

(b) 8 Projections

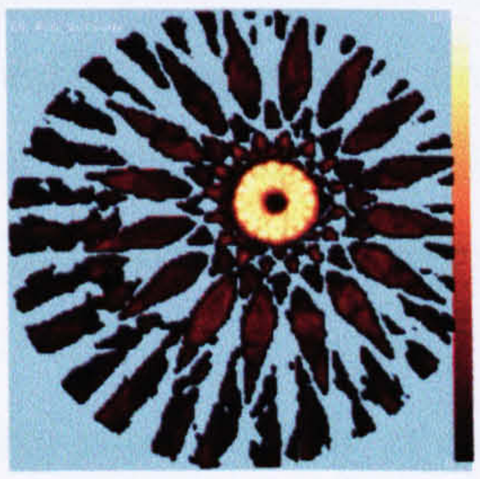

(c) 16 Projections

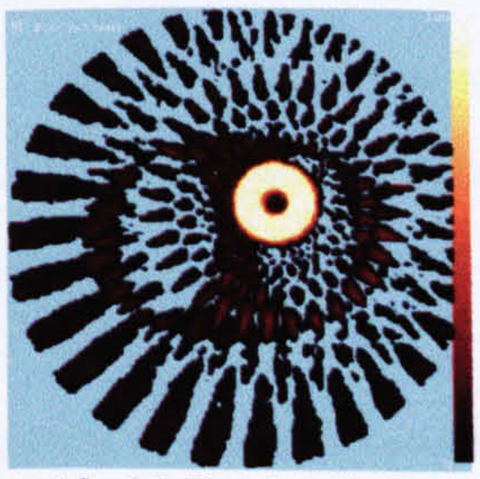

(d) 32 Projections

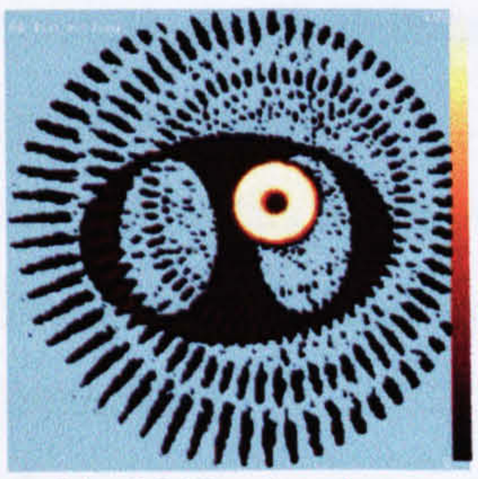

(e) 64 Projections

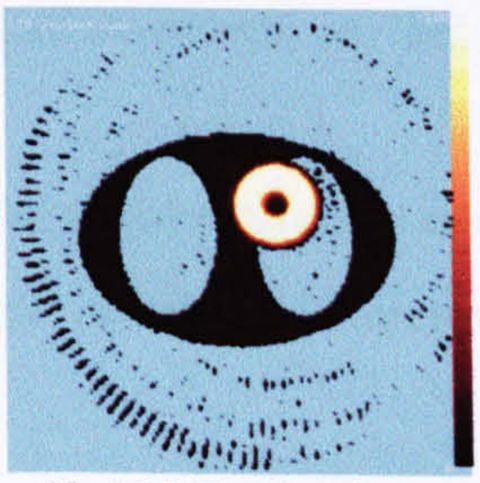

(f) 128 Projections

Figure 2-9 (a) computer-simulation phantom reconstructed by FBP using different number of projections; 8, 16, 32, 64, and 128.

FBP is not the only reconstruction method used in nuclear medicine, although it is by far the most common algorithm used in clinical SPECT studies due to its low computational costs. However, the disadvantage of using the FBP algorithm in SPECT is that it cannot incorporate any corrections for spatially varying physical factors, such as photon attenuation, collimator geometric response, and scatter [33]. In the following section the iterative algorithm, which can incorporate these effects, will be discussed

2.4.2 Iterative algorithm

Another approach to image reconstruction is to use an iterative algorithm, where all physical effects can be modelled and image reconstruction based on finding the relationship between the projection data and the object function. The most frequently used iterative algorithm is the Maximum Likelihood Expectation Maximization (MLEM). The MLEM is an iterative reconstruction which aims to maximize the probability (likelihood) of detected counts and to produce an image that has the greatest likelihood of matching a given measured image data set.

The iterative reconstruction algorithm is implemented by iterations requiring both forward projection and back-projection. In brief, the values of all pixels is initially guessed using a simulated uniform image; then those initial values are slightly altered several times (iterations) until they converge to a final result consistent with the available count profiles. Figure 2-10, shows the flow chart of a typical iterative reconstruction algorithm method that uses the maximum-likelihood (ML) expectation-maximization (EM). The following steps show how this algorithm works;

- An initial estimate of the reconstructed image is created. It can be a uniform disk enclosed in the field of view or an image obtained by FBP [34]. It is often a nonzero image that has the same total projection counts as the measured projection data.
- Projection data that would have resulted from this initial estimate is calculated.
- The ratio (or difference) of the measured and calculated projection data is determined.
- The ratio data are then back-projected to obtain a correction image

- The initial image estimate is then multiplied by (or added to) the correction image estimate to form a new image estimate.
- The new image estimate is then tested using a specific criterion.
- If the criterion is not met, the new image estimate is used to generate the calculated projection data and the iterative steps repeat.
- If the criterion is met, the new image estimate is considered the final image estimate and the iteration stops

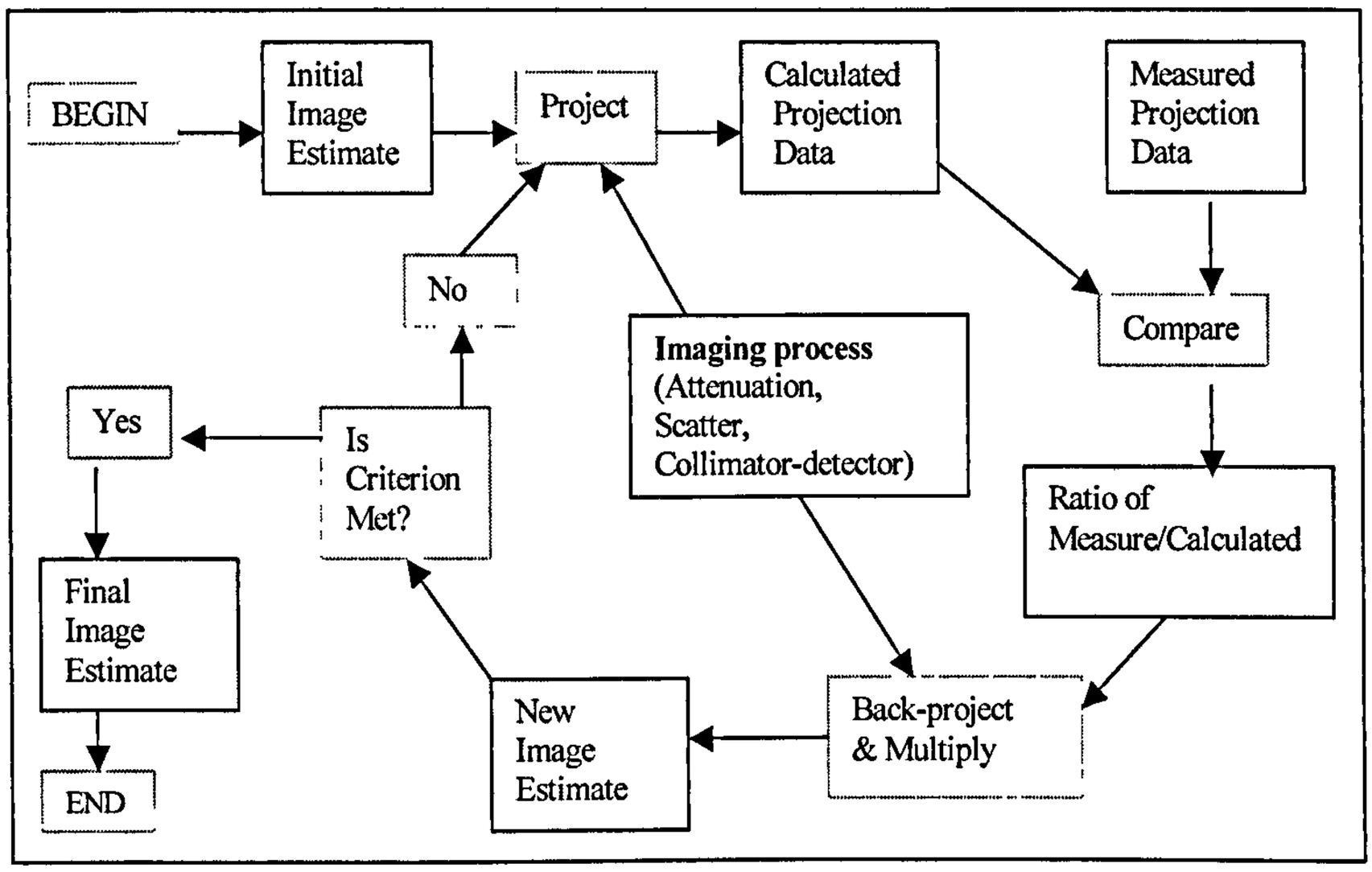

Figure 2-10 Flow chart of the MLEM iterative reconstruction algorithm [35].

The criterion is a comparison between a pre-selected small value and the difference between the previous and new image estimate. If the model of the imaging process accurately includes the image-degrading factors, such as attenuation, collimator-detector response, and scatter response, the iterative process will converge to an image compensated for the degrading factors [35].

Mathematically the MLEM algorithm is a set of successive forward projections/back-projection procedures [34]. The iteration process starts with a simulated uniform image with positive values (current estimate). The ratio between the simulated and computed projections is used to modify the current estimate to produce an updated estimate, which becomes iteration $k+1$. This process is then repeated many times. The MLEM

algorithm is applied pixel by pixel as

$$f_j^{(k+1)} = \frac{f_j^{(k)}}{\sum_{i=1}^{n} a_{ij}} \sum_{i=1}^{n} \left(\frac{g_i}{\sum_{j=1}^{m} a_{ij} f_j^{(k)}} \right) a_{ij} \qquad \text{Eqn 2-3}$$

Where $f^{(k)}$ denotes the image estimate after k iterations and g represents the measured data. The factor a_{ij} is the contribution of object element i to projection pixel j. The expression $\sum_{j=1}^{m} a_{ij} f_j^{(k)}$ can be interpreted as the forward projection of the kth iteration object estimate resulting in a set of projection images. The expression $\sum_{i=1}^{n} a_{ij}$ is a normalizing factor. The update $\left(\frac{g_i}{\sum_{j=1}^{m} a_{ij} f_j^{(k)}}\right)$ is the ratio of the measured number of counts to the counts estimate of the mean number of counts in bin i. The $\left(\sum_{i=1}^{n} \left(\frac{g_i}{\sum_{j=1}^{m} a_{ij} f_j^{(k)}} \right) a_{ij}\right)$ is the back-projection of this ratio for pixel j. This equation 2.3 can be extended to the whole image and interpreted as:

$$Image^{(k+1)} = Image^{(k)} \times Normalized\ back\text{-}projection\ of\ [measured\ proj / proj\ of\ image^{(k)}] \qquad \text{Eqn 2-4}$$

One advantage of iterative reconstruction is that the final image has a different noise appearance, with reduced noise in areas with low counts (background regions) and virtually no streak artefacts. More importantly complex corrections (i.e. for attenuation) can also be directly incorporated.

On the other hand, the disadvantage with iterative reconstruction is that it takes several, possibly many, iterations to reach an acceptable solution. A single iteration takes at least as much time (computational power) as a single filtered back projection; therefore, it is much slower than filtered back projection. With fast computers and efficient reconstruction programs this is no longer a major obstacle. As the number of iterations increases, the image gets sharper but also noisier. The effect is a little like increasing the cut-off frequency for a smoothing filter. Clinically, the iterative procedure can be stopped at a relatively small number of iterations at a point that the image looks reasonably sharp, and with the noise remaining controlled. Alternatively a larger number

of iterations can be performed, and then a post-reconstruction smoothing filter can be applied smoothing with an appropriate cut-off. This thesis considers this issue.

Recently, an accelerated version of the iterative algorithm has been introduced with a reduction of computation time to clinically acceptable periods of time. This commercially available version is called "Ordered-Subset Expectation Maximization (OSEM)" [36]. This is the algorithm that will be used in this thesis and will be discussed in next section.

2.4.3 OSEM algorithm

The OSEM algorithm was proposed as an alternative to the MLEM algorithm, aiming at speeding up the low convergence rate of the latter. It belongs to the class of ordered-subset, or block-iterative methods, that are based on the idea of partitioning the data into disjoint, equally sized subsets or blocks and using a single block at each iteration step, instead of the whole data volume. In turn, each subset is used in the iterative step to update the reconstructed image estimate. The resulting reconstruction becomes the starting value for use with the next subset. A single iteration of OSEM is a single pass through all the specified subsets. Passing through the same ordered subsets and using as a starting point the reconstruction provided by the previous iteration, one may perform further iterations. Hudson [36] claims that OSEM can accelerate convergence by a factor proportional to the number of subsets, achieving an image quality that is similar to standard MLEM.

Mathematically, let y_i be the number of photon emissions recorded in the i^{th} projection bin and let Y_θ be the set of parallel projections $\{yi,yi+1,\ldots\}$ that view the object at angle θ, orthogonal to the tomography axis. The projection data are grouped into n subsets, denoted $S_1,S_2,\ldots S_n$. If there are P projections bins in total, the element of each subset, in no particular order, are:

$$S_1 = \{y_1, y_2, \ldots\ldots, y_{P/n}\} S_2 = \{y_{P/n+1}, y_{P/n+2}, \ldots\ldots, y_{2P/n}\} \ldots\ldots, S_n = \{y_{(n-1)P/n+1}, y_{(n-1)P/n+2}, \ldots\ldots, y_P\} \quad \text{Eqn 2-5}$$

The subsets normally consist of projection views separated by some fixed angle about

the object. For example, each subset might consist of two sets of parallel projection views, spaced 90 degree apart:

$$S_1 = \{y_0, y_{\pi/2}\}, S_2 = \{y_{\pi/4}, y_{3\pi/4}\} \text{....And so on} \qquad \text{Eqn 2-6}$$

The MLEM is then applied to each subset in turn until the n subsets have been processed. The processing of all subsets represents a single iteration. MLEM is a special case of OSEM with a number of subsets set to n=1. As an example, using two subsets would accelerate convergence by nearly a factor of 2 compared with standard MLEM and thus considerably shorten the computing time needed for reconstruction.

The fast OSEM algorithm in combination with the new generation of fast computers has significantly reduced the processing time while maintaining good image quality for quantitative SPECT image reconstruction [35]. Iterative reconstruction methods have been gaining increased acceptance in their ability to compensate for the non-uniform attenuation of the patient's chest region in myocardial perfusion SPECT [37, 38].

2.5. Quantification of SPECT images

Before interpretation, the projection data is reviewed in a cine mode to detect any artefacts and their cause. The artefact sources may include patient motion, upward creep, breast shadow due to attenuation, and diaphragmatic attenuation. The data will be reconstructed into transaxial images, which represent planes perpendicular to the long axis of the patient, and therefore, are not perpendicular to the long axis of the left ventricle. The transaxial slices are then oriented to produce three sets of images [short axis (SA), vertical long axis (VLA), and horizontal long axis (HLA)] (Figure 2-11(a)). Stress and rest images are aligned serially adjacent to each other and viewed for qualitative interpretation (Figure 2-11(b)). Short-axis images, which are perpendicular to the long axis of the left ventricle, can be used to present 3D information in 2D polar maps (a standard tool for quantification of the myocardial SPECT study). This polar map image is called a bull's-eye display (Figure 2-11(c)).

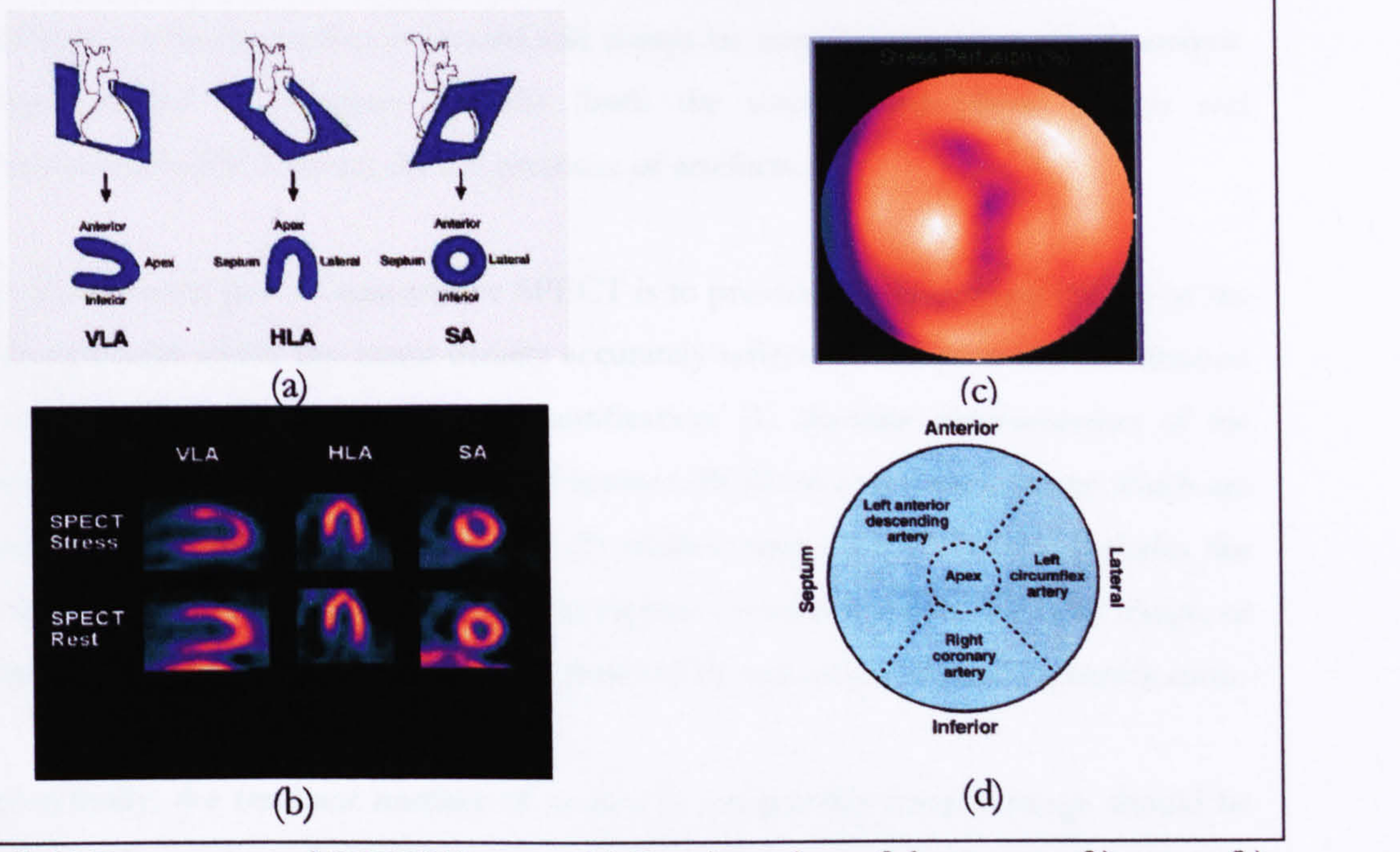

Figure 2-11 Reconstructed SPECT images: (a) Reorientation of three sets of images. (b) Stress-rest sequential images. (c) bull's-eye image. (d) Coronary artery territories.

The bull's-eye image consists of extracting maximal count circumferential profiles on each of the short-axis slices. The bull's-eye plot consists of a series of concentric circles made from apex to base (the apex is at the centre and the base at the periphery). Two bull's-eye images are constructed for the stress and rest studies. The pixel with the highest number of counts in the stress and rest images is given a constant value (e.g. 100) to normalize the images (in order to make images comparable to a database of normal patients' bull's-eye images). By using standard deviation, the difference between the normal database and the patient bull's-eye image (or the difference between stress and rest bull's-eye images) can be displayed and identified as a myocardial defect. The bull's-eye image is divided into segments corresponding to the myocardial areas supplied by the coronary arteries (Figure 2-11(d)).

The assessment of myocardial SPECT images can be done by either qualitative or quantitative analyses. Quantitative analysis is widely used to objectify and standardize the process of interpreting and analysing images. Whereas visual interpretation is subjective and more prone to observer variability, quantitative analysis offers an objective approach, providing a more accurate means to assess the extent, severity, and reversibility of perfusion defects or to estimate their functional significance. Moreover, quantitative techniques are well suited to analysing a study objectively over a period of

time or after medical or surgical intervention. Although quantification provides great confidence in interpretation, it should still always be complementary to visual analysis. Images should be inspected visually (both the unprocessed planar images and reconstructed SPECT slices) for the presence of artefacts.

The fundamental goal of quantitative SPECT is to provide cross-sectional images of the heart uptake in which the count density accurately reflects the amount and distribution of activity. There are two types of quantification; (1) absolute representation of the number of counts detected in a region of interest (ROI) on a transverse image which are translatable to actual heart activity and (2) relative representation which includes the comparison of counts within two different regions of interest within the same image, or from two or more different images. This thesis will focus only on relative quantification.

Theoretically, the resultant number of counts in a transverse section image should be related to the total number of detected counts acquired in the set of projection images; however, image processing modifies the detected counts (by scaling process) in order to save image memory (or speed up image processing) and improve the image display for review by the physician. This scaling process and other image processing parameters such as attenuation correction should be considered for accurate quantification.

2.6. Attenuation artefacts

Attenuation is believed to be one of the most important of the physical causes of image degradation. Some of the photons emitted by the injected radiopharmaceutical are lost (attenuated) due to interaction with the surrounding tissue as they pass through the body. At diagnostic energies photons interact with tissue by two different mechanisms; Compton and photoelectric interactions. In the Compton Effect, photons are deflected from their linear path, giving up some of their energy, and continuing in a new direction with lower energy. The other type of interaction causes total elimination of the photons (Figure 2-12). Attenuation means there is a loss of useful photons, emitted from a source within the body, so that the numbers that interact with the detector are reduced compared with the total emitted. The fraction of photons that are attenuated from a narrow beam after passing through 5 cm of water-equivalent tissue is about 50% for 140 keV (^{99m}Tc). This results in a large decrease in intensity toward the centre of the reconstructed image.

Mathematically, photon attenuation for homogenous medium (constant linear attenuation coefficient) can be expressed by the exponential equation 2-7):

$$I = I_0 e^{-\mu L} \qquad \text{Eqn 2-7}$$

For the non-uniform attenuation coefficient the previous equation will be:

$$I(x, z) = I_0 \; e^{-\int \mu(x, y, z)dy} \qquad \text{Eqn 2-8}$$

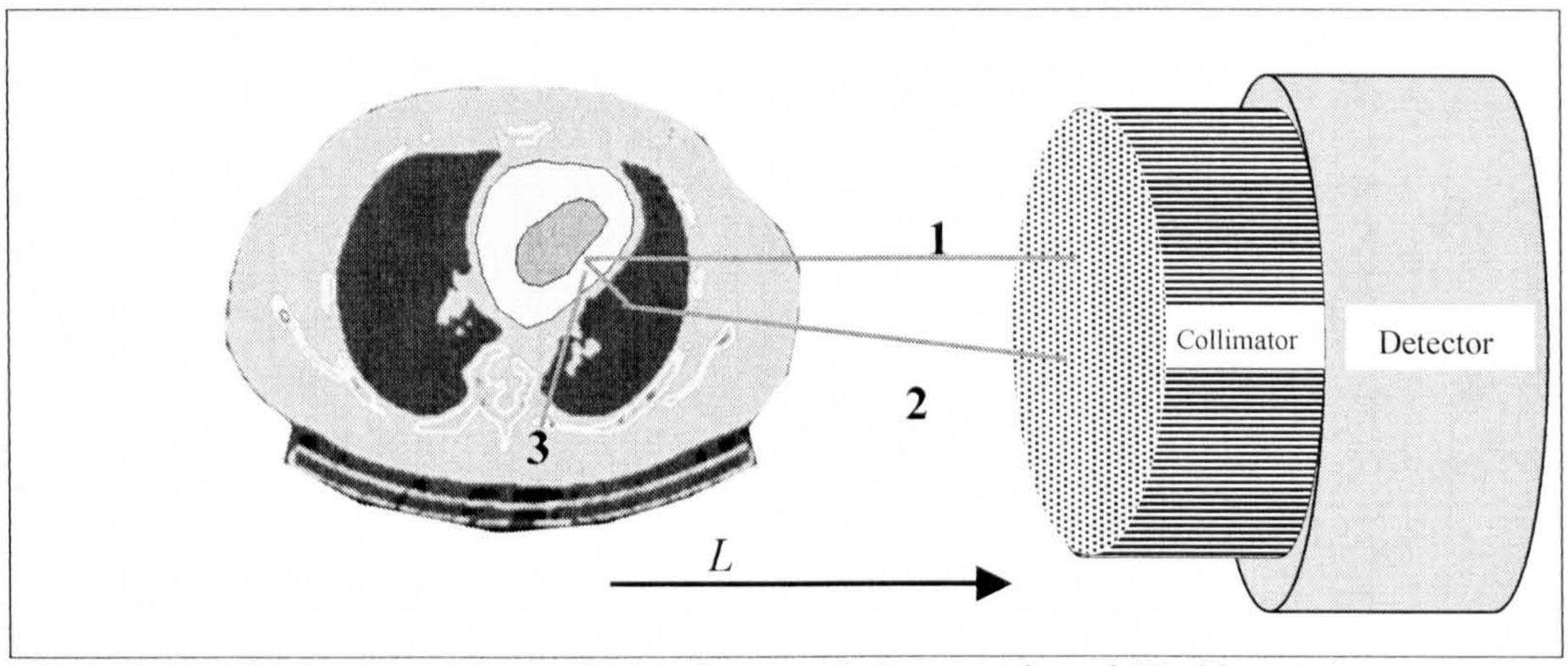

Figure 2-12 Photons interactions; (1) Primary, (2) Scattered, and (3) Absorption.

Where I is the detected photons that have traversed the tissue without interactions, I_0 is the initial number of photons, μ is the linear attenuation coefficient of the tissue, and L is the thickness. The parameter μ represents the probability that the photon will undergo an interaction while passing through a unit thickness of tissue. The linear attenuation coefficient is a complicated function of photon energy and attenuating material. It combines the photoelectric and Compton components.

The degree of attenuation is influenced by (1) the distance between the radiation source and the body surface, (2) the average attenuation coefficient of the tissue along the path of gamma rays and (3) the energy of the emission. In addition, the attenuation coefficient depends upon the experimental geometry used to make the measurement; either narrow-beam or broad-beam geometry. Using narrow-beam geometry (in which no scatter is detected), in which the beam is highly collimated, the attenuation coefficient for 140-keV photons in water is 0.15 cm^{-1}. If the measurement is instead made with a broad beam (scattered photons are detected), photons from regions other than that of the beam may be scattered into the detector, thereby increasing the detected

intensity and the attenuation coefficient obtained (0.12 cm^{-1}) is smaller [17]. The probability of absorption decreases as photon energy increases. This is the reason why attenuation artefacts are reported to be less severe (but still significant) with ^{99m}Tc agent rather than with ^{201}Tl [39]. Narrow beam attenuation coefficients for selected materials in the body at two main energies used in nuclear medicine (140 keV for ^{99m}Tc, and 73 keV for ^{201}Tl) are given in Table 2.1.

Table 2.1 Narrow beam Attenuation coefficient (μ) values for selected material [40].

	μ Values (cm^{-1})	
Type of tissue	^{201}Tl	^{99m}Tc
Tissue (muscle)	0.191	0.153
Lung	0.063	0.051
Bone	0.429	0.286

The attenuation effect causes the pixel counts values in the reconstructed image to not proportional is to the true tracer distribution. This means that deep structures will appear to have lower counts than more superficial structures. This leads to a typical reconstruction artefacts (depression of activity concentration in the centre and a "bowl-shaped" profiles) of a SPECT reconstruction of a uniform source (Figure 2-13), and degrades the ability to obtain accurate quantitative information from a SPECT image.

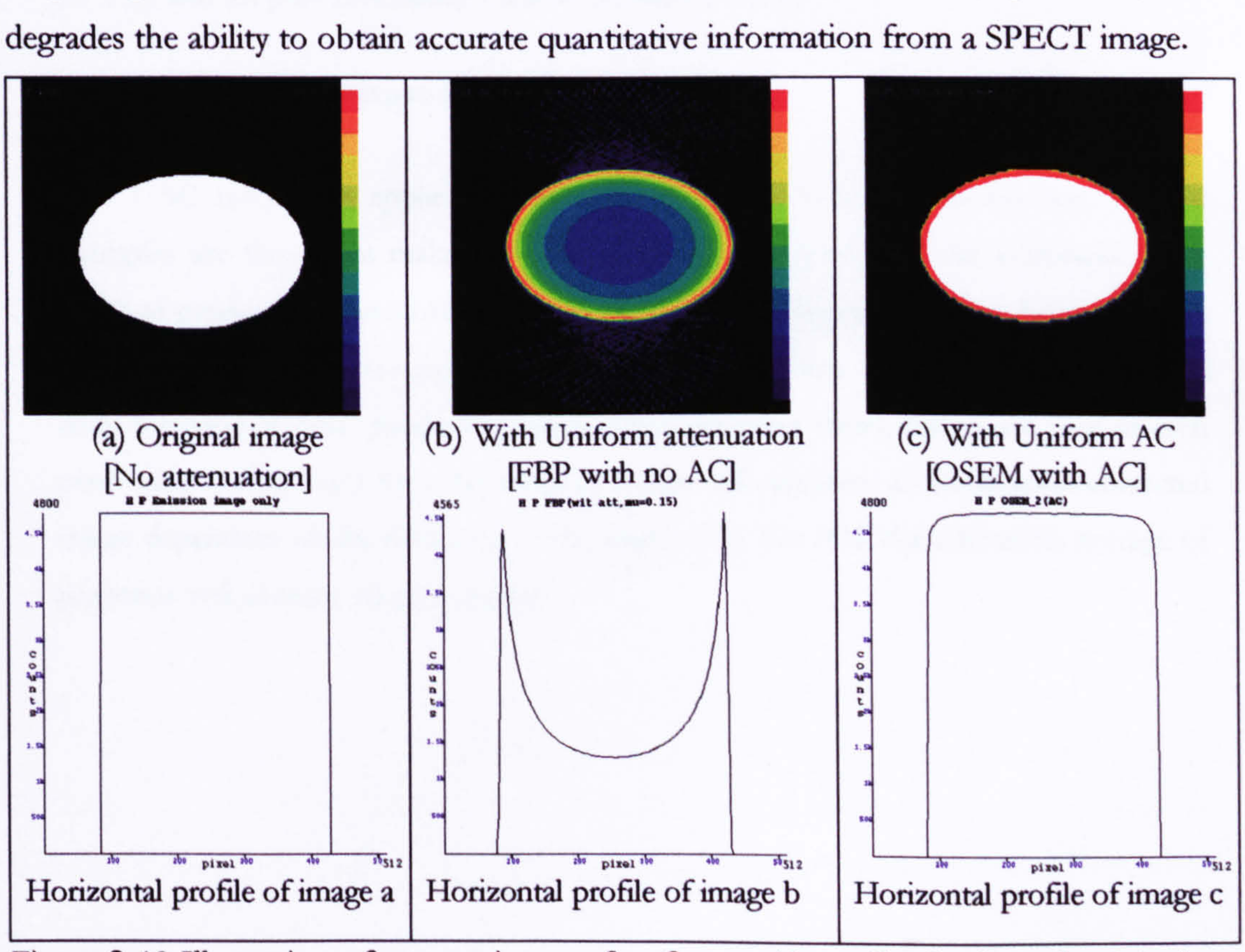

Figure 2-13 Illustration of attenuation artefact for a uniform distribution of activity in a 2D simplified elliptical model.

2.7. Attenuation correction methods

Attenuation Correction (AC) methods can be grouped in two general categories. The first category assumes that the attenuation coefficient is uniform (UAC = Uniform Attenuation Correction) throughout the body and therefore μ is constant. In a uniform medium (e.g. abdomen and brain), the activity located deeper in the body is attenuated more than activity near the surface, which would result in a trans-axial slice with decreasing counts near its centre. The second category of AC methods assumes that the attenuation coefficient is non-uniform (NUAC = Non-uniform Attenuation Correction) and applicable in the thorax where there is a specific μ distribution.

2.7.1 Uniform attenuation correction methods

There are several algorithms available for uniform AC and these can be categorized into three groups; (1) pre-processing method (section 2.7.1.1), (2) intrinsic method (section 2.7.1.2), and (3) post-processing method (section 2.7.1.3).

2.7.1.1. Pre-processing method

This UAC method is applied to the projection data before reconstruction. Typical examples are those that make use of geometric mean (GM) and the arithmetic mean (AM) of conjugate projections views. Conjugate views (Figure 2-14) can be used under the assumption the source and tissue distribution is uniform. For GM a data set formed from the pixel-by-pixel product of anterior and posterior views, the square root of each pixel value is taken and then the resulting image will represent an attenuation corrected image dependent on the thickness of the object [41]. For AM, the arithmetic average of posterior and anterior views is found.

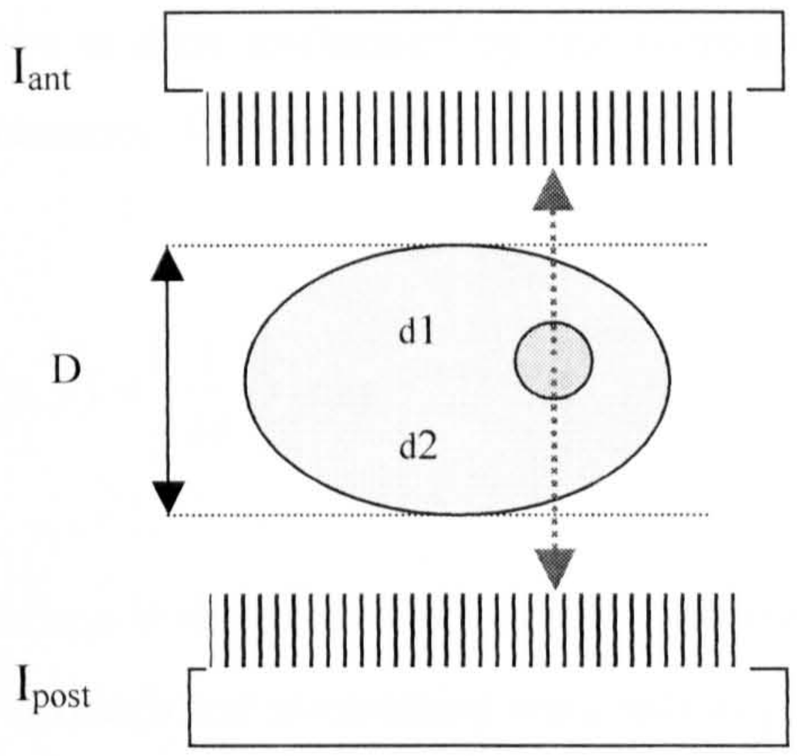

GM

$I_{ant}=I_0.[e^{(-\mu d1)}]$
$I_{post}=I_0.[e^{(-\mu D-d1)}]$
$I_{GM}=[I_{ant}.I_{post}]^{1/2}$
$I_{GM}=I_0.[e^{(-\mu D/2)}]$

AM

$I_{ant}=I_0.[e^{(-\mu d1)}]$
$I_{post}=I_0.[e^{(-\mu D-d1)}]$
$I_{AM}=[(I_{ant}+I_{post})/2]$
$I_{AM}=0.5.I_0.[e^{(-\mu d1)}+e^{(-\mu D-d1)}]$
In the centre d_1 and $D-d_1=D/2$
$I_{AM}=I_0.[e^{(-\mu D/2)}]$

Figure 2-14 The acquisition of point source within an object of thickness D using conjugate projections views [41].

The GM and AM work well for a single radioactive source in a uniform attenuating medium. The limitations of GM and AM pre-processing AC methods are most evident in situations where multiple sources are involved and knowledge of source thickness and source depth is required [42].

2.7.1.2. Intrinsic method

This UAC is applied during the reconstruction steps. It involves multiplying the projection data with an exponential function whose exponent is a function of body thickness, filtering with a modified ramp filter in the frequency domain, and back-projecting the filtered projections with an exponential weighting. A body contour is needed. The modified ramp filter is the same as the regular filter, except that its value is zero in the frequency range between zero and $\mu/2\pi$. This AC method is simple to implement and works well even for multiple sources but it tends to generate high-reconstructed image noise. As a result, an additional smoothing filter is necessary to reduce image noise [17, 42].

2.7.1.3. Post-processing method

Chang's method is the most commonly implemented post-correction method [43]. This method consists of two steps; calculating a multiplicative factor and multiplying the reconstructed image by this factor. The measured projection data are reconstructed without attenuation compensation. A correction factor is then calculated at each image

point as the average attenuation factor over all projection angles. The reconstructed image is then multiplied by the correction factors. The correction factor [$C(x,y)$] for attenuation for each point is defined as;

$$C(x,y) = \left[\frac{1}{M} \sum_{i=1}^{M} \exp^{-\mu l(x,y,\theta_i)} \right]^{-1} \qquad \text{Eqn 2-9}$$

Where μ is the linear attenuation coefficients, $l(x,y,\theta_i)$ is the distance that the projection i go through the attenuating materials at projection angle θ and M is the total number of projections.

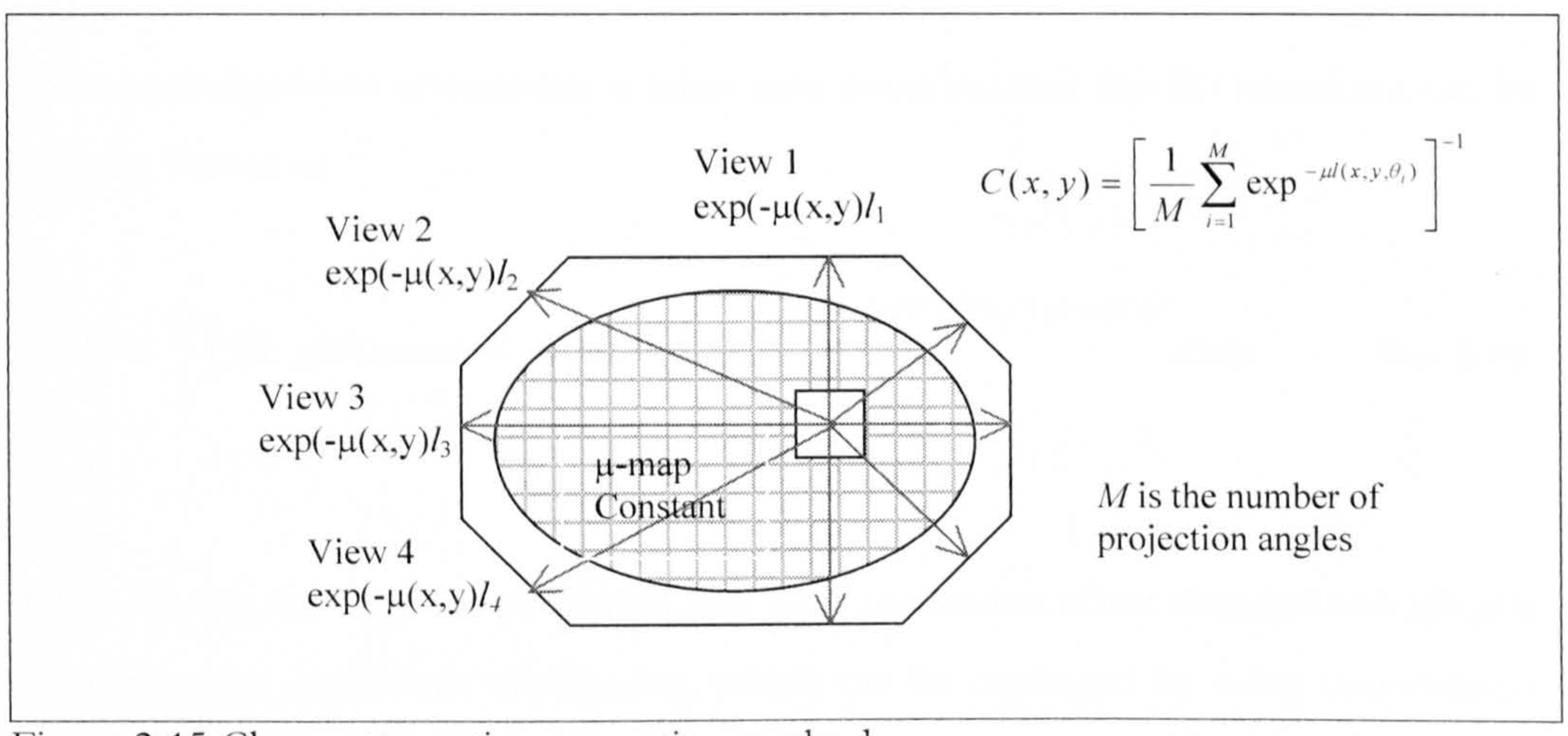

Figure 2-15 Chang attenuation correction method.

Chang's method performs well for uniform attenuation and is supplied with most commercial systems. It is mainly used in the reconstruction process for brain scans where the assumption that there is a constant attenuation coefficient in the brain itself, but the surrounding skull can create artefacts when using UAC [44].

When performing Chang AC the correct boundary of the body must be selected. For example the required boundary is the edge of the head, not the edge of the brain, and this boundary is different in each transverse slice through the head. Due to the assumption that there is a constant attenuation coefficient distribution it does not work well in the thorax (e.g. cardiac SPECT imaging) since the heart is surrounded by tissue of varying density (lung, chest wall, and bone), with different attenuation coefficients. A direct estimation of the variable attenuation in the chest is necessary.

2.7.2 Non-uniform attenuation correction methods

In the chest, the attenuation in lungs is approximately 1/3 of the attenuation in other tissues (since the lungs are full of air), and there will be increased counts detected by the gamma camera due to the increased transmission of photons through the area of decreased attenuation. The gamma camera cannot distinguish increased counts originating from increased activity (heart) or because of low attenuation. In order to accurately correct this non-uniform attenuation in chest one needs an estimate of the attenuation coefficient distribution of the patient. A large number of methods have been proposed to estimate the attenuation coefficient distribution. Many manufacturers now offer, as optional equipment, a means to measure attenuation distribution (transmission imaging) for each patient.

Mathematically, when attenuation is taken into consideration, the 2D transform can be formally written as

$$P(t,\theta) = \int_{-\infty}^{\infty}\int f(x,y)\delta(x\cos\theta + y\sin\theta - t)\exp^{-\int\int_{x,y}^{\infty}\mu(x',y')\delta(x'\cos\theta+y'\sin\theta-t)dx'dy'} dxdy \qquad \text{Eqn 2-10}$$

Where $P(t,\theta)$ is the emission projection data with attenuation effect included and $\mu(x,y)$ is the attenuation coefficient distribution, which can be measured by using transmission imaging and $P(t,\theta)$ is the emission. In transmission imaging, both blank scan[9] (in which there is no patient in the scanner) (Figure 2-16(a)) and the transmission scan (where the patient remains in the scanner and is exposed to an external radiation source) (Figure 2-16(b)) are acquired. This allows the measurement of the transmitted intensity (the attenuated intensity $P(t,\theta)$.

This represents the measurements of the un-attenuated (I_0) intensity. The blank and attenuated scans are related by

$$T(t,\theta) = \int_{-\infty}^{\infty}\int \mu(x,y)\delta(x\cos\theta + y\sin\theta - t)dxdy \qquad \text{Eqn 2-11}$$

[9] Blank scan is required for each detector and each collimator used for transmission scanning.

$$M(t,\theta) = I_0(t,\theta)exp^{-\int\int \mu(x,y)\delta(x\cos\theta + y\sin\theta - t)dxdy} \quad \text{Eqn 2-12}$$

Where $T(t,\theta)$ is the transmission data when no patient present and $M(t,\theta)$ is the transmission data when patient remains in the scanner. The projections can be calculated as follows

$$\therefore T(t,\theta) = \log\left[\frac{I_0(t,\theta)}{M(t,\theta)}\right] \quad \text{Eqn 2-13}$$

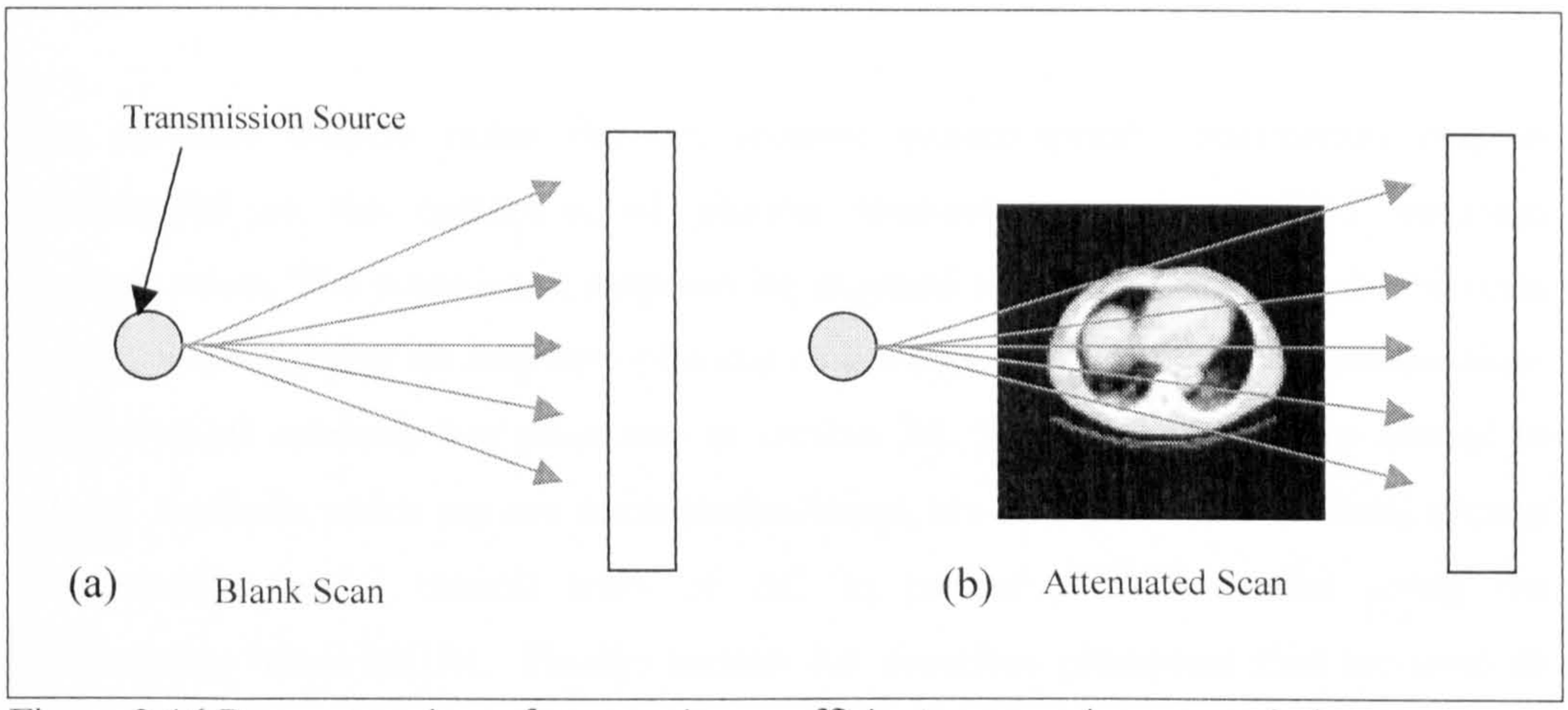

Figure 2-16 Reconstruction of attenuation coefficients map using transmission source.

This patient specific attenuation map can be incorporated into the iterative reconstruction algorithm in order to correct for non-uniform attenuation artefacts in cardiac SPECT studies. Thus accurate compensation for non-uniform attenuation is essential in cardiac SPECT reconstruction and processing in order to produce an artefact-free image, and quantitatively accurate data.

The use of an external radioactive source (or conventional x-ray CT equipment) to acquire a transmission scan during SPECT acquisition is gaining popularity, and has been implemented by most SPECT instrumentation manufacturers. A review of these transmission-based NUAC methods will be covered in chapter 3.

Chapter Three Correction methods for non-uniform attenuation

The previous chapter notes that an accurate patient-specific attenuation map is fundamental to the correction of photon attenuation in the SPECT emission reconstruction. The attenuation map can be acquired using a transmission-based scan. Firstly, in this chapter an overview of some of the commercially available transmission-based NUAC methods are presented in section 3.1. In section 3.2, issues related to NUAC methods which are not transmission-based, are briefly discussed. Then, section 3.3 considers some clinical trials of AC in cardiac SPECT studies using the transmission-based NUAC. Finally, section 3.4 describes phantoms that are used to evaluate (or validate) NUAC.

3.1. Transmission-based methods

A variety of transmission hardware modifications and external sources have been proposed for commercial SPECT systems. The designs of these transmission systems differ with regard to; (1) whether to use sequential or simultaneous emission/transmission imaging; (2) the radionuclide used for transmission; and (3) the number and configuration of detectors.

3.1.1 Sequential or simultaneous emission/transmission imaging

The majority of procedures for NUAC using measured transmission data in SPECT are applied either during or after emission reconstruction [45]. Emission/transmission data are either acquired at separate points in time (sequential scanning) or at the same time (simultaneous scanning). Sequential acquisition can increase the potential for patient motion leading to misregistration between the emission and transmission images and the introduction of artefacts [46]. Misalignment between emission/transmission data

will introduce errors into the AC images. To overcome this, emission/transmission data may be acquired simultaneously. The disadvantage of simultaneous acquisitions is the contamination of the emission data with cross-talk from the transmission source into the emission data (or vice versa).

3.1.2 Transmission source

Ideally the transmission source should; (1) minimize cross-talk between transmission and emission data, (2) provide an accurate attenuation coefficient map, (3) be simple to use in a clinical environment and (4) be available at an acceptable cost. There are a number of transmission sources available commercially. Table 3-1, adapted from the data presented in Ficaro [47], summarizes the physical properties of some of these sources.

Table 3-1 Isotopes commercially available for performing transmission imaging [47].

Transmission source	Photon emission energy	$T_{1/2}$
^{99m}Tc	140 keV	6 hours
^{153}Gd	95.1-103.2 keV (51%); 40.9-54.7 keV (147%)	242 days
^{241}Am	59.5 keV	432 years
^{57}Co	122 keV (86%); 136.5 keV (10%)	271 days

Abundance is quoted in the brackets

The first instance of using a transmission source to obtain the body contour was by Jaszczak [48] who developed a technique to estimate the body contour using a ^{133}Xe (74 and 85 keV) transmission line source attached to the camera head. The body contour is then used to compute the correction matrix to be applied for Chang AC. Using ^{133}Xe as a transmission source has some limitations, including a slightly increased radiation dose to both patient and technician, and the necessity for mounting and periodically replenishing the line source. To largely overcome the extra time of mounting the source, Ljungberg [49] used a standard, commercially available ^{57}Co sheet source as a transmission source. This transmission source can be mounted on the camera quickly and easily with a comparative reduction in time for the transmission scan.

For ^{99m}Tc radiotracers, Bailey [50] used ^{153}Gd as a transmission source whereas for ^{201}Tl radiotracers, Frey [51] chose ^{99m}Tc as a transmission source (due to its availability as an inexpensive source). Ficaro [47] proposed the use of ^{241}Am as a transmission source for both ^{99m}Tc and ^{201}Tl as it has a low photon energy (60 keV) and therefore contributes the least amount of contamination to the emission data. The long half-life of ^{241}Am transmission sources eliminates periodic replacement (daily for ^{99m}Tc, yearly for ^{153}Gd and ^{57}Co). It is also relatively inexpensive. In general, ^{153}Gd is the most commonly used transmission source in SPECT imaging for several practical reasons; appropriate energy, sufficiently long half-life (242 days), high activity, and reasonable cost.

These transmission sources can be in different forms including; a sheet source, a point source, a single line source, multiple line sources, a scanning line source, and multiple array sources. Some of these forms will be discussed in the next sections.

It is also possible to use an x-ray tube (CT scanner) as a transmission source as it offers the advantages of higher photons rates and a faster transmission scan. Using images from two modalities suffers from the usual problems of working with multi-modality images, namely, accurate co-registration from different modalities [45]. .

3.1.3 Configurations of transmission scanning geometries

In commercial transmission scanning systems, there are several different geometries for the transmission source and the collimator. Each configuration has its advantages and drawbacks. The first combination is of a cone-beam collimator and a point source [52] [53]. The second is a moving line source and a parallel-hole collimator [54]. The third is a line source and a fan-beam collimator [51] [55] [56] [57]. The fourth combination is of a fillable flood source and a parallel-hole collimator [58] [59]. The third method provides advantages including a small fraction of scattered photons in the transmission and emission data, and easy handling of the transmission source. This method uses lower activities for the transmission source than those using the second method. The advantages of the fourth method include the absence of truncation artefacts and the lower cost of the instruments. For this method, the problems are; a larger number of scattered photons which affect the images, and the inconvenience of the preparation of the transmission source. To overcome the problem of transmission source preparation, Hashimoto [60] and Ichihara .[61] designed a new type of ^{99m}Tc transmission source

called "sheet line source". This is a narrow fluoroplastic tube filled with ^{99m}Tc by an automatic injector and is almost the same as a uniform flood source. This source offers easy handling of the radioisotope during preparation and reduces the absorbed dose to the technologists and physicians. In general, sheet sources and uniform-activity line sources are relatively easy to produce, but the routine use of a refillable source is not desirable because of the radiation exposure received during filling and the difficulty of achieving a uniform activity distribution. Compared to line sources, point sources cost less and are easier to shield and collimate.

Some of these published geometries are summarized on Table 3-2 and reviewed in the next sections.

Table 3-2 Configurations of transmission scanning geometries

Configuration	Advantages	Disadvantages
Point source	Cost less, Easy to shield and collimated.	Truncation effect
Moving line sources	Less radiation dose to staff.	Mechanical motion problems, More expensive than a fixed line source
Fixed line sources	No mechanical motion problems	
Flood source	Easy to use and produced Low cost	Radiation dose to staff

3.1.3.1. Single-head system

Bailey [50] used an uncollimated ^{153}Gd flood source in front of a single parallel-hole collimator (Figure 3-1(a)) to perform simultaneous transmission scan. The transmission source irradiates the whole face of the camera head without needing to move the source. The limitations in this technique are the cross-talk with emission data and the measurement of μ from a broad-beam.

Frey [51] developed a method of using a ^{99m}Tc flood source fitted with a collimator and attached to the gantry on the opposite side of the patient. This reduces the number of transmission-scattered photons and also reduces patient dose. Moreover, if the transmission source collimator is attached to a single-head camera, the increased weight is too heavy for most single-head SPECT systems.

Also for a single camera, Tsui [62] used a collimated ^{99m}Tc sheet source mounted opposite the detector (Figure 3-1(b)). A special parallel-hole collimator was placed in front of the transmission sheet source in order to reduce radiation exposure to the patient and the image degrading effects of scattered transmission photons. The emission scan was acquired first then the transmission source was put in place and the transmission scan was acquired (sequentially, moving only the transmission source to eliminate artefacts from patient motion).

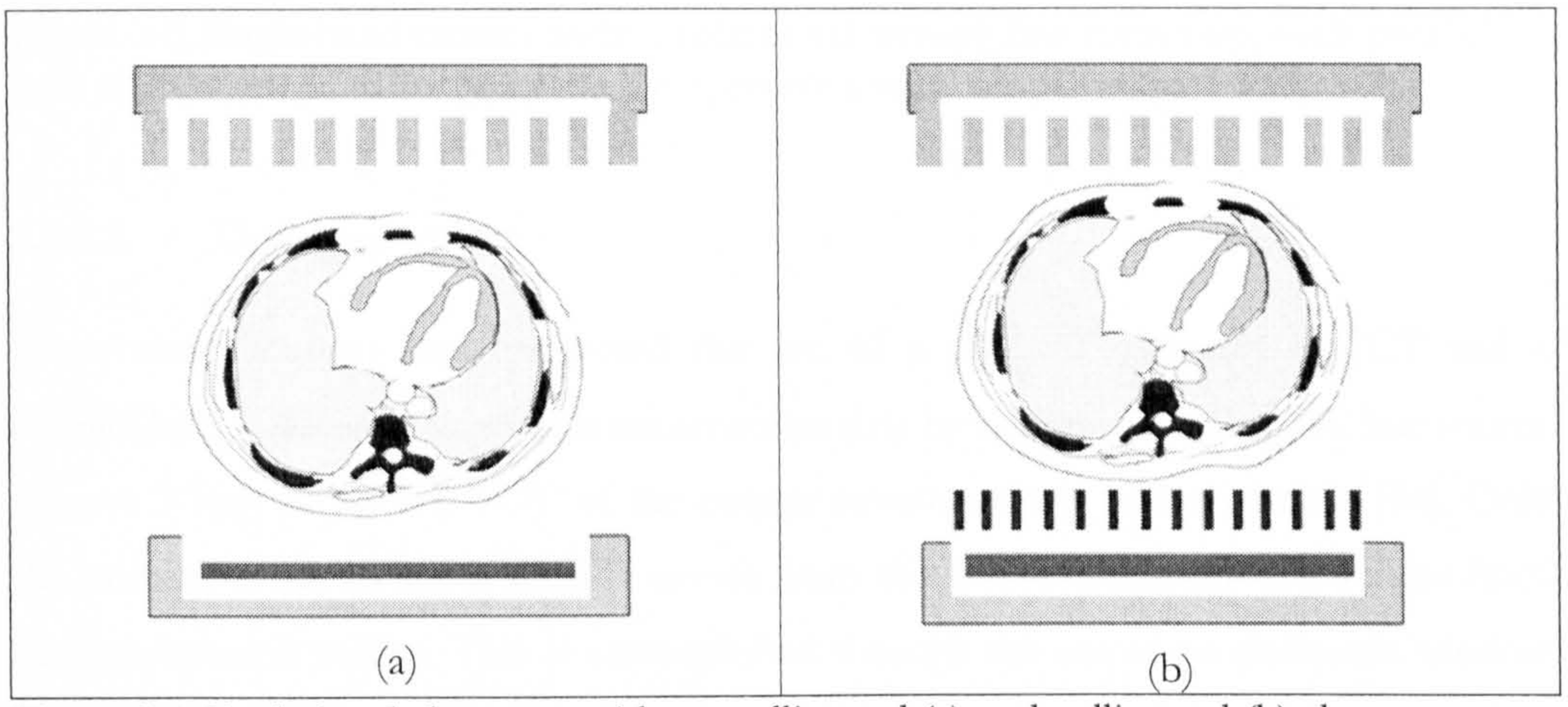

Figure 3-1 Single headed camera with un-collimated (a) and collimated (b) sheet-source.

Another approach was proposed by Tan [63] [54] using a collimated ^{153}Gd moving line source that transverses the field of view (FOV) at each acquisition angle. The transmission source was attached on a frame parallel to the FOV of the camera (Figure 3-2(a)). It was microcomputer controlled and could be programmed for different acquisition times in synchrony with the SPECT acquisition. Also, an electronic spatial window was used to reduce the emission photons in the transmission window and vice versa. This technique has some advantages; radiation dose to the staff is reduced, and the same nuclide can be employed for both transmission and emission.

Manglos [52, 64], performed emission/transmission measurements using a ^{99m}Tc point source opposite a cone-beam collimator (Figure 3-2(b)). With this system, there was a significant increase in resolution in the attenuation maps, which measured the narrow-beam attenuation coefficient. The major disadvantage of this system derives from the producing of truncated projected data.

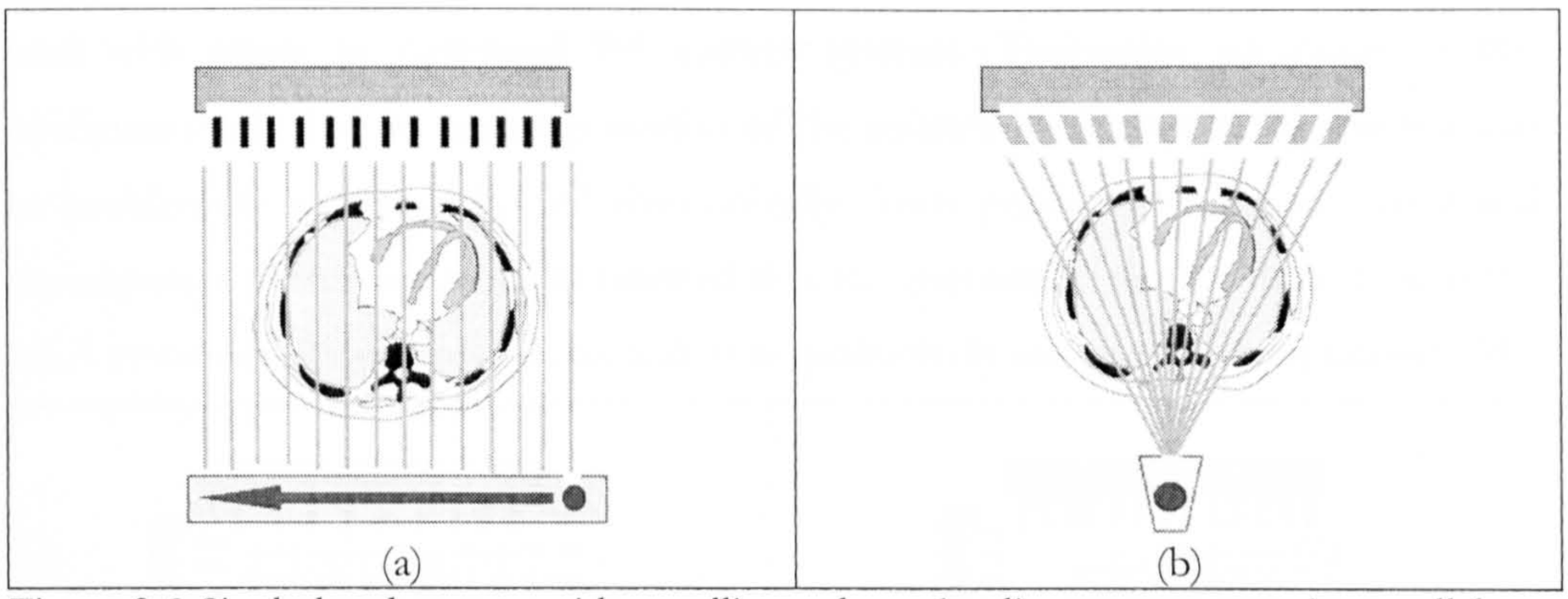

Figure 3-2 Single-head camera with; a collimated moving line source opposite parallel-hole collimator (a), and a point source opposite a cone-beam collimator (b).

3.1.3.2. Dual-head system

Some manufacturers have proposed the use of a dual 90° detector SPECT and a parallel-hole collimator to acquire transmission data by scanning a collimated line source (Figure 3-3(a)) across the FOV of the camera simultaneously or sequentially [54]. Only the portion of the detector directly across from the line source receives photons from the transmission source. This is accomplished through the use of an electronic window or masking that moves in unison with each of the line sources. The remainder of the detector surface acquires the emission scan in the usual manner. The scanning electronic mask coupled with energy discrimination circuitry minimizes energy cross-talk between transmission and emission photons. This configuration does have the drawback of requiring synchronized mechanical motion of the source with the electronic windowing employed to accept the transmission photons.

The other widely implemented configuration for commercial acquisition is the multiple line source array (MLA) approach [65]. It uses a group of collimated line sources (^{153}Gd) positioned close enough together that they appear as a continuous distribution of transmission source photons over the FOV [40]. The activity in the central lines of the MLA was higher than at the edges, so that greater transmission photon flux near the centre of FOV would be directed toward the thicker parts of the human body (where the attenuation is greater) (Figure 3-3(b)). As the line sources decay, two line sources are inserted into the centre of the array. The rest of the lines are moved outward one position, and the weaker pairs (at the edges) removed. The whole set of line sources was placed in a lead box to shield the back and the sides of the system. The system can be

used with single or dual-head 90° camera systems. The major advantage of this configuration is that no scanning motion of the sources is required as this motion can be problematic mechanically and electronically. Tests performed using simulated and experimental phantom data demonstrated that the attenuation maps obtained using the MLA system displayed no artefacts and were qualitatively and quantitatively correct [65].

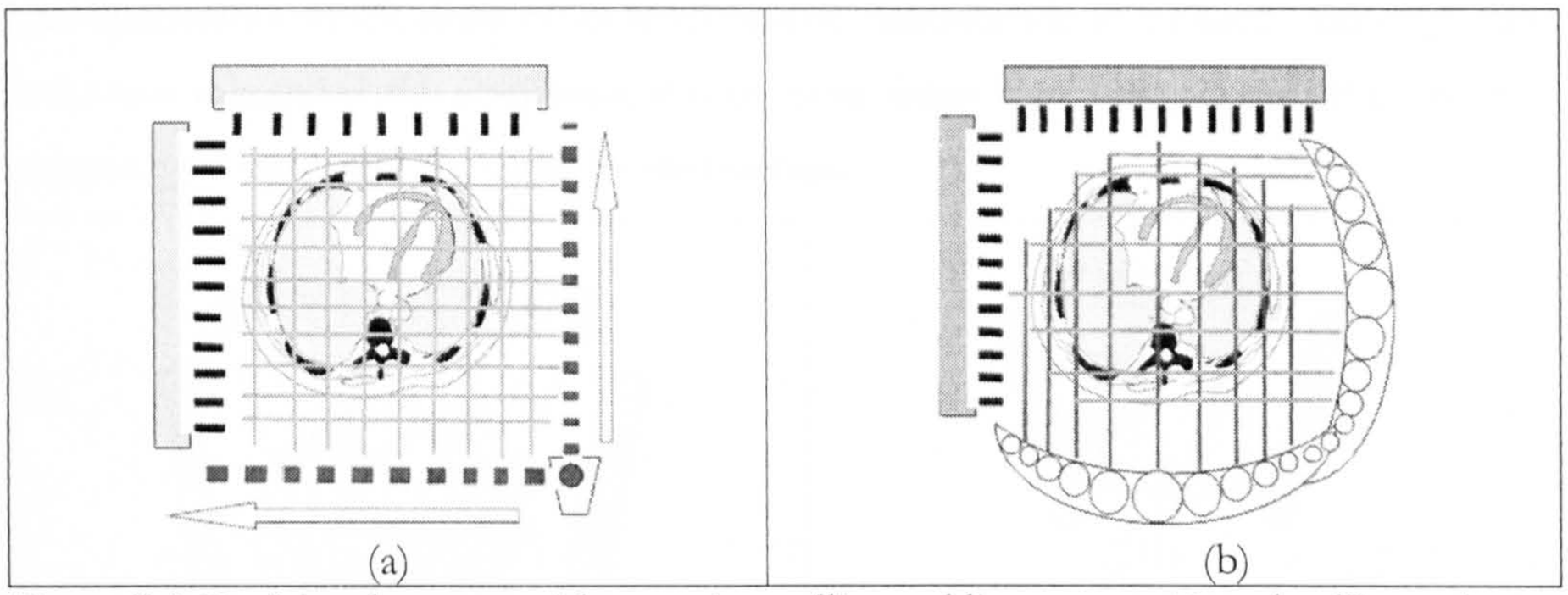

Figure 3-3 Dual-head camera with scanning collimated line source (a) and collimated multiple line sources array (b).

Hashimoto [60] developed a practical method for attenuation correction in ^{201}Tl myocardial SPECT (for a dual-headed SPET gamma camera system equipped with parallel-hole collimators). The attenuation map was obtained from a sheet source (^{99m}Tc), which was composed of a long narrow fluoroplastic tube embedded in a rectangular acrylic board. The tube was first injected with ^{99m}Tc by automatic injector, and then attached opposite the collimator surface of one of the two detectors. This method was validated by several phantom and clinical cardiac studies. They conclude that this ^{99m}Tc sheet line source may not produce truncation in transmission images, and is cost-effective and easy to prepare in clinical studies. The other advantages of this sheet line source are that it is light and easy to handle, and only a small amount of activity needs to be injected [61] .

3.1.3.3. Triple-head system

Tung [55], used a triple-detector SPECT system with a collimated line source opposite a detector fitted with a short focal-length fan-beam collimator (Figure 3-4(a)). This approach offers the advantage of simultaneous acquisition of transmission and emission data using a lightweight, low-dose line source with minimum cross-talk between

emission and transmission data. The major disadvantage was severe truncation of the trans-axial FOV (small FOV from small focal length) for most applications apart from brain imaging [52] [66]. To reduce the truncation of the transmission projection, Jaszczak [56] have used longer focal length fan-beam collimators (Figure 3-4(b)). The transmission source used was a removable ^{99m}Tc line source and rotatable air-copper-lead attenuators which allow other transmission radionuclide to be used. Although this technique minimizes the scan time, shorter scan times would be possible if more line sources were used with the triple-headed camera.

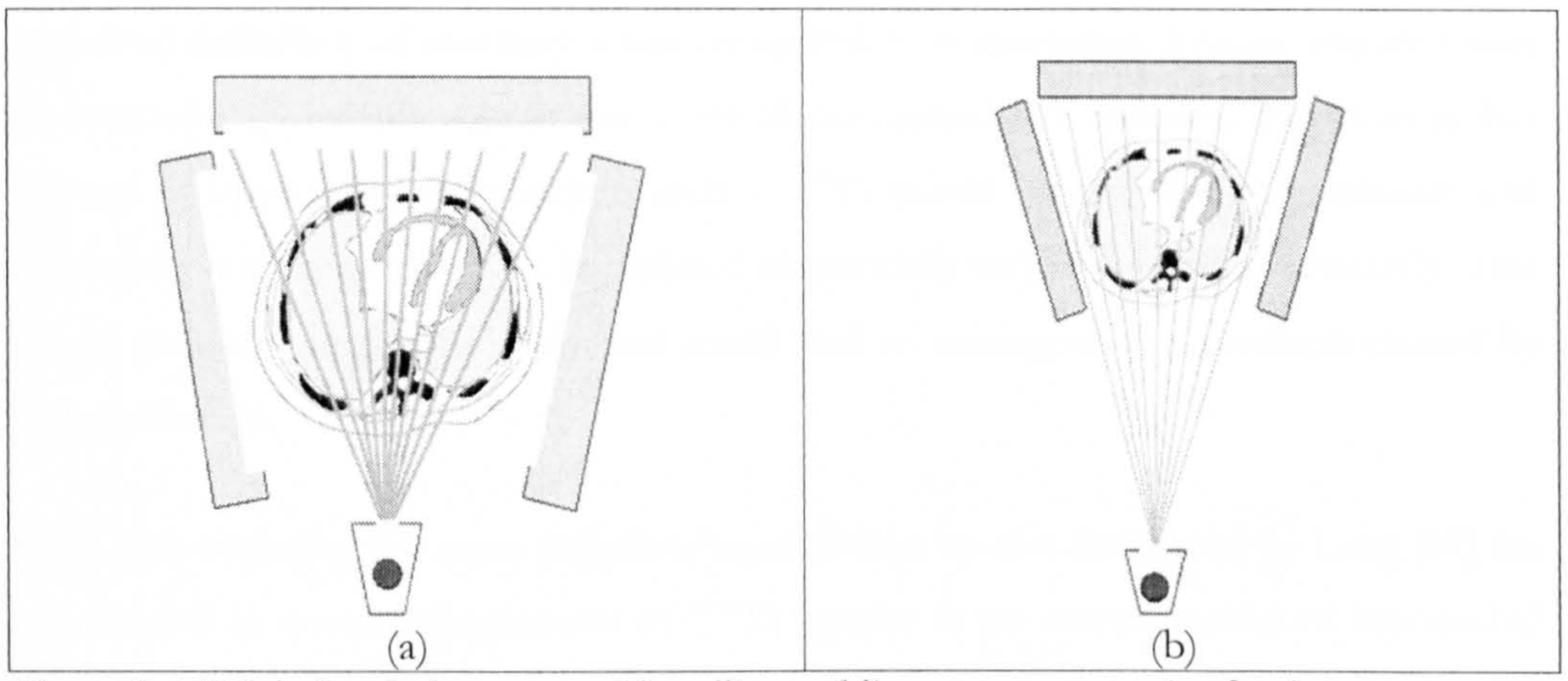

Figure 3-4 Triple-headed camera with collimated line source opposite fan-beam collimator with short (a) and long focal length (b).

3.1.3.4. X-ray source and CT

Patient-specific attenuation maps obtained from a CT system using a conventional x-ray tube and detector have recently been used in attenuation correction technique. Initially, the transmission scan was obtained with the patient in the CT scanner and then moving the patient to a SPECT system for acquisition of the emission image. However, there is a need to register both transmission and emission images accurately and convert the linear attenuation coefficients obtained with the x-ray source into attenuation coefficients for emission photon energy. To obtain accurate registration, it is necessary incorporate a full x-ray CT system with a SPECT gantry. This is an expensive solution that has only recently been made commercially available.

Lang [67], developed a prototype imaging system that can perform simultaneous x-ray transmission CT and SPECT. This emission/transmission system employs a detector array coupled to a collimator with septa angled toward the focal spot of an x-ray tube,

providing spatial localisation for SPECT and scatter rejection for x-ray CT. The detectors move in an arc in conjunction with fast pulse-counting electronics to simultaneously detect and energy-resolve x-ray photons from an external source and higher-energy γ-ray photons from an internally administered radionuclide source. This system allows the SPECT images to be registered on the x-ray CT map, by acquiring the emission and transmission data with the same detector and reconstructed with the same geometry. This superposition of the SPECT image on the high-resolution x-ray CT map improved anatomical localisation. The x-ray CT image acquired with this device shows improved definition of anatomy when compared to transmission images acquired with an external radionuclide source and a scintillation camera. A technical limitation is that the use of low-energy radionuclide such as ^{201}Tl would require that the emission and transmission measurements be performed sequentially rather than simultaneously. This would prolong the patient study and could lead to misregistration artefacts caused by patient motion.

Kalki [68] evaluated the same emission/transmission system developed by Lang [67] for quantitative in vivo measurements of ^{99m}Tc uptake in an animal model of myocardial perfusion. They found that the additional anatomical information from the x-ray CT image was helpful in defining regions of interest for quantitation of the SPECT image. They reported that their system precluded clinical studies on humans, because of the long scan times and the small reconstruction circle.

Bocher [69] developed a gamma camera-mounted anatomical x-ray tomograph (GMAXT) that is a hybrid[10] gamma camera/CT scanner. It provides high resolution, high-contrast, cross-sectional x-ray transmission images that facilitate anatomical localisation of the radioisotope uptake and allows for patient specific AC in both PET and SPECT imaging. The patient attenuation is measured using an x-ray imaging system that rotates around the patient to acquire cross-sectional data in a way similar to third-generation CT systems. The x-ray imaging system is composed of an x-ray tube and a set of 384 detectors located on opposite sides of the gantry. The tube and x-ray detectors are fixed to the gantry and rotate around the patient along with the gamma detectors. The x-ray images were used for AC of emission images. They examined the

[10] Although the combination of two or more pre-existing imaging device from one company into a single gantry is referred as a hybrid imaging system, still others use the term "hybrid" referring to fusion imaging that combines two independent imaging modalities to produce a diagnostically and clinically superior image.

performance of this system with a phantom and also imaged 6 patients. A left ventricular phantom filled with ^{99m}Tc placed inside an anthropomorphic torso phantom was scanned and the quality of the images with AC and NC were visually evaluated. The phantom images exhibit visually good AC of cardiac attenuation defects. Clinically, the usefulness of functional-anatomical mapping was assessed by inspection of co-registered and fused images of patients referred for tumour imaging. In all six patients, this system contributed a more precise anatomical localization of the scintigraphic findings. The most significant limitation is the long scanning time (14-s per slice), which is constrained by the heavy gamma camera detector. This long scanning time may result in breathing motion artefacts.

Today these hybrid-imaging systems (CT/SPECT) are in clinical use. One of these is the "Hawkeye" system manufactured by General Electric Medical. The Hawkeye hybrid imaging system consists of a CT x-ray tube and CT detector mounted on a dual-head variable-angle gamma camera (SPECT/CT). It is completely integrated with both modalities on a single gantry. Although this system was developed for anatomic registration with emission images for oncology studies (cancer treatment planning), it provides a high quality transmission image (patient specific attenuation map) for use in attenuation correction (AC) of cardiac and other images [69]. But quantification of attenuation corrected images remains an issue. The hybrid Emission/Transmission imaging systems have received much attention as a recent development in the field of non-uniform attenuation correction (NUAC).

3.1.3.5. Hawkeye CT/SPECT system

The state-of-art Hawkeye system is a fully integrated system which permits SPECT (or PET) acquisition and x-ray transmission imaging using a single gantry (Figure 3-5). The x-ray transmission and emission scans are acquired by moving the patient from one detector to the other while the patient remains on the scanning table. After both sets of images are acquired and reconstructed, then both images are fused in way that can be displayed in colour on a grey-scale CT image to co-register the anatomical and physiological features. The anatomical localization intends to improve evaluation of disease, in comparison to SPECT (or PET) alone. In addition, CT data can be used to generate a patient-specific map of attenuation coefficients to correct the emission image for photon attenuation [70]. Due to the high quality attention map and accurate co-

registration, the Hawkeye system is a very promising development in AC of cardiac SPECT imaging.

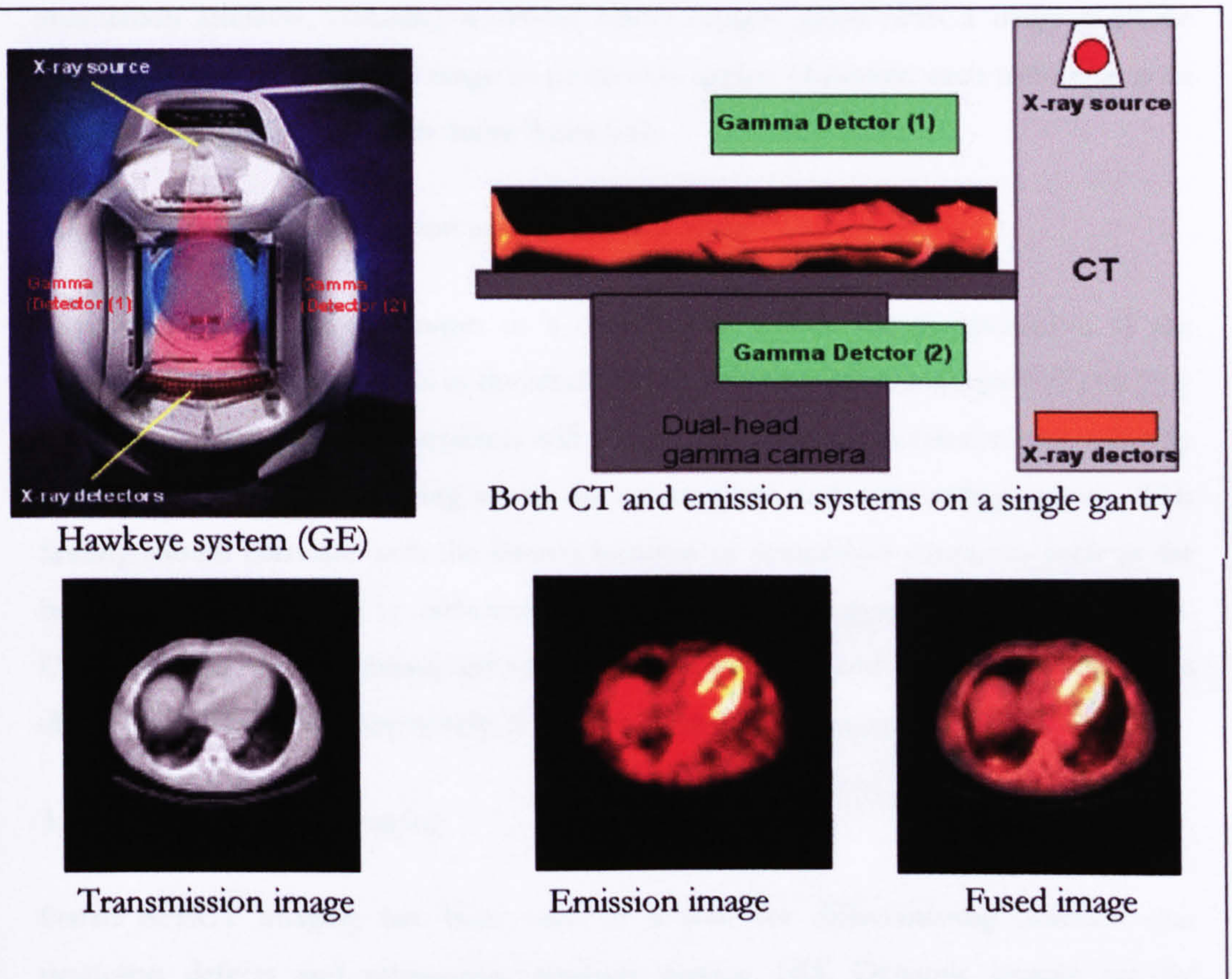

Figure 3-5 Hawkeye GE hybrid CT/SPECT system.

The CT scanner is designed with a lower spatial resolution than conventional CT scanners in a way that is still suitable for AC. Fundamentally conventional CT image has a higher spatial resolution (512×512) and should be compressed to the same format of the emission image (64×64 or 128×128). The x-ray source produces higher photon density that allows the transmission data to be acquired faster and with a higher statistical quality giving lower noise attenuation map than can be obtained from other external transmission sources. Furthermore, the x-ray source does not decay, and does not need frequent replacement [71]. However, with a slow CT system, respiratory motion artefacts at the level of the diaphragm can occur and may result in unsatisfactory correction of the adjacent inferior cardiac walls [72].

There are other methods, which help to minimize (and/or recognize) attenuation artefacts. The following section summarizes the literature for some of these methods.

3.2. Methods of minimizing (or recognizing) attenuation artefacts

Various techniques have been described in the literature to recognize and minimize attenuation artefacts, including reviewing planar images, gated SPECT imaging, prone imaging, and using a selected range of projection angles. However, each technique is an indirect solution and possesses some limitations.

3.2.1 Reviewing the projection images in a cine form

Reviewing the projection images in a cine format before the interpretation of the tomograms is an effective tool in the identification of attenuation artefacts [73] [74] [39]. Attenuation that may cause artefacts will appear as a decrease in relative count density and resemble a shadow moving across the myocardium and surrounding regions. This finding should correlate with the known location of anatomical structures such as the breast and should help to differentiate true defect (hypo-perfusion) from artefacts. Unfortunately, the combined effects of hypo-perfusion and attenuation are often difficult to differentiate objectively, leading to reduced test sensitivity [40].

3.2.2 Gated SPECT imaging

Gated SPECT imaging has been used as a tool for differentiating between true perfusion defects and attenuation artefacts motion [40]. Dynamic images can be obtained when SPECT acquisition data is gated with the electrocardiogram (ECG). A gated-SPECT study is generally performed using 8 to 16 frames acquired throughout the cardiac cycle. The display of gated SPECT study can be as simple as side-by-side static displays of end-diastolic and end-systolic images. Regional LV function can be assessed by measuring the distance that a region of the LV moves between end-systole and end-diastole. Gated SPECT imaging provides information about wall motion and thickening of myocardial segments, as well as ventricular function. In general Gated SPECT can differentiate scar from artefact since fixed defects should demonstrate decreased wall motion and wall thickening, whereas attenuation artefacts should move and thicken normally [75]. When a perfusion defect is not consistently visible at both diastole and systole, it is more likely an attenuation artefact than a true defect [39].

3.2.3 SPECT imaging in prone position

Esquerre [76] reported SPECT imaging in a prone position as a method of minimizing attenuation artefacts. With the patient positioned this way, the heart and diaphragm are shifted to reduce inferior wall attenuation while potentially increasing anterior wall attenuation. For assessing suspected inferior wall attenuation, a planar static lateral decubitus view can be acquired with the patient on his/her right side and used for comparison with the corresponding lateral projection of the SPECT acquisition. The shifting position of the organs relative to the myocardium in this view often reveals an increase in inferior wall counts relative to the anterior regions correlating with diaphragmatic attenuation artefacts in the supine SPECT [40] .

3.2.4 Using a selected range of projection angles

Bateman [77] argue that a selected range of projection angles determined to be minimally affected by attenuation can be used as a method that minimizes the effects of attenuation artefacts. A sinogram representation of the projection data is examined to identify the angular views that are most affected by attenuation. A 180° angular range is defined that excludes these projections as much as possible. Although, this technique reduces the effects of attenuation, it cannot provide complete compensation [40].

In recent years, there has been much interest in the clinical application of AC to cardiac SPECT with the promise that accurate quantitative images can be obtained to improve clinical diagnosis. It is hypothesised that SPECT reconstruction with AC would enhance the diagnostic accuracy of CAD. "Recent published results suggest that the real world performance of AC is improving for a range of manufacturer's systems and techniques" [78].

While the majority of the published clinical studies of AC cardiac SPECT have reported a significant improvement in specificity or sensitivity, especially for high-risk patterns of CAD [79] [6] [80], and helped in the diagnosis of patients with low pre-test likelihood of disease [81], others have reported little or no benefit, especially with intermediate pre-test likelihood of CAD [11] [9] [12]. Some of the published clinical trials are reviewed in the next section.

3.3. Clinical trials of AC in cardiac SPECT studies

The first clinical trial using AC was reported by Bailey [50]. A total of 11 patients were studied with ^{201}Tl myocardial perfusion scanning. In 7 cases, there was no difference in final diagnosis between AC images and no AC images (NC) and the use of AC led to 3 cases being correctly reported as normal [82].

Ficaro [47] developed a system that uses a triple-detector camera equipped with ^{241}Am transmission line source opposite a fan-beam collimator on one detector to collect transmission and emission projection data. This system was used by Ficaro [79] to study forty patients with CAD and ten normal volunteers (50 patients) with simultaneous transmission/emission ^{201}Tl SPECT. They found that the attenuation artefacts were effectively eliminated from the reconstructed emission image and they anticipated improved specificity for myocardial perfusion SPECT when AC is applied

Ficaro [6] assessed the effect on the diagnostic accuracy of AC for ^{99m}Tc myocardial SPECT for the detection and localization of CHD in 119 patients (60 patients with angiographically documented CHD and 59 patients with a very low likelihood of CHD). Corrected (AC) and uncorrected (NC) emission images were visually and quantitatively interpreted and compared for the presence or absence of CHD. Each patient underwent simultaneous transmission/emission imaging with the previously discussed system developed by the same group, Ficaro [47, 79]. They found that the normalcy rates[11] increased from 88% to 98% and from 76% to 95% for visual and quantitative analysis respectively [83]. Corrected images demonstrated a significant increase in test specificity from 46% to 82% by both visual and quantitative analysis.

Prvuolovich [80] evaluated the effect of AC on myocardial ^{201}Tl distribution in 36 patients (14 men and 22 women) with low risk of CAD (<5%). Emission and transmission data were acquired sequentially. Transmission data were obtained using a pair of collimated ^{153}Gd scanning line sources mounted permanently on the rotating gantry in parallel to the two detectors. Two experienced observers assessed the images qualitatively. The result was that the AC images showed improved homogeneity of tracer distribution compared to NC images. Also, there was no significant difference in

[11] Normalcy rate is the ratio of the number of subjects with definitely normal or probably normal scans divided by the total number of subjects in the cohort (X100 for percentage).

count density observed between corresponding myocardial segments in the AC images of men and women.

Hendel [9] performed a multi-centre clinical trial of AC with ^{99m}Tc perfusion imaging using a dual-head gamma camera equipped with a moving ^{153}Gd line source. Ninety-six patients involved in this study had angiographically documented CAD and 88 patients had a low likelihood of disease. The uncorrected (NC) and attenuation corrected (AC) images were read in a blinded manner. The results of this study demonstrate that the normalcy rate of tomographic myocardial perfusion imaging was significantly improved (86% to 96%) by the use of AC. There were only 16 patients with normal angiograms and specificity was not significantly improved (44% NC to 50% AC). False-positive perfusion images were reduced by more than 4-fold, from 14% to 3% and the confidence for the reporting of a normal image was increased.

Further clinical results using the same method of AC as by Hendel [9], were reported by Kluge [7] for a small group of patients (25 male, with ≥ 50% stenoses of RCA) undergoing myocardial SPECT studies using ^{99m}Tc. Sensitivities of 84% in uncorrected and 100% in AC SPECT studies were found. A significant increase in count density after AC was observed in inferolateral, inferior, inferoseptal, septal and anteroseptal segments. This was compensated by a significant reduction in relative count densities in anterior segments. This study considered only patients with abnormalities of vessels supplying the inferoposterior wall segments [8]. The major limitation of this study was that the results were obtained exclusively in male patients; otherwise it shows a positive result for the case of AC.

Vidal [8] studied 56 patients (46 men and 10 women) with suspected CAD using the same system as Ficaro [6] (triple-head camera and ^{99m}Tc line source). Simultaneous SPECT images with and without AC were blindly interpreted for reversible or fixed defects in the RCA and LAD regions. The ^{201}Tl emission data were corrected for cross talk and truncation effects and then reconstructed using an MLEM algorithm with and without AC. They found that with AC, the specificity of reversible or fixed defect detection was significantly increased in the inferior wall, and the sensitivity of defect detection was significantly reduced in the anteroseptal region.

Chouraqui [84] studied 42 patients (male and female) with low likelihood of CAD using a ^{153}Gd moving line source (synchronized with a moving electronic acquisition window to avoid cross-talk with a ^{201}Tl emission scan). The resulting NC and AC polar maps were visually interpreted and showed clear improvement in homogeneity after correction among male patients and female patients at stress and redistribution. The male and female mean polar maps showed very little differences in regional count distribution after correction. There was a slight relative increase in inferior wall counts at redistribution, which was most likely caused by scatter from the relatively higher liver activity than during stress.

The diagnostic accuracy of myocardial SPECT is closely related to the pre-test likelihood of CAD. In patients in whom the pre-test likelihood is high, myocardial SPECT is performed to determine which arterial territory is ischemic or related to the infarct. In patients with a very low likelihood of CAD (<5%), myocardial SPECT is performed to confirm normal perfusion. For patients with intermediate pre-test likelihood of CAD, Lee [12] found that the incremental value of AC SPECT did not differ significantly from the value of conventional SPECT.

Whilst Ficaro [79] and Prvulovich [80] studied only volunteers or patients with low likelihood of CAD, Lee [12] studied patients with an intermediate pre-test likelihood of CAD. They investigated whether using AC could improve specificity in the diagnosis of CAD. Sixty-eight patients with coronary artery stenoses ≥ 70 % underwent rest AC ^{201}Tl SPECT and stress gated AC ^{99m}Tc SPECT with a dual-head camera. A ^{153}Gd source was used as the transmission source. The sensitivity, specificity, and areas under ROC curves were compared for each operator (three physicians who had read stress gated SPECT images in the clinical setting for 3 years before this study) for three assessment techniques; (1) NC rest/stress SPECT, (2) gated stress SPECT plus NC rest/stress SPECT, and (3) AC rest/stress SPECT plus gated stress SPECT plus NC rest/stress SPECT. They found that, for a group of patients with an intermediate likelihood of CAD, there was no difference between these three techniques and no significant difference between the three operators. On the other hand, Cullom [78] reported some comments on the study of Lee [12]; (1) they should perform correction for photo-peak scatter and non-stationary resolution to get optimal AC, (2) compensation for ^{99m}Tc down-scatter into the ^{153}Gd-derived attenuation map was essential to avoid attenuation

map errors, and (3) the AC was assessed clinically even before quality control for transmission instrumentation performance had been adequately described.

Patton [85] evaluated AC in the commercially available x-ray CT/Dual head (GE Millennium) camera system. X-ray CT and SPECT images were acquired from two cardiac patients (one normal and one with an inferior wall defect). The AC images were compared to the NC images using count profiles, bull's-eye plots and visual analysis. The result showed normal distribution with AC for the normal patient and the inferior wall defect remaining in the abnormal patient.

Pretorius [2] studied 200 patients (90 men and 110 women) with a large range of body shapes, identified as having normal cardiac perfusion with ^{99m}Tc SPECT imaging (using a triple head camera with a ^{153}Gd transmission line source). Semi-quantitative comparison was made between OSEM (AC) and OSEM (AC+scatter correction (SC)). They found that for patients identified as having a possible attenuation-caused decrease in the inferior wall, AC+SC improve the counts in the inferior region, and for the subset of patients identified as having breast-like attenuation artefacts causing a decreased count in the anterior wall, both AC or AC+SC failed to show significant improvement in the counts in the anterior region (for both male and female patients). They suggested that the decrease in counts in the anterior region in the subset of patients interpreted as having anterior attenuation artefacts in the FBP-reconstructed slices needs further investigation.

A summary of the clinical trials is shown in Table 3-3. From the previously mentioned clinical trials of NUAC on cardiac SPECT, some studies have reported significant improvements in specificity or specificity and sensitivity; others have reported no improvement or a decrease in accuracy resulting from the introduction of artefacts [4]. Whilst Hendel [86], found significantly improved overall specificity but a reduced sensitivity in the right coronary artery territory, Lee [12], found no impact of either gating or AC in patients with intermediate likelihood of CAD. Neither of these studies used quality-control measures [87].

These differences may be the result of differences in patient populations, acquisition protocols, hardware/external transmission source modifications, different likelihood of CAD in the patient groups, and the reconstruction strategies used. Other factors that

affect the variable success of the previous clinical studies may include: insufficient compensation for down-scatter from the transmission source and lack of critical quality-control evaluation of the transmission data and the attenuation map quality [78, 87]. This suggests that the present commercially available state-of-the-art AC devices are not sufficiently robust for routine use in clinical practice [1]. An editorial suggested that the design and testing of software for AC is a complex and iterative process [88].

Although, the clinical validation of AC has been performed for several commercially available hardware/software systems, there are only limited studies including some new hardware (x-ray CT high quality transmission scan, Hawkeye GE) and algorithms (such as OSEM algorithm). In addition, in some studies, no female patients were involved or no gender was mentioned. This means that the AC in the anterior wall was not evaluated fully in some studies.

Table 3-3 Summary of some of the clinical trials of AC on cardiac SPECT studies.

Author	Patients	Comments
Bailey [50]	11 (No gender)	-3 cases being correctly reported after AC.
Ficaro [79]	50 (No gender)	-Reduced lateral-posterior activity ratio.
Ficaro [6]	119 (No gender)	-Improvement in specificity (from 48 % to 82 %),
Prvulovich [80]	36 (14 M+22 F)	-AC images improved homogeneity compared with NC -No difference between men and women AC images.
Kluge [7]	50 (M only)	-Improvement in sensitivity (84% NC to 100% AC). -Normalcy rates (82% NC to 94% of circumflex and 65% NC to 97% for right territories)
Gallowitsch [89]	51 (45 M+6 F)	-Specificity was improved from 69% (NC) to 84% (AC) -AC and NC should be interpreted in a complementary manner.
Vidal [8]	56 (46 M+10 F)	-Improvement of RCA specificity (12% NC to 65% AC).
Hendel [9]	184 (No gender)	- Improvement in normalcy rate from 86% NC to 96% AC for patients with single vessel disease. -No improvement in sensitivity (76% NC versus 75 % AC) of multi-vessels CHD 69% NC to 92% AC. -False-positive images were reduced by > 4-fold from 14% to 3%
Lee [12]	68 (29 M +39 F)	-No difference between AC and NC
Pretorius [2]	200 (90 M+110 F)	-AC and SC improve the counts in inferior wall region. - (Either AC or AC+SC) failed to compensate the counts in anterior wall region. -OSEM reconstruction and SC were used.
Banzo [10]	99 (71 M + 28F)	-Specificity increased from 46% (NC) to 71% (AC+SC) -Sensitivity decreased from 92% (NC) to 71%(AC+SC)
M=Male, F=Female, AC= with attenuation correction, NC=without attenuation correction, SC= with scatter correction, CHD=coronary heart disease, RCA=right coronary artery,		

There are patient related parameters, which may change the attenuation pattern such as diaphragmatic attenuation in men and breast attenuation in women [73] [39]. The main

complicating factor of validating AC in women is the wide variability of breast attenuation.

3.3.1 Breast attenuation and AC

Breast attenuation artefacts are commonly identified as a region of decreased count density over the anterior region of the left ventricle. The severity and extent of the breast attenuation effects depends on the thickness, density, shape and position of the breast relative to the myocardium [73] [90]. For instance, in women with firm breasts that lie on the anterior chest wall with the patient supine, the attenuation effect will be most marked over the anterior wall of the left ventricle. In contrast, in women with large, pendulous breasts that lie adjacent to the lateral chest wall the lateral myocardial wall will be more markedly attenuated. In women with breast implants, which are denser than normal breast tissue, the anterior attenuation artefact is more marked. In contrast women with small breasts or who have undergone mastectomy have little, if any, anterior myocardial wall attenuation. In such cases count density distribution is similar to that of a normal male, with inferior count density relatively decreased [73].

Manglos [90] measured the effects of breast attenuation on myocardial polar maps using a thorax phantom with a cardiac insert and added breast tissue. Simulated breast tissue was from a RANDO phantom[12], which is radiographically equivalent to soft tissue. Transmission data were acquired using a cone-beam collimator and a ^{99m}Tc point source. The phantom was removed and an emission source (^{99m}Tc) was added to the cardiac insert and the SPECT emission acquisitions were performed. The polar map showed a reduction in counts (15% lower than the most active region) at the inferior region when the thorax phantom was imaged without breast tissue. In comparison, with AC, the polar map was more symmetric in appearance and the regional variations were no greater then 5%. One limitation of this study was that the thorax model was relatively small (simulates only limited patient data).

An alternative explanation for the counts reduction in anterior wall can be related to diaphragmatic respiratory motion. Pitman *et al* (2002) [91] studied the combination of diaphragmatic motion and attenuation artefacts on cardiac SPECT images using a physical phantom data. Phantom images with respiratory motion (simulated by

[12] It is constructed with a natural human skeleton cast inside material that is radiologically equivalent to soft tissue.

mechanically moving the phantom on a gantry with different vertical amplitudes) reconstructed with FBP show a reduction in counts density in both anterior and inferior walls relative to that of the lateral wall. AC (using MLEM) fails to correct this artefact, even though it successfully corrects the effect of attenuation. They also suggest that respiratory gating should be applied (equally to both emission and transmission data to avoid any misregistration artefacts) clinically with AC to produce the best possible AC images.

A recent study by Pretorius [2] found that AC and AC+SC failed to show significant count improvements in 23 patients (1 male and 22 females) identified as having a possible breast-like attenuation artefact causing a decreased polar map counts in the anterior wall (relative to the inferior wall). They also concluded that the decreased count in the anterior wall needs further investigation. This supports the findings by Bailey [82] who, reported that: "If we accept the proposal that AC does work, we are then left with the question as to what is causing the confusing results, especially in the anterior wall and apex of the heart" [78].

Therefore, there is a need to study the attenuation from breast tissue with varying degrees of photon attenuation by simulating patient data (or/and a physical phantom with added breast mimicking material) before the validation of AC on real patients.

3.3.2 Arm attenuation and AC

Image count density is additionally decreased if the arm is positioned between the detector and the heart, increasing attenuation. Cardiac SPECT perfusion imaging is routinely performed with patients' arms above their heads to avoid potential attenuation artefacts and reduced image quality [92].

Prvulovich [93] studied the effect of imaging arms down and arms up for ^{201}Tl cardiac SPECT with AC (FBP-NC and MLEM-AC) using a dual-head gamma camera with two ^{153}Gd line sources. Twenty-eight patients (10 male and 18 female) were investigated in this study. They found that there was an apparent lateral under-correction in approximately 10% of attenuation-corrected arms-down studies and that image quality is reduced in about one-third of studies compared with uncorrected arms-up studies. The anterolateral under-correction in this study may due to truncation or spatial

misregistration between emission and transmission data. They suggested that the AC is not sufficiently robust to allow routine acquisition of myocardial perfusion imaging data with arms down.

Toma [92] reported different findings in an abstract. They studied 41 patients (^{99m}Tc SPECT-NC) scanned with arms down and with arms above their heads. They found no significant difference in the location of myocardial perfusion imaging defects between the two arm positions. The possible explanation of the findings in this study is that photon attenuation is less marked with the higher energy (140 keV) ^{99m}Tc tracers than with ^{201}Tl (60-80 keV) [93]. There was no AC implemented in this study. Therefore, attenuation from arms requires validation in addition to the attenuation from breast tissue.

3.3.3 Scanning couch and AC

O'Connor [94] investigated the attenuation of the imaging table on a supine and prone imaging of the heart using a cardiac phantom. They showed that the table attenuation [low (Graphite) and medium (Aluminium/Foam) attenuation table] has a minimal effect on myocardial count distribution for either prone or supine studies of the heart. Also, they showed that high-attenuation imaging tables (made of Aluminium) might cause subtle changes in the apparent activity in the anterior or anterolateral wall in prone imaging. They anticipated that future development in the area of AC would lead to accurate correction for any errors introduced by the table tomographic imaging. The robustness of AC to correct attenuation error from the scanning couch can be studied.

3.3.4 180° versus 360° acquisition and AC

Image reconstruction from data acquired over 180° was preferred for the ^{201}Tl agent because of reduced attenuation over these angles and the improved spatial resolution due to the shorter source-to-collimator distance. Tamaki [95] recommended 180° data acquisition over 360° data acquisition for cardiac SPECT imaging. This study has shown that images reconstructed from 180° data generally have better contrast and resolution than the images reconstructed from 360°. Another study also has shown that images reconstructed from 180° data generally have more artefacts and spatial distortion as

compared to images reconstructed from 360° data, especially toward the basal region of the myocardium [96]. A simulation study by Knesaurek [97] showed that the difference in count density between 180° and 360° images were largely due to the effects of non-uniform attenuation, which had not been compensated for in reconstruction [98].

With ^{99m}Tc agent, the situation has changed as compared to ^{201}Tl because of increased counts and less severe attenuation. When non-uniform attenuation correction (phantom study) is included in the reconstructing of ^{201}Tl, LaCroix [98] found that both SPECT images from 180° and 360° data have identical count density in the LV wall. Clinically, Araujo [99], studied 39 patient with less than 5% likelihood of CAD (using ^{99m}Tc agent) and showed that there was an incremental benefit on the myocardial uniformity with the progressive use of 360° acquisition, and attenuation correction. A more recent ^{99m}Tc simulation study [100] showed that with AC (using OSEM algorithm) the detection performances for both male and female phantoms were increased with 360° acquisitions. Also, for 180° scans, the detectability increased a little with AC for male phantom and decrease for female phantom. They indicated that more comparison phantom studies with AC would be made in the future [100].

Although the evaluation of attenuation correction (AC) performance in a clinical setting is always of interest [78], these newly developed methods for AC should be validated using general accepted standardized testing protocols before launching clinical trials in patients. Wackers [1] stated that "Because AC deals with a physics problem, it seems rational to first perform testing of AC devices in a well-designed series of physics experiments with cardiac phantoms that resemble as closely as feasible the human chest, including attenuating and fillable organs"[1]. In order to address the problems associated with the validation studies of AC mentioned above, further validation studies are recommended.

3.4. Phantoms

New developments in both hardware and software techniques for attenuation correction must be carefully evaluated (or/and validated) under realistic conditions to improve results in clinical practice. Obviously, phantoms are a useful tool for evaluating problems where clinical studies are too complicated and expensive. The main advantage of using phantoms in validating studies is that the exact dimensions and functions of the

phantom are known. This provides a gold standard from which to evaluate image processing and reconstruction techniques (such as AC). A validation technique should involve simulating (or modelling) the imaging process and the patient anatomy (and or physiology). Accurate simulation of the human anatomy can be achieved by using hardware (physical) and software (computerized) phantoms. Using these phantoms it is possible to evaluate the attenuation correction on quantitative cardiac SPECT imaging.

In simulations using physical phantoms, the exact shape of the object is known but everything else is executed as in a real clinical study. In the use of computer-generated phantom, a synthetic object in the form of a 2D or 3D image can be generated and its projections can be computed by software program that simulate the acquisition performed by the tomograph. Such a program should also account for other factors such as the attenuation, in order to compute projections that are as close as possible to those obtained by a real scan. The resulting data from different simulations can then be reconstructed and compared. The advantage of this method is that the "ideal" image can be used as a reference in the evaluation of the effectiveness of an algorithm.

3.4.1 Physical phantoms

3.4.1.1. RSD phantom

The RSD (Radiology Support Devices), also known as the Alderson, phantom is a fully-tissue-equivalent anthropomorphic phantom which simulates an average male patient. It is made of a skeleton enclosing a chest region and embedded in a tissue-equivalence material with heart, liver, and lungs inserts simulating a semi-realistic thoracic human model (Figure 3-6(a)). The heart insert is accurately modelled using high-resolution patient data with slight modification to facilitate its use[13]. The narrow beam linear attenuation coefficient measured at 140 keV for all simulated tissue of this phantom were 0.160 cm^{-1}, 0.043 cm^{-1}, 0.280 cm^{-1}, for tissue, lungs, bone respectively. However, there are two limitations of this phantom; (1) The slight modification of the heart leads to a heart model might not simulate the real anatomy of the human heart, and (2) The attenuation coefficient values were claimed to simulate 140 keV, but when these values compared to some published values [37] (0.153 cm^{-1}, 0.051 cm^{-1}, 0.286 cm^{-1}, for tissue, lungs, bone respectively for 140 keV ^{99m}Tc only), it is clear that attenuation coefficient

[13] Normalcy rate is the ratio of the number of subjects with definitely normal or probably normal scans divided by the total number of subjects in the cohort (X100 for percentage)
[13] http://www.pi-medical.nl/rsd/rs-thorax.htm

value of tissue material cannot model the attenuation coefficients which reflect the ^{99m}Tc emission source.

3.4.1.2. Data Spectrum phantom

The Data Spectrum phantom consists of a cylindrical elliptical tank made of Plexiglas and different inserts (two lungs, bone, liver, and heart). The lung inserts are made of Styrofoam beads that have a density close to that of air (Figure 3-6(b)). The cardiac insert can be filled with radioactivity and filled with a simulated defect. This phantom has been widely used in the literature for evaluating non-uniform attenuation in cardiac SPECT.

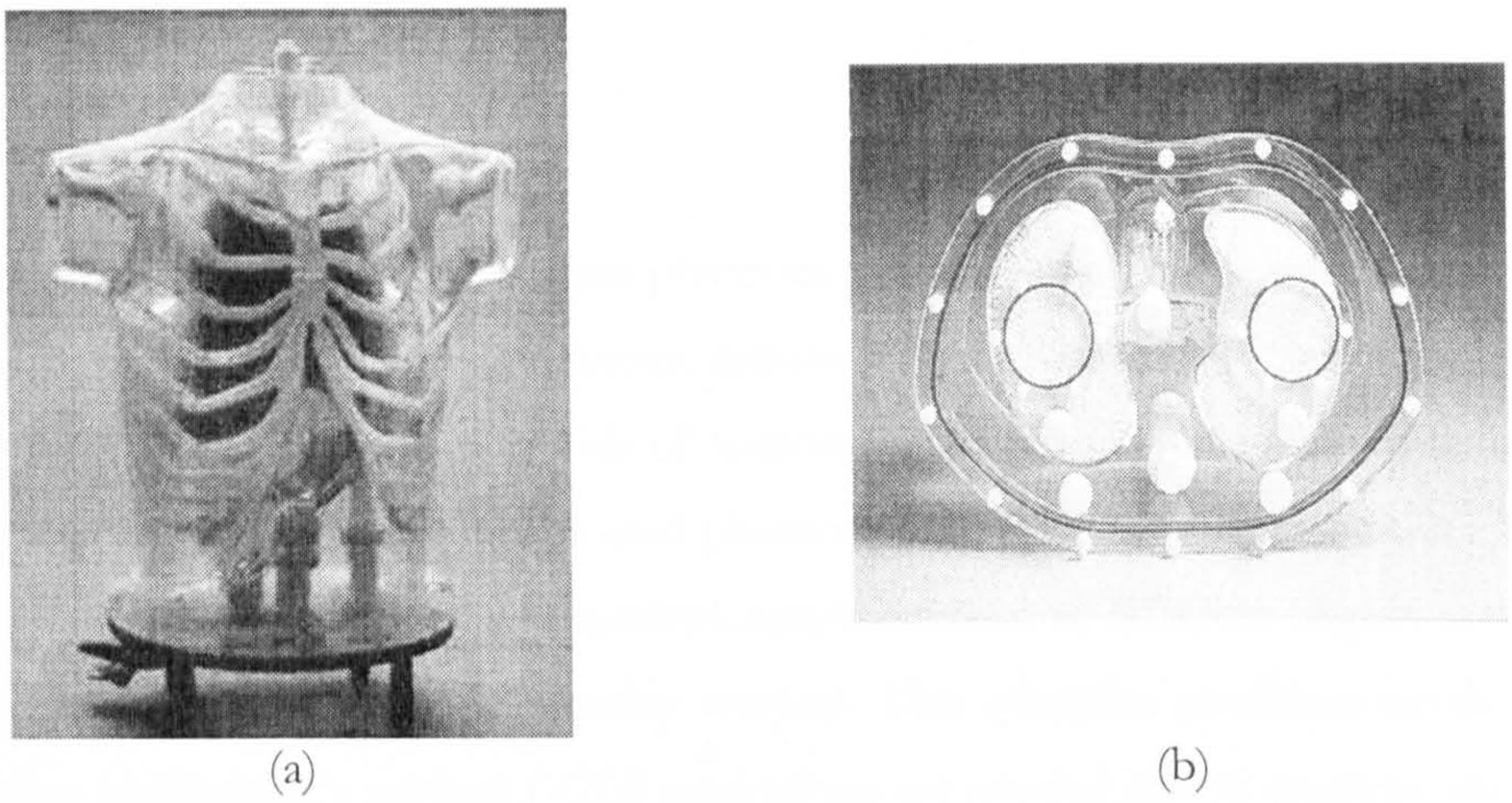

(a) (b)

Figure 3-6 Physical phantoms: (a) RSD phantom, and (b) Data Spectrum phantom.

3.4.2 Computerized phantoms

In general, computerized anthropomorphic phantoms can either be defined by mathematical (analytical function), or digital (voxel-based) volume arrays [101]. Analytic phantoms consists of regularly shaped continuous objects defined by combinations of simple mathematical geometries whereas voxel-based phantoms are mainly derived from segmented tomographic images of the human anatomy obtained by either x-ray CT or Magnetic Resonance Imaging (MRI) [102].

3.4.2.1. MCAT phantom

The Mathematical CArdiac Torso phantom is a popular 3D mathematical phantom used in medical imaging research and developed at the University of North Carolina at Chapel Hill .It models the internal organs of the human torso using a combination of geometric objects and surfaces, such as ellipsoids, cylinders, and planes, which are described by simple mathematical equations (Figure 3-7(a)). It permits modelling of different patient sizes, various shapes and compositions of female breasts, and one or two arms. The new 4D version of this MCAT phantom can simulate a dynamic, beating heart including changes in myocardial thickness and chamber volume [103]. Furthermore, it allows simulation of activity uptake from various radionuclide agents and for simulation of attenuation distributions corresponding to either mono-energetic or poly-energetic (spectrum) sources [104]. It has a great deal of flexibility and simplicity but is not very realistic.

3.4.2.3. NURBS phantom

The Non-Uniform Rational B-Splines phantom is a mathematically complex phantom, based on CT data from the visible human dataset (Figure 3-7(b)) [105]. It was developed to provide realistic and flexible models of anatomy and physiology to be used in nuclear medicine simulation. It is a sophisticated phantom, which can simulate the distribution of attenuation coefficients and radioactivity concentrations in different organs as well as motion, such as cardiac and respiratory motion. This complex phantom needs many parameters to describe a surface (>200 parameters are needed just to describe the heart surface [106].

The 4D version of NURSB was developed to simulate cardiac and respiratory motion. Tsui [105] investigated the effect of most common sources of involuntary patient motion (respiratory motion) in myocardial perfusion SPECT images using this 4D phantom. The respiratory motion was modelled by moving the diaphragm up and down in a sinusoidal fashion over an extent of 2 cm and by tilting of the rib cage (to simulate normal tidal breathing) over the emission and transmission data acquisition.

The simulated emission data including the effects of attenuation were then reconstructed using FBP (no AC) and OSEM algorithm with attenuation correction (5 iterations). The FBP reconstructed image of the simulated upward creep of 2 cm shows a reduced intensity at the inferior-septal wall and overlapped with the attenuation

artefacts in the same region. The upward creep motion artefacts remain after attenuation compensation

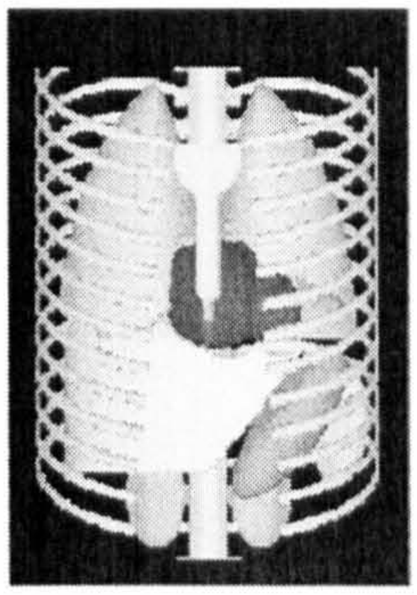

(a) MCAT phantom[14]

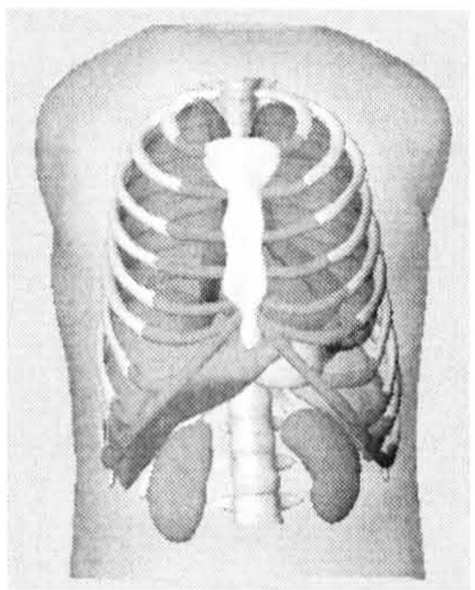

(b) NURBS phantom[15]

(c) Coronal slice through Zubal phantom[16]

Figure 3-7 Examples of computerized phantoms.

It is clear that the human anatomy is too complex to be realistically modelled using mathematical phantoms. A few research groups have successful constructed image-based models using advanced high resolution imaging techniques, such as CT and MRI.

3.4.2.4. Zubal phantom

Researchers at Yale University developed a digital voxel-based (or "voxel man") phantom, known as the Zubal phantom [107]. This 3D anthropomorphic phantom closely resembles a typical male anatomy (Figure 3-7(c)). Medical experts manually segmented the original x-ray CT images of a living human male into different types of tissue. Each voxel of the volume contains an index number designating it as belonging to a given tissue type. These indices can then be assigned a value, corresponding to, e.g. activity or attenuation coefficient. Although the voxel-based phantom is very realistic, it is very inflexible. However, it is still can be used to investigate the quantitative accuracy of different reconstruction algorithm and the effects of physical factors that degrade medical images.

[14] http://www.bme.unc.edu/mirg/mcat/

[15] http://elm.bme.unc.edu/~wsegars/

[16] http://noodle.med.yale.edu/zubal/

A number of methods (including both hardware and software) have been proposed for using non-uniform attenuation maps for SPECT attenuation correction. Each method has its own advantages and drawbacks, and no one method has been singled out as the standard. Some of these non-uniform attenuation techniques are commercially available and are expected to contribute greatly to the production of attenuation artefact-free, and quantitatively accurate, cardiac SPECT images. Cullom [78] expected that in the future AC techniques will become routine and make a valuable contribution to the diagnosis and management of patients with CAD. However, there is little information available about the validity of NUAC using the Hawkeye system. Also in general there are still some controversies regarding its usefulness in routine clinical cardiac SPECT studies.

In this thesis, simulation studies, a physical phantom experiment, and one patient study were performed to investigate the usefulness of NUAC for routine clinical cardiac SPECT. These validation studies of AC aimed to answer the question "Does AC produce quantitatively accurate cardiac SPECT images and does it introduce new unfamiliar artefacts".

Three phantoms were used in this thesis; (1) 2D simplified computer-generated phantom, (2) Zubal voxel-based phantom, and (3) Data spectrum hardware phantom. The Zubal phantom has been selected to be the main model in this thesis. In the first part of this thesis, 2D simplified models were used to obtain familiarity with AC and to identify the factors, which need to be considered when validating AC using the 3D realistic Zubal models. In the final part of this thesis, the hardware phantom and patient data were used to provide a comparison.

Chapter Four

Two-dimensional computer-simulated models

This chapter covers a series of experiments performed in order to validate AC using simulated two-dimensional (2D) simplified numerical models and to obtain familiarity with the two reconstruction algorithms (FBP and OSEM). In addition, the results of these investigations were used to identify the factors, which needed to be considered when AC was validated by using three-dimensional (3D) realistic models. The 3D models will be discussed in detail in chapter 5.

Four sets of experiments were performed using the 2D simplified computer-simulated models. Each experiment is presented separately with the summary of all the experiments discussed at the end of the chapter. The specific aims for each experiment are as follows:

Experiment	Aim(s)
1-Calculation of Scaling factor (Section 4.1)	To find out the additional scaling factor for both the FBP and OSEM reconstruction algorithms, and to demonstrate that this calculated scaling factor could be used to restore the counts per pixel in simulated data.
2-Elliptical uniform emission model without attenuation effect (Section 4.2)	To compare the two algorithms (FBP and OSEM) on reconstructing an elliptical emission model (No attenuation), and to verify how the number of iterations with OSEM affects the reconstruction of the emission image.
3-Left Ventricle (LV) emission model with and without AC. (Section 4.3)	To validate AC using 2D LV emission model with both uniform and non-uniform attenuation models.
4-The effect of additional attenuation from breasts, arms, and the scanning couch on AC. (Section 4.4)	To test the effects of adding these attenuating objects (breasts, arms, and scanning couch) on the non-uniform AC in a realistic 2D segmented model

All models were generated using the Link Medical software (MAPS 10000 version 5.4) and Sun workstation (SPARC station 4 and Solaris open windows version 3.6).

The first simulation was based on a 2D elliptical uniform emission model with homogenous activity and no attenuation. The second simulation is a 2D ring emission model representing the left ventricle (LV), and with and without elliptical transmission models (providing both uniform and non-uniform attenuation maps). Also, a non-uniform attenuation model was simulated from the segmentation of a patient CT slice. No scatter effects and noise effect were simulated in this model. The two reconstruction techniques used were the FBP and OSEM algorithms. The projection data of both algorithms were generated by using a C-based program called "fwdprj" which was developed by Professor David Barber (Appendix A). The projection images can then be filtered (only a Ramp filter was used in this chapter), and back-projected to produce FBP axial images. The OSEM algorithm is a commercial algorithm based on an iterative reconstruction algorithm (a block iterative version known as Ordered Subset Expectation Maximization) [36] (Appendix B). Because of the main interest in iterative reconstruction algorithm is the noise amplification as the number of iterations increases, we focus here on increasing the number of iterations and keeping the number of subset constant (one subset). Although, when using one subset in OSEM algorithm is equivalent to MLEM algorithm, we decided to name all the images reconstructed with one subset and different number of iteration as images reconstructed by OSEM algorithm. However, in chapter 5, the impact of changing both the number of subsets within OSEM algorithm on AC images will be studied.

4.1. Calculation of scaling factor

4.1.1 Forward-projection "fwdprj" program

The planar (projection) images profiles were constructed by using a C-based program called "fwdprj". This program takes an emission image and an attenuation (transmission) image of the same resolution and constructs projection images by forward projection.

The emission image, which typically has a resolution of 256×256 or 512×512 pixels, is an image of the distribution of radioactivity. The pixel values represent Bequerels per pixel. The attenuation image is in terms of linear attenuation coefficients. The pixel

dimensions are assumed to be 1×1 mm in all cases. Thus to simulate a chest with a diameter of 40-50 cm, a 512×512 image was large enough.

The values in the emission image can be of arbitrary magnitude, and represent different concentrations of radioactivity. However, the values in the attenuation image represent true attenuation values. In all simulations, the convention that 100 represent an attenuation coefficient of 0.1 cm^{-1}, was followed. Therefore a value of 153 (0.153 cm^{-1}) was used to represent the attenuation for ^{99m}Tc in tissue.

Clinically the projected counts are stored in a pre-selected matrix size. The matrix size is always a power of two, typical values being 64×64, 128×128, 256×256 and 512×512. Each pixel in the matrix is designed to accommodate a maximum number of counts depending on the acquisition mode. There are two common types of acquisition mode; byte and word modes[17]. The byte mode allows 8 bits per pixel and the word mode typically allows 16 bits per pixel (Link software uses 16 bits per pixel). The data is normally considered as an unsigned integer. Therefore, in byte acquisition mode, the pixel values can register no more than 256 (2^8) counts, and a word acquisition mode can register over 65000 (2^{16}) counts. In situations where the number of events recorded in a pixel exceeds the capacity of the system, pixel overflow artefacts appear. Overflow effect needs to be eliminated before starting to process the simulated models.

4.1.2 Scaling factor

When using "fwdprj" program, the projection data is stored on disc in integer format (to make it compatible with Link Medical data storage conventions). In order to accommodate projection values, which exceed the maximum value storable in integer form the "fwdprj" programme scales the projection data and stores the multiplication factor with the data in the image header of the projection data. This multiplication factor (S) can be used to restore the post-reconstruction pixel value to its original value (pre-reconstruction). When axial images are reconstructed from projection data using both FBP and OSEM, ideally the final image should represent the activity distribution in Bequerels per pixel.

[17] Other systems sometimes use an intermediates value of 12 pits per pixel.

In practice the activity distribution will not be quantitatively accurate for two main reasons. Firstly, the projection data is scaled with the internal scaling factor and the axial image data needs to be rescaled with the multiplication factor to undo this. Secondly, there will be an additional scaling factor specific (SF) to the details of both the FBP and OSEM algorithms. This additional scaling factor is harder to derive theoretically so it will be derived experimentally before starting simulation. This additional scaling factor will be used in all subsequent simulated experiments to restore the post-processing pixel count values to their "true" value.

4.1.3 Method

To calculate the additional scaling factor (SF), a simple 2D numerical model was used. It simulates a uniform elliptical chest model, which has the dimensions of 342×228 mm [108]. Figure 4-1 shows the uniform model with a resolution of 512×512 and a pixel value of one count per pixel.

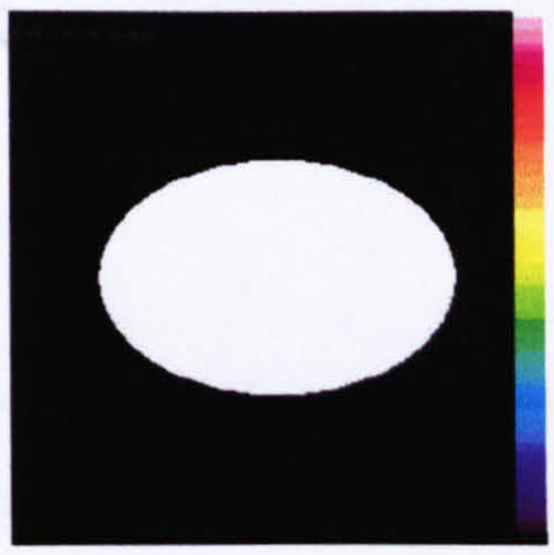

Figure 4-1 2D uniform emission model.

This uniform model was used to simulate different emission models with different pixel values ranging from 10 to 1000 counts per pixel. Each 2D model represents an emission image with uniform uptake values. The model was reconstructed using the "fwdprj" program with parameters and flags representing an emission image of one slice, 128 projections, and 128 bins over 360°. The output images were filtered (using a Ramp filter) and converted into an axial FBP image Figure 4-2(a). The same projections were used to reconstruct an OSEM (using one subset and eight iterations) image as shown in Figure 4-2(b).

(a) FBP

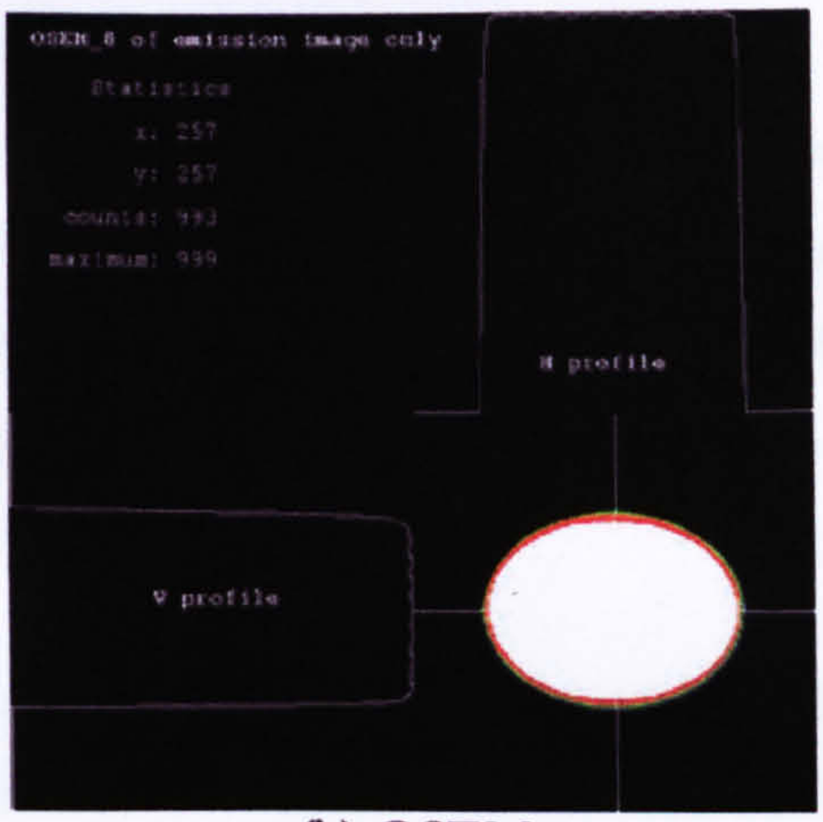

(b) OSEM
(Count density profiles are shown)

Figure 4-2 Emission uniform model (without attenuation) reconstructed by (a) FBP and (b) OSEM algorithms.

The maximum counts in ellipse region of interest in the reconstructed images and other factors, which are shown in Table 4-1, were used to calculate the additional Scaling Factor (SF) as shown in Eqn 4-2.

$$SF = \left[S \times \left(\frac{A}{P} \right) \right] \times \frac{1}{V} \qquad \text{Eqn. 4-1}$$

Where

S is the internal multiplication factor stored in the header file of the planar data.

A is the additional associated factor with FBP

P is the number of profiles (=128)

V is the volume of each pixel (=64)

The additional associated factor with FBP (A) was calculated as shown in Eqn 4-2

$$A = \left[\frac{(V \times C)}{B} \right] \times \frac{P}{S} \qquad \text{Eqn. 4-2}$$

Where

S is the internal multiplication factor stored in the header file of the planar data.

P is the number of profiles (=128)

V is the volume of each pixel (=64)

B is the maximum counts in ellipse ROI after reconstruction

C is the maximum counts in ellipse ROI before reconstruction

4.1.4 Results

Figure 4-2 shows that the OSEM algorithm produced a more uniform image, free from streaking artefacts. In comparison to the FBP algorithm, OSEM produces count density, which agrees closely with the original emission model shown in Figure 4-1. Although the scaling factor was applied to both algorithms, FBP produces a lower count density since the process only applies a Ramp filter.

The FBP and OSEM axial images were compared using count density profiles (horizontal and vertical curves), (Figure 4-3). These show some edge artefacts for the image reconstructed by the OSEM algorithm.

The reconstructed images shown in Figure 4-2 and Figure 4-3 were only made for one emission model with 1000 counts per pixel. The calculation results of the other emission models with different uptake values are summarised in Table 4-1 (The values are also presented in Figure 4-4).

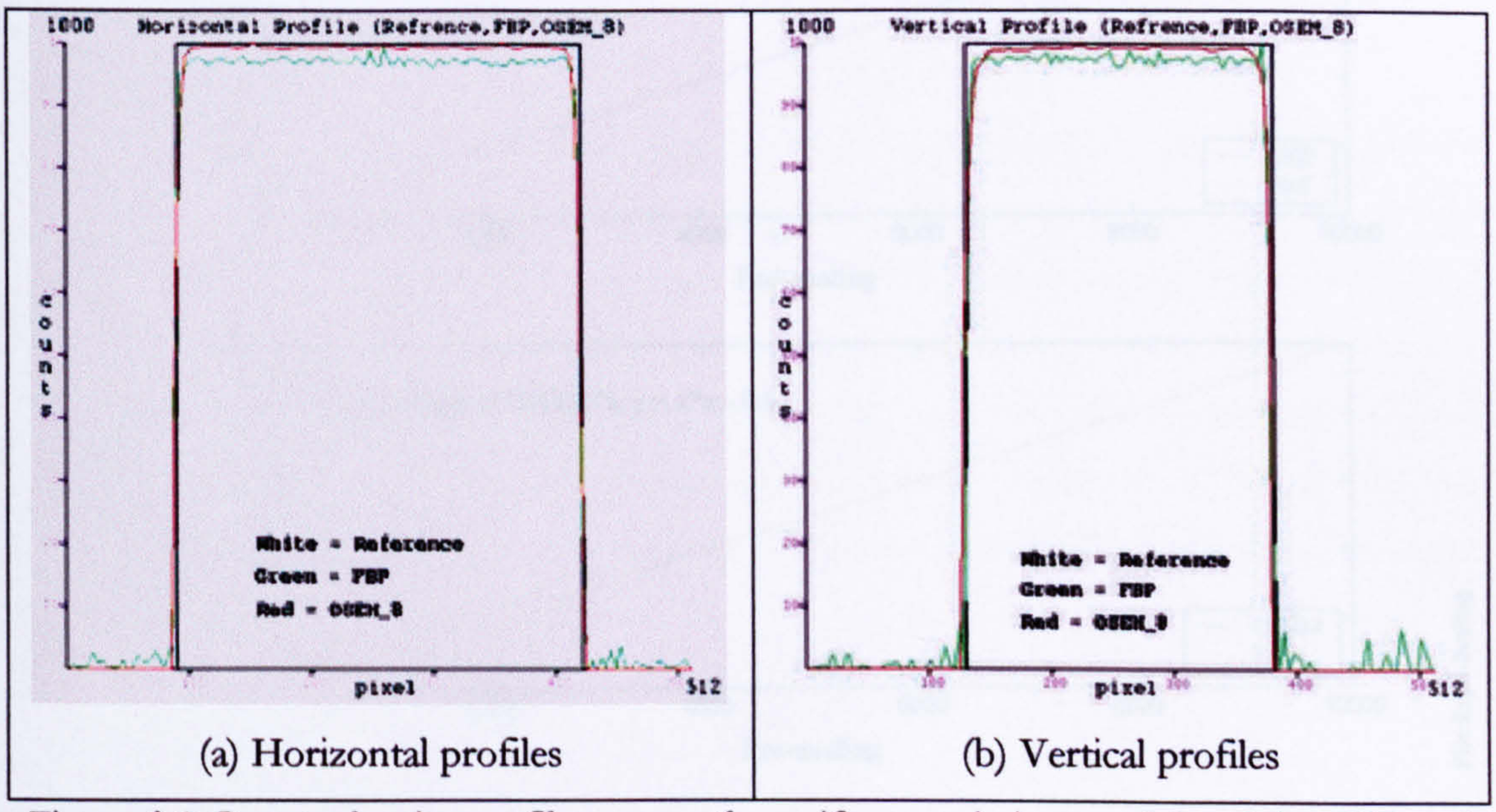

(a) Horizontal profiles (b) Vertical profiles

Figure 4-3 Counts density profiles across the uniform emission model and the FBP and OSEM reconstructed images.

In Table 4-1, the internal multiplication factor was obtained from the header file of the planar data. The maximum counts inside the elliptical region were measured pre and post application of the calculated scaling factor and are shown in Figure 4-4. The results

show that applying the calculated scaling factor can restore the mean counts back to their original values before reconstruction.

Table 4-1 Calculated Scaling Factors and the restored count values for both FBP and OSEM reconstructions.

							Counts/Pixel (After applying *SF*)	
C	*S*	*B*	*P*	*V*	*A*	*SF*	FBP	OSEM
10	54.84	1532	128	64	0.975	0.006526	8	9
100	548.40	1532	128	64	0.975	0.06526	96	98
1000	5484.00	1532	128	64	0.975	0.6526	976	998
10000	54840.00	1532	128	64	0.975	6.526	9779	9994

P = number of profiles (=128)
S = Internal multiplication factor
V = volume of each pixel (4×4×4=64)
C = counts/pixel (pre-reconstruction)
B = counts/pixel (post-reconstruction)
A = additional factor associated with FBP

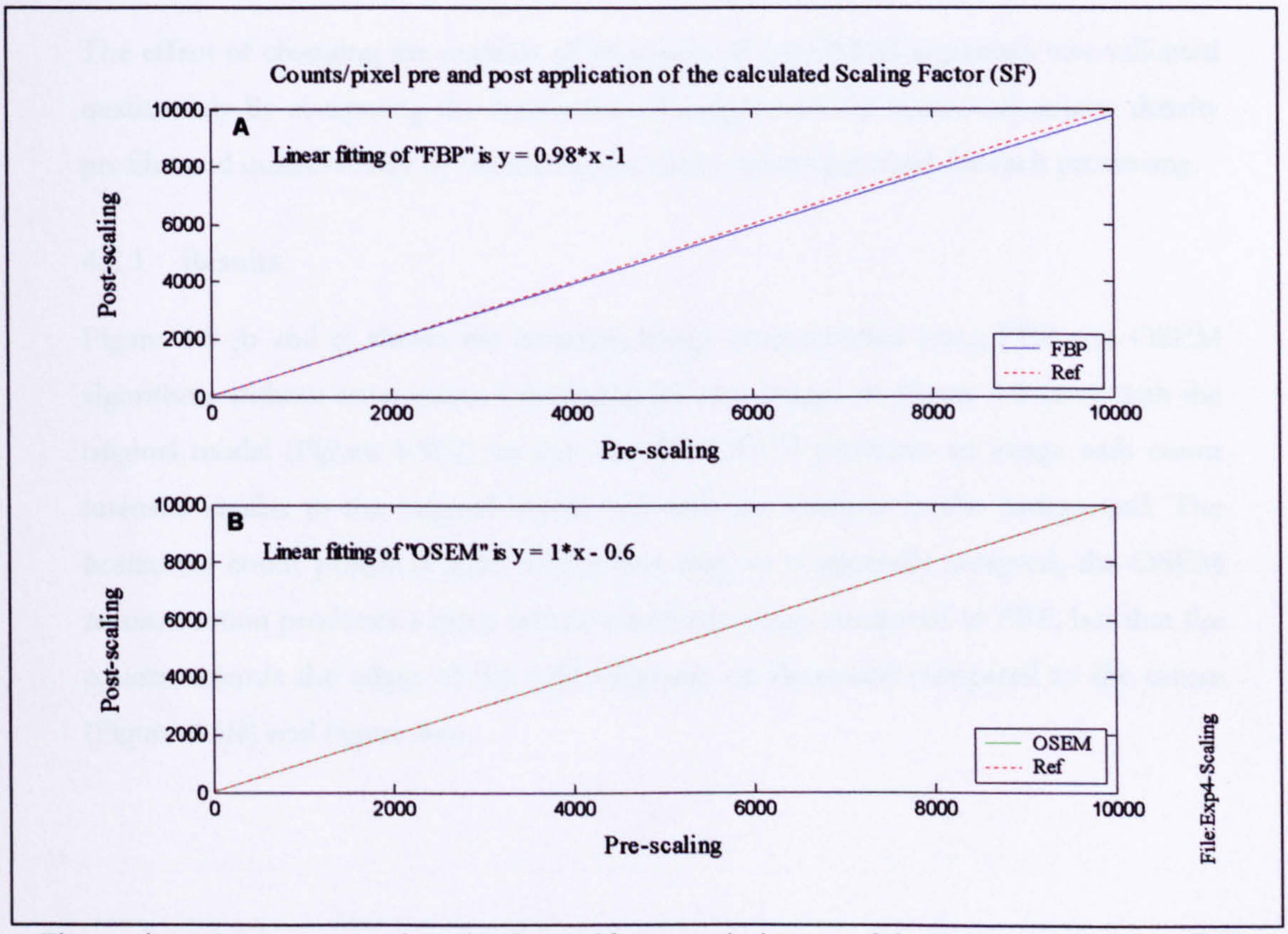

Figure 4-4 Mean count values in the uniform emission model reconstructed with FBP and OSEM algorithm before and after applying the calculated Scaling Factors (SF).

As it is illustrated in Figure 4-4, the mean counts values were restored 100% with OSEM and 98% with FBP algorithm. This is evident from the linear fit shown in Figure 4-4

The results showed that the application of the calculated scaling factor (SF) could accurately restore the post-reconstruction pixel value of both FBP and OSEM algorithms to its original value (pre-reconstruction).

4.2. Elliptical uniform emission model without attenuation effect

A two-dimensional numerical elliptical model was generated (Figure 4-5(a)). This simulates a cross section through the thorax, with the ellipse representing uniform activity in the body with 300 counts per pixel (this pixel value was selected based on the pixel value in the LV should exceed 200 counts for a ^{99m}Tc)[18].

The emission model was reconstructed using the FBP and OSEM (one subset and three iterations) reconstruction algorithms (Figure 4-5(b-c)). The reconstructed image was multiplied by the scaling factor as calculated using the formula determined in section 4.1.

The effect of changing the number of iterations of the OSEM algorithm was validated qualitatively by comparing the reconstructed images and the horizontal counts density profiles and quantitatively by measuring the mean counts per pixel for each processing.

4.2.1 Results

Figure 4-5 (b and c) shows the emission image reconstructed using FBP and OSEM algorithms without attenuation. Comparing the two images on Figure 4-5 (b-c), with the original model (Figure 4-5(a)) we can see that OSEM produces an image with count intensity similar to the original model and with no artefacts in the background. The horizontal count profile (Figure 4-6) shows that, as is generally accepted, the OSEM reconstruction produces a more accurate uniform image compared to FBP, but that the counts towards the edges of the OSEM image are decreased compared to the centre (Figure 4-5(c) and Figure 4-6).

[18] http://www.belnuc.be/pages/download/Guidelines_Cardio.pdf

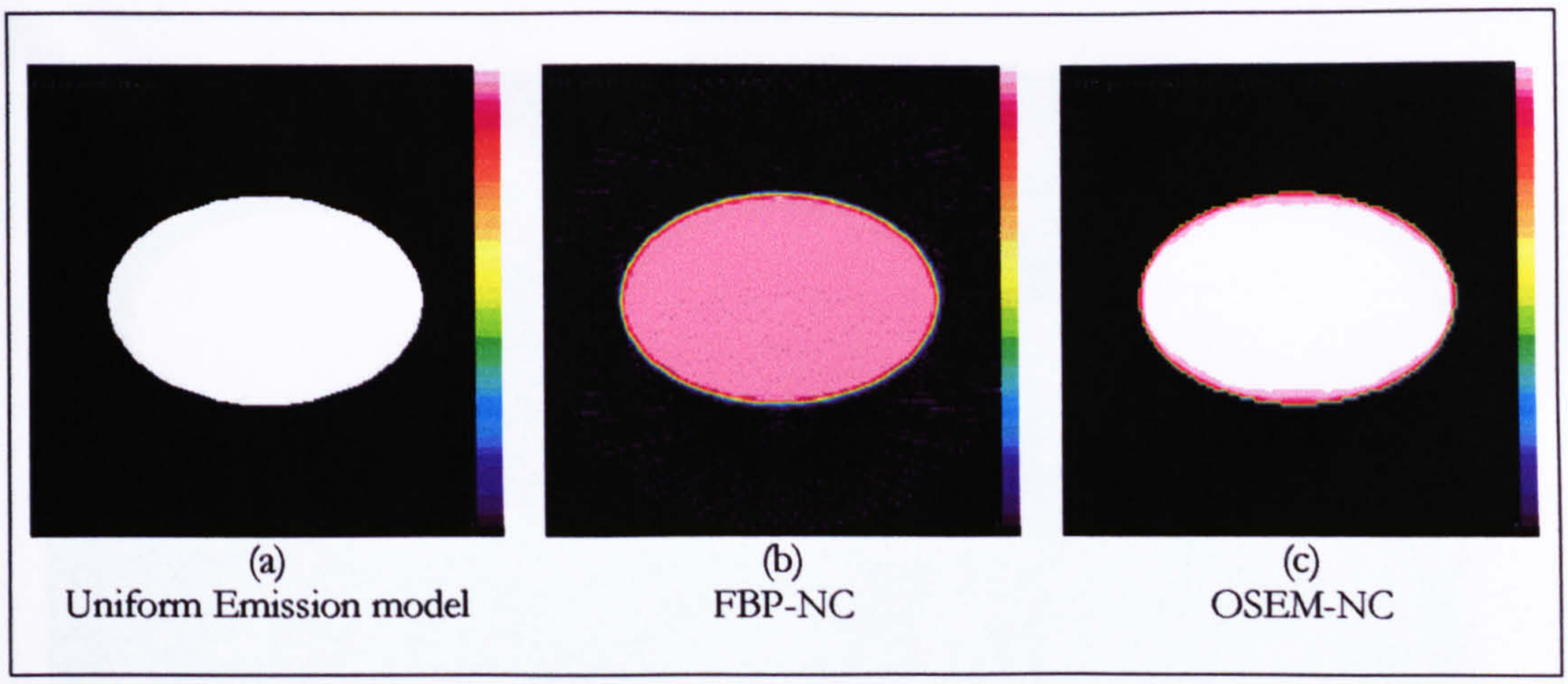

Figure 4-5 Reconstructed transaxial slices of uniform emission model.

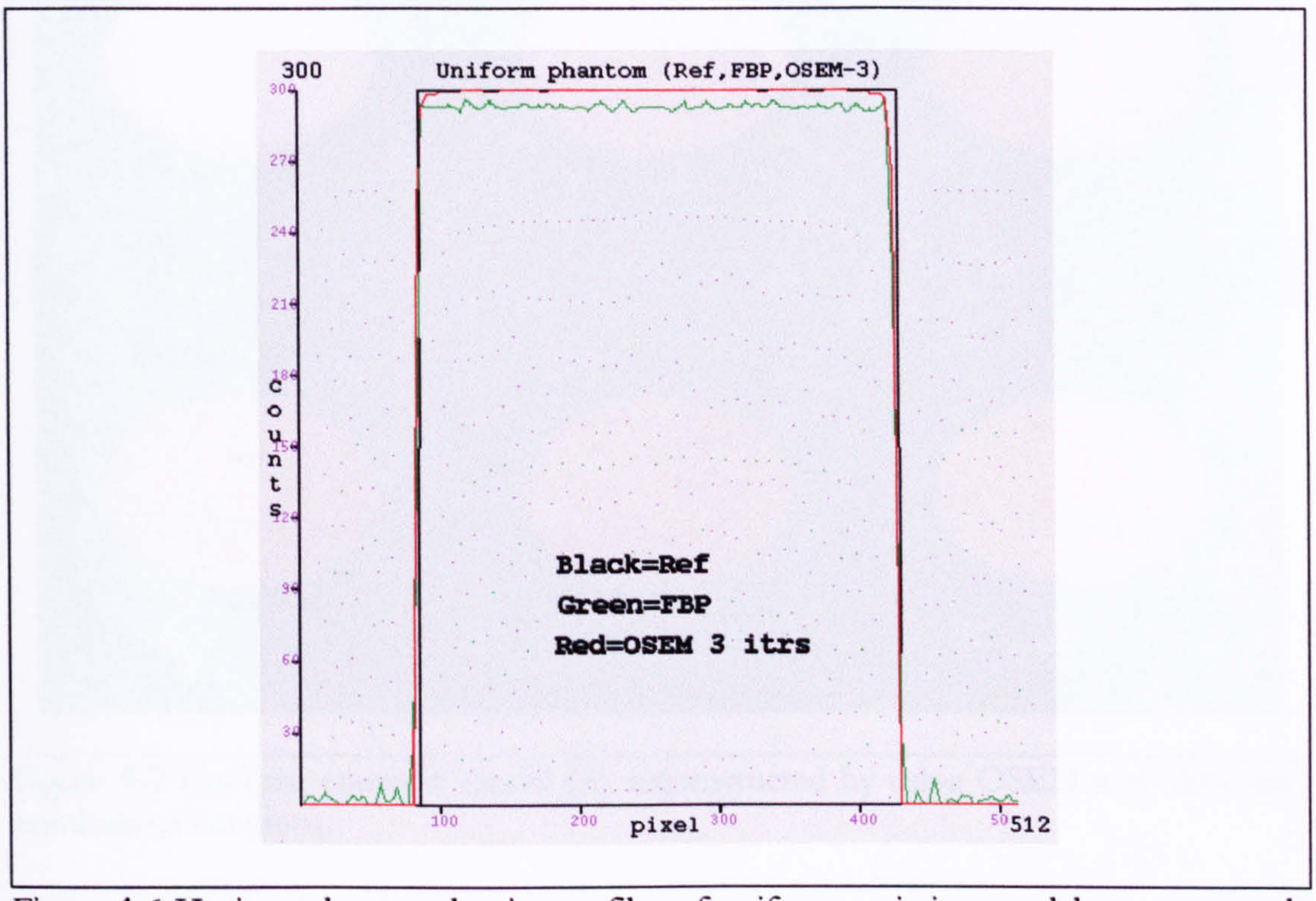

Figure 4-6 Horizontal count density profiles of uniform emission model reconstructed by FBP and OSEM.

This experiment shows that OSEM produces count profiles, which match the counts of the original model in the centre and with some count reduction at the edges.

Figure 4-7 shows OSEM reconstruction of the emission model shown in Figure 4-5(a), using different numbers of iterations. As is clearly seen, as the number of iterations increases beyond 6, artefacts (fluctuating peaks) start appearing with increasing peaks toward the edges of the reconstructed image (Figure 4-8).

Figure 4-7 Uniform emission model (A) reconstructed by using OSEM with different numbers of iterations.

It can be seen from Figure 4-8, that as the number of iterations increases, the counts per pixel in the emission image are not uniform as in the original image (fluctuating green curve in comparison with the flat black curve of the original image). For each image shown on Figure 4-8, the mean and maximum counts per pixel (after applying the Scaling Factor) are shown in Table 4-2 and Figure 4-9.

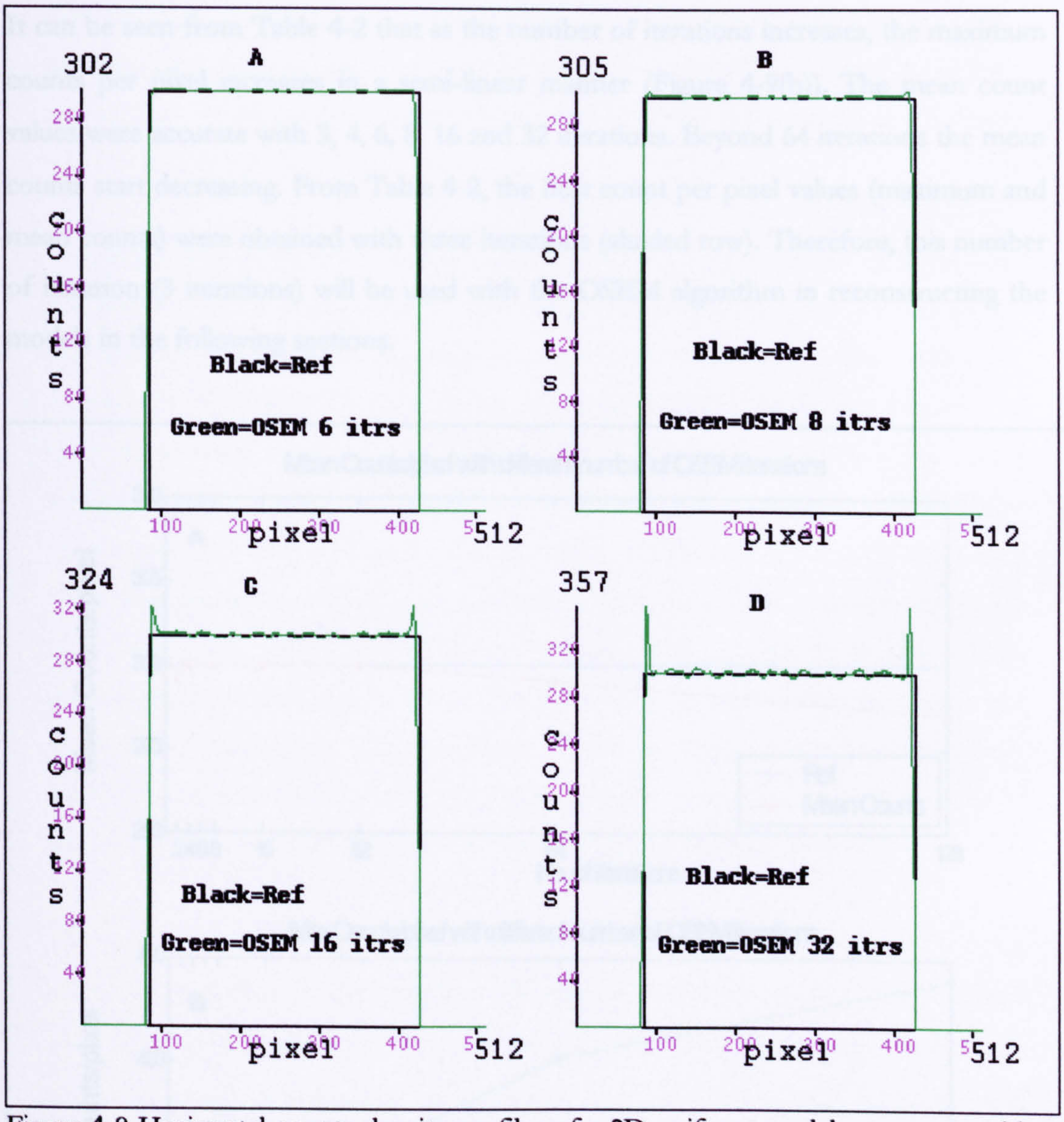

Figure 4-8 Horizontal counts density profiles of a 2D uniform model reconstructed by using OSEM with different number of iterations.

Table 4-2 Mean and maximum counts in the uniform image (no attenuation) reconstructed by OSEM with different number of iterations.

	OSEM (After applying Scaling Factor)	
Number of iterations	Mean Counts	Maximum counts
2	299	300
3	300	300
4	300	301
6	300	302
8	300	305
16	300	324
32	300	357
64	299	402
128	297	439

It can be seen from Table 4-2 that as the number of iterations increases, the maximum counts per pixel increases in a semi-linear manner (Figure 4-9(b)). The mean count values were accurate with 3, 4, 6, 8, 16 and 32 iterations. Beyond 64 iterations the mean counts start decreasing. From Table 4-2, the best count per pixel values (maximum and mean counts) were obtained with three iterations (shaded row). Therefore, this number of iteration (3 iterations) will be used with the OSEM algorithm in reconstructing the models in the following sections.

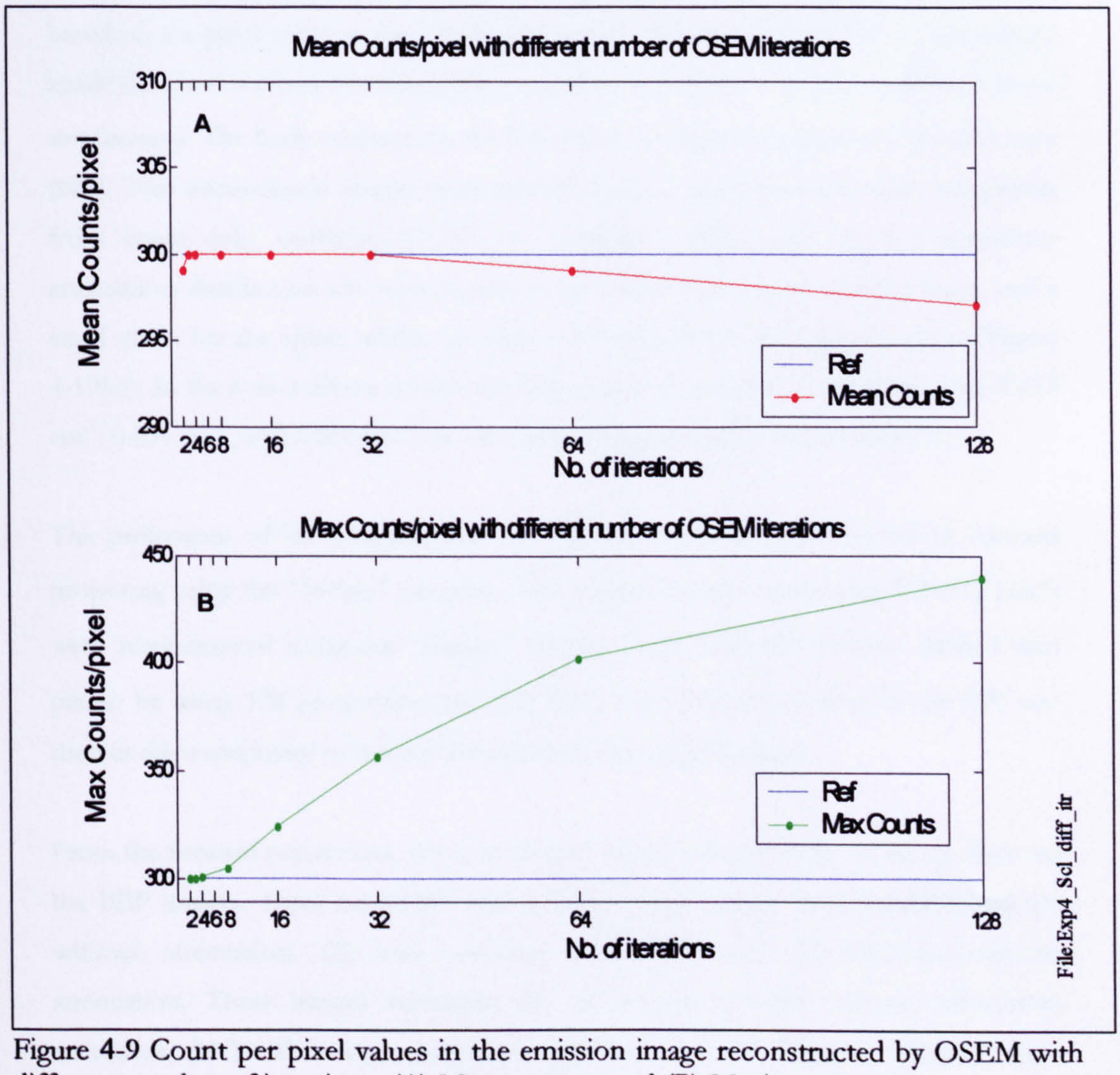

Figure 4-9 Count per pixel values in the emission image reconstructed by OSEM with different number of iterations. (A) Mean counts, and (B) Maximum counts.

4.3. Validation of AC using 2D left ventricle emission model.

In this section, 2D computer generated models were used to perform three experiments; the simulated left ventricle emission model was reconstructed without attenuation and

with two types of attenuation distribution maps. The attenuation maps were 2D images representing a uniform and non-uniform attenuation distribution inside an elliptical region. The two reconstruction algorithms used were FBP (no attenuation correction) and OSEM (with AC).

Two-dimension numerical models were generated representing emission and transmission (attenuation) images. The emission model (activity uptake in LV myocardium) was simulated as a ring–shaped left ventricle chamber and a LV cavity with no activity (Figure 4-10(a)) with 300 counts per pixel (this pixel value was selected based on the pixel value in the LV should exceed 200 counts for a ^{99m}Tc). The uptake inside the chest was not simulated (Photon scatter and noise were not modelled in these simulations). The body contour for the transmission image was elliptical (342×228 mm) [108]. Two transmission images were modelled; (1) a uniform ellipse with attenuation from tissue only, coefficient=0.153 cm^{-1} (Figure 4-10(b)), and (2) a non-uniform attenuation distribution was represented by two ellipses associated with the lungs, and a small circle for the spine, within an ellipse for the soft tissue inside the chest (Figure 4-10(c)). In the non-uniform attenuation map, linear attenuation coefficients were 0.153 cm^{-1}, 0.051 cm^{-1}, and 0.286 cm^{-1} for soft tissue, lungs and bone respectively [37].

The projections of the emission and transmission data were constructed by forward projecting using the "fwdprj" program. The original models comprising 512×512 pixels were reconstructed using the "fwdprj" program into 128×128 matrices (with 4 mm pixels) by using 128 projections, and 128 bins over 360°. The scaling factor (SF) was used in this experiment to restore the counts to the original values.

From the forward projections, the axial images were produced using the Ramp filter for the FBP images. Three axial FBP Left Ventricle (LV) images were reconstructed; (1) without attenuation, (2) with uniform attenuation, and (3) with non-uniform attenuation. These images represent the LV emission model without attenuation correction (NC). The same projections produced by the "fwdprj" program were reconstructed using OSEM (one subset and three iterations) algorithm. Again using three scenarios; (1) without attenuation correction, (2) with uniform attenuation correction (UAC), and (3) with non-uniform attenuation correction (NUAC). The LV

emission image with non-uniform attenuation was also reconstructed using different numbers of OSEM iterations in order to study the effect on AC.

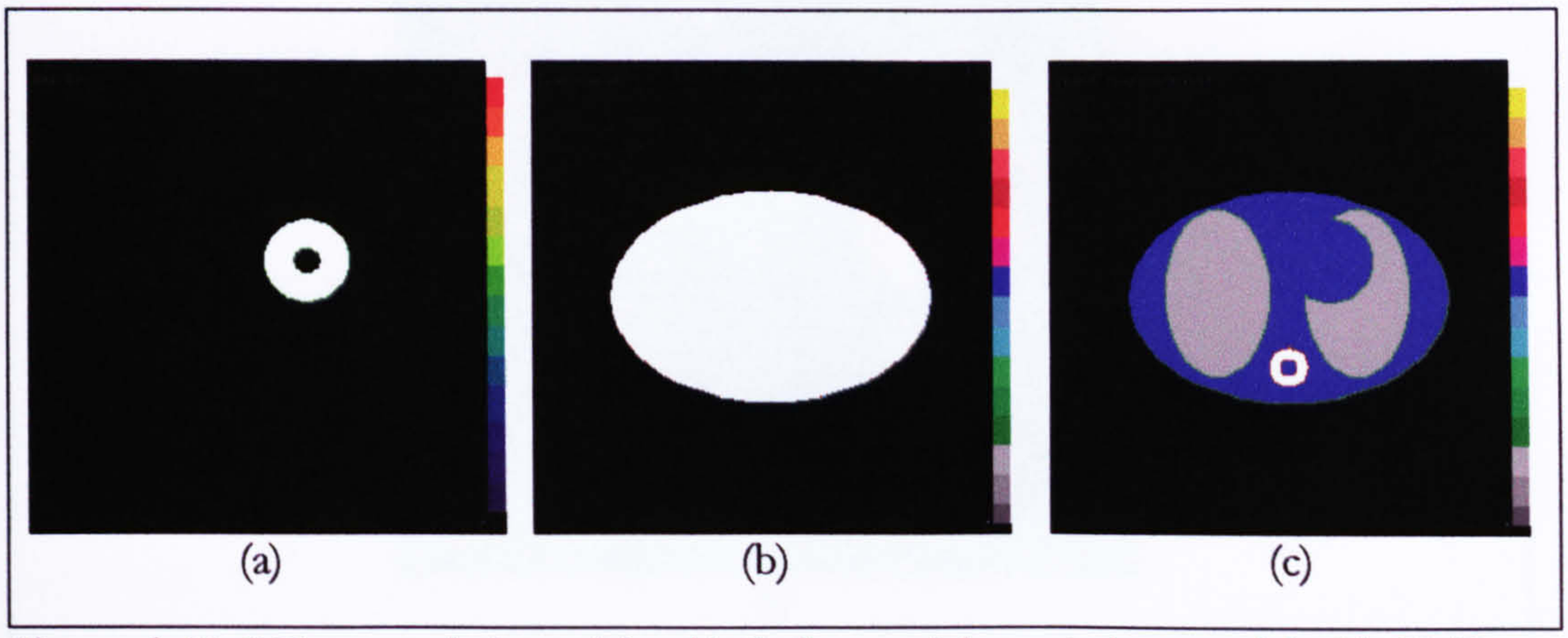

Figure 4-10 2-D numerical models: (a) Left ventricle emission model. (b) Uniform attenuation map model. (c) Non-uniform attenuation map model.

The reconstructed images were evaluated quantitatively by using count density profiles and measured mean counts in four regions of interest (Figure 4-11(b)). Two count density profiles were drawn through the left ventricle image; one vertical profile, which passes through the anterior and posterior walls of the LV image, and a horizontal line profile, which passes through right and left walls (Figure 4-11(a)). Four elliptical regions of the same size were marked at four locations in the left ventricle image corresponding to the anterior, right, posterior, and left walls (Figure 4-11(b)). These ROIs and counts density profiles were used for all of the evaluation in this chapter.

The mean counts pre and post-processing were compared in terms of the percentage change. These were used to; (1) compare FBP and OSEM reconstruction of a LV emission model with and without attenuation, and (2) find out how accurately OSEM reconstructs the LV emission model with and without correcting for the attenuation effect from uniform and non-uniform attenuation maps, and (3) find out the effects of changing the number of iterations within OSEM when non-uniform attenuation correction is incorporated

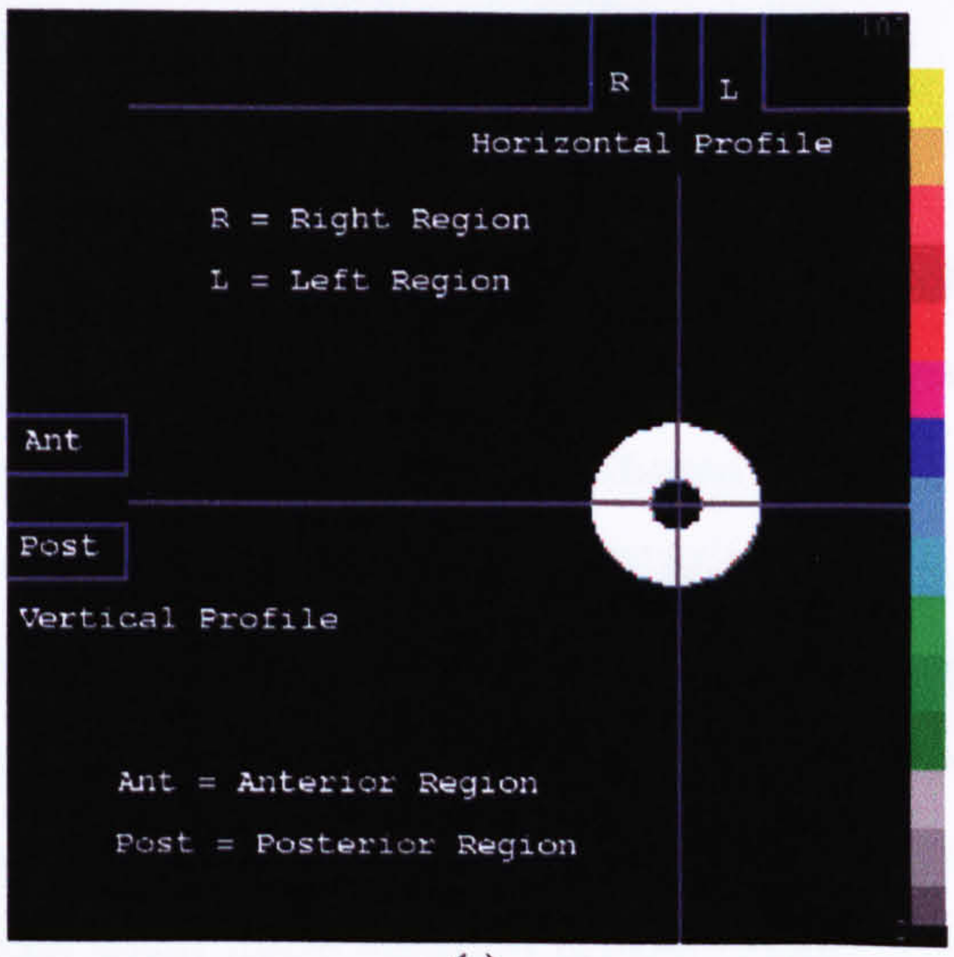

(a)

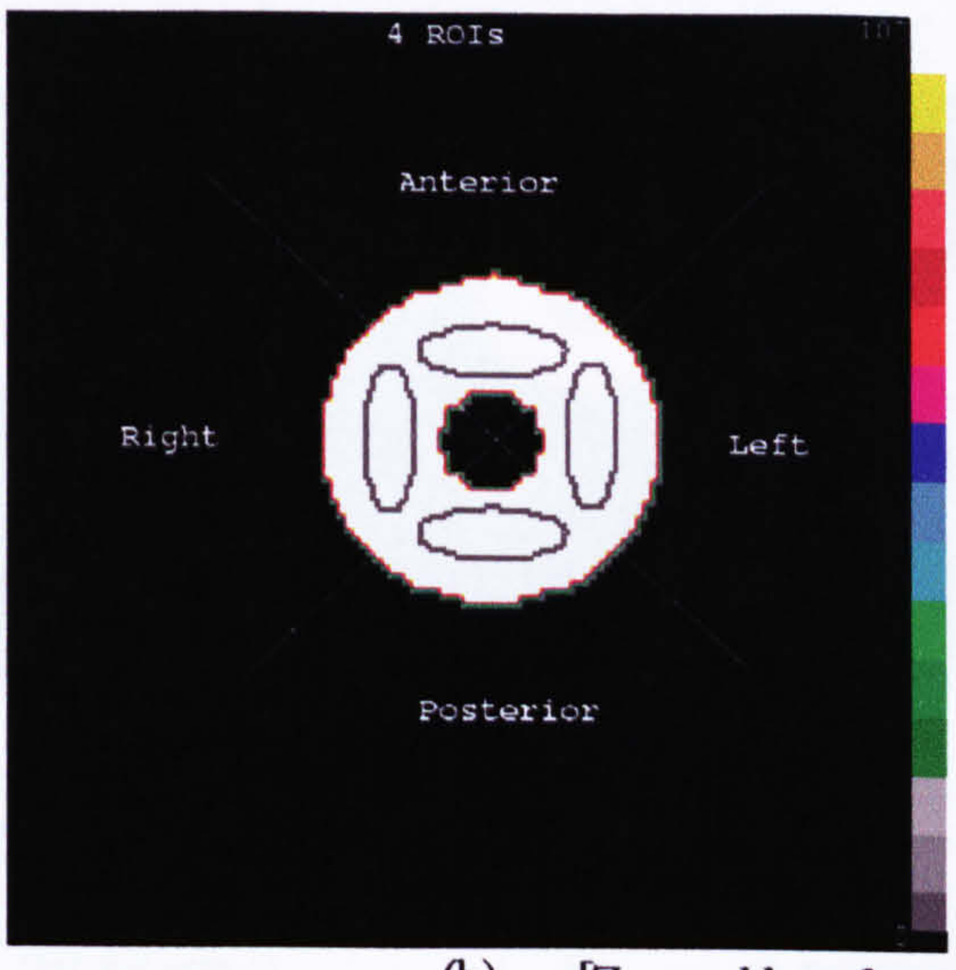

(b) [Zoomed by a factor of 2]

Figure 4-11 (a) Counts density profiles and (b) the position of the four ROIs inside LV model.

The quantitative comparison was performed by using the count density profiles and by using the percentage change over the four regions of the LV emission model (Figure 4-11(b)).

$$\%Change = \left[\frac{(C_{Measured} - C_{True})}{C_{True}}\right] \times 100 \qquad \text{Eqn. 4-3}$$

Where $C_{Measured}$ is the measured mean counts in the ROI after reconstruction and the C_{True} is the mean counts in the ROI in the original model.

4.3.1 Results

4.3.1.1. Left ventricle emission model without attenuation effect

As shown in Figure 4-12(b-c), the FBP-NC reconstruction produces an image with streak artefacts and the OSEM-NC produces a ring free of streak artefacts. Figure 4-13 shows the count density profiles of the images shown on Figure 4-12. As can be seen from Figure 4-13, the counts density of the OSEM-NC image is close to the counts density of original model than is the FBP image. Also, the counts density of the OSEM image shows lower contrast than FBP image, this was due to the small number of iterations (3 iterations) used with OSEM. The contrast of OSEM image shows an improvement in contrast when more iteration is used (Figure 4-15).

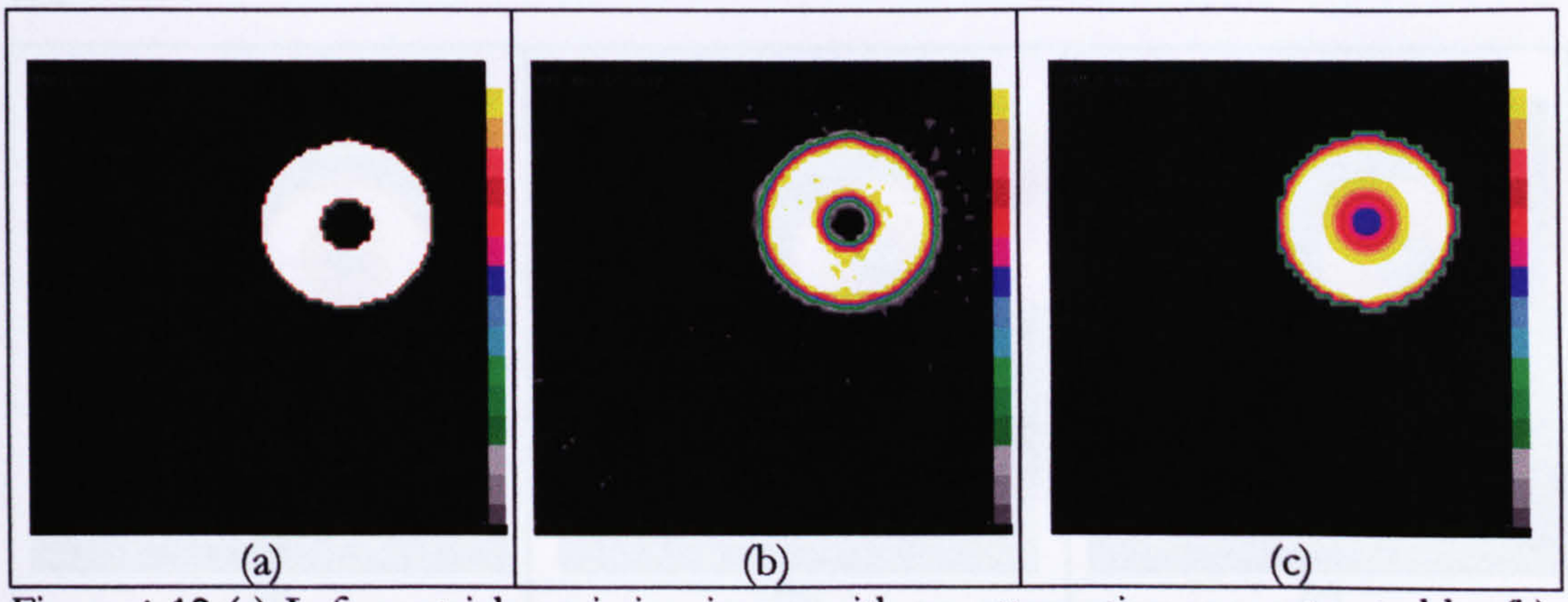

Figure 4-12 (a) Left ventricle emission image with no attenuation reconstructed by (b) FBP-NC and by (c) OSEM-NC.

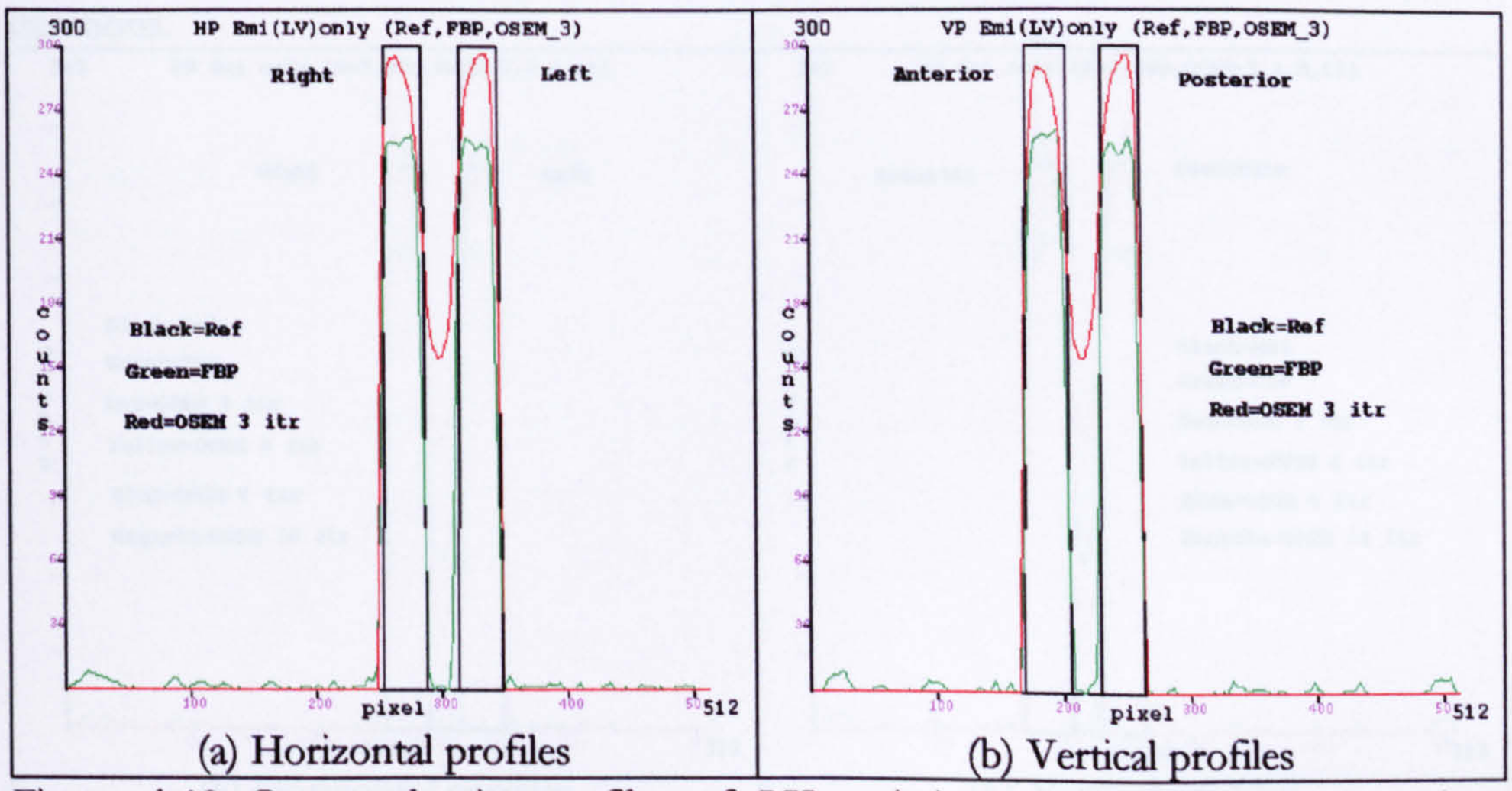

Figure 4-13 Counts density profiles of LV emission model without attenuation reconstructed by FBP-NC and OSEM-NC algorithms.

Figure 4-13 shows that the count density profile curves of the image reconstructed by FBP-NC are lower than the reference image in all regions with a percentage change of -15% (Table 4-3). Table 4-3 shows the counts per pixel and the percentage change of mean counts in the four LV regions of the images shown in Figure 4-12. Also, the curves in Figure 4-13 show that, OSEM-NC produces a count density close to the reference model before reconstruction with a percentage change of -4.65% in all regions and a maximum percentage change of -6.0% at the anterior region (as shown on Table 4-3). The possibility of improving the counts in all LV regions, and especially the counts in the anterior region, is discussed next.

The emission model reconstructed by OSEM-NC with 4, 8, and 16 iterations are shown in Figure 4-14. Also, the count density profiles of these images are shown on Figure 4 -15

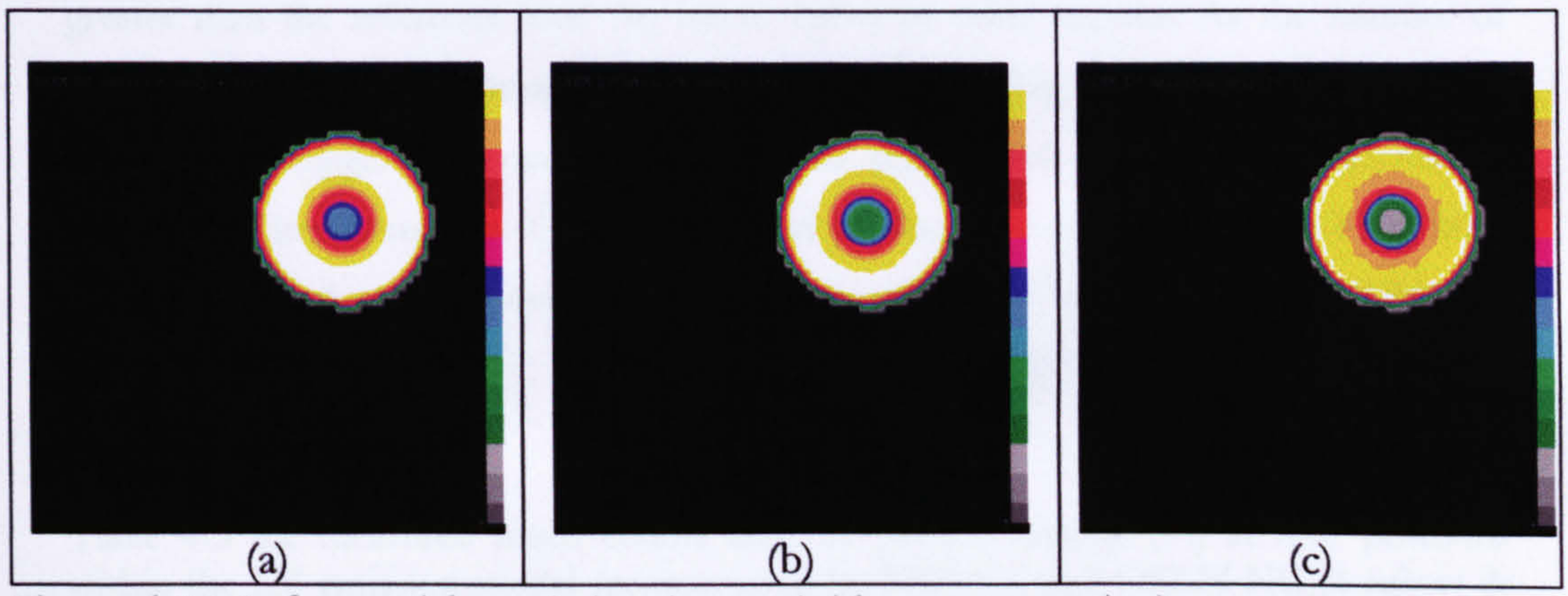

Figure 4-14 Left ventricle emission image (with no attenuation) reconstructed using OSEM with different number of iterations; (a) 4 iterations, (b) 8 iterations, and (c) 16 iterations.

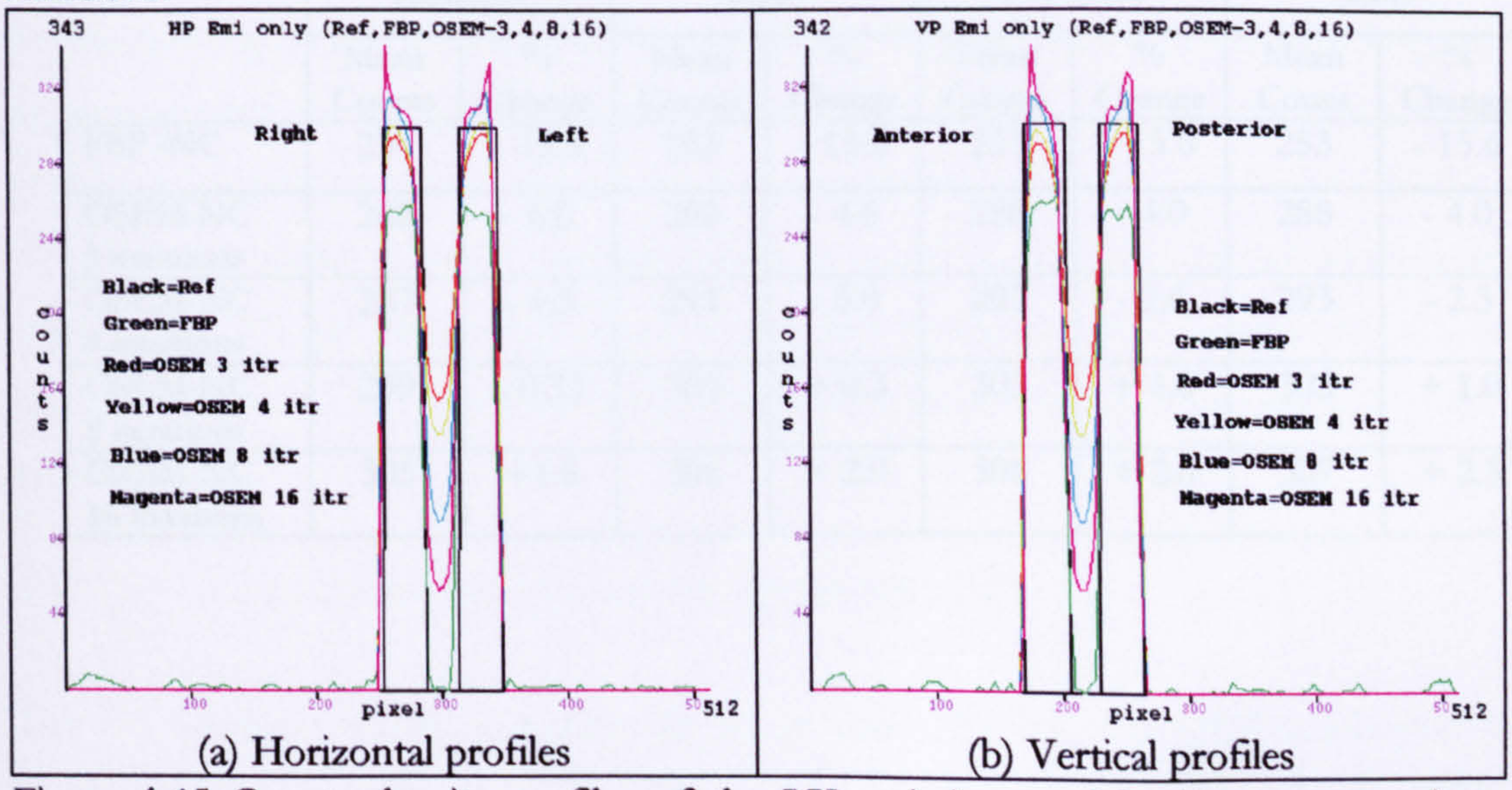

Figure 4-15 Counts density profiles of the LV emission model without attenuation, reconstructed by OSEM with different number of iterations.

As can be seen from Figure 4-14 and Figure 4-15, as the number of iterations is increased, the counts in the image are increased toward the edges and the edge artefacts become more prominent. The selection of the number of iterations is based on the finding that as the number of iterations increased to 8, some ring-like artefacts are seen at the boundary of the LV image and the percentage change of mean counts exceed the reference mean counts (Figure 4-15). Thus, for this LV ring emission model reconstructed by OSEM-NC, 3 or 4 iterations are enough to give agreement with the reference model.

It can also be seen from both Table 4-3 and Figure 4-16, that, for the OSEM-NC algorithm, the percentage change of mean counts was similar to the reference model (pre-reconstruction) only after 3 or 4 iterations. As the number of iteration goes beyond 8, the percentage change is improved in the anterior region (from -4.3% to -0.3%) and greater than the reference level (by up to 1.0%) in other regions. As the number of iterations is increased the image contrast is improved and but the edge artefacts increase for the LV image. Percentage changes in all regions are increased with increasing numbers of iterations. The OSEM algorithm produces a better image than FBP, both qualitatively and quantitatively, (percent change of OSEM was -4% and for FBP was -15%).

Table 4-3 the measured mean counts and the percent change (%) at four positions within the LV emission model reconstructed by FBP-NC and OSEM-NC (1 subset & different numbers of iterations) algorithms.

	Anterior		Right		Posterior		Left	
	Mean Counts	% Change	Mean Counts	% Change	Mean Counts	% Change	Mean Count	% Change
FBP -NC	254	- 15.3	253	- 15.6	253	- 15.6	253	- 15.6
OSEM-NC 3 iterations	282	- 6.0	286	- 4.6	288	- 4.0	288	- 4.0
OSEM-NC 4 iterations	287	- 4.3	291	- 3.0	292	- 2.6	293	- 2.3
OSEM-NC 8 iterations	299	- 0.33	301	+ 0.3	303	+ 1.0	303	+ 1.0
OSEM-NC 16 iterations	305	+1.6	306	+ 2.0	308	+ 2.6	307	+ 2.3

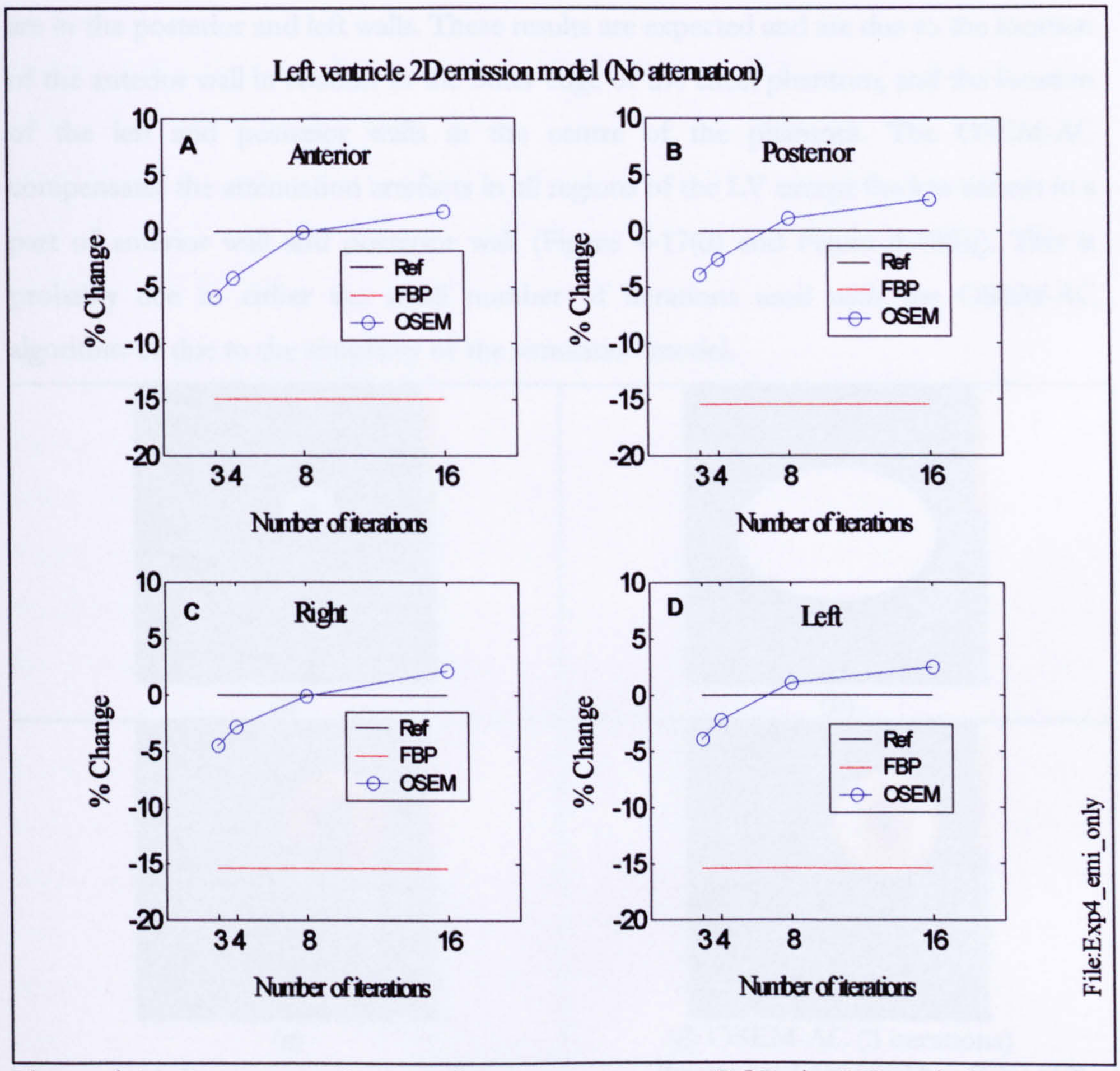

Figure 4-16 Percentage change of mean counts at 4ROIs in LV emission model reconstructed with FBP-NC and OSEM-NC with number of iterations.

In Figure 4-16, it can be seen that the percentage change with 8 iterations was in good agreement with the true image in anterior and right regions; whereas the percentage change at posterior and left regions were overestimated compared to the true image. Therefore, in order to avoid overestimation in some regions and as the percentage change of – 5% can be ignored we chose to select 3 iterations to be considered when validating the same LV emission model with both uniform and non-uniform AC in the next section.

4.3.1.2. Left ventricle emission model with uniform AC

The LV emission model reconstructed using both FBP-NC and OSEM-AC with a uniform attenuation map is shown in Figure 4-17. In the image reconstructed by FBP-NC, it can be seen that the highest counts are in the anterior wall and the lowest counts

are in the posterior and left walls. These results are expected and are due to the location of the anterior wall in relation to the outer edge of the chest phantom, and the location of the left and posterior walls in the centre of the phantom. The OSEM-AC compensates the attenuation artefacts in all regions of the LV except the low counts in a part of anterior wall and posterior wall (Figure 4-17(d) and Figure 4-18(b)). This is probably due to either the small number of iterations used with the OSEM-AC algorithm or due to the simplicity of the simulation model.

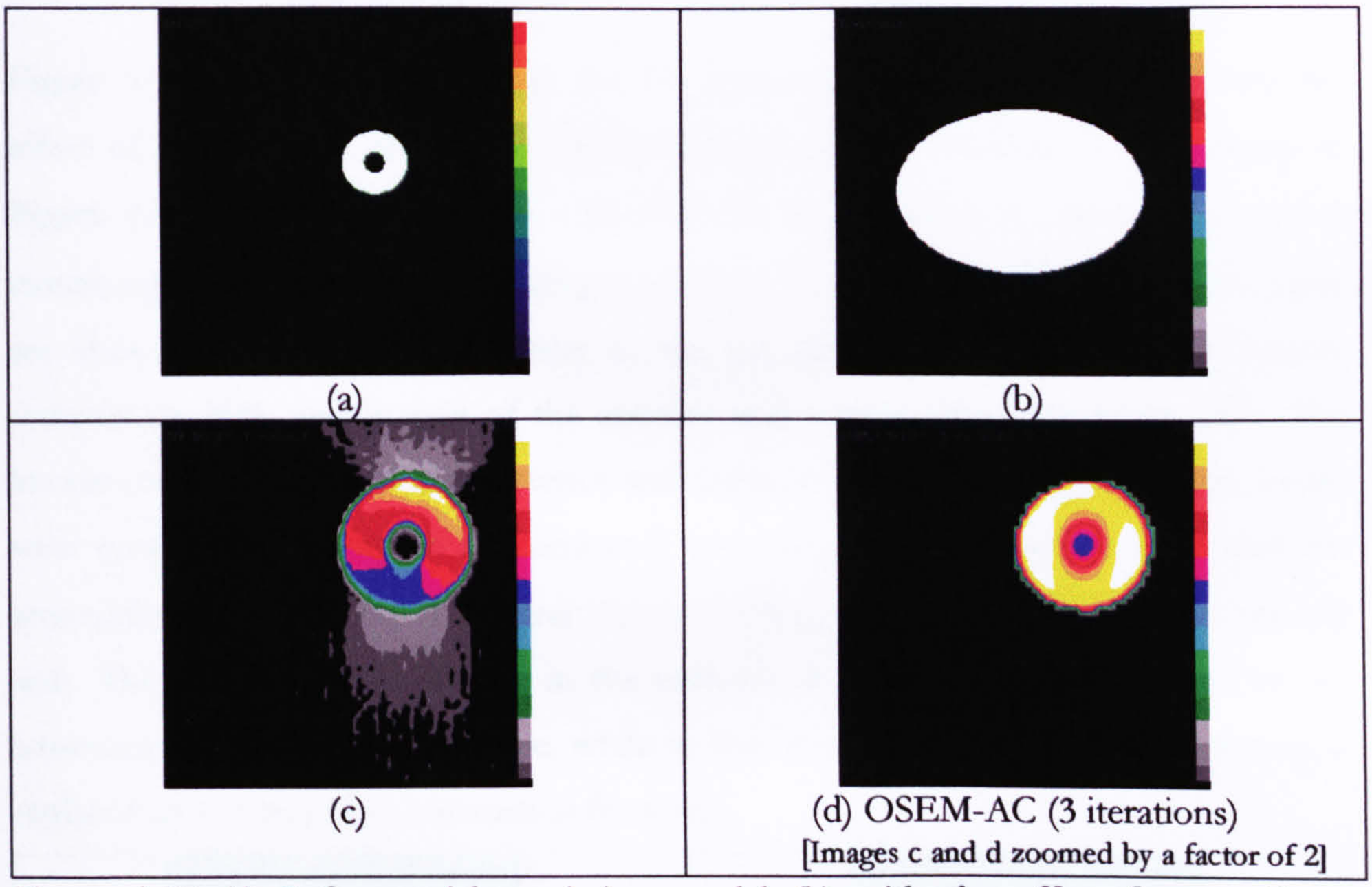

Figure 4-17 (a) Left ventricle emission model (b) with the effect from uniform attenuation model reconstructed by (c) FBP-NC, and (d) OSEM-AC.

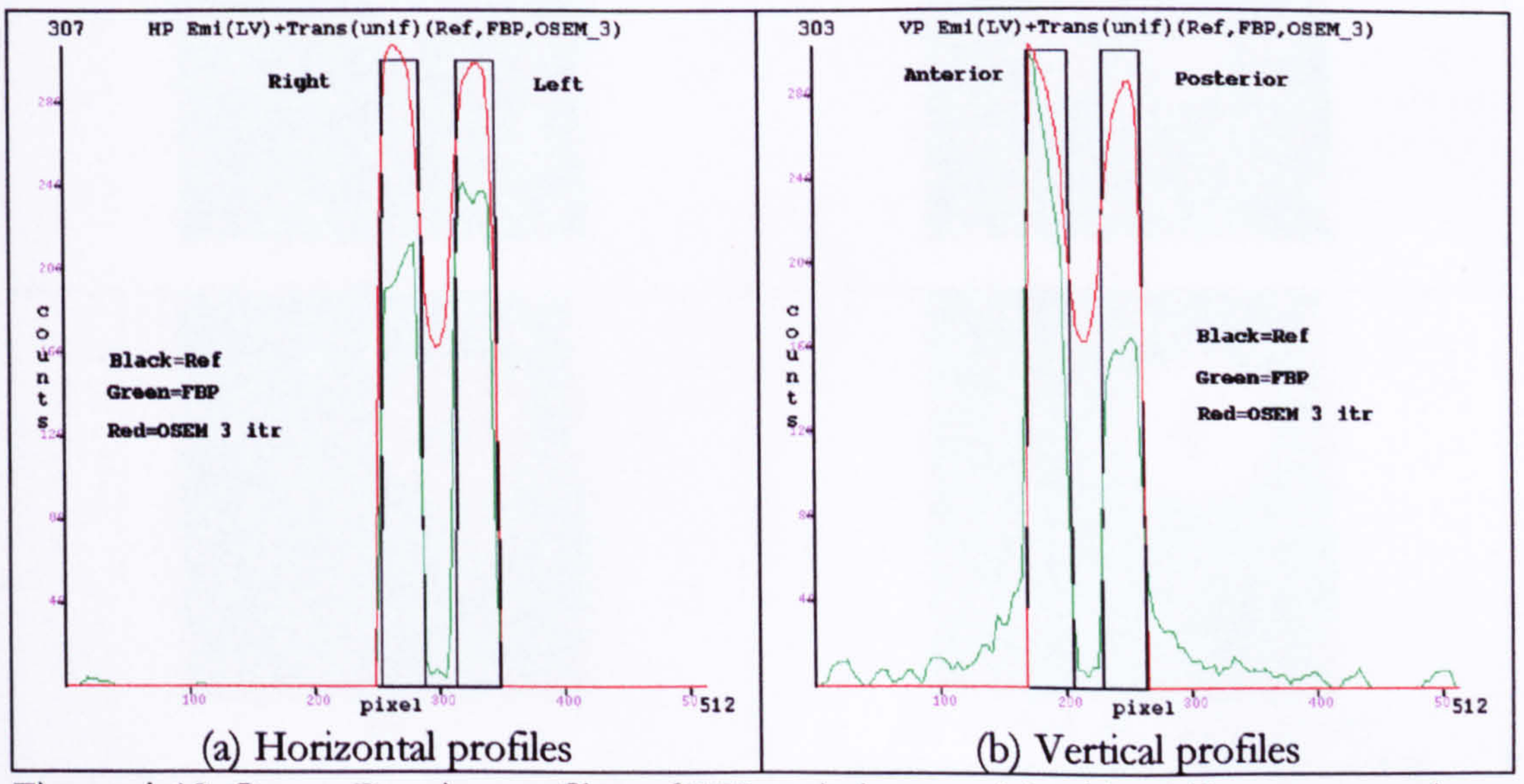

Figure 4-18 Count Density profiles of LV emission model with uniform attenuation effect; reconstructed by FBP-NC and OSEM-AC.

In this experiment it was found that OSEM-AC produces similar counts in the left and right LV walls and reduced counts in the anterior and posterior walls. The compensation of counts in the anterior wall from uniform attenuation is of interest and it will be considered again with non-uniform attenuation and OSEM-AC with different number of iterations in the experiment in section 4.3.1.4.

4.3.1.3. Left ventricle emission model with non-uniform AC

Figure 4-19 and Figure 4-20 show the LV emission model, taking into account the effect of non-uniform attenuation (using the non-uniform attenuation map shown in Figure 4-19(b) and reconstructed with FBP-NC and OSEM-AC (one subset and 3 iterations). In the FBP-NC image (Figure 4-19(c)), it can be seen that the highest counts are shown in the left wall (adjacent to the low attenuation, left lung) with counts reduced by 21%, and in part of the anterior wall with counts reduced by 28%. The lowest counts are seen in the posterior wall (adjacent to the highest attenuation, bone) with counts reduced by 38%. Compared with the FBP-NC image from a uniform attenuation (experiment 4.3.1.2 and Figure 4-17(c)), there are high counts in the left wall. The reason for this is that, in the uniform attenuation, this area represents an attenuation coefficient from tissue, while in the non-uniform attenuation; this area is replaced by left lung (low attenuation from air).

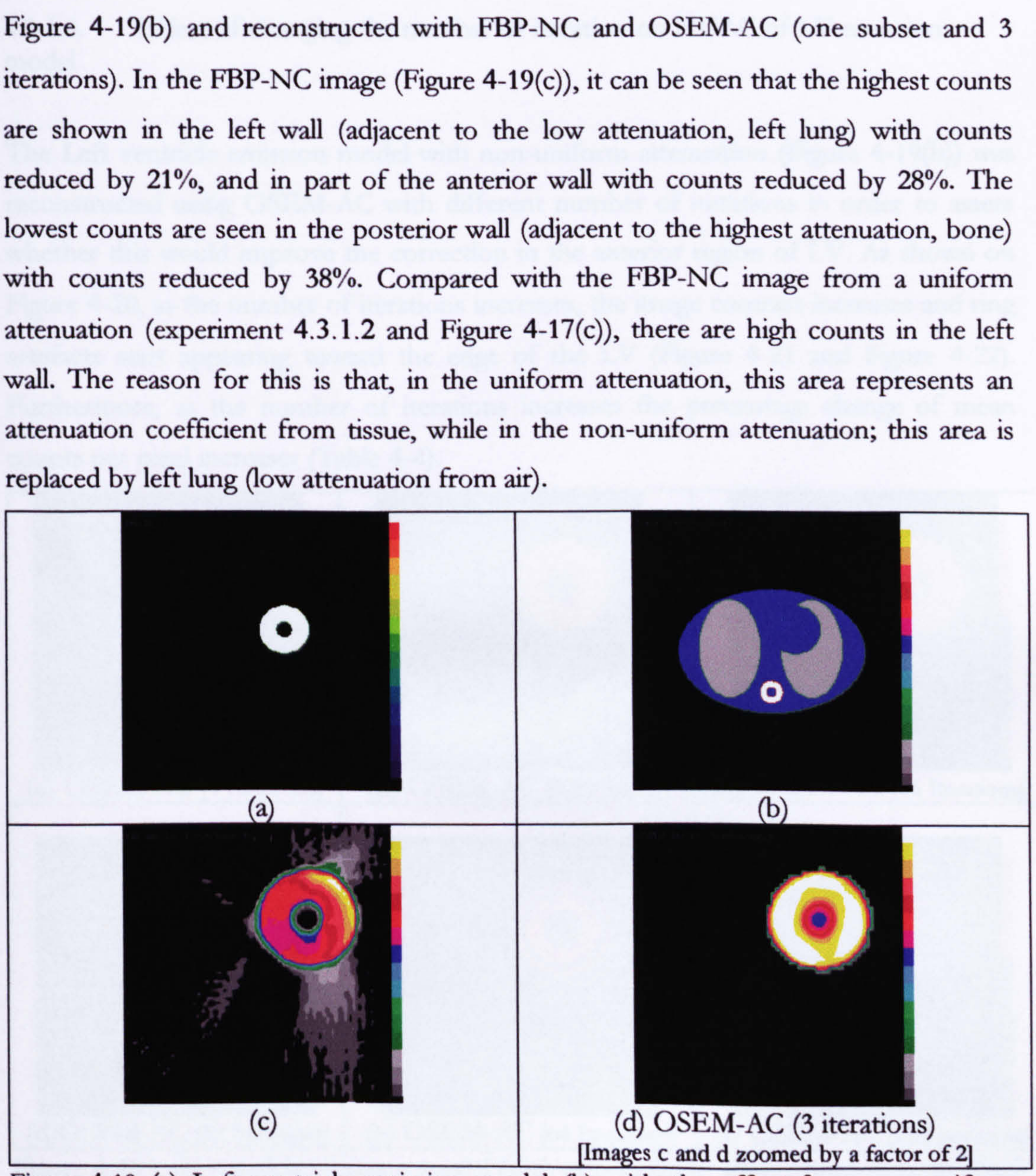

Figure 4-19 (a) Left ventricle emission model (b) with the effect from non-uniform attenuation model reconstructed by (c) FBP-NC, and (d) OSEM-AC.

The OSEM-AC for the non-uniform attenuation (Figure 4-19(d)) under-corrects the non-uniform attenuation artefacts in all LV regions, seen most clearly in Figure 4-21 (red profile curves) and Figure 4-19. The percentage change for the mean counts after AC was under-corrected in the four walls (anterior, right, posterior, and left by -7.0%, -3.0%, -3.6%, and -5.6%, respectively). From the profiles (Figure 4-21(a-b)) one can see that the anterior wall with OSEM-AC (3 iterations) shows the lowest counts profile compared to the other walls of the LV (This finding also was noted in the previous experiment (section 4.3.1.2)). Increasing the number of iterations, which might improve the mean counts in the anterior wall, will be investigated next (section 4.3.1.4)

4.3.1.4. Effect of changing the number of iteration on NUAC of LV emission model

The Left ventricle emission model with non-uniform attenuation (Figure 4-19(b)) was reconstructed using OSEM-AC with different number of iterations in order to assess whether this would improve the correction in the anterior region of LV. As shown on Figure 4-20, as the number of iterations increases, the image contrast increases and ring artefacts start appearing toward the edge of the LV (Figure 4-21 and Figure 4-22). Furthermore, as the number of iterations increases the percentage change of mean counts per pixel increases (Table 4-4).

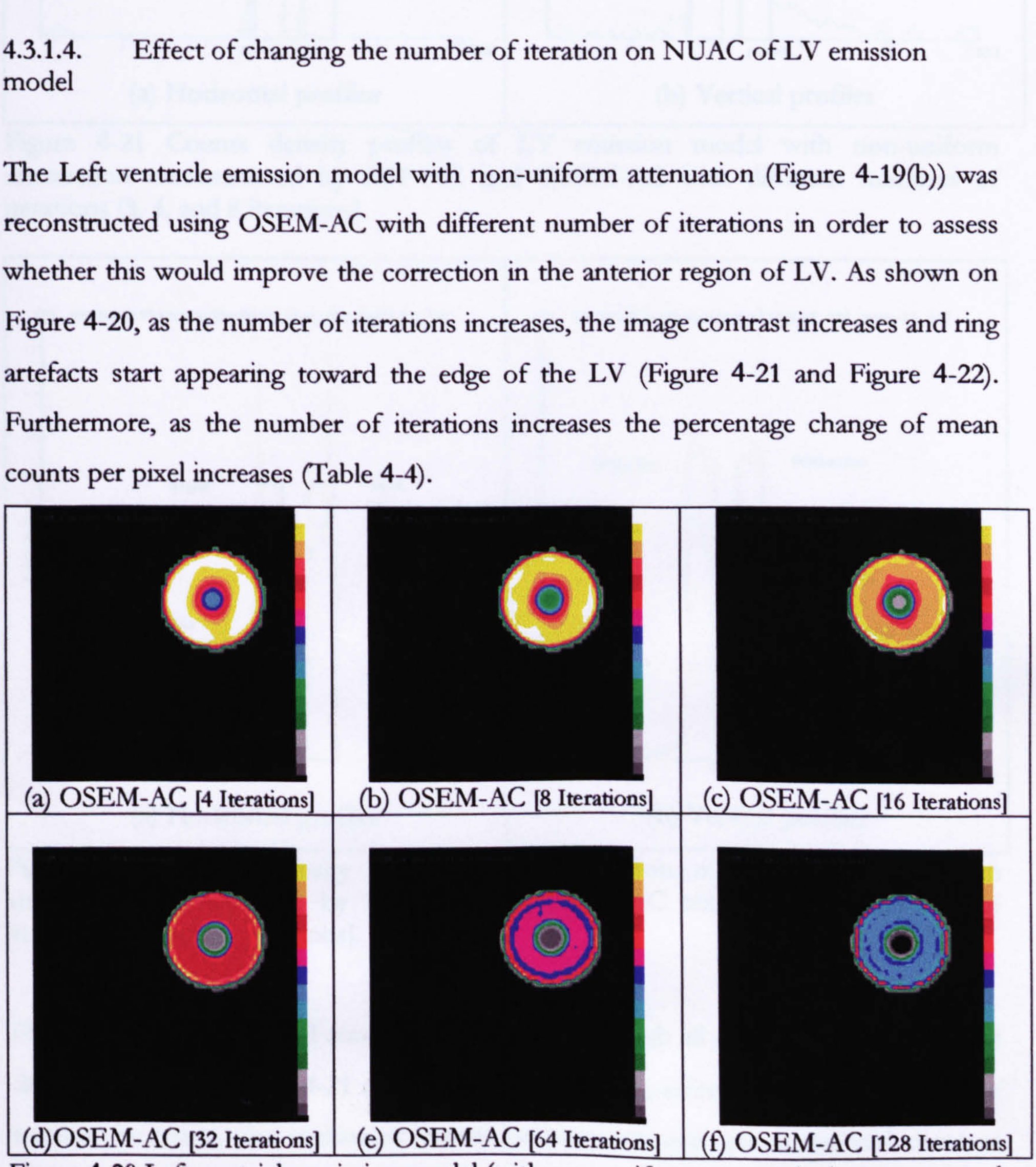

Figure 4-20 Left ventricle emission model (with non-uniform attenuation) reconstructed by OSEM-AC with different iterations as indicated in (a)-(f).

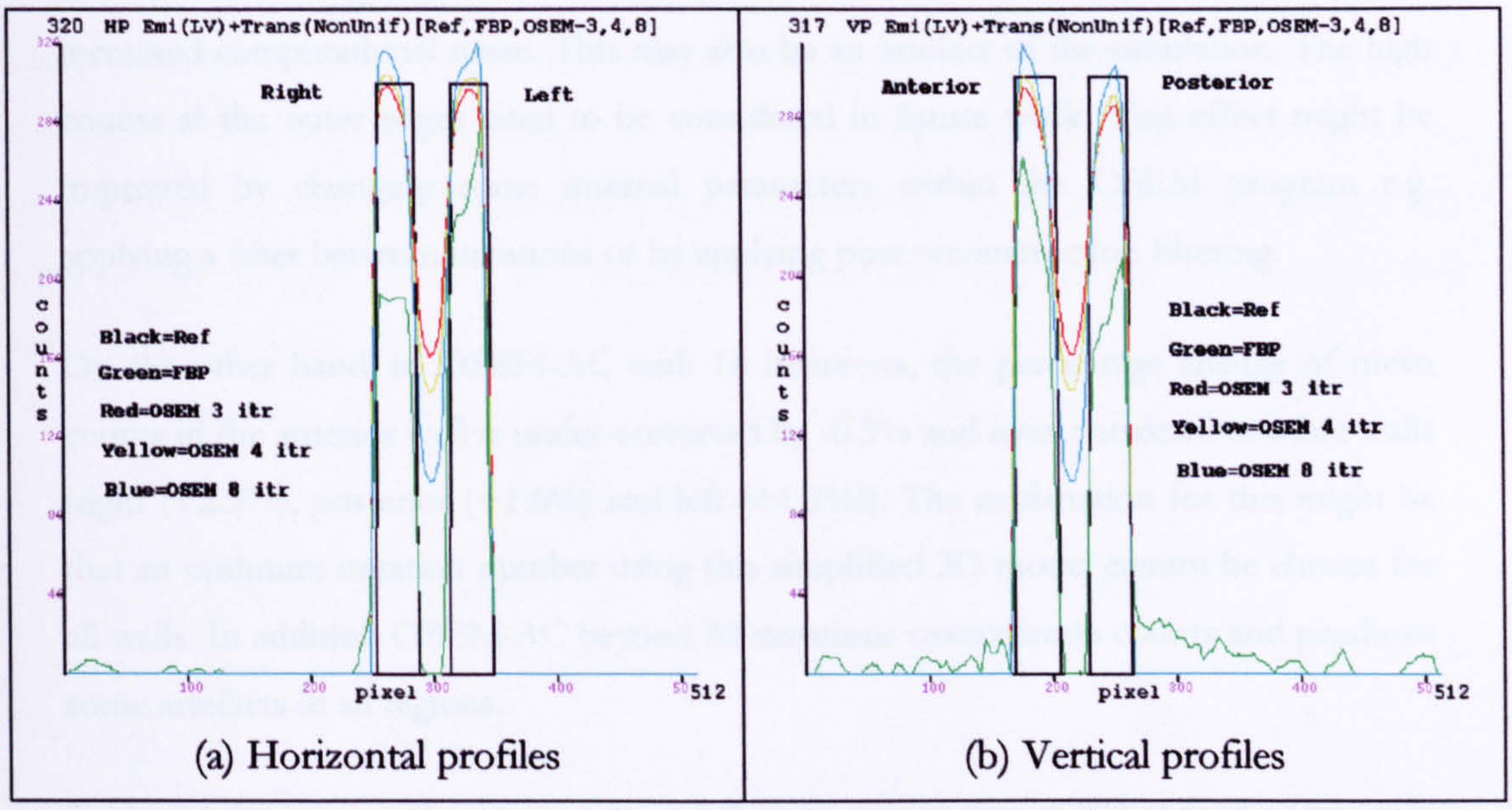

(a) Horizontal profiles (b) Vertical profiles

Figure 4-21 Counts density profiles of LV emission model with non-uniform attenuation reconstructed by FBP-NC and OSEM-AC with different numbers of iterations [3, 4, and 8 iterations].

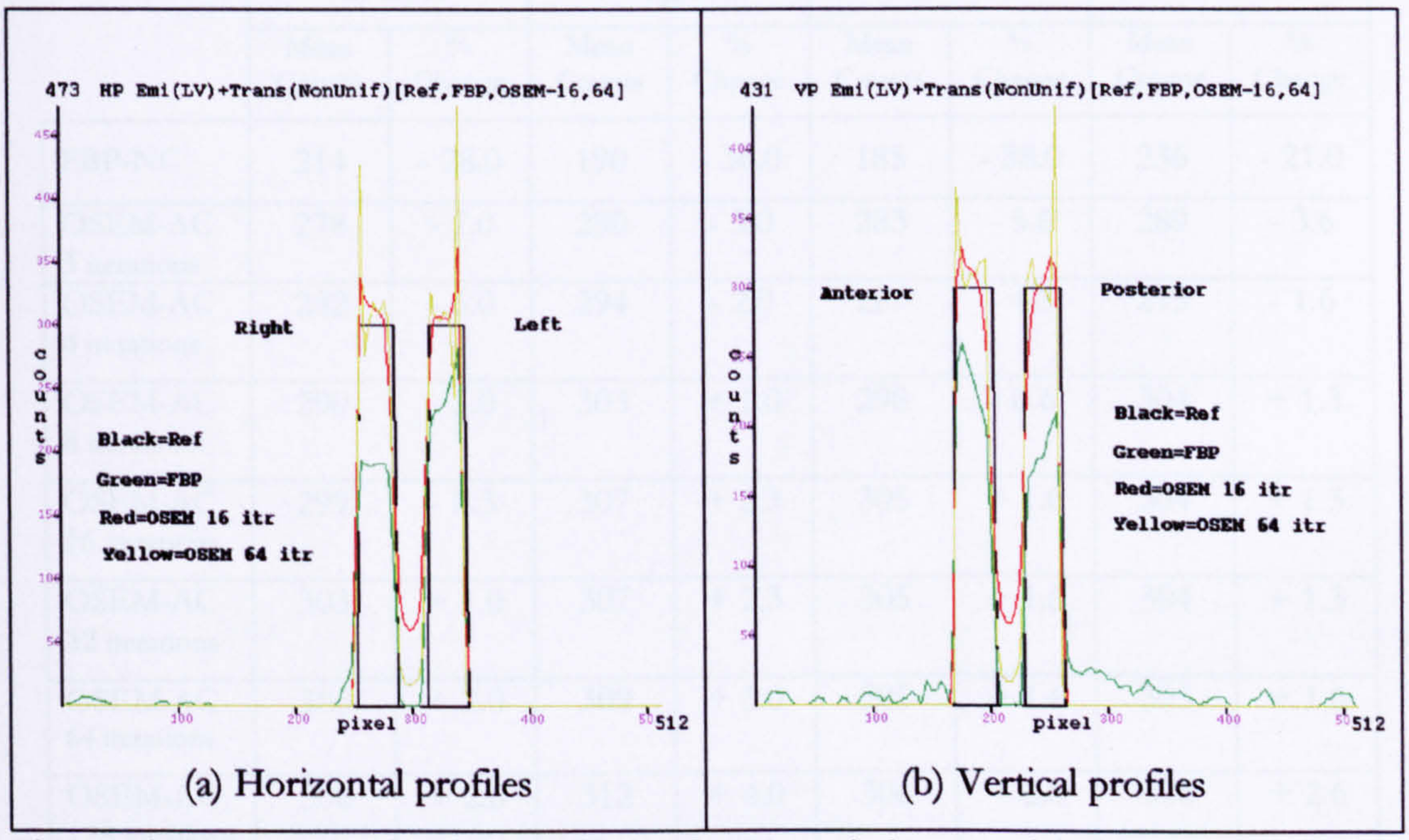

(a) Horizontal profiles (b) Vertical profiles

Figure 4-22 Counts density profiles of LV emission model with non-uniform attenuation reconstructed by FBP-NC and OSEM-AC with different numbers of iterations [16 and 64 iterations].

The horizontal and vertical count density profiles through all of the images in Figure 4 -20 are shown on Figure 4-21 and Figure 4-22. These confirm that, as the number of iteration increases, the maximum counts increase towards the edges and decrease toward the centre of the LV emission image and ring artefacts appear. This indicates

that with increasing the number of iterations, the contrast increases, and the image has increased computational noise. This may also be an artefact of the simulation. The high counts at the outer edges need to be considered in future work. This effect might be improved by changing some internal parameters within the OSEM program e.g. applying a filter between iterations or by applying post-reconstruction filtering.

On the other hand, in OSEM-AC with 16 iterations, the percentage change of mean counts in the anterior wall is under-corrected by -0.3% and over-corrected in other walls [right (+2.3%), posterior (+1.6%) and left (+1.3%)]. The explanation for this might be that an optimum iteration number using this simplified 2D model cannot be chosen for all walls. In addition OSEM-AC beyond 32 iterations overcorrects counts and produces some artefacts in all regions.

Table 4-4 the measured mean counts and the percentage change (%) at four positions in the LV emission model (with non-uniform attenuation) reconstructed by FBP-NC and OSEM-AC (with different number of iterations).

	Anterior		Right		Posterior		Left	
	Mean Counts	% Change	Mean Counts	% Change	Mean Counts	% Change	Mean Counts	% Change
FBP-NC	214	- 28.0	190	- 36.0	185	- 38.0	236	- 21.0
OSEM-AC 3 iterations	278	- 7.0	290	- 3.0	283	- 5.6	289	- 3.6
OSEM-AC 4 iterations	282	- 6.0	294	- 2.0	287	- 4.3	295	- 1.6
OSEM-AC 8 iterations	290	- 3.0	303	+ 1.0	298	- 0.6	304	+ 1.3
OSEM-AC 16 iterations	299	- 0.3	307	+ 2.3	305	+ 1.6	304	+ 1.3
OSEM-AC 32 iterations	303	+ 1.0	307	+ 2.3	305	+ 1.6	304	+ 1.3
OSEM-AC 64 iterations	306	+ 2.0	309	+ 3.0	305	+ 1.6	305	+ 1.6
OSEM-AC 128 iterations	308	+ 2.6	312	+ 4.0	306	+ 2.0	308	+ 2.6

Figure 4-23 illustrates that; the best percentage change of mean counts is produced with 8 iterations in all walls and with 16 iterations in the anterior wall alone. It is important to point out here that, with 3 and 4 iterations, the mean counts are under-corrected but without introduction of artefacts in the reconstructed image. Also, for more than 8

iterations, the mean counts in both the right and left walls are overcorrected. However, the percentage change of mean counts were not beyond – 10% in some undercorrection cases (low number of iterations; 3, 4, 8, and 16) and not beyond +5% in all overcorrection cases (with high number of iterations; 32, 64, and 128) (Figure 4-23). This indicates that OSEM-AC successfully corrects attenuation artefacts in this simplified 2D model.

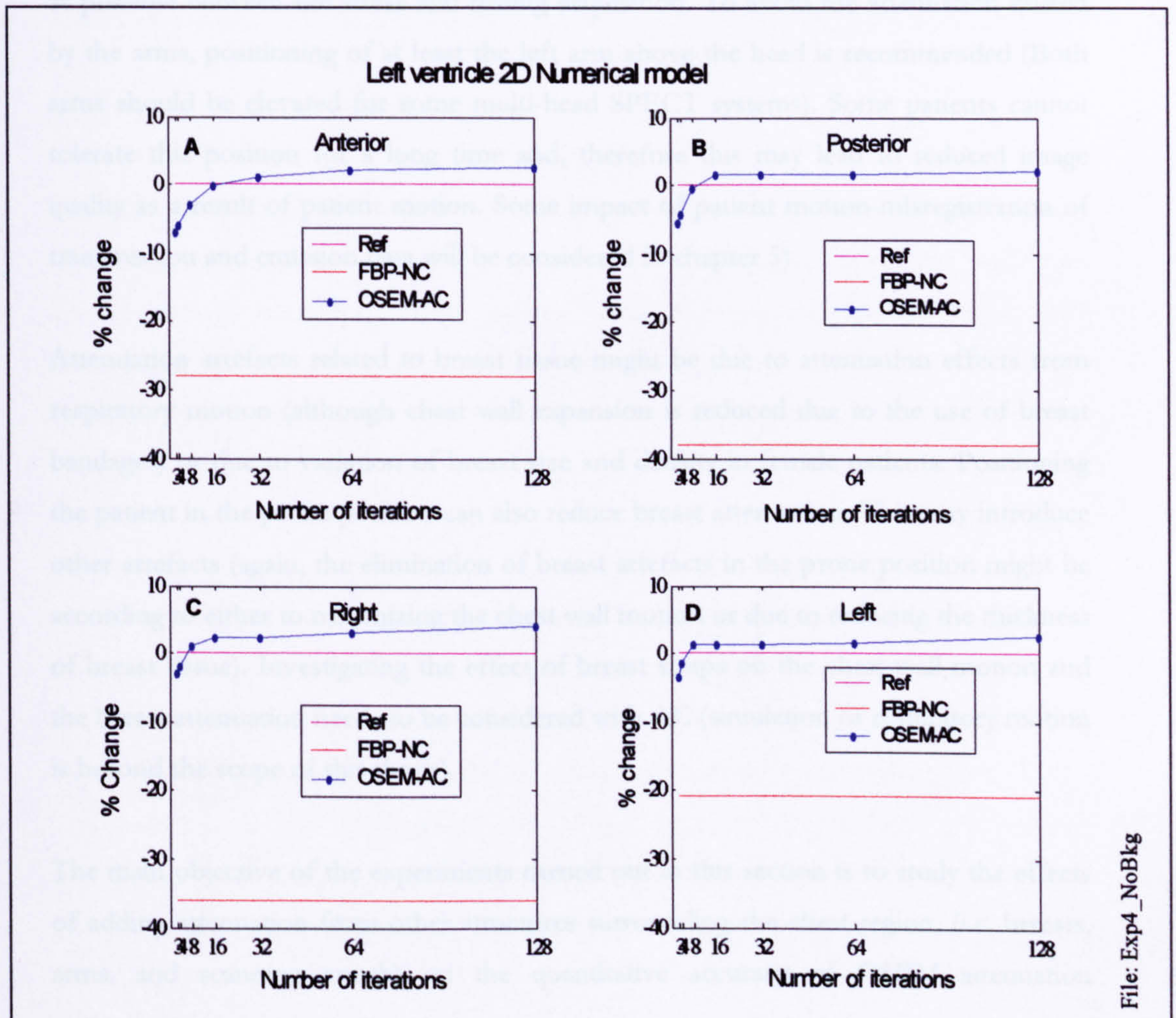

Figure 4-23 Percentage change of the mean count in 4ROIs in the LV emission model reconstructed by FBP-NC and OSEM (with different number of iterations) with non-uniform AC.

4.4. The effects of additional attenuation from breasts, arms, and scanning couch on AC.

The anterior artefact is commonly believed to be the result of breast attenuation whereas lateral artefacts have been attributed to the left arm if the arm is positioned at the patient's side during data acquisition. To avoid breast attenuation, breasts are commonly restrained with an elasticated bandage and should be positioned as identically as possible between the stress and resting acquisition. To avoid the attenuation caused by the arms, positioning of at least the left arm above the head is recommended (Both arms should be elevated for some multi-head SPECT systems). Some patients cannot tolerate this position for a long time and, therefore this may lead to reduced image quality as a result of patient motion. Some impact of patient motion-misregistration of transmission and emission data will be considered in chapter 5)

Attenuation artefacts related to breast tissue might be due to attenuation effects from respiratory motion (although chest wall expansion is reduced due to the use of breast bandages) or due to variation of breast size and density in female patients. Positioning the patient in the prone position can also reduce breast attenuation. This may introduce other artefacts (again, the elimination of breast artefacts in the prone position might be according to either to minimizing the chest wall motion or due to reducing the thickness of breast tissue). Investigating the effect of breast straps on the chest wall motion and the breast attenuation needs to be considered with AC (simulation of respiratory motion is beyond the scope of this thesis).

The main objective of the experiments carried out in this section is to study the effects of adding attenuation from other structures surrounding the chest region, (i.e. breasts, arms, and scanning couch) on the quantitative accuracy of OSEM attenuation correction.

In order to study this, a 2D CT image was segmented into an attenuation coefficient map to simulate different attenuation models (chest with breasts, chest with arms, and chest with scanning couch). The aims of these experiments are: 1) to evaluate the influence of adding attenuation from breasts, arms, and scanning couch upon the non-uniform AC, and 2) to find out whether OSEM can provide a robust AC technique with different attenuation maps.

4.4.1 Segmentation of a non-uniform CT attenuation model

The segmentation strategy used in this experiment is based on a counts-threshold-based technique. It is the simplest and most widely used segmentation technique. It uses the grey-level histogram counts to identify regions of pixels in an image. All pixels whose value (grey level or colour) is between two values belong to one region. The result of threshold segmentation is a binary image, which is 1 everywhere the threshold condition is met and 0 otherwise. Mathematically it is written as;

$$g(i,j) = 1 \quad for \;\; T_{lower} < f(i,j) < T_{upper}$$
$$= 0 \quad Otherwise \qquad \text{Eqn. 4-4}$$

The purpose of image segmentation is to subdivide the CT image into anatomic regions of the attenuation values corresponding to soft tissue, lungs and bone. The upper and lower threshold values for different regions within an image are obtained by using the histogram for the image. A trans-axial CT slice image from a set of clinical CT images acquired by a Hawkeye GE hybrid system for a thin female patient with arms down was used in these experiments (Figure 4-24(a)). The smoothed histogram of attenuation values is shown on Figure 4-24(b).

As can be seen from Figure 4-24(b), on the horizontal axis, the intensity level represents the attenuation values and the vertical axis shows number of pixels. The histogram has four main peaks, which are attributed to background and air (peak 1), lung (peak 2), soft tissue (muscle and also including the scanning couch-peak 3) and bone (peak 4). The two peaks representing attenuation values for soft tissue and muscles were grouped into one region. This was made in order to make the simulation simple and to simulate attenuation from only three types of tissue; soft-tissue, bone, and lungs.

The upper and lower threshold values of each peak were used to produce a mask image (where all values are 0 and 1). Once the segmented mask image for each type of tissue was obtained, each pixel in the mask image was multiplied by a factor representing the attenuation coefficient values for 140 keV ^{99m}Tc. The attenuation coefficients for air, lungs, soft tissue, and bone were 0.001 cm^{-1}, 0.051 cm^{-1}, 0.153 cm^{-1}, and 0.286 cm^{-1}, respectively [37] (Table 4-5). The previous images were combined to produce a 2D static slice, which will be used as the 2D segmented attenuation map (Figure 4-24(c)).

Table 4-5 The selected threshold values replaced by theoretical attenuation coefficient values [37].

Regions	Threshold values (lower-upper) (Hounsfield Units)*	Replaced theoretical μ (cm^{-1})
Air	0-60	0.001
Lungs	60-800	0.051
Soft tissue	800-1100	0.153
Bone	1100-1800	0.286

* Hounsfield Unit or CT-number of tissue = $[(\mu_{tissue}-\mu_{water})/\mu_{water}] \times 1000$

It is obvious from comparing the final segmented attenuation map, with the pre-segmented CT slice (Figure 4-24(a)) that in the segmented slice there are only four distinct regions, the air (background), the soft tissue, the lungs, and the bone (Figure 4-24(c)). However, there are still some high intensity pixels shown within the bone region. The probable explanation is that the segmentation was based on the user selection of threshold levels, which can lead to some pixels, being included or excluded from the bone region. Despite this, the 2D non-uniform attenuation map obtained by threshold segmentation can be used to correct the emission data for non-uniform attenuation effects simulated from a realistic CT image.

As well as the attenuation map simulation, the 2D ring-shape LV emission model was simulated and each pixel was multiplied by a factor of 300. The LV emission was located in the heart position inside the 2D segmented slice as shown on Figure 4-24(d). The 2D segmented slice was used to simulate different attenuation map models by subtracting some organs around the chest region and leaving only the attenuation from others. For instance, to investigate the influence of adding attenuation from breasts, all structures around the chest region such as arms, and scanning couch were subtracted. The process was repeated to simulate the attenuation from adding either arms or the scanning couch. Similarly to this, subtracting all organs around the chest also simulates attenuation from the chest region only.

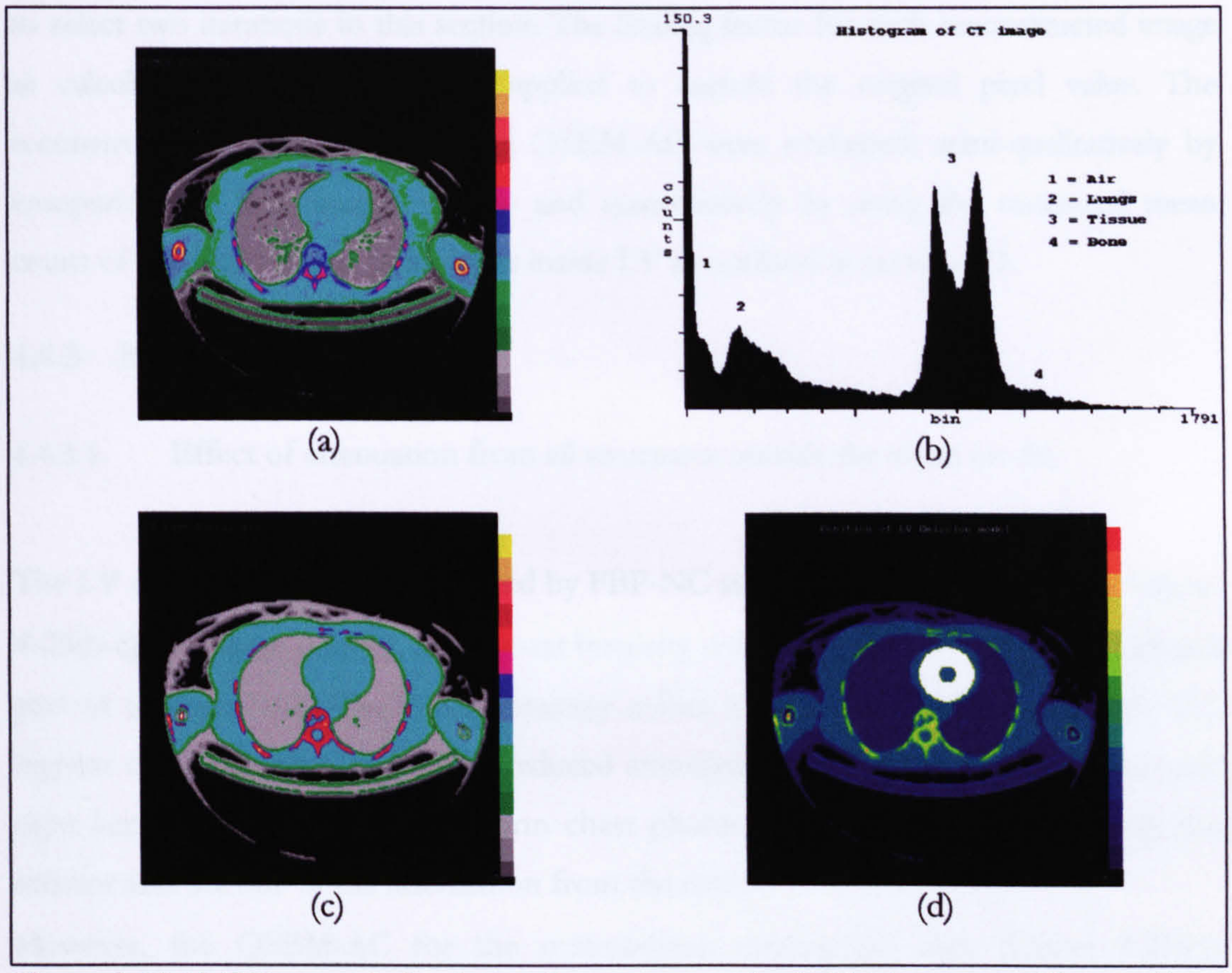

Figure 4-24 (a) CT transmission image [pre-segmentation], (b) histogram of image (a), (c) the new-segmented attenuation map and (d) the position of left ventricle emission model inside attenuation model (d).

4.4.2 Method:

The LV emission model was reconstructed using FBP, and different types of non-uniform attenuation were simulated. The FBP reconstruction comprises the following simulated transmission images; (1) chest with attenuation from breasts, arms, and scanning couch (Figure 4-25(a)), (2) Chest only [excluding breasts, arms, and scanning couch] (Figure 4-26(a)), (3) chest with breasts [excluding arms and scanning couch] (Figure 4-27(a)), (4) chest with arms [excluding breasts and scanning couch] (Figure 4 -28(a)), and (5) chest with scanning couch [excluding breasts and arms] (Figure 4-29(a)).

The FBP-NC was reconstructed with attenuation effect included and without AC. The previous transmission images were also used to correct attenuation artefacts. For the OSEM-AC only two iterations were employed. From previous experiments, we notice that anterior wall was overcorrected when 3 iterations was used. Therefore, we decided

to select two iterations in this section. The Scaling factor for each reconstructed image as calculated in section 4.1 was applied to restore the original pixel value. The reconstructions from FBP-NC and OSEM-AC were evaluated; semi-qualitatively by comparing the final images visually and quantitatively by using the measured mean count of the four regions of interests inside LV as outlined in section 4.3.

4.4.3 Results:

4.4.3.1. Effect of attenuation from all structures outside the chest on AC

The LV emission image reconstructed by FBP-NC and OSEM-AC are shown in Figure 4-25(b-c). In Figure 4-25(b), the highest intensity colours are shown in the left wall and part of the right wall. The lowest intensity colour is shown in the posterior wall. The highest count areas are due to the reduced attenuation from the lungs (at the left and right lateral sides of the non-uniform chest phantom), and the lowest counts in the inferior wall are due to the attenuation from the spine.

However, the OSEM-AC for the non-uniform attenuation map (Figure 4-25(c)) produces an emission image of almost uniform colour in all regions except for small parts of both the anterior and posterior regions, which show reduced counts. This reduction of counts after AC in the anterior wall is probably due to the presence of attenuation from breasts and in the posterior wall due to the presence of attenuation either from the scanning couch or from the left arm. The percentages of the mean counts in the four walls of LV emission image are shown inn Table 4-7 and Figure 4-30.

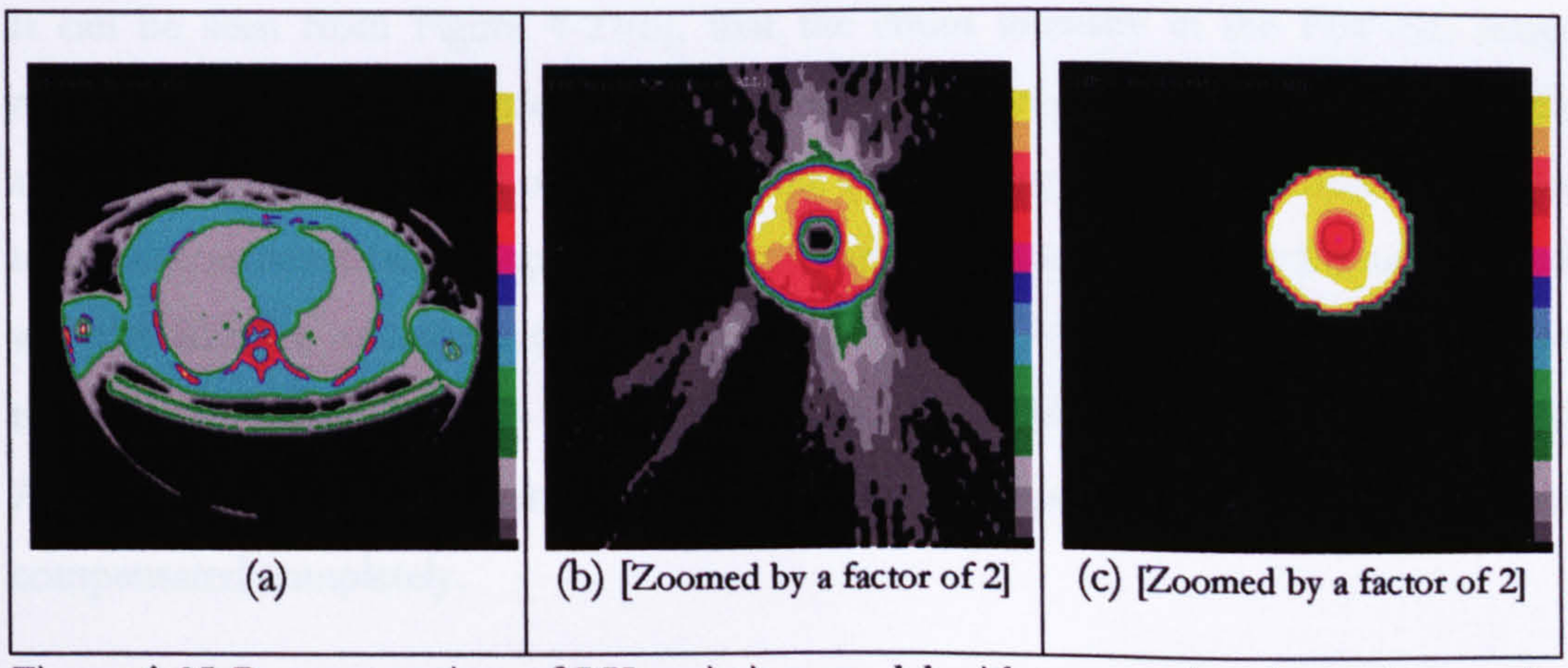

(a) (b) [Zoomed by a factor of 2] (c) [Zoomed by a factor of 2]

Figure 4-25 Reconstruction of LV emission model with attenuation from chest region and all attenuating materials around chest. (a) Attenuation map from chest region and all attenuating structures around chest region (included; breasts, arms, and scanning couch). (b) FBP-NC. (c) OSEM-AC.

4.4.3.2. Effects of attenuation from the chest region only on AC

Figure 4-26, illustrates the effect of attenuation from the chest region only on the OSEM-AC. It can be seen that this is more uniform in all regions compared to the OSEM-AC image with attenuation from all regions around chest (Figure 4-25(c)). This demonstrates that the OSEM-AC can compensate well for the attenuation from only the tissue inside chest region. The main difference between the OSEM-AC image shown in Figure 4-25(c) and image shown in Figure 4-26(c) is that the attenuating structures around the chest have had a significant impact on the AC of the anterior and posterior walls of the LV.

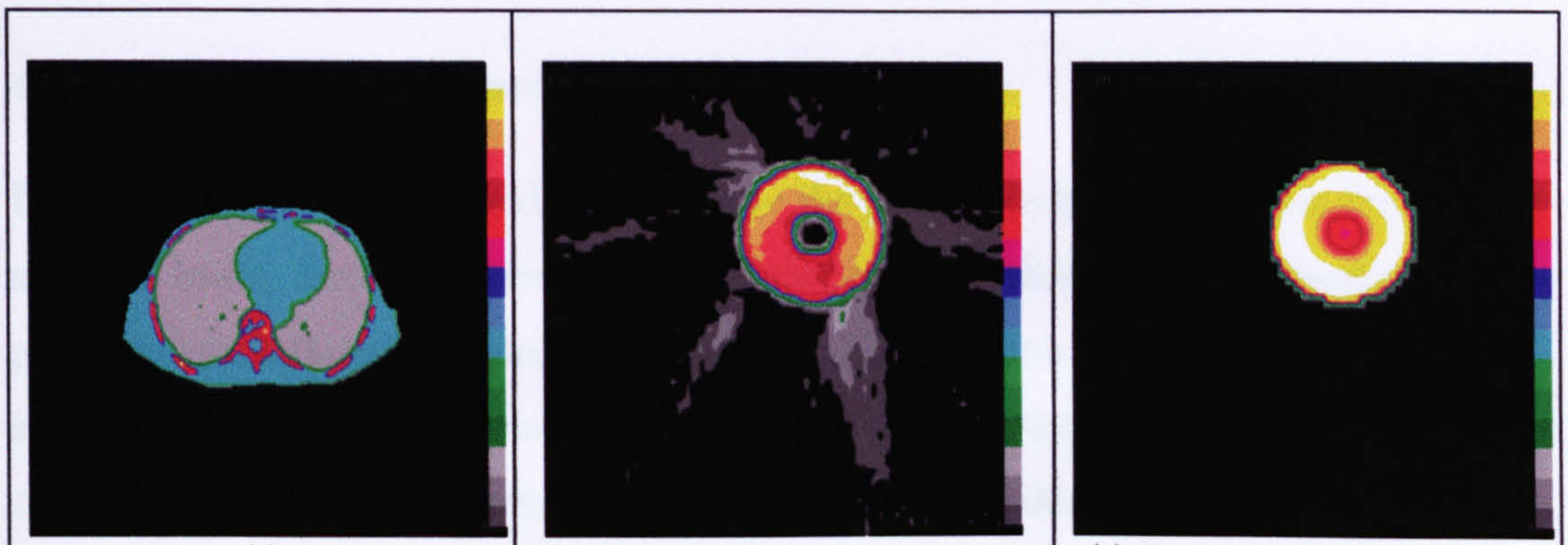

(a) (b) [Zoomed by a factor of 2] (c) [Zoomed by a factor of 2]

Figure 4-26 Reconstruction of LV emission model with attenuation from chest region only. (a) Attenuation map from chest region only. (b) FBP-NC. (c) OSEM-AC.

4.4.3.3. Effect of breast attenuation on AC

It can be seen from Figure 4-27(b), that the count intensity in the FBP-NC image reconstructed with attenuation effect from breasts only, was reduced in both the anterior and posterior walls of LV. While the count reduction in the posterior was due to the attenuation from the spine, the reason for the count reduction in the anterior wall was the addition of attenuation to the outer margins of chest on the non-uniform transmission image (Figure 4-27(a)). When this image was reconstructed using OSEM-AC (Figure 4-27(c)), count in the anterior, and part of posterior walls of LV was not compensated completely.

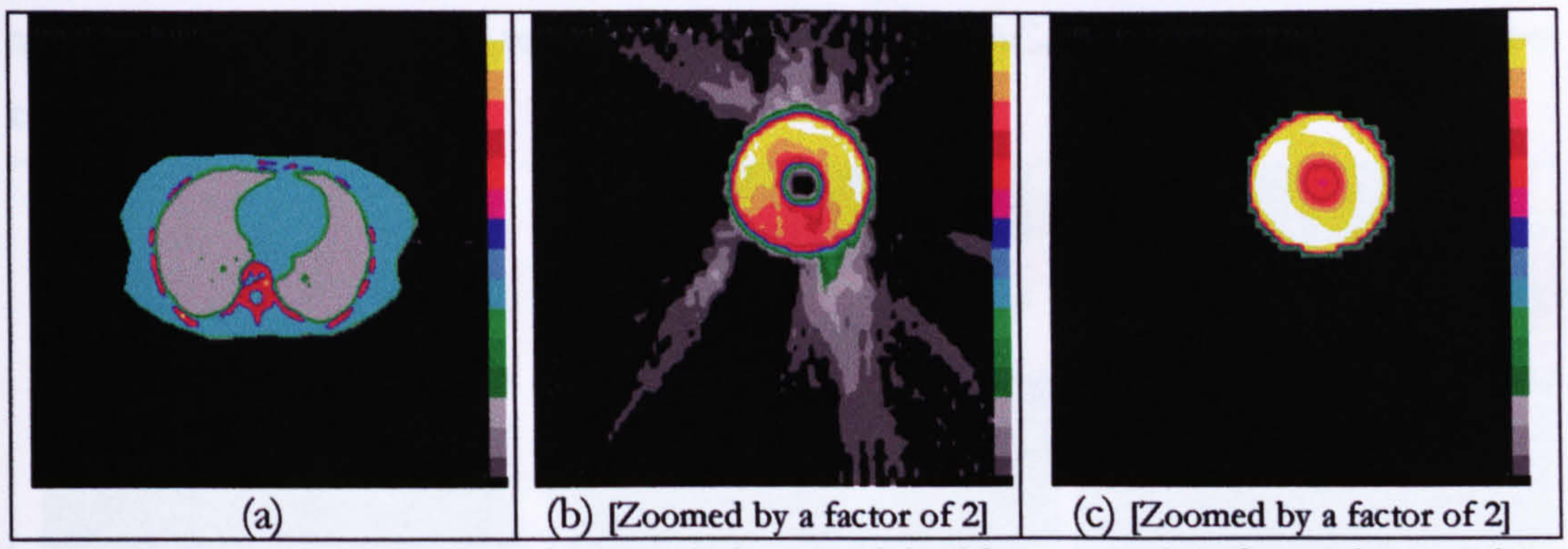

(a) (b) [Zoomed by a factor of 2] (c) [Zoomed by a factor of 2]

Figure 4-27 Reconstruction of LV emission model with attenuation from chest region with additional attenuation from breasts. (a) Attenuation map form chest region and breasts. (b) FBP-NC. (c) OSEM-AC.

4.4.3.4. Effect of arm attenuation on AC

Image count density may be decreased once the arm is positioned between the detector and the heart, increasing attenuation. A study by Prvulovich [93] showed that arm position does influence regional myocardial ^{201}Tl distribution in the reconstructed image, and they found that there was under-correction in the lateral wall of the LV in 10% of AC arms-down studies. Possible explanations of these findings include attenuation map truncation or misregistration between emission and transmission data.

Another study, by Toma and colleagues [92] found no significant difference in the location of defects between the two arms positions using ^{99m}Tc as a tracer instead of ^{201}Tl. The most likely explanation of the differences between these studies is that photon attenuation is less marked with the higher energy (140 keV) ^{99m}Tc tracers than ^{201}Tl (60-80 keV). Clinically, it is recommended that SPECT data should be acquired while the arms of the patients are placed over the head to decrease the attenuation from arms when held down. This is uncomfortable position, especially for elderly patients, (also movement of the arms during acquisition might cause misalignment between emission and transmission data), and therefore data can be acquired with arms down. This experiment is just to show whether the AC is sufficiently robust to allow acquisition of cardiac SPECT imaging data with the arms held down.

When attenuation from two arms (Figure 4-28(c)) is added to the non-uniform chest, the attenuation was corrected on all regions except for part of the anterior wall, when compared to the AC image with the attenuation from chest only (Figure 4-26(c)). This also, might be improved if more iteration were used in the reconstruction. This indicates that AC of the anterior wall is significantly influenced breast and arms more than by the

attenuation from the chest region alone. The issue of AC of anterior wall needs to be considered further.

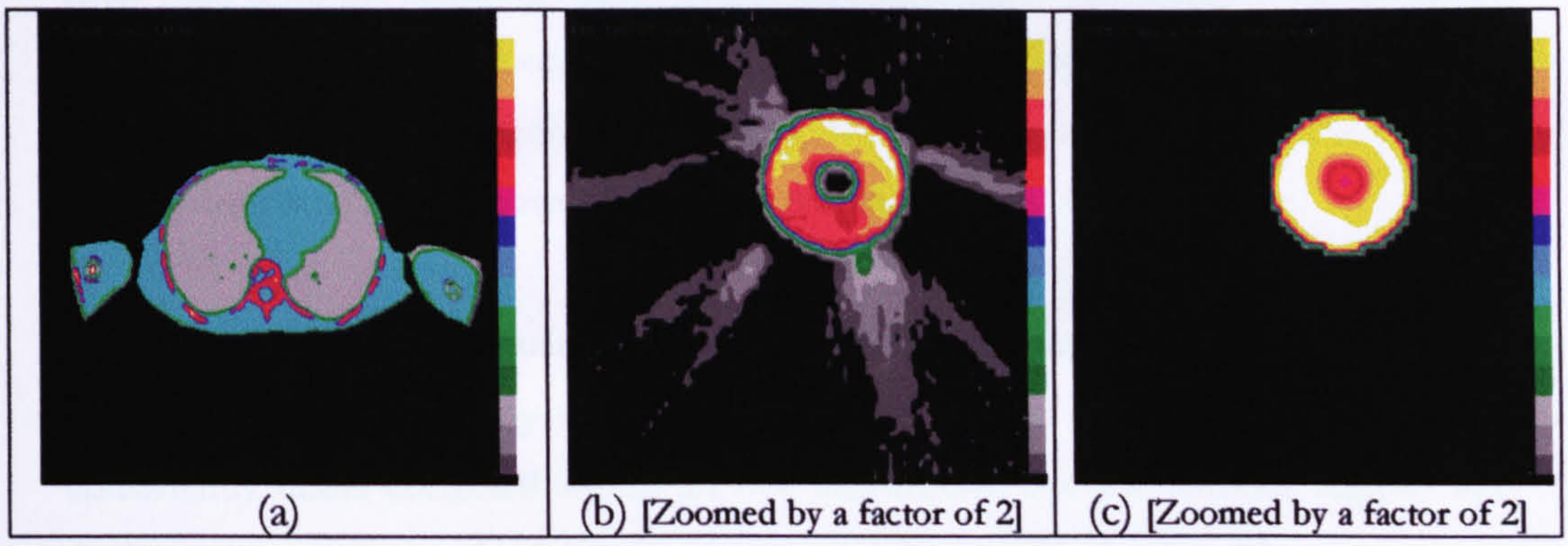

(a) (b) [Zoomed by a factor of 2] (c) [Zoomed by a factor of 2]

Figure 4-28 Reconstruction of LV emission model with attenuation from chest region and both arms. (a) Attenuation map form chest region and attenuation from arms. (b) FBP-NC. (c) OSEM-AC.

4.4.3.5. Effect of attenuation from scanning couch on AC

The counts in the posterior wall were reduced by 39.3% with the attenuation from both arms compared to a count reduction of 33.3% with attenuation from the scanning couch alone (Table 4-7). This indicates that the arms influence the attenuation in the posterior wall more than the scanning couch.

The scanning couch of the GE system used in this experiment was constructed from a low-attenuation material (Graphite/Foam) [94], and has more of an effect on the counts in the posterior wall (reduced by 33%) than the anterior wall (reduced by 22%). This change in counts in the posterior wall with the scanning couch was the same as the change of the counts at the same wall with the chest only (reduced by 33.3%). As seen in Table 4-7, the counts in the posterior wall showed a significant improvement with AC (reduced by 1.3%).

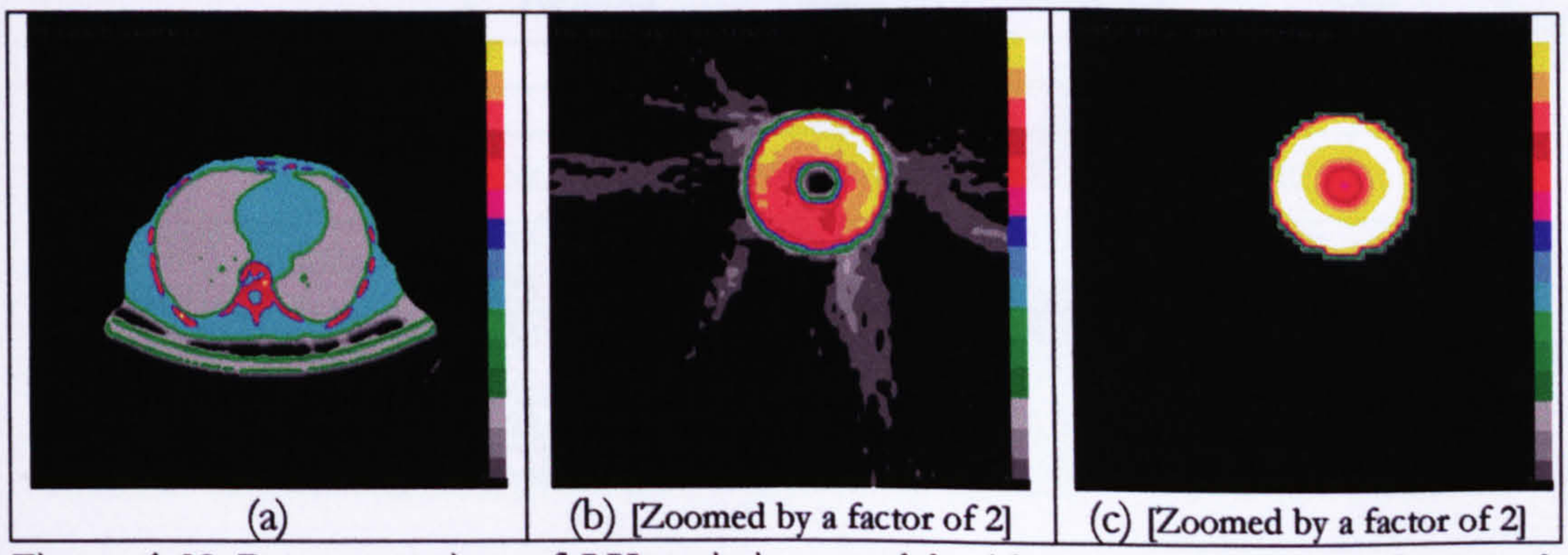

(a) (b) [Zoomed by a factor of 2] (c) [Zoomed by a factor of 2]

Figure 4-29 Reconstruction of LV emission model with attenuation from chest and scanning couch. (a) Attenuation map from chest region and scanning couch. (b) FBP-NC. (c) OSEM-AC.

This indicates that the AC is influenced by the attenuation from the breast and arms more than from the scanning couch. The best attenuation compensation can be seen on the images which incorporate attenuation effects from the chest region only. Furthermore, attenuation from the scanning couch (made of low attenuation material, such as Graphite/foam) shows that it has a minimal impact on AC.

In summary, as more attenuation is added to the non-uniform attenuation from chest, the OSEM-AC increasingly fails to correct the walls of the LV. The only region consistently under-corrected within all five simulations was the anterior region. This finding supports the results from the experiments discussed in section 4.3.

The calculated mean counts in 4 ROIs applied to the LV images reconstructed with and without AC are shown in Table 4-6. The percentage change of the mean counts values is shown inn Table 4-7.

Table 4-6 Calculated Mean counts for 4 ROIs applied to the LV emission model reconstructed with and without AC.

	Anterior		Right		Posterior		Left	
FBP (No attenuation)	251		249		249		250	
OSEM_2 (No attenuation)	295		298		298		298	
	NC	AC	NC	AC	NC	AC	NC	AC
Chest (All)	193	287	198	304	168	294	210	301
Chest only	231	293	209	298	200	299	228	296
Chest + Breasts	208	288	208	302	185	295	219	298
Chest +Arms	212	291	197	299	182	298	214	297
Chest + Scanning couch	234	293	208	298	200	299	228	294
NC = FBP with no attenuation, and AC= attenuation correction by OSEM_2.								

Table 4-7 the percentage change (%) for all data presented in Table 4-6.

	Anterior		Right		Posterior		Left	
FBP (No attenuation)	-16.3		-17.0		-17.0		-16.6	
OSEM_2(No attenuation)	-1.6		-0.6		-0.6		-0.6	
	NC	AC	NC	AC	NC	AC	NC	AC
Chest (All)	-35.6	-4.3	-34.0	1.3	-44.0	-2.0	-30.0	0.03
Chest only	-23.0	-2.3	-30.3	-0.6	-33.3	-0.3	-24.0	-1.3
Chest + Breasts	-30.6	-4.0	-30.6	0.6	-38.3	-1.6	-27.0	-0.6
Chest +Arms	-29.3	-3.0	-34.3	-0.3	-39.3	-0.6	-28.6	-1.0
Chest + Scanning couch	-22.0	-2.3	-30.6	-1.3	-33.3	-0.3	-24.0	-2.0
NC = FBP with no attenuation, and AC= attenuation correction by OSEM_2.								

As shown in Table 4-7 and Figure 4-30, the OSEM-AC produces counts in all walls consistently similar to the counts in the reference image (within ±10%). In the anterior wall OSEM-AC produces counts consistently reduced in comparison to the other walls and to the counts in the reference image

Considering the anterior wall, the percentage change of mean counts was the same for both; attenuation from the chest only and from the scanning couch (reduced by -2.3%). In contrast the percentage changes of mean counts of AC were - 4.0% and - 4.3% in the presence of attenuation from the chest and breast tissue and from all structures around chest respectively Figure 4-30.

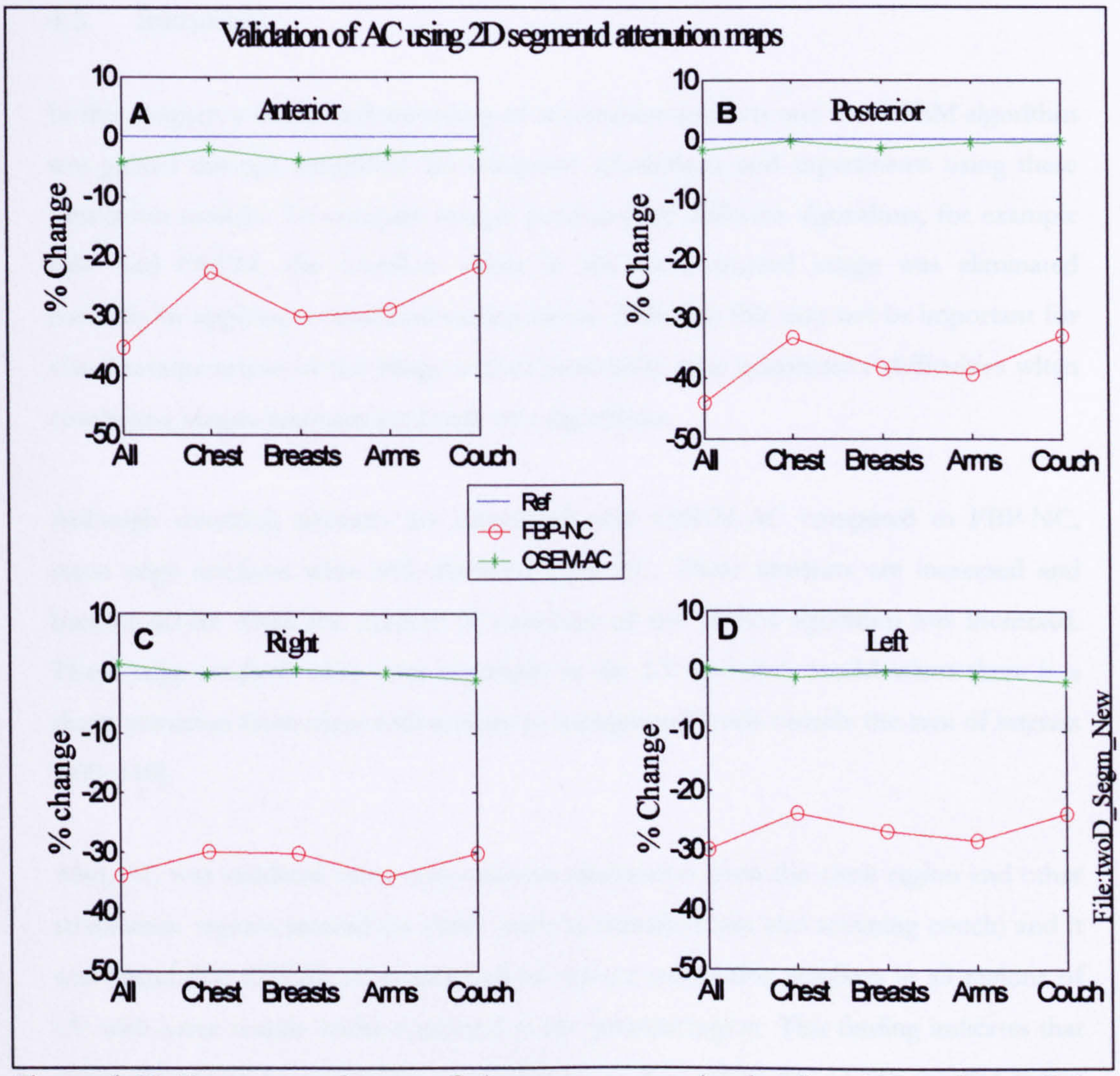

Figure 4-30 Percentage change of the mean count in the four LV regions of the emission image with non-uniform attenuation; reconstructed by FBP-NC, and OSEM-AC.

The performance of the histogram-based threshold segmentation technique strongly depends on the choice of the threshold. This choice is problematic, and there is a lot of variation in acceptable limits. The attenuation coefficient for air and the background may be neglected allowing consideration of just three types of tissues; lungs, soft tissue, and bone. The patient bed in the attenuation map image may be omitted (set to zero). The heart emission simulation needs to be more realistic by obtaining the true dimensions of the Left ventricle wall. In addition, the OSEM reconstruction might be modified in future work by applying a smoothing filter during iterations. The segmented attenuation map slices can be interpolated in the future work to produce a 3D simulation.

4.5. Summary

In this chapter, a better understanding of attenuation artefacts and the OSEM algorithm was gained through simplified 2D computer simulations and experiments using these simulation models. To compare images produced by different algorithms, for example FBP and OSEM, the overflow effect in the reconstructed image was eliminated correctly by applying a calculated scaling factor. Although this may not be important for visual interpretation of the image it does potentially raise quantitative difficulties when comparing images reconstructed with two algorithms.

Although streaking artefacts are eliminated with OSEM-AC compared to FBP-NC, some edge artefacts were still observed after AC. These artefacts are increased and became severe when the number of iterations of the OSEM algorithm was increased. These edge artefacts were seen especially in the LV emission model when there is a sharp transition from areas with activity to background levels outside the area of interest [109, 110].

Also, AC was validated using non-uniform attenuation from the chest region and other attenuation regions around the chest (such as breasts, arms, and scanning couch) and it was found that OSEM-AC works well to correct attenuation artefacts in all regions of LV with some counts under-corrected in the anterior region. This finding indicates that attenuation from breasts might be significant on the OSEM-AC on the anterior region of LV. Baily 2000, [82] reported that "if we accept the proposal that AC does work, we are then left with the question as to what is causing the confusing results, especially in

the anterior wall and apex of the heart". Also, Hendrik [111] suggest that "a decrease in counts in the anterior region in the subset of patients interpreted as having anterior attenuation artefacts in the FBP-reconstructed slices needs further investigation".

Although the experimental simulated images presented in this chapter were not representative of typical clinical cardiac SPECT images, the main benefit of simulation rather than clinical data is that the anatomy of patients could be varied. Simulations that were not involved in this experiment are; attenuation from ribs cage and sternum bone, and uptakes from liver, background, and noise. Also, other image degrading effects in SPECT such as scatter were not simulated in these experiments.

In conclusion, from the previous simple 2D simulation experiments it is shown that OSEM algorithm was able to correct attenuation artefacts and produce a percentage change values within ± 5%. The percentage of ± 5% was selected to be criteria of the acceptable results in validating AC using the 2D simplified models. Also, it was accepted that OSEM-AC within the chest with non-uniform attenuation (no added breasts or arms), needs further investigations (to clarify the reason for the reduction of counts at anterior wall with AC). This will be investigated in 3D realistic models (Chapter 5).

Chapter Five Three-dimensional computer-simulated models

This chapter focuses on the use of more realistic 3D models for validation purposes and is arranged as follows. In section 5.1, the aims are summarized. In section 5.2, details of how the 3D models were simulated are described. In sections 5.3 to 5.9 results of a series of experiments on the validation of AC using 3D models are presented, and both the qualitative and quantitative measurements are discussed. Finally, in section5.10, summary remarks are presented.

5.1. Aims

The specific aims of the experiments carried out in this chapter were:

- To simulate realistic 3D digital models of the heart and thoracic (emission and transmission 3D models).
- To validate AC using the 3D emission model with both uniform and non-uniform attenuation present reconstructed by FBP (no AC) and OSEM (with AC) algorithms.
- To evaluate the influence of changing the OSEM parameters (number of iterations and subsets) on the AC reconstructed image.
- To evaluate the effect of misregistration error between transmission and emission scans on the AC of cardiac SPECT.
- To validate AC using noisy data and to study the effect of applying a post-reconstruction filter on the noisy AC images.
- To validate AC with two common acquisition arcs 180° and 360°.

5.2. Materials and methods

The simulated 3D models used here to validate AC in cardiac SPECT were constructed from a series of CT transaxial images taken from the Zubal phantom. This phantom was obtained from the Yale University through George Zubal [107]. Researchers at Yale University have developed a voxel-based computerized phantom ("voxel man") by manually segmenting the transverse x-ray CT slices of a living human male (Figure 5 -1(a)). Each slice is a 512×512 matrix (pixel size of 1×1mm), with a 10 mm space between slices. Each type of organ or structure in each slice has a unique organ index number. The assignments of integers to the organs are shown in Table 5-1 with a total of 64 index numbers covering the human body from neck to mid-thigh

Using these indices, different anatomical structures of human body can be modelled. This Zubal phantom is an anthropomorphic phantom suitable for many computer-based modelling techniques. It is an extremely useful resource for simulation and is being used by many researchers to verify the quantification of tumours and organ uptake of radioactivity by SPECT. Complex activity and attenuation distributions can be modelled by using this computerized phantom [102].

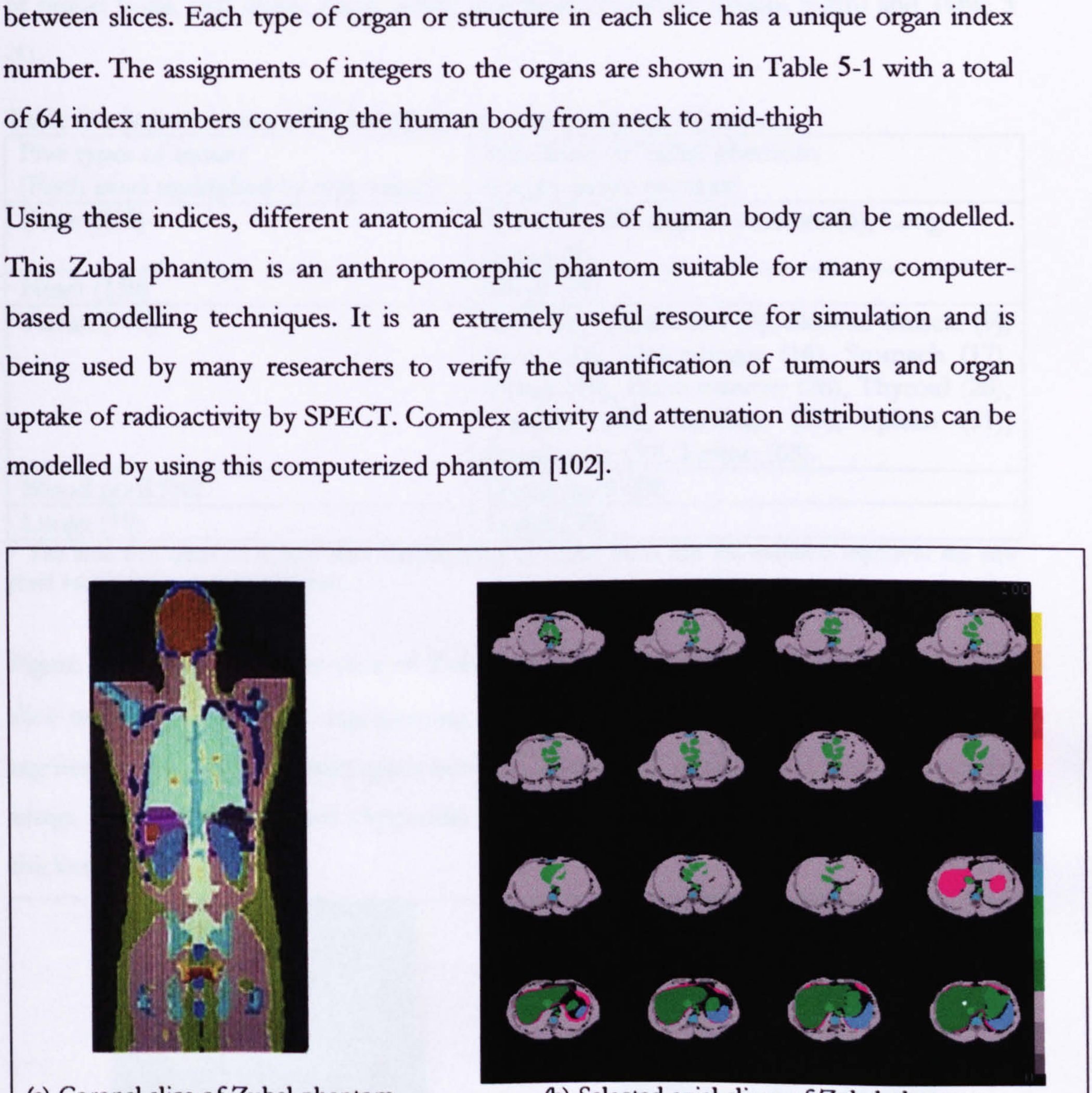

(a) Coronal slice of Zubal phantom (b) Selected axial slices of Zubal phantom

Figure 5-1 Zubal phantom[19]

[19] http://noodle.med.yale.edu/zubal/

The 26 transaxial slices covering the thoracic region were included in the 3D simulations (Figure 5-1(b)) shows 16 of the 26 slices). Each structure was selected by using threshold segmentation to create a masked image with the organ index number selected as both the upper and lower threshold values. The mask image was converted into a 256×256 (pixel size of 2×2mm) image with one count per pixel. Then, the pixel value for different types of tissue was multiplied by a new value, grouping those tissues into a single tissue type. These newly segmented Zubal transaxial slices represented five groups of tissue; bone, soft tissue, lungs, heart, and heart chambers (Figure 5-2(b) and Table 5 -1).

Table 5-1 Segmentation of Zubal phantom into five types of tissue.

Five types of tissues (Each pixel multiplied by new value)*	Structures of Zubal phantom (Organ index number)
Bone (200)	Spine (5), Rib cage & sternum (6), Long bones (8)
Heart (150)	Heart (11)
Tissue (100)	Skin (1), Spinal cord (3), Skeletal muscle (9), Liver (12), Oesophagus (16), Stomach (17), Colon (19), Bone marrow (26), Thyroid (28), Trachea (29), Cartilage (30), Spleen (31), Diaphragm (39), Lesion (63).
Blood pool (50)	Blood pool (23)
Lungs (10)	Lungs (10)

* The new five types of tissues after segmentation of Zubal slices and the numbers represent the new pixel values for each type of tissue.

Figure 5-2(a-b), shows one slice of Zubal phantom (Figure 5-2(a)) and the segmented slice with the new values representing only five types of tissues (Figure 5-2(b)). All segmented slices (with 10 mm space between slices) were interpolated using an in-house image registration algorithm (Appendix C) and smoothed to make images with a slice thickness of 2 mm.

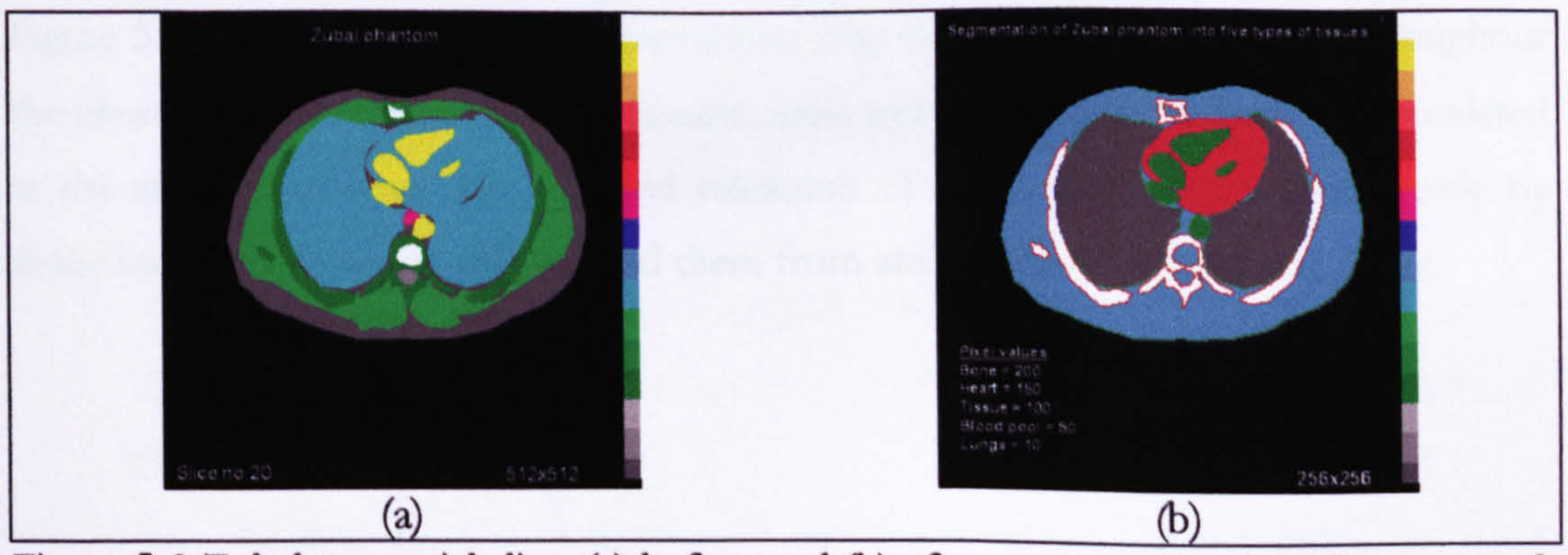

(a) (b)

Figure 5-2 Zubal transaxial slice; (a) before and (b) after segmentation into five types of tissue.

By assigning appropriate values to various structures in the segmented Zubal model (Figure 5-2(b)); emission (radioisotope uptake) and transmission (both uniform and non-uniform attenuation distribution) models were simulated. Shown in Figure 5-3 are three transverse slices (256×256) of these models. Figure 5-3(a), shows the simulated activity uptake with myocardium, soft tissue and lungs defined with a ratio of 10.0:1.0:0.1 respectively (Table 5-2). The background activity in the body was one tenth the activity of the heart, simulating the typical occurrence in practical cardiac imaging [112].

Table 5-2 Pixel values allocated in all simulated emission and transmission (uniform and non-uniform) models.

Interpolated Model (pixel value)	Emission Model	Uniform Transmission Model*	Non-Uniform Transmission Model*
Bone (200)	30	153	286
Tissue (100)	30	153	153
Heart (150)	300	153	153
Blood pool (50)	30	153	153
Lungs (10)	3	153	51

* The pixel value simulates an attenuation coefficient for 140 keV photons (^{99m}Tc). e.g. the pixel value of 153 simulates μ of 0.153 cm^{-1} in soft tissue.

These uptake values simulate the uptake in a ^{99m}Tc myocardial perfusion study (Liver uptake was not simulated). The attenuation distribution was simulated by multiplying each pixel by a value representing the attenuation coefficient of 140 keV photons (^{99m}Tc). Figure 5-3(c), shows the non-uniform attenuation map for which $\mu = 0.286\ cm^{-1}$ in bone, $\mu = 0.153\ cm^{-1}$ in soft tissue and $\mu = 0.051\ cm^{-1}$ in the lungs (Table 5-2). Figure 5-3(b), shows the uniform attenuation map for which $\mu = 0.153\ cm^{-1}$ throughout the chest region. Attenuation from breasts, arms and scanning couch were not simulated in the attenuation map. This allowed validation of attenuation effects caused only by tissue inside chest region and isolated them from any additional attenuating tissue.

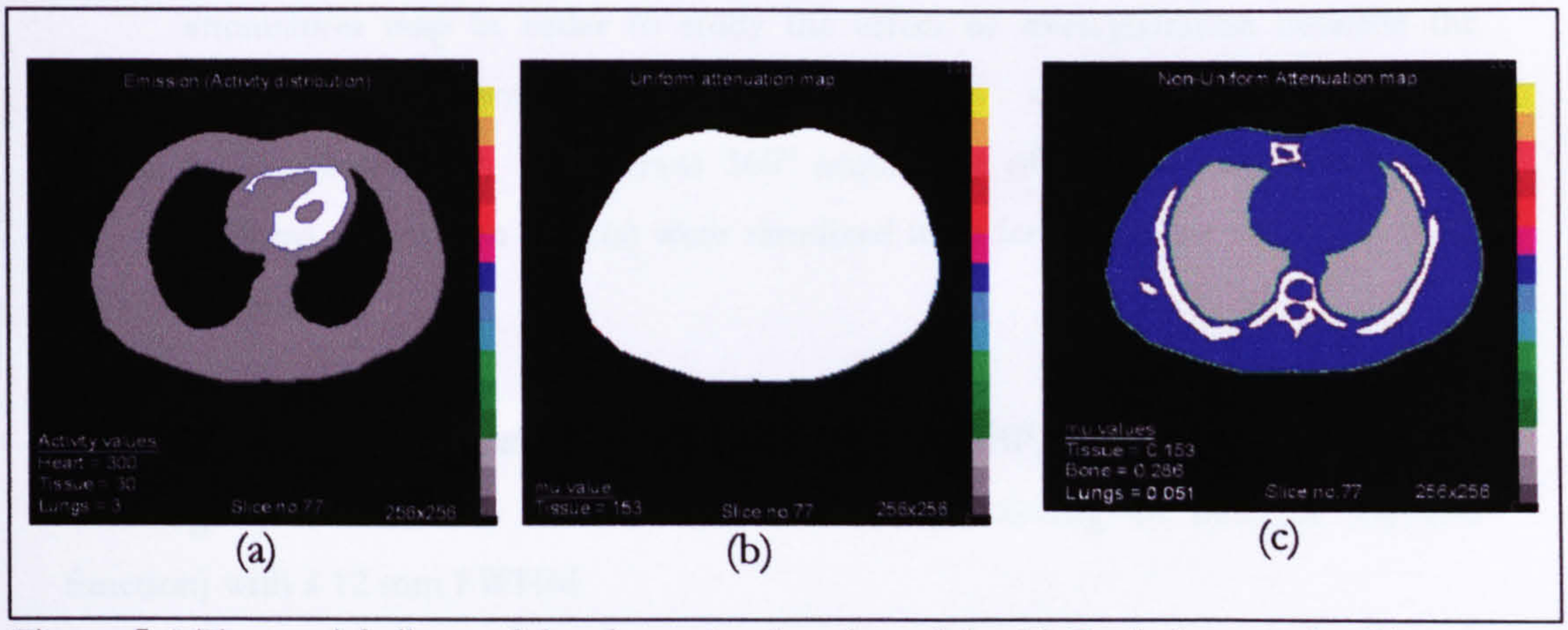

Figure 5-3 Transaxial slices of the three simulated models: (a) Emission mode. (b) Uniform transmission model. (c) Non-uniform transmission model.

Each set of two adjacent slices in the three models were joined to create a slice thickness of 4 mm in the z-axis and then forward projected (using "fwdprj") slice by slice. The projection data was simulated for 128 projections with parallel-beam collimation (matrix size = 128×128) over a 360° circular orbit. The reconstructed pixel size was 4.0 mm × 4.0 mm with slice thickness of 4.0 mm. Scatter and noise were not simulated in the first models (Noise was introduced in experiment 5.6 to produce a noisy projection data).

Multiple sets of projections data were created to perform six validation experiments:

1) In experiment 5.3, the projections of the emission model (Figure 5-3(a)) were generated without the inclusion of attenuation effects. The aim of this was to find the gold standard model to be used for a comparison purposes.
2) In experiments 5.4 and 5.5, projections of the emission model (Figure 5-3(a)) with both uniform (Figure 5-3(b)) and non-uniform (Figure 5-3(c)) attenuation effects were generated in order to validate uniform AC (UAC) and non-uniform AC (NUAC).
3) In experiment 5.6, noise was added to the projections generated in experiment 5.5 and these were reconstructed with OSEM-AC, both with and without post-filtering.
4) In experiment 5.7, the projection generated in experiments 5.3 and 5.5 were used, but with changes to the OSEM parameters (including the number of both iterations and subsets).
5) In experiment 5.8, the projections generated in experiment 5.5, were reconstructed using OSEM-AC with a misregistration error in the non-uniform

attenuation map in order to study the effect of misregistration between the transmission and emission models on AC.

6) In experiment 5.9, 180° versus 360° acquisition of emission data (with non-uniform attenuation effects) were simulated in order to validate AC using these techniques.

Before the projections were reconstructed using either FBP or OSEM algorithms, they were slightly smoothed by 2D Gaussian functions (mimicking the detector response function) with a 12 mm FWHM.

The planar images were first smoothed using a Butterworth filter (cut-off 0.2, order 10) before reconstruction with filtered back-projection using a Ramp filter. This produced the transaxial slices without AC. The smoothed planar images were used with the OSEM algorithm to reconstruct axial images.

Where the attenuation effect was included in the forward projection process, the transaxial images were reconstructed using filtered back projection without attenuation correction (FBP-NC). For OSEM-AC, the transmission model was included and compensates for the attenuation effect. For each reconstructed model, a set of 128 ×128 transaxial images were obtained. The image counts were scaled after each reconstruction using the scaling factor, which was presented in Chapter 4, section 4.1. This factor was used to restore the post-reconstruction pixel values. The major steps of reconstructions are shown in Figure 5-4.

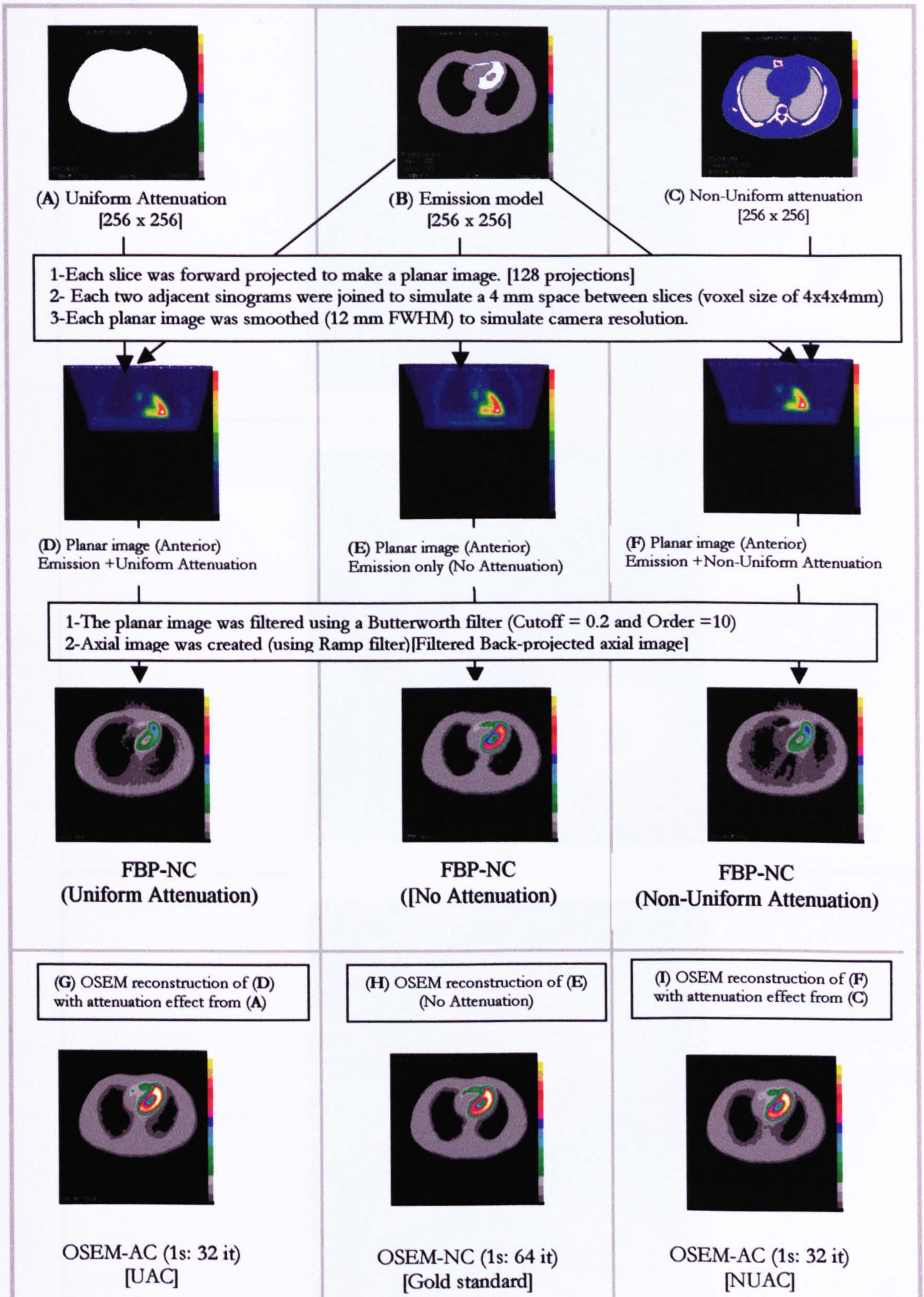

Figure 5-4 Flow chart of how transaxial slices with and without AC were reconstructed using both FBP and OSEM reconstruction algorithms.

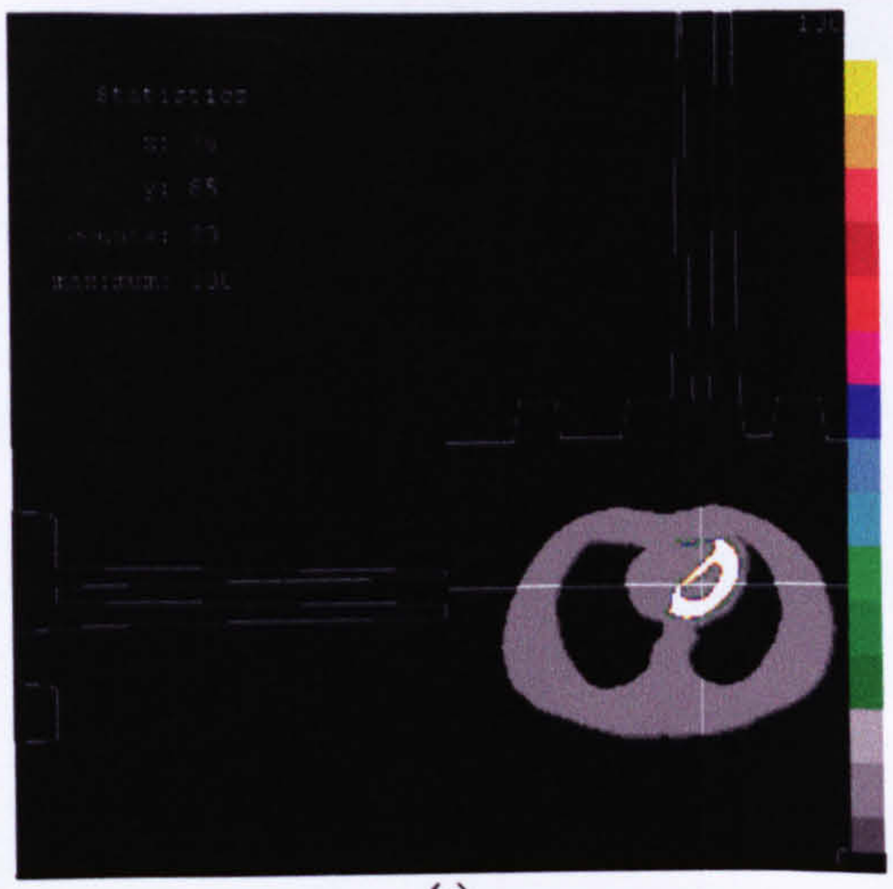

(a)

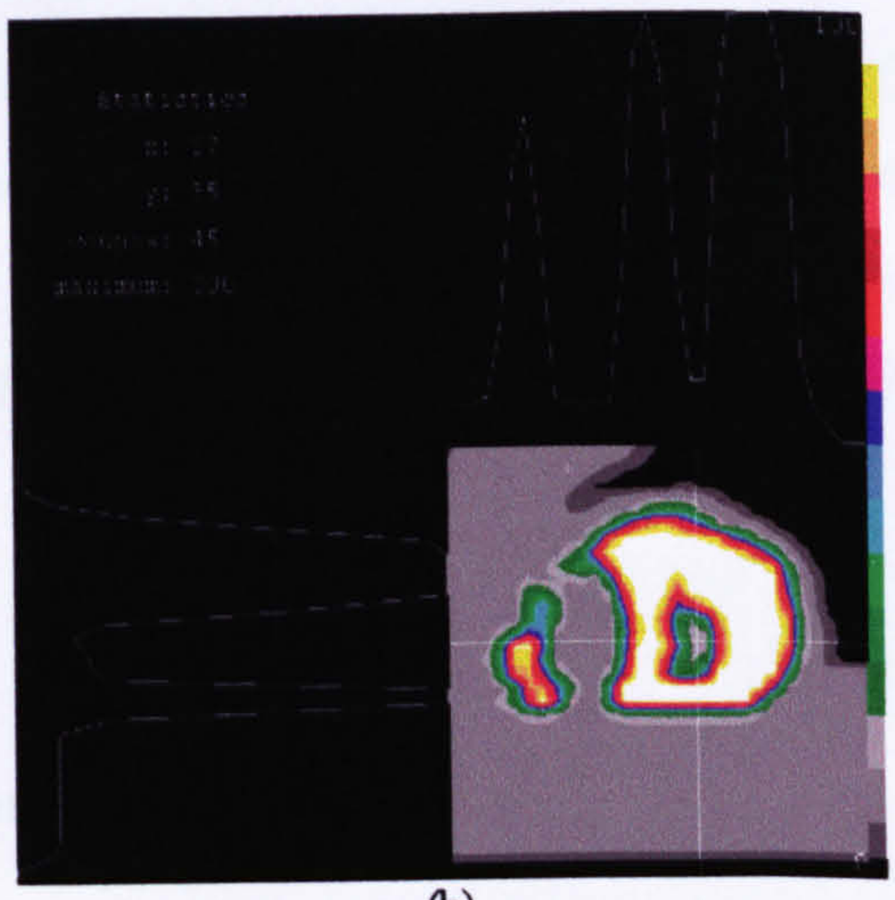

(b)

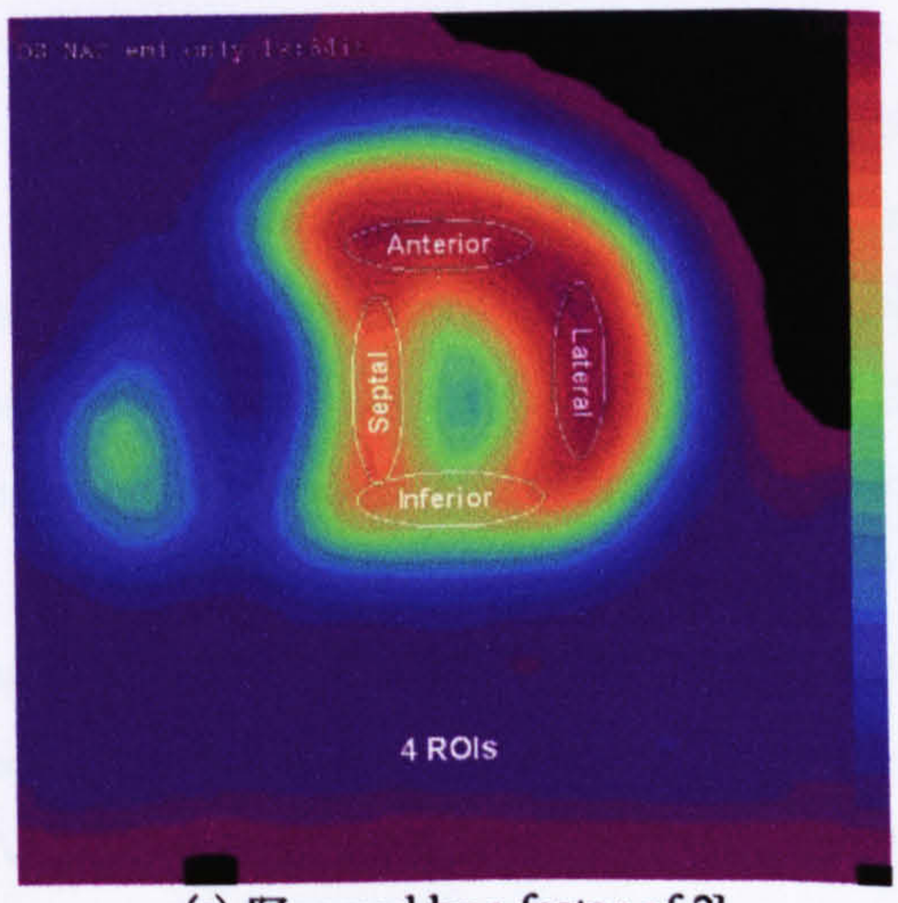

(c) [Zoomed by a factor of 2]

Figure 5-5 (a) and (b) demonstrate the position of the count density profiles for the transaxial image and short axis image respectively. The positioning of the 4ROIs inside the short-axis slice is shown in (c).

The reconstructed transaxial images were reoriented into short-axis, vertical long-axis and horizontal long-axis views, and one transaxial and short-axis slice were selected for comparison purposes. A mid-range short-axis slice was selected and four regions were drawn in which the mean counts was calculated corresponding to the anterior, septal, inferior, and lateral walls of the LV. Furthermore, using 64 short-axis images, a two-dimensional polar map of the heart model was generated (a bull's-eye plot).

All reconstructed images were qualitatively and quantitatively evaluated using the following measures:

- A selected transaxial slice (128×128)
- A selected short-axis slice (64×64)
- Horizontal and vertical count density profiles (one-pixel-wide) (Figure 5-5(a-b).
- Regional quantification by measuring mean counts at four locations (anterior, septal, inferior, and lateral) in a short-axis slice of the LV (Figure 5-5(c)).
- Short-axis, vertical and horizontal long axis images in the format of a single report image.
- Bull's-eye plot

5.3. Gold standard emission model

In order to test the effectiveness of the OSEM algorithm to correct attenuation artefacts, the number of iterations has to be selected to produce the "gold standard" reference model. The gold standard model is the emission model with a-priori known activity reconstructed using OSEM without attenuation present. In this experiment planar emission images (without attenuation), were reconstructed using OSEM, with 1 subset and different numbers of iterations (4, 8, 16, 32, 64 and 128) in order to find the optimum number of iterations to produce a gold standard emission model.

All reconstructed images (transaxial and short axis) were qualitatively compared to the transaxial and short-axis slices shown in Figure 5-6. As can be seen from Figure 5-6, the septum wall of the LV looks thinner compared to other walls. Because of the thinness of the membranous septum, it is often appear to be shorter than the other walls.

Clinically, activity at the base of the septum is generally further reduced, due to normal anatomic thinning of the septum [113].

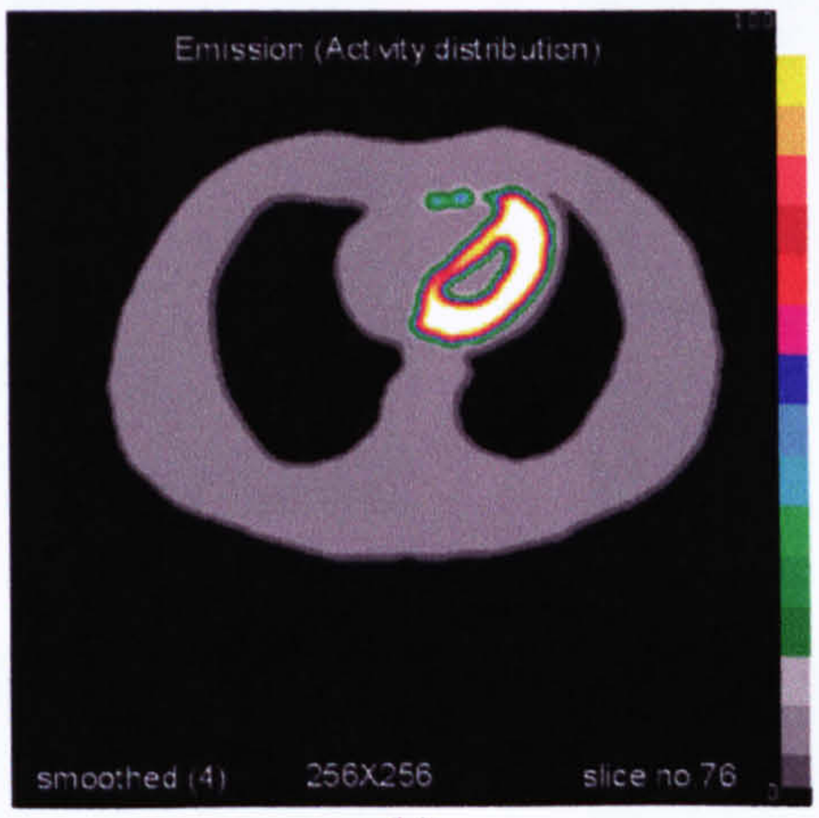

(a)

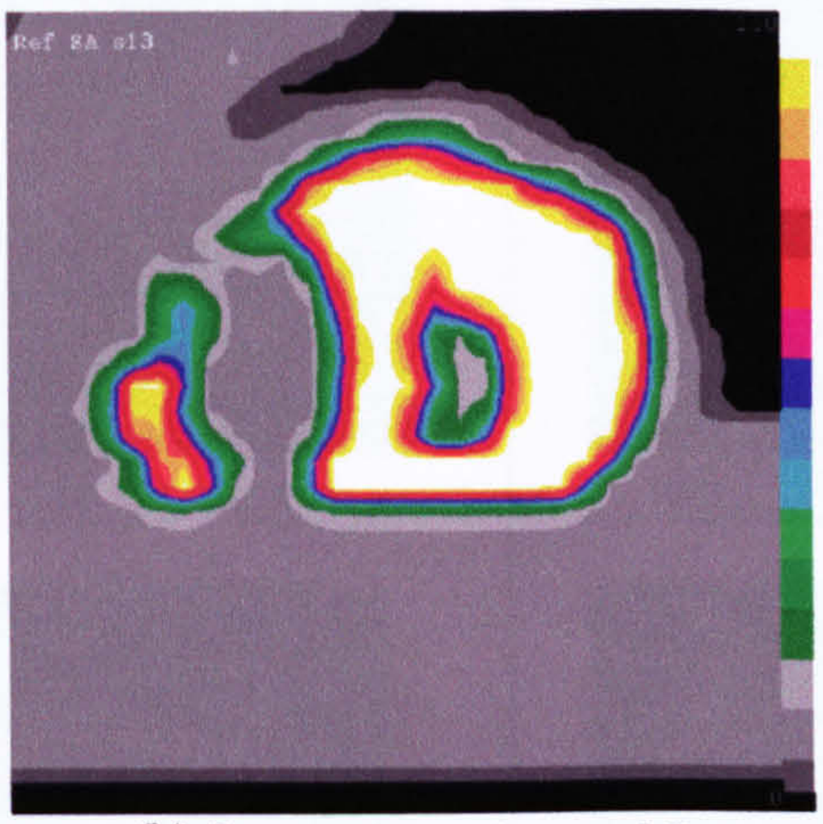

(b) [Zoomed by a factor of 2]

Figure 5-6 Emission model before reconstruction: (a) transaxial slice, and (b) short-axis slice.

Figure 5-7(a-f) and Figure 5-8(a-f) display the emission images (transaxial and short-axis slices) without attenuation, reconstructed by the OSEM algorithm with one subset and different number of iterations. As can be seen from these images, as more iteration is performed, the image contrast improves and the image has increased computational noise. Qualitatively, at only 64 iterations, the reconstructed image most closely matches the reference image.

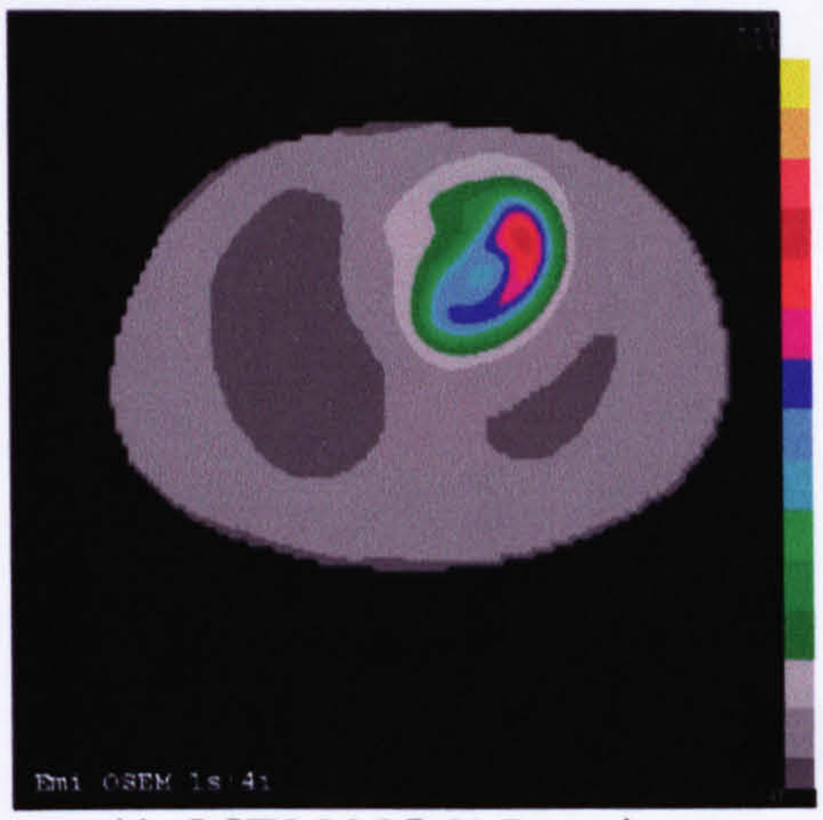

(a) OSEM-NC [4 Iterations]

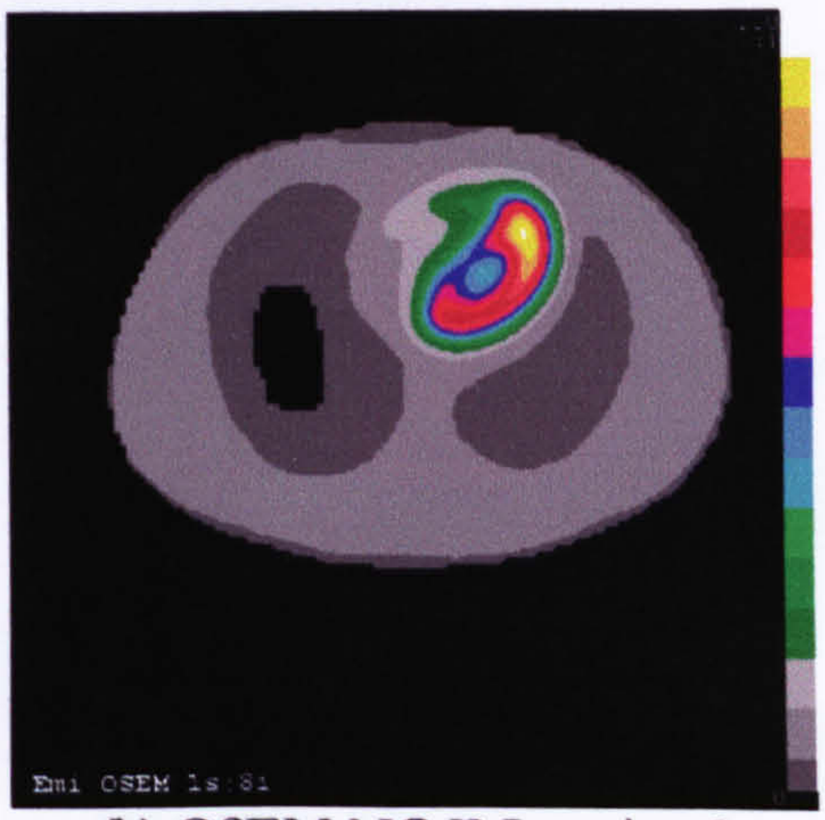

(b) OSEM-NC [8 Iterations]

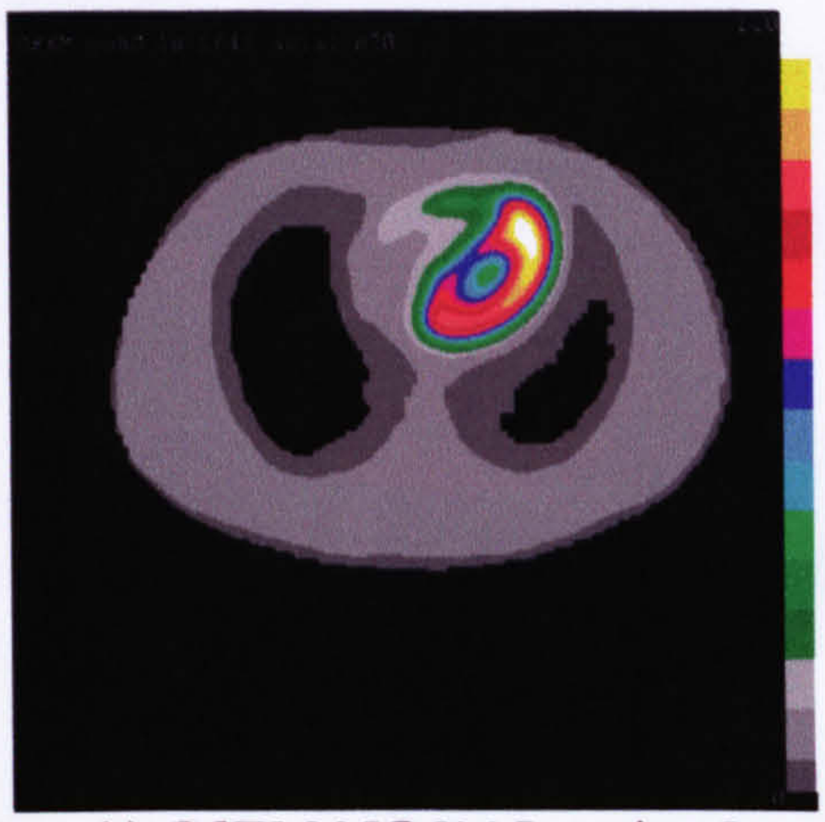

(c) OSEM-NC [16 Iterations]

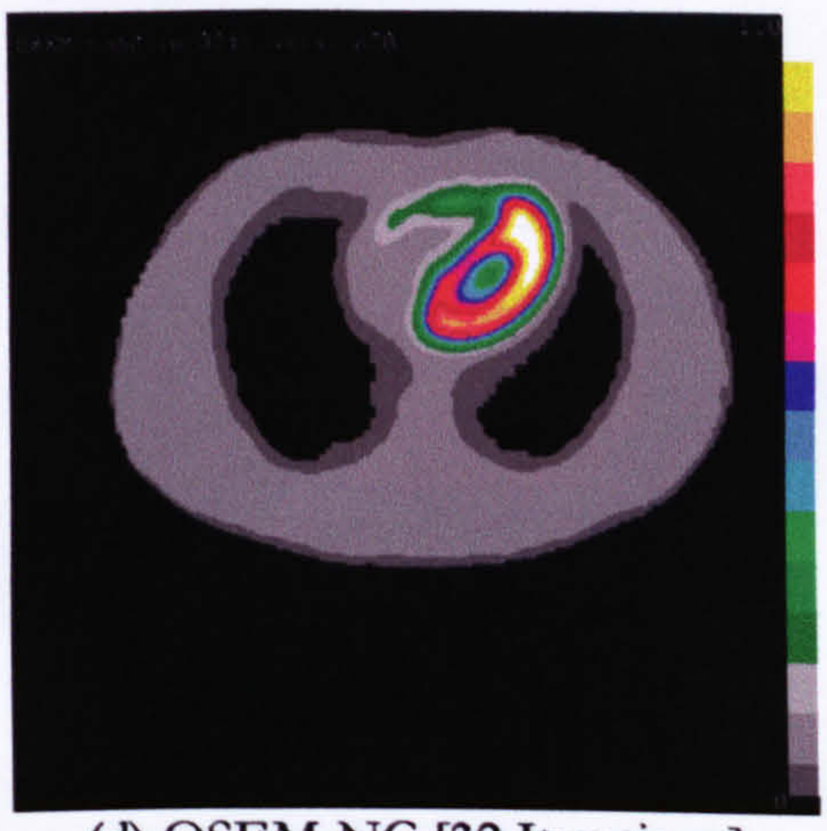

(d) OSEM-NC [32 Iterations]

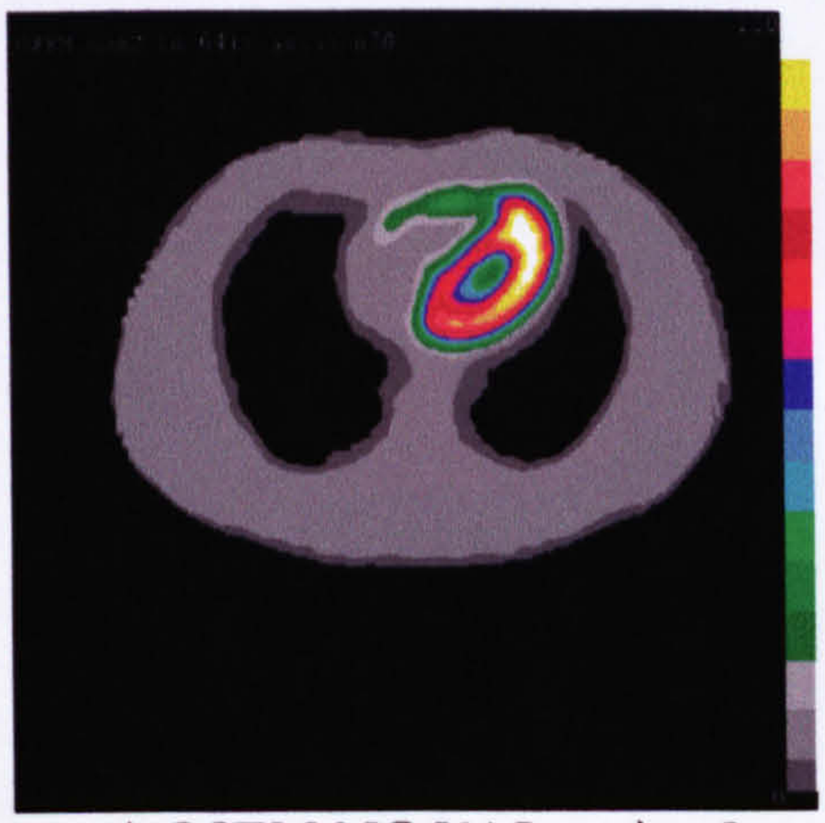

(e) OSEM-NC [64 Iterations]

(f) OSEM-NC [128 Iterations]

All slices are 128×128

Figure 5-7 Reconstructed transaxial slices of the emission model (without attenuation) using OSEM algorithm with one subset and the indicated number of iterations.

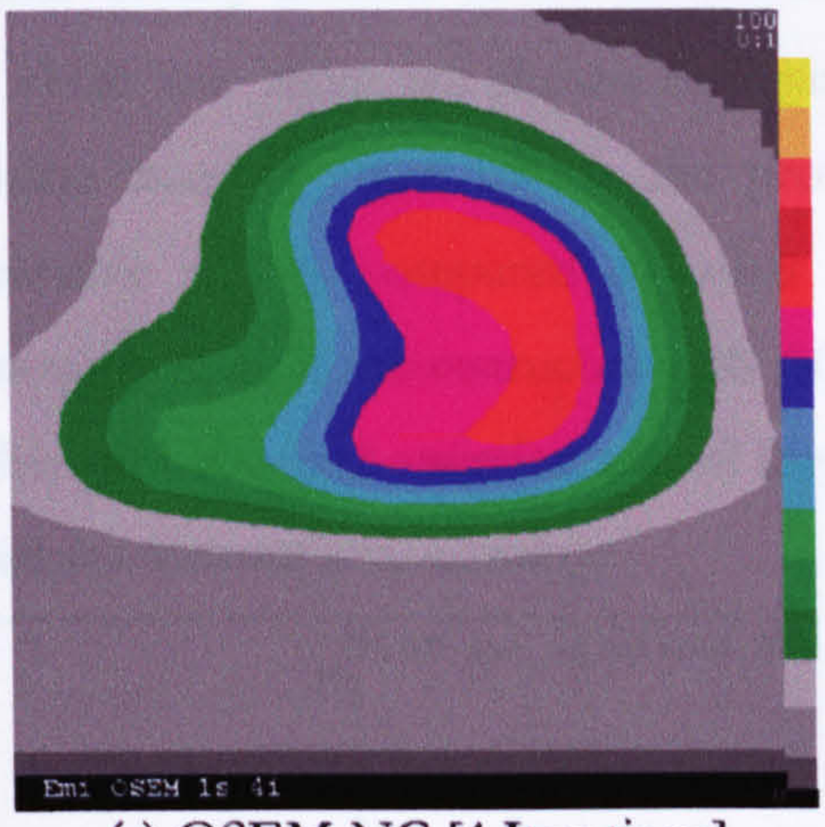

(a) OSEM-NC [4 Iterations]

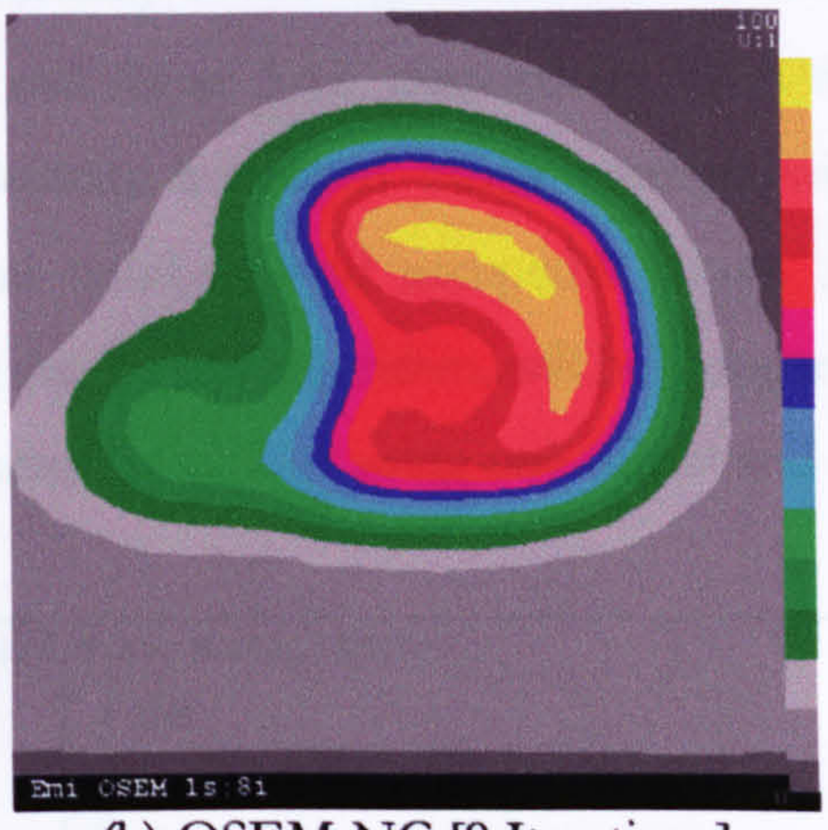

(b) OSEM-NC [8 Iterations]

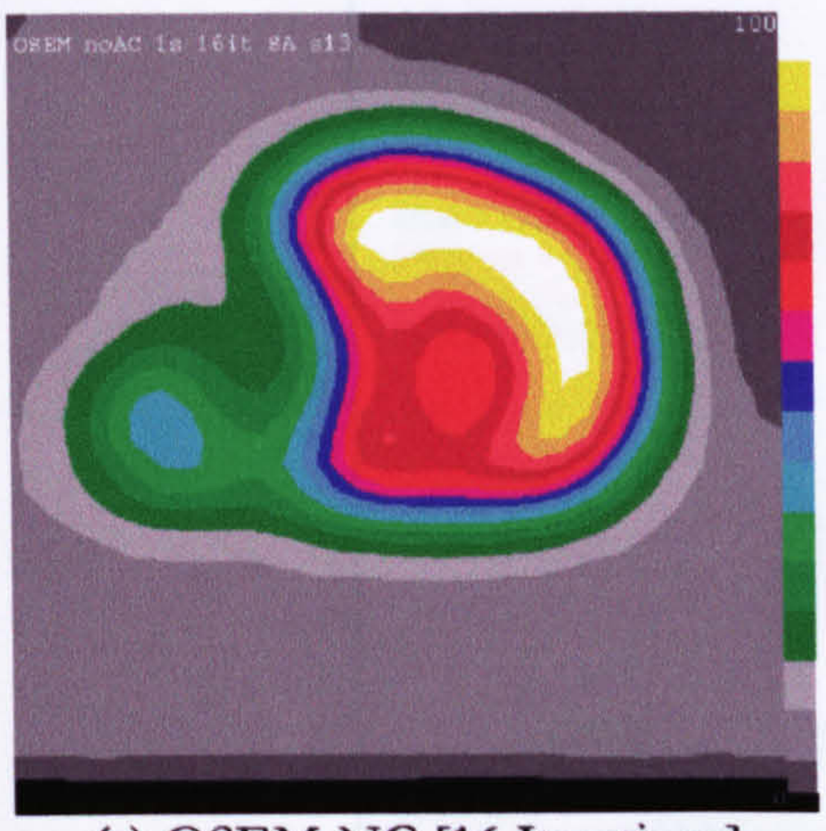

(c) OSEM-NC [16 Iterations]

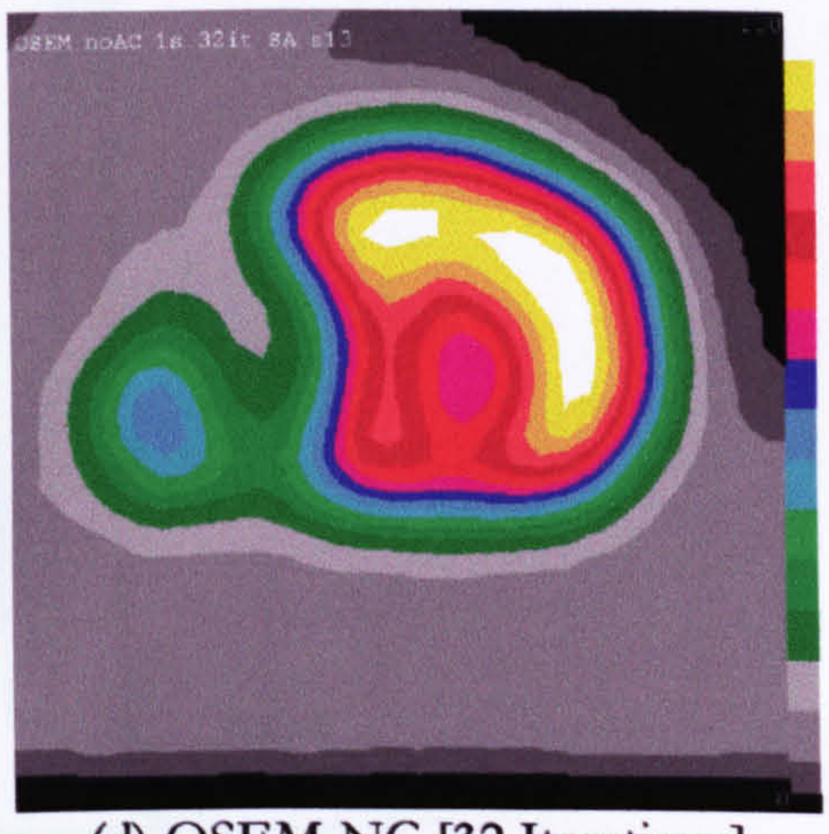

(d) OSEM-NC [32 Iterations]

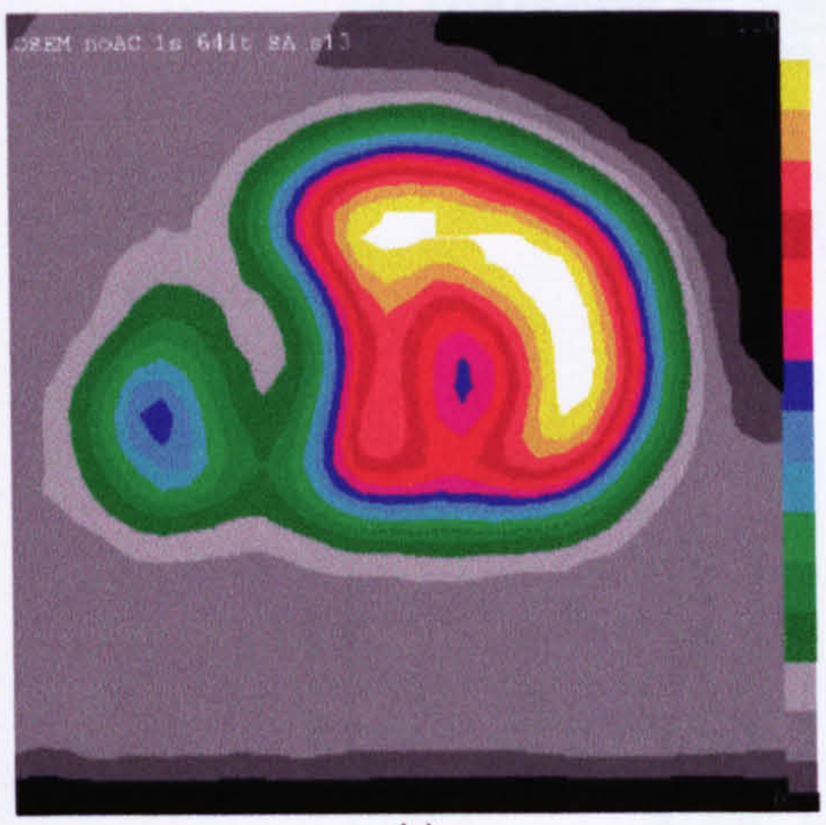

(e)
OSEM-NC [64 Iterations]

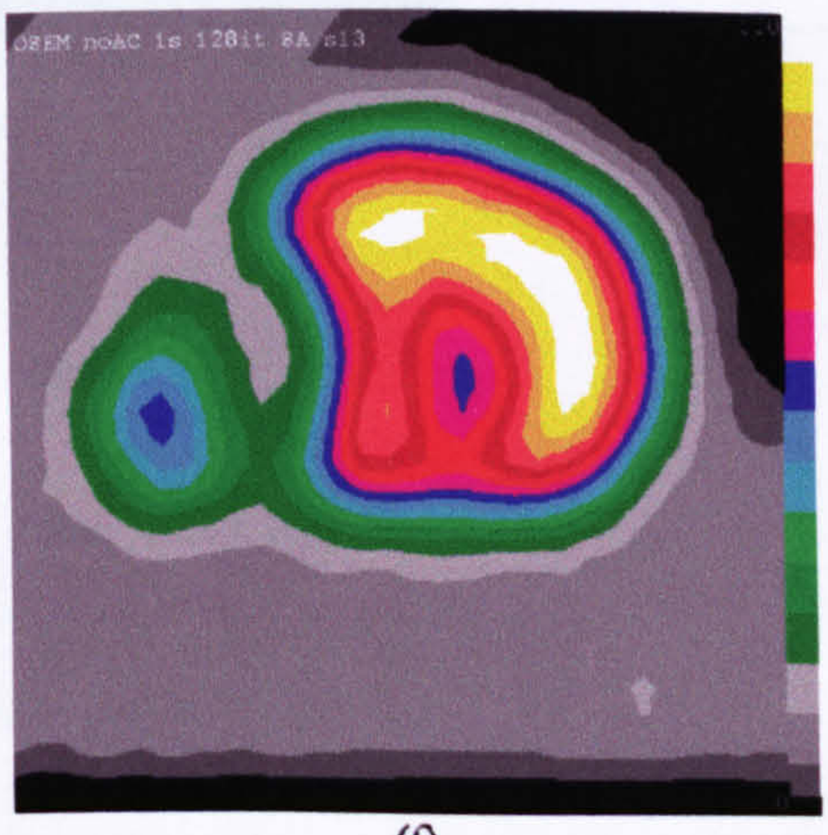

(f)
OSEM-NC [128 Iterations]

All slices are 64×64

Figure 5-8 Reconstructed short-axis slices of the emission model (without attenuation) using OSEM algorithm with one subset and the indicated number of iterations.

Counts density profiles (both horizontal and vertical) of the representative transaxial and short axis slices are shown in Figure 5-9 and Figure 5-10, respectively. With the iteration number equal to 64, the profiles illustrate improved image contrast with reasonable counts compared to other iteration numbers and acceptable noise. All subsequent images reconstructed with AC using the OSEM algorithm, will be compared to this gold standard emission model (reconstructed by OSEM using one subset and 64 iterations without attenuation).

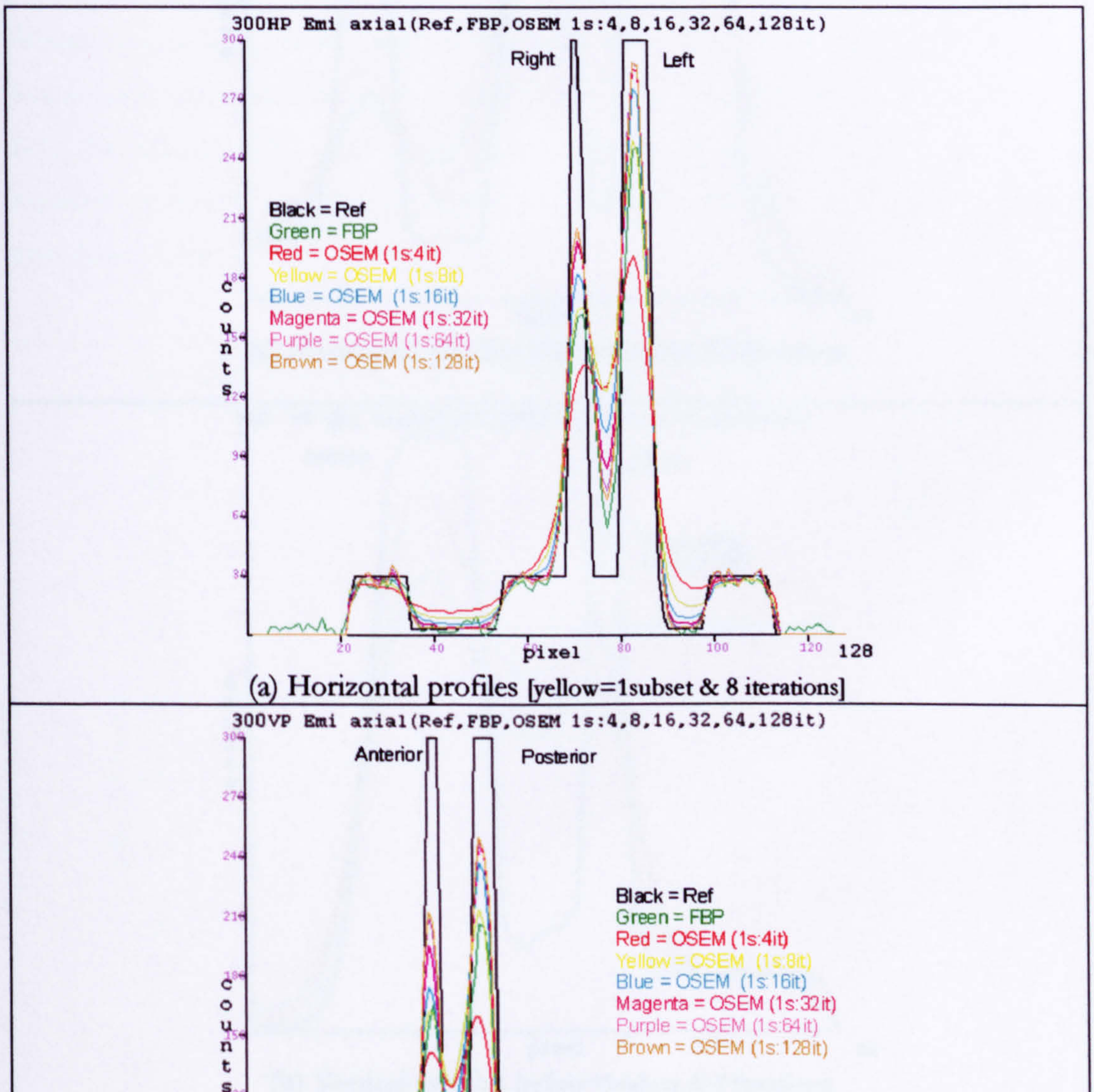

(a) Horizontal profiles [yellow=1subset & 8 iterations]

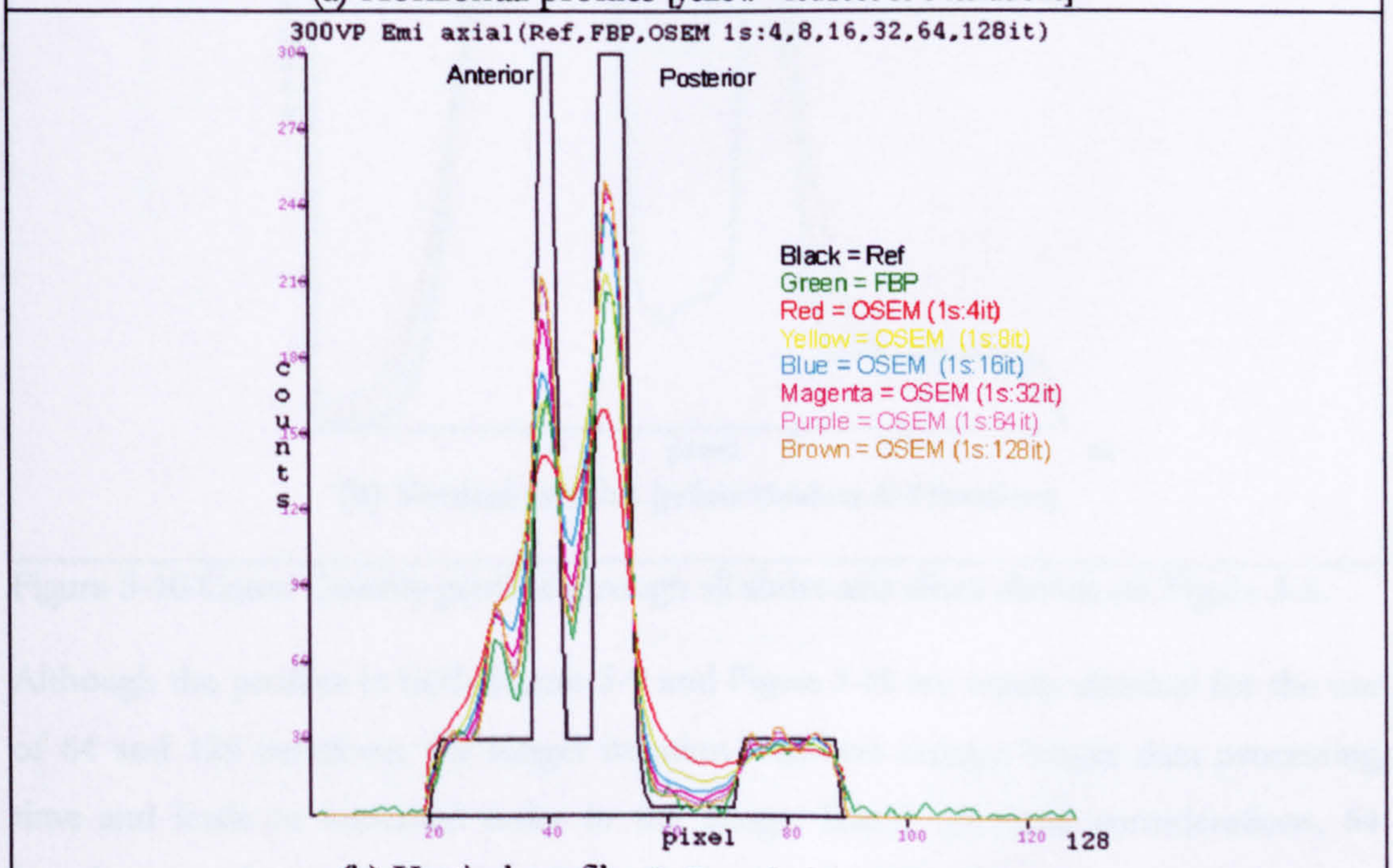

(b) Vertical profiles [yellow=1subset & 8 iterations]

Figure 5-9 Count Density profiles through all transaxial slices shown on Figure 5-7.

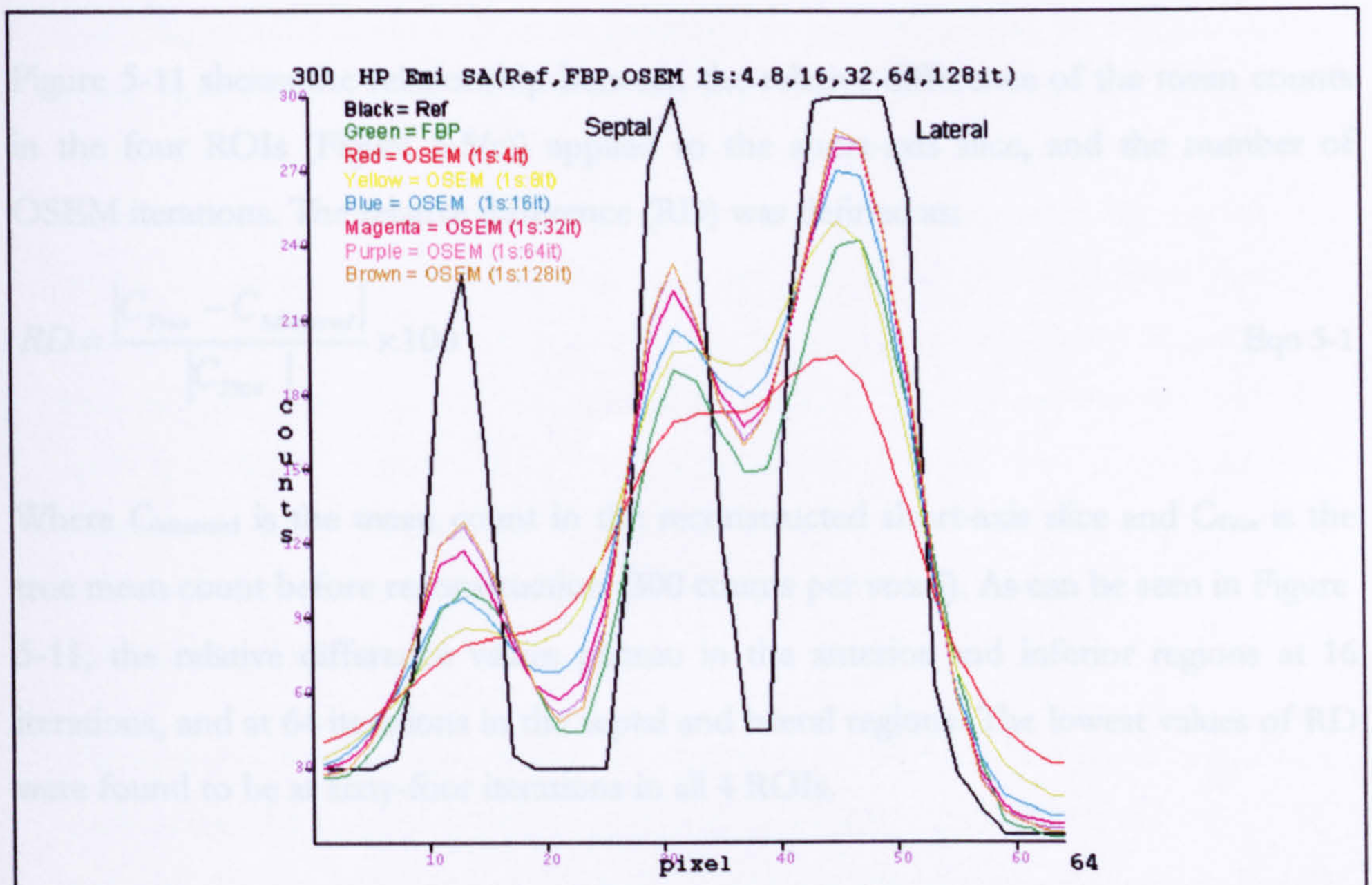

(a) Horizontal profiles [yellow=1subset & 8 iterations]

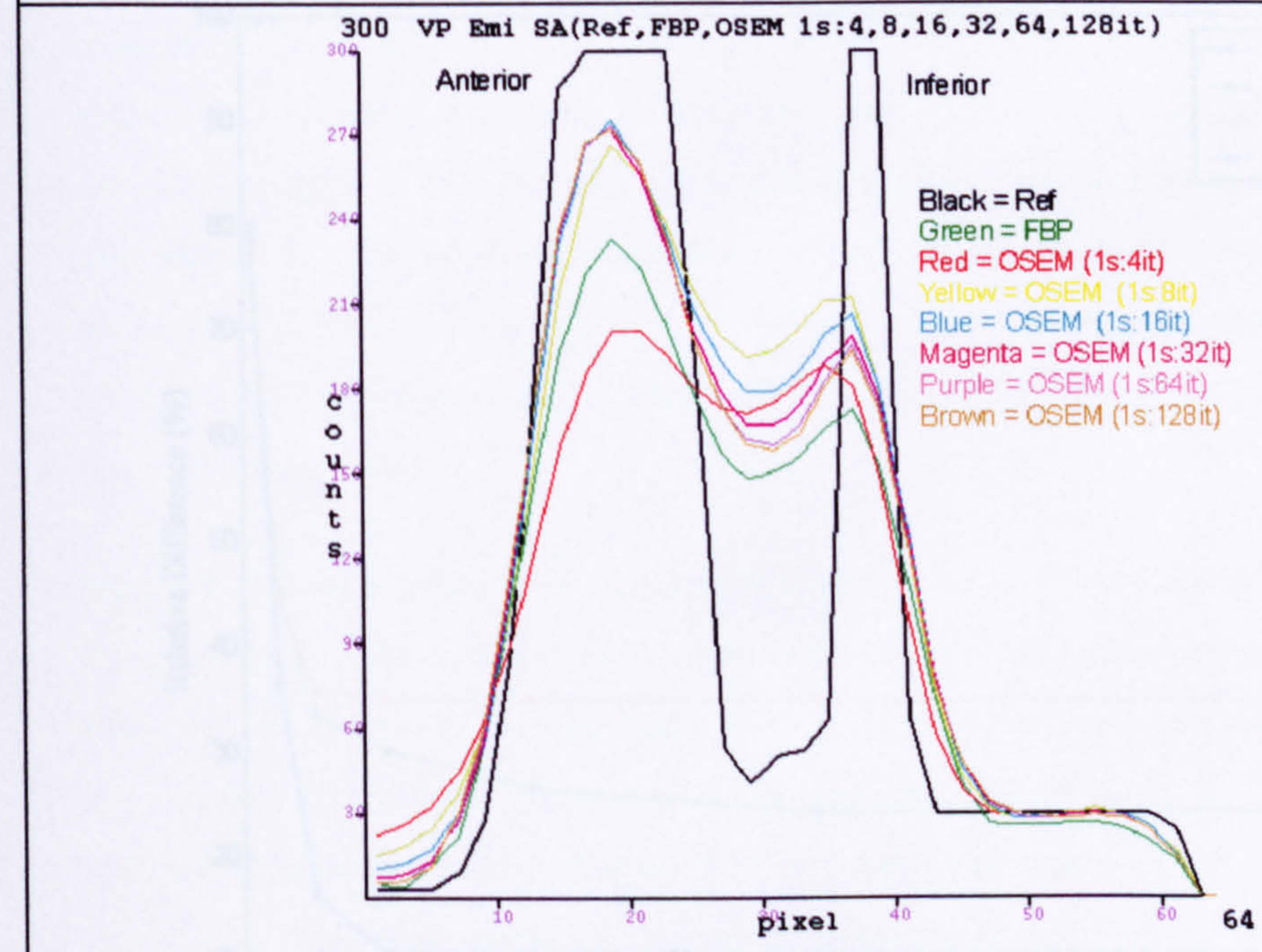

(b) Vertical profiles [yellow=1subset & 8 iterations]

Figure 5-10 Count Density profiles through all short-axis slices shown on Figure 5-8.

Although the profiles in both Figure 5-9 and Figure 5-10 are nearly identical for the use of 64 and 128 iterations, the longer iteration numbers require longer data processing time and leads to increased noise in the image. Based on these considerations, 64 iterations was the appropriate number of iterations for the gold standard model.

Figure 5-11 shows the relationship between the relative difference of the mean counts in the four ROIs (Figure 5-5(c)) applied to the short-axis slice, and the number of OSEM iterations. The relative difference (RD) was defined as;

$$RD = \frac{|C_{True} - C_{Measured}|}{|C_{True}|} \times 100 \qquad \text{Eqn 5-1}$$

Where $C_{Measured}$ is the mean count in the reconstructed short-axis slice and C_{True} is the true mean count before reconstruction (300 counts per voxel). As can be seen in Figure 5-11, the relative difference values plateau in the anterior and inferior regions at 16 iterations, and at 64 iterations in the septal and lateral regions. The lowest values of RD were found to be at sixty-four iterations in all 4 ROIs.

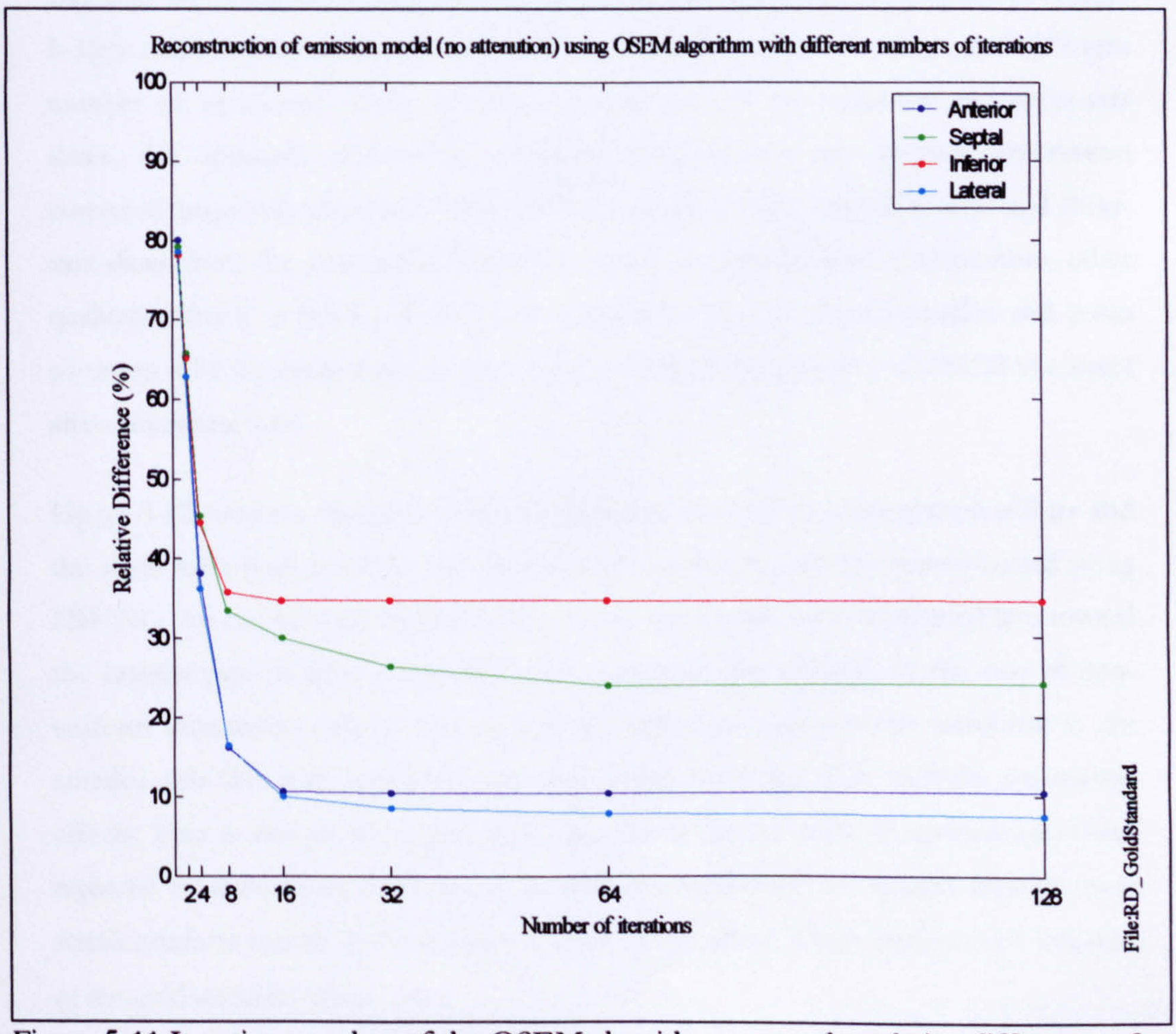

Figure 5-11 Iteration number of the OSEM algorithm versus the relative difference of the mean counts for the four ROIs applied to the short-axis slices.

Tsui [35], found that about 30 to 60 iterations are required for the MLEM to reach a stable, final image estimate of clinical myocardial SPECT data without attenuation correction. Since the number of subsets used with the OSEM reconstruction of the emission model was equal to one, this means that the OSEM algorithm corresponds to the MLEM original version of the algorithm. From Figure 5-9, it was clear that the best count uniformity and image contrast were achieved with iterations beyond 32 iterations. However, the increase in iterations beyond 64, requires longer processing time and will result in a higher noise level in the image. Therefore, from these simulations, the emission model reconstructed by OSEM (1 subset and 64 iterations) without attenuation present was selected to be the gold standard model in all-following validation experiments.

The emission model (Figure 5-3(a)) was reconstructed with uniform and non-uniform attenuation. The attenuated projection data were reconstructed without AC using FBP and with AC using both uniform (Figure 5-3(b)) and non-uniform attenuation (Figure 5-3(c)) maps incorporated into the OSEM algorithm (using 1 subset and different number of iterations). Using qualitative assessment of the transaxial and short-axis slices, the optimum number of iterations that produce the accurate attenuation corrected image was identified. Only one selected slice of the transaxial slices and short-axis slices from the attenuation corrected images are shown here. Furthermore, other qualitative (such as bull's-eye plot) and quantitative (counts density profiles and mean counts at 4 ROIs) measurements were used to validate the accuracy of OSEM to correct attenuation artefacts.

Figure 5-12 presents the gold standard transaxial slice without attenuation effects and the slices with both uniform and non-uniform attenuation effects reconstructed using FBP-NC. As can be seen from Figure 5-12(b), the counts were attenuated less toward the anterior side of chest compared to the posterior side of chest. In the case of non-uniform attenuation effects (Figure 5-12(c)), still there was a count reduction in the anterior side but with improved counts in comparison the with uniform attenuation effects. This is due to the attenuation from tissue (in the uniform attenuation) being replaced by attenuation from lungs. In addition, both FBP-NC images contain some streak artefacts mainly at the anterior surface of the chest. These artefacts are not seen in the gold standard image.

(a) Gold standard

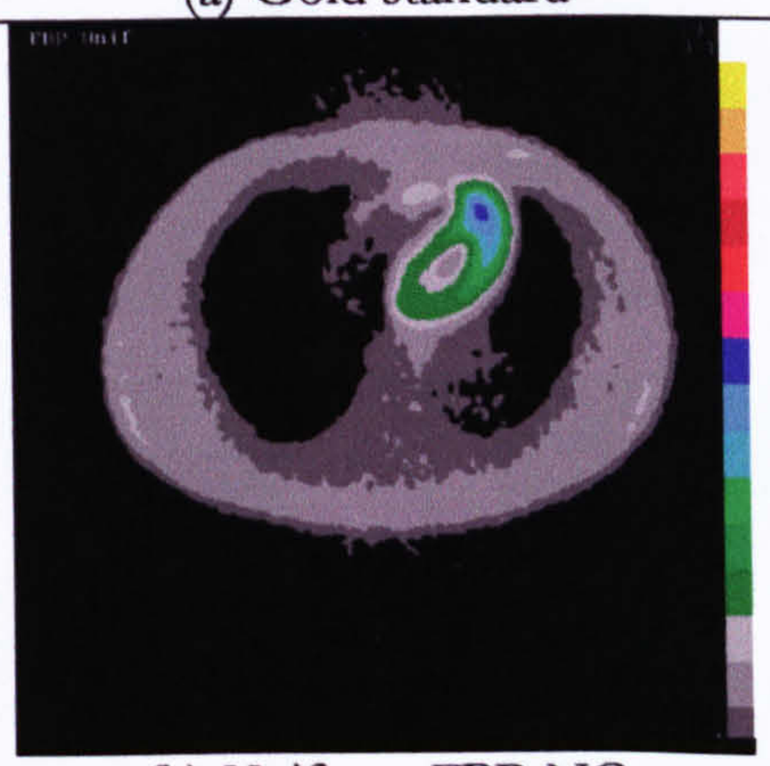

(b) Uniform FBP-NC

(c) Non-uniform FBP-NC

Figure 5-12 Reconstructed transaxial slices of the emission model (with both uniform and non-uniform attenuation effects included) using FBP-NC.

5.4. Validation of uniform AC

Figure 5-13(a-f) shows the uniform attenuation correction transaxial slices obtained using the OSEM algorithm with a single subset and different numbers of iterations (4, 8, 16, 32, 64 and 128). The corresponding short-axis slices are shown in Figure 5-14(a-f). Comparison of the images without (Figure 5-12(b)) and with AC (Figure 5-13) AC clearly demonstrates that streak artefacts shown in the anterior surface of the chest were

eliminated using OSEM-AC. Based on the results obtained from both transaxial and short-axis slices, 32 iterations was the optimal number for uniform AC.

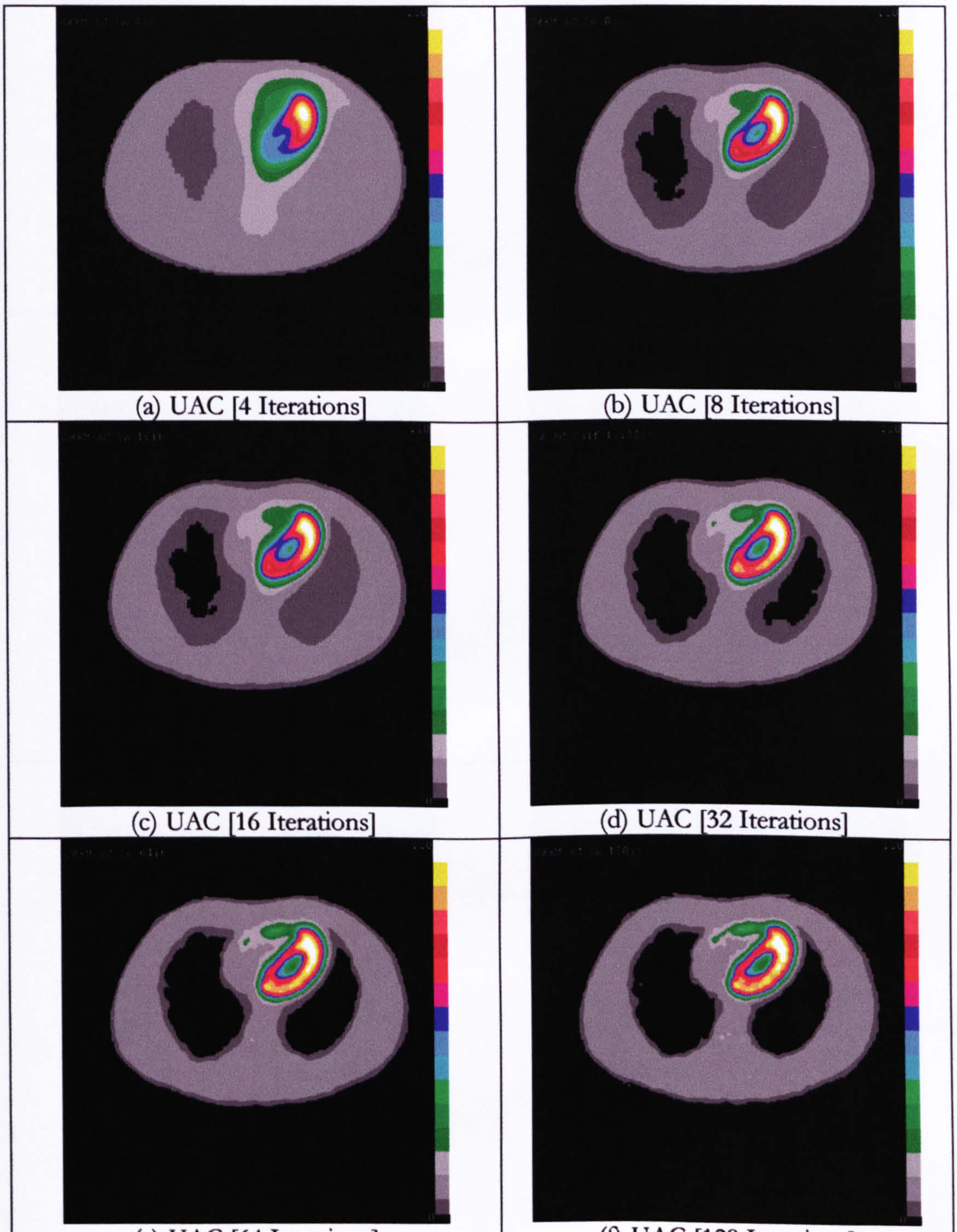

(a) UAC [4 Iterations]

(b) UAC [8 Iterations]

(c) UAC [16 Iterations]

(d) UAC [32 Iterations]

(e) UAC [64 Iterations]

(f) UAC [128 Iterations]

All slices are 128×128

Figure 5-13 Reconstructed transaxial slices of uniform AC using OSEM with 1 subset and a number of iterations ranging from 4 to 128 as indicated.

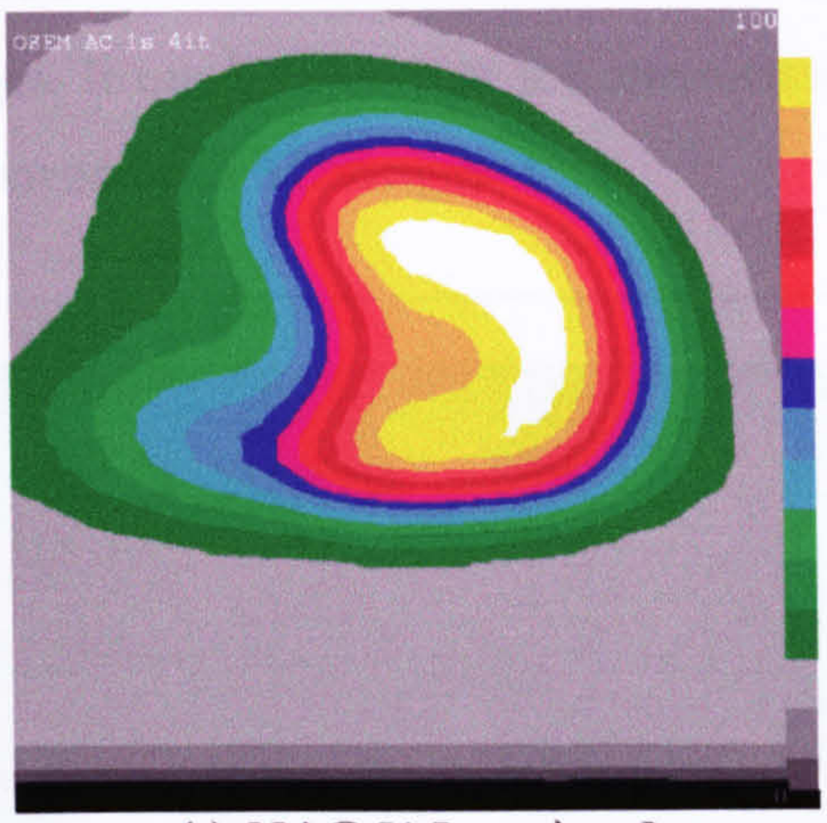

(a) UAC [4 Iterations]

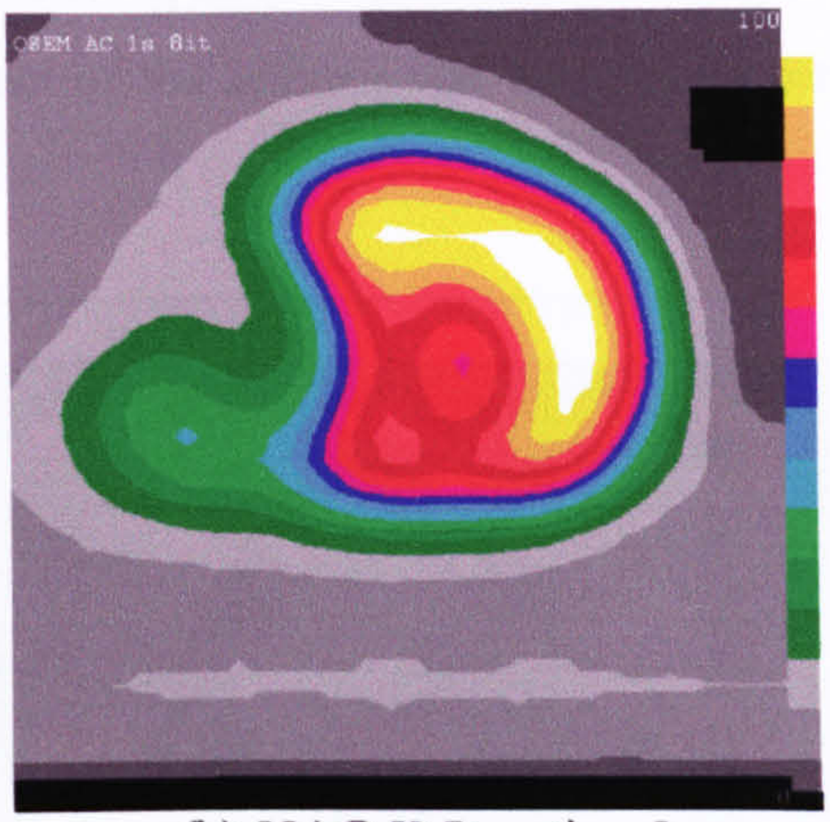

(b) UAC [8 Iterations]

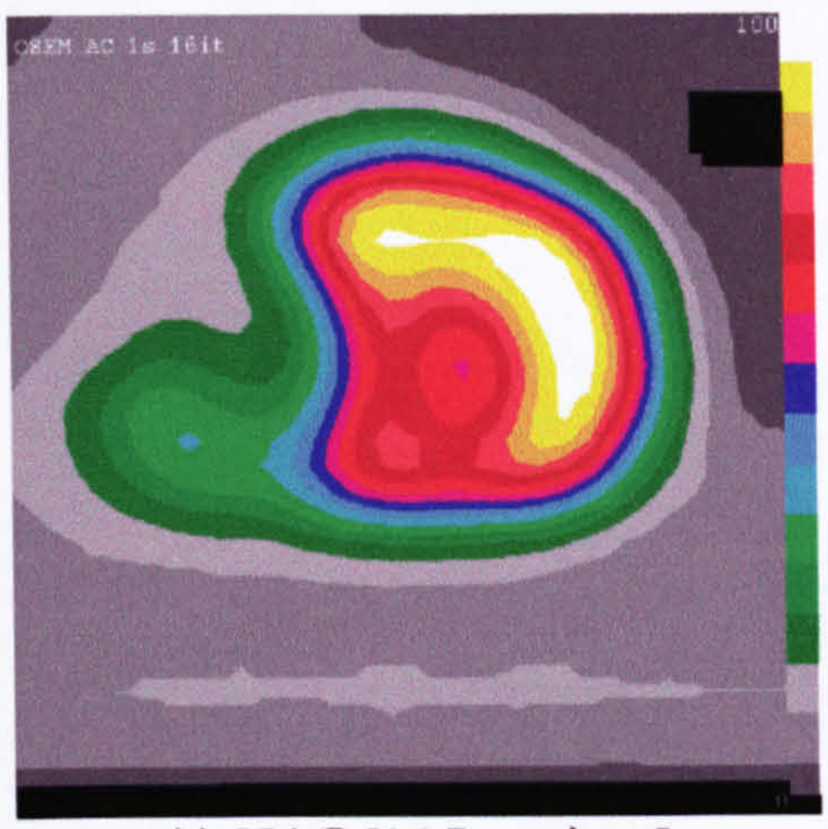

(c) UAC [16 Iterations]

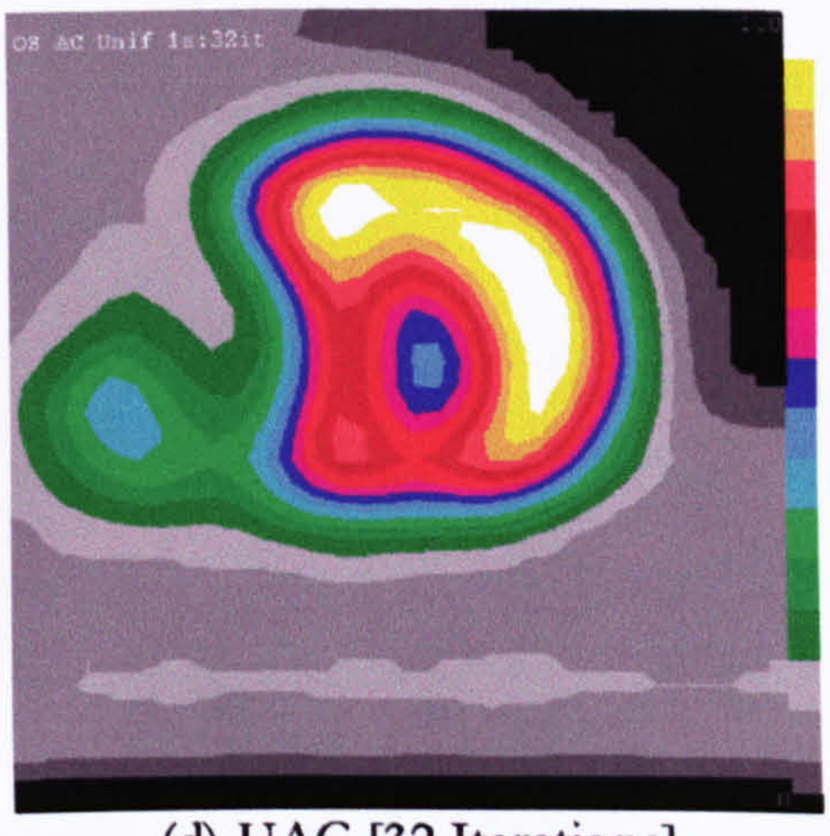

(d) UAC [32 Iterations]

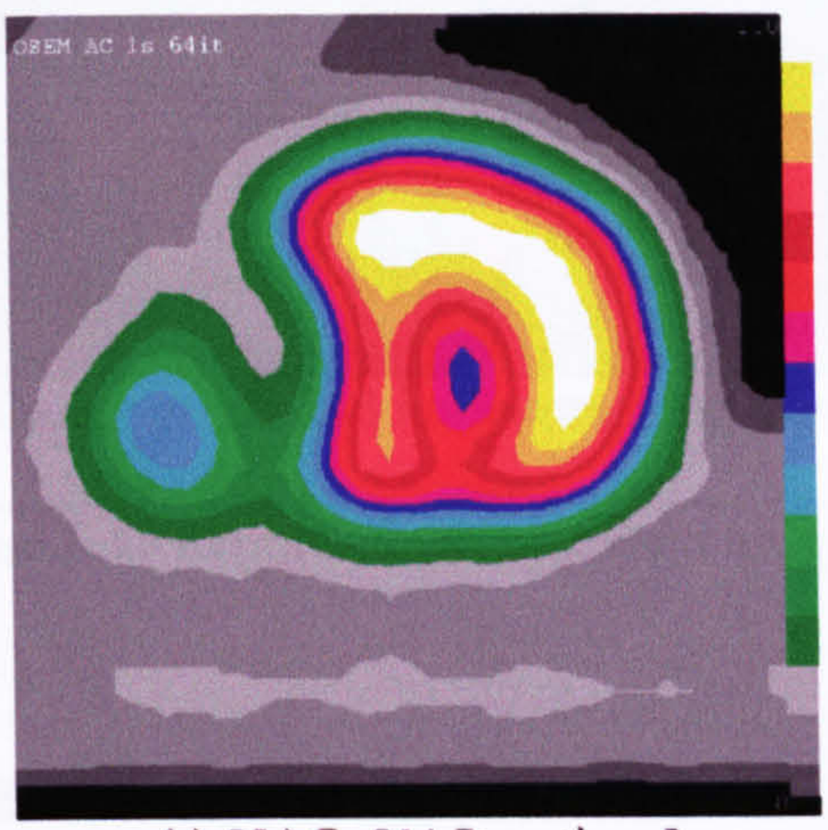

(e) UAC [64 Iterations]

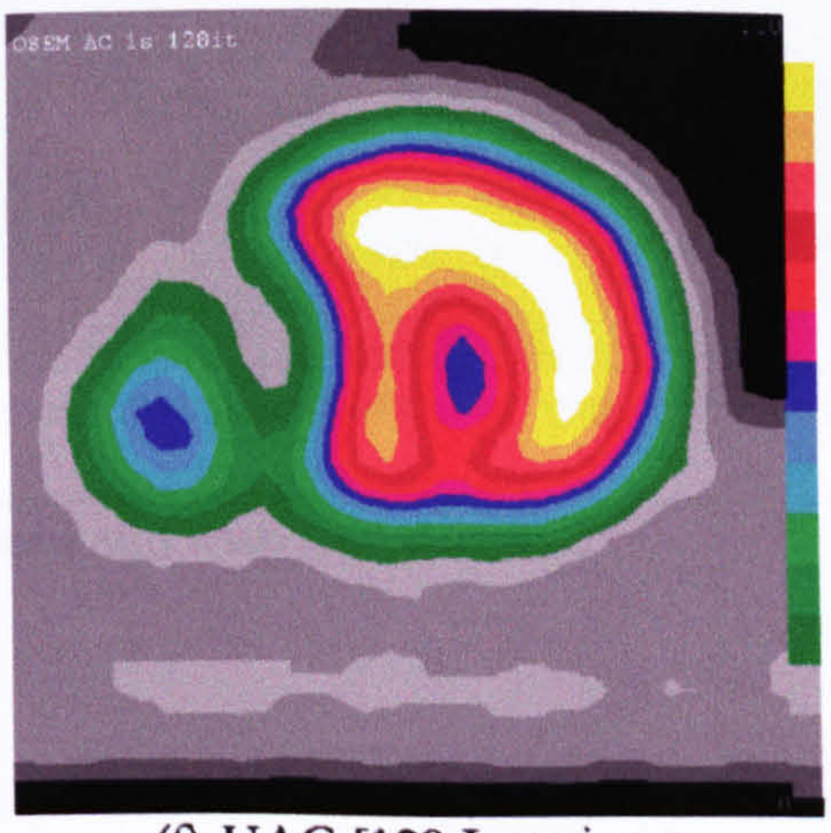

(f) UAC [128 Iterations]

All slices are 64×64

Figure 5-14 Reconstructed short-axis slices of uniform AC using OSEM with 1 subset and a number of iterations ranging from 4 to 128 as indicated.

Figure 5-15 demonstrates the validation of the AC using all short, vertical and long-axis images. It can be seen that the attenuation artefact of the inferior wall was significantly improved in all AC images.

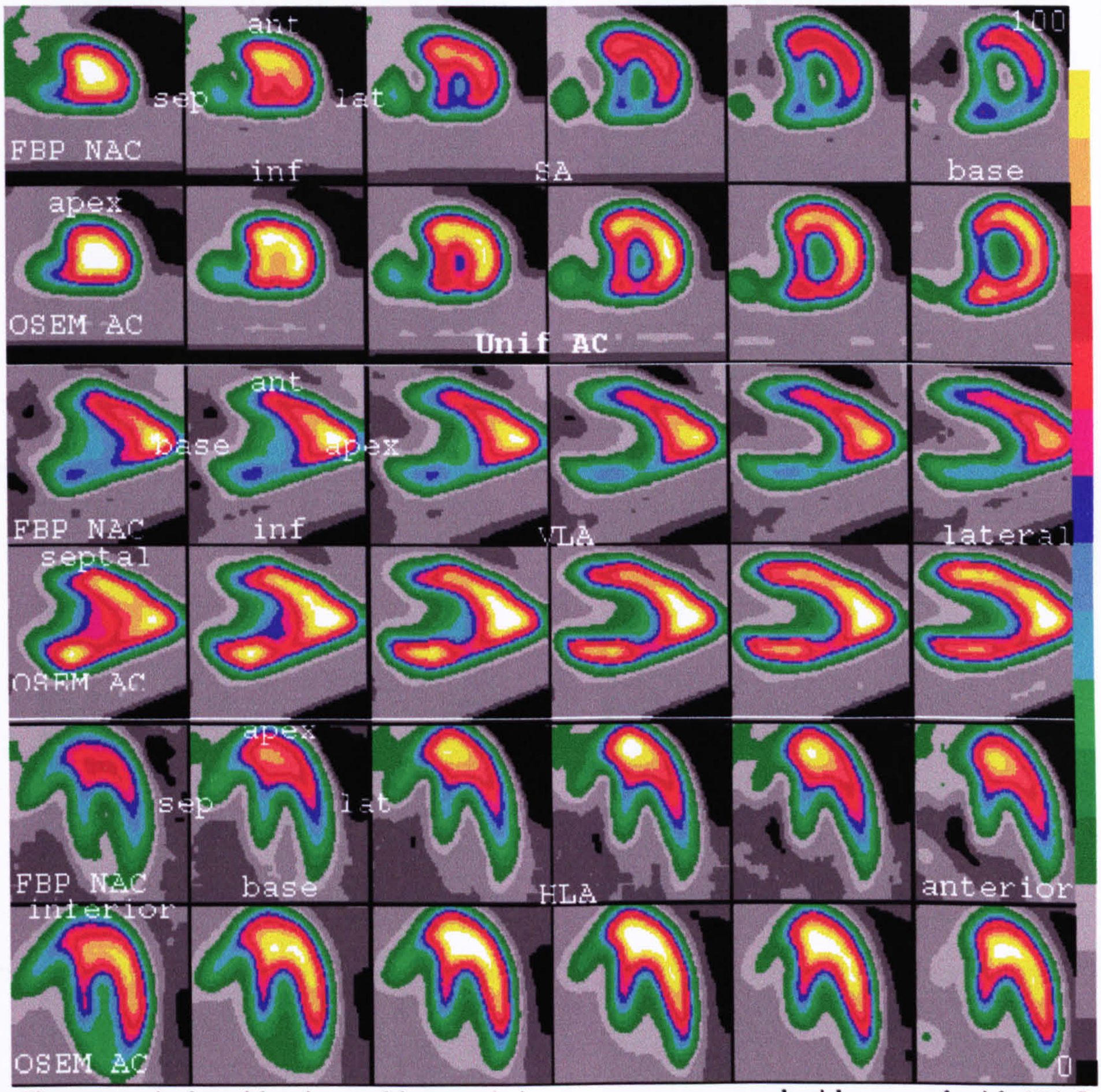

Short, vertical and horizontal long axis images reconstructed without and with UAC

Figure 5-15 Report of reconstructed images without and with uniform AC.

OSEM produces AC images free from streak artefacts. In addition, the attenuation artefacts in all LV walls in the uncorrected images were significantly improved in the OSEM-AC images.

5.5. Validation of non-uniform AC

Figure 5-16 shows the transaxial slices of non-uniform AC data reconstructed with 4, 8, 16, 32, 64 and 128 iterations, respectively.

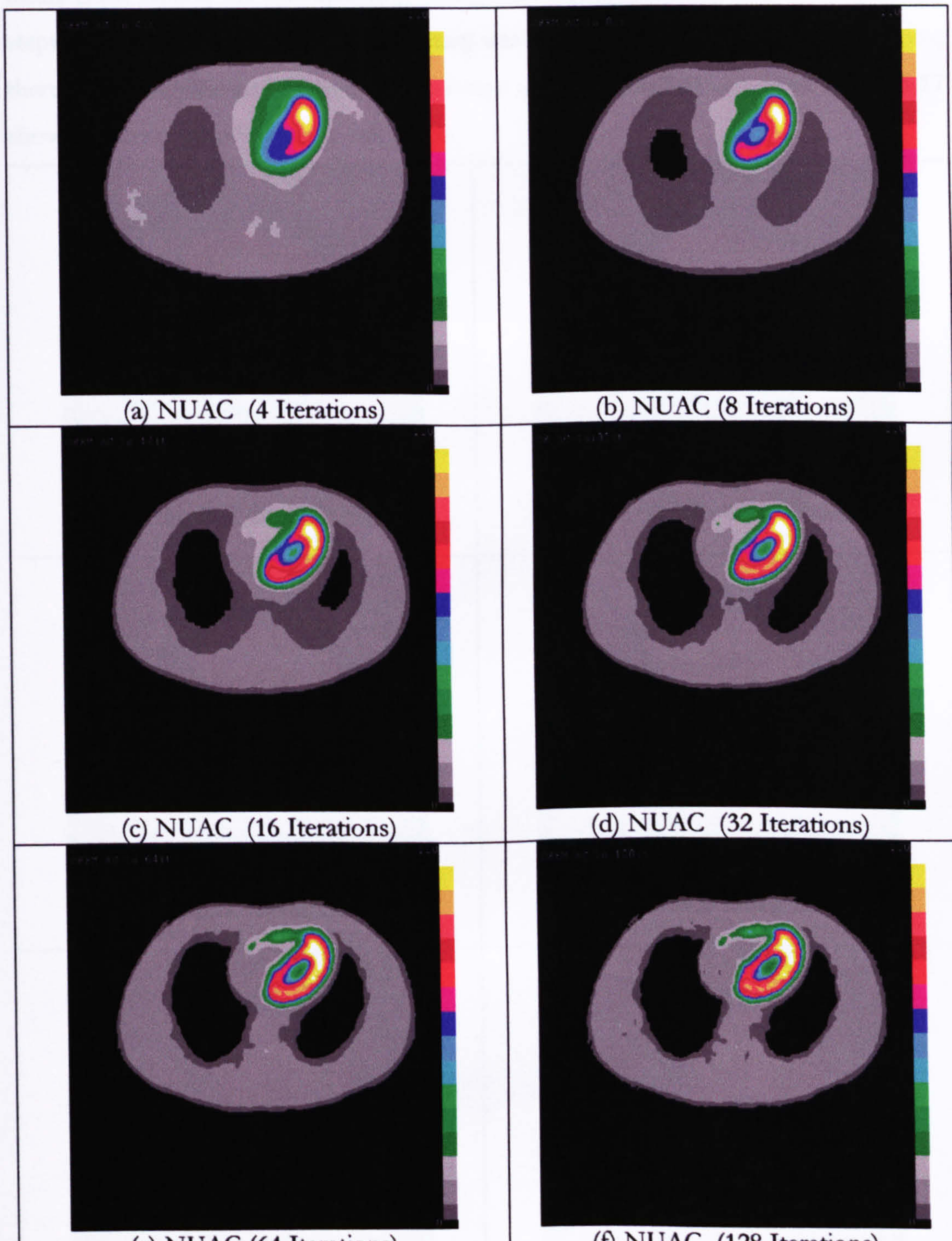

(a) NUAC (4 Iterations)

(b) NUAC (8 Iterations)

(c) NUAC (16 Iterations)

(d) NUAC (32 Iterations)

(e) NUAC (64 Iterations)

(f) NUAC (128 Iterations)

All slices are 128×128

Figure 5-16 Reconstructed transaxial slices of non-uniform AC using OSEM with 1 subset and a number of iterations ranging from 4 to 128 as indicated.

The visual evaluation of all slices shown in Figure 5-16 demonstrates that the low frequency components of activity distribution (e.g. myocardium) is visualized clearly even after four iterations compared to the high frequency region (e.g. uptake in tissue inside chest around the myocardium), which starts to be visualized only with additional steps. Although, the image quality (contrast) was improving with increasing of iterations, there was no significant improvement in image quality beyond 64 iterations. Figure 5-17 shows the corresponding short-axis slices.

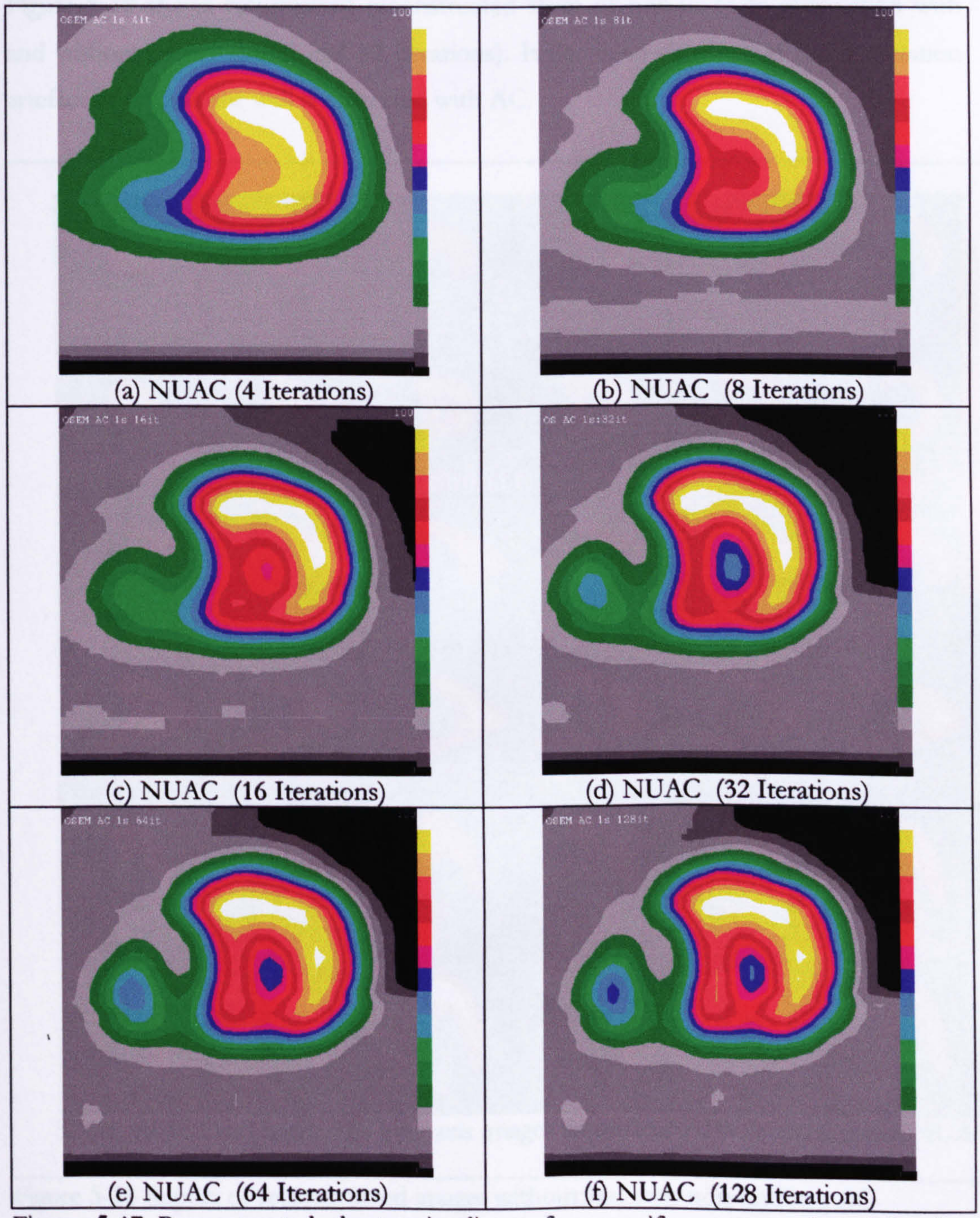

(a) NUAC (4 Iterations)
(b) NUAC (8 Iterations)
(c) NUAC (16 Iterations)
(d) NUAC (32 Iterations)
(e) NUAC (64 Iterations)
(f) NUAC (128 Iterations)

Figure 5-17 Reconstructed short axis slices of non-uniform attenuation AC using OSEM with 1 subset and a number of iterations ranging from 4 to 128 as indicated.

Again Figure 5-17, shows that there was no significant quantitative improvement between images reconstructed with 64 and 128 iterations in the LV (except some improvement in contrast at the centre of the LV). Also, there was a significant count reduction in the lateral wall with iterations beyond 64 compared to 32 iterations. The results obtained from both transaxial and short-axis slices suggest that 32 iterations was the optimal number for non-uniform AC.

Figure 5-18 shows reformatted reconstructed slices of non-uniform attenuation with and without AC (1 subset and 32 iterations). It has been shown that the attenuation artefact in the inferior wall is corrected with AC.

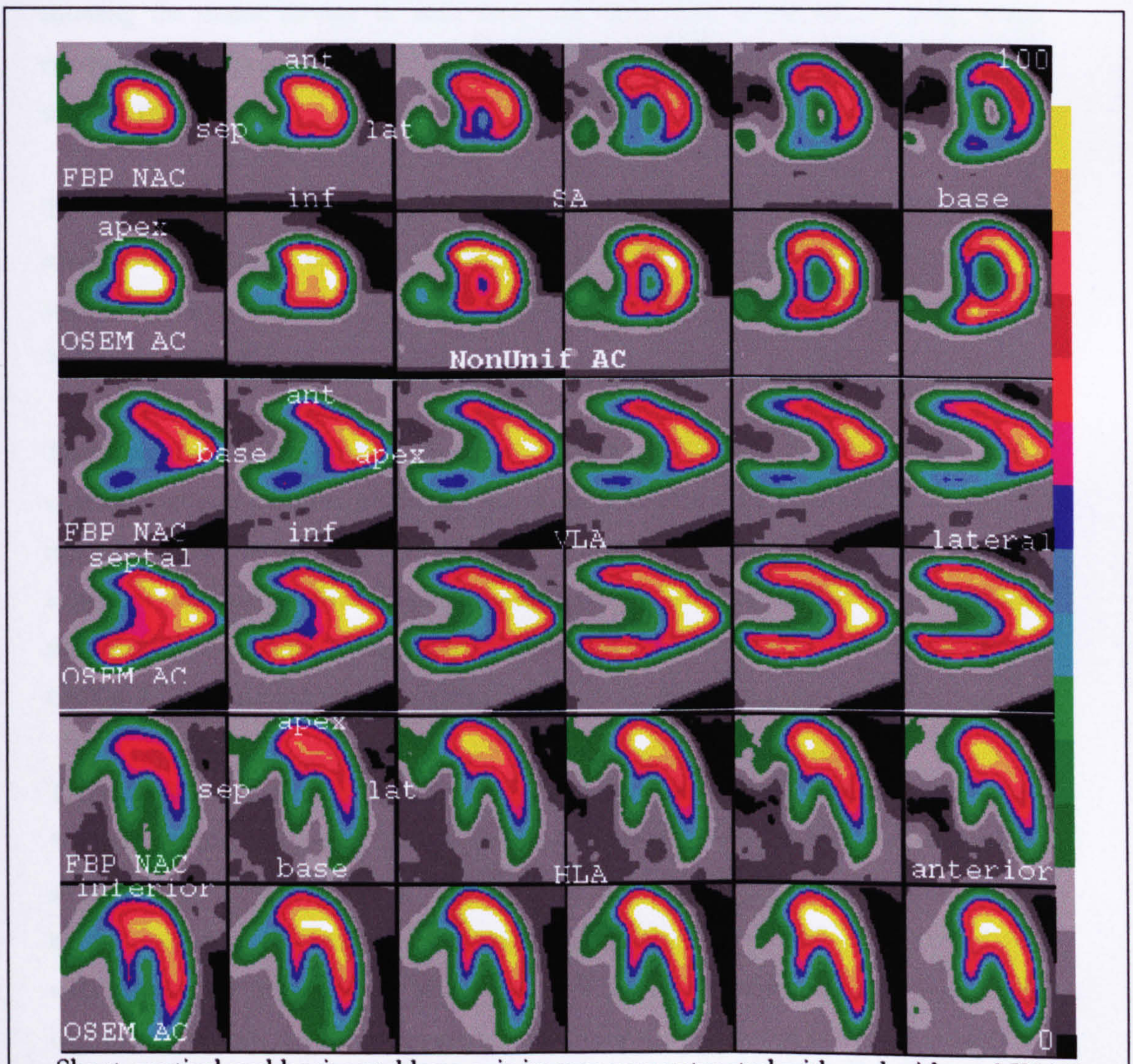

Short, vertical and horizontal long axis images reconstructed with and without NUAC

Figure 5-18 Report of reconstructed images without and with non-uniform AC

From a qualitative assessment of the transaxial and short axis slices shown in Figures 5-16 and 5-17; 32 iterations was selected for both uniform and non-uniform AC reconstruction for comparison with the gold standard image for validation purposes.

Validation of both uniform and non-uniform AC was performed with the emission model (without attenuation) reconstructed using OSEM (1 subset and 64 iterations) used as the gold standard. Quantitative and qualitative assessment of the AC images after AC was performed.

To analyse the LV count density from apex to base, a bull's-eye polar map was generated from all reconstructed short-axis slices. It consists of concentric rings showing the count density in each short-axis slice. The centre of the polar map represents the apex of the LV, and subsequent rings short-axis slices progressing towards the base.

To summarize the results of the AC validation using both uniform and non-uniform models, all images are listed in the Figure 5-19 and the count density profiles of both transaxial (Figure 5-20 and Figure 5-21) and short-axis slices (Figure 5-22 and Figure 5-23) are compared.

Transaxial slices of the gold standard and reconstructed images with and without both uniform and non-uniform AC are shown in the left column of Figure 5-19. The polar maps are shown in the right column. The top row of Figure 5-19(a) displays the three images of the gold standard model; transaxial, short-axis, and bull's-eye plot. To assess the accuracy of the OSEM algorithm to correct attenuation artefacts, we compared the OSEM-AC reconstructed images with the gold standard images.

The reduction of counts in the bull's-eye image reconstructed with both uniform (Figure 5-19(b)) and non-uniform (Figure 5-19(d)) attenuation were accurately compensated in all walls except in the septal wall. This can be attributed to partial volume effects caused by the smoothing of the true Zubal model. Generally, the bull's-eye images produced with OSEM-AC (Figure 5-19(c and e)) show a substantial qualitative improvement in uniformity through the LV, compared to the bull's-eye image computed from the FBP reconstruction with no AC (Figure 5-19(b and d)).

(a) Gold Standard

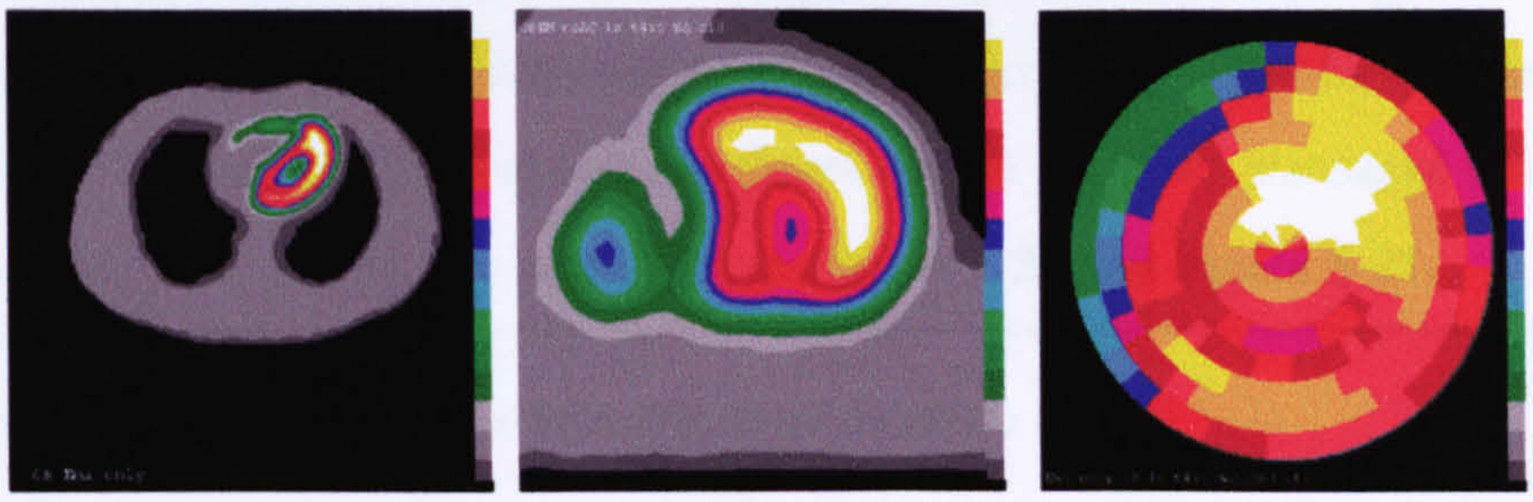

(b) Uniform FBP-NC

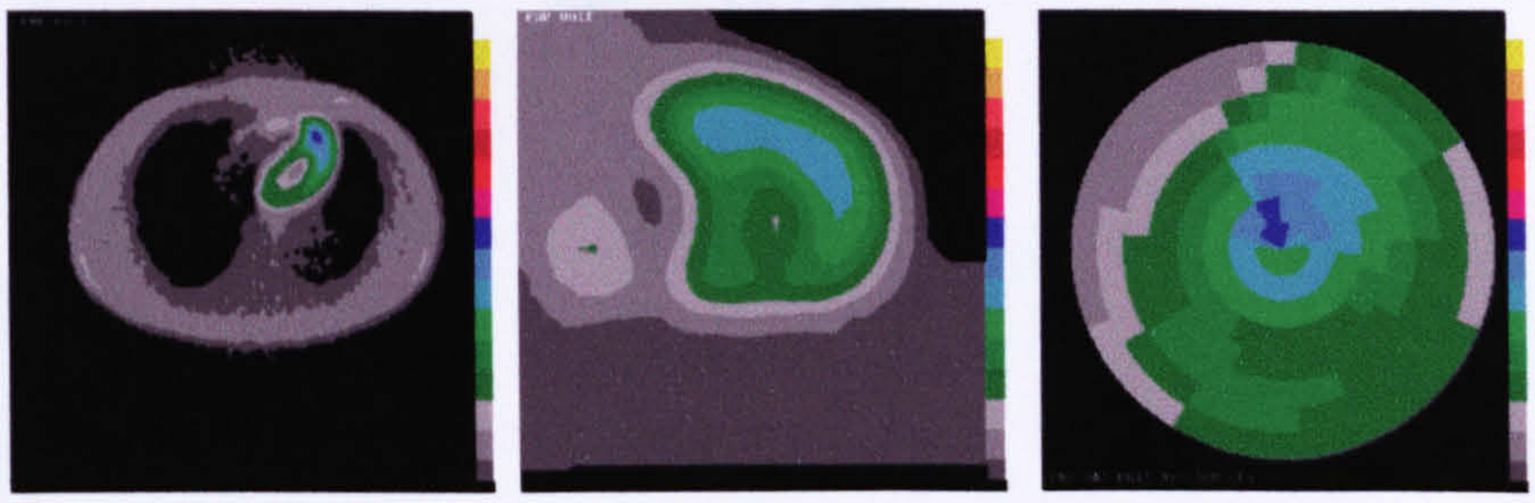

(c) Uniform OSEM-AC

(d) Non-uniform FBP-NC

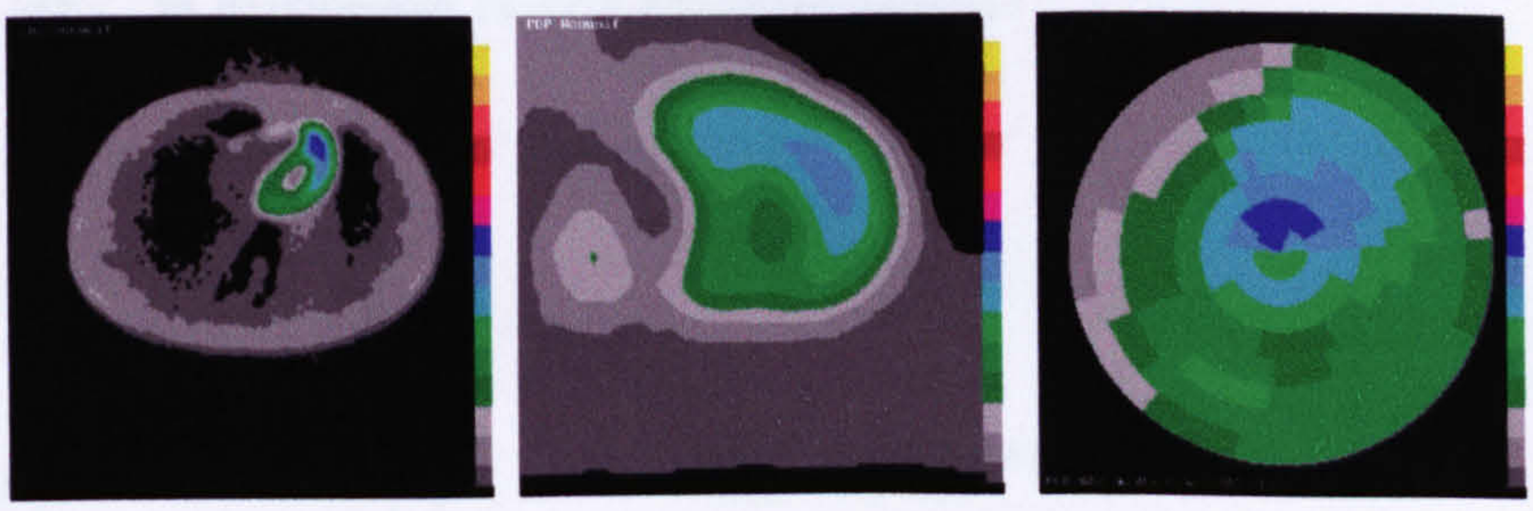

(e) Non-uniform OSEM-AC

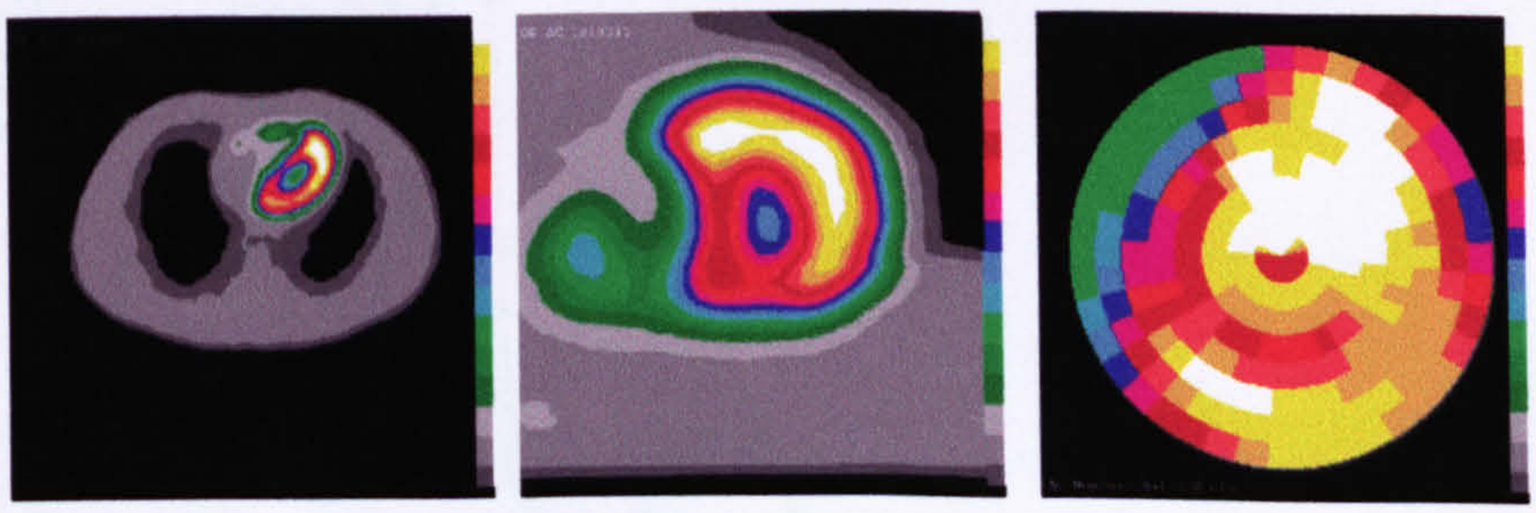

Figure 5-19 Reconstructed images of both uniform and non-uniform attenuation with and without AC: transaxial slices (left column), short-axis slices (middle column) and bull's-eye plots (right column).

In addition to the qualitative assessment of the transaxial and short axis images and polar images, other quantitative measurements (such as count density profiles) were used. Horizontal and vertical profiles through the heart region on both transaxial and short axis slices with and without AC are presented in Figure 5-20 and Figure 5-21.

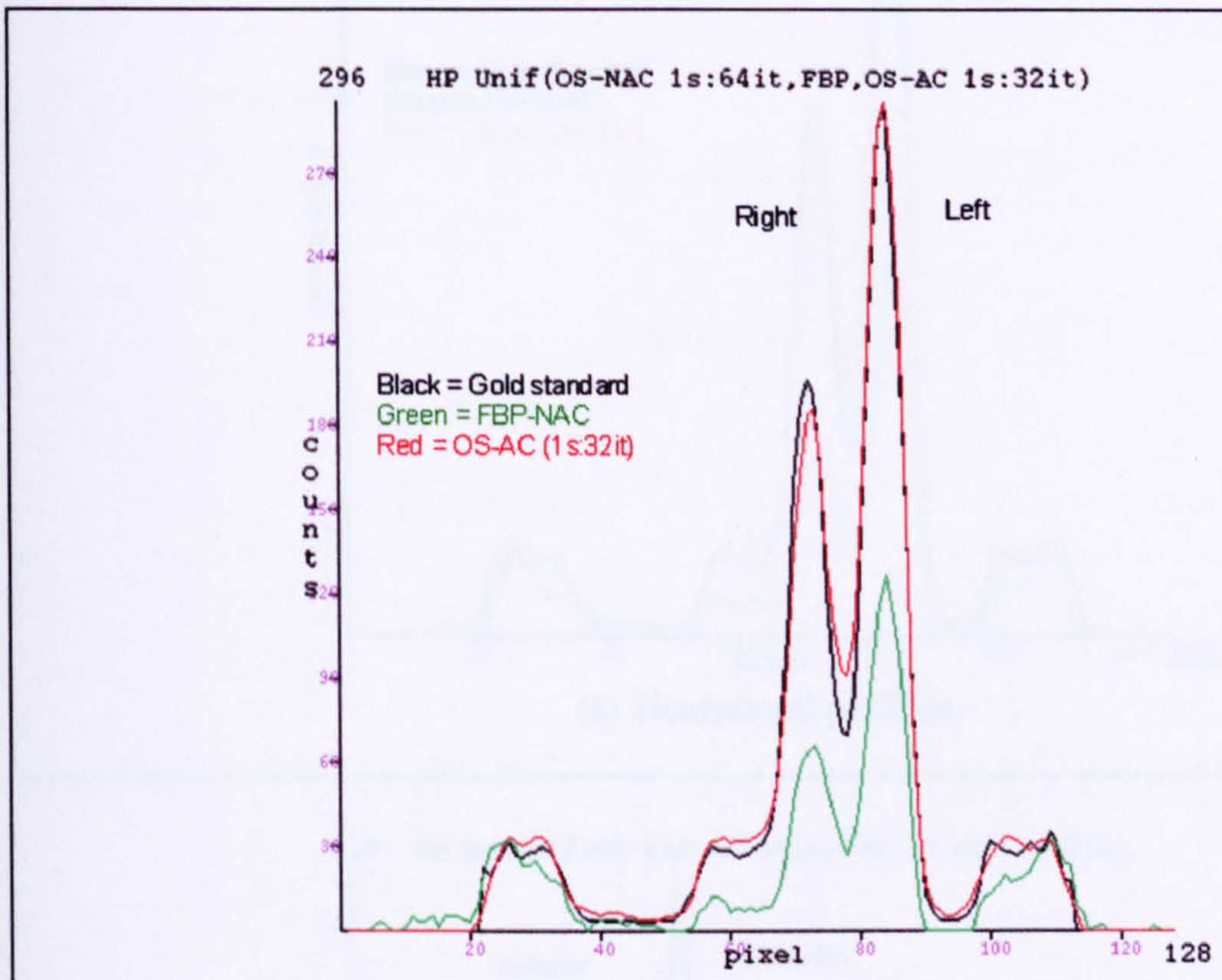

(a) Horizontal profiles

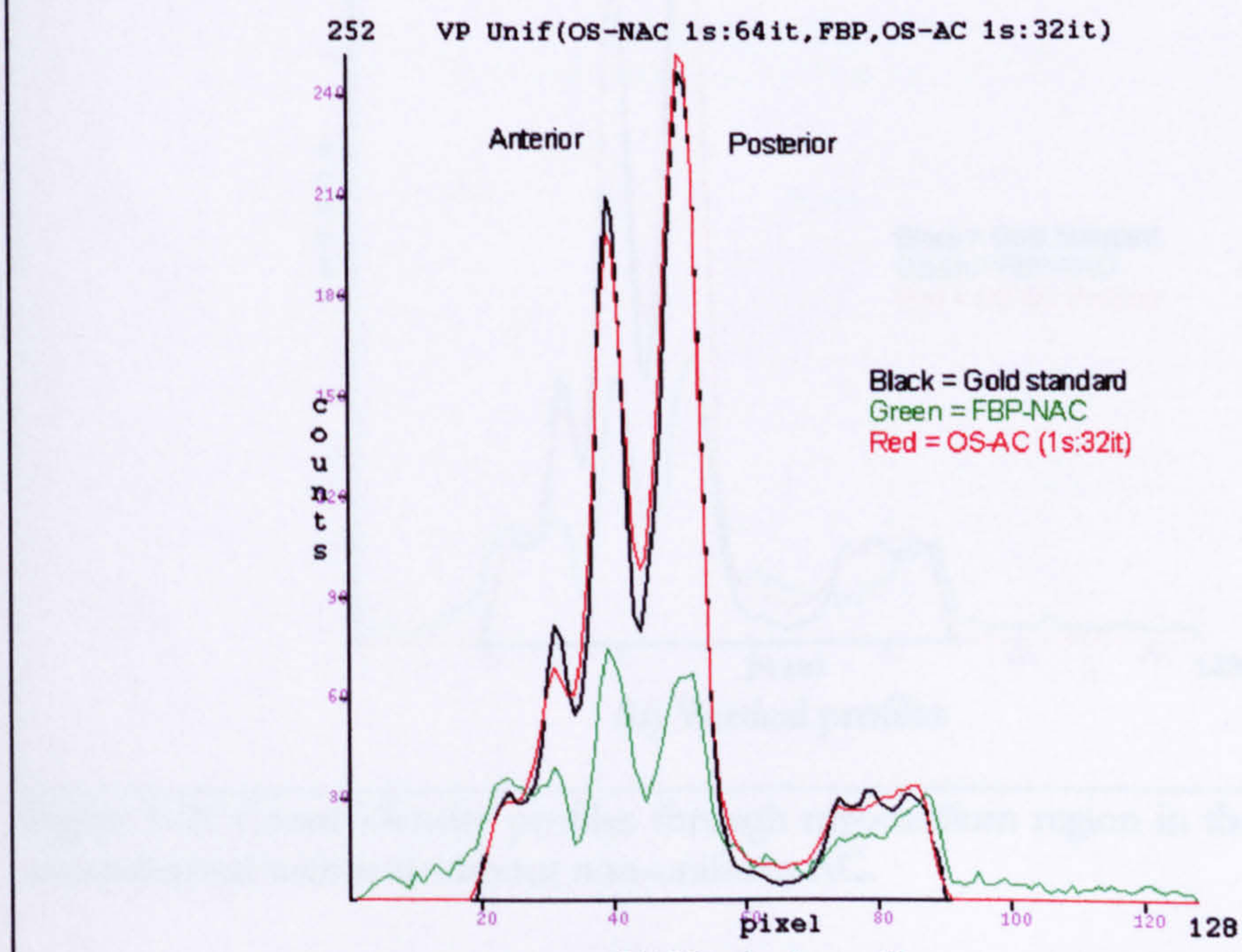

(b) Vertical profiles

Figure 5-20 Count Density profiles through myocardium region in the transaxial slices reconstructed with and without uniform AC.

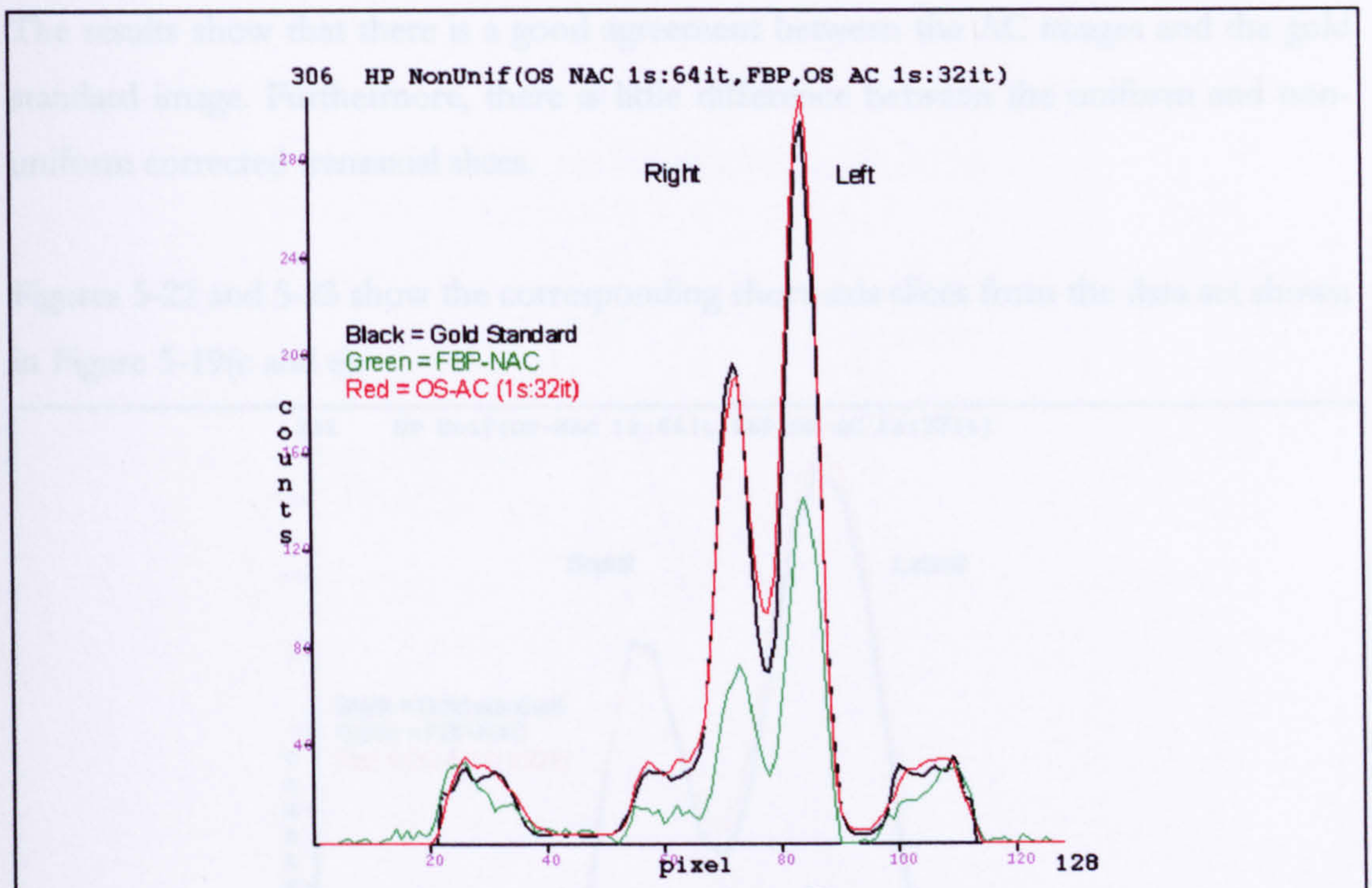

(a) Horizontal profiles

(b) Vertical profiles

Figure 5-21 Count Density profiles through myocardium region in the transaxial slices reconstructed with and without non-uniform AC.

The results show that there is a good agreement between the AC images and the gold standard image. Furthermore, there is little difference between the uniform and non-uniform corrected transaxial slices.

Figures 5-22 and 5-23 show the corresponding short-axis slices from the data set shown in Figure 5-19(c and e).

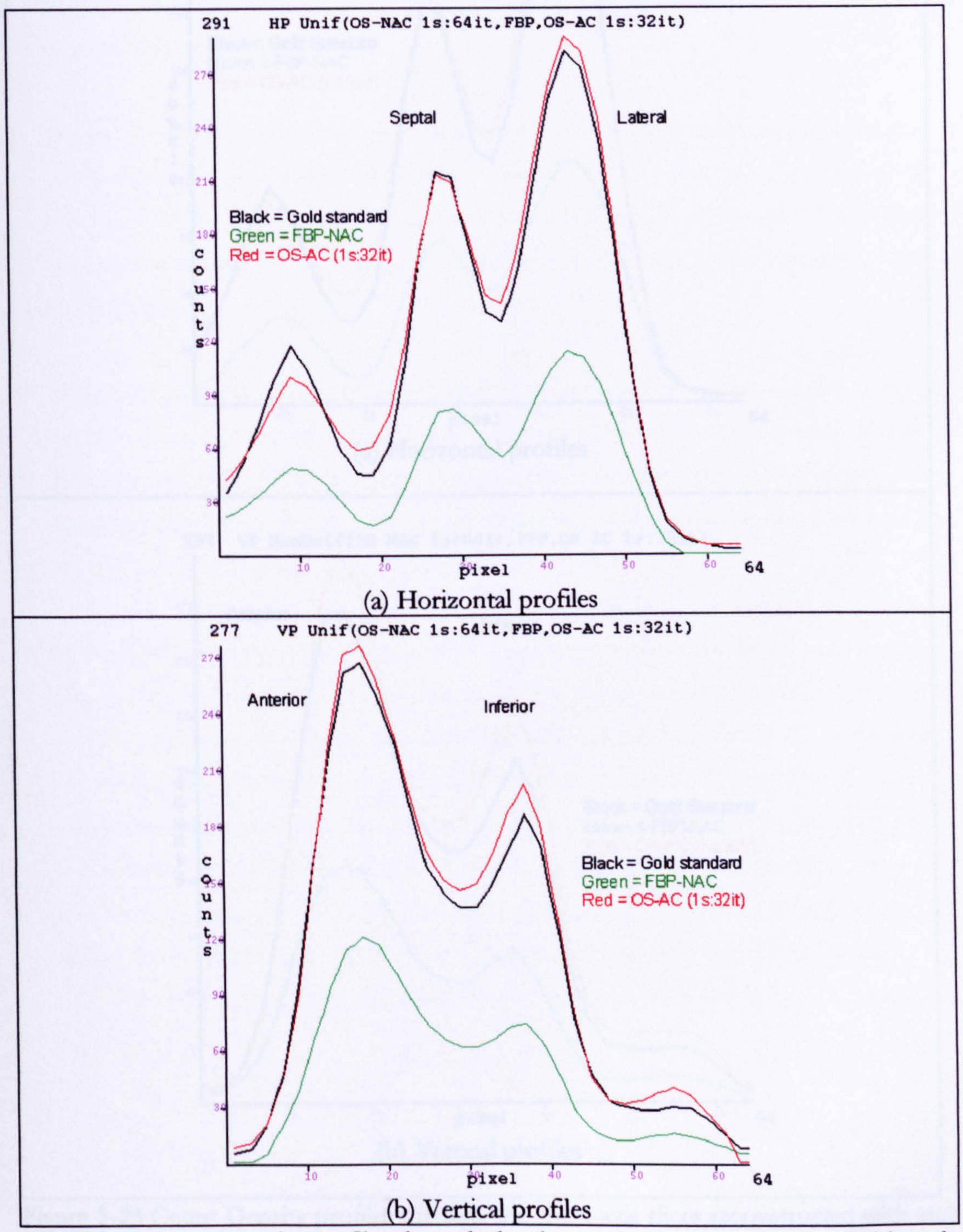

Figure 5-22 Count Density profiles through the short-axis slices reconstructed with and without uniform AC.

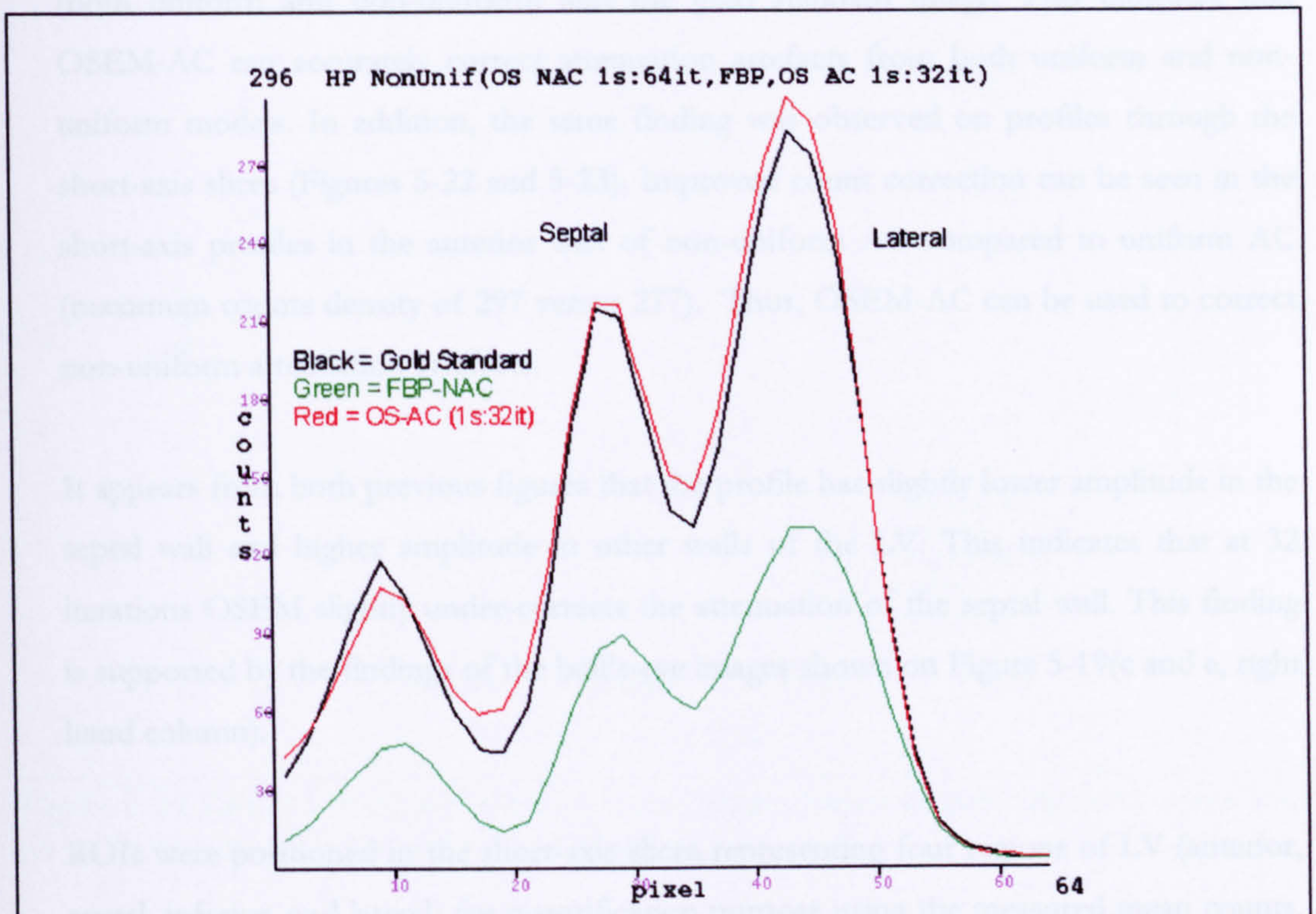

(a) Horizontal profiles

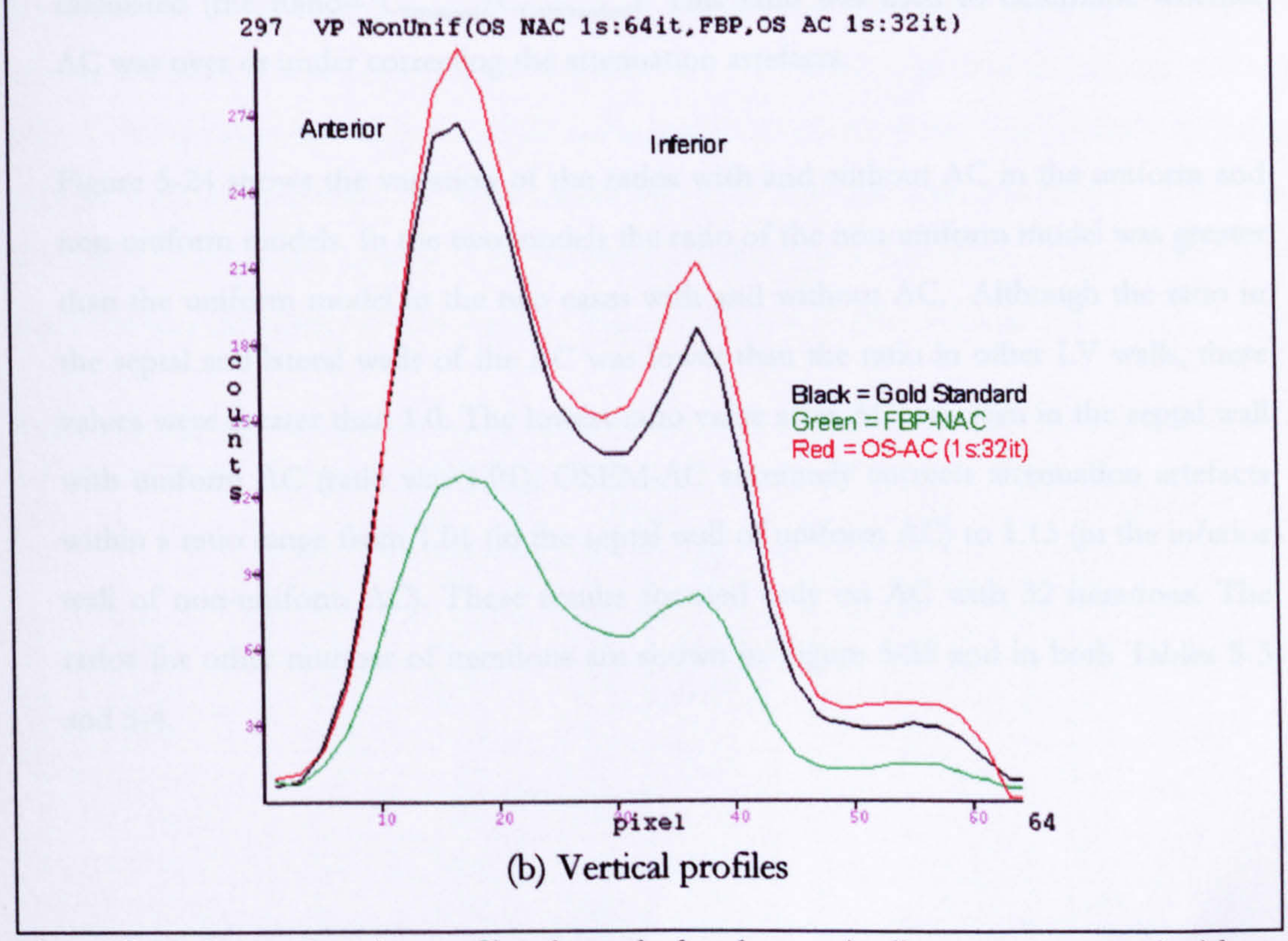

(b) Vertical profiles

Figure 5-23 Count Density profiles through the short-axis slices reconstructed with and without non-uniform AC.

The profiles in Figures 5-20 and 5-21 show a good agreement between the AC images (both uniform and non-uniform) and the gold standard image. This indicates that OSEM-AC can accurately correct attenuation artefacts from both uniform and non-uniform models. In addition, the same finding was observed on profiles through the short-axis slices (Figures 5-22 and 5-23). Improved count correction can be seen in the short-axis profiles in the anterior wall of non-uniform AC compared to uniform AC (maximum counts density of 297 versus 277). Thus, OSEM-AC can be used to correct non-uniform attenuation artefacts.

It appears from both previous figures that the profile has slightly lower amplitude in the septal wall and higher amplitude in other walls of the LV. This indicates that at 32 iterations OSEM slightly under-corrects the attenuation of the septal wall. This finding is supported by the findings of the bull's-eye images shown on Figure 5-19(c and e, right hand column).

ROIs were positioned in the short-axis slices representing four regions of LV (anterior, septal, inferior, and lateral) for quantification purpose using the measured mean counts. The ratio of measured mean count to the mean counts of the gold standard was calculated (the Ratio= $C_{Measured}/C_{GoldStandard}$). This ratio was used to determine whether AC was over or under correcting the attenuation artefacts.

Figure 5-24 shows the variation of the ratios with and without AC in the uniform and non-uniform models. In the two models the ratio of the non-uniform model was greater than the uniform model in the two cases with and without AC. Although the ratio in the septal and lateral walls of the AC was lower than the ratio in other LV walls, these values were greater than 1.0. The lowest ratio value after AC was seen in the septal wall with uniform AC (ratio was 1.01). OSEM-AC accurately corrects attenuation artefacts within a ratio range from 1.01 (in the septal wall of uniform AC) to 1.13 (in the inferior wall of non-uniform AC). These results focused only on AC with 32 iterations. The ratios for other number of iterations are shown in Figure 5-25 and in both Tables 5-3 and 5-4.

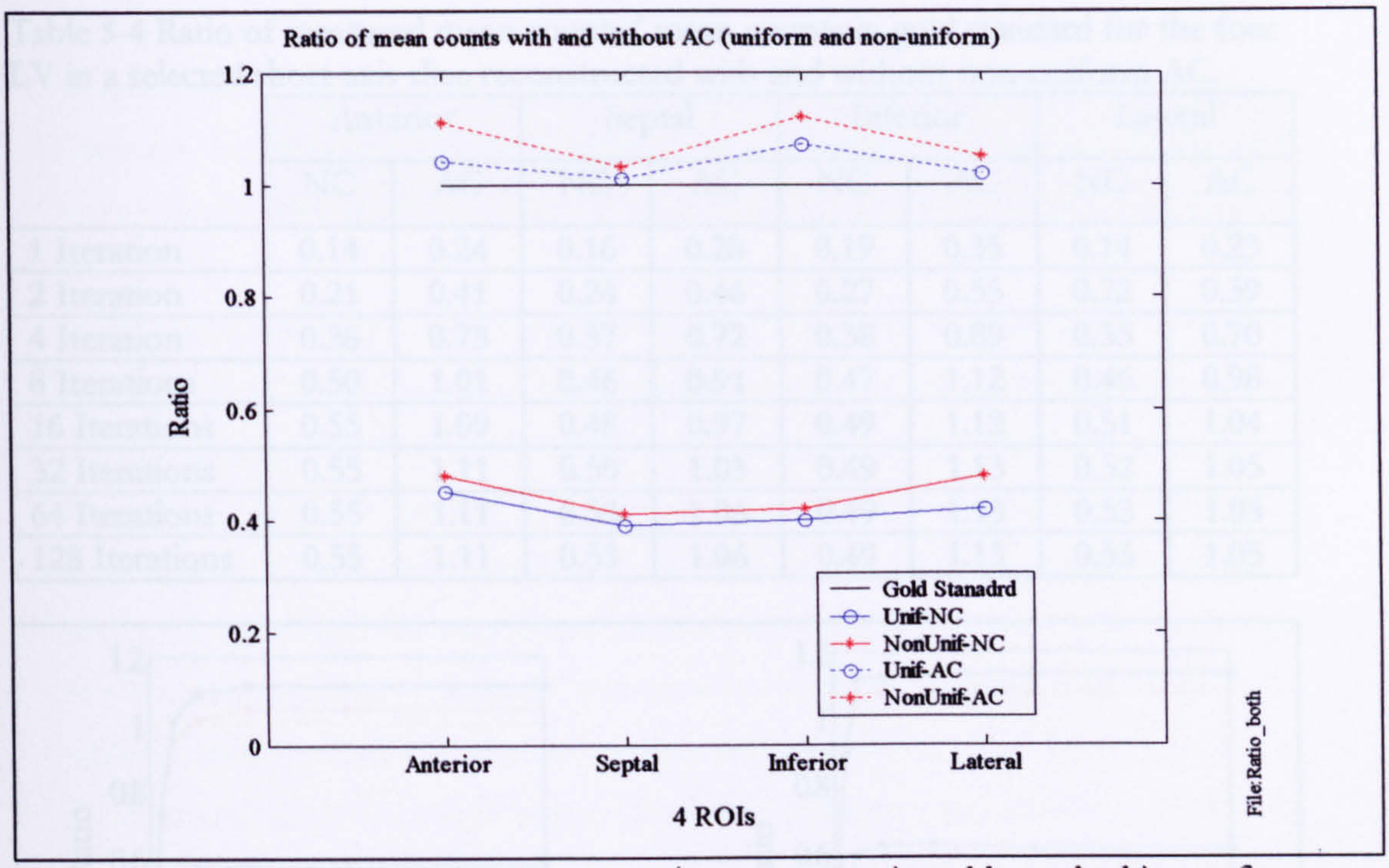

Figure 5-24 Ratio of measured mean counts/ mean counts in gold standard image for no AC and with uniform and non-uniform AC.

In order to show whether the OSEM algorithm over or under corrects attenuation artefacts, the same models used in previous section were reconstructed with attenuation effects included (both uniform and nonuniform attenuation effects) and reconstructed with OSEM algorithm only (no FBP used here). Reconstruction was performed using OSEM without and with AC with subset size of 1 and different number of iterations. The ratio of the mean counts of the reconstructed image to the mean counts of the gold standard was calculated and shown on Figure 5-25 and Tables 5-3 and 5-4.

Table 5-3 Ratio of measured mean counts/ mean counts in gold standard for the four LV in a selected short-axis slice reconstructed with and without uniform AC.

	Anterior		Septal		Inferior		Lateral	
	NC	AC	NC	AC	NC	AC	NC	AC
1 Iteration	0.14	0.23	0.17	0.29	0.22	0.34	0.14	0.23
2 Iteration	0.22	0.40	0.24	0.46	0.32	0.53	0.20	0.39
4 Iteration	0.37	0.70	0.35	0.71	0.48	0.84	0.32	0.68
8 Iterations	0.53	0.85	0.45	0.89	0.60	1.07	0.43	0.96
16 Iterations	0.57	1.01	0.50	0.96	0.62	1.07	0.48	1.02
32 Iterations	0.57	1.04	0.55	1.01	0.62	1.07	0.49	1.03
64 Iterations	0.57	1.04	0.60	1.01	0.61	1.07	0.48	1.03
128 Iterations	0.57	1.04	0.63	1.01	0.61	1.07	0.48	1.03

Table 5-4 Ratio of measured mean counts/ mean counts in gold standard for the four LV in a selected short-axis slice reconstructed with and without non-uniform AC.

	Anterior		Septal		Inferior		Lateral	
	NC	AC	NC	AC	NC	AC	NC	AC
1 Iteration	0.14	0.24	0.16	0.28	0.19	0.35	0.14	0.23
2 Iteration	0.21	0.41	0.24	0.46	0.27	0.55	0.22	0.39
4 Iteration	0.36	0.73	0.37	0.72	0.38	0.89	0.35	0.70
8 Iterations	0.50	1.01	0.46	0.91	0.47	1.12	0.46	0.98
16 Iterations	0.55	1.09	0.48	0.97	0.49	1.12	0.51	1.04
32 Iterations	0.55	1.11	0.50	1.03	0.49	1.13	0.52	1.05
64 Iterations	0.55	1.11	0.53	1.06	0.49	1.13	0.53	1.05
128 Iterations	0.55	1.11	0.53	1.06	0.49	1.13	0.53	1.05

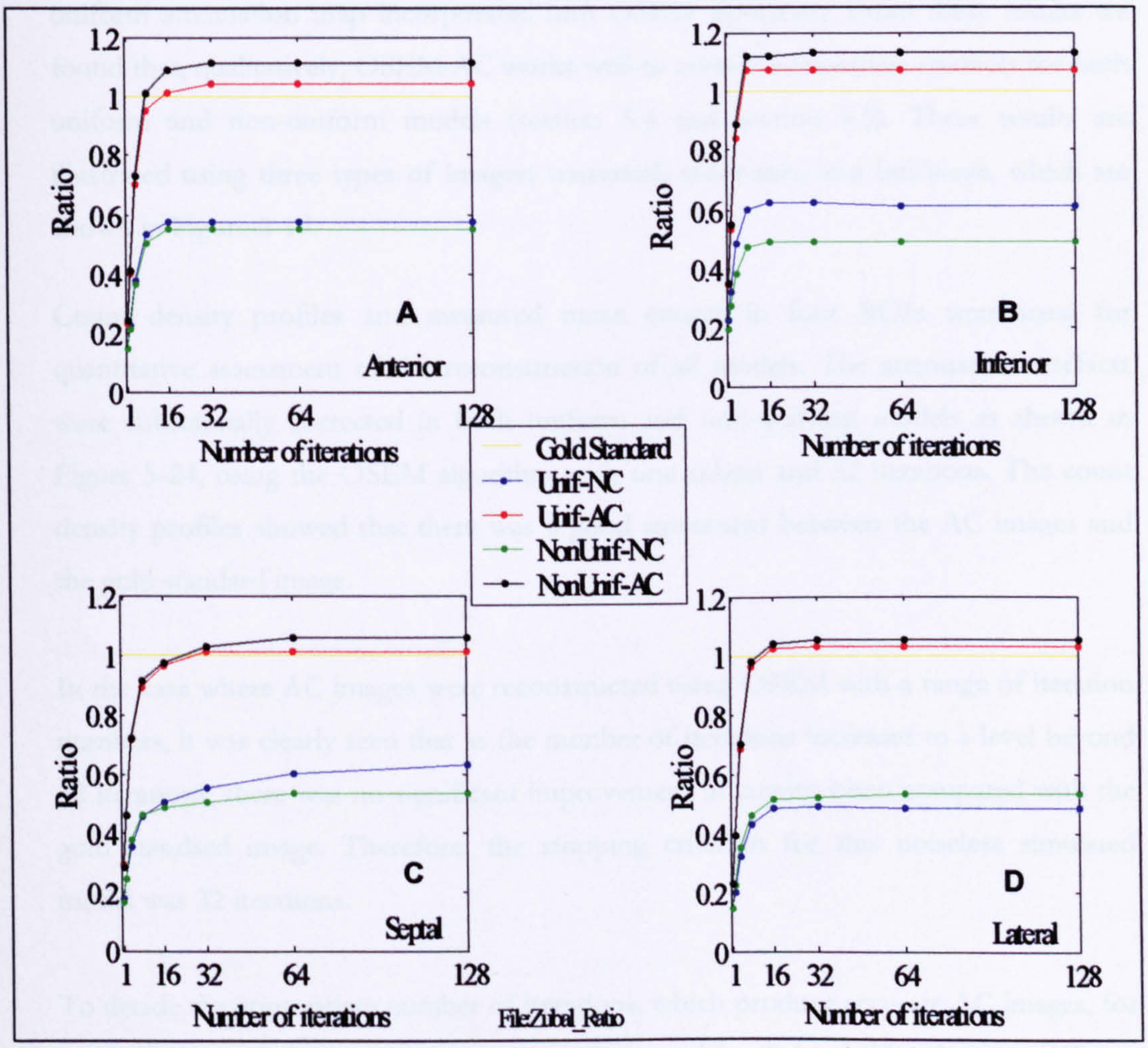

Figure 5-25 the ratio of measured mean counts to mean counts in gold standard for no AC and with AC with uniform and non-uniform AC.

Based on Figure 5-25, in all four walls of the LV, the ratio initially increases rapidly with the number of iterations. After approximately 32 iterations in all LV walls, the ratio does not change greatly with further iterations. In all cases, the maximum ratio was obtained with non-uniform AC in the inferior wall reconstructed with 128 iterations (Ratio

=1.13). Practically, higher number of iterations will not be used due to noise in the reconstructed image and the long processing time. Therefore, the selection of 32 iterations can be used to accurately correct for attenuation since the ratio values were acceptable (1.0 to 1.1).

In the previous experiments, realistic 3D cardiac SPECT data were simulated to validate AC using the OSEM algorithm. The emission model without attenuation effects was reconstructed by OSEM (1 subset and 64 iterations) and used as the gold standard for comparison purposes (section 5.3). Furthermore, attenuated projection data were reconstructed without AC using FBP, and with AC using both uniform and non-uniform attenuation map incorporated into OSEM algorithm. From these results we found that, qualitatively, OSEM-AC works well to correct attenuation artefacts for both uniform and non-uniform models (section 5.4 and section 5.5). These results are illustrated using three types of images; transaxial, short-axis, and bull's-eye, which are shown in Figure 5-19.

Count density profiles and measured mean counts in four ROIs were used for quantitative assessment of the reconstruction of all models. The attenuation artefacts were substantially corrected in both uniform and non-uniform models as shown in Figure 5-24, using the OSEM algorithm with one subset and 32 iterations. The count density profiles showed that there was a good agreement between the AC images and the gold standard image.

In the case where AC images were reconstructed using OSEM with a range of iteration numbers, it was clearly seen that as the number of iterations increases to a level beyond 32 iterations, there was no significant improvement in counts when compared with the gold standard image. Therefore, the stopping criterion for this noiseless simulated model was 32 iterations.

To decide the appropriate number of iterations, which produce accurate AC images, for real patients, a noisy non-uniform attenuation model will be validated using different numbers of subsets and iterations in the following sections (section 5.6 and 5.7).

5.6. Impact of noise and post-filtering on AC

Image noise is the degree of variability of the pixel values caused by the statistical nature (Poisson distribution) of the radioactive decay and detection process. In order to simulate realistic SPECT images, the raw data should contain some generated noise and reconstructed with AC. Clinically, in order to reduce the effect of Poisson noise, the number of photon counts has to be increased[20]. This can be achieved by using one or a combination of the following methods:

a) Firstly, increasing the acquisition time with increased risk of patient motion and a reduction of camera throughput.
b) Secondly, by increasing the amount of administered radioactive material, which will lead to increased patient dose.
c) The last solution is to use gamma camera with multiple detectors or very high efficient detectors with a drawback of increasing costs and technical difficulties.

Given the limitation of each of the above methods, image-processing techniques are often used to reduce the noise level without increasing photon counts. The simplest technique to reduce noise is to use filtering, where each pixel value is replaced with the mean of its surrounding neighbours. Therefore, post-filtering technique will be used in this section as the technique to reduce noise.

The aims of this section were to validate AC using a noisy data, and to study the usefulness of using post-filtering on AC.

Using the previous noise-free projection data obtained from emission models with non-uniform attenuation effect, noisy projection data was simulated by adding random Poisson noise. Noise was added with a Poisson generator program called "poisson_noise" (Appendix D). Poisson noise was added to the projection data prior to reconstruction. To make the simulation comparable to the expected real clinical data, the maximum counts in the clinical data was calculated and the noise simulated according to this level of noise.

---

[20] High quality image can be obtained by increasing the signal-to-noise-ratio (SNR). SNR is equal to the square root of the mean counts. Therefore, a higher number of counts contribute to the value of each pixel, decreasing the noise variance and then increasing the SNR.

In order to find the level of the simulated noise, a ROI was placed (in the same position) to measure maximum counts on both projection images; one obtained from real noisy patient data and the other obtained from the simulated noisy data. The simulated noisy data was 60% relatively higher than the real noisy patient data. Although this level of noise represent only one level of noise, other level of noise either equal or lower than the clinical level of noise can be simulated. The selection of this level of simulated noise was selected to be as one of the worst case of noise level.

Both the noise-free and noisy attenuated projection data were reconstructed with and without AC (The AC images were corrected using a noise-free non-uniform attenuation map and no noise was simulated in the transmission image). In addition, the resulting reconstructions from the noisy data with AC were examined with and without post-reconstruction filtering using a Butterworth filter with order = 10, cut-off = 0.2 cm^{-1}. This is the filter normally used locally with FBP for reconstructing cardiac SPECT data.

The noise-free and noisy reconstructed images were compared in two ways. First, the reconstructed slices (both transaxial and short-axis) and their count density profiles were compared to that of the noise-free gold standard model, and second, the fractional root mean square error (FRMSE) was calculated and discussed in section 5.7.

Figure 5-26 shows a representative projection view of the noise-free and noisy anterior projection views. The profiles through the myocardium show the low noise level compared to the noise-free projection view.

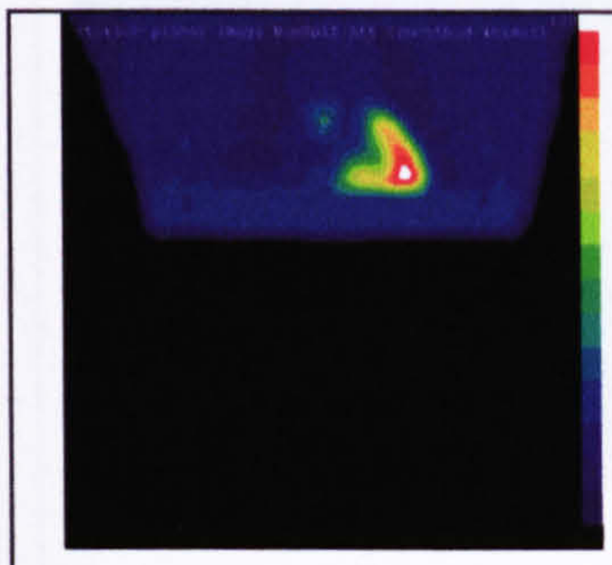

(a) Noise-free Projection image

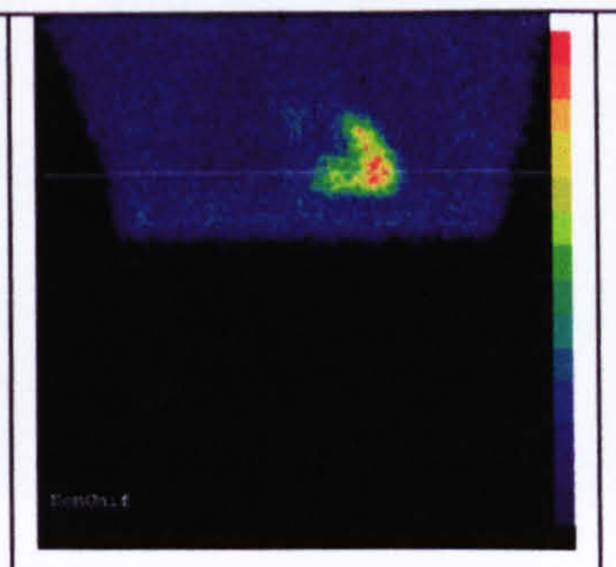

(b) Noisy Projection image

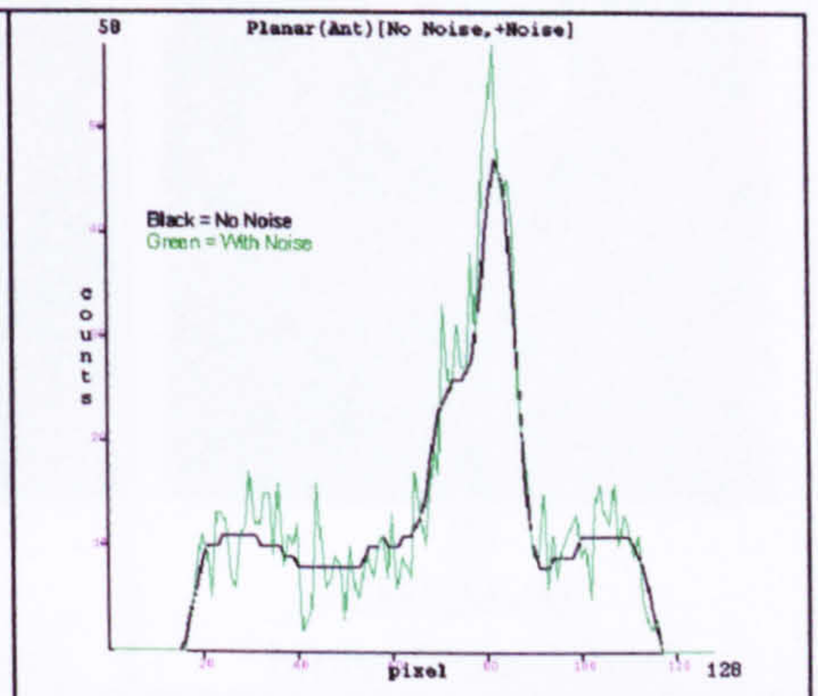

Horizontal profiles of images (a) and (b)

Figure 5-26 Simulation of noisy projection data.

The noise-free and noisy attenuated projection data were reconstructed without AC (Figure 5-27 (b and c respectively)) and with AC (Figure 5-27(d and e respectively)) and a comparison was made using the count density profiles as shown in Figure 5-28. The noisy image with post-filtering is also shown in Figure 5-27(f). In addition, the corresponding short-axis slices are shown in Figure 5-28.

Examining both Figure 5-27 and Figure 5-28, one can see that OSEM-AC can accurately correct attenuation artefacts in the noisy data. Visual evaluation of the reconstructed short-axis slices in Figure 5-29 demonstrates that post-filtering of the AC images improves the noise mainly in the lateral wall. In contrast, part of the inferior wall in the post-filtering slice had lower counts than the slice reconstructed with AC without post-filtering. As expected, it can be seen that, using post-filtering is a useful tool to reduce the noise in AC reconstructed slices.

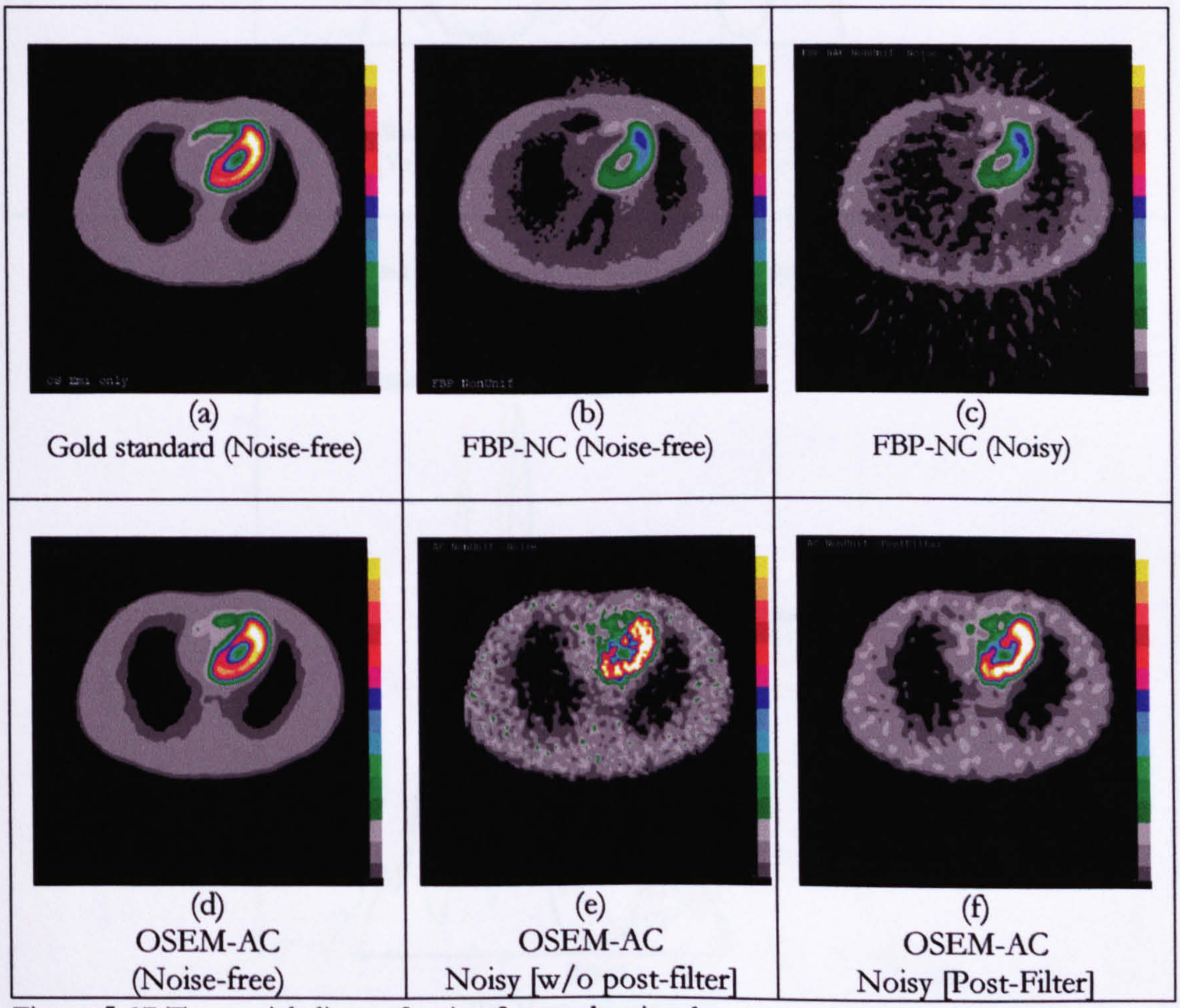

(a) Gold standard (Noise-free)

(b) FBP-NC (Noise-free)

(c) FBP-NC (Noisy)

(d) OSEM-AC (Noise-free)

(e) OSEM-AC Noisy [w/o post-filter]

(f) OSEM-AC Noisy [Post-Filter]

Figure 5-27 Transaxial slices of noise-free and noisy data reconstructed with and without AC. [(f) with post-filtering applied].

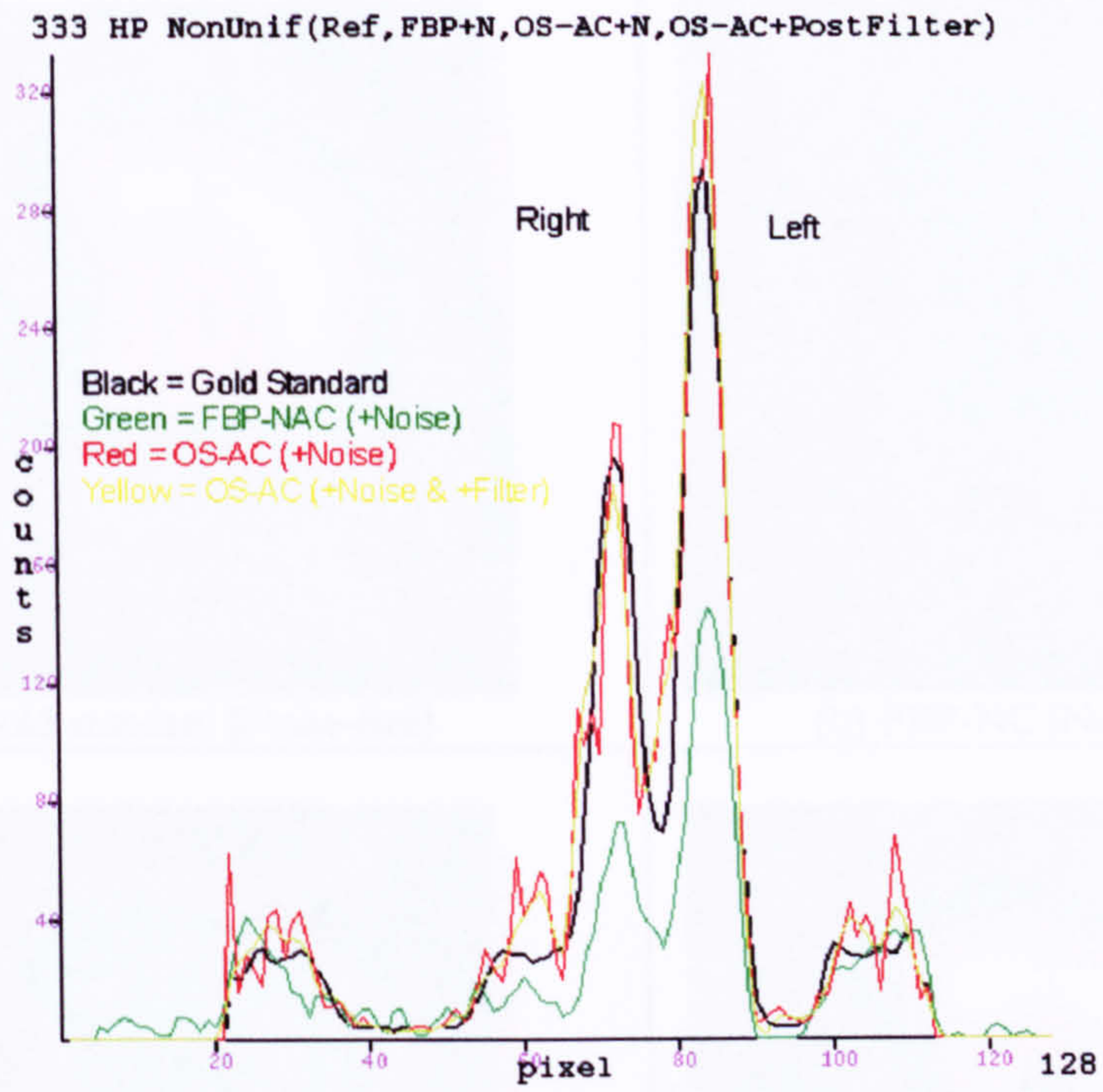

(a) Horizontal profiles
[Red= AC with Noise & without Filter]
[Yellow= AC with Noise & with Filter]

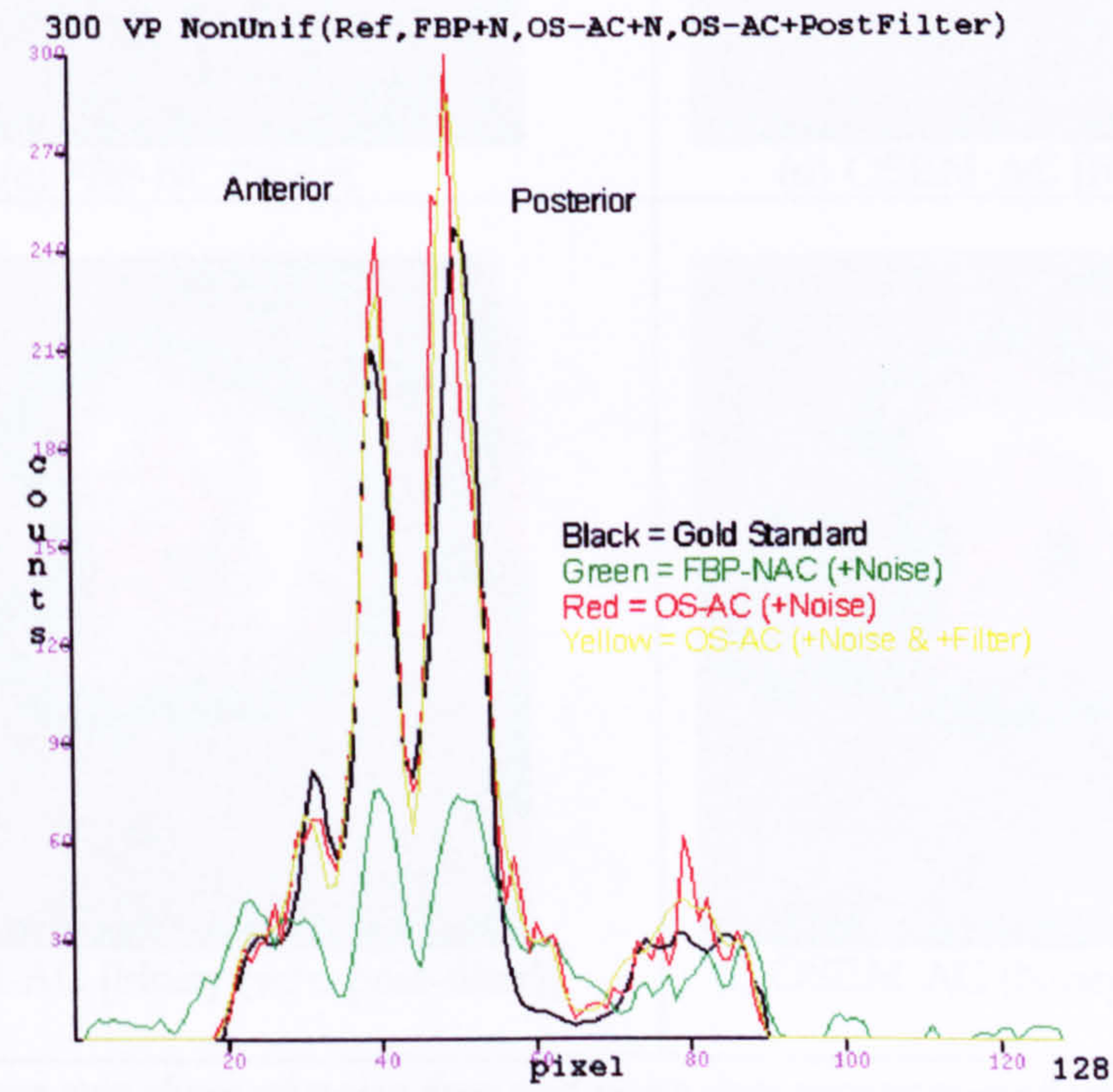

(b) Vertical profiles
[Red= AC with Noise & without Filter]
[Yellow= AC with Noise & with Filter]

Figure 5-28 Count Density profiles through the transaxial slices shown in Figure 5-27.

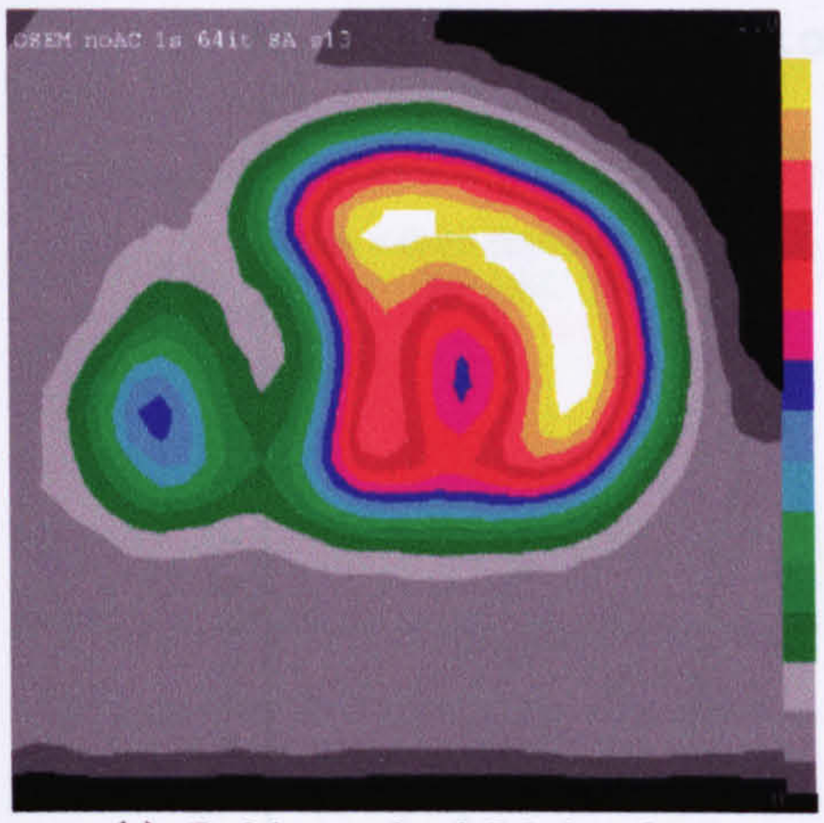

(a) Gold standard [Noise-free]

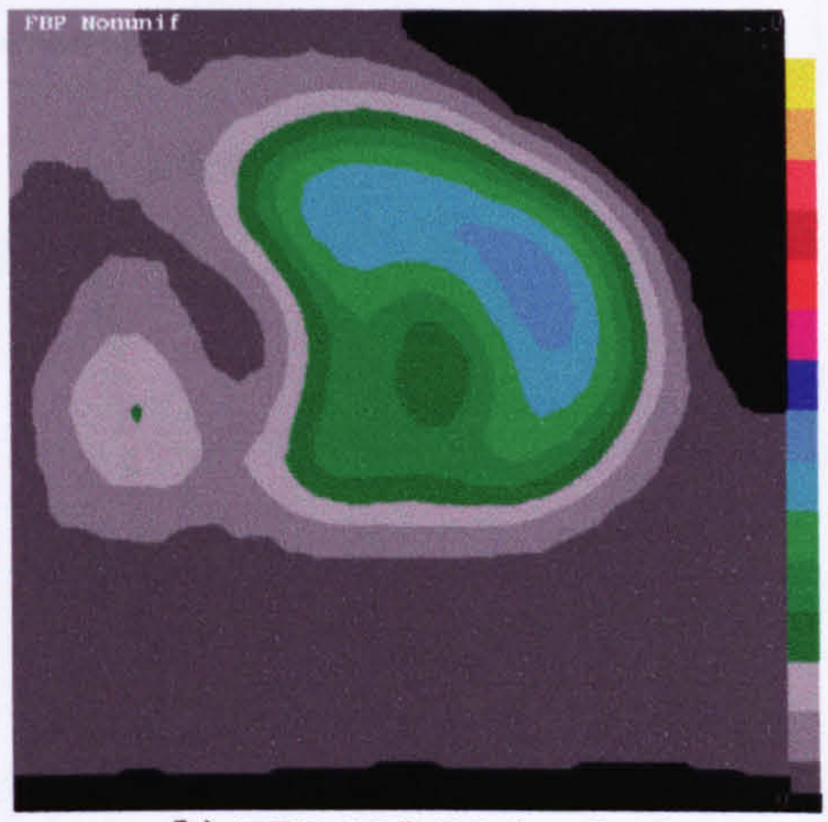

(b) FBP-NC [Noise-free]

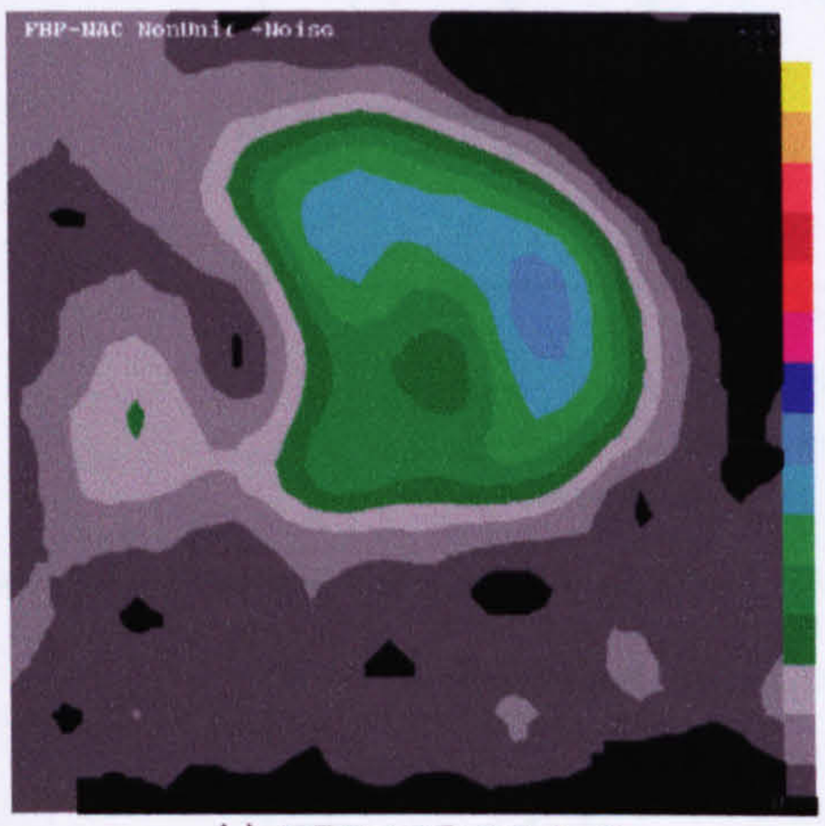

(c) FBP-NC [Noisy]

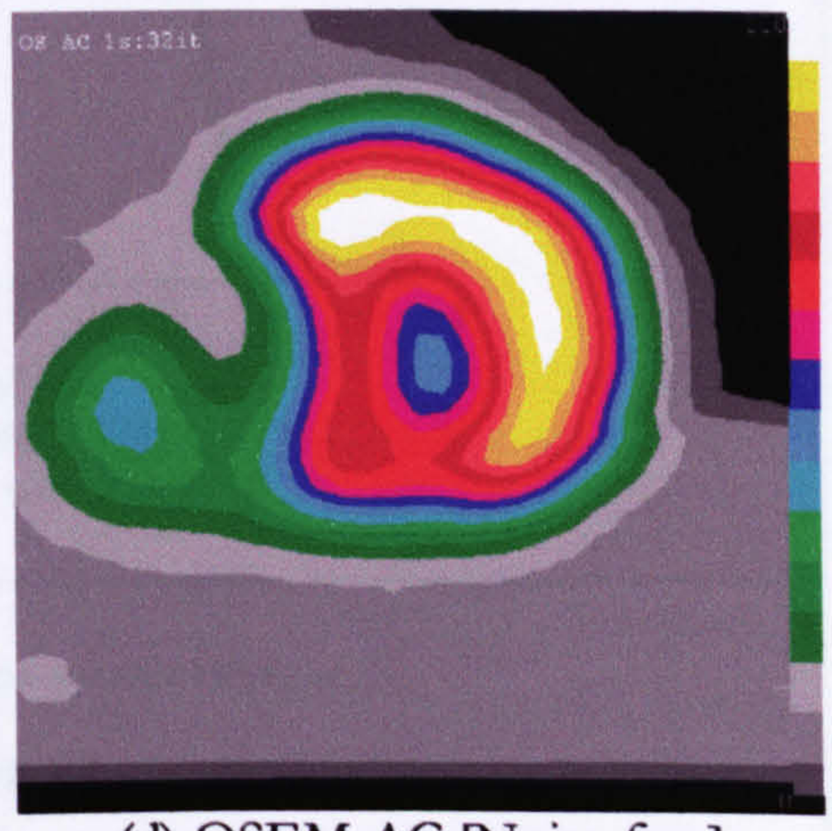

(d) OSEM-AC [Noise-free]

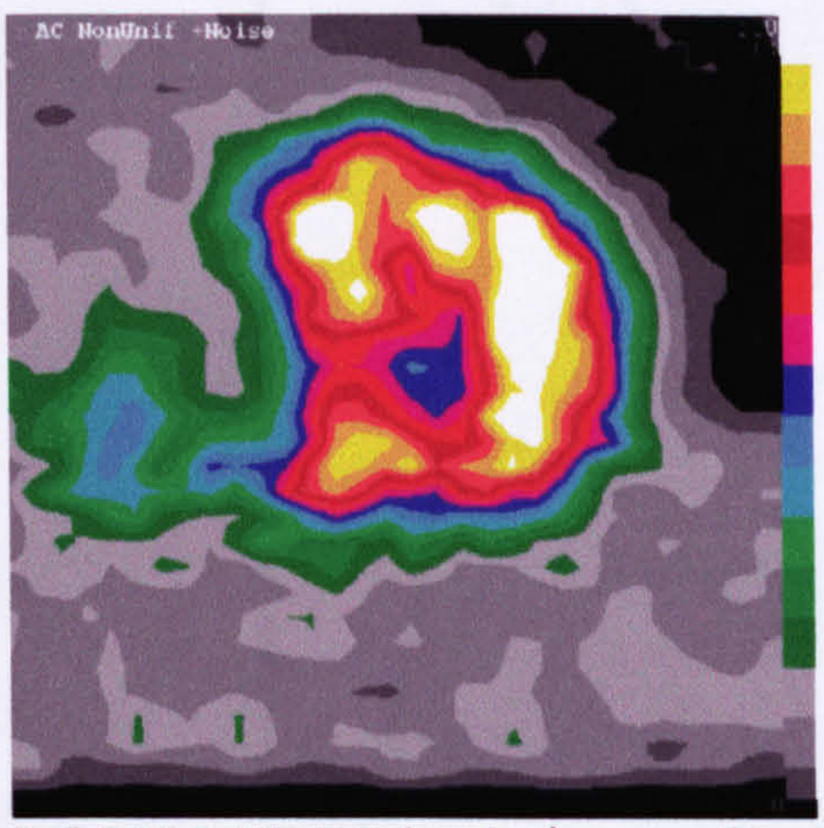

(e) OSEM-AC [Noisy (w/o post-filter)]

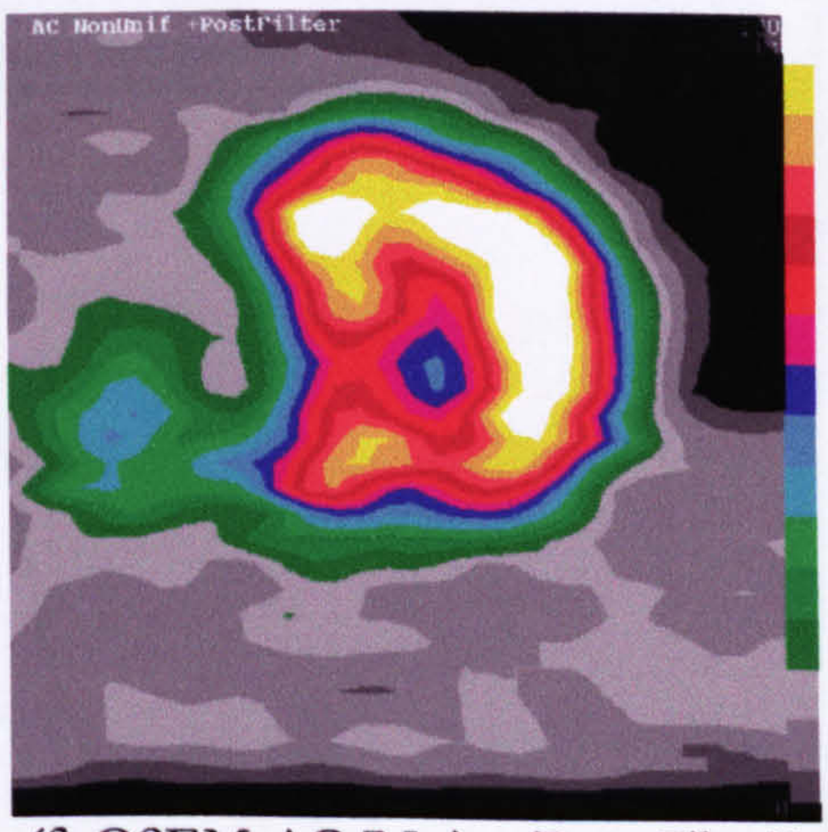

(f) OSEM-AC [Noisy (Post-Filter)]

Figure 5-29 Short-axis slices of noise-free and noisy data reconstructed with and without AC. [(f) with post-filtering applied].

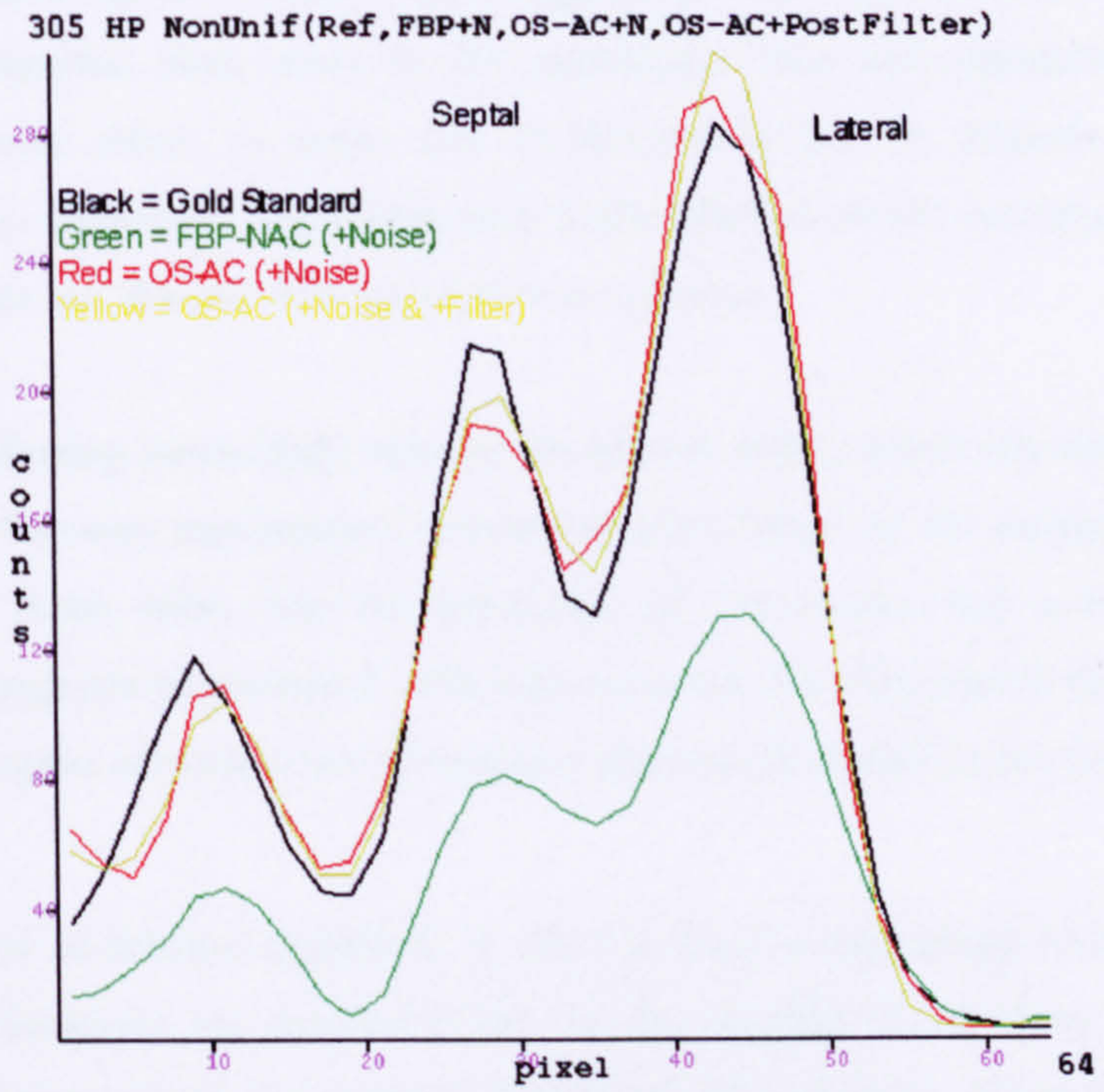

(a) Horizontal profiles
[Red= AC with Noise & without Filter]
[Yellow= AC with Noise & with Filter]

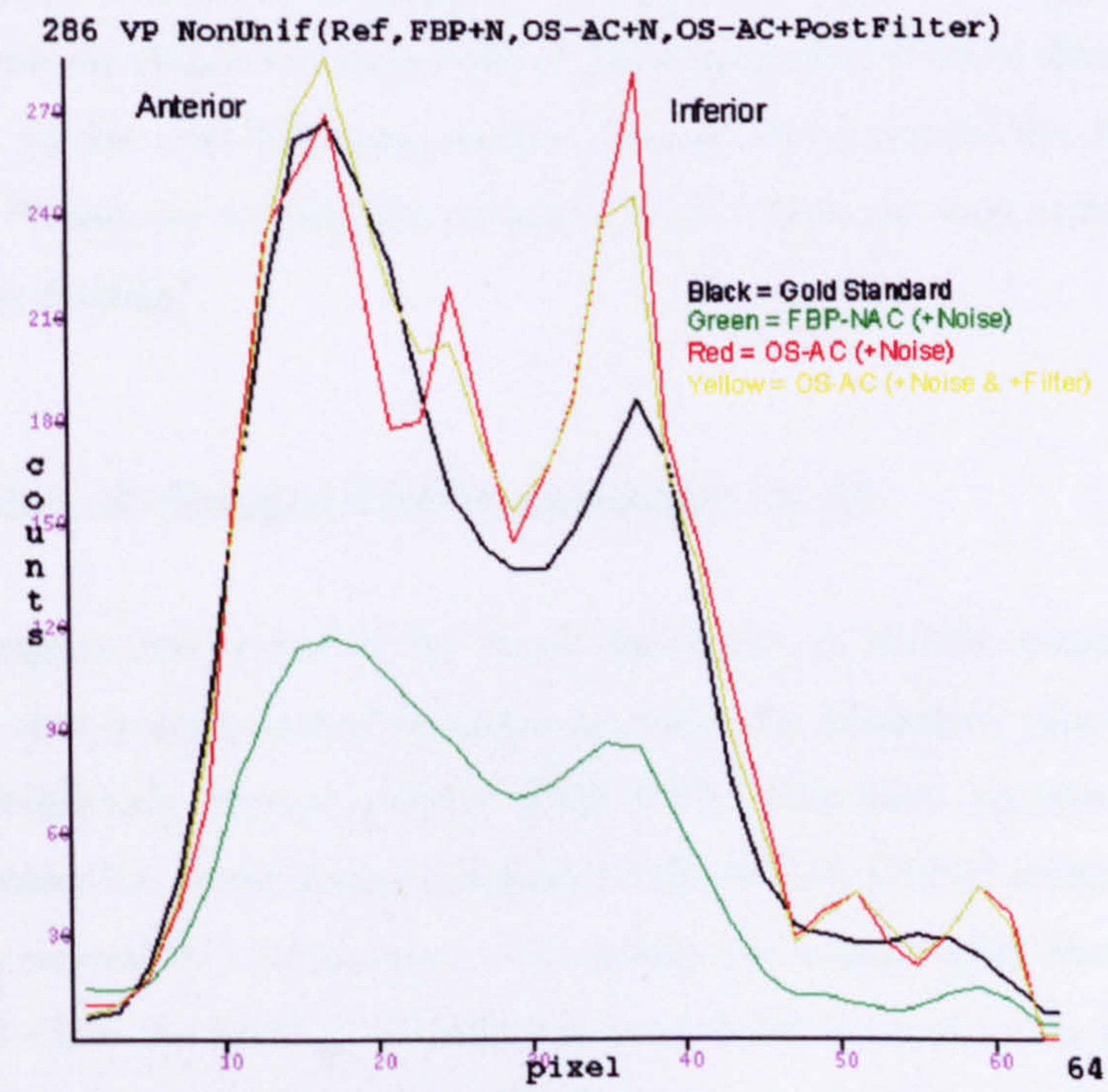

(b) Vertical profiles
[Red= AC with Noise & without Filter]
[Yellow= AC with Noise & with Filter]

Figure 5-30 Count Density profiles through the transaxial slices shown in Figure 5-29.

Liew [114] pointed that three sources of noise can be identified in SPECT reconstruction using the iterative MLEM algorithm. These are the photon noise in the emission projection data, noise in the attenuation map and algorithm noise. The algorithm noise refers to noise that is introduced due to imperfections in the reconstruction algorithm, which may arise if the physical model incorporated into the algorithm does not describe the actual photon emission.

Using post-filtering successfully reduced the photon noise, which was simulated in this experiment. Previous transmission simulations were based on the assumption that the CT system (x-ray tube) has the advantage of low noise, and a high-resolution attenuation map can be generated. Although noise was not simulated in the transmission model, the impact of noise in the attenuation map can be studied in the future.

In the case of an iterative algorithm, in order to reach a high image resolution, a large number of iterations are required [115]. As the number of iterations increases, the contrast and the noise in the reconstructed image also increases. Noise can be reduced by either early termination of the algorithm before the noise becomes significant or by smoothing the images after reconstruction by the use of post-reconstruction filters [116]. In clinical studies it is likely that reconstruction may be stopped after fewer iterations (with the choice of a larger subset size if necessary) so as to obtain a smoother result [117]. In the next following section, we will try to answer the Hutton's [117] question of "When can we stop the iterations" and , "if we can stop earlier, what about applying post-filtering".

5.7. Effects of changing OSEM parameters on AC

Slow convergence rate is one of the major drawbacks of MLEM iterative algorithms. This means that it takes several iterations to reach the maximum value of the object function (likelihood). Several authors [118] [119] [120] have reported that OSEM produces similar but faster images compared with MLEM. OSEM reduces the number of iterations needed by a factor equal to the number of subsets used. Similar results can be obtained when the number of iterations for MLEM is equal to the product of the number of iterations "*Itr*" and the number of subsets "*Sbs*" for OSEM. However, a problem associated with iterative algorithms (both MLEM and OSEM) is the lack of a

robust stopping rule that can dictate the termination of the iterative process. Some manufacturers of SPECT scanners have recently started to include OSEM algorithms in the software of their systems. The users, however, do not have the opportunity to easily change the various reconstruction parameters and optimise them to their acquisition protocols. This makes it another black box for the user [119].

The OSEM algorithm depends on two free parameters, the number of iterations and the number of subsets. These parameters control both the speed of convergence and the regularization (i.e. the stability for Poisson noise)[121]. In the OSEM algorithm package (Version 5.201 which is licensed only for research purposes) used in this project, only limited free parameters such as the number of subsets and iterations can be changed in the reconstruction process. To this end the purpose of this experiment was two-fold:

1) To optimise the OSEM algorithm in terms of both the number of iterations and subsets for the noise-free emission model with and without non-uniform AC.
2) To compare the usefulness of using post-filtering with the early stopping criteria in noisy data.

These two goals were studied using just one figure of merit; fractional root mean square error (FRMSE). The FRMSE was calculated between the noise-free gold standard image $C_{GoldStd}$ and the reconstructed $C_{Measured}$ and is given by:

$$FRMSE = \frac{\sqrt{\frac{1}{n}\sum_{n}(C_{Measured} - C_{GoldStd})^2}}{C_{Average}} \qquad \text{Eqn 5-2}$$

Where

$C_{GoldStd}$ is the counts in the LV region of gold standard model

$C_{Measured}$ is the counts in the LV region after reconstruction

$C_{Average}$ is the average counts in the LV regions after reconstruction

n is the number of region of interest (4) where measurements were carried out (4 ROIs as shown previously on Figure 5-5(c))

In the case of simulation studies, where the pixel count (or activity density in the source) is known in advance, the FRMSE can be used, and expresses a normalized measure of agreement between the reconstructed and actual image. As the FRMSE gets smaller

(and reaches zero), this indicates that the reconstructed image converges with the gold standard with minimum error. The significant FRMSE value was selected to be any error greater than 0.1 (=10 %.).

In order to investigate the effects of changing the OSEM parameters, the same noise-free and noisy models as used in sections 5.3, 5.5 and 5.6 were reconstructed with AC using the OSEM algorithm with different numbers of iterations and subsets. These models were performed as follows;

- Noise-free and noisy emission model only without attenuation effect (noisy data with and without post-filtering).
- Noise-free and noisy emission model with non-uniform AC (noisy data with and without post-filtering)

Different numbers of iterations (1, 2, 4, 8, 16, 32, 64, and 128 iterations) were used in combination with 1, 2, 4, and 8 subsets (The two subsets includes 64 projections per subset, and the four and eight subsets include 32 and 16 projections per subset, respectively). Although the highest number of subsets should be used to speed up the reconstruction process, the number of selected subsets should contain at least four projections per subset. Blocklet [122] claims that "below four projections per subset, significant difference could arise between MLEM and OSEM". Based on this the minimum number of projection per subsets was selected to be 16 projections per subset (8 subsets with a total of 128 projections).

5.7.1 Emission model only without attenuation effect

Table 5-5 and Figure 5-31 show the FRMSE with different numbers of subsets and iterations for the noise-free emission model reconstructed without attenuation. This figure shows that as the number of iterations increased, the FRMSE significantly decreased (and got closer to zero) with early iteration numbers and reached a plateau at 64 iterations. These results indicate that with the four different number of subsets (1, 2, 4, and 8 subsets) OSEM converges and reach the gold standard model when the combination of $Itr \times Sbs = 64$. These results agreed with the gold standard model, which was reconstructed by using OSEM with 1 subset and 64 iterations.

Table 5-5 The FRMSE as a function of iterations for a combination of four subsets groups (1, 2, 4 and 8) for noise-free emission model only (no attenuation).

No. Of iterations	1 subset	2 subsets	4 subsets	8 subsets
1	0.750	0.576	0.229	0.067
2	0.576	0.283	0.079	0.039
4	0.283	0.086	0.040	0.015
8	0.086	0.040	0.015	**0.002**
16	0.040	0.015	**0.002**	0.002
32	0.016	**0.000**	0.002	0.002
64	**0.000**	0.002	0.002	0.005
128	0.002	0.002	0.002	0.005
Minimum FRMSE values are shown in bold.				

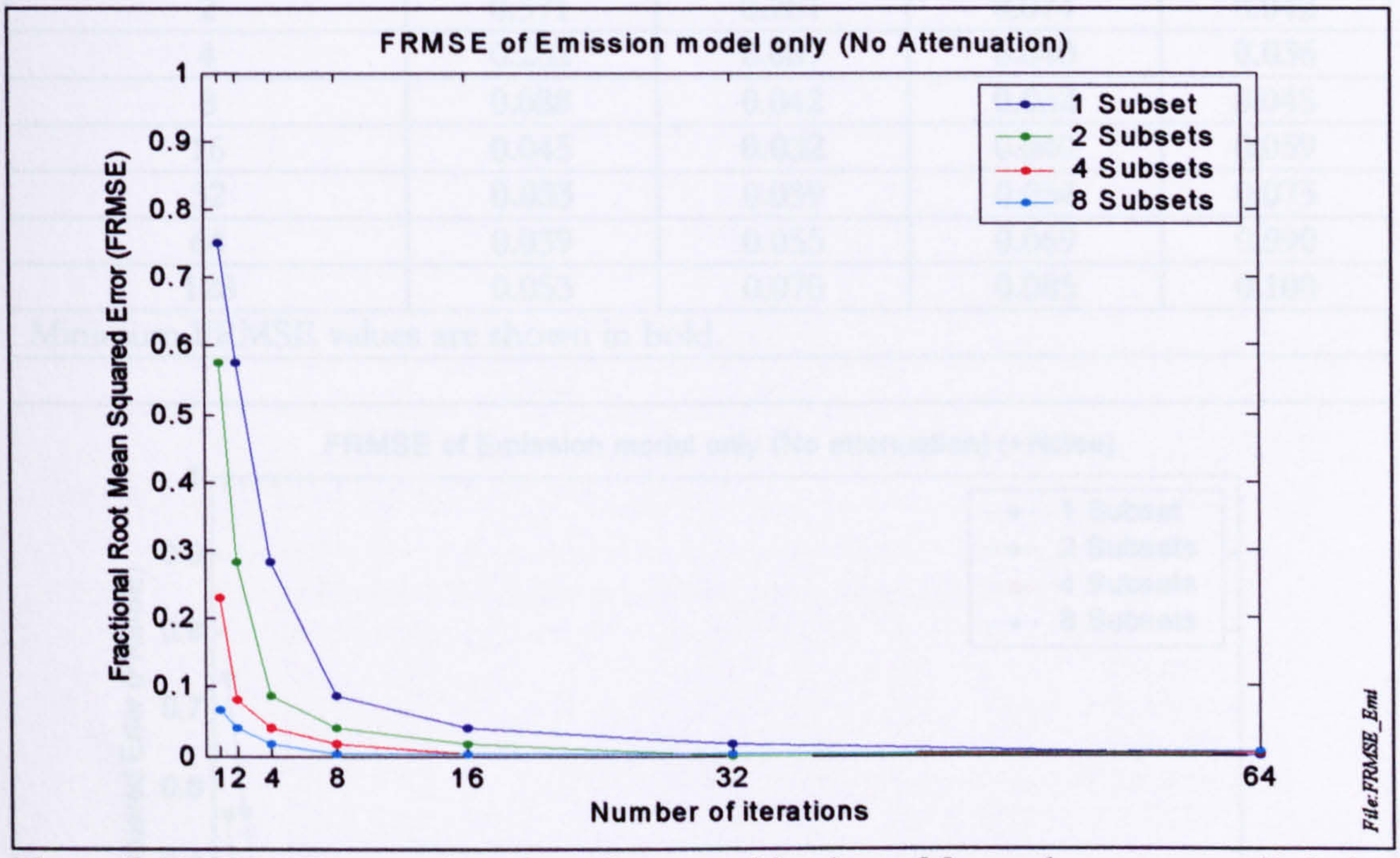

Figure 5-31 FRMSE versus iterations for a combination of four subsets groups (1, 2, 4 and 8) for noise-free emission model only (no attenuation).

Table 5-6 and Figure 5-32 present the FRMSE of the noisy emission model reconstructed with OSEM (no attenuation) with different number of iterations for four different numbers of subsets. Post-filtering was not applied in these reconstructions. It is seen that when noise is included in the reconstruction, the FRMSE increases (compared to the noiseless emission model) as the number of both iteration and subsets are increased. For the same combination of number of iterations and number of subsets ($Itr \times Sbs = 64$), the FRMSE in the noisy data (Table 5-6 and Figure 5-32) were (0.039, 0.055, 0.069, and 0.090) compared to the noise-free data (Table 5-5 and Figure 5-31) which were (0.00, 0.00, 0.002, and 0.002) for 1, 2, 4, and 8 subsets, respectively. Despite

these increased values of FRMSE, still these errors are considered insignificant since all values were below 0.1 (10%). These results indicate that the OSEM reconstruction works quite well to reconstruct the emission model (noise-free and noisy models) with insignificant errors especially, when attenuation effect was not incorporated in the reconstruction. These results only represent one level of noise. When other levels of noise are simulated, the FRMSE values will change according to the noise level.

Table 5-6 The FRMSE as a function of iterations and a combination of four groups of subsets for noisy emission model without attenuation (w/o post-filtering).

No. Of iterations	1 subset	2 subsets	4 subsets	8 subsets
1	0.745	0.569	0.225	0.059
2	0.571	0.281	0.074	0.042
4	0.282	0.087	0.040	**0.036**
8	0.088	0.042	**0.032**	0.045
16	0.045	**0.032**	0.040	0.059
32	**0.033**	0.039	0.054	0.075
64	0.039	0.055	0.069	0.090
128	0.053	0.070	0.085	0.100
Minimum FRMSE values are shown in bold.				

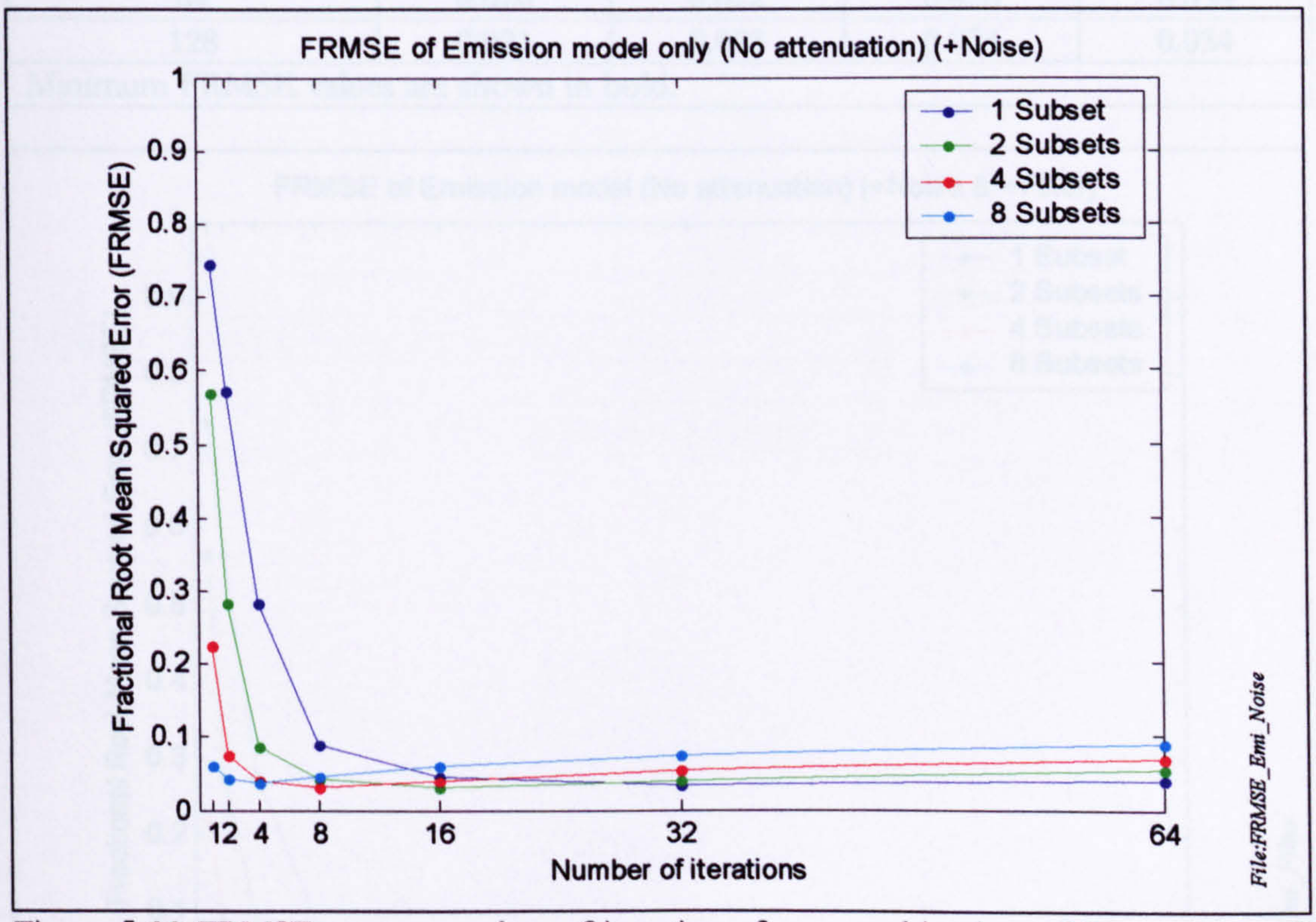

Figure 5-32 FRMSE versus number of iterations for a combination of four groups of subsets (1, 2, 4, and 8 subsets) with noisy emission model and reconstructed without attenuation (w/o post filtering).

In the case where post-filtering was applied to the noisy emission model, the FRMSE values for a combination of ($Itr \times Sbs = 64$), were decreased (0.020, 0.020, 0.023, and 0.032) (Table 5-7 and Figure 5-33) compared to the noisy data without post-filtering (0.039, 0.055, 0.069, and 0.090) (Table 5-6 and Figure 5-32) for 1, 2, 4, and 8 subsets, respectively. These results indicate that applying post-filtering to a noisy emission data (no attenuation) can significantly reduce the error in the OSEM reconstruction.

Irrespective of the importance of applying post-filtering on noisy emission data, the FRMSE values after post-filtering did not reach zero (i.e. equal to the gold standard).

Table 5-7 The FRMSE as a function of iterations and number of subsets for noisy emission model without attenuation (post-filtering).

No. Of iterations	1 subset	2 subsets	4 subsets	8 subsets
1	0.740	0.567	0.218	0.0544
2	0.567	0.274	0.066	0.036
4	0.276	0.078	0.032	**0.028**
8	0.081	0.035	**0.022**	0.032
16	0.036	0.021	0.023	0.033
32	0.022	**0.020**	0.024	0.033
64	**0.020**	0.022	0.026	0.034
128	0.021	0.023	0.024	0.034
Minimum FRMSE values are shown in bold.				

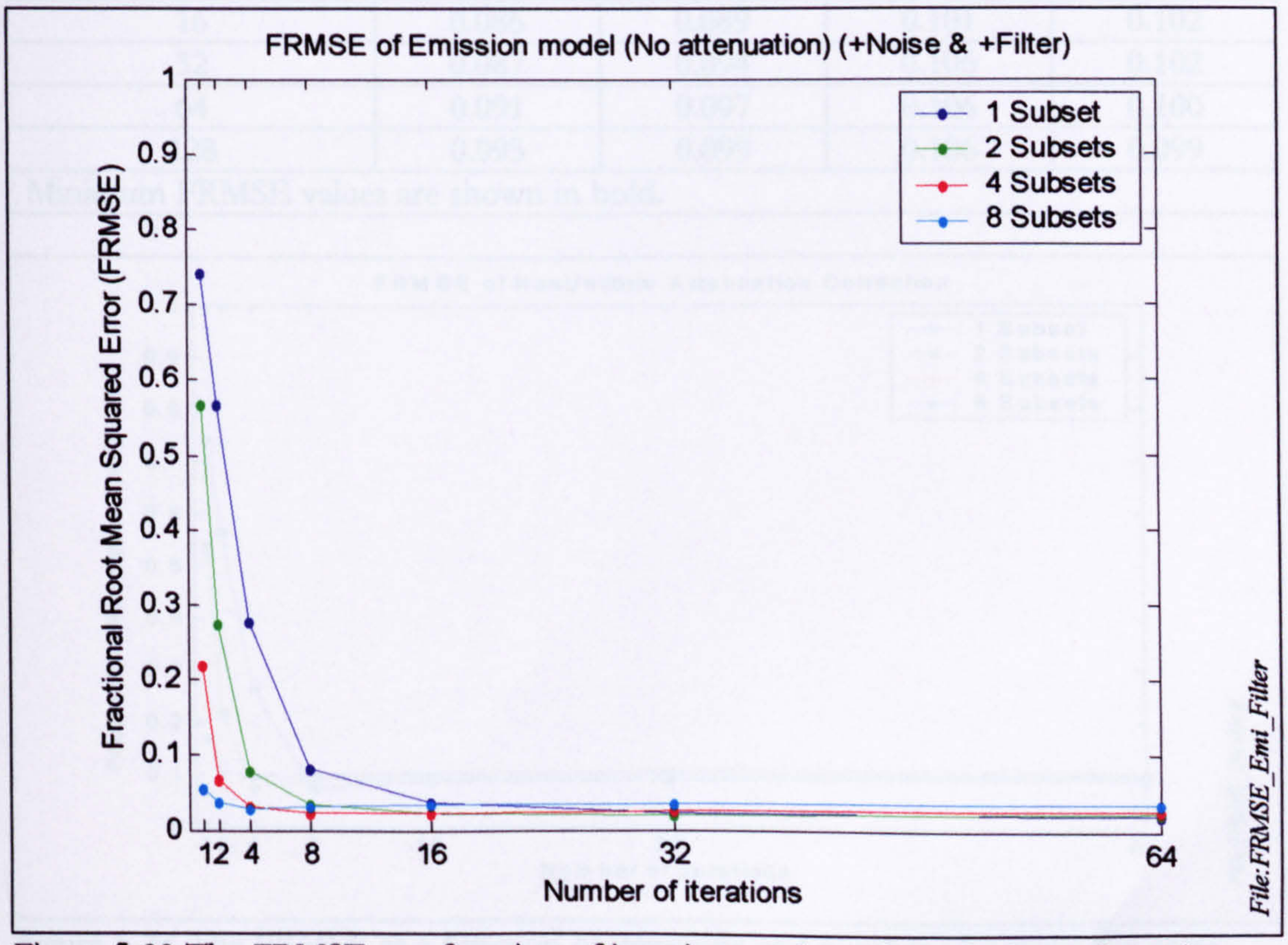

Figure 5-33 The FRMSE as a function of iterations and number of subsets for noisy emission model without attenuation (post-filtering).

5.7.2 Emission model with non-uniform attenuation effect

The FRMSE of the noise-free emission model reconstructed with non-uniform AC are shown in Table 5-8 and Figure 5-34. From these data it can be seen that the FRMSE is decreased as the number of iterations increases for the same subset and also decreases as the number of subset increases for the same iteration number. In general the minimum FRMSE values were obtained (0.071, 0.076, 0.076, and 0.094) for a combination of; [(1 *Sbs : 8 Itr*), (2 *Sbs* : 4 *Itr*), (4 *Sbs* : 2 *Itr*), and (8 *Sbs* : 2 *Itr*)], respectively. The previous data indicates that as the number of subsets was increased from 2 subsets to 4 subsets, the FRMSE values remained the same (0.076) but still higher than the FRMSE with one subset (0.071). According to this, the combination of 1 subset and 8 iterations was selected to be the optimum for reconstruction of this noise-free model.

Table 5-8 The FRMSE as a function of iterations and number of subsets for noise-free emission model reconstructed with non-uniform AC.

No. Of iterations	1 subset	2 subsets	4 subsets	8 subsets
1	0.741	0.539	0.225	0.168
2	0.566	0.217	**0.076**	0.104
4	0.261	**0.076**	0.096	**0.094**
8	**0.071**	0.088	0.097	0.099
16	0.086	0.089	0.101	0.102
32	0.087	0.094	0.106	0.102
64	0.091	0.097	0.106	0.100
128	0.093	0.099	0.106	0.099
Minimum FRMSE values are shown in bold.				

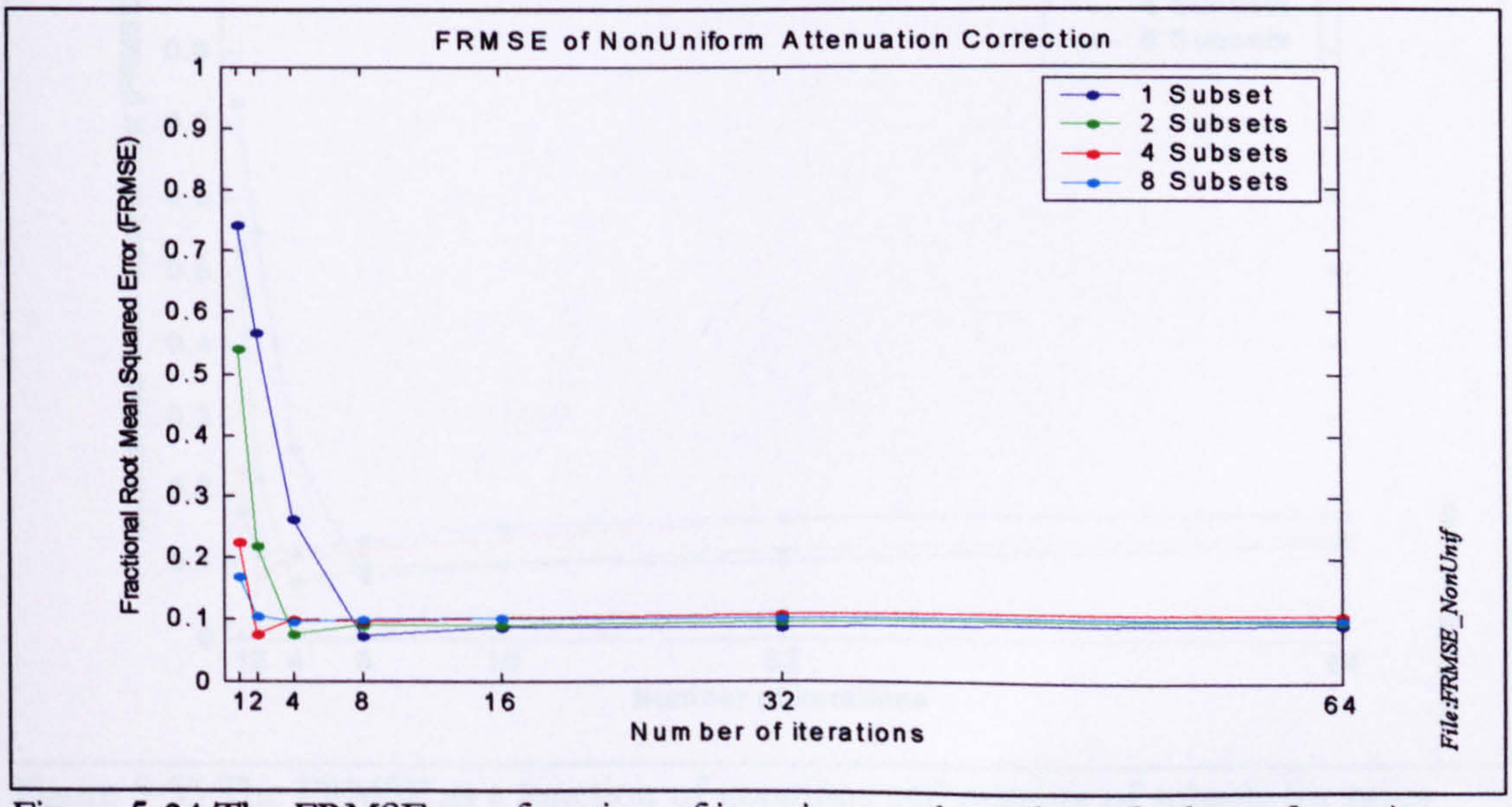

Figure 5-34 The FRMSE as a function of iterations and number of subsets for noise-free emission model with non-uniform attenuation.

Figure 5-35 plots the FRMSE of the reconstructed non-uniform AC images for the noisy data. The FRMSE values show a rapid decrease during the first iteration (up to 8 iterations) of OSEM algorithm. After this rapid convergence phase, the FRMSE reaches an optimum point then dramatically starts increasing. All FRMSE values after the optimum point were significantly greater than the acceptable limit (~ 0.1 and above) due to the noisy nature of the data. Based on Figure 5-35, it was noted that at all subsets levels, the FRMSE increased as the number of iterations is increased, due to the build-up of noise in the image as the iteration increases.

Table 5-9 The FRMSE as a function of iterations and number of subsets for noisy emission model with non-uniform attenuation (w/o post-filtering).

No. Of iterations	1 subset	2 subsets	4 subsets	8 subsets
1	0.730	0.530	0.229	0.175
2	0.555	0.218	**0.084**	**0.112**
4	0.259	**0.075**	0.109	0.115
8	**0.080**	0.096	0.117	0.133
16	0.101	0.102	0.135	0.152
32	0.105	0.119	0.159	0.161
64	0.126	0.140	0.172	0.165
128	0.148	0.150	0.172	0.169
Minimum FRMSE values are shown in bold.				

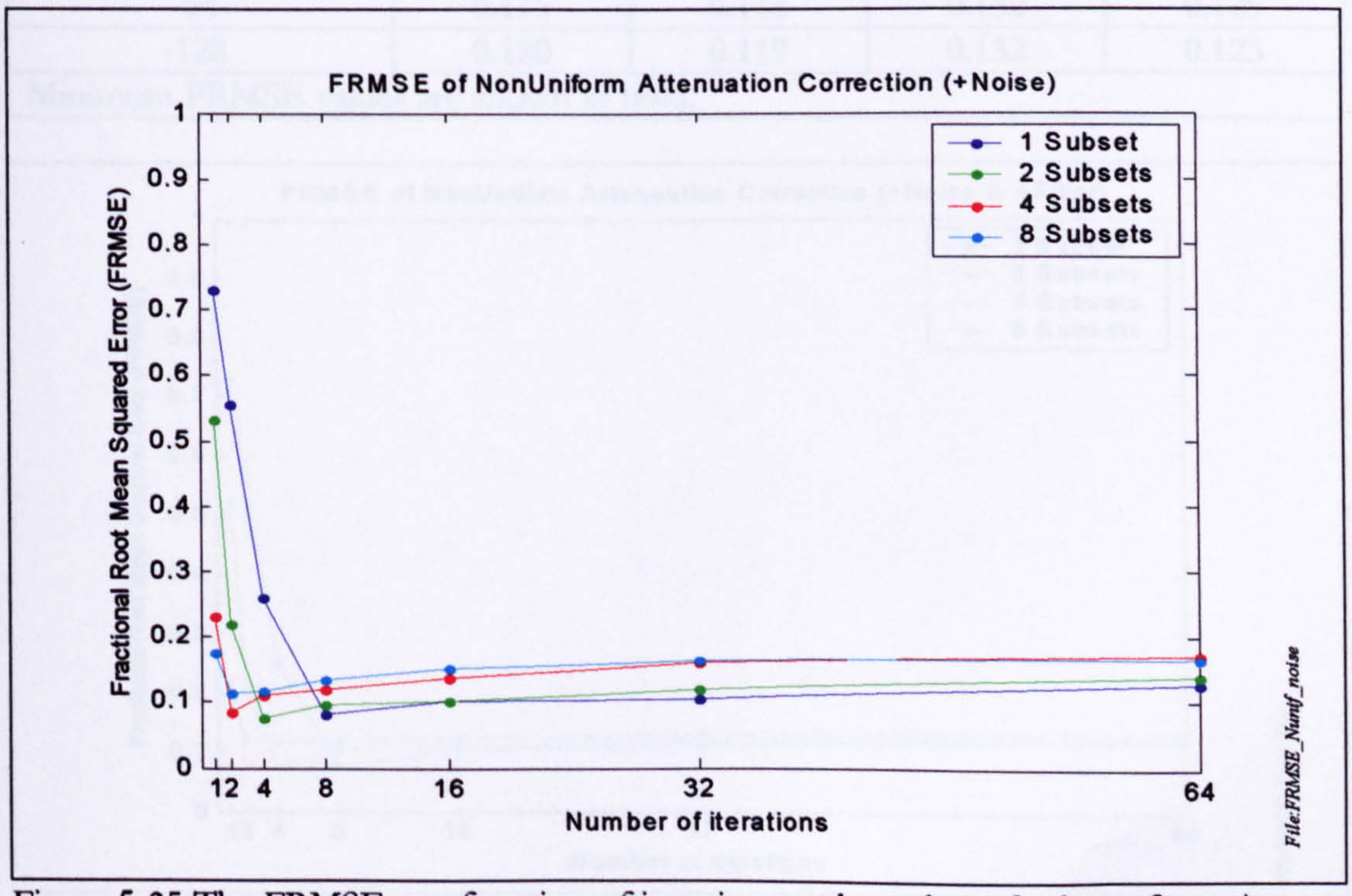

Figure 5-35 The FRMSE as a function of iterations and number of subsets for noisy emission model with non-uniform attenuation (w/o post-filtering).

Figure 5-36 shows the FRMSE when the post-filtering was applied to the noisy non-uniform AC reconstructed data. When the post-filtering was used, the FRMSE was improved (0.076, 0.074, 0.080, and 0.117) (Table 5-10 and Figure 5-36) compared to the noisy data without applying of post-filtering (0.080, 0.075, 0.084, and 0.112) (Table 5-9 and Figure 5-35) for a combination of; [(1 *Sbs : 8 Itr)*, (2 *Sbs :* 4 *Itr)*, (4 *Sbs :* 2 *Itr*), and (8 *Sbs :* 2 *Itr*)], respectively.

OSEM algorithm has the remarkable feature that iterating has to stop early to achieve a low-noise solution (as the number of iterations increases the noise will be increased as well). Because some structures of the reconstructed image will not be reconstructed completely with small number of iterations, it is recommended that more iteration are used (despite the noise) to obtain an accurate image, and post-filtering can be used after reconstruction to reduce the noise.

Table 5-10 The FRMSE as a function of iterations and number of subsets for noisy emission model with non-uniform attenuation (post-filtering).

No. Of iterations	1 subset	2 subsets	4 subsets	8 subsets
1	0.727	0.523	0.218	0.185
2	0.553	0.207	**0.080**	**0.121**
4	0.250	**0.074**	0.115	0.117
8	**0.076**	0.104	0.119	0.118
16	0.105	0.111	0.122	0.123
32	0.110	0.115	0.129	0.125
64	0.115	0.118	0.132	0.125
128	0.120	0.119	0.132	0.125
Minimum FRMSE values are shown in bold.				

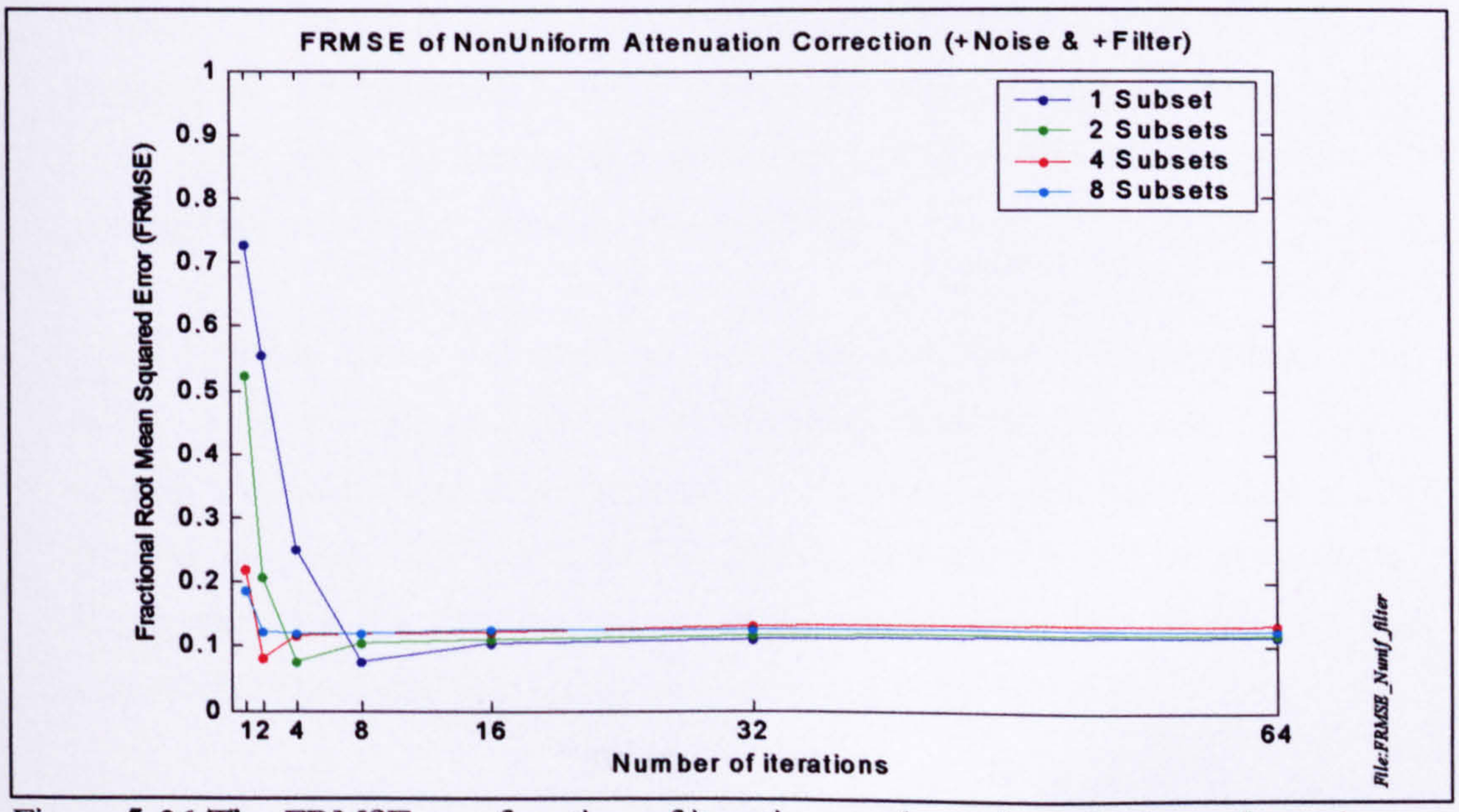

Figure 5-36 The FRMSE as a function of iterations and number of subsets for noisy emission model with non-uniform attenuation (post-filtering).

attenuation modelling was included or not. Hutton [109] believed that the optimal number of iterations is dependent on whether other modelling such as scatter is employed. In general the estimation of optimal values for these two parameters (iterations and subsets) is extremely complex since they depend on the organ under study, and on the number of photons collected [121].

From all data shown in previous section (5.7), four main conclusions can be drawn:

- It has been demonstrated that the product of the number of iterations and subsets for OSEM is equivalent to the number of iterations for MLEM.
- OSEM algorithm converges but never reaches the gold standard in both noisy and noiseless non-uniform AC.
- In noisy data, the FRMSE improves in early iterations and then increases due to increasing noise.
- Post-filtering reconstructed images show a decreased noise whatever the selection of iteration (and subset) number.
- It has been shown that, to get accurate image we should go for more iterations and then applying post filtering (to reduce noise) compared to stopping early to control noise (with inaccurate image).

5.8. Effect of misregistration error between transmission and emission scan on AC

In the Hawkeye multi-modality imaging system, both SPECT emission and CT transmission scans are intended to be acquired with minimum misregistration error between both scans as both systems are combined into a single device and there is no need to move the patient between both scans. Due to the long acquisition time (total scanning time of both transmission and emission scans is about 45 minutes [123], motion artefacts created either by patient motion or rib cage breathing can occur and can be the most important obstacle to exact matching (misregistration) of the SPECT and CT images.

The effect of such misregistration error can be significant in cardiac SPECT and might have an impact on the AC. For instance, a 7-mm misregistration may result in a modification of regional activity by 17% in the LV wall [46] [124]. Consequently such misregistration should be avoided in order to obtain more accurate quantitative measurements. Therefore, the quality of the image corrected for attenuation effects largely depends on registration of the transmission and emission scans [125]. The main objective of this experiment was to evaluate the influence of misregistration between emission and transmission scans on AC.

The effect of misregistration (registration error between the emission and transmission data) was simulated by shifting each slice of transmission model by 3 pixels (12 mm) in the back-front direction relative to the imaging couch. Shifting along the right-left direction was not considered, since it requires the patient to move sideways on the couch. In addition to this horizontal motion, other types of motion such as rotation and twisting were also not considered in this experiment.

Figure 5-37(a-b) shows the transaxial slices with and without misregistration error reconstructed with AC. The profiles of the same transaxial slices shown in Figure 5-37(c-d) indicated that profiles after attenuation corrections were higher than the gold standard (this might show that there were slightly overcorrected with the misregistered data compared to the AC data without misregistration error). This finding was also supported and presented in short-axis slices shown in Figure 5-38(a-b).

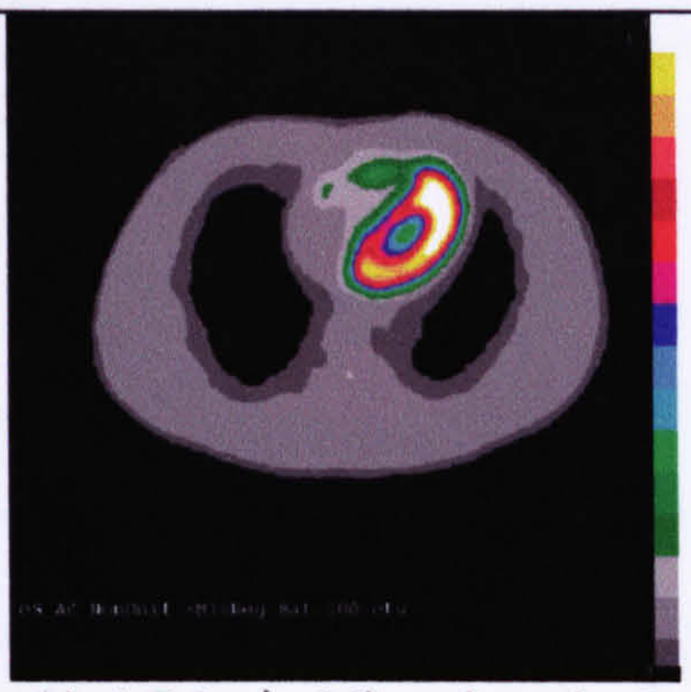

(a) AC [w/o Misregistration]

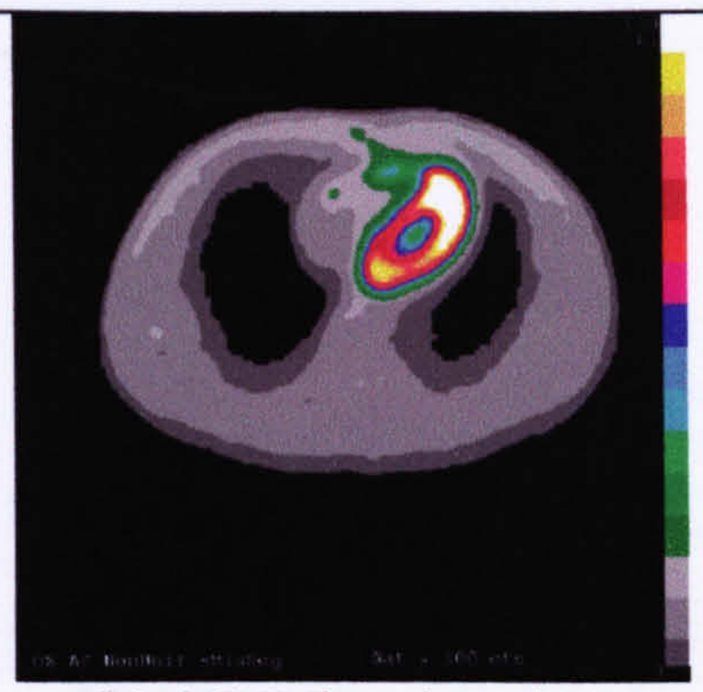

(b) AC [Misregistration]

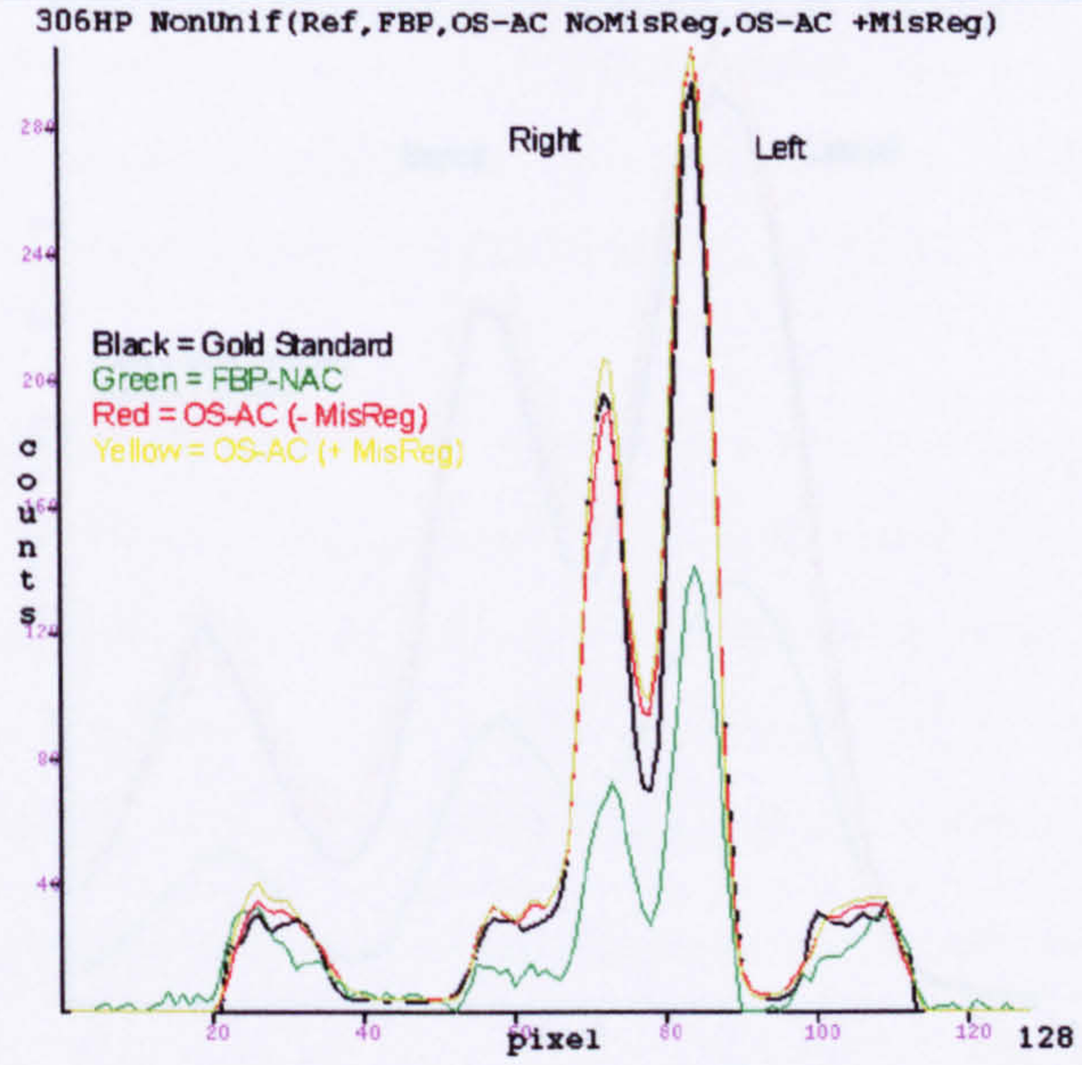

(c) Horizontal profiles

[Red= AC without misregistration] [Yellow= AC with misregistration]

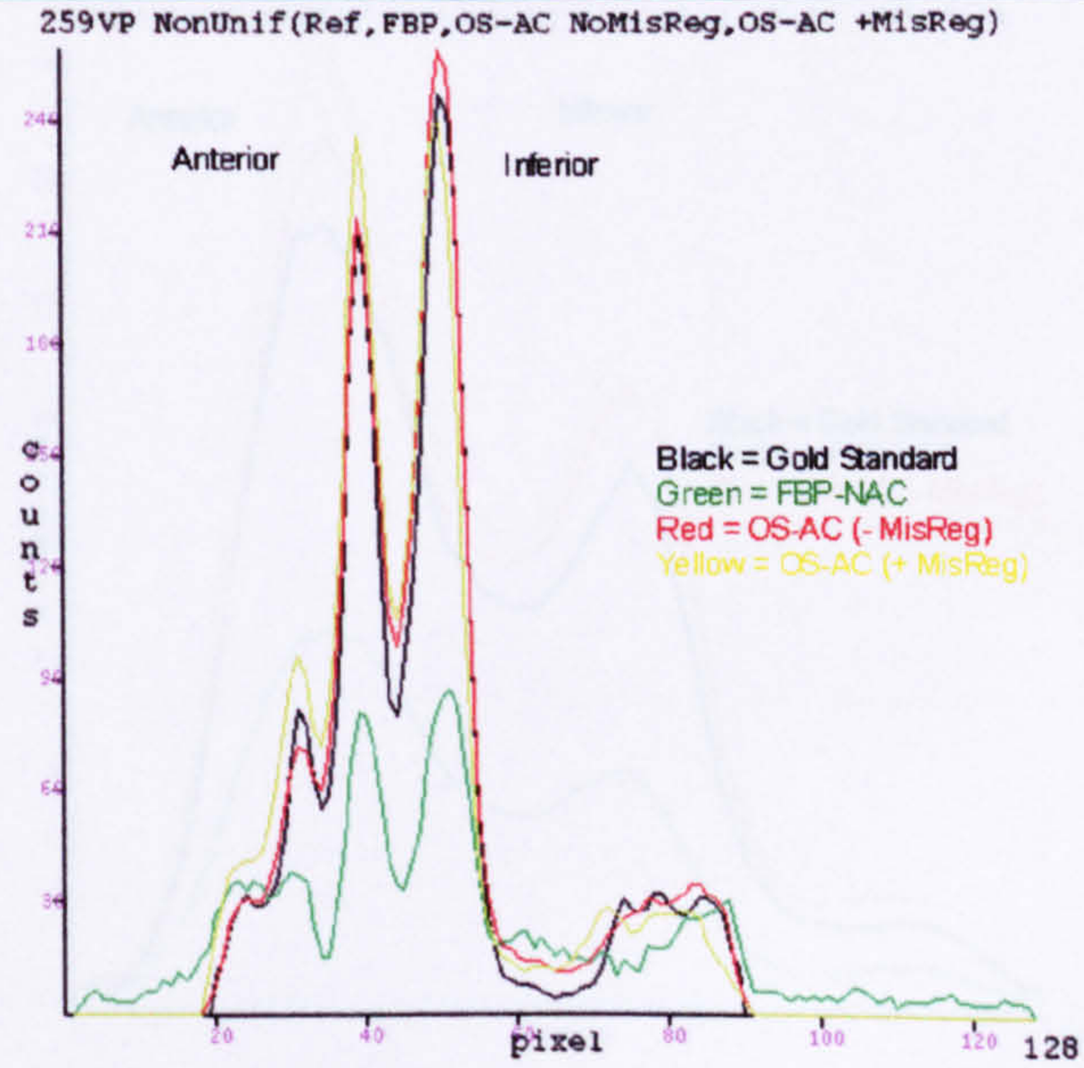

(d) Vertical profiles

[Red= AC without misregistration] [Yellow= AC with misregistration]

Figure 5-37 Transaxial slices and count density profiles of non-uniform attenuation models reconstructed with and without misregistration error.

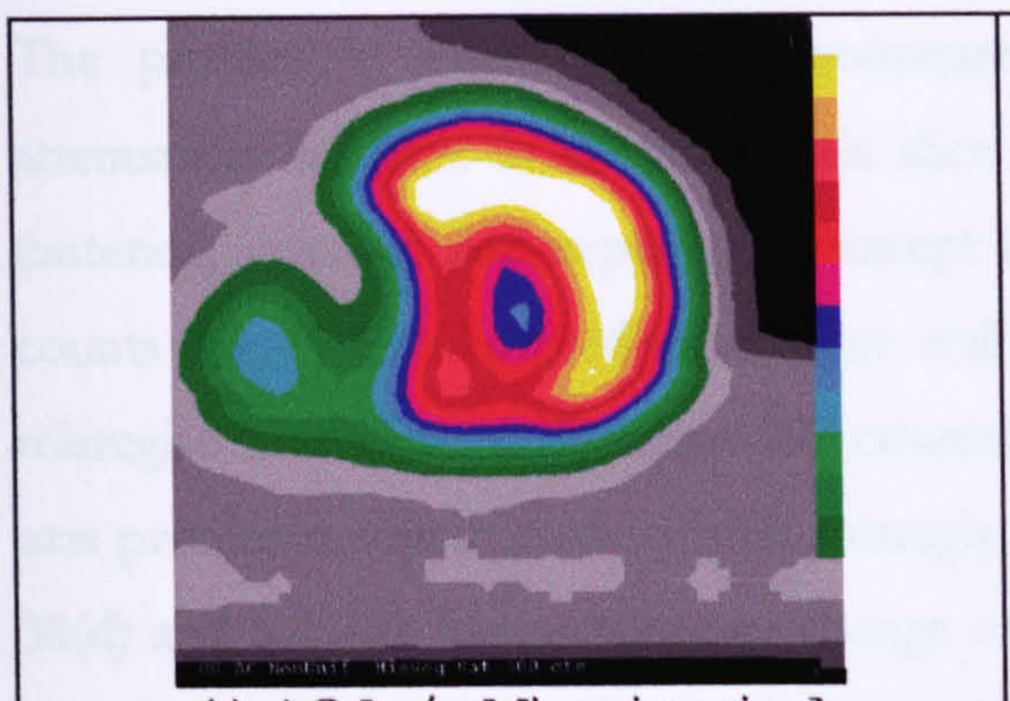

(a) AC [w/o Misregistration]

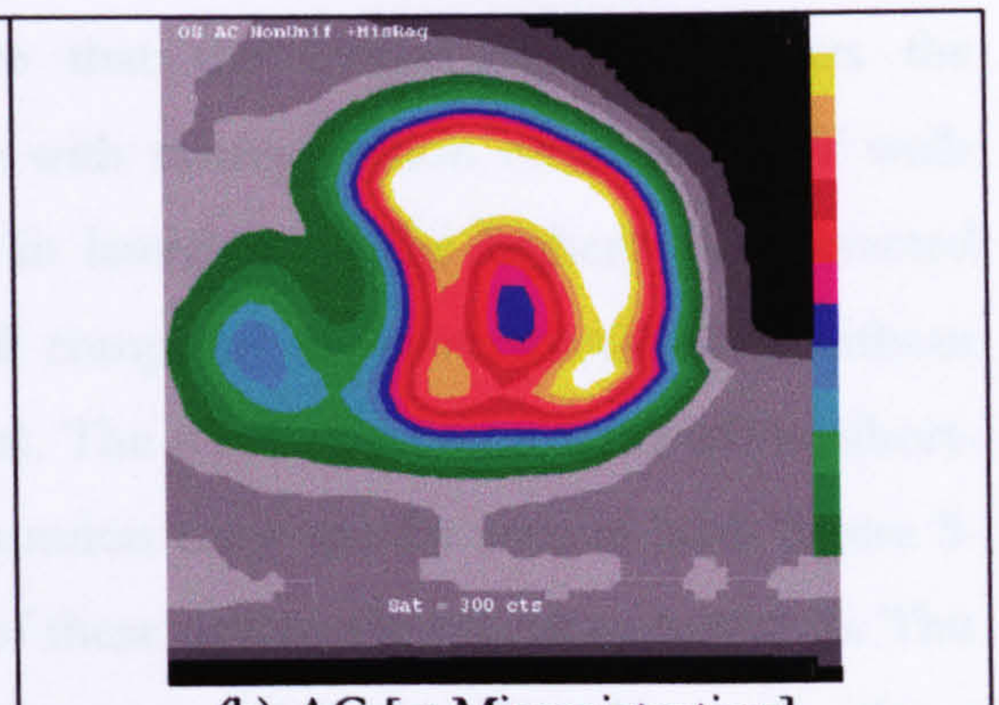

(b) AC [w Misregistration]

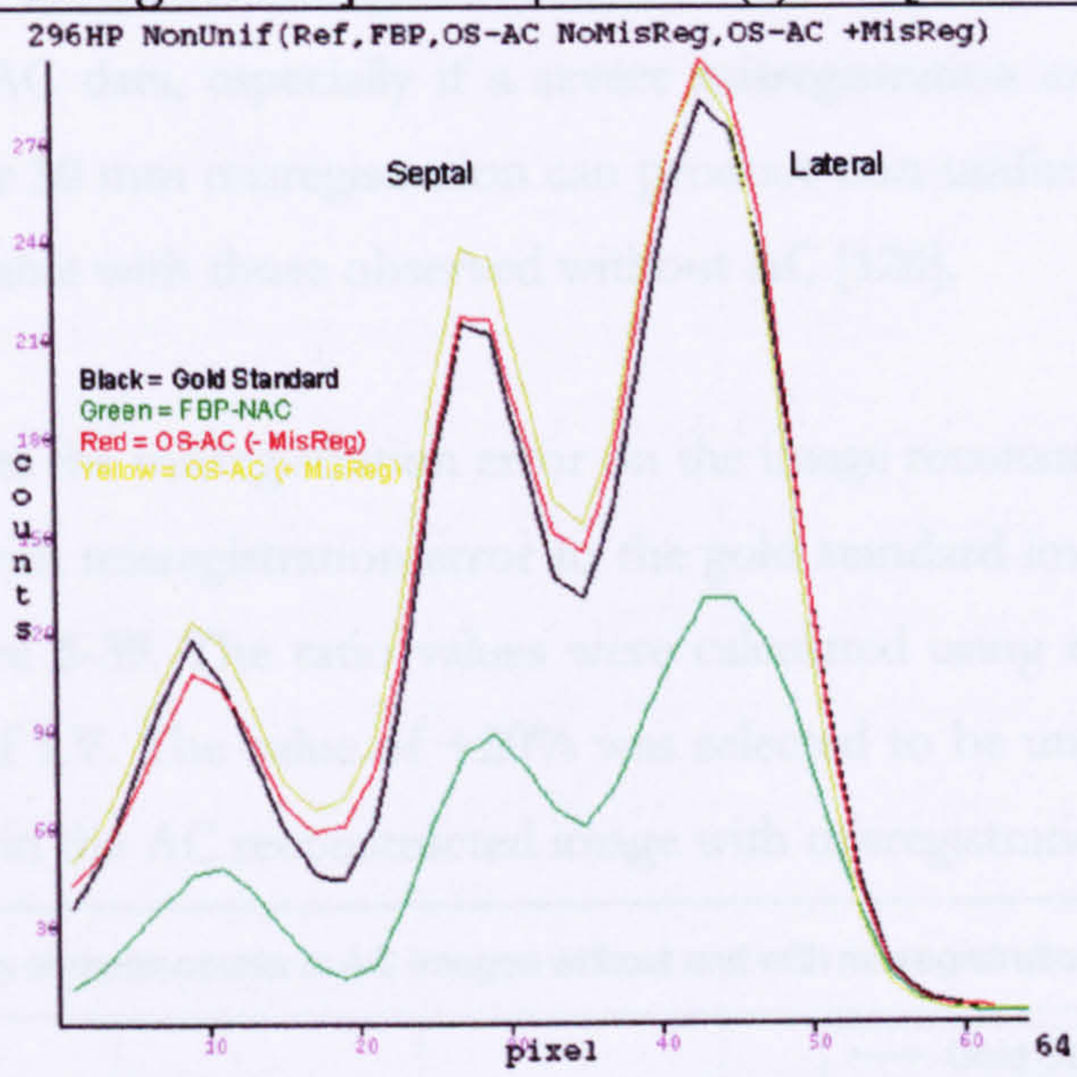

(c) Horizontal profiles

[Red= AC without misregistration][Yellow= AC with misregistration]

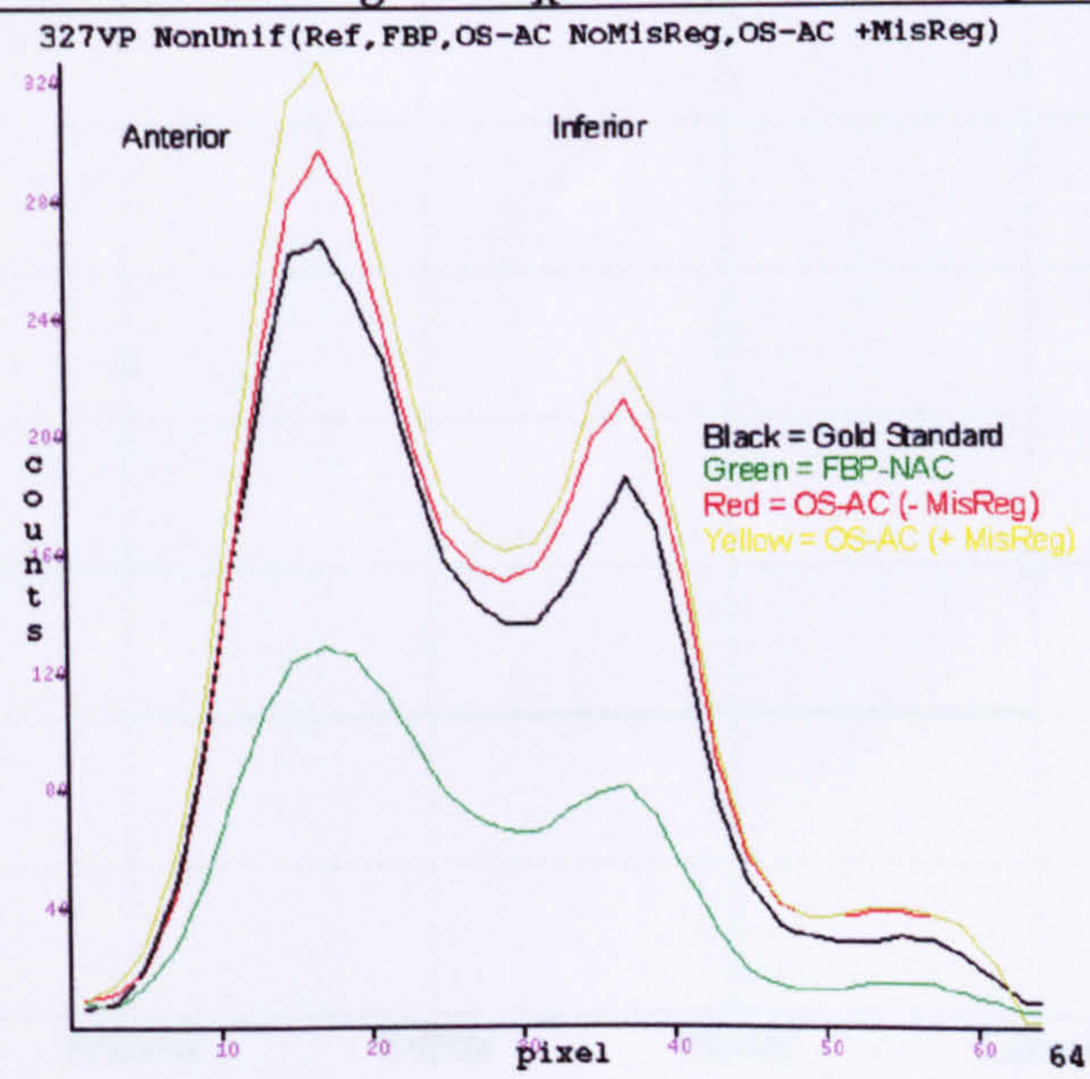

(d) Vertical profiles

[Red= AC without misregistration][Yellow= AC with misregistration]

Figure 5-38 Short-axis slices and count density profiles of non-uniform attenuation models reconstructed with and without misregistration error.

The profiles in Figure 5-38 demonstrate that the OSEM-AC overcorrects the attenuation artefacts in the short-axis slice with misregistration error at all LV walls (anterior, inferior, and septal) and except in lateral wall. The highest overcorrected counts value was observed at anterior wall compared to reconstructed slice without misregistration error (327 versus 297 counts). The maximum count value of the short-axis profiles reconstructed without misregistration error can be seen in both Figure 5-38(d) and 5-37(d). The percentage change of these overcorrected values is 10.1 %. This moderate degree of simulated misregistration error (12 mm) can lead to a significant over-correction in AC data, especially if a severe misregistration error was simulated. For instance, a 20 or 30 mm misregistration can produce non-uniformity of LV activity distribution comparable with those observed without AC [126].

In order to quantitate the misregistration error on the image reconstructed with AC, the ratio in the image with misregistration error to the gold standard image were calculated and shown in Figure 5-39. The ratio values were calculated using the measured mean counts in 4 ROIs of LV. The value of +20% was selected to be unacceptable value of producing artefacts in the AC reconstructed image with misregistration effect.

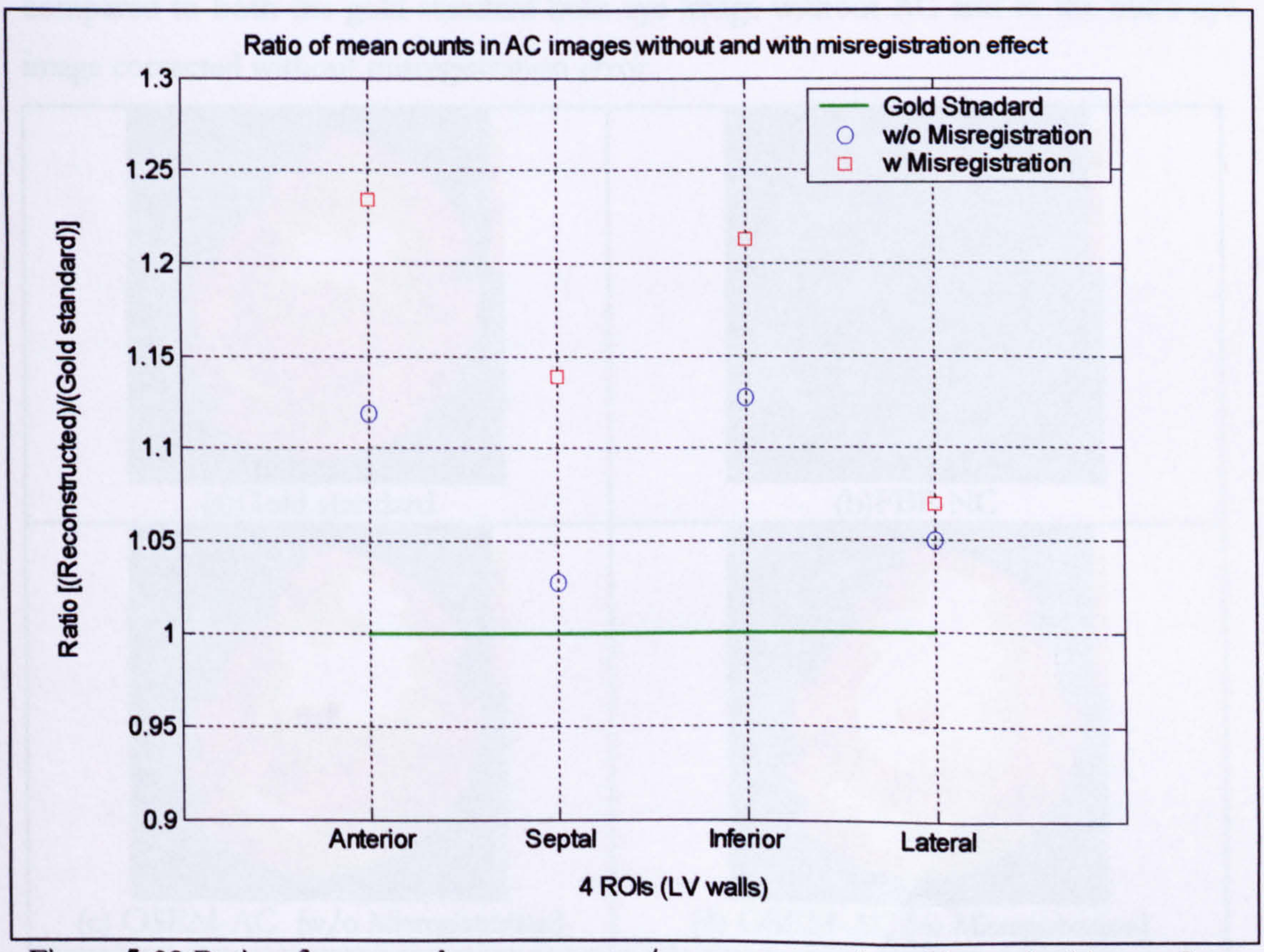

Figure 5-39 Ratio of measured mean counts / mean counts in gold standard image for AC image without and with misregistration effect.

As can be seen from Figure 5-39, the ratio values with misregistartion effect were 1.23, 1.13, 1.21, and 1.07 for anterior, septal, inferior and lateral walls respectively. The ratio values that exceed the acceptable limit (+20%) at anterior and inferior walls indicated that, the misregistration error between emission and transmission images (simulation of 13 mm misregistration) produce a significant relative change in AC compared with AC image without misregistartion effect. Fricke *et al* [127] believe that "the artefacts in the anterior wall in AC image may be due to underestimation of the attenuation effects of the anterior wall in the case of misalignment and the overestimation of the attenuation effects in the inferior wall may explain the phenomenon of overcorrection in the left wall of left myocardium"

Figure 5-40 shows the bull's-eye images of (a) the gold standard, (b) with FBP-NC, (c) attenuation correction without misregistration error and (d) attenuation correction with misregistration error, respectively. From these bull's-eye images, it is clear that the misregistration error between emission and transmission data have a significant impact on AC. In addition, the bull's-eye image corrected with misregistration error (Figure 5-40(d)) shows considerable over-correction of counts at anterior wall and apex region compared to both the gold standard bulls-eye image without AC and to the bull's-eye image corrected without misregistration error.

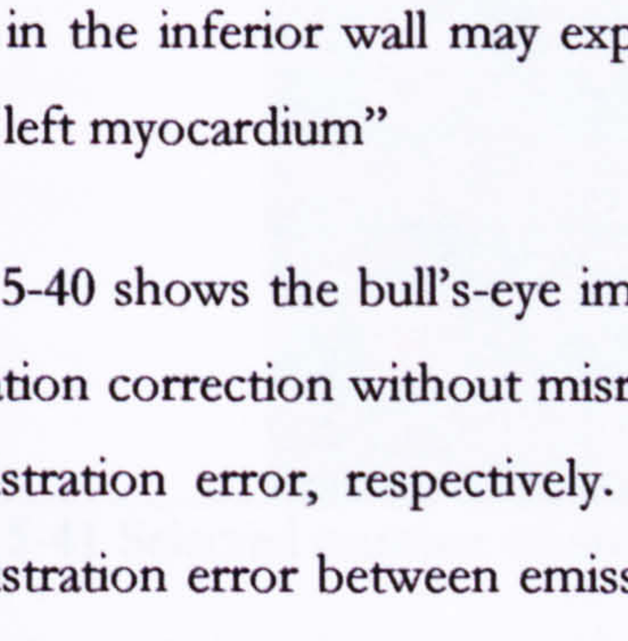

(a)Gold standard

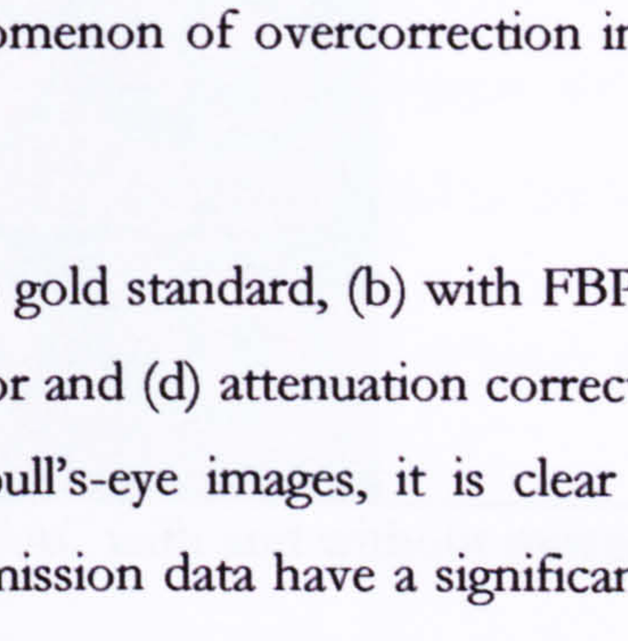

(b)FBP-NC

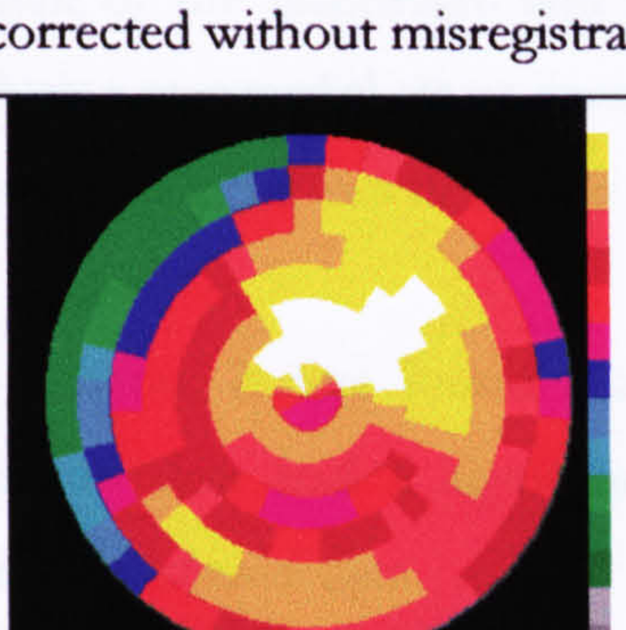

(c) OSEM-AC [w/o Misregistration]

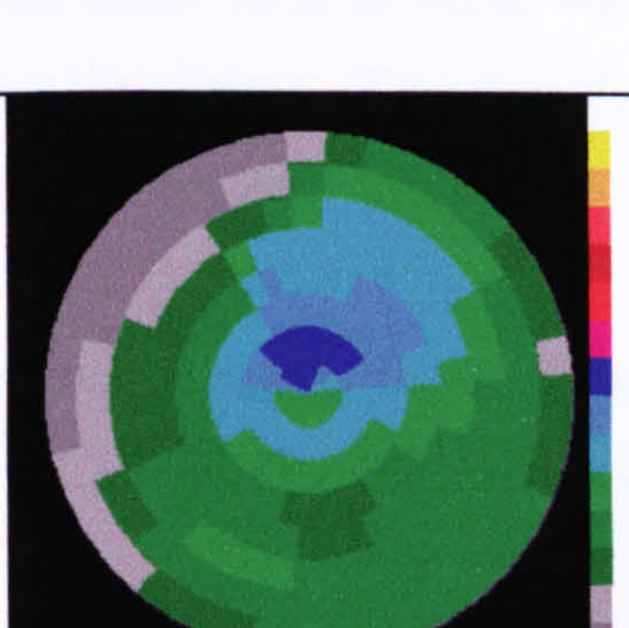

(d) OSEM-AC [w Misregistration]

Figure 5-40 the bull's-eye images of AC with and without misregistration error.

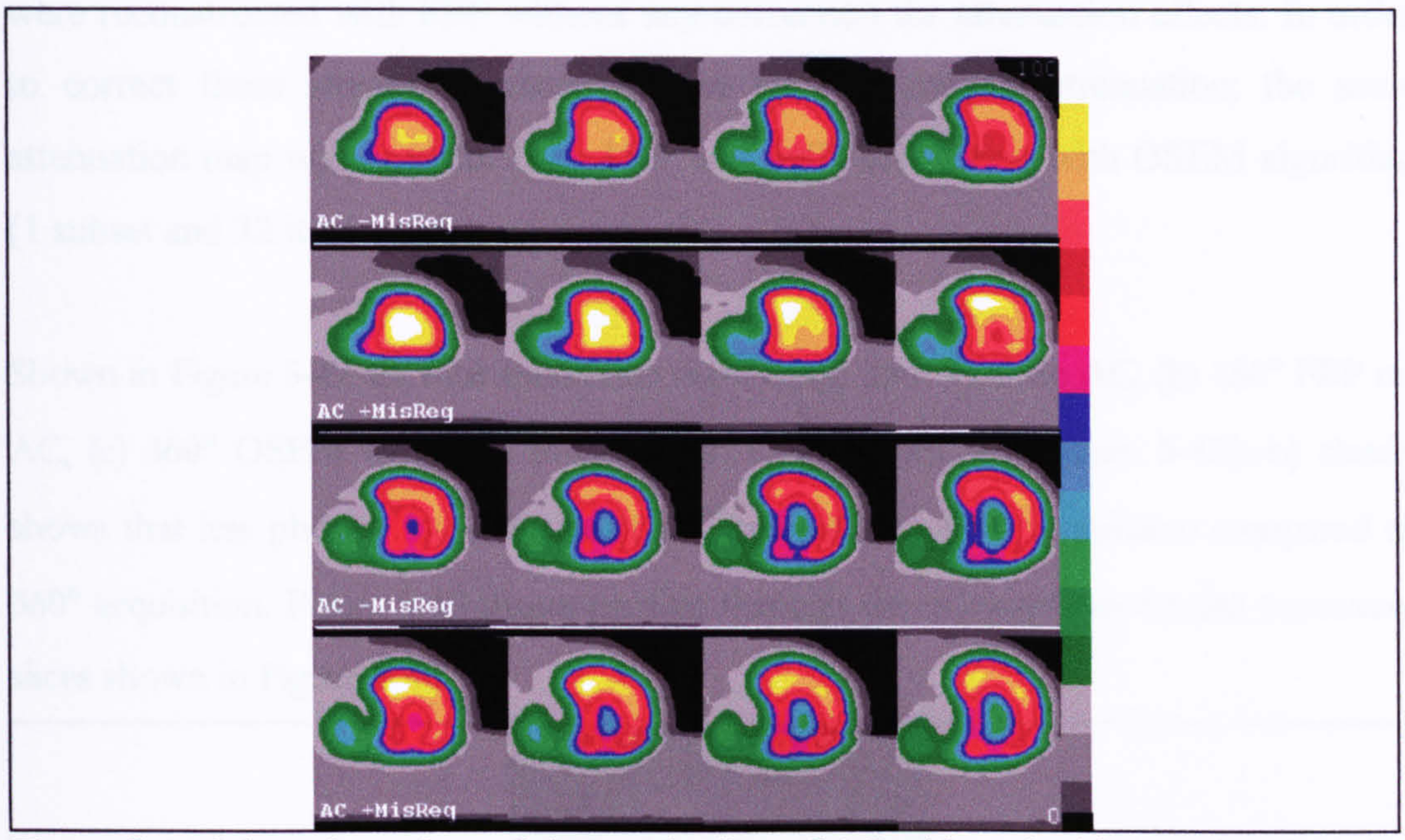

Figure 5-41 Selected number of short-axis slice of AC with and without misregistration error.

The simulation of misregistration error in this experiment was simple and in one direction and it is possible to simulate other sources of misregistration. For example movement of the diaphragm and movement of the heart such as occur with cardiac creep during myocardial stress imaging. Therefore, various types of motion that lead to misregistration error also need to simulated and studied with AC.

In this section, it was found that the misregistration error between emission and transmission data had a significant impact on AC, and therefore it needs to be considered in clinical data.

5.9. Impact of 180° versus 360° acquisition on AC

The aim of this investigation was to evaluate AC with two common acquisition techniques, 180° and 360°.

The same planar projections data, which were obtained with 360° simulations, were used to simulate 180° acquisitions. This was achieved by taking into account only projection views covering the area from left posterior oblique (LPO) to right anterior oblique (RAO). These sets of projection views represent the angles where attenuation

of the heart is minimal. The simulated projections using an acquisition over 180° were reconstructed with FBP without any correction for attenuation effects. In order to correct these attenuated planar images for non-uniform attenuation; the same attenuation map was used for both 180° and 360° acquisition with OSEM algorithm (1 subset and 32 iterations).

Shown in Figure 5-42 are four transverse slices of (a) 360° FBP no AC, (b) 180° FBP no AC, (c) 360° OSEM with AC, and (d) 180° OSEM with AC. Figure 5-42(a-b) clearly shows that less photon from the heart are attenuated in 180° acquisition compared to 360° acquisition. Figure 5-43 shows profiles through the myocardium for the transverse slices shown in Figure 5-42.

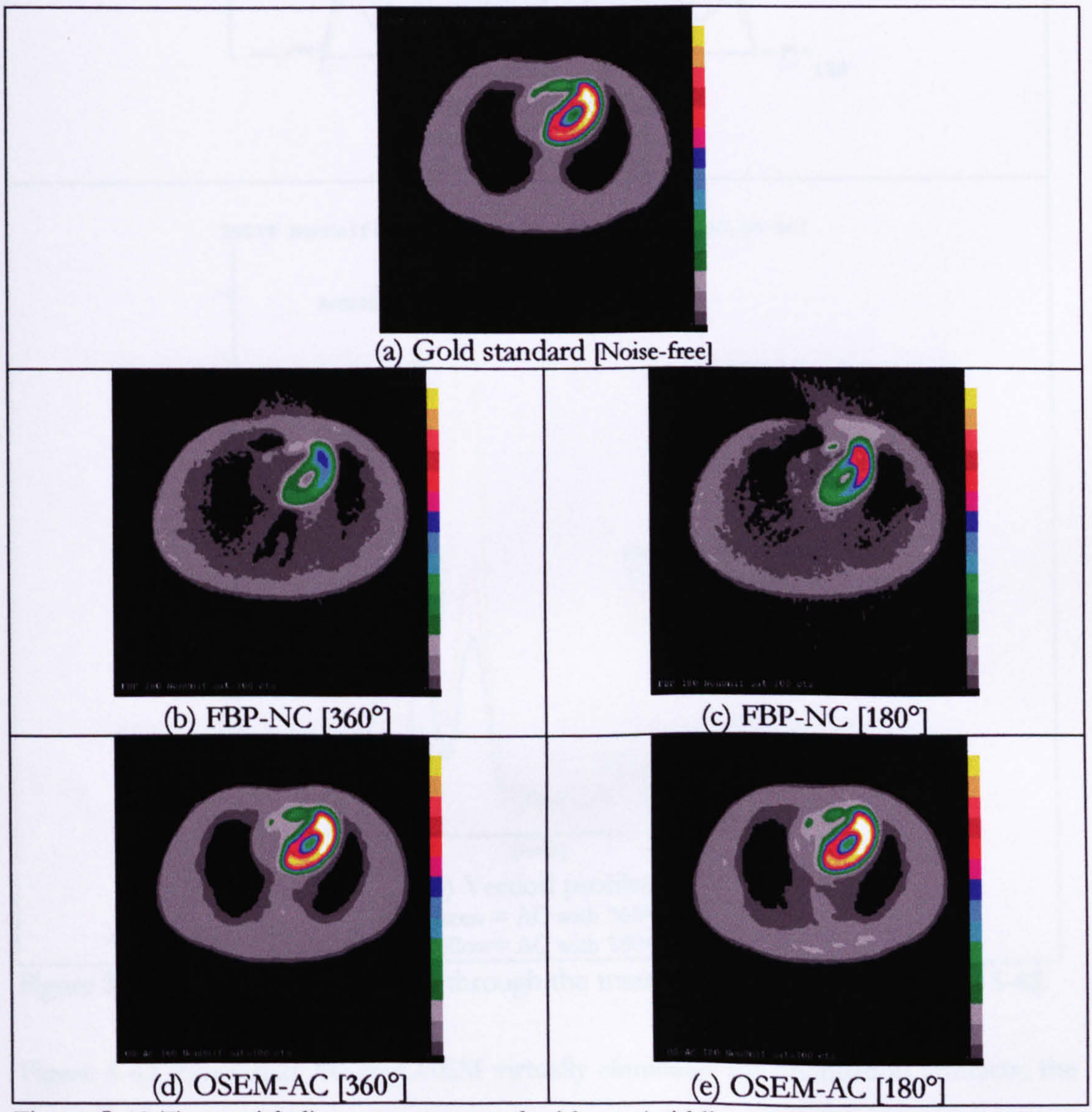

(a) Gold standard [Noise-free]

(b) FBP-NC [360°]

(c) FBP-NC [180°]

(d) OSEM-AC [360°]

(e) OSEM-AC [180°]

Figure 5-42 Transaxial slices reconstructed without (middle row) and with AC (bottom row) using two acquisition techniques; 360° (left) and 180° (right).

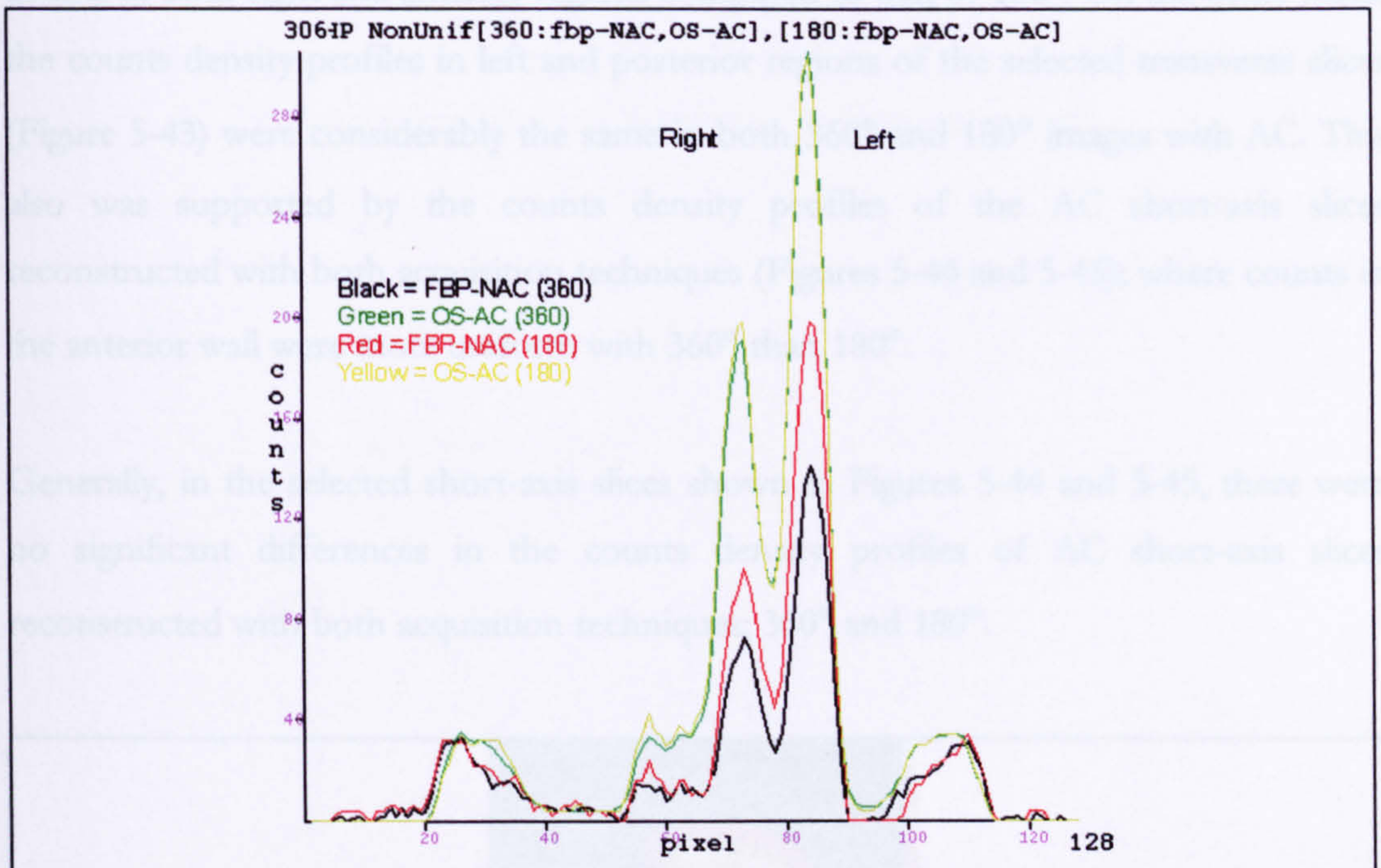

(a) Horizontal profiles
[Green = AC with 360°]
[Yellow = AC with 180°]

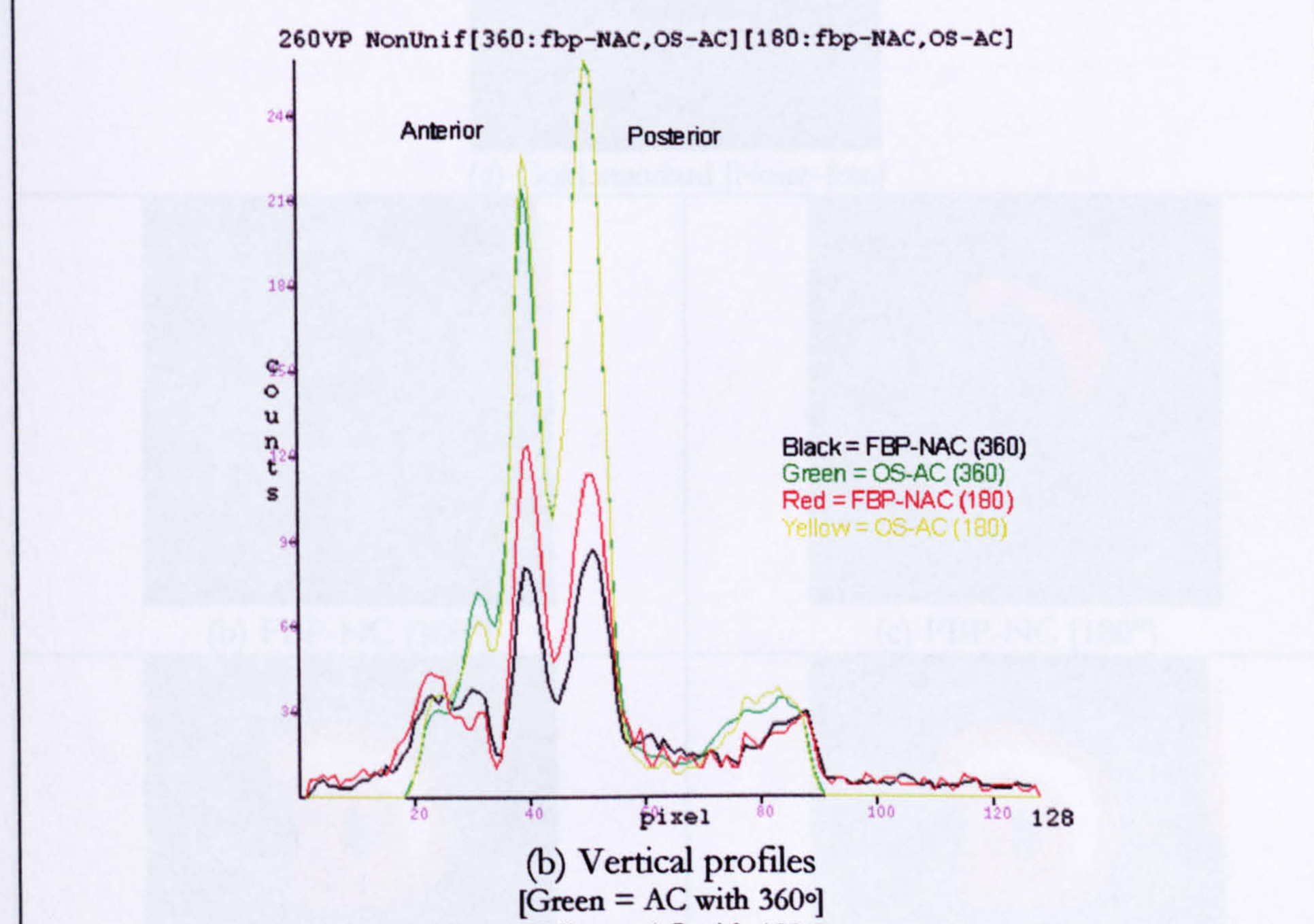

(b) Vertical profiles
[Green = AC with 360°]
[Yellow= AC with 180°]

Figure 5-43 Count Density profiles through the transaxial slices shown in Figure 5-42.

Figure 5-43 shows that AC by OSEM virtually eliminates the attenuation artefacts; the OSEM-AC reconstruction of the 360° acquisition seems to produce slightly better

counts in both right and anterior regions compared to that of 180°. On the other hand, the counts density profiles in left and posterior regions of the selected transverse slices (Figure 5-43) were considerably the same in both 360° and 180° images with AC. This also was supported by the counts density profiles of the AC short-axis slices reconstructed with both acquisition techniques (Figures 5-44 and 5-45); where counts in the anterior wall were more uniform with 360° than 180°.

Generally, in the selected short-axis slices shown in Figures 5-44 and 5-45, there were no significant differences in the counts density profiles of AC short-axis slices reconstructed with both acquisition techniques; 360° and 180°.

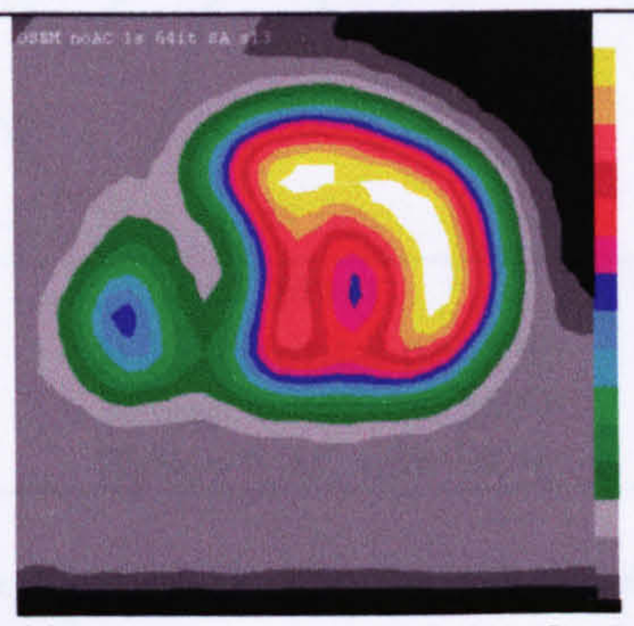

(a) Gold standard [Noise-free]

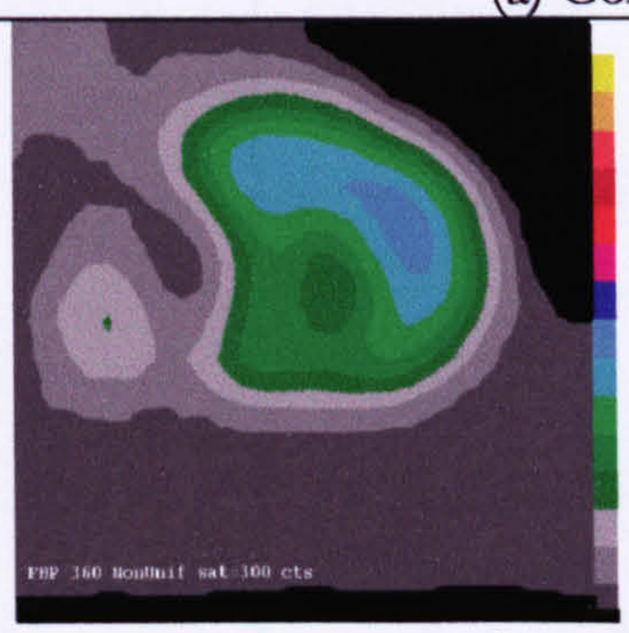

(b) FBP-NC [360°]

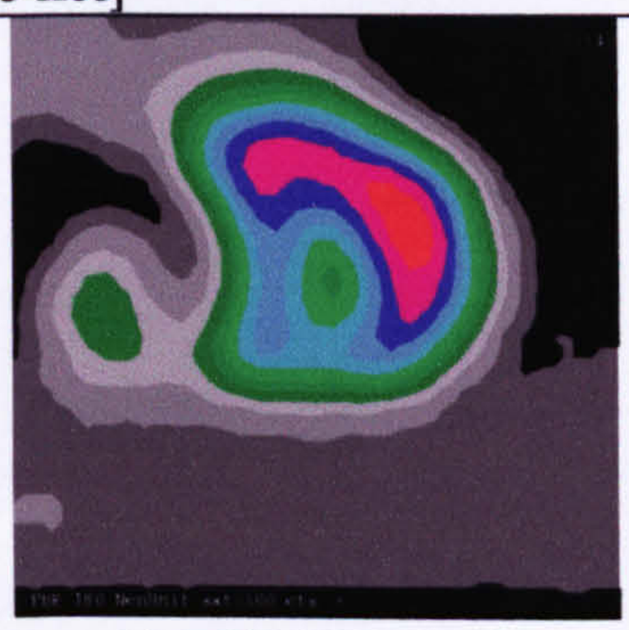

(c) FBP-NC [180°]

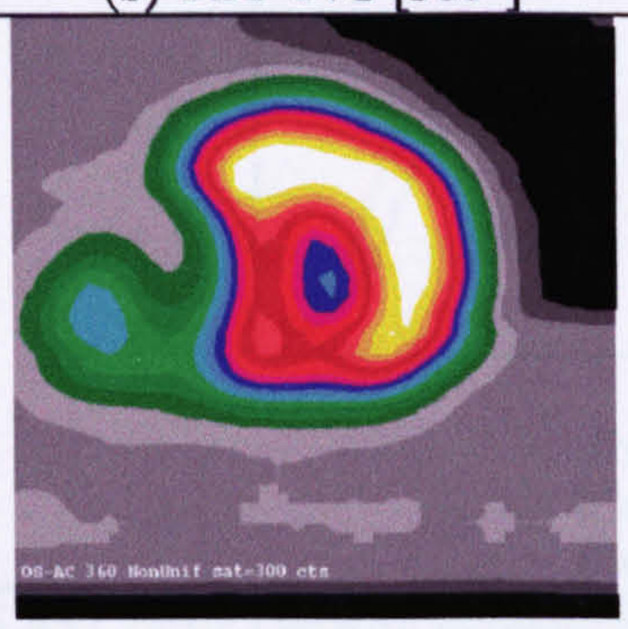

(d) OSEM-AC [360°]

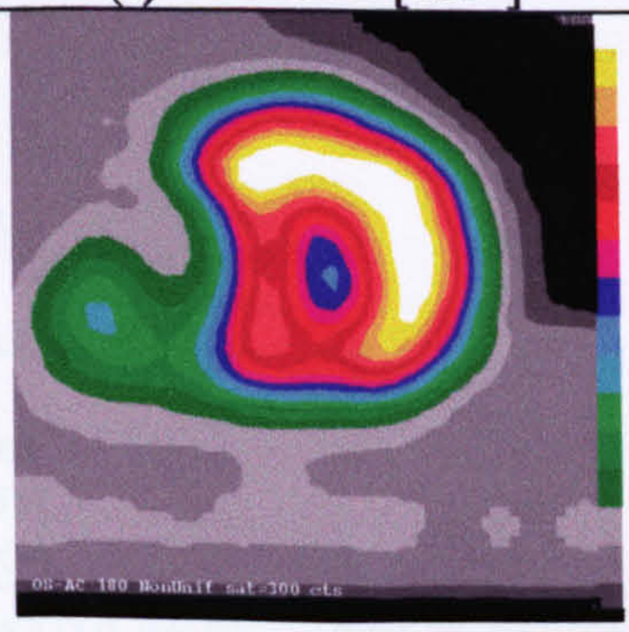

(e) OSEM-AC [180°]

Figure 5-44 Short-axis slices reconstructed without (middle row) and with AC (bottom row) using two acquisition techniques; 360° (left) and 180° (right).

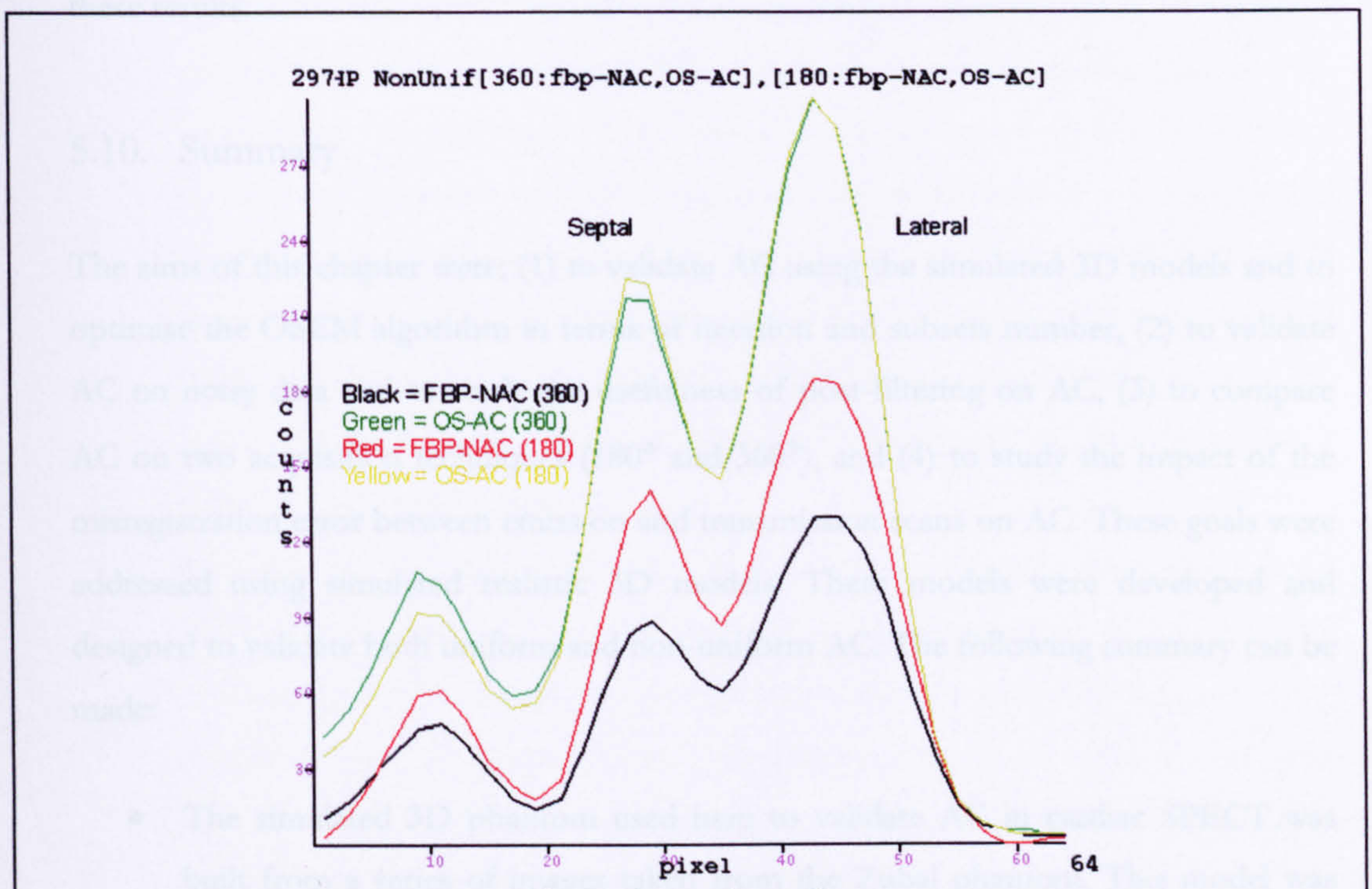

(a) Horizontal profiles
[Green = AC with 360°]
[Yellow= AC with 180°]

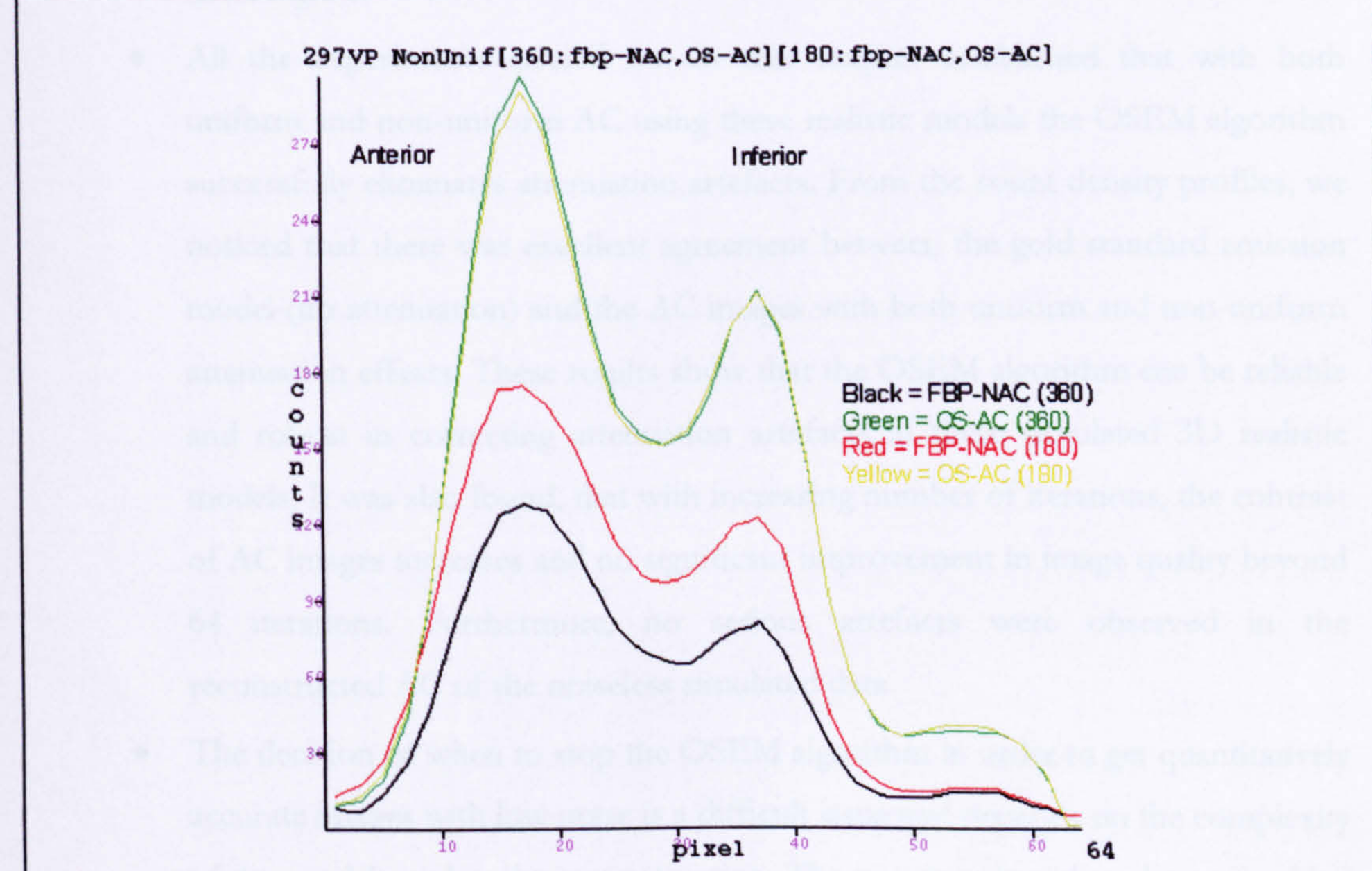

(b) Vertical profiles
[Green = AC with 360°]
[Yellow= AC with 180°]

Figure 5-45 Count Density profiles through the transaxial slices shown in Figure 5-44.

It is clear from the previous results that OSEM with AC corrects attenuation artefacts to an equivalent degree as shown in short-axis slices with both acquisition techniques

(180° and 360°). The counts density profiles in both Figures 5-43 and 5-45 confirm these results.

5.10. Summary

The aims of this chapter were; (1) to validate AC using the simulated 3D models and to optimise the OSEM algorithm in terms of iteration and subsets number, (2) to validate AC on noisy data and to study the usefulness of post-filtering on AC, (3) to compare AC on two acquisition techniques (180° and 360°), and (4) to study the impact of the misregistration error between emission and transmission scans on AC. These goals were addressed using simulated realistic 3D models. These models were developed and designed to validate both uniform and non-uniform AC. The following summary can be made:

- The simulated 3D phantom used here to validate AC in cardiac SPECT was built from a series of images taken from the Zubal phantom. This model was used to generate both the emission and transmission images from a male patient chest region.
- All the experiments carried out in this chapter established that with both uniform and non-uniform AC using these realistic models the OSEM algorithm successfully eliminates attenuation artefacts. From the count density profiles, we noticed that there was excellent agreement between the gold standard emission model (no attenuation) and the AC images with both uniform and non-uniform attenuation effects. These results show that the OSEM algorithm can be reliable and robust in correcting attenuation artefacts in these simulated 3D realistic models. It was also found, that with increasing number of iterations, the contrast of AC images increases and no significant improvement in image quality beyond 64 iterations. Furthermore, no serious artefacts were observed in the reconstructed AC of the noiseless simulated data.
- The decision of when to stop the OSEM algorithm in order to get quantitatively accurate images with low noise is a difficult issue and depends on the complexity of the model used in the reconstruction. The iterative algorithms have an added complication of finding where to stop the number of iterations, which may be a function of patient size and activity distribution near the area of interest [128].

Although, the minimum FRMSE was used to determine the optimal OSEM parameters (iterations and subsets), using FRMSE remains controversial as a criteria of stopping the reconstruction in these simulated studies. Meikle [129] found that the minimum mean square error was reached after a different number of iterations for three types of simulated tumours using MLEM algorithm. These results suggest that an optimal iteration number for OSEM cannot be chosen in advance, but rather must be selected on a case-by-case basis. This strongly suggests that the lack of a robust stopping rule is one of the major drawbacks of the iterative algorithm. The optimal number of iterations remains a matter of debate.

- In noisy data reconstructed with AC and without applying post-filtering, the FRMSE value showed that the iteration can be stopped at 1 subset and 8 iterations and if the iterations continued after that the FRMSE starts increasing (Figure 5-35). As expected, using post-filtering was shown to be a significant tool to reduce the buildup noise artefacts, and reduce the FRMSE significantly for the same number of iteration (Figure 5-36).
- In order to get accurate result; we should go for higher iterations and using post-filtering after that to control the buildup noise. This will give a chance to all structures of the image to be reconstructed completely, compared to if we stop the iteration early.
- Other experiments carried out in this chapter demonstrated that (a) there was a significant impact from misregistration errors between emission and transmission scans on AC, and (b) the OSEM algorithm was capable to correct non-uniform attenuation artefacts accurately in both 180° and 360° acquisition techniques.
- The simulation models did not perfectly model the clinical situation. In particular scatter was not modelled and the attenuation map contains no noise. Only a single male patient model was simulated and did not mimic the variability and complexity of the true patient. Wackers [88] believed that "Simulation is never close enough to real patient imaging to replace clinical testing in patient". However, the model simulating clinical realistic activity distribution and non-uniform attenuation map that was used in this chapter is a realistic anatomical model which we believe is adequate for validation purposes. During the next

few years, it is believed that such realistic models will become more widely available in clinical setting.

Although, validation of AC using realistic 3D phantom studies are important, they have to be followed by studies on patients to check the results are clinically relevant [120]. Validating and evaluating attenuation effects from clinical images or ordinary phantom studies is generally a difficult task since other artefacts may arise. Therefore, physical phantom and one patient (used for a demonstrative purpose) data will be used to evaluate AC in chapter 6.

Chapter Six Physical phantom and patient data

In this chapter, AC was evaluated using data obtained from both a physical phantom and one patient study, using a CT system to determine the attenuation distribution. The two reconstruction algorithms were evaluated: OSEM without AC and OSEM with AC. Filtered-back projection reconstruction algorithm were not considered for any of the reconstructions carried out in this chapter. The patient data consists of a high quality transmission image (attenuation map) and attenuated SPECT emission data of a male patient acquired using the multi-modality Hawkeye GE system. Also, an acquisition of an anthropomorphic cardiac phantom was performed using the Hawkeye GE system. The availability of this state-of-the-art multi-modality imaging system in addition to availability of the iterative reconstruction algorithm (OSEM) in the Medical Physics Department at the Royal Halamshire Hospital was a good opportunity to evaluate AC by scanning a physical phantom and using real clinical data.

In this chapter, two main experiments were carried out to demonstrate whether the OSEM-AC was effective and capable of correcting the attenuation effect of real patient data and a physical phantom. Firstly, AC was evaluated using a real patient data (section 6.2). Secondly, acquisition of data from a physical anthropomorphic phantom was performed for a comparison purposes (section 6.3). The physical phantom was borrowed from the Medical Physics Department at the Bradford Royal Infirmary.

6.1. Method

6.1.1 Patient study

Attenuated emission patient projection data and a CT transmission scan (attenuation map) were obtained from the GE Hawkeye system (gamma camera with CT system). The injected radiopharmaceutical was ^{99m}TC Tetrofosmin with a dose of 400 MBq. The attenuated planar images consist of 60 projections (30 seconds per projection) over 180° in 128×128 format and with 4.417 mm pixel size. Figure 6-1(a) shows only one lateral projection view. The CT scan consists of 128 axial slices in 128×128 format with 4.417 mm pixel size and 4.417 mm spacing between slices. Figure 6-1(b) shows only one slice of the CT slices. All the sixty attenuated emission projected data were reconstructed without and with AC by using the OSEM algorithm with one subset and different number of iterations. All the attenuation map slices were incorporated into the OSEM reconstruction algorithm and used for AC.

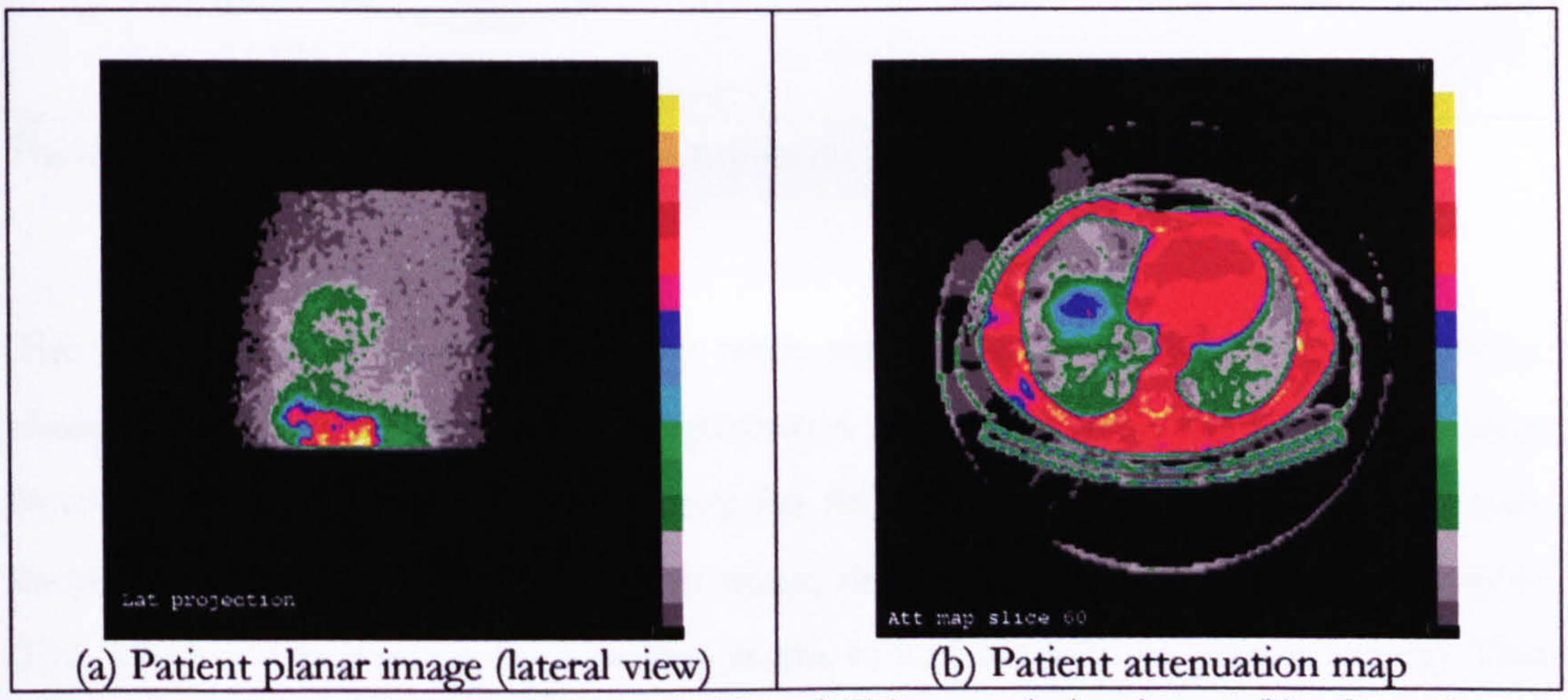

(a) Patient planar image (lateral view) (b) Patient attenuation map

Figure 6-1 Attenuated projection image (a) and CT transmission image (b) of a male patient.

6.1.2 Physical phantom

Attenuated correction of cardiac SPECT was also evaluated by reconstructing experimentally acquired data from an anthropomorphic phantom with cardiac insert (Data-Spectrum, Hillsborough, NC). The physical phantom used in this experiment is shown in Figure 6-2(a) and the cardiac insert is shown in Figure 6-2(b). This thorax phantom has a natural body contour and contains a cardiac insert, a Teflon spine, a liver, and lungs filled with Styrofoam beads. The side-to-side dimension of the phantom is 380 mm and front-to-back is 260 mm. This phantom provided a realistic physical

object for assessing cardiac image quality including the effects of non-uniform attenuation. Technetium ^{99m}Tc was distributed in the water of the myocardium, liver and background regions with a radioactivity of 45, 25, 15 MBq/l respectively. The heart/liver ratio was 1.8 (moderate liver activity). The heart insert consists of two compartments, the myocardium and the ventricle. The myocardium was filled with activity and the ventricle was filled with water (defect was not used).

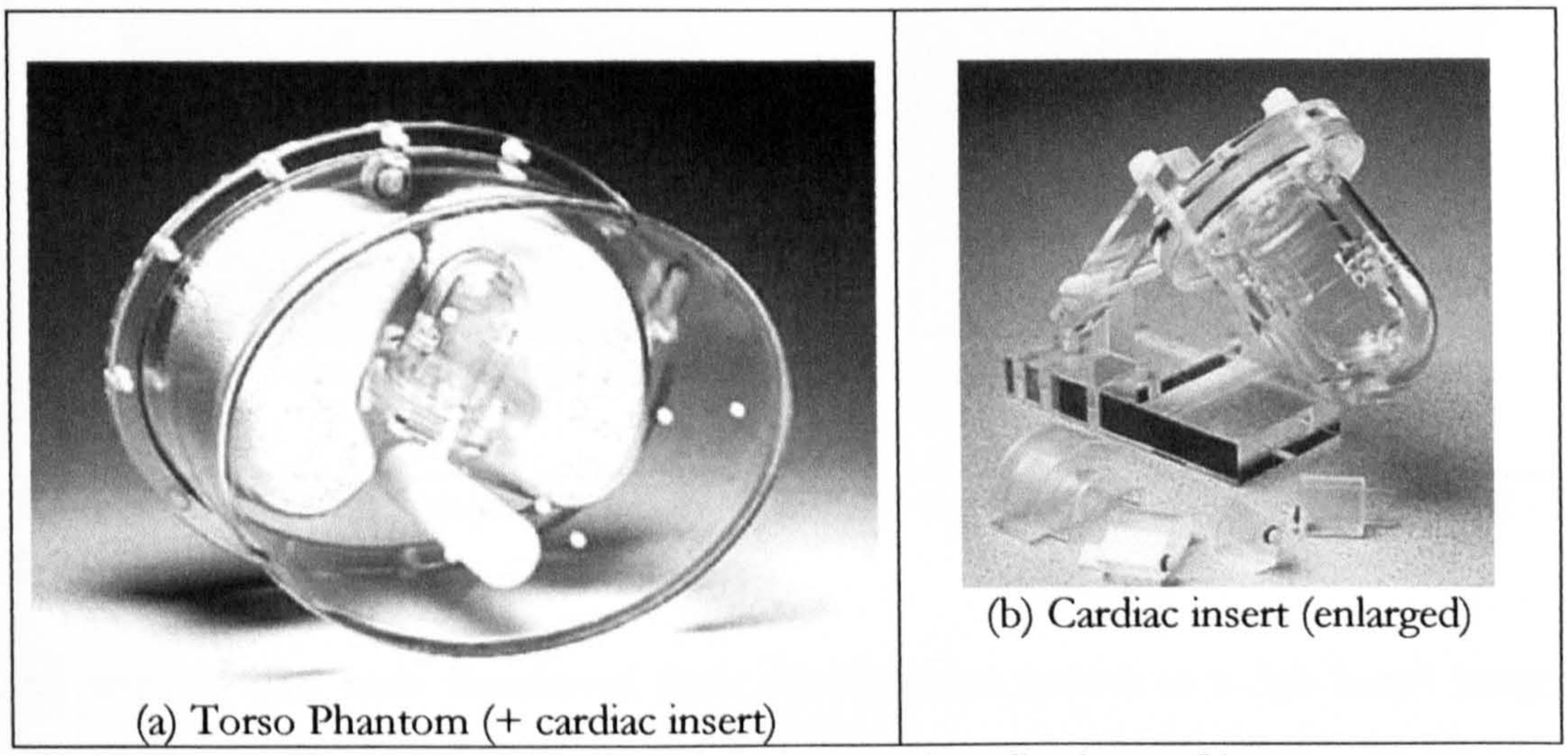

(a) Torso Phantom (+ cardiac insert)

(b) Cardiac insert (enlarged)

Figure 6-2 Anthropomorphic torso phantom (a) and cardiac insert (b).

The phantom was scanned using the same acquisition parameters used for routine clinical SPECT acquisition in our department. The non-uniformity attenuation map (one slice) of the physical phantom used for AC is shown in Figure 6-3(b). The body section of the phantom was filled with water, despite the transverse slice on Figure 6-3(b), which shows that the body section seems to be filled with air (or was empty). This was due to the fact that the transverse slice image is displayed with a saturation level selected to be 200 as the maximum level of the colour scale. This saturation level value was selected in order to show the position of the cardiac insert inside the phantom. SPECT projection data were collected in 128×128 matrices (pixel size = 4.417 mm) using two general-purpose parallel-hole collimators. A total of 60 projections (30 seconds per projection) were acquired over 180° and the number of detector bins was 128 (pixel size = 4.417 mm). One projection view of the torso phantom is shown in Figure 6-3(a).

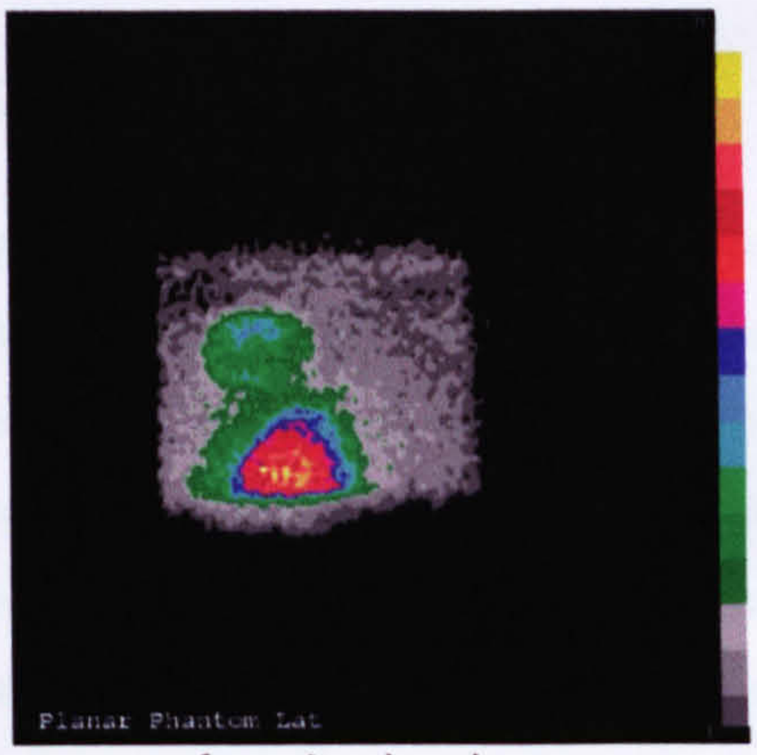

(a) Attenuated projection image [lateral view]

(b) Attenuation map [transaxial slice]
Saturation level selected to be 200 as the maximum level of the colour scale

Figure 6-3 Attenuated projection image (a) and CT transmission image (b) of physical phantom.

All acquired data were transferred from the Hawkeye system to a Sun based image processing system (Sun Solaris version 3.6) for processing and handling. The analysis and quantification were carried out using Link software (Link Medical MAPS 10000, version 5.4). The iterative reconstruction program (OSEM version 5.201) by Larkin [36] was installed on to the Unix-system.

The planar data were reconstructed using OSEM reconstruction with a subset size of 1 and different numbers of iterations (1, 2, 4, 8, 16, 32, 64 and 128) without and with correction for attenuation effect. The AC was evaluated by comparing the images reconstructed by using OSEM-AC with the images reconstructed from OSEM-NC (no AC). The OSEM reconstruction of the projection images produces transaxial images, which were reoriented into short-axis images. One transaxial slice and one short-axis image were selected for qualitative and quantitative analysis. In addition, multiple short--axis images that cover the entire myocardium, and the bull's-eye images were used in the next evaluation studies.

All images were quantitatively compared using counts density profiles (horizontal and vertical one pixel thick profiles) and the measured mean counts in 4 regions of interest (ROIs). Four ROIs were drawn over the selected short-axis slice to obtain the mean counts in anterior, septal, inferior, and lateral walls of left ventricle. As the original

activity is unknown, the AC images were compared to the NC images only (not to a reference image).

6.2. Patient study

Figure 6-4 shows the reconstructed transaxial slices without (Figure 6-4(a)) and with AC (Figure 6-4(b)) using OSEM algorithm (one subset) for different number of iterations. The visual evaluation of all images (without and with AC) demonstrates that as the number of iterations increases, the contrast increases and the image become noisier. The noise becomes more visible as the number of iterations increases especially for the results beyond 64 iterations. The best attenuation corrected image was obtained with 32 iterations. At low number of iterations (1, 2, 4, and 8), the attenuation artefacts were not completely corrected.

It was found that attenuation leads to areas of decreased counts in anterior-septal and inferior wall in the short-axis images shown in Figure 6-5(a-6). As it can be seen in Figure 6-5 (b-6), the AC images show improved counts in all LV walls except part of inferior wall. Also, it was found that as the number of iterations increases beyond 32 iterations, the noise increases. The noise was increasing with higher number of iterations for both NC and AC images (Figure 6-5(a-b)). Therefore, for the patient data included here, the reconstructed images after 32 iterations were chosen as an optimum solution that had good resolution with an acceptable noise level. By qualitative assessment of all AC images shown in both Figure 6-4(b) and 6-5(b), it is recommended that we should go to more iteration (32 iterations) to get a corrected image for attenuation artefacts and then the issue of building up noise can be resolved by applying post-filtering with high number of iterations (Post-filtering was not applied in this chapter, but the simulation data presented in Chapter 5 showed this effect clearly). The issue of stopping the iteration early might be one of the explanations of why AC does not receive widespread acceptance in routine clinical practice.

In addition, counts density profiles of these selected transaxial and short-axis slices, which were reconstructed with OSEM (32 iterations), are shown in both Figure 6-7 and Figure 6-8.

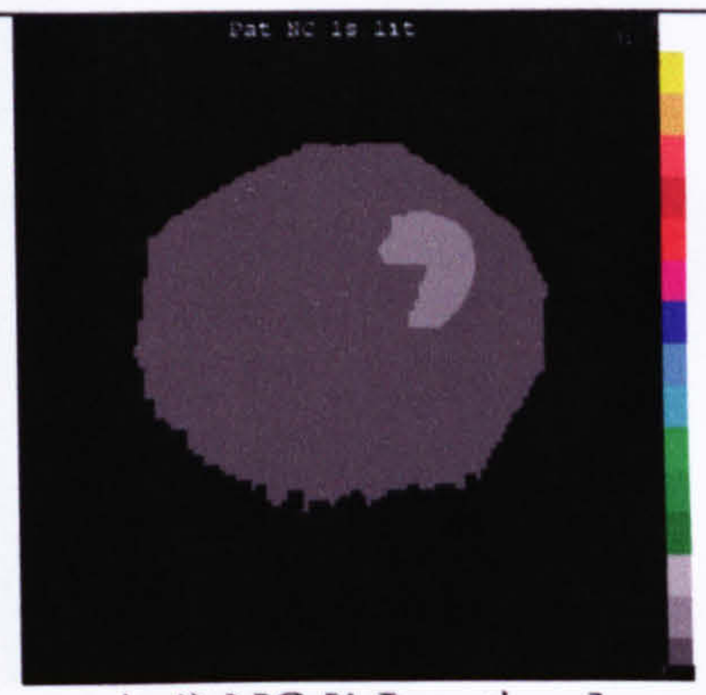

(a-1) NC [1 Iterations]

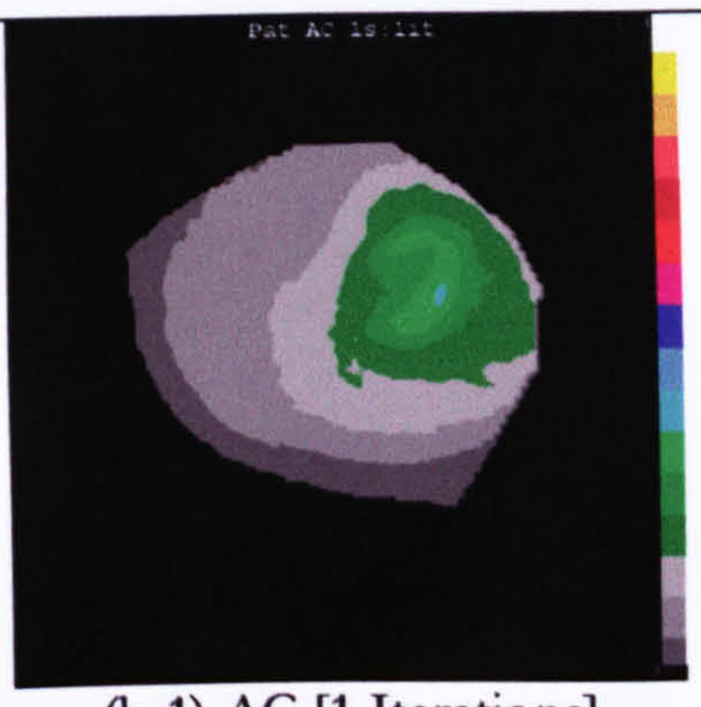

(b-1) AC [1 Iterations]

(a-2) NC [2 Iterations]

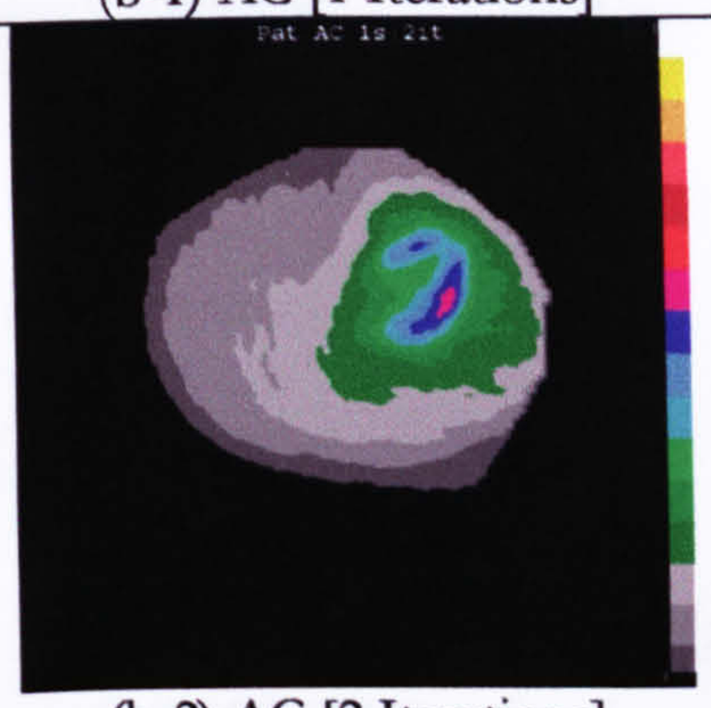

(b-2) AC [2 Iterations]

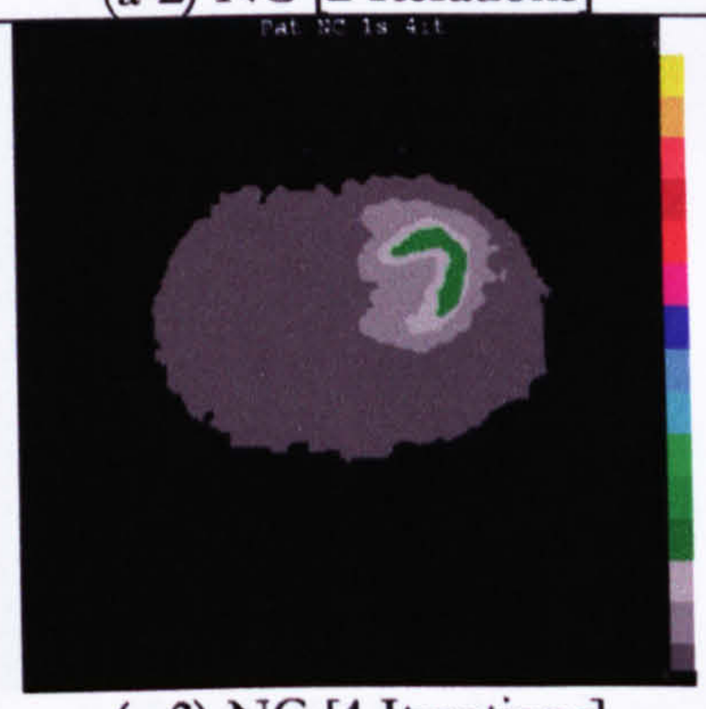

(a-3) NC [4 Iterations]

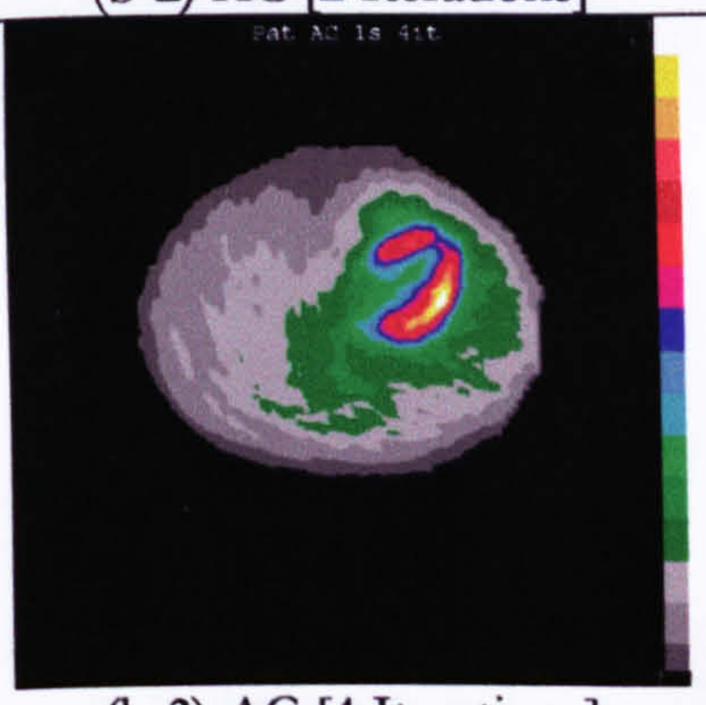

(b-3) AC [4 Iterations]

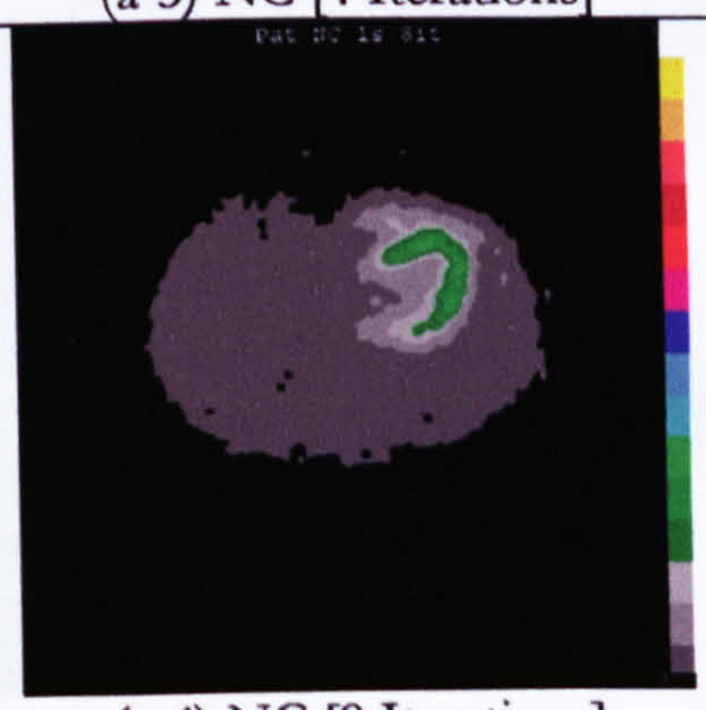

(a-4) NC [8 Iterations]

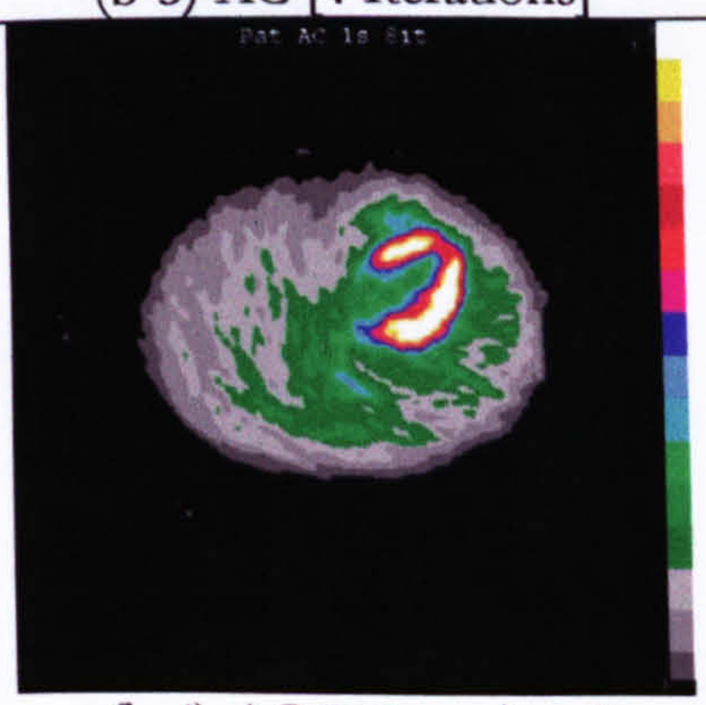

(b-4) AC [8 Iterations]

[The legend of these images is continued in next page]

(a-5) NC [16 Iterations]

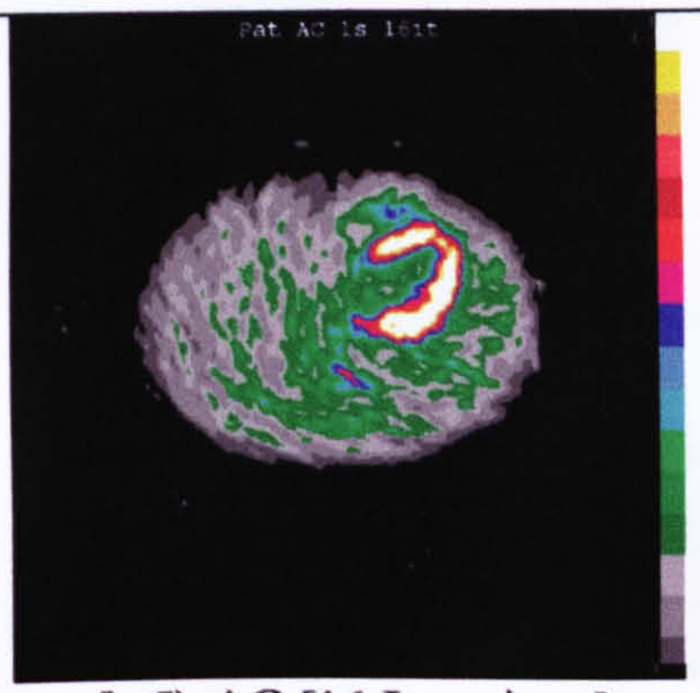

(b-5) AC [16 Iterations]

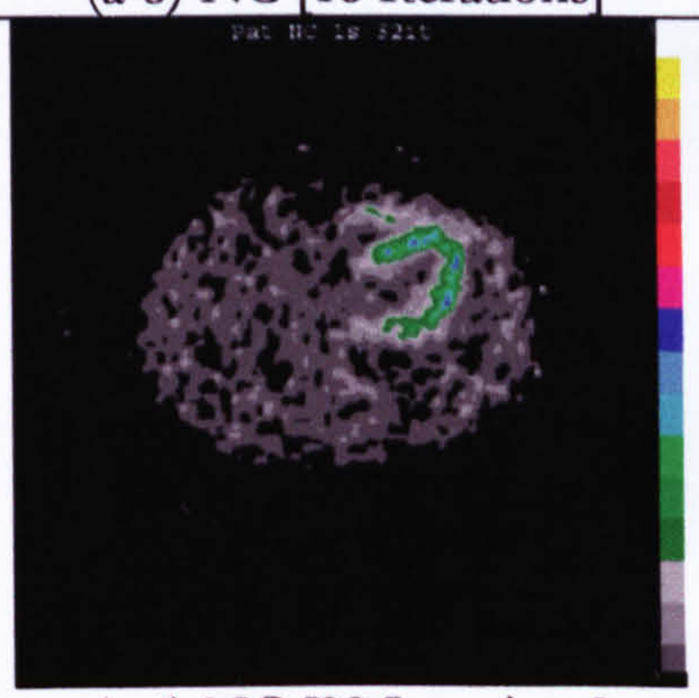

(a-6) NC [32 Iterations]

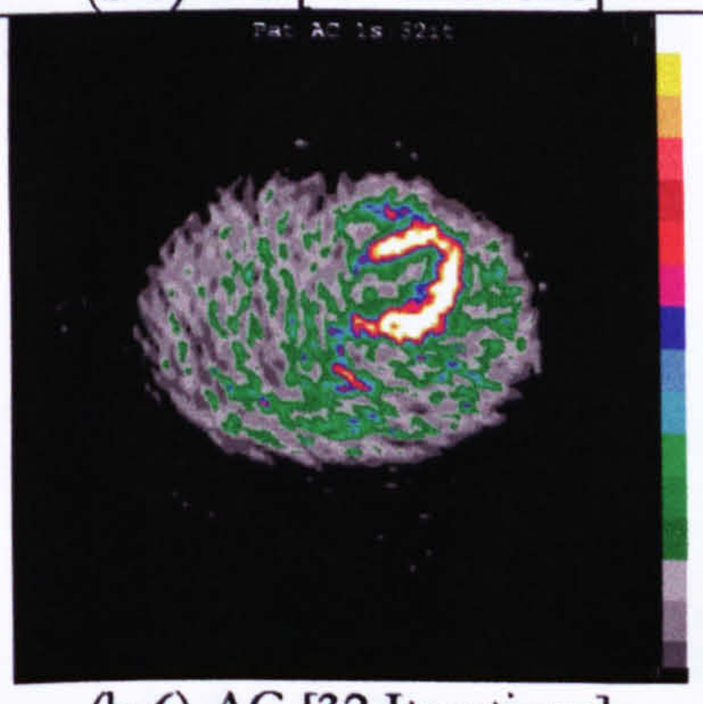

(b-6) AC [32 Iterations]

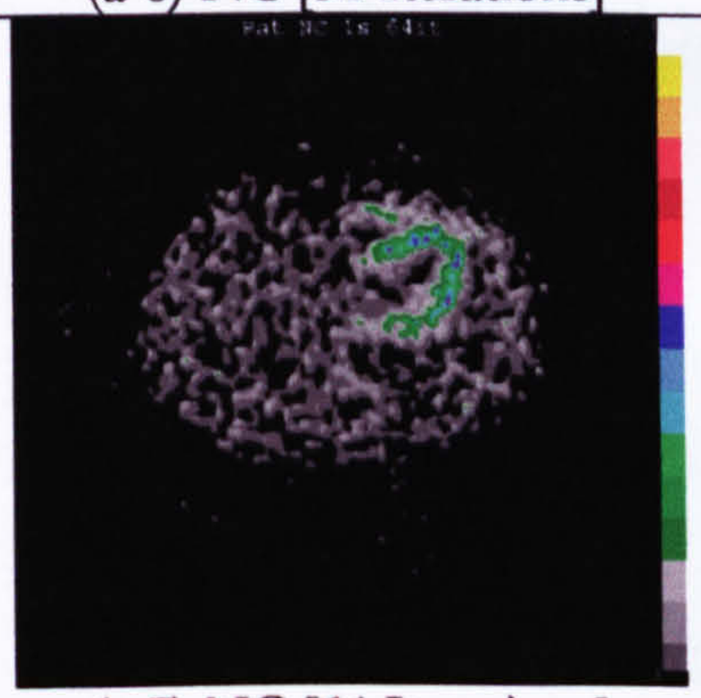

(a-7) NC [64 Iterations]

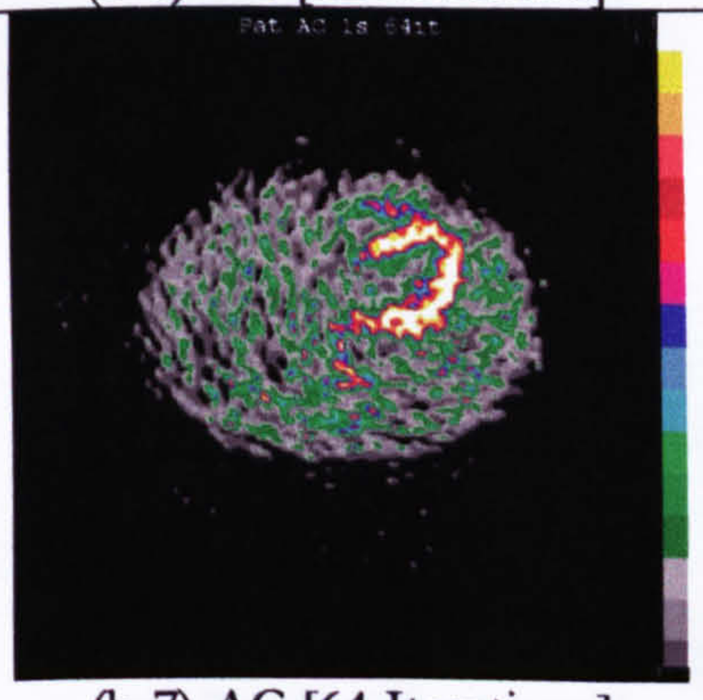

(b-7) AC [64 Iterations]

(a-8) NC [128 Iterations]

[NC = without AC, AC = with AC]

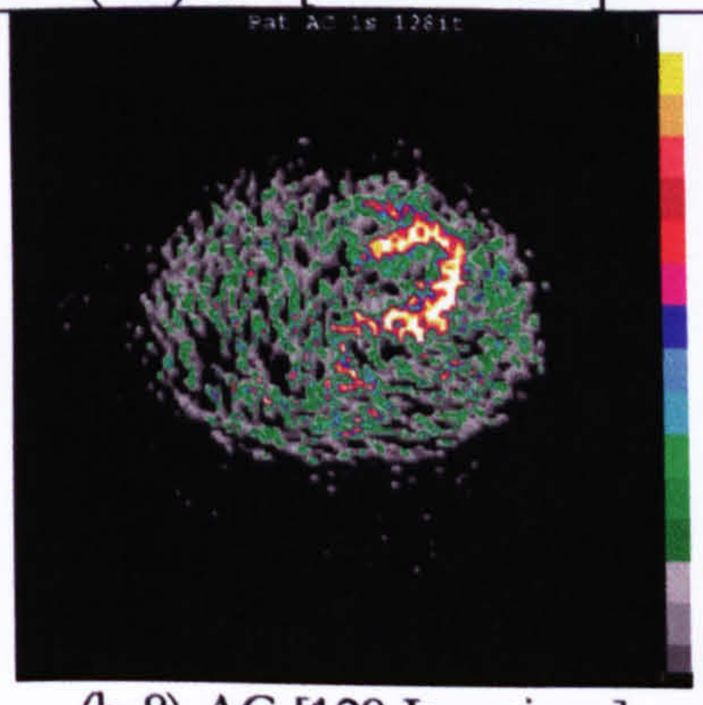

(b-8) AC [128 Iterations]

All images are 128×128

Saturation level selected to be 320 counts as the maximum level of the colour scale in all images

Figure 6-4 Reconstructed transaxial slices from patient study using the OSEM algorithm without AC (a) and with AC (b) (with 1 subset and different numbers of iterations).

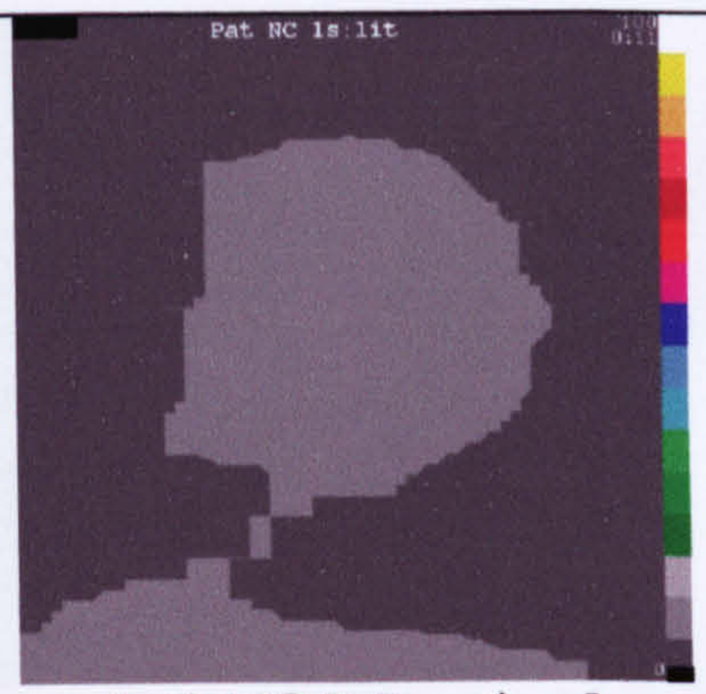

(a-1) NC [1 Iterations]

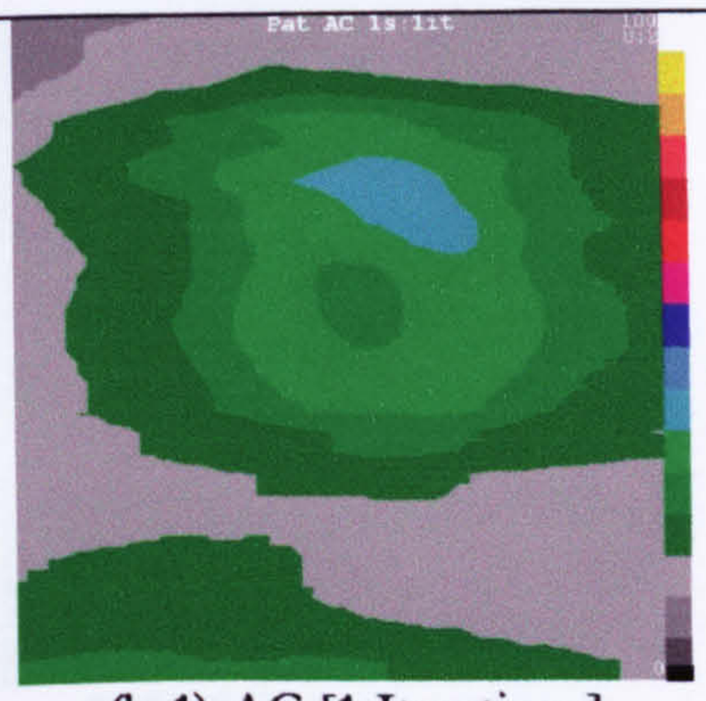

(b-1) AC [1 Iterations]

(a-2) NC [2 Iterations]

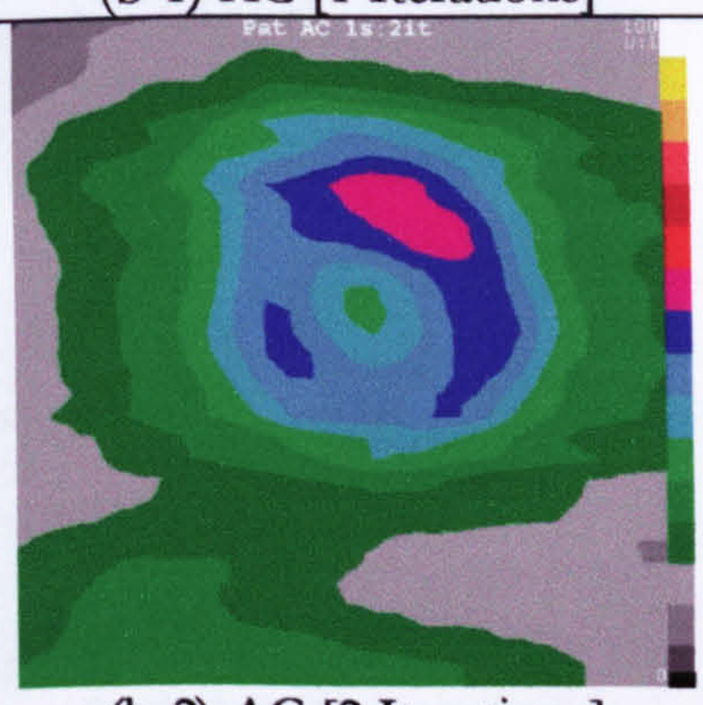

(b-2) AC [2 Iterations]

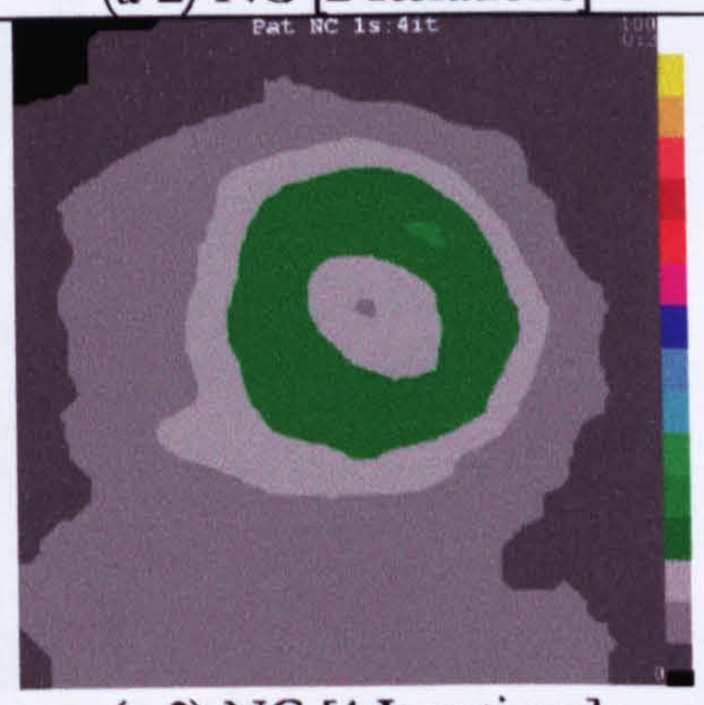

(a-3) NC [4 Iterations]

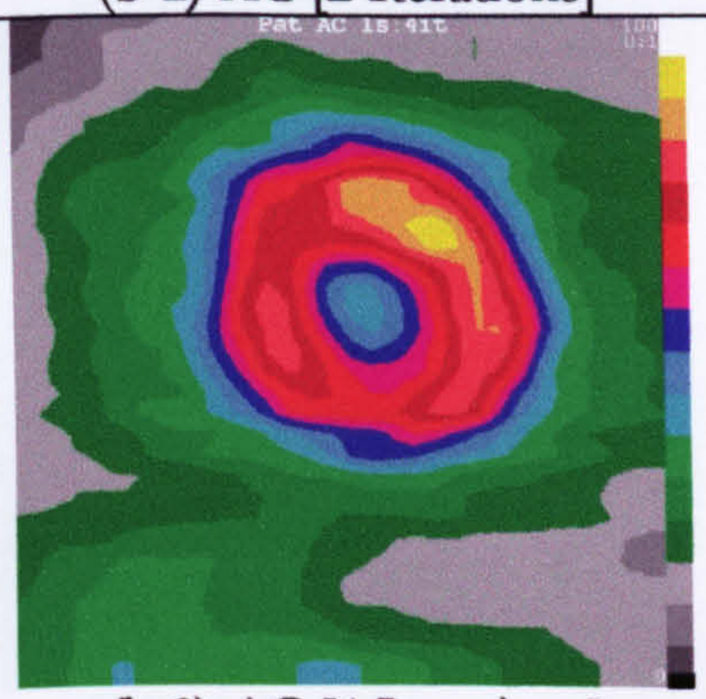

(b-3) AC [4 Iterations]

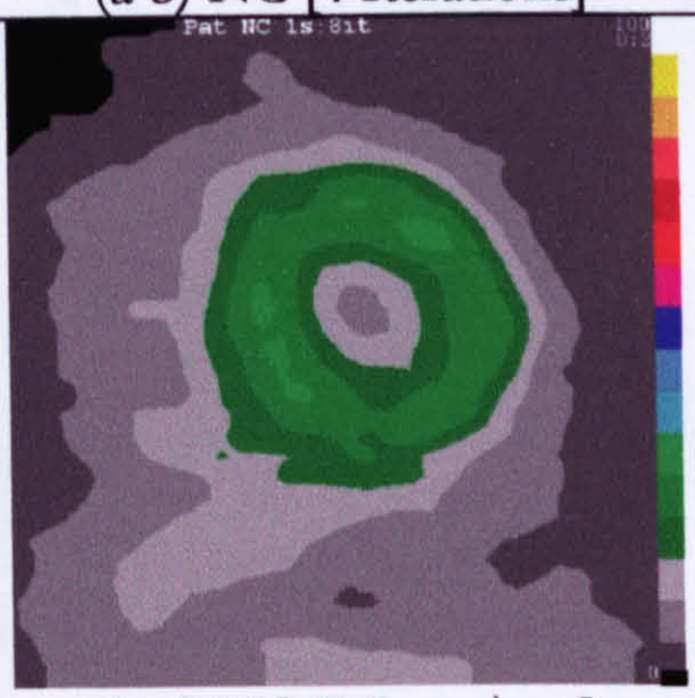

(a-4) NC [8 Iterations]

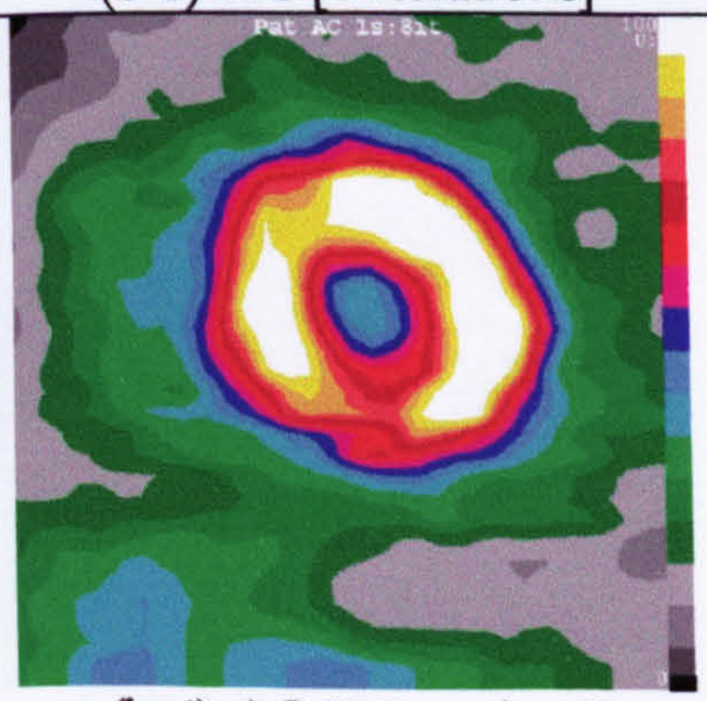

(b-4) AC [8 Iterations]

[The legend of these images is continued in next page]

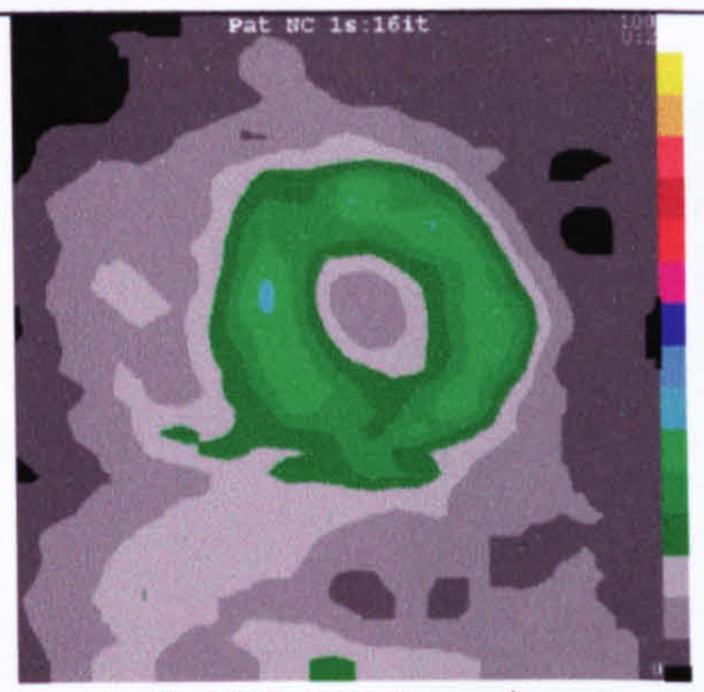

(a-5) NC [16 Iterations

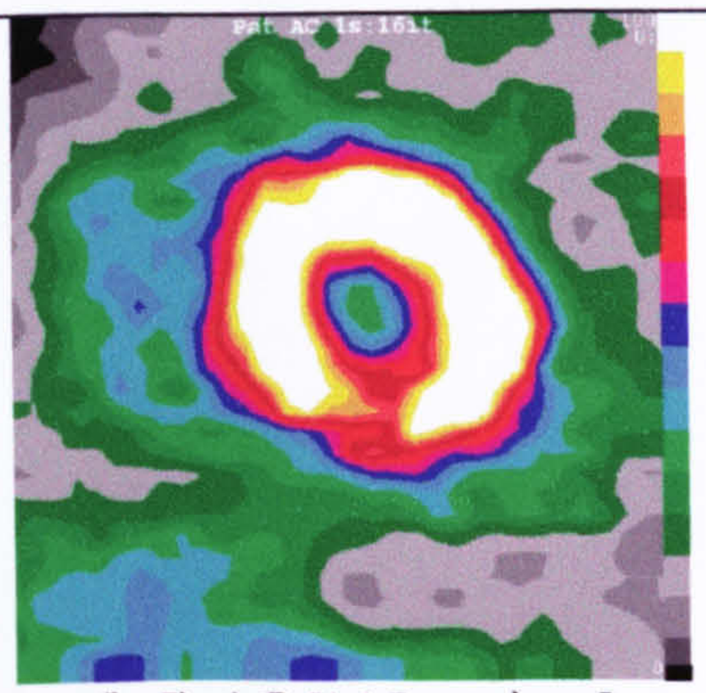

(b-5) AC [16 Iterations

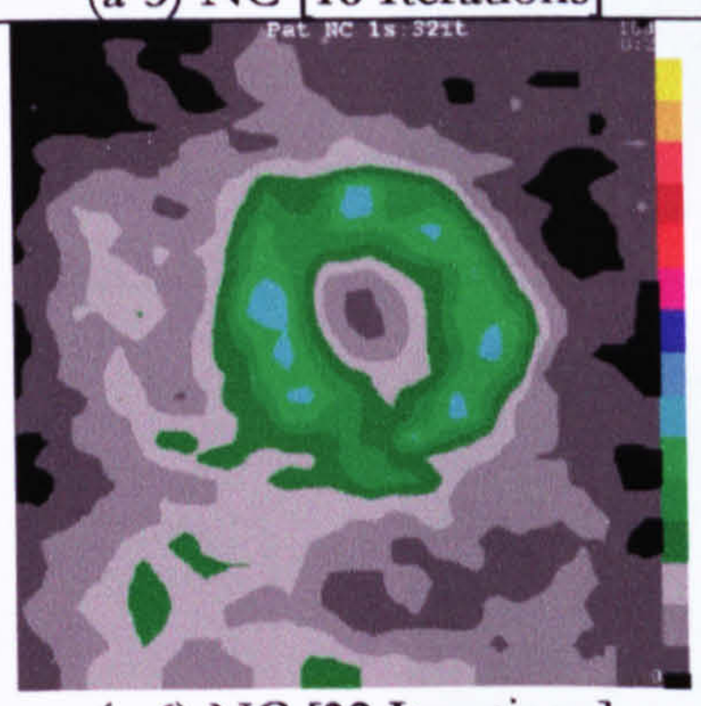

(a-6) NC [32 Iterations

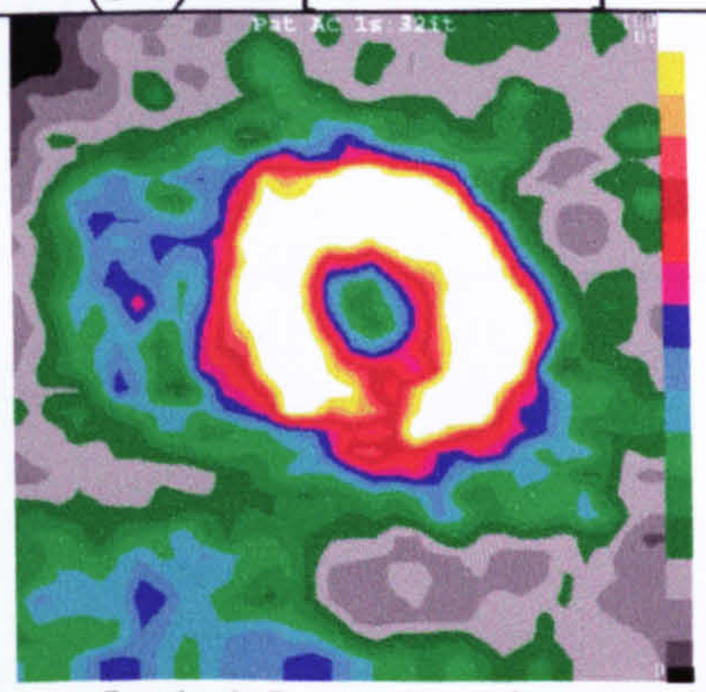

(b-6) AC [32 Iterations

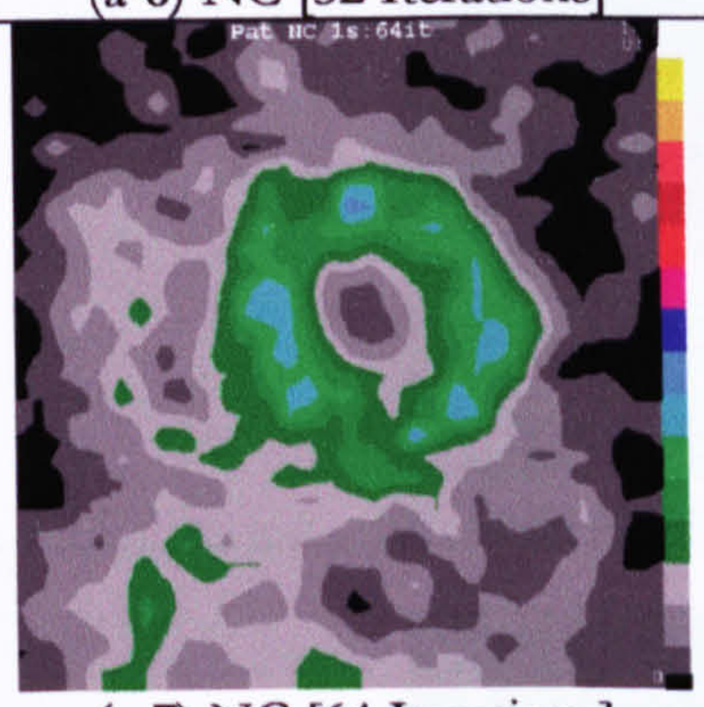

(a-7) NC [64 Iterations

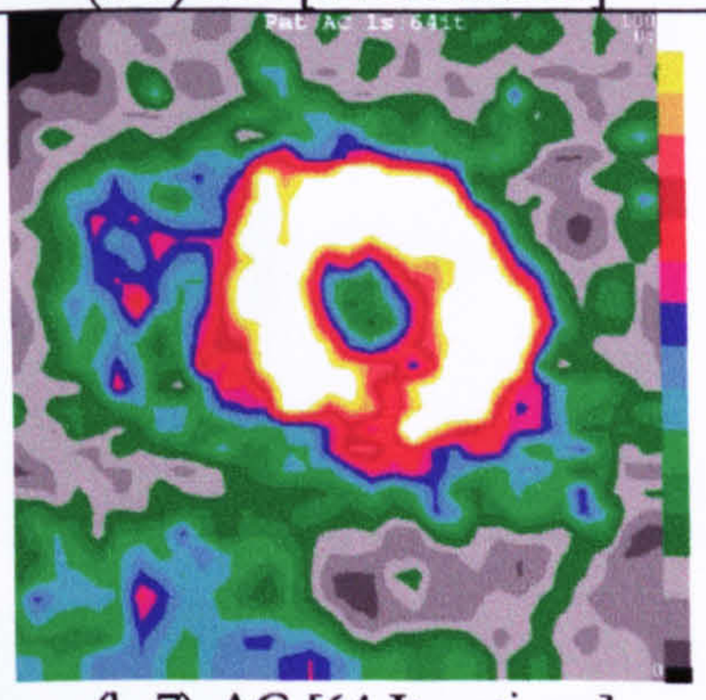

(b-7) AC [64 Iterations

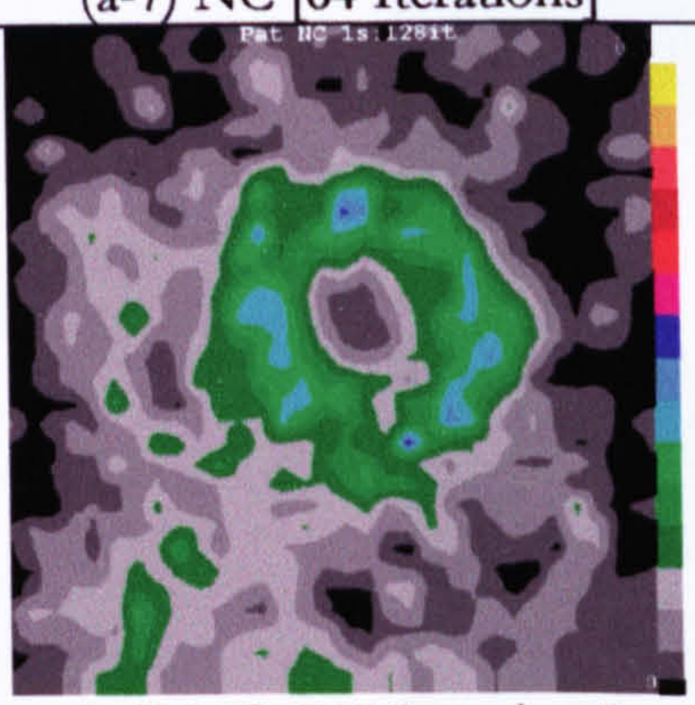

(a-8) NC [128 Iterations]

[NC = without AC, AC = with AC]

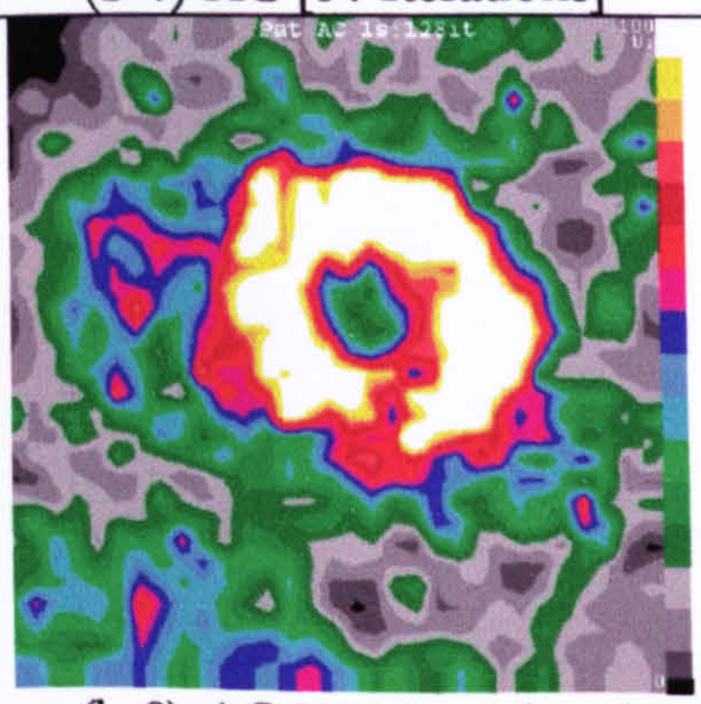

(b-8) AC [128 Iterations]

All images are 64×64

Saturation level selected to be 320 counts as the maximum level of the colour scale in all images

Figure 6-5 Reconstructed short-axis slices from patient study using the OSEM algorithm without AC (a) and with AC (b) (with 1 subset and different numbers of iterations).

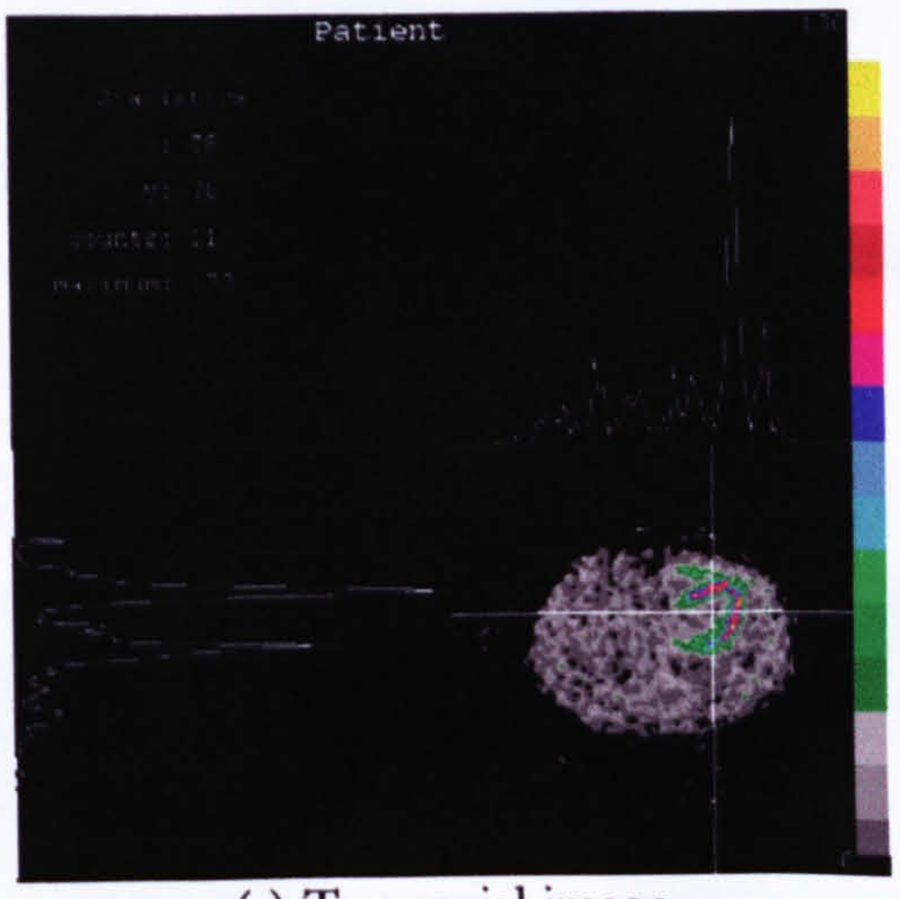

(a) Transaxial image

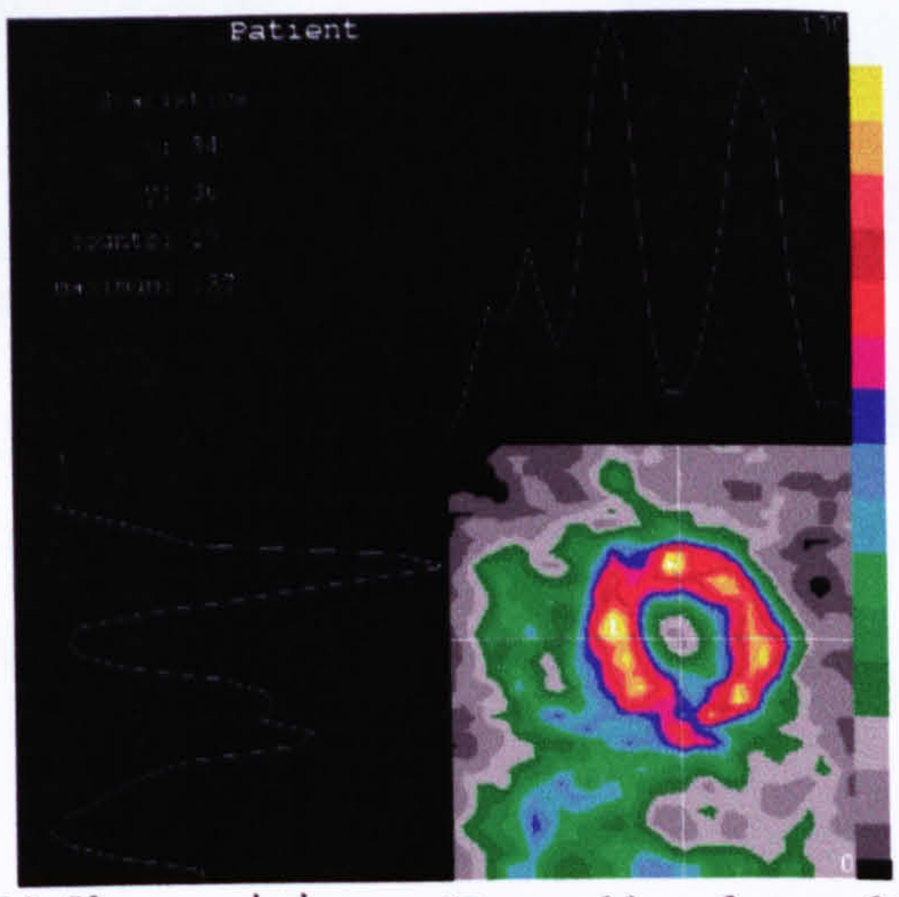

(b) Short-axis image [Zoomed by a factor of 2]

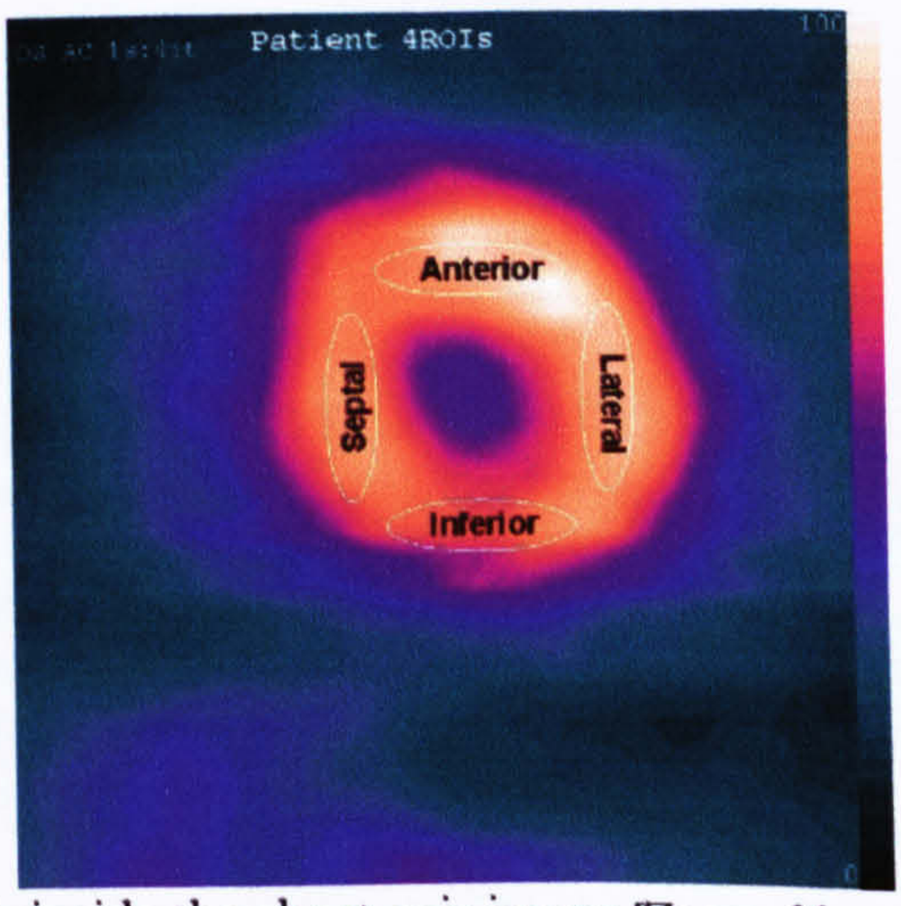

(c) 4ROIs inside the short-axis image [Zoomed by a factor of 2]

Figure 6-6 (a) and (b) demonstrate the position of the counts density profiles (horizontal and vertical) for the transaxial image (a) and short-axis image (b) of patient data. The positioning of the 4ROIs inside the short-axis image is shown in (c).

Figure 6-7 shows transaxial slices and count density profiles of these slices. These show that the attenuation artefacts were corrected in all regions of LV (anterior, left, posterior, and right) except a small part at the apex of the LV. On the other hand, the profiles of short-axis slices with AC (Figure 6-8) showed that attenuation artefacts were corrected in all LV regions with some artefacts remaining at inferior wall. The artefacts shown in inferior wall was due to a real defect (Figure 6-9 (c-d)).

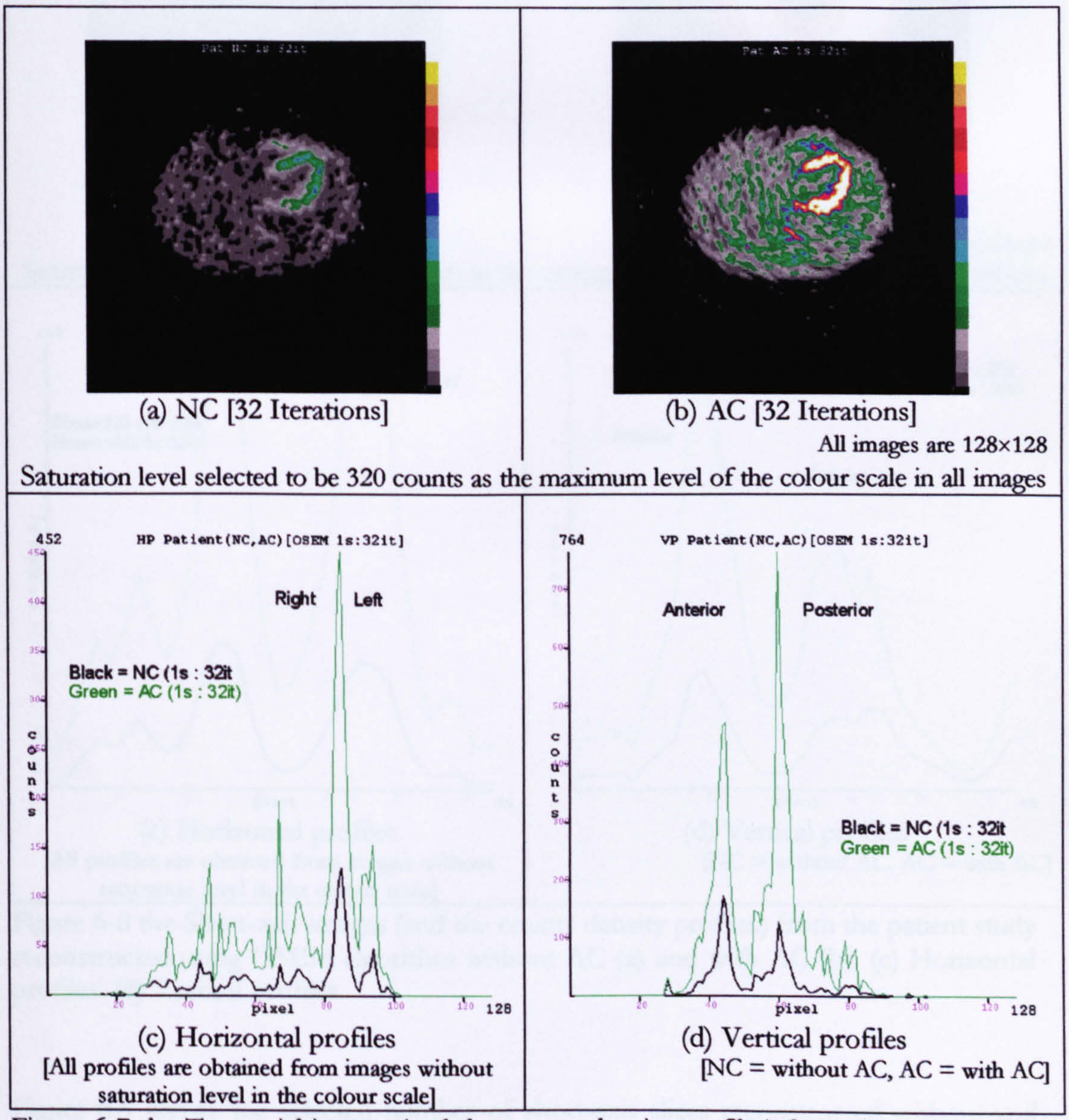

Figure 6-7 the Transaxial images (and the counts density profiles) from the patient data reconstructed using OSEM algorithm without AC (a) and with AC (b). (c) Horizontal profiles. (d) Vertical profiles.

According to the vertical counts density profiles of short-axis slices reconstructed with AC (green curve) shown in Figure 6-8(c-d), OSEM was correcting the counts density to a level mostly equal in all LV walls (anterior, septal, and lateral) with low non-uniform

counts density peak representing inferior wall (Figure 6-8(d)). This might be due to new artefacts being generated by the AC algorithm or a real defect (Figure 6-9 (c-d)).

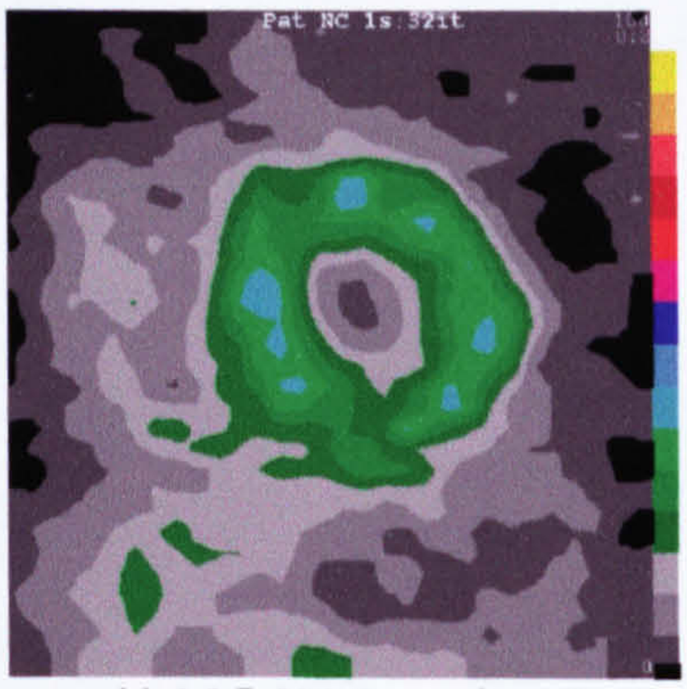

(a) NC [32 Iterations]

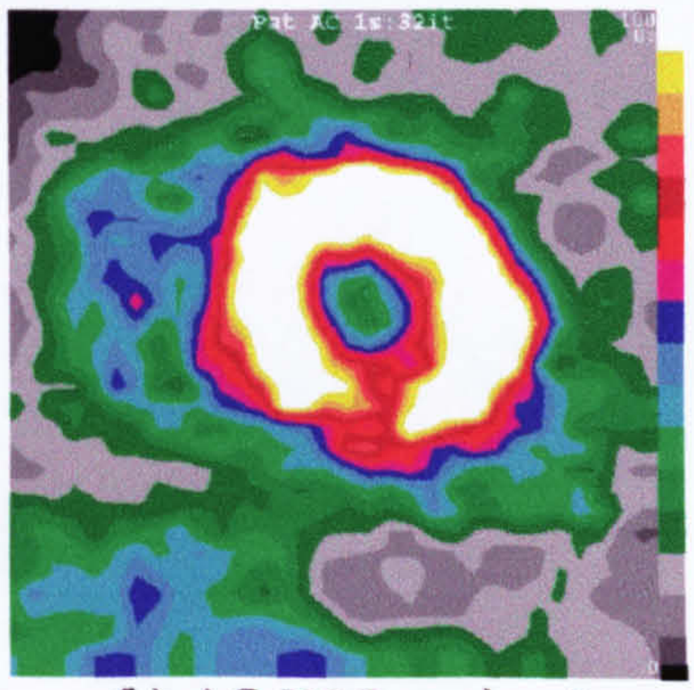

(b) AC [32 Iterations]

All images are 64×64

Saturation level selected to be 320 counts as the maximum level of the colour scale in all images

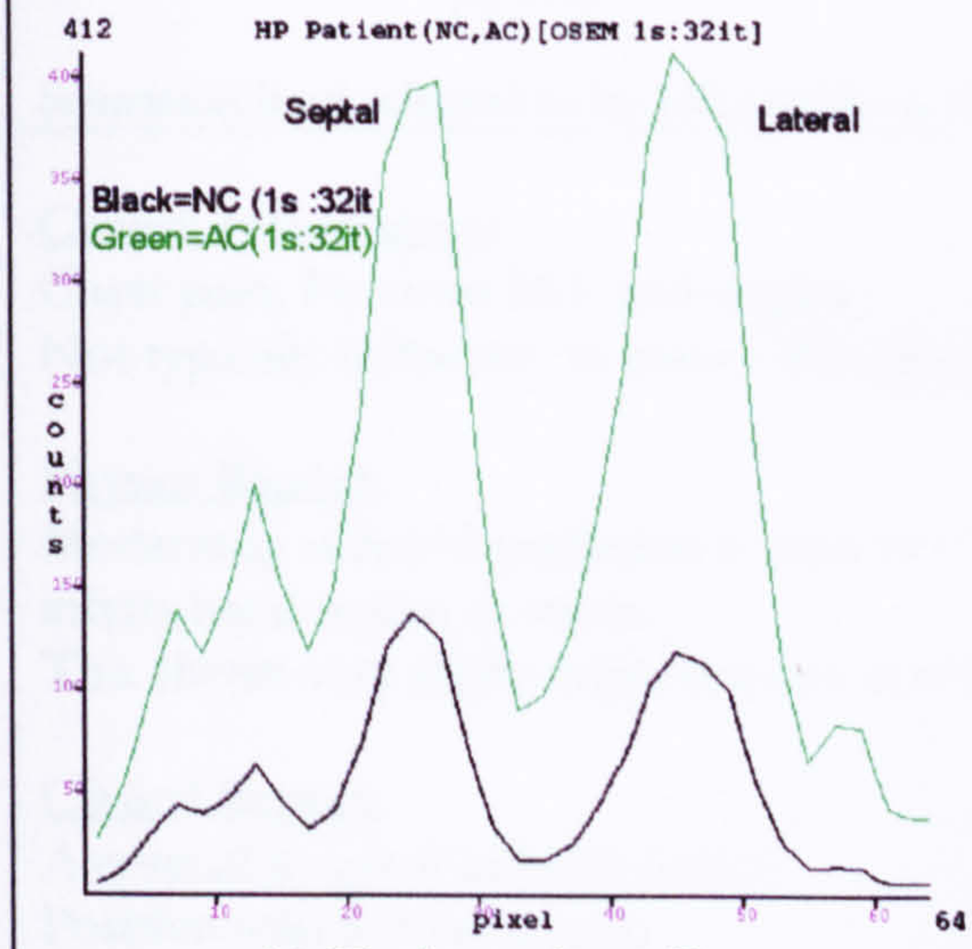

(c) Horizontal profiles

[All profiles are obtained from images without saturation level in the colour scale]

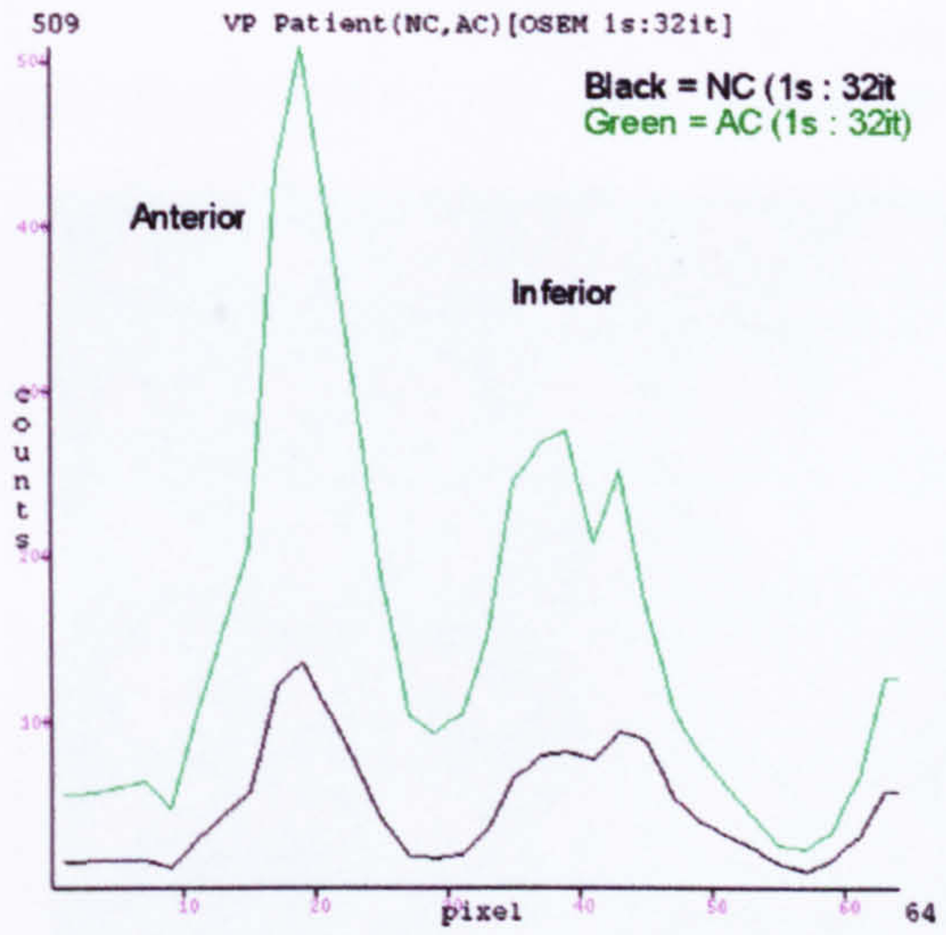

(d) Vertical profiles

[NC = without AC, AC = with AC]

Figure 6-8 the Short-axis images (and the counts density profiles) from the patient study reconstructed using OSEM algorithm without AC (a) and with AC (b). (c) Horizontal profiles. (d) Vertical profiles.

Figure 6-9 shows the selected number of short-axis slices reconstructed without and with AC (using 1 subset and 32 iterations). As can be seen from Figure 6-9, the attenuation artefacts were not corrected in inferior region and part of septal region of LV. This might be due to a true defect or under-correction of counts at these regions. On the other hand, the improvement of counts at anterior and lateral walls with AC compared to NC slices indicates that attenuation artefacts were corrected in these regions. This finding also can be seen in Figure 6-10 (b).

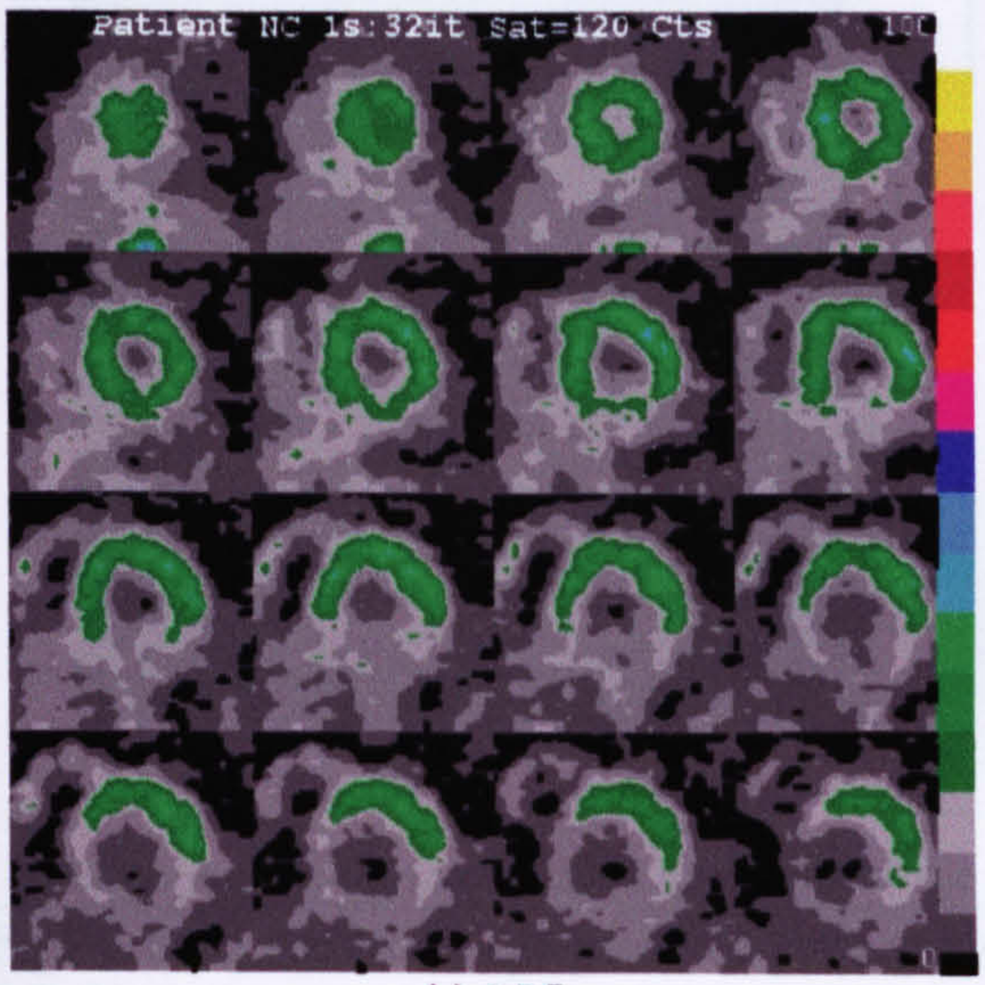

(a) NC (b) AC

[NC = without AC, AC = with AC]

Saturation level selected to be 120 counts as the maximum level of the colour scale in all images

Clinical Information:
Chest pain, Previous M.I. and angina
Not typically ischaemic in nature this time.

Physics Report:
Moderately reduced perfusion is seen in the infero-basal region at stress.
This shows very slight improvement at rest.

Clinical Report:
A reversible apical-inferior lesion.
Positive scan for ischaemia.

(C)

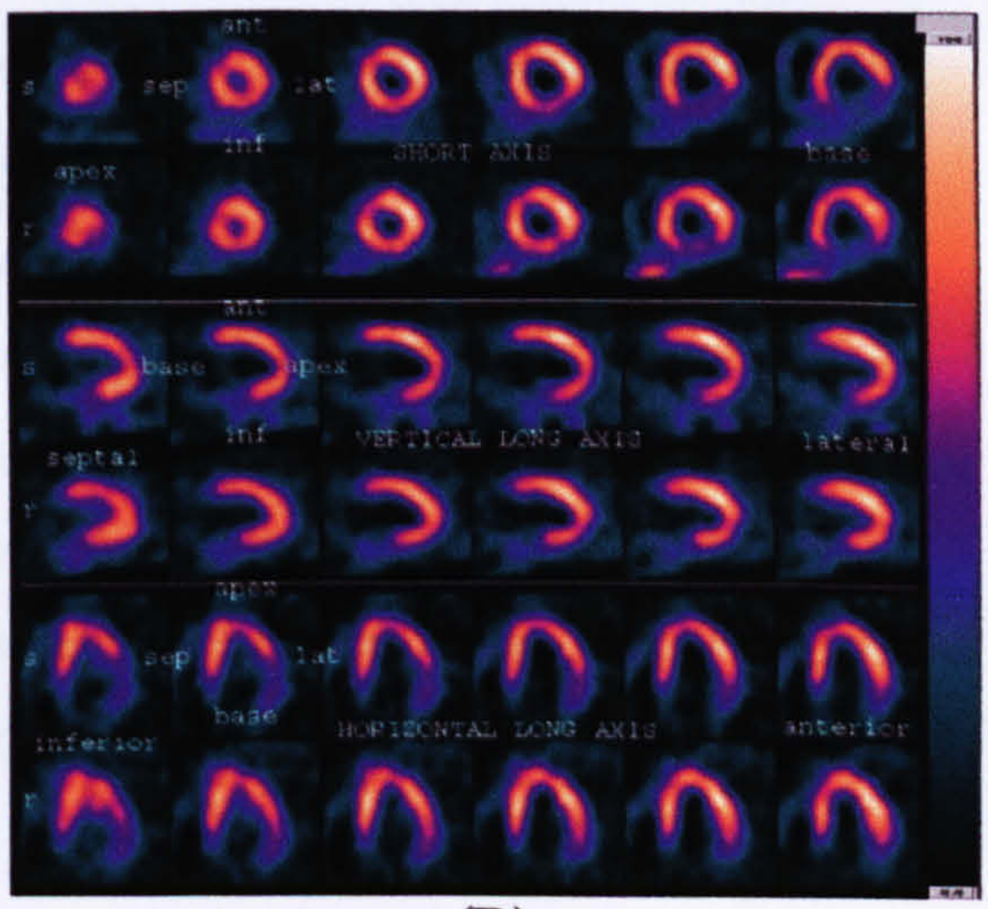

(D)

Figure 6-9 Selected number of short-axis slices of patient data reconstructed without AC (a) and with AC (b). Clinical report of patient data (C and D).

To analyse the counts density with LV from apex to base, a 'bull's-eye image was generated from all reconstructed short-axis slices. The bull's-eye images without and with AC are shown in Figure 6-10. With respect to the bull's-eye image, it appears that AC can correct attenuation artefacts in all LV walls with some artefacts still shown at the inferior wall and part of septal wall of LV (especially toward the base level of LV).

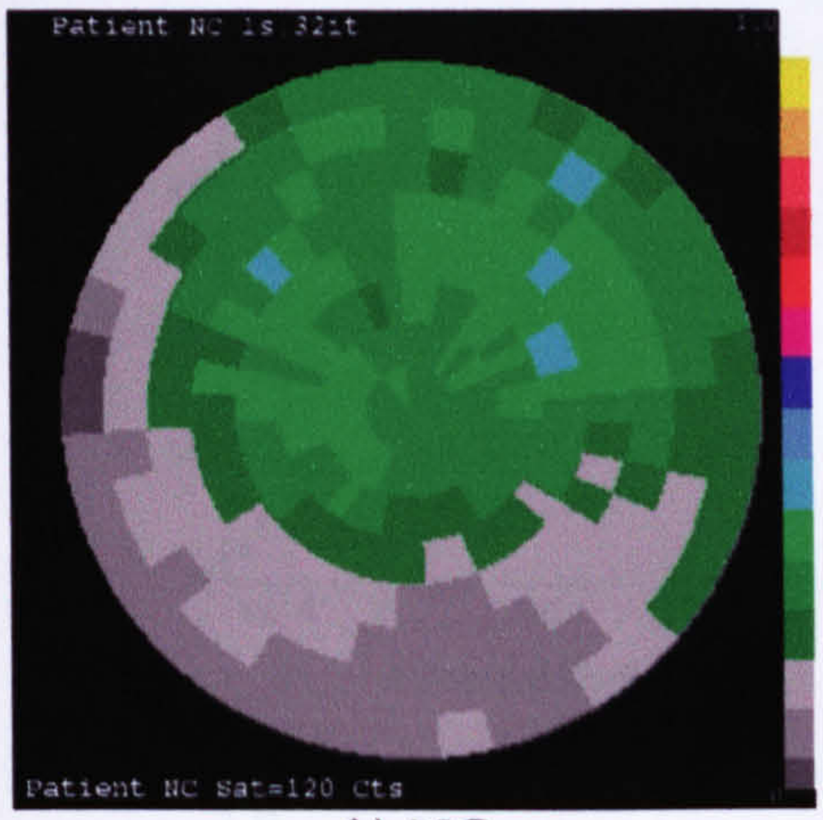

(a) NC

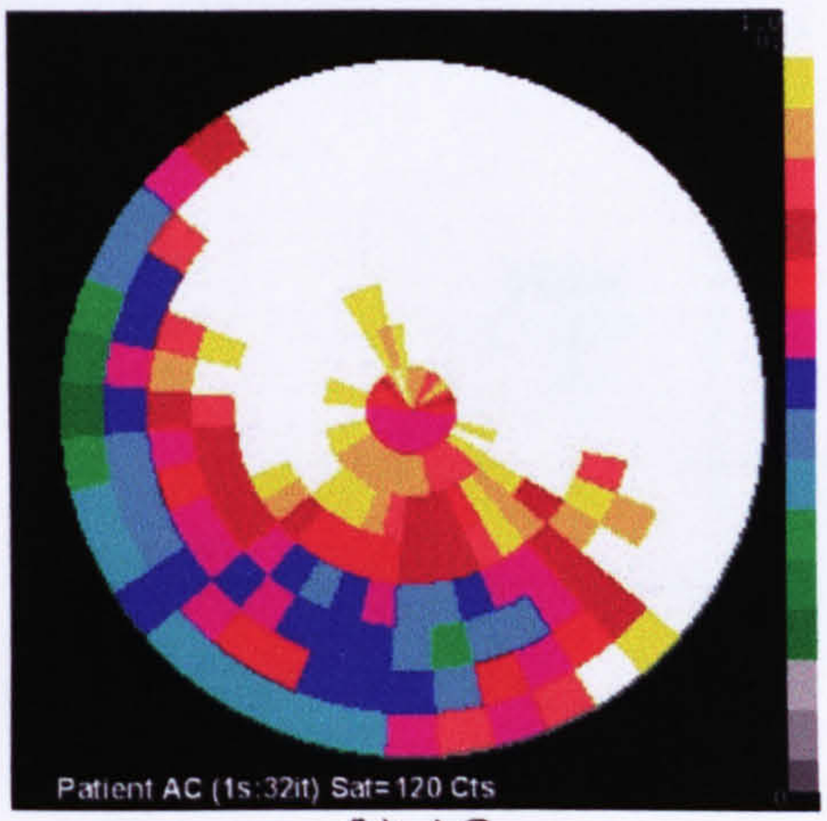

(b) AC

[NC = without AC, AC = with AC]

Saturation level selected to be 120 counts as the maximum level of the colour scale in all images

Figure 6-10 the bull's-eye plots of patient data reconstructed without AC (a) and with AC (b).

To provide quantitative assessment of AC, measured mean counts (at 4ROIs shown in Figure 6-6(c)) without and with AC at a selected short-axis slice reconstructed with OSEM using different number of iterations, are shown in both Table 6-1 and Figure 6 -11. From Figure 6-11 it was observed that the measured mean counts with AC were higher than the measured mean counts without AC. Although, this indicates that OSEM-AC can provide an accurate compensation for attenuation artefacts in all LV walls, still this has not fully addressed the question of how severe this correction (or over-correction) is compared to a reference level. Since the original activity was unknown and scatter correction was not applied, this question is difficult to answer.

Table 6-1 Measured mean counts at four walls of LV in a selected short-axis slices reconstructed without and with non-uniform AC (patient data).

	Anterior		Septal		Inferior		Lateral	
	NC	AC	NC	AC	NC	AC	NC	AC
1 Iteration	26	120	24	106	25	101	24	115
2 Iterations	45	180	42	158	43	150	42	171
4 Iterations	73	256	72	236	70	214	69	252
8 Iterations	91	321	97	314	86	260	90	331
16 Iterations	98	364	110	350	87	275	101	369
32 Iterations	102	388	116	354	86	280	106	381
64 Iterations	103	397	116	343	85	282	109	387
128 Iterations	103	399	113	331	85	282	110	393

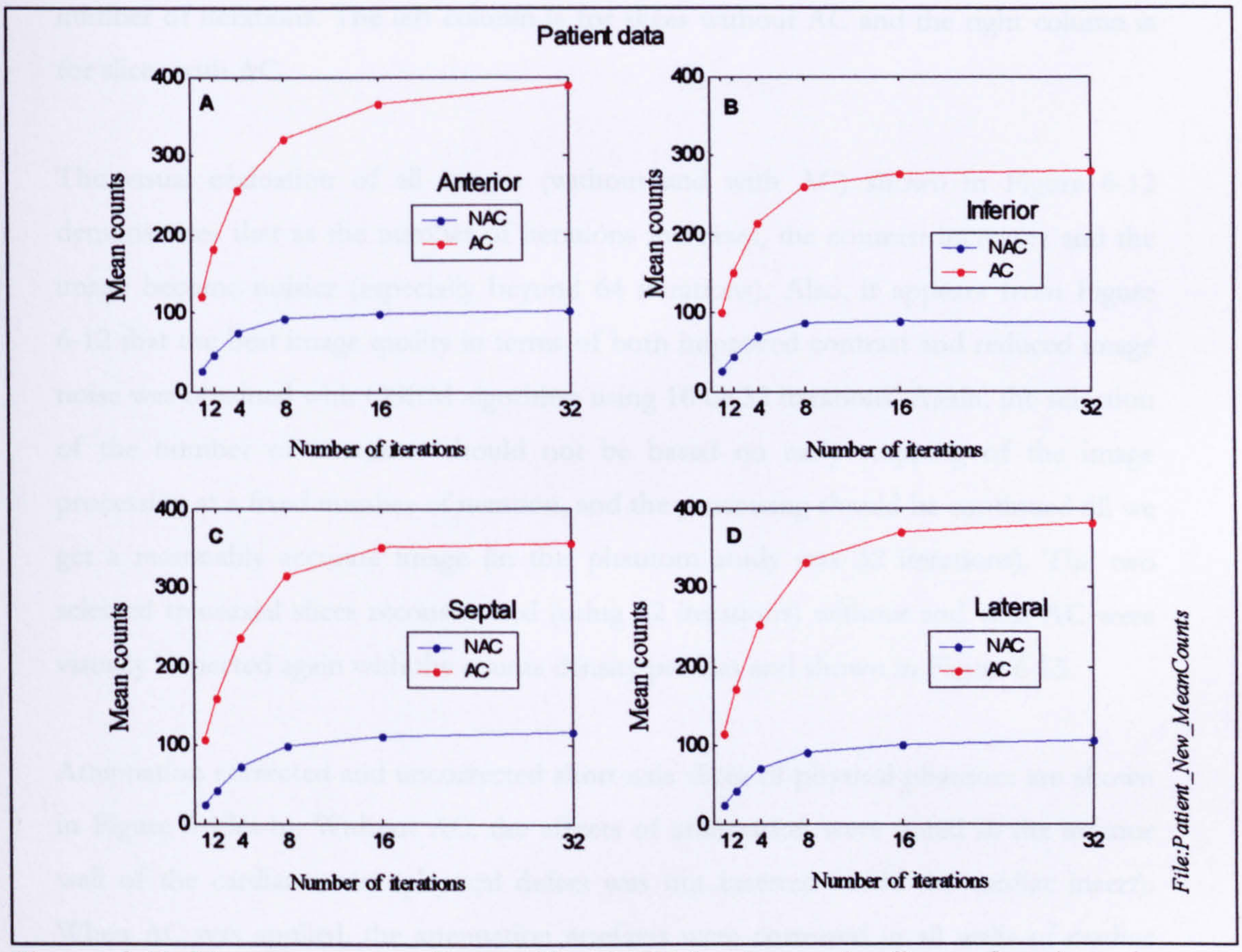

Figure 6-11 Mean counts at four walls of LV in short-axis slices of patient data reconstructed without and with AC.

The results indicate that, for a patient data without scatter correction, OSEM algorithm can significantly corrects attenuation artefacts in all walls of LV. However, some artefacts remain in inferior wall and part of septal wall after correction. These artefacts might be improved if scatter correction was applied. Therefore, the combinations of both scatter correction and AC should be validated in future work.

6.3. Physical phantom

The data for the physical phantom were reconstructed in two different ways, using OSEM algorithm. In the first case, no AC was performed for attenuation. In the second case, AC was performed with incorporating the attenuation map obtained from the Hawkeye system into OSEM algorithm.

Figure 6-12 (a-b) shows the transaxial slices through the cardiac insert of the physical phantom without and with AC reconstructed using OSEM algorithm with different

number of iterations. The left column is for slices without AC and the right column is for slices with AC.

The visual evaluation of all images (without and with AC) shown in Figure 6-12 demonstrates that as the number of iterations increases, the contrast increases and the image become noisier (especially beyond 64 iterations). Also, it appears from Figure 6-12 that the best image quality in terms of both improved contrast and reduced image noise was obtained with OSEM algorithm using 16 or 32 iterations. Again, the selection of the number of iterations should not be based on early stopping of the image processing at a fixed number of iteration, and the processing should be continued till we get a reasonably accurate image (in this phantom study was 32 iterations). The two selected transaxial slices reconstructed (using 32 iterations) without and with AC were visually inspected again with the counts density profiles and shown in Figure 6-15.

Attenuation corrected and uncorrected short-axis slices of physical phantom are shown in Figure 6-13(a-b). Without AC, the effects of attenuation were noted in the inferior wall of the cardiac insert (physical defect was not inserted inside the cardiac insert). When AC was applied, the attenuation artefacts were corrected in all walls of cardiac insert except parts of both septal and inferior walls and the image become relatively uniform in lateral wall compared with other walls as the number of iterations was increased. Furthermore, the noise was increasing with higher number of iterations for both NC and AC images.

It was noticed that at images reconstructed with AC, small number of iterations (1 to 8 iterations) produce images with non-uniform uptake. When theses AC compared to NC images, we can see that NC produce more uniformity in counts than AC images and this result might suggest that NC is better than AC. However, more iteration reverses this finding. Beyond 16 iterations (Figure 6-13(a/b-5)) a clear preference for AC emerges. There is still some non-uniformity but these may be due either to geometric effects or scatter. This strongly showed that stopping at a low number of iterations produces artefacts of uptake. Therefore, the artefacts produced after AC in some published literature could be due to the early stopping criteria.

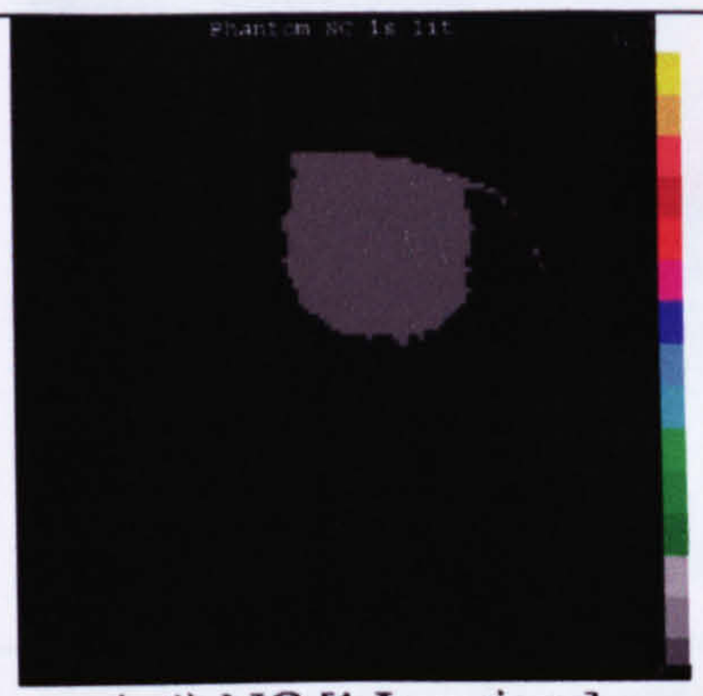

(a-1) NC [1 Iterations]

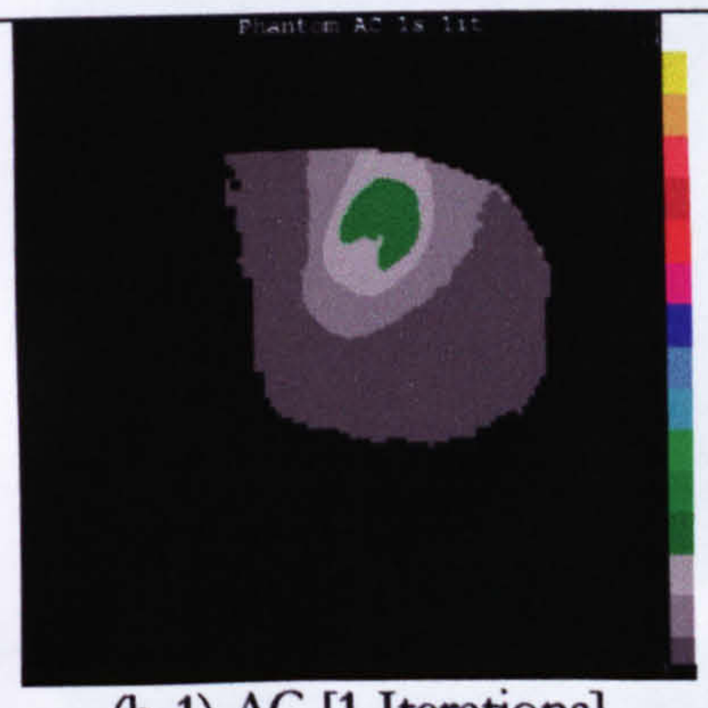

(b-1) AC [1 Iterations]

(a-2) NC [2 Iterations]

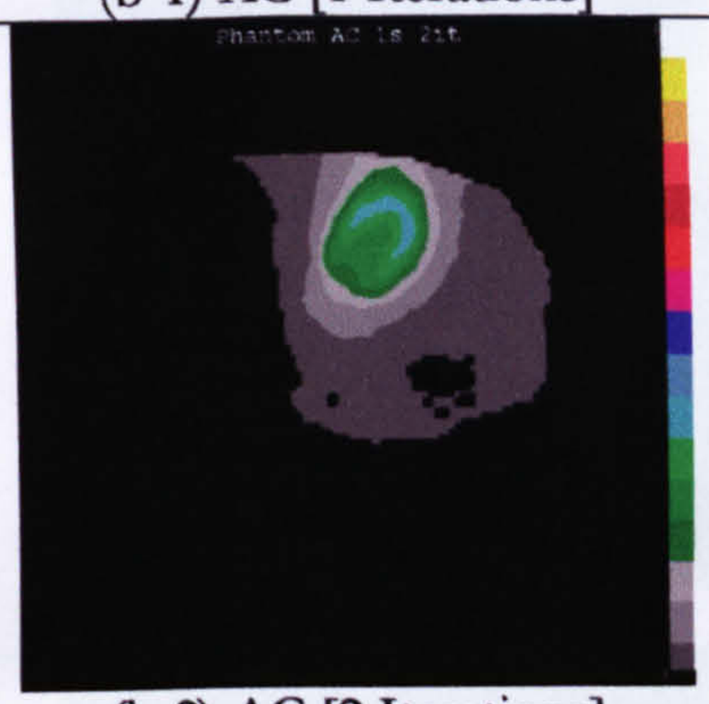

(b-2) AC [2 Iterations]

(a-3) NC [4 Iterations]

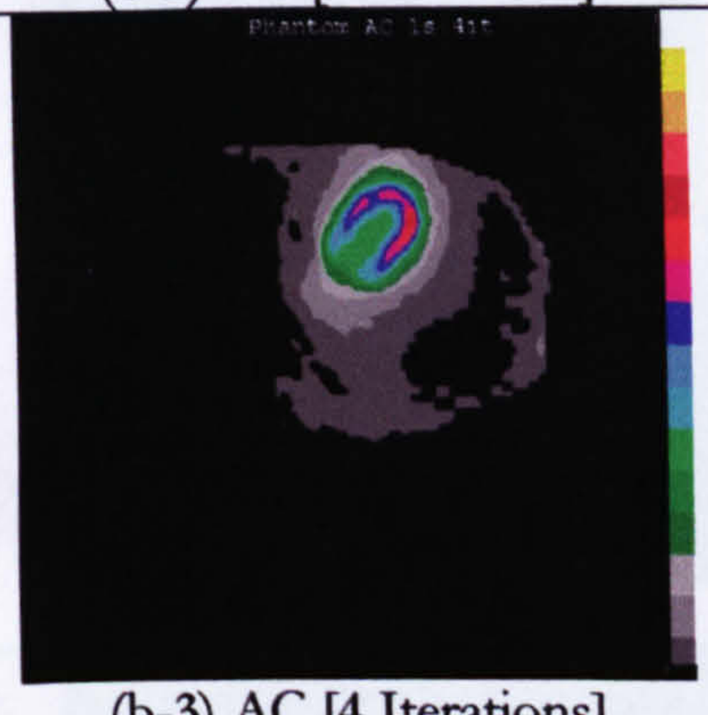

(b-3) AC [4 Iterations]

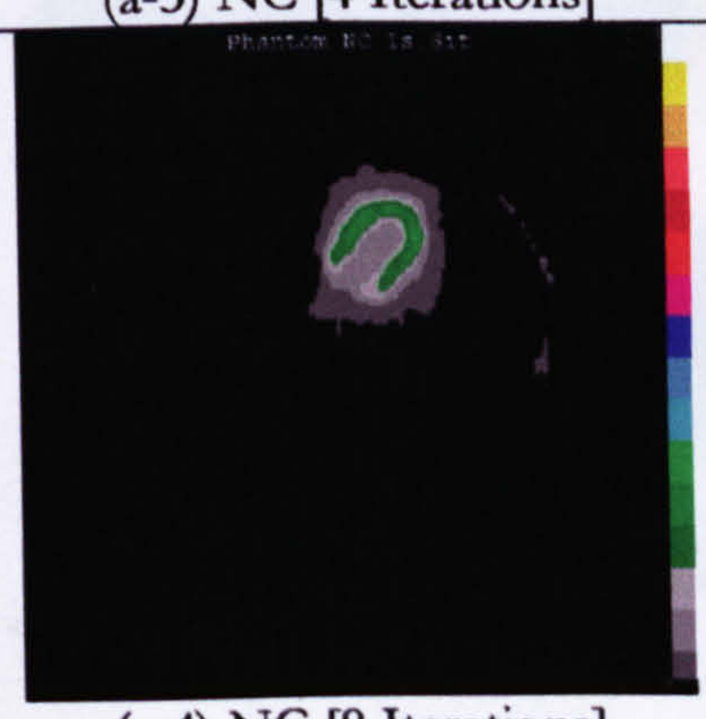

(a-4) NC [8 Iterations]

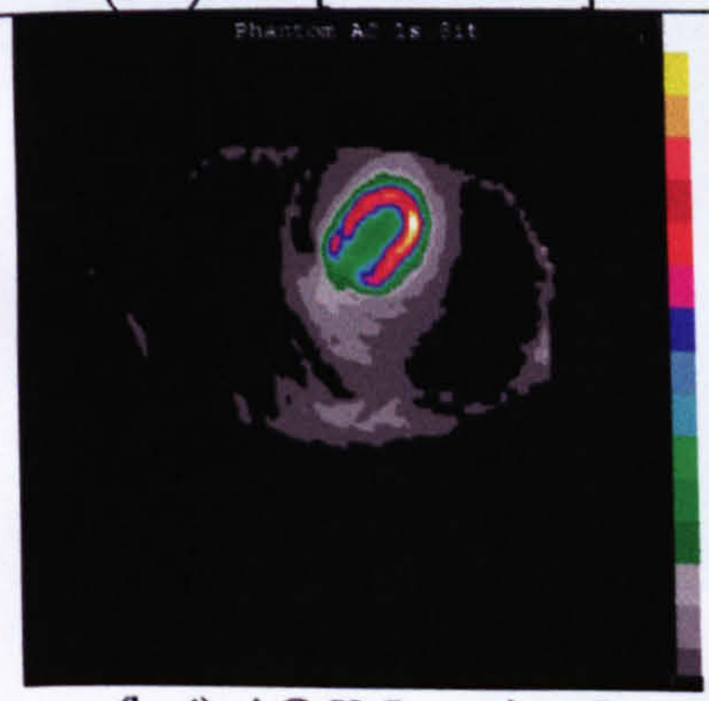

(b-4) AC [8 Iterations]

[The legend of these images is continued in next page]

(a-5) NC [16 Iterations]

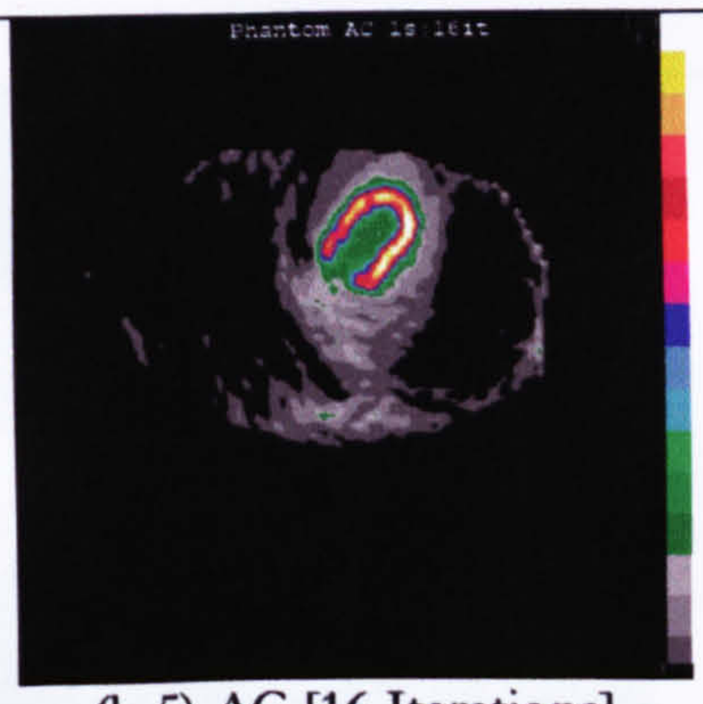

(b-5) AC [16 Iterations]

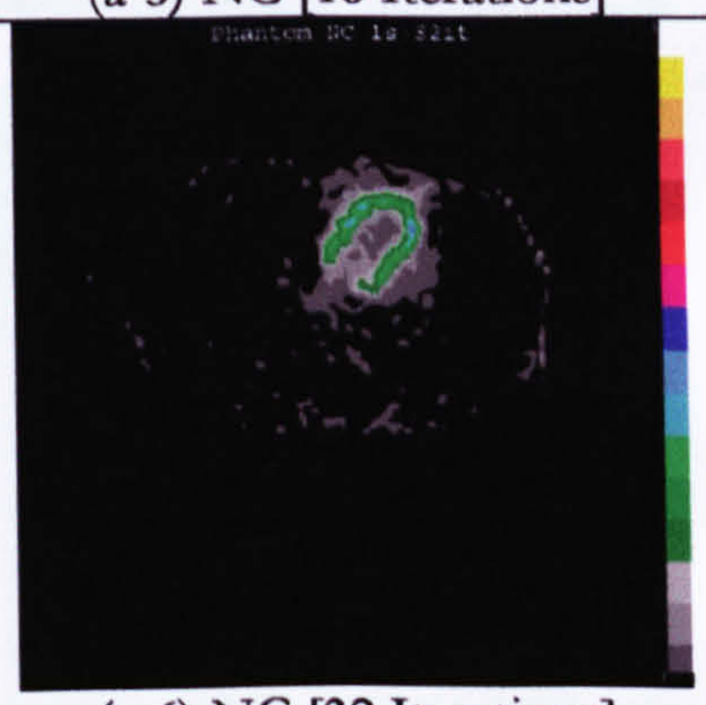

(a-6) NC [32 Iterations]

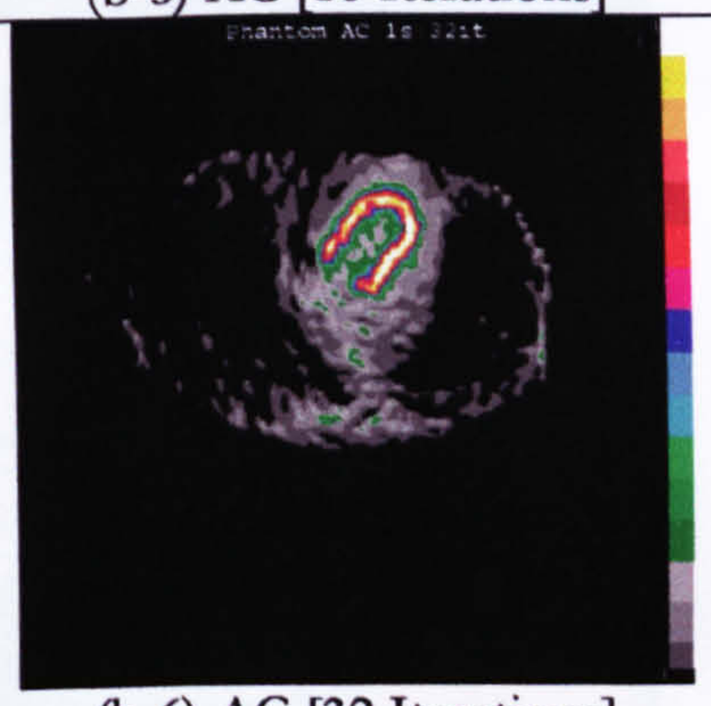

(b-6) AC [32 Iterations]

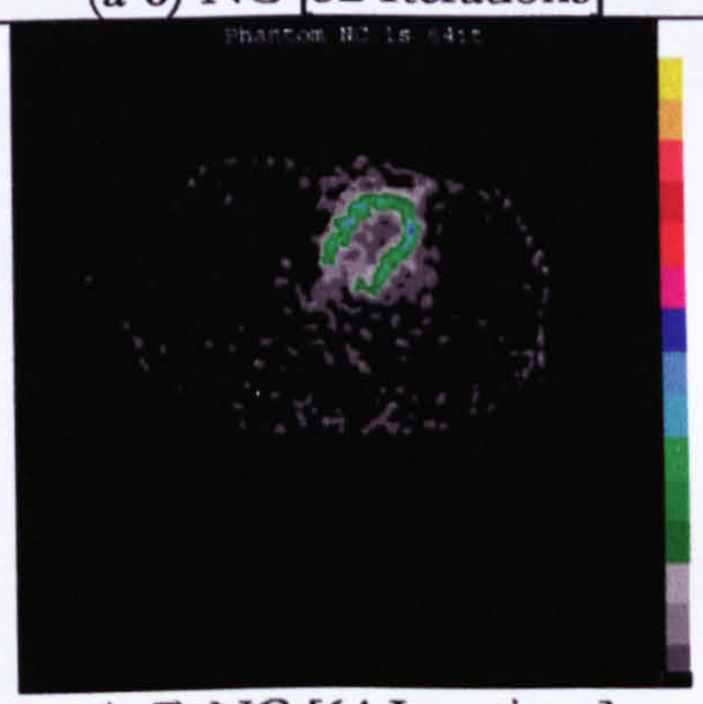

(a-7) NC [64 Iterations]

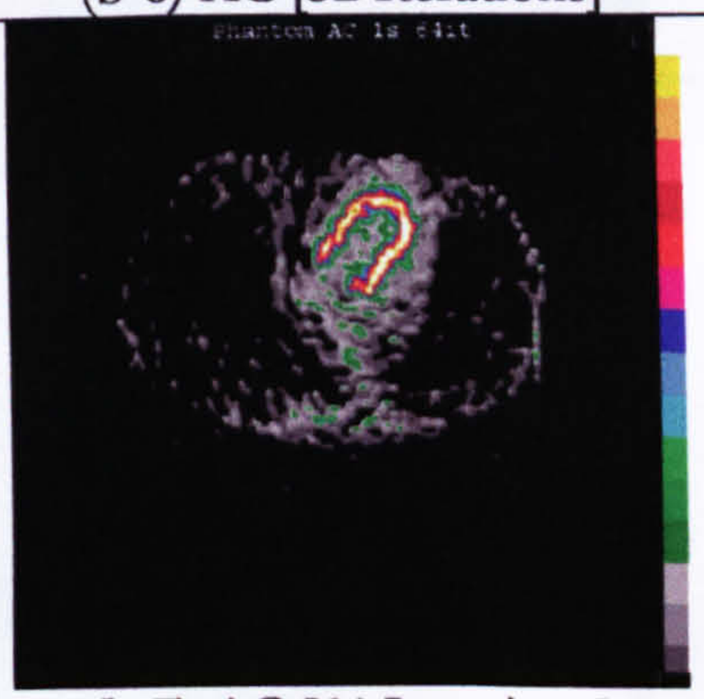

(b-7) AC [64 Iterations]

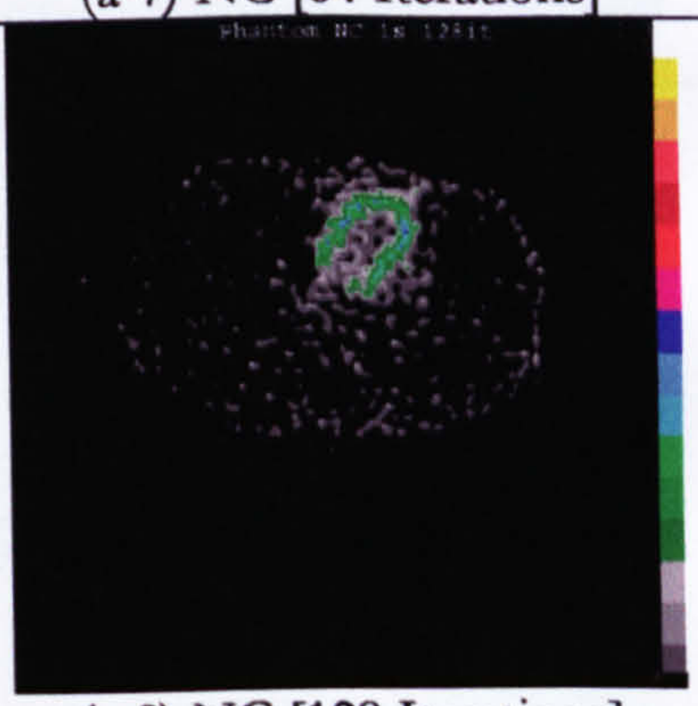

(a-8) NC [128 Iterations]

[NC = without AC, AC = with AC]

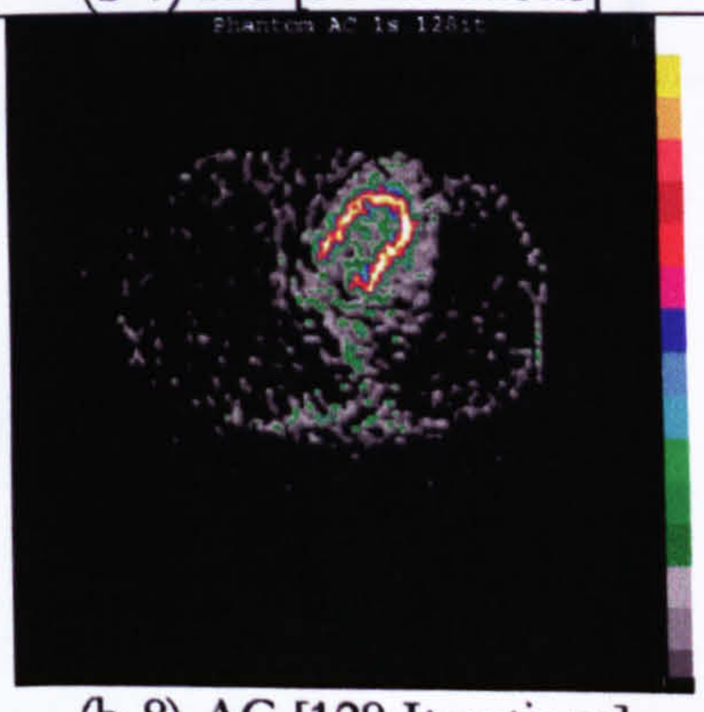

(b-8) AC [128 Iterations]

All images are 128×128

Saturation level selected to be 550 counts as the maximum level of the colour scale in all images

Figure 6-12 Reconstructed transaxial slices using OSEM algorithm (with 1 subset and different numbers of iterations) without AC (a) and with AC (b).

(a-1) NC [1 Iterations]

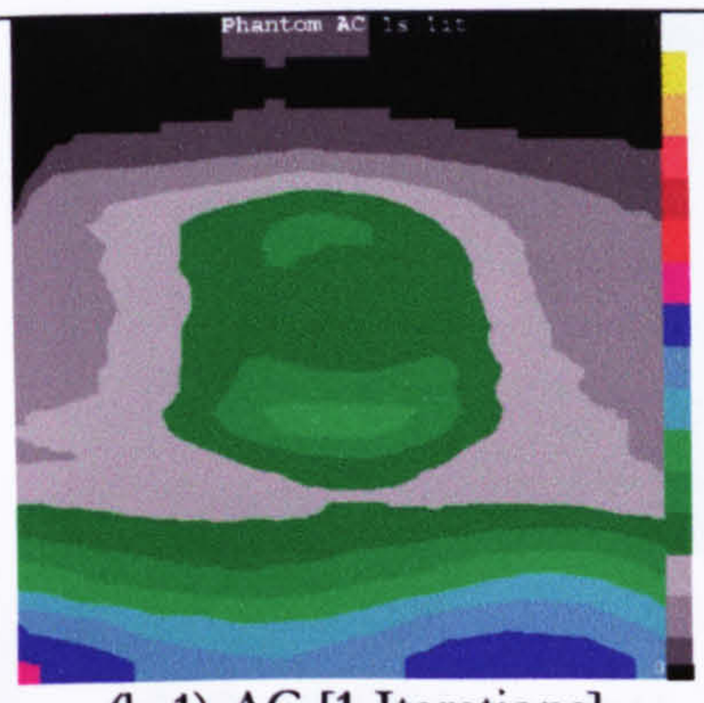

(b-1) AC [1 Iterations]

(a-2) NC [2 Iterations]

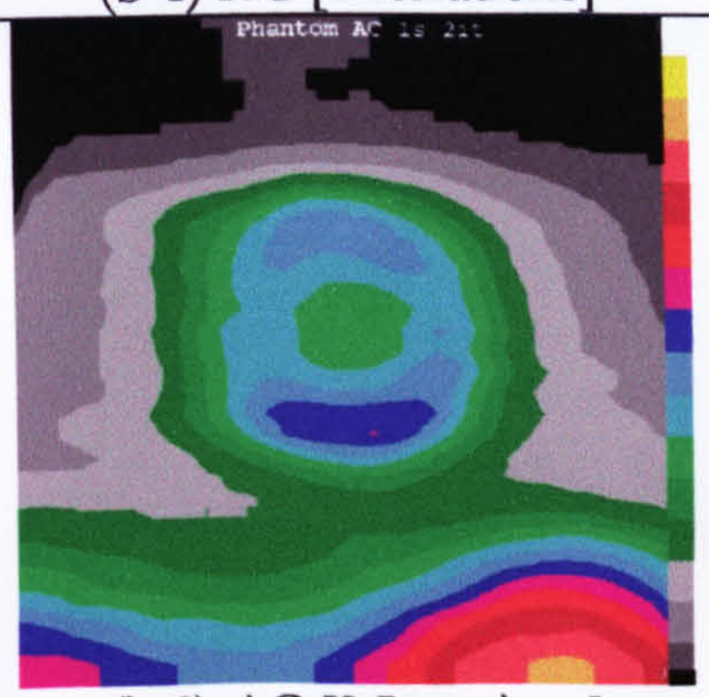

(b-2) AC [2 Iterations]

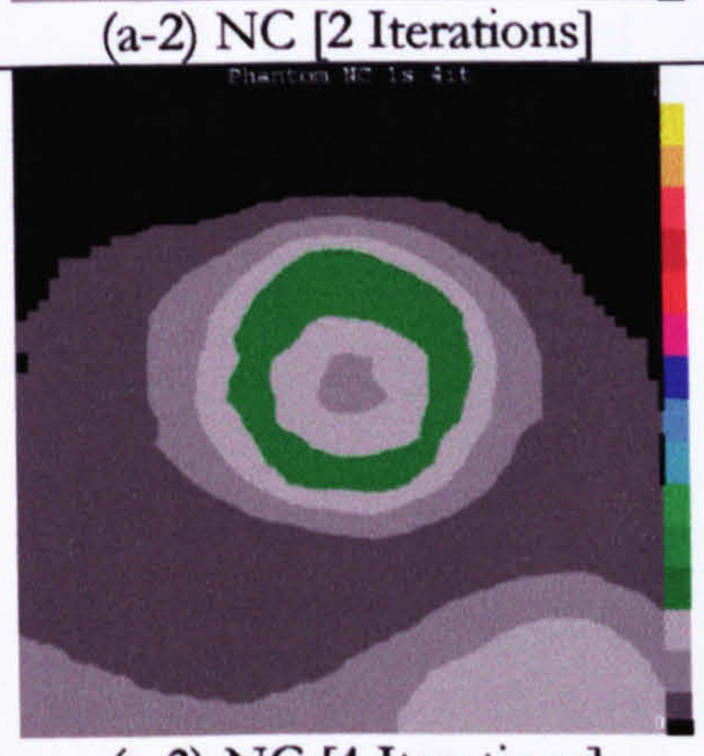

(a-3) NC [4 Iterations]

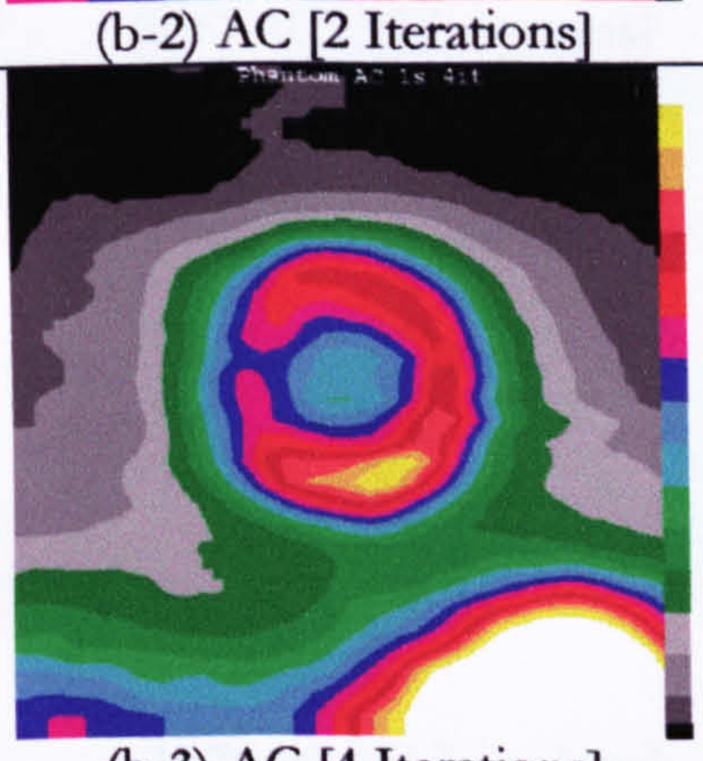

(b-3) AC [4 Iterations]

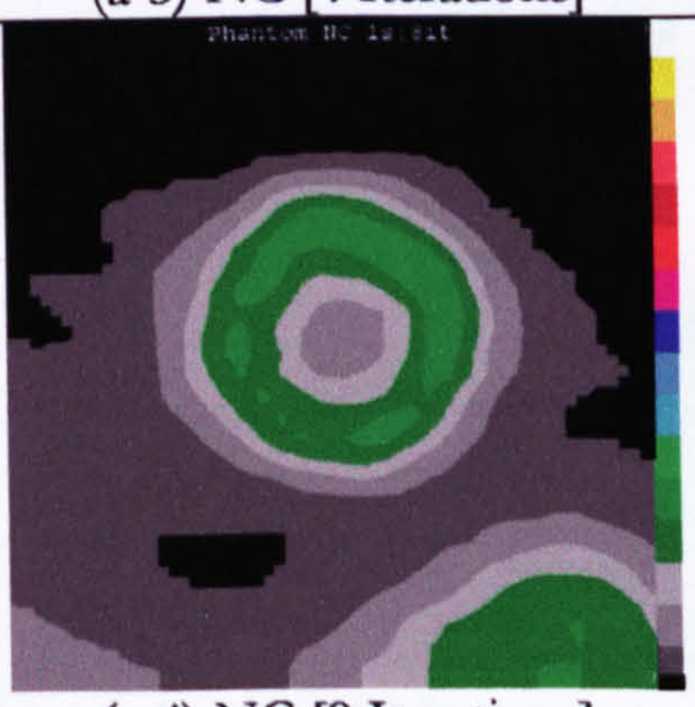

(a-4) NC [8 Iterations]

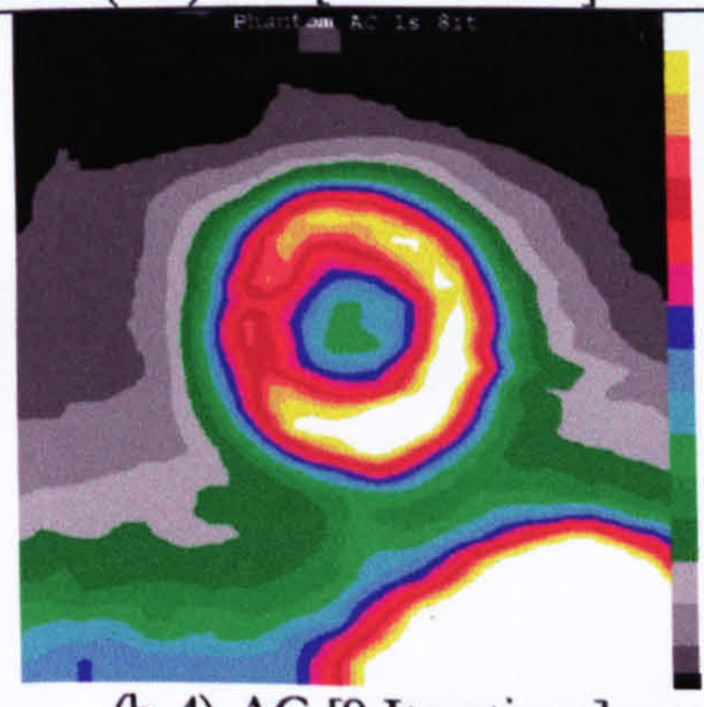

(b-4) AC [8 Iterations]

[The legend of these images is continued in next page]

(a-5) NC [16 Iterations]

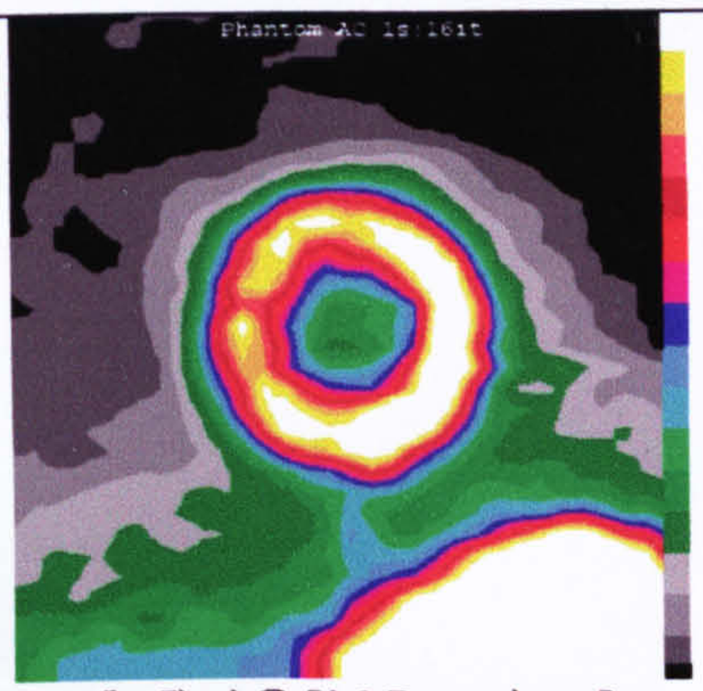

(b-5) AC [16 Iterations]

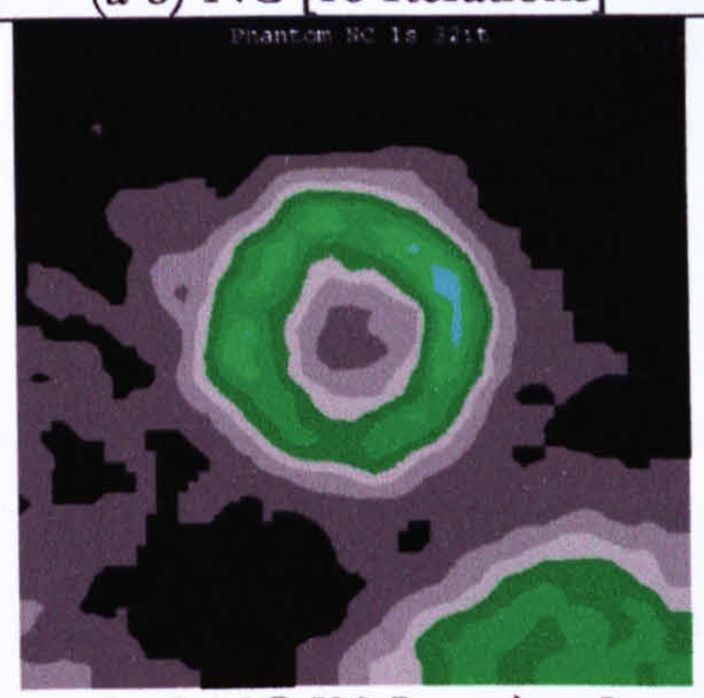

(a-6) NC [32 Iterations]

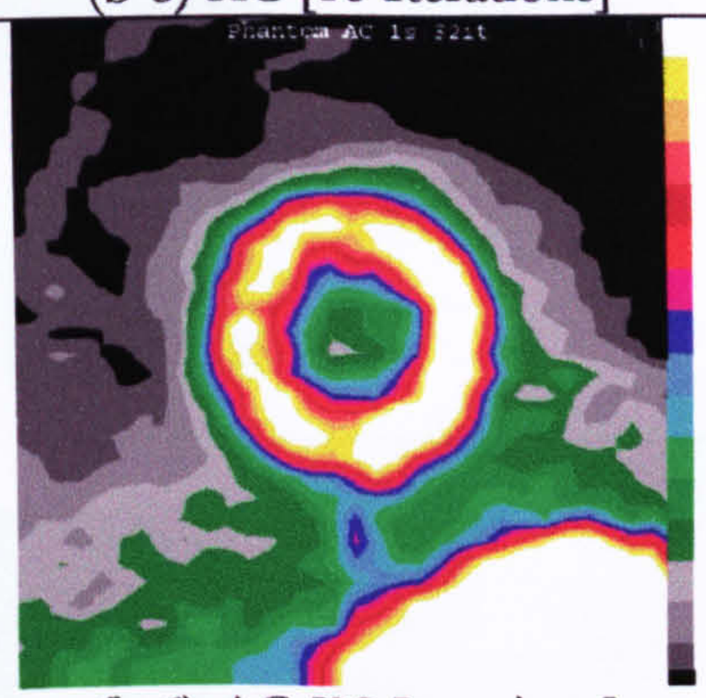

(b-6) AC [32 Iterations]

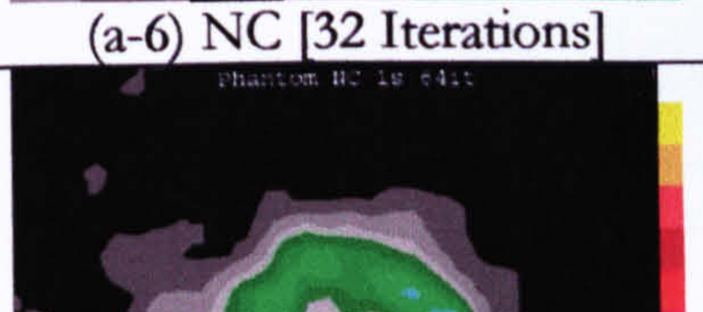

(a-7) NC [64 Iterations]

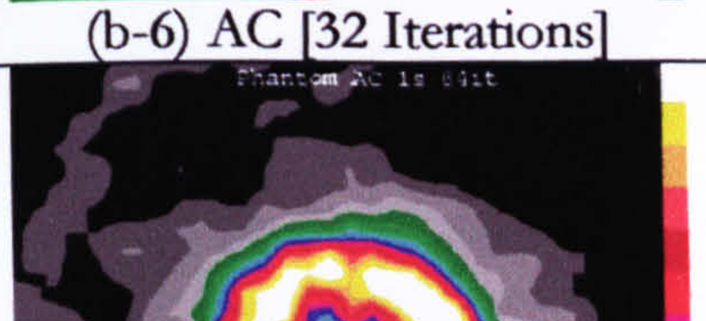

(b-7) AC [64 Iterations]

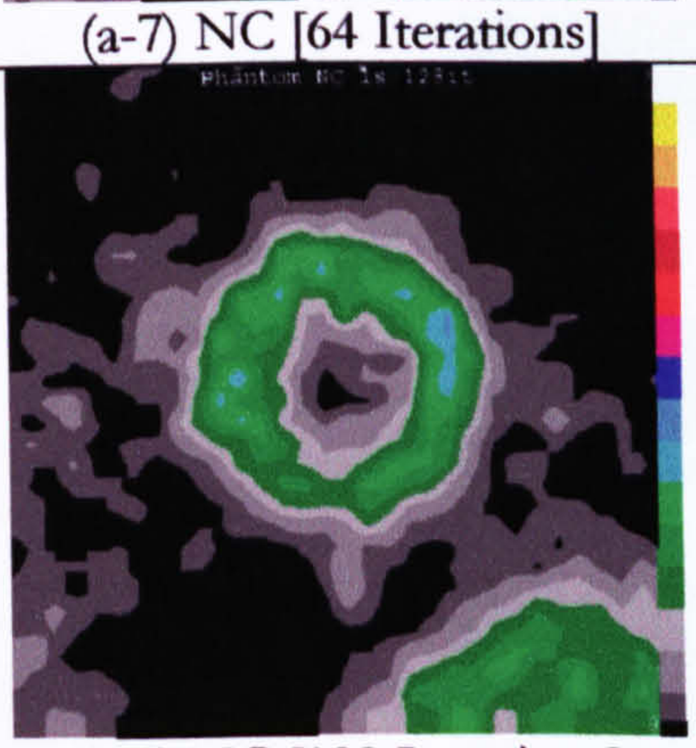

(a-8) NC [128 Iterations]

[NC = without AC, AC = with AC]

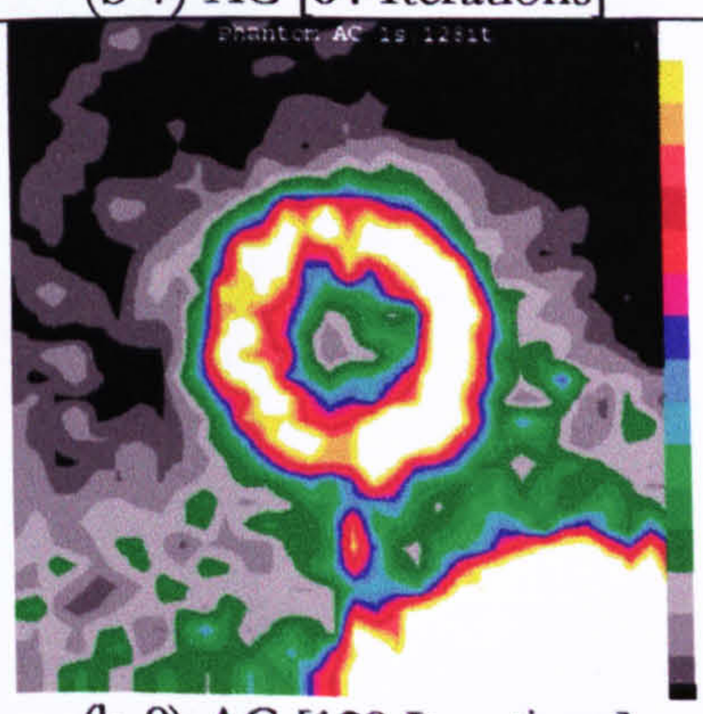

(b-8) AC [128 Iterations]

All images are 64×64

Saturation level selected to be 550 counts as the maximum level of the colour scale in all images

Figure 6-13 Reconstructed short-axis images using OSEM algorithm (with 1 subset and different numbers of iterations) without AC (a) and with AC (b).

For further assessment, reconstructed images and the counts density profiles through the transaxial and short-axis slices reconstructed without and with AC using OSEM algorithm (32 iterations) are shown on both Figure 6-15 and Figure 6-16.

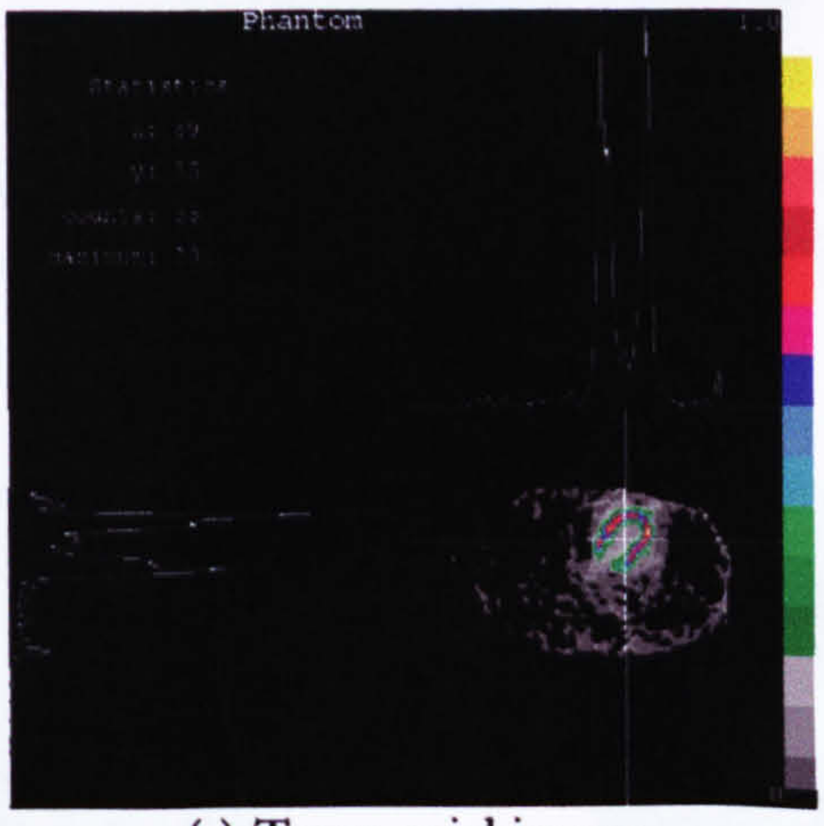

(a) Trans-axial image

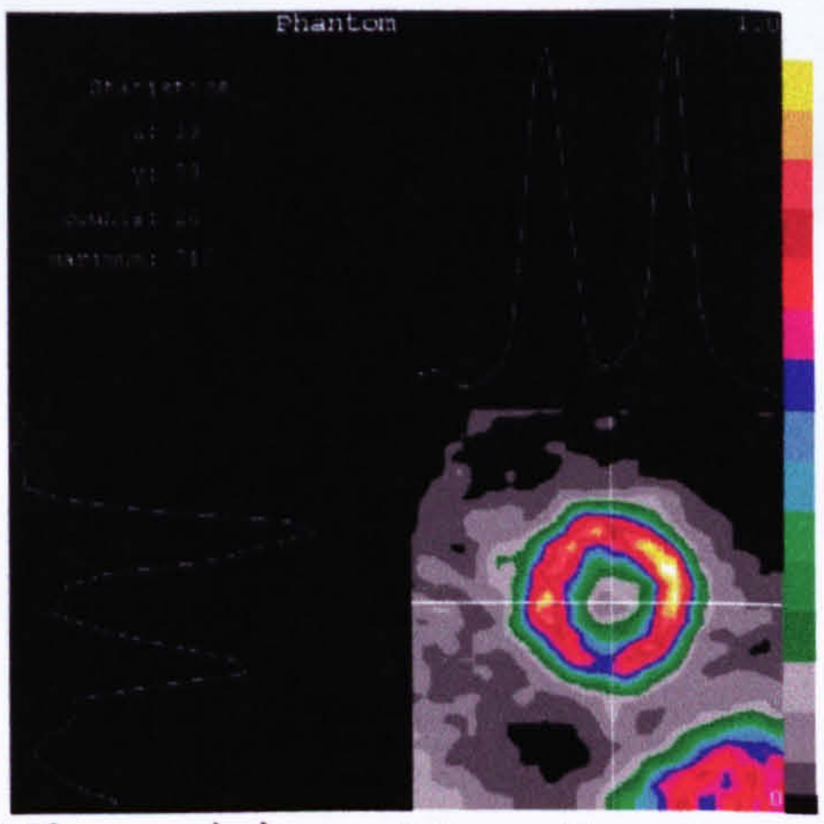

(b) Short-axis image [Zoomed by a factor of 2]

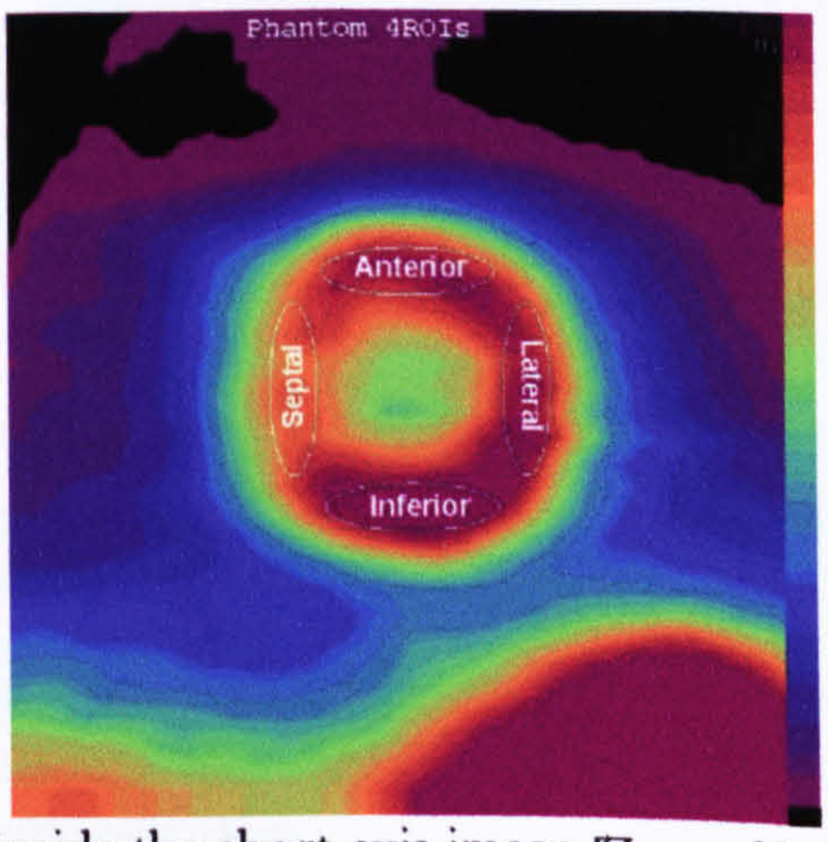

(c) 4ROIs inside the short-axis image [Zoomed by a factor of 2]

Figure 6-14 (a) and (b) demonstrate the position of the counts density profiles (horizontal and vertical) for the transaxial image (a) and short-axis image (b) of physical phantom data. The positioning of the 4ROIs inside the short-axis image is shown in (c).

Figure 6-15(c-d) shows the counts density profiles for the transaxial slices shown in Figure 6-15(a-b). With AC, the profiles illustrate that OSEM was accurately correcting the counts density in all sides of the cardiac insert. While a significant increase in counts density after AC was observed in posterior side of cardiac insert, there was some noise buildup (green curve in Figure 6-15(d)) at this side compared to the profile without AC. However, the details of how severe this noise at posterior side was not addressed because post-filtering were not applied.

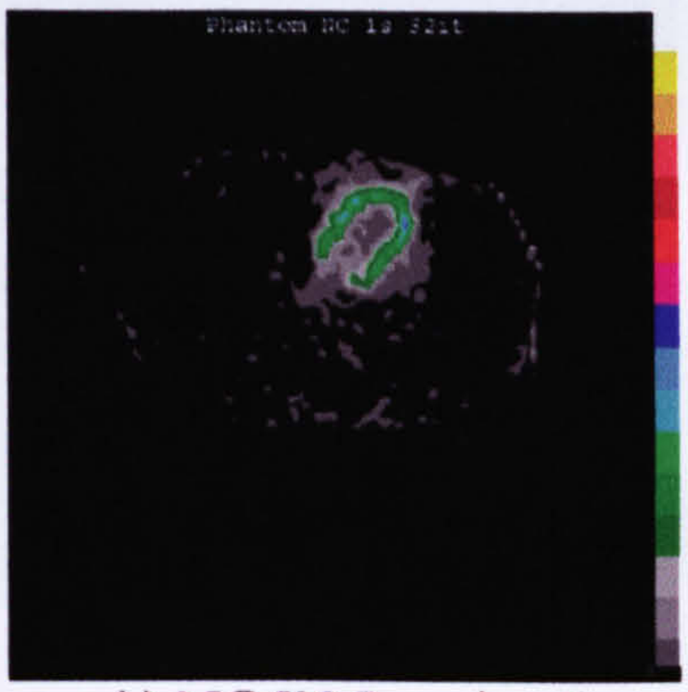

(a) NC [32 Iterations]

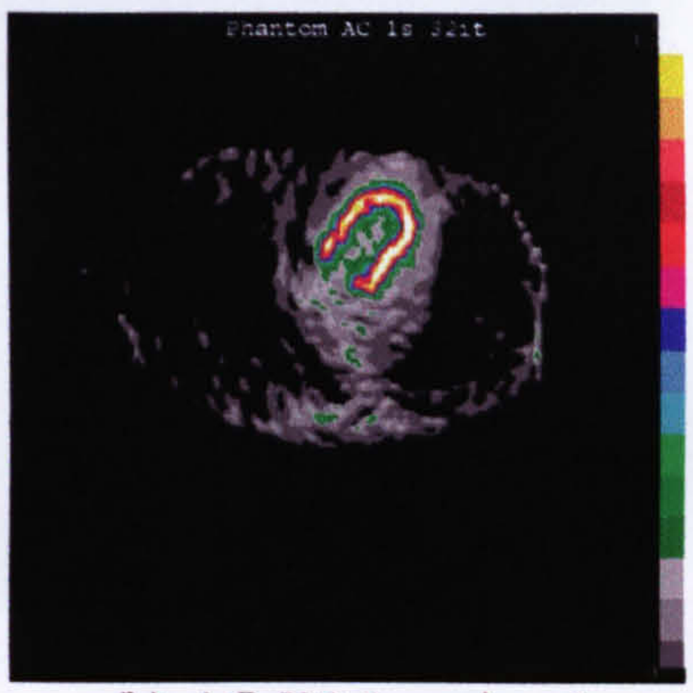

(b) AC [32 Iterations]

All images are 128×128

Saturation level selected to be 550 as the maximum level of the colour scale in all images

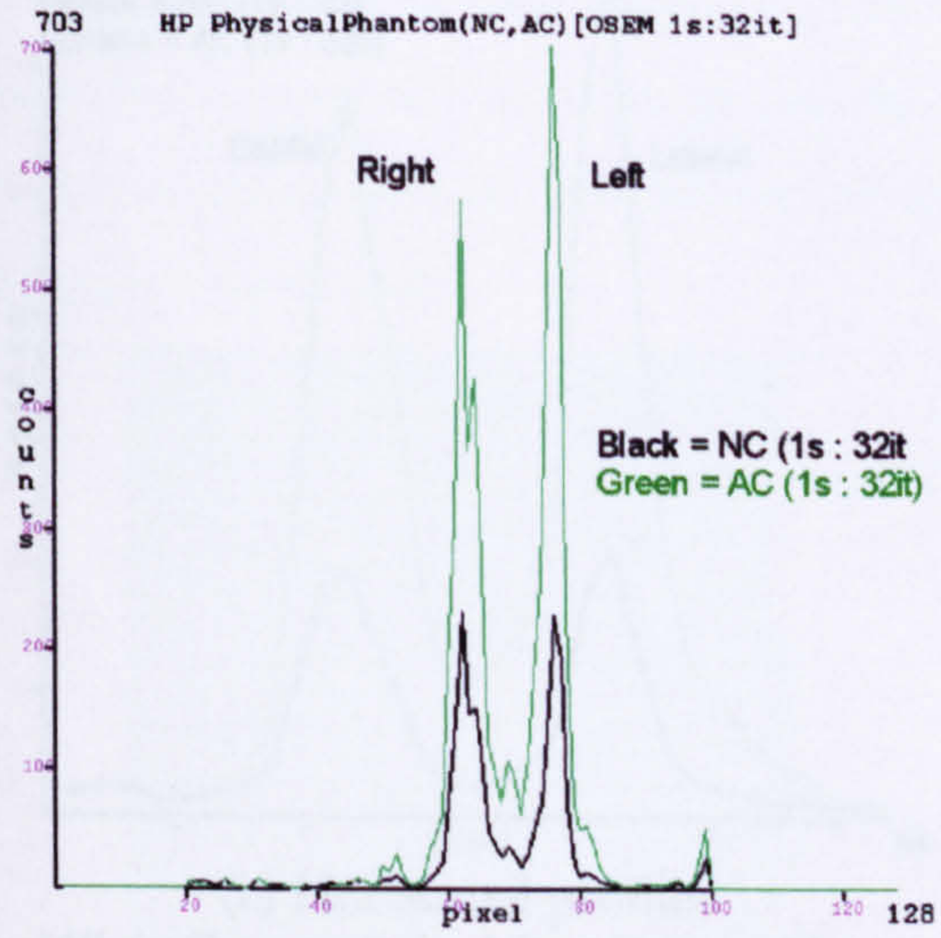

(c) Horizontal profiles

[All profiles are obtained from images without saturation level in the colour scale]

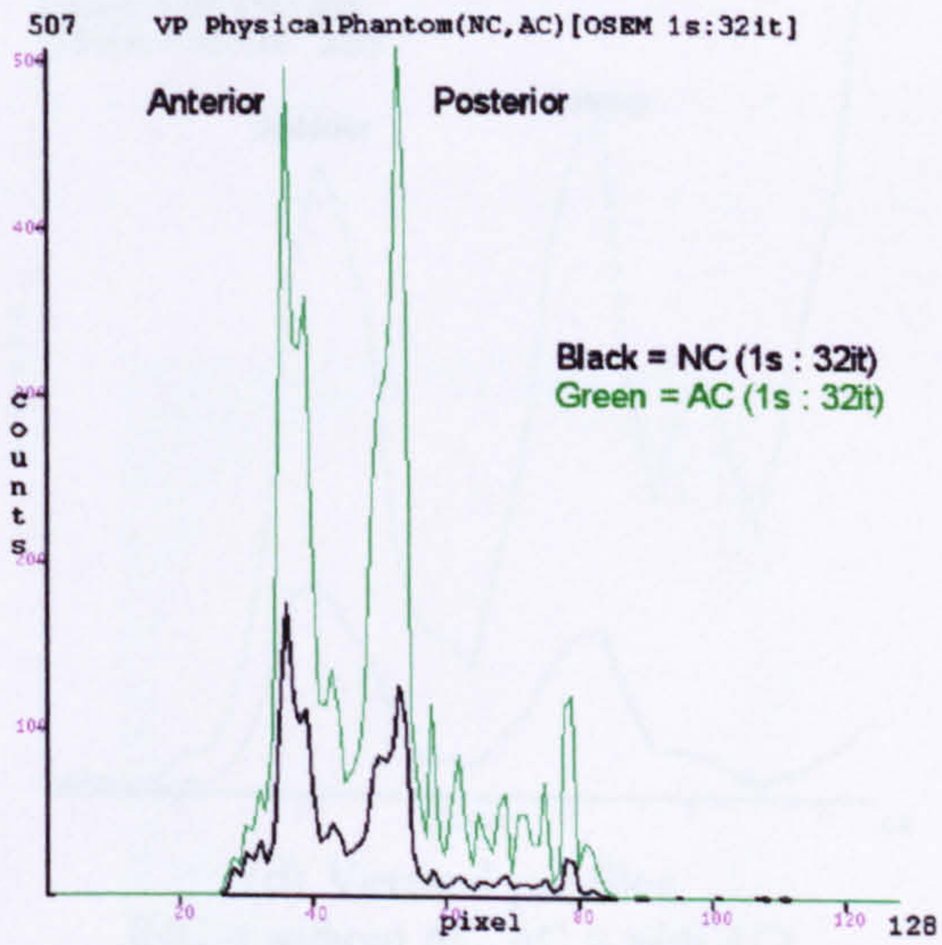

(d) Vertical profiles

[NC = without AC, AC = with AC]

Figure 6-15 the Transaxial slices (and the counts density profiles) from the physical phantom reconstructed using OSEM algorithm without AC (a) and with AC (b). (c). Horizontal profiles. (d) Vertical profiles.

Short-axis slices and corresponding profiles through the cardiac insert, without and with AC are shown in Figure 6-16. Without AC, the profiles illustrate a lower uptake in the septal, anterior and inferior walls of cardiac insert. With AC the counts after correction (green curves in Figure 6-16(c-d)) was higher in lateral wall compared to the counts at all other walls of LV (anterior, septal, and inferior). The explanation of this was not clear whether from the OSEM algorithm itself or whether due to the presence of scatter photons in the inferior wall originated from the high uptake in liver. This might be improved by using scatter correction in a combination with AC.

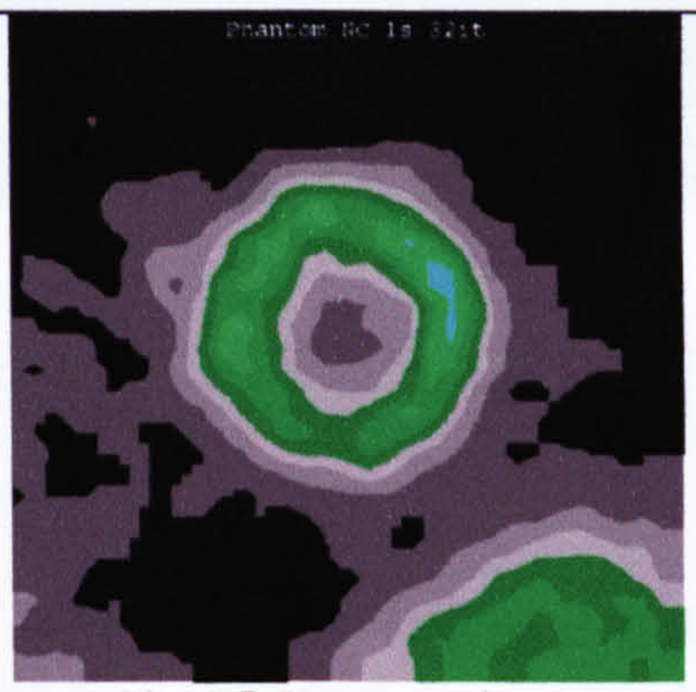

(a) NC [32 Iterations]

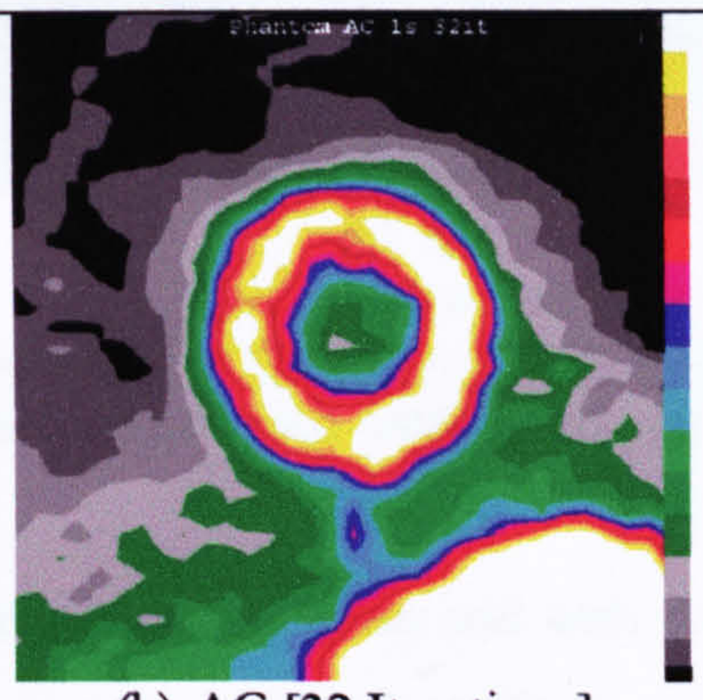

(b) AC [32 Iterations]

All images are 64×64

Saturation level selected to be 550 counts as the maximum level of the colour scale in all images

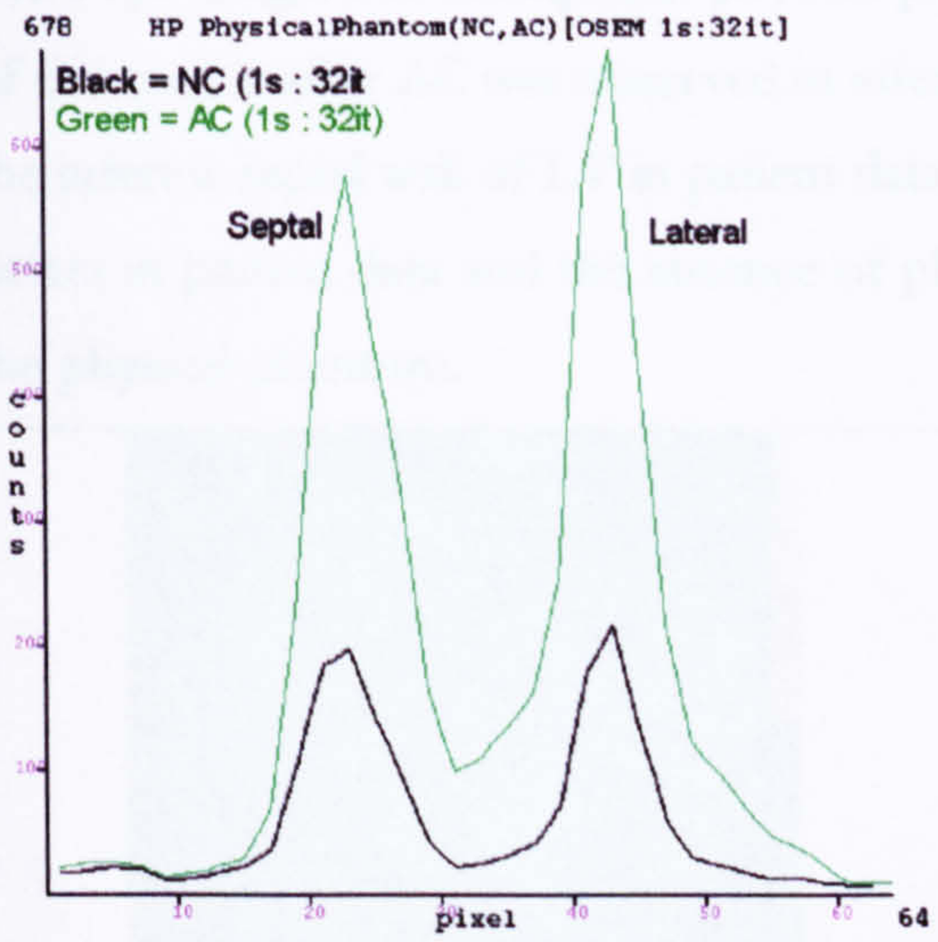

(c) Horizontal profiles

[All profiles are obtained from images without saturation level in the colour scale]

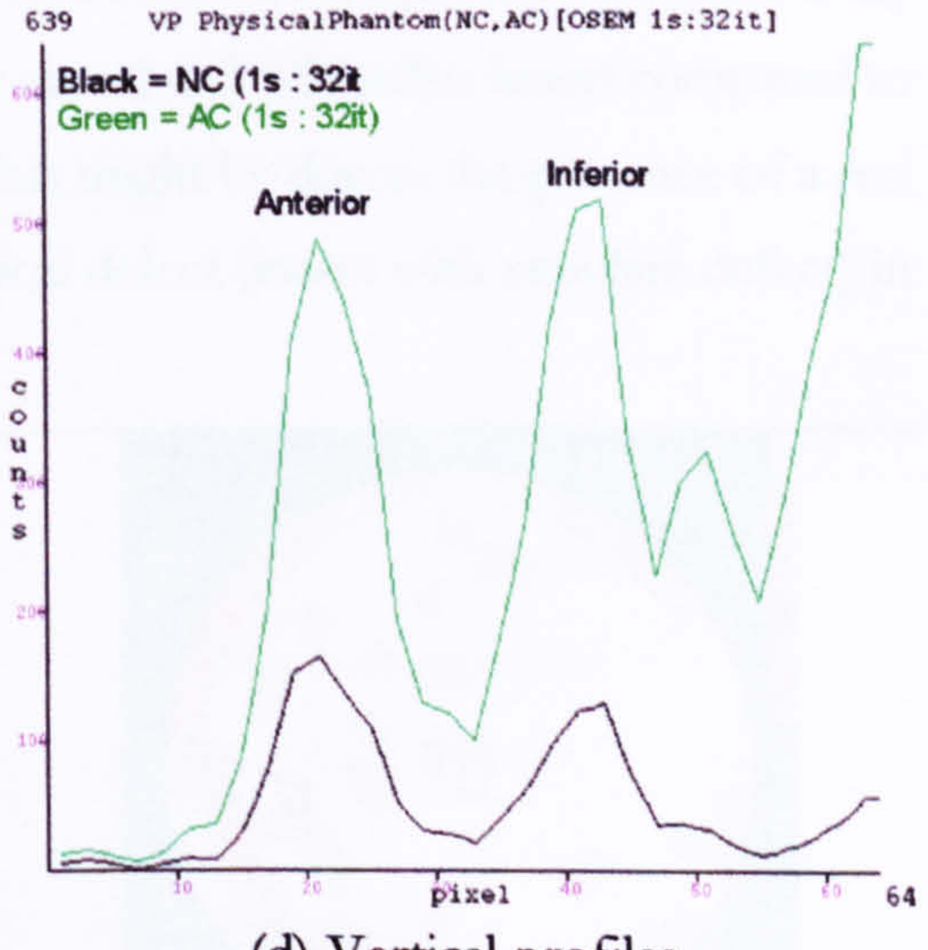

(d) Vertical profiles

[NC = without AC, AC = with AC]

Figure 6-16 the Short-axis slices (and the counts density profiles) from the physical phantom reconstructed using OSEM algorithm without AC (a) and with AC (b). (c). Horizontal profiles. (d) Vertical profiles.

It appears from the short-axis slices shown in Figure 6-17, that OSEM corrects attenuation artefacts quite accurately in all walls of cardiac insert.

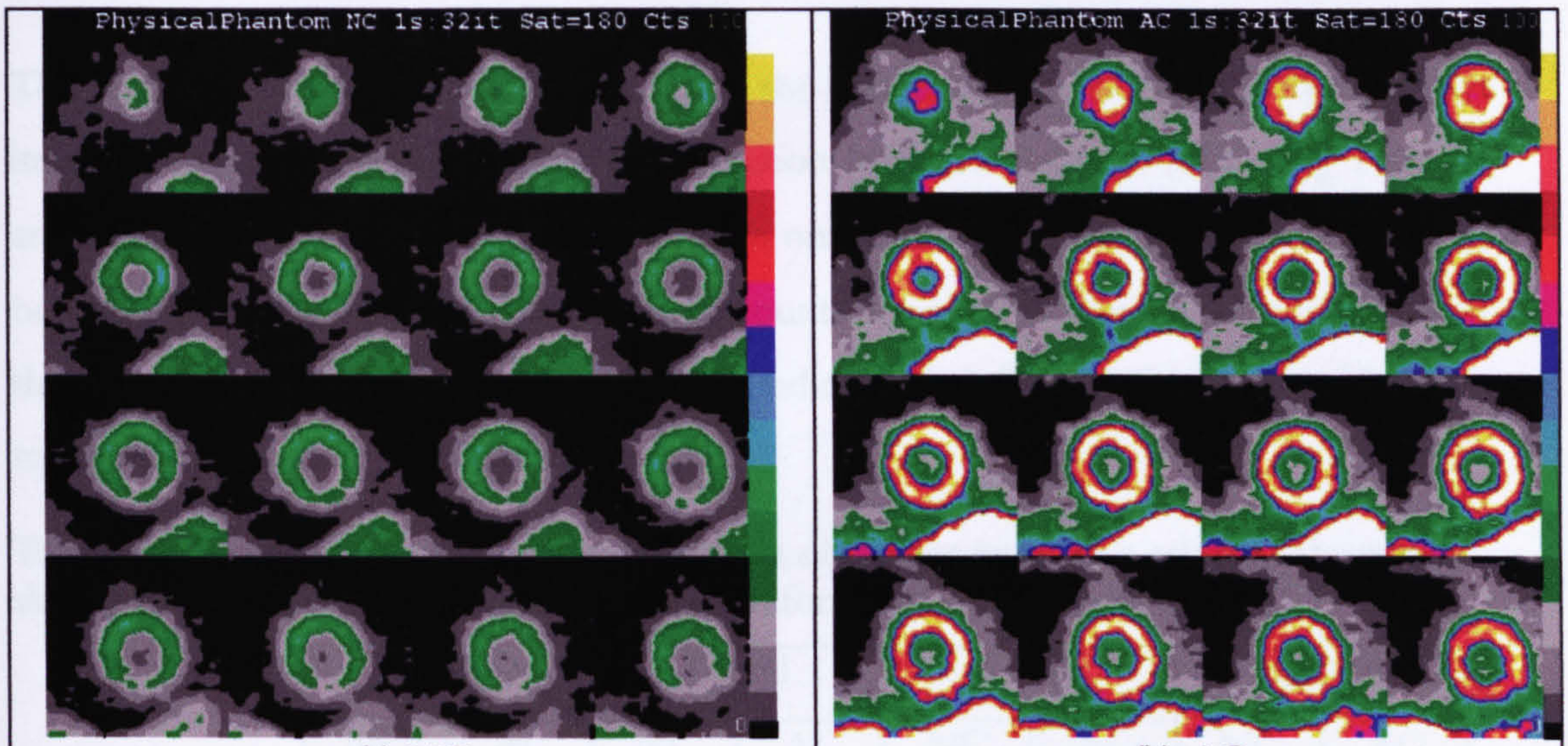

(a) NC (b) AC

[NC = without AC, AC = with AC]

Saturation level selected to be 180 counts as the maximum level of the colour scale in all images

Figure 6-17 the Short-axis slices for phantom data reconstructed without AC (a) and with AC (b).

Figure 6-18 shows the bull's-eye images of all reconstructed without and with AC. It was noted that the attenuation artefacts that remain not completely uniform were at different small parts of the outer rings (toward the base level of the cardiac insert) of bull's-eye image. For example, in physical phantom bull's-eye image, the non-uniformity of the counts after AC was observed in inferior-septal wall of cardiac insert compared to the inferior-septal wall of LV in patient data. This might be due to the presence of a real defect in patient data and the absence of physical defect (insert with simulate defect) in the physical phantom.

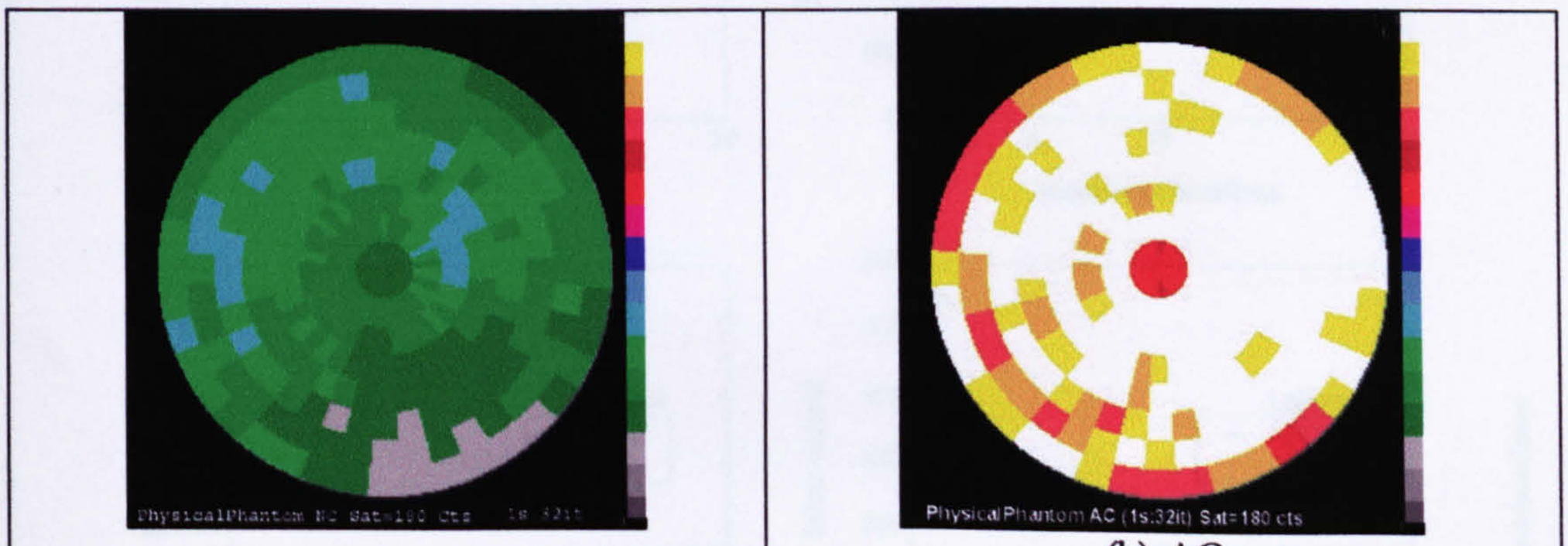

(a) NC (b) AC

[NC = without AC, AC = with AC]

Saturation level selected to be 180 counts as the maximum level of the colour scale in all images

Figure 6-18 the bull's-eye plots of physical phantom reconstructed without AC (a) and with AC (b).

The measured mean counts at 4ROIs (using the regions shown in Figure 6-14(c)) versus iteration number of both OSEM reconstruction (without and with AC) using 1 subset and different number of iterations are shown on both Table 6-2 and Figure 6-19. It can be noted from Figure 6-19, that the mean counts after AC in all walls were higher than the measured mean counts before AC. This indicates that OSEM-AC significantly helps to correct attenuation artefacts in all walls.

Table 6-2 Measured mean counts at four walls of cardiac insert in a selected short-axis slices reconstructed without and with non-uniform AC (physical phantom).

	Anterior		Septal		Inferior		Lateral	
	NC	AC	NC	AC	NC	AC	NC	AC
1 Iteration	33	136	31	134	32	175	31	130
2 Iterations	70	247	62	223	61	291	61	235
4 Iterations	120	365	107	307	108	442	110	381
8 Iterations	148	446	134	381	131	537	147	506
16 Iterations	160	479	153	446	133	550	168	562
32 Iterations	163	490	164	482	132	546	181	586
64 Iterations	166	496	168	495	130	544	186	593
128 Iterations	168	501	170	500	128	544	187	591

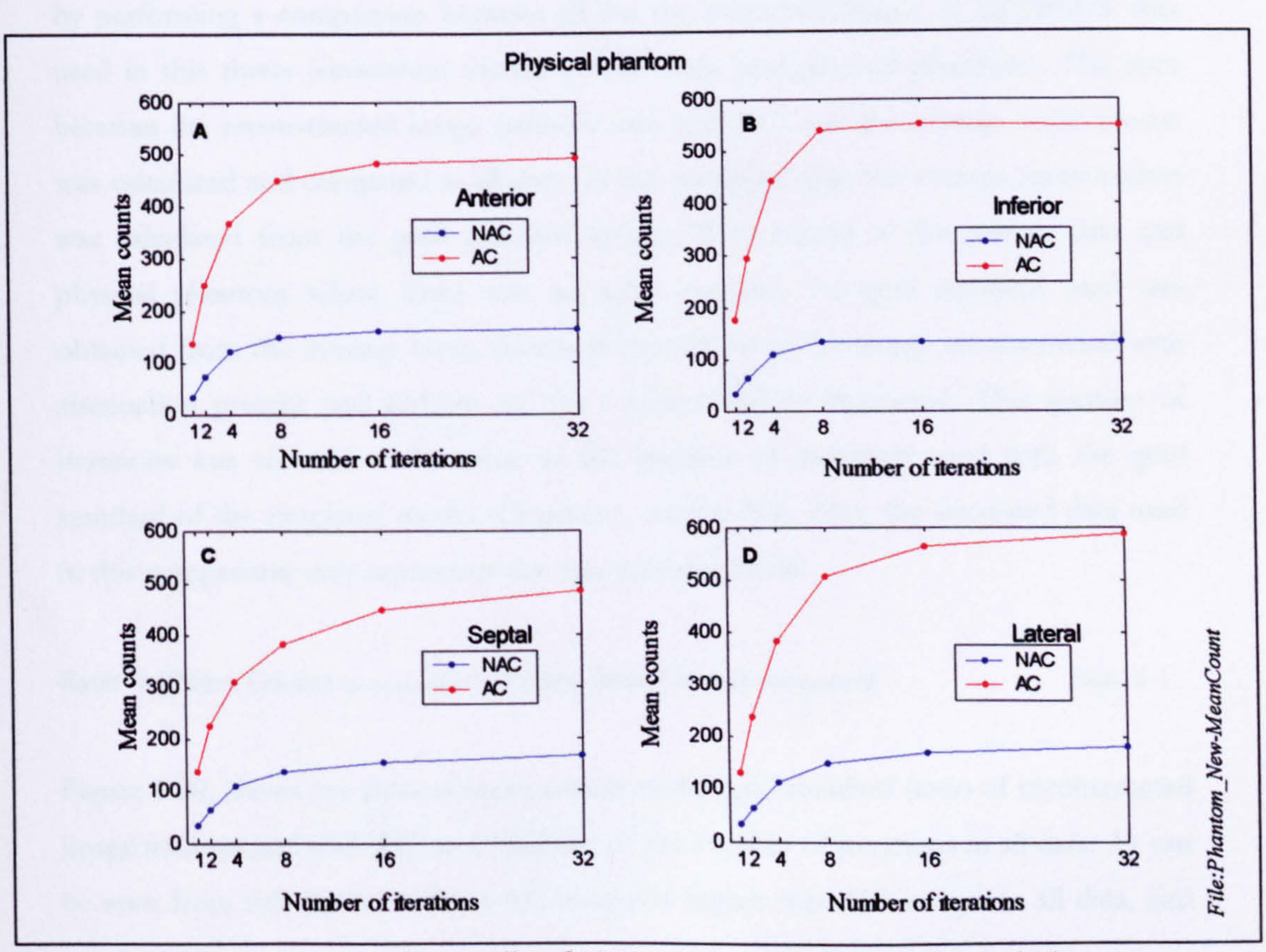

Figure 6-19 Mean counts at four walls of LV in short-axis slice of physical phantom reconstructed without and with AC.

In general, AC improves image quality and quantifications of physical phantom by correcting the attenuation artefacts mainly at inferior wall. In the physical phantom experiment, activity was simulated only in the LV walls and in the liver. In patient study, non-specific activity can also be observed in the LV activity, in the lungs, or in the digestive tract [126]. Despite the presence of scattering counts from liver (and scatter correction was not applied), AC successfully corrects attenuation artefacts at inferior region. This was likely due to the simulated ratio concentration between the myocardium and the liver used in the physical phantom was (1.8) higher than the ratio which can be observed in a healthy subject (0.6) [126]. This ratio was assumed to simulate moderate ratio and was suggested by Mr. Mike Avison from Bradford Hospital. However, this ratio can be higher than 1.8 or even lower than 0.6. Therefore, further investigations should be carried out with a simulation of different myocardium/liver ratio (low, moderate, and high) and with applying scatter correction in a combination of AC.

6.4. Comparison of AC in all SPECT data used in this thesis

The ability of the OSEM algorithm to correct attenuation artefacts has been examined by performing a comparison between all the reconstructed images of all SPECT data used in this thesis (simulation model, patient data, and physical phantom). The ratio between the reconstructed image (without and with AC) and the average mean counts was calculated and compared in all data (in the simulated data the average mean counts was calculated from the gold standard image). With regard to the patient data and physical phantom where there was no gold standard, the gold standard used was obtained from the average mean counts in four ROIs of the image reconstructed with attenuation present and without AC (at 1 subset and 64 iterations). This number of iterations was selected to be same as the number of iterations used with the gold standard of the simulated model (Chapter 5, section 5.3). Also, the simulated data used in this comparison only represents the non-uniform model.

$$\text{Ratio} = [(\text{Mean Counts}_{\text{Reconstructed}})/(\text{Average Mean Counts}_{\text{Gold standard}})] \qquad \text{Eqn. 6-1}$$

Figure 6-20, shows the ratio of mean counts to the gold standard (ratio of reconstructed image without and with AC) as a function of the number of iterations in all data. As can be seen from this figure, ratio of AC images is higher than NC images in all data, and

this indicates that OSEM-AC was able to correct attenuation artefacts successfully in all data. Also, it was noticed that, generally, ratio values were low in the simulated data in both NC and AC (Figure 6-20(a)), moderate in physical phantom data (Figure 6-20(c)), and high with patient data (Figure 6-20(b)). Figure 6-20(b) shows that the ratio values in patient data of the AC image (AC at 32 iterations/average of NC image at 64 iterations) and NC image (NC at 32 iterations/average of NC image at 64 iterations) were 4.9 for AC and 1.3 for NC. These ratios become smaller (Figure 6-20(a)) in the simulated data with 1.02 in AC image and 0.6 in NC image (AC or NC at 32 iterations/gold standard). Ratio values in the simulated data were low because all NC and AC images were reconstructed from noise-free data (and no simulation of liver uptake). On the other hand, the ratio values in the patient data was high because all NC and AC images were calculated with respect to average mean counts of NC image instead of the gold standard (as the true counts are impossible to be known in patient data). This Figure 6-20 shows that in general attenuation artefacts were corrected in all models.

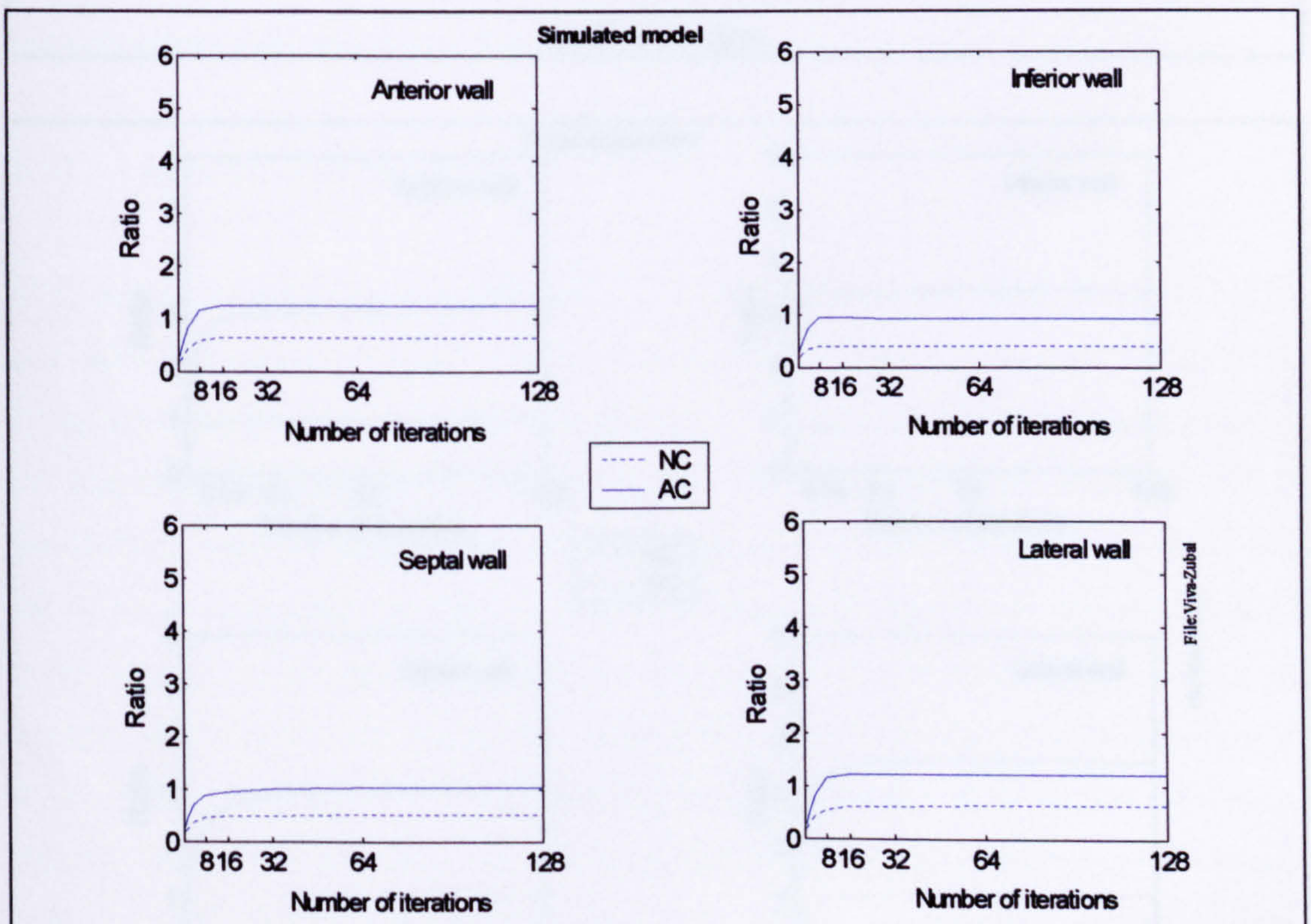

(a) Simulated model (non-uniform attenuation model)

[The legend of this figure is continued in next page]

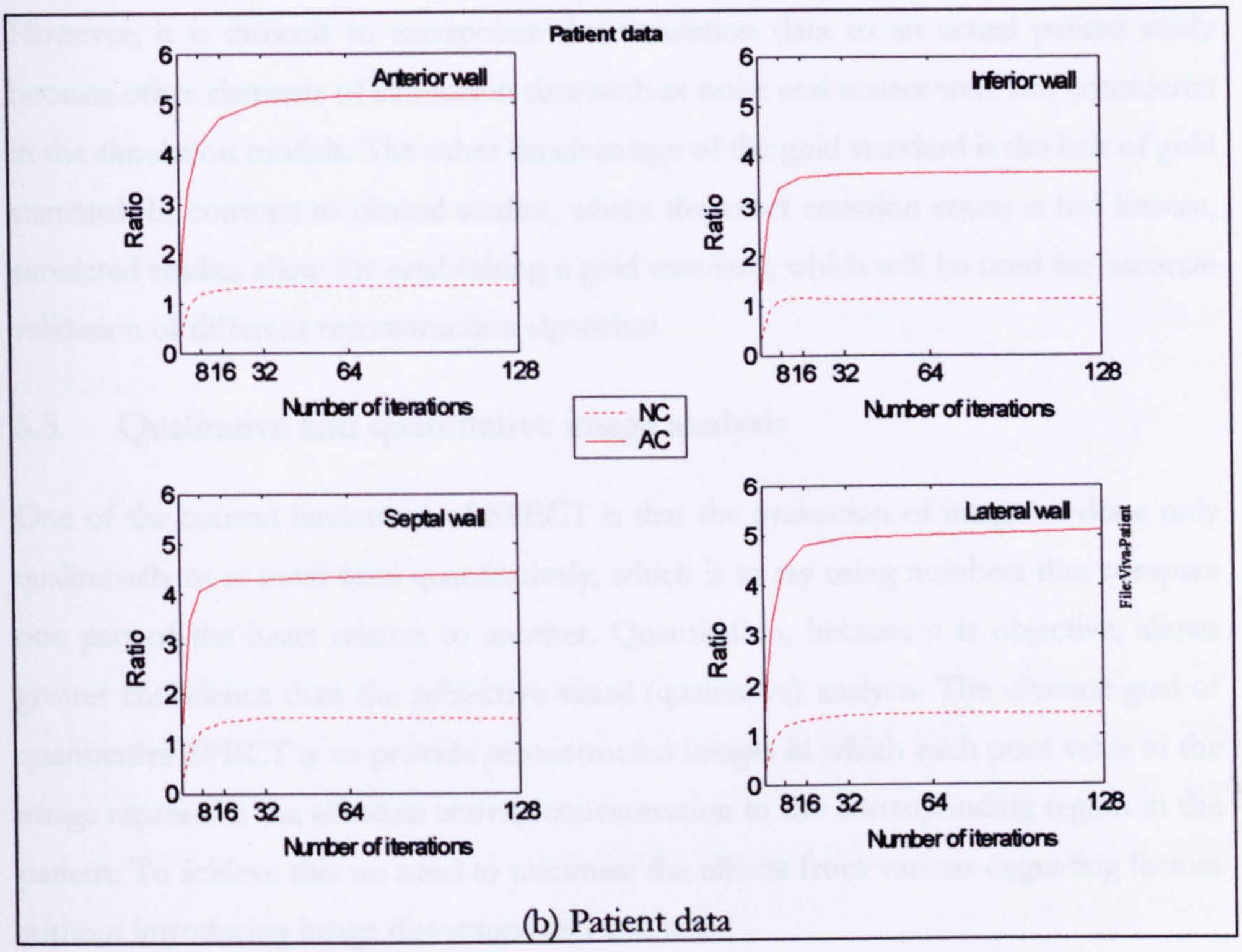

(b) Patient data

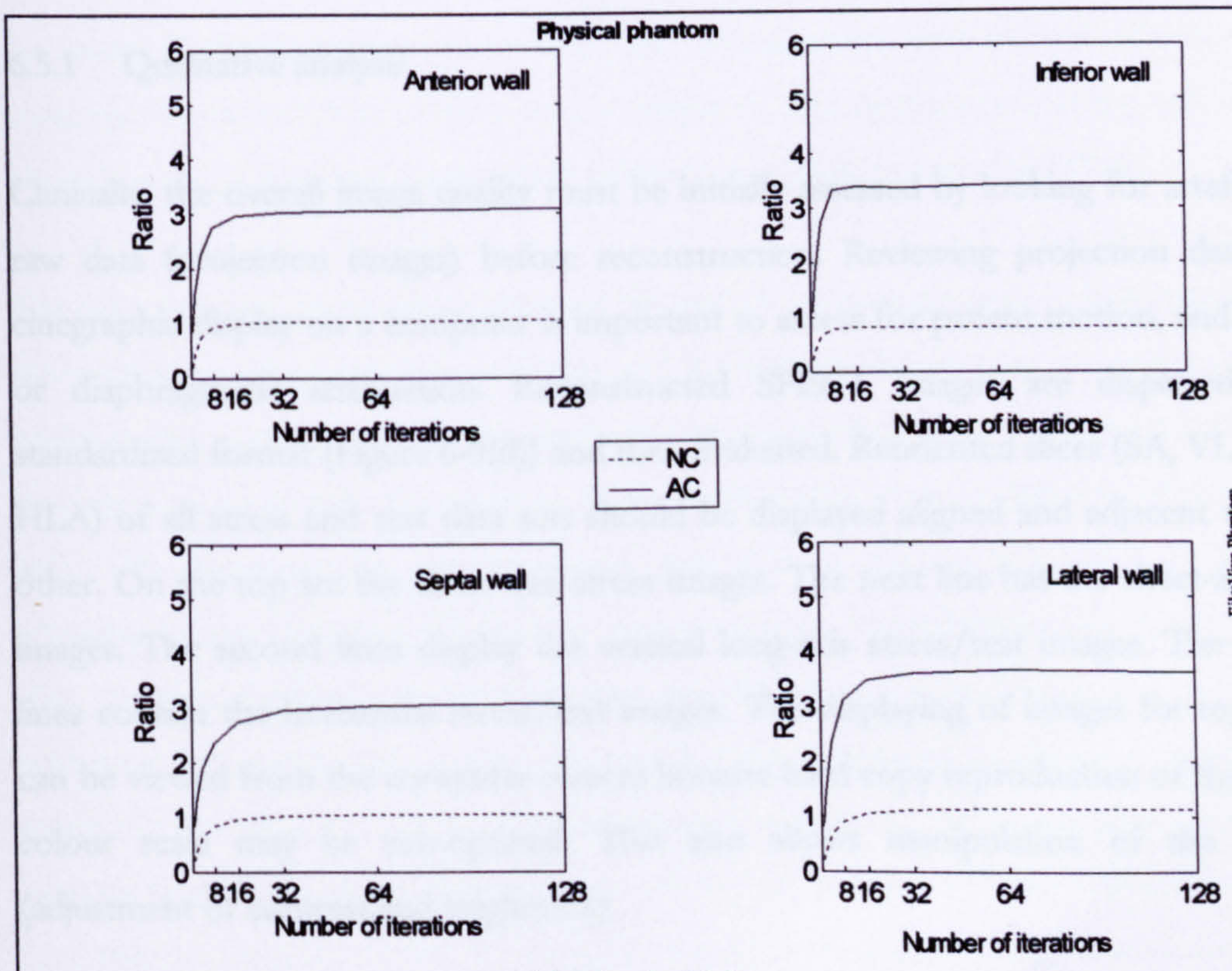

(c) Physical Phantom

Figure 6-20 Ratio of mean counts at four walls of LV in all SPECT data (a: Simulated model, b: Patient data, and c: Physical Phantom) reconstructed with and without AC using OSEM algorithm (one subset and different number of iterations).

However, it is difficult to extrapolate the simulation data to an actual patient study because other elements of simulation data such as noise and scatter were not considered in the simulation models. The other disadvantage of the gold standard is the lack of gold standard. In contrast to clinical studies, where the exact emission count is not known, simulated studies allow for establishing a gold standard, which will be used for accurate validation of different reconstruction algorithm.

6.5. Qualitative and quantitative image analysis

One of the current limitations of SPECT is that the evaluation of images is done only qualitatively or at most semi quantitatively, which is to say using numbers that compare one part of the heart relative to another. Quantitation, because it is objective, allows greater confidence than the subjective visual (qualitative) analysis. The ultimate goal of quantitative SPECT is to provide reconstructed images in which each pixel value in the image represents the absolute activity concentration in the corresponding region in the patient. To achieve this we need to minimize the effects from various degrading factors without introducing image distortions and artefacts.

6.5.1 Qualitative analysis

Clinically, the overall image quality must be initially assessed by looking for artefacts in raw data (projection images) before reconstruction. Reviewing projection data in a cinegraphic display on a computer is important to assess for patient motion, and breast or diaphragmatic attenuation. Reconstructed SPECT images are displayed in a standardized format (Figure 6-9(d)) and then evaluated. Reoriented slices (SA, VLA, and HLA) of all stress and rest data sets should be displayed aligned and adjacent to each other. On the top are the short-axis stress images. The next line has the short-axis rest images. The second lines display the vertical long-axis stress/rest images. The final 2 lines contain the horizontal stress/rest images. The displaying of images for reporting can be viewed from the computer screen; because hard copy reproduction of the image colour scale may be sub-optimal. This also allows manipulation of the images (adjustment of contrast and brightness).

Images can be displayed using two main colour scale format; continuous colour format, such as grey scale, and discrete colour format, such as spectrum scale. The colour scale involves assigning an appropriate display level to each pixel, such that its displayed brightness is proportional to the counts it contains. Pixels containing the highest counts are displayed at the maximum brightness and those with the lowest counts at minimum brightness. Pixels containing counts between these limits are displayed in intermediate shades of grey.

6.5.2 A relative perspective

It is acknowledged that in the clinical environment, images are typically normalised to the maximum of the peak value in the data set and compared on that basis. According to Anagnostopoulos [130] "Each tomographic acquisition should be displayed with the top of the colour scale at the maximum within the myocardium for each set. Displays with the top of the colour scale at the maximum of each individual tomogram and those that use the same maximum for stress and rest images should not be used. Care should be taken if the maximum lies outside the myocardium, and manual adjustment or masking for extra-cardiac activity may be required. The bottom end of the colour scale should be set to zero and background subtraction should be avoided" [130].

For our purposes, comparison between NC and AC images provides information about the correction of attenuation artefacts and indicates which images are better (with or without AC). An example is the short-axis reconstructed slices without and with AC displayed with normalisation relative to the peak counts in each data sets (Figures 6-22 and 6-23). Contrast this set of images with that of Figures 6-5 and 6-13 and the advantages/disadvantages of absolute versus relative normalisation can be examined. The absolute method compromises the breadth of the colour scale that is used to represent the counts data in the low counts images, whereas subtleties in contrast are much more evident if the grey scale maximum is equated to the counts peak. This is not such an issue when observing the counts density profiles, but relative comparison in this case requires suitable choice of normalisation in both profiles (Figures 6-16 and 6-18). The user must answer this question, "Where do we normalise to?'- inevitably this involves subjective manipulation of that data.

The value of the absolute method is that it removes all subjectivity and provides a completely objective comparison. Note that, it is assumed that appropriate correction of the absolute counts implicity reflects a similarly corrected and accurate description of the count distribution in the image. Thus, the mean absolute count becomes the metric used to quantify the effectiveness of AC. There is perhaps no a priori reason why mean counts should correlate with accuracy of reconstructed contrast across the slice, but the qualitative images presented in this thesis imply acceptable correlation. It is for reasons of objectivity and the necessity for a simple quantitative metric that absolute normalisation has been used throughout this work.

Images are best displayed and viewed with a continuous colour scale (e.g. hot metal) rather than a discrete colour scale (e.g. rainbow). This is important because several of the other colour scales can artificially enhance count difference. For example, a discrete rainbow scale can affect perception of defects at the sharp interfaces between colours [131]. This also can accentuate regional differences in counts density, leading to over-reporting of a perfusion defect [132]. For example in Figure 5-21, the same short-axis slice is displayed in two different colour scale format (continuous hot body colour scale, and a discrete rainbow colour scale for images a and b respectively). Although, the only difference in these images is the colour scale, yet the two images look very different. The septal perfusion defect shown in Figure 5-21(a) is over-emphasised when the colour scale is changed (Figure 5-21(b)) [132]. It is clear that the variation in the method of representing the SPECT images on different colour scales can significantly influence the user's perception and interpretation of the images.

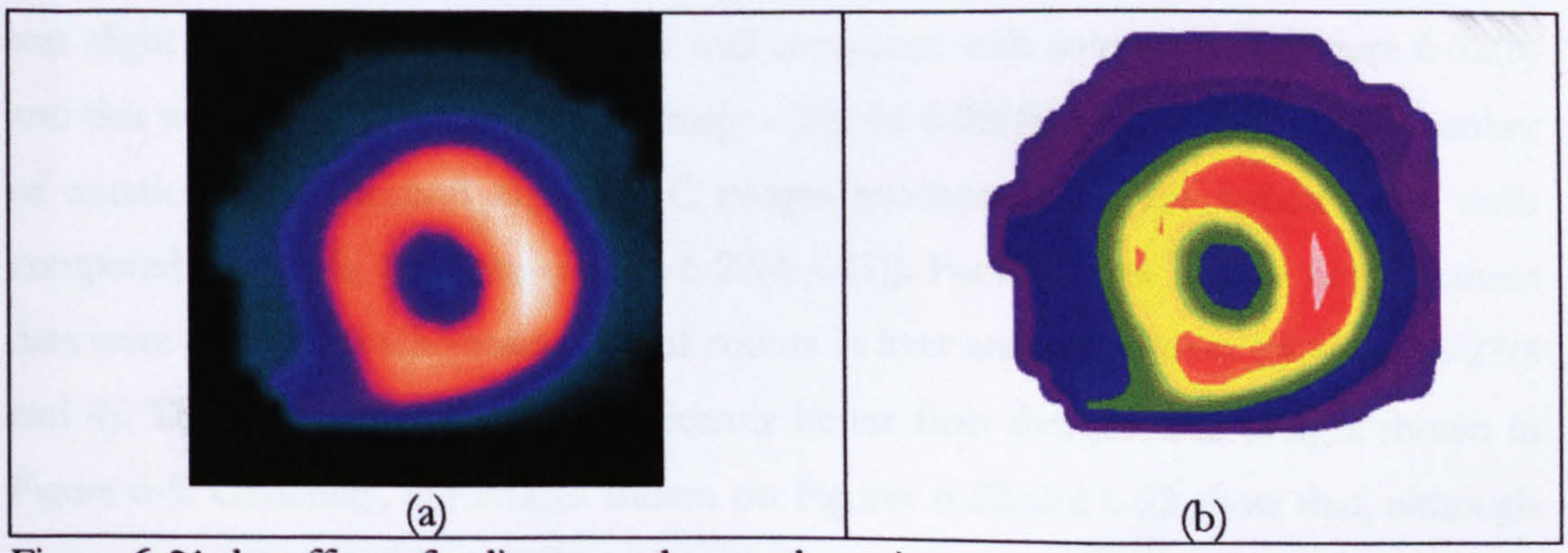

Figure 6-21 the effect of a discrete colour scale on image appearance. (a) A short-axis slices view in a continuous hot colour scale. (b) The same image as (a) in a discrete rainbow colour scale [132].

However, "it is also possible that the user can control the colour scale saturation, although care must be taken as artefactual defects may be produced by over-zealous adjustment of the scale [131]. All reconstructed images in this chapter were displayed by using the same maximum for both AC and NC images in order to show the relative difference between two sets (NC and AC images). The same short-axis slices without and with AC in both physical phantom and patient data were displayed without changing the colour scale saturation (each slice was displayed by individual maximum counts as the high level of colour scale) in order to show the absolute qualitative difference of each set of images (e.g. NC images) not in a relative manner with AC images which normalized to peak counts (as it is commonly done in the clinical setting) other set.

Individual qualitative analysis of AC images in phantom data with different numbers of iterations (Figure 6-22(2:A-G)) showed that the counts density in liver was increased as the number of iterations increases and is marginally stable after 32 iterations. This is the reason for selecting 32 iterations to make a comparison between NC and AC images (this is also supported by the counts density profiles shown on Figure 6-24). However, it is difficult to compare NC slices (Figure 6-22(1)) with AC slices due to the presence of high counts in the liver region. Therefore, counts in liver (and other counts in background) were subtracted in all slices and displayed in Figure 6-22(3 and 4). Thus, in these images OSEM with AC was compared to OSEM without AC to determine whether the OSEM algorithm can improve image quality after attenuation correction.

In Figure 6-22(4), images demonstrated increased relative counts densities in the inferior wall after AC, compared with anterior wall in AC images. Also, in the NC images there was slight counts reduction in inferior wall compared with anterior wall (Figure 6-22(3) and this was clearly corrected in AC images (Figure 6-22(4)) In addition, as the number of iterations goes beyond 32, the AC images produce a uniform uptake in all walls compared with early iterations (Figure 6-22(4:A-G)). Furthermore, images of the patient data were displayed with subtraction of counts in liver area and shown on Figure 6-23(3 and 4). These images were not significantly better than the previous images shown in Figure 6-5. Generally, the images shown on Figures 6-22 and 6-23 show that, although images were displayed in a different manner than all images showed previously in this chapter (Figures 6-13 and 6-5), still the same conclusion can be obtained.

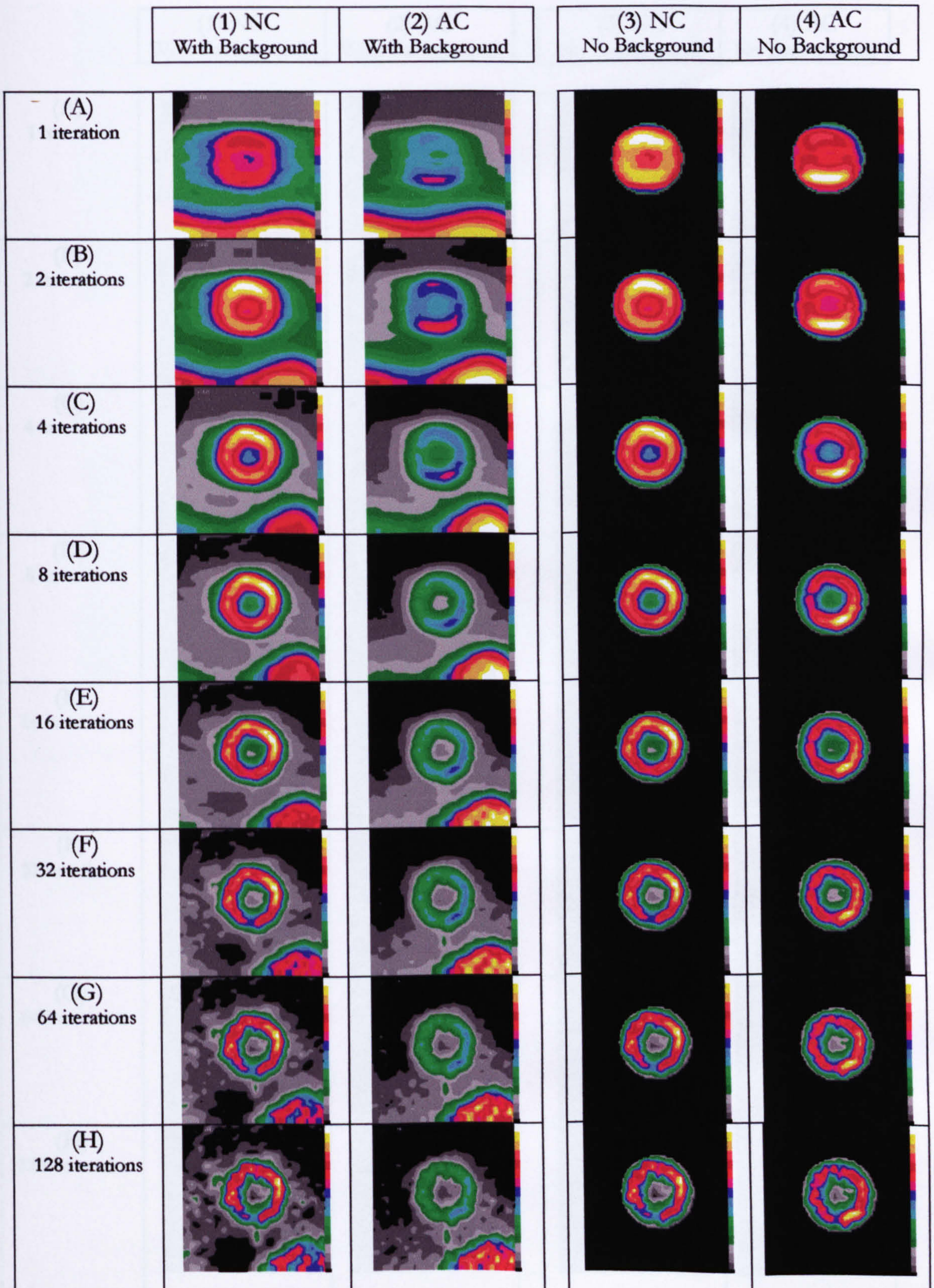

Figure 6-22 Images of Physical phantom data are reconstructed without and with AC (using 1 subset and different number of iterations; A-H). Short-axis slices are displayed properly without (1 and 2) and with background subtraction (3 and 4).

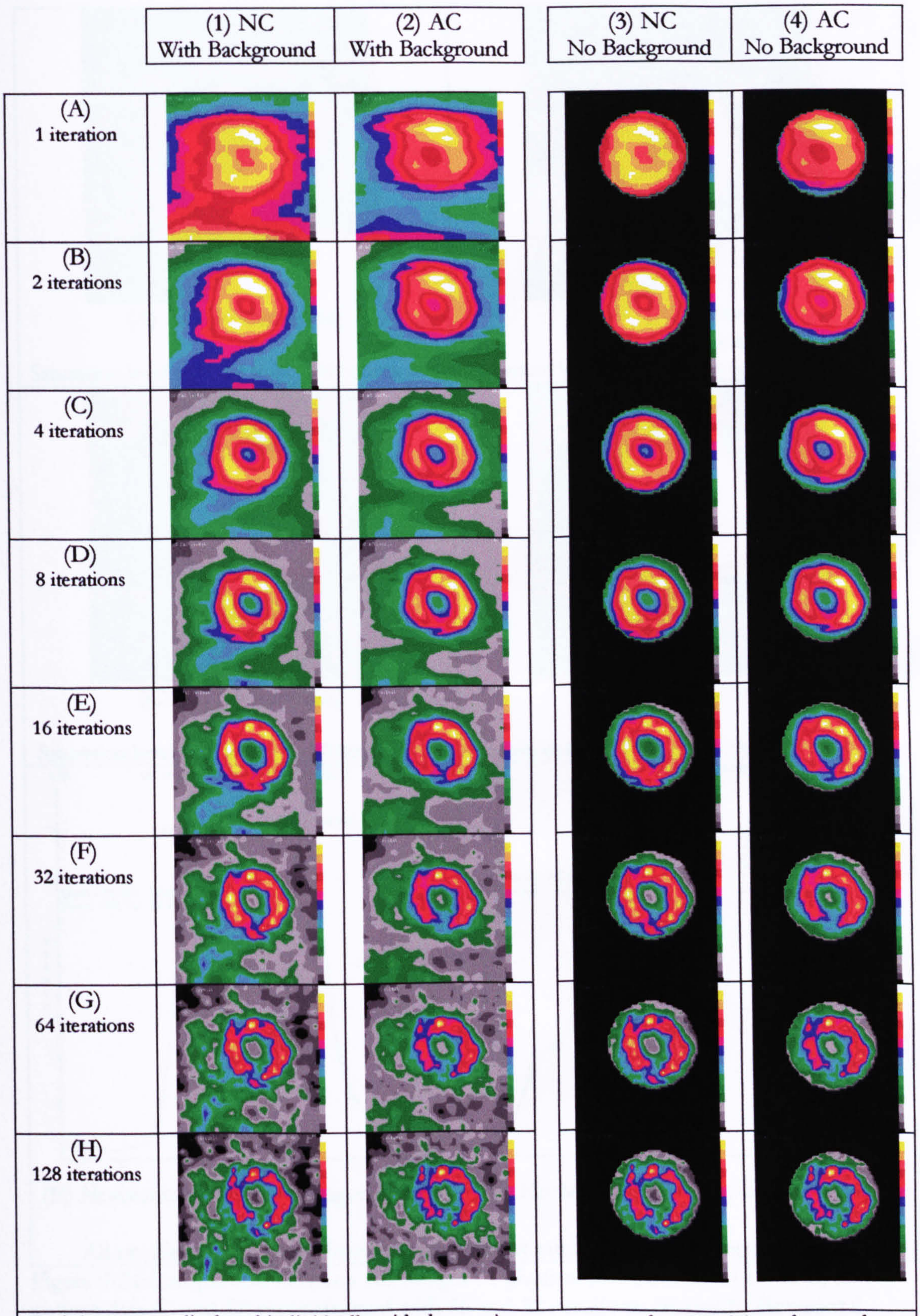

Each image was displayed individually with the maximum counts as the top of the colour scale.

Figure 6-23 Images of the patient data are reconstructed without and with AC (using 1 subset and different number of iterations; A-H). Short-axis slices are displayed properly without (1 and 2) and with background subtraction (3 and 4).

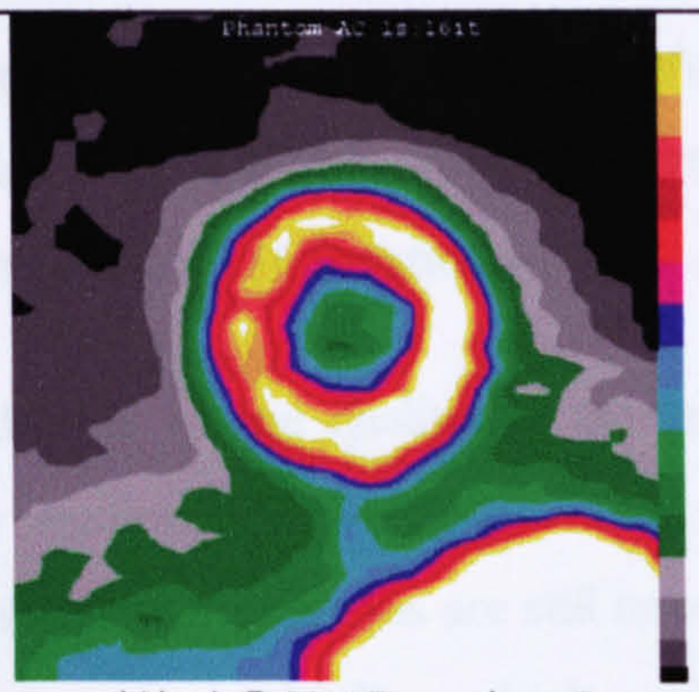

(A) AC [16 Iterations]

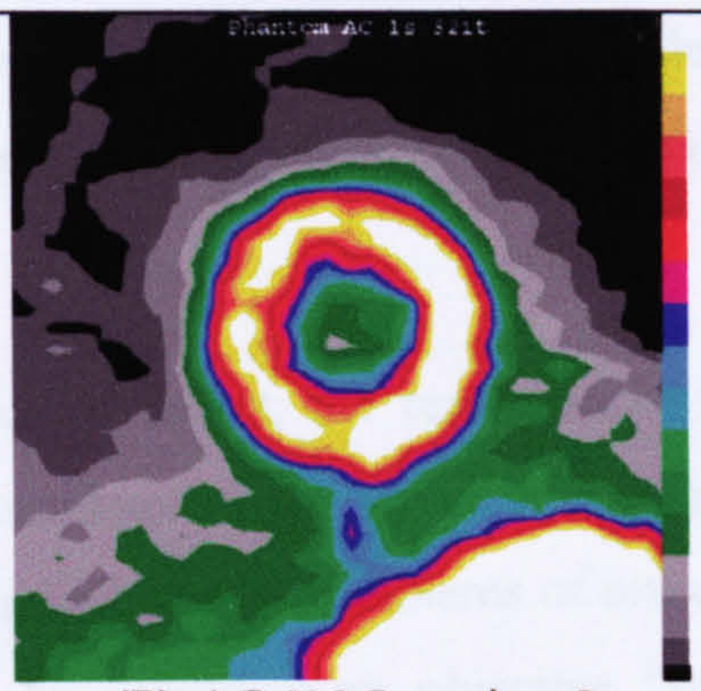

(B) AC [32 Iterations]

Physical phantom data

Saturation level selected to be 550 counts as the maximum level of the colour scale in all images

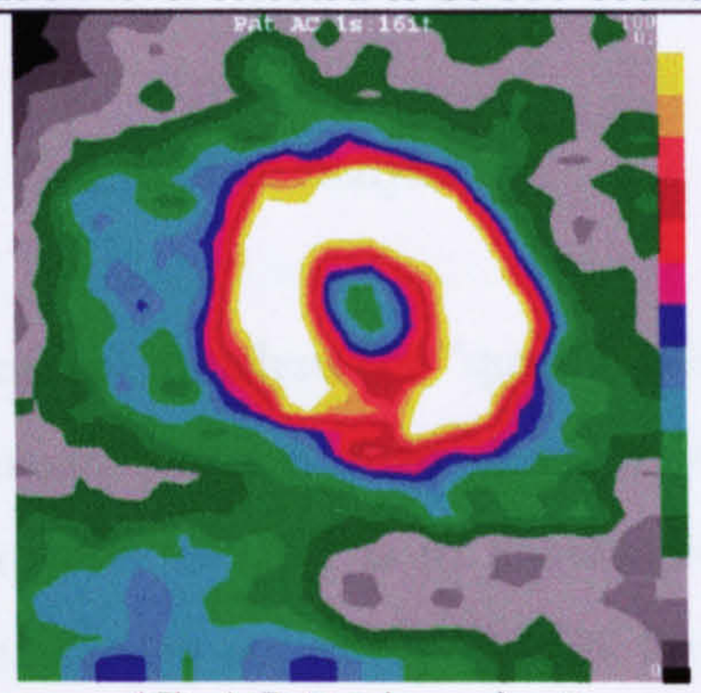

(C) AC [16 iteration]

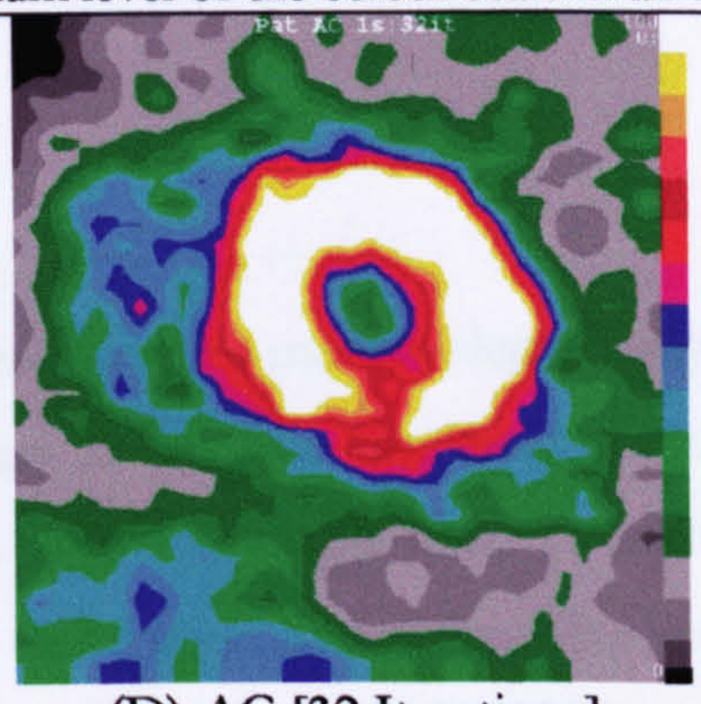

(D) AC [32 Iterations]

Patient data

Saturation level selected to be 320 counts as the maximum level of the colour scale in all images

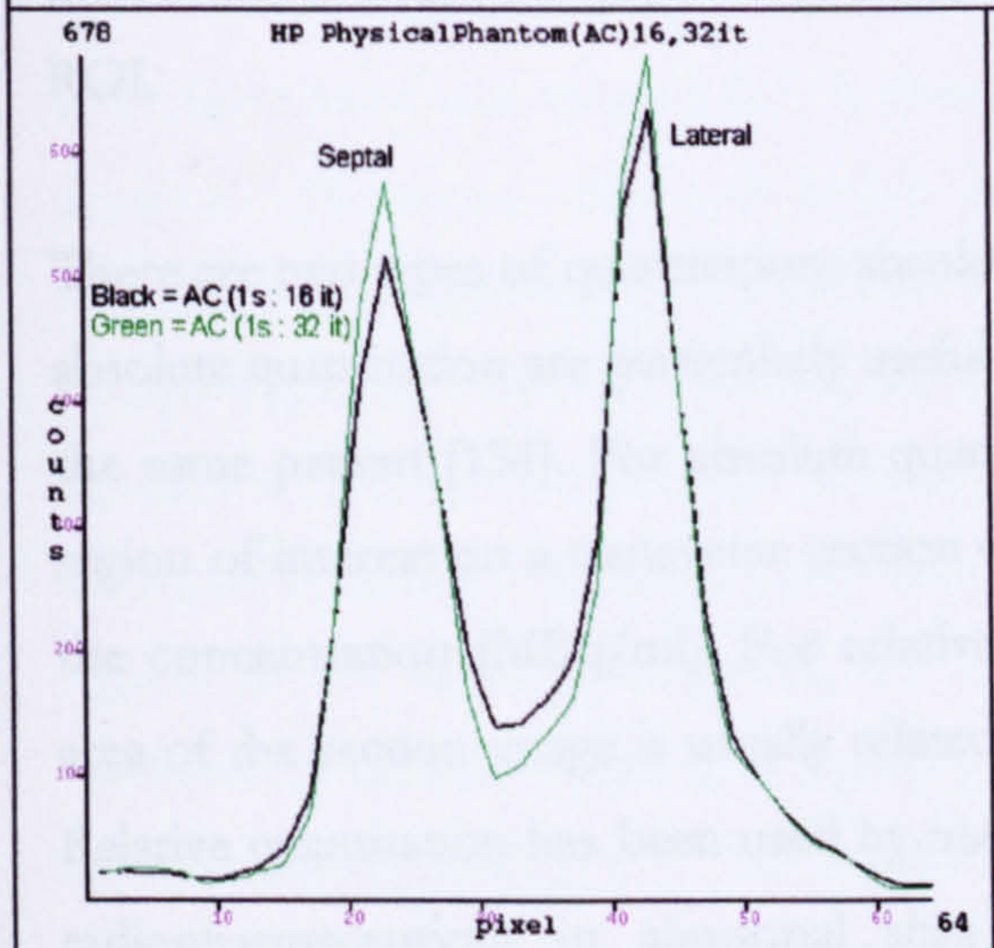

(E) Horizontal profiles of images A and B

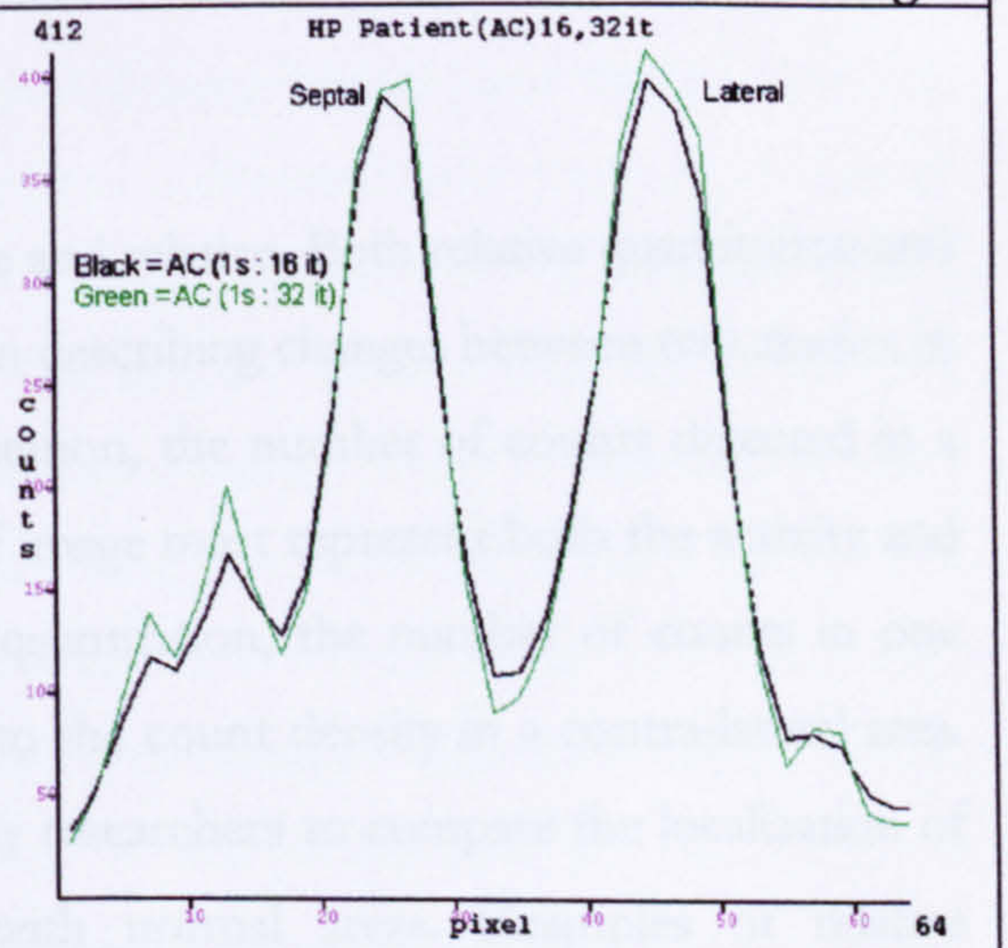

(F) Horizontal profiles of images C and D

All profiles are obtained from images without saturation level in the colour scale

Figure 6-24 Comparison between AC images of physical phantom data (A and B) and patient data (C and D) reconstructed with 16 and 32 iterations. (E and F) Horizontal counts density profiles.

Figure 6-24 shows why the AC image reconstructed with 32 iterations was selected to be the best for a comparison purpose. As it can be seen, from the horizontal counts density profiles (Figure 6-24(E and F), AC images with 32 iterations produce better counts than AC images with 16 iterations.

In addition to the qualitative assessment of perfusion defect, the reader should also apply semiquantitative approaches, which can complement the visual interpretation. Quantitative approaches are still important in circumventing the problems of intra- and interobserver variability, which assists observers by providing an objective "second opinion" and have a high degree of reproducibility [133].

6.5.3 Quantitative analysis

Quantitative analysis (or "quantitation") attempts to provide a more in-depth analysis of perfusion patterns than does visual interpretation alone. The fundamental goal of quantitative SPECT is to provide section images of uptake in the heart in which the count density accurately reflects the amount and distribution of activity. This involves drawing a region of interest (ROI) around a structure of interest in a SPECT image and then commanding the computer to compute the mean of values of the pixels within the ROI.

There are two types of quantitation: absolute and relative. Both relative quantitation and absolute quantitation are particularly useful in describing changes between two studies in the same patient [134]. For absolute quantitation, the number of counts detected in a region of interest on a transverse section of image must represent both the activity and the concentration (MBq/ml). For relative quantitation, the number of counts in one area of the section image is usually related to the count density in a contra-lateral area. Relative quantitation has been used by many researchers to compare the localization of radiopharmaceuticals in abnormal sites with normal areas. Examples of relative quantitation include the comparison of counts within two different regions of interest within the same image, or from two or more different images. It can also be the comparison of counts (or intensities) between abnormal and normal database, and the results can be displayed automatically in terms of the number of abnormal pixels or the

total number of standard deviations below the normal mean for all defective regions [135].

However, absolute quantitation of radionuclide localization in the various tissues of the body can provide more fundamental information related to our understanding of the many physiological processes in both healthy and disease tissue [136]. The absolute quantitation can be made for an area or a volume and can determine either the concentration of radioactivity or the total activity in the defined region. The activity can also be compared to the injected dose. Results can be compared from case to case without regard to imaging method or size of patient [17].

In this chapter, the semiquantitative analysis that was carried out was based on the comparison of counts within two different regions of interest from two different images (AC and NC images). The reason for using a relative quantitation is that there was no gold standard (the true activity without attenuation effect). Despite, this, relative quantitative analysis was a useful tool used to show the effectiveness of AC algorithm.

6.6. Summary

The objective of this chapter was to evaluate AC using both patient data and physical phantom. The patient data was mainly used for a demonstrative purpose. A further objective was to investigate the influence of changing the number of iterations within OSEM algorithm on AC. The results in this chapter showed that the attenuation artefacts were corrected when an attenuation map obtained from CT scan was included in OSEM algorithm. Although, attenuation artefacts were corrected in the majority of all regions of LV and cardiac insert, still some artefacts existed (either not completely corrected or partially reduced) in some regions. For example, attenuation artefacts were not completely corrected at the inferior wall of the patient data (we do not know whether this a real defect or a false defect due to uncorrected attenuation artefacts) and at part of the inferior wall (toward the base level) of the physical phantom. In addition, the results also showed that stopping reconstruction at a low number of iterations produces artefacts of uptake, and therefore, this might be an explanation of why some artefacts produced after AC in some published literature. Zaidi *et al* [71] recently believed that "the stopping criteria remain a good academic problem although iterative

algorithms used clinically are stopped after a fixed number of iterations and therefore are not run into convergence". The under-correction of counts after AC may have been due to the fact that scatter correction was not considered in these experiments. Recently Watson 2004 [137] pointed out that the "Attenuation artefacts are reduced but not eliminated and some artefacts are introduced". Despite this AC appears to have worked well.

Several factors that may affect the AC were not considered in these experiments. First, post-filtering of the reconstructed AC images was not used as a technique to decrease noise whatever the number of iteration number used in the reconstruction. Second, patient motion can be a significant source of misregistration between emission and transmission images. Third, other factors such as scatter correction might influence counts at the inferior wall. This was simply because the main objective of this chapter was a demonstrative evaluation of OSEM algorithm without and with AC only excluding any corrections methods for other physical effects (e.g. scatter, and geometric effect). Narayanan *et al* [138] demonstrated through human-observer-receiver-operating-characteristic (ROC) that OSEM algorithm with a combination of attenuation, scatter, and depth-dependent resolution compensation strategies would provide a large improvement in diagnostic accuracy for CAD than would correcting solely for attenuation. Therefore, these factors need to be considered in future studies of AC.

Chapter Seven Conclusion

The conclusion of the work presented within this thesis will be broken down into three main sections. First, the discussion of the impact of AC on the reconstructed cardiac SPECT images and some simulation issues will be discussed in section 7.1 Secondly, the results of the validation studies using all models will be summarised in section 7.2. Finally, future work will be suggested in section 7.3.

7.1. Discussion

The diagnostic accuracy of cardiac SPECT for the detection of CAD is significantly improved when attenuation correction (AC) is performed [6]. Various techniques have been proposed to correct for attenuation artefacts. Most state-of-the-art SPECT systems include the option of transmission scanning and new iterative reconstruction algorithms (OSEM), attempting to reconstruct cardiac SPECT images free from attenuation artefacts. Despite the extensive literature on AC of physical phantoms and patient studies, it appears that the use of AC in cardiac SPECT is not as widely accepted as might be expected. This is due to the perception that attenuation correction, while reducing some artefacts, appears to introduce others [139]. Published results suggest that unacceptable artefacts can be produced in myocardial SPECT images using attenuation correction, although not all workers are agreed on this. Whether the artefacts are worse or simply different is unclear.

The lack of use of AC in routine clinical practice leads naturally to the following questions; does AC produce quantitatively accurate cardiac SPECT images? and does AC create additional unfamiliar artefacts?. To answer these two questions, a series of experiments validating AC were carried out in this thesis using cardiac SPECT data and

OSEM reconstruction algorithm. The cardiac SPECT data were obtained from simulation models, physical phantoms and patient data. AC reconstructed images were inspected (qualitatively and quantitatively) to assess if the OSEM algorithm has corrected the attenuation effects and to inspect the reconstructed images for unfamiliar artefacts which might have been produced. Validation of AC using simulations and physical phantom experiments is essential prior to investing the effort in a full clinical validation [140].

7.1.1 Attenuation effect

Despite high levels of diagnostic accuracy for CAD, SPECT cardiac imaging still has several drawbacks including the production of artefacts due to interrelated physical effects. These artefacts result from the fact that the most common method for reconstructing SPECT images, the filtered back-projection (FBP) method, does not accurately model the physics of the imaging process. The physical effects not modelled include, attenuation, scatter, depth-dependent collimator response and partial volume effects. Studying the impact of these physical effects (whether individually or in combination) and methods for their correction in the reconstructed image has been an area of research over the last two decades.

If the physics of the imaging situation is modelled correctly, and incorporated into an iterative reconstruction algorithm, (such as the OSEM algorithm) this theoretically allows the production of artefact-free cardiac SPECT image (within the limit set by noise). This improves the qualitative and quantitative accuracy of SPECT imaging for the detection of CAD.

The effect of photon attenuation has a greater impact than scatter. El-Fakhri *et al* [141] investigated the influence of attenuation and scatter upon the image characteristics in cardiac SPECT in a phantom-based study and found that attenuation causes underestimation of the activity in reconstructed slices by 90%, scatter causes an overestimation the activity by about 20% after reconstruction of a 10-mm thick left ventricle wall. This study indicates that attenuation is the major physical effect limiting cardiac SPECT imaging accuracy. Attenuation artefacts are thought to be a major cause of the high incidence of false-positive diagnoses of CAD using cardiac SPECT

perfusion images [37] and therefore, in this study, attention was only paid to the impact of attenuation in cardiac SPECT data.

Attenuation is the loss of useful photons whereas scatter causes an increase in the number of photons in the background and reduces contrast. When both scatter and attenuation factors are modelled accurately and corrected, the improvement of one may be at the expense of the other. Correcting of one may produce an image, which looks worse than the uncorrected one even though the corrected image is closer to the true distribution than the uncorrected one. Some artefacts will not be particularly visible and clinically significant whereas others may be much more critical. Until it is clear that a completely correct imaging model is being used, and the images produced can be assumed to be correct representations of the underlying activity distribution, some effort must be made to assess the accuracy of a given algorithm for a specific clinical use. The errors due to the combination of two effects such as scatter and attenuation make it difficult to analyse the precise origin of errors observed on the reconstructed slice. Therefore the major focus of this work was on modelling and validating the correction method for attenuation artefacts independently from other physical factors.

7.1.2 Simulation issues

Monte Carlo modelling techniques have been widely used to simulate a variety of emission tomography (e.g. SPECT and PET) [106] [101]. Monte Carlo methods are mathematical experiments in which statistical probabilities, random numbers, and computers are combined to solve problems. The knowledge of radioactivity concentration inside the attenuation medium (as simulation of anthropomorphic voxel-based computer phantom, e.g. Zubal phantom) is commonly used in Monte Carlo simulations for simulating a very realistic clinical configuration [107] [102]. However, the Zubal phantom does not simulate the whole body (covers only head to mid-thigh). This was tackled by a voxel based whole body model, called VIP-man [142]. It is an adult male model which has been constructed from the colour photographic images of the famous Visible Human Project[21]. It is a realistic model which contains much more anatomical information (containing small tissues, such as skin, eyes, and red bone marrow). Although, this model simulates the world's finest and most complete human anatomical model [142], it simulates only the adult male model. More recently [143] a

[21] http://www.nlm.nih.gov/research/visible

GSF voxel phantom family were reconstructed using high-resolution CT data of real patients. These phantoms tend to cover persons of two paediatric ages and adult middle age, as well as both sexes, and stature, and several others are under construction [102]. They simulate the human body realistically and can find a wide spectrum of applications in medical physics where the detailed modelling of the human body is required.

These models have been adopted into the state-of-the-art Monte Carlo codes and can be used for validating image reconstruction algorithm, developing of correction methods, and evaluating of attenuation/scatter corrections [144] [126]. The major problem of Monte Carlo simulations can be due to the long time needed to run and generate enough simulated data in a time compatible with clinical use. However, the rapid progress in computational power helps Monte Carlo simulation to play an increasing role for increasing quantitative accuracy in SPECT imaging [106].

We used simulated projections with attenuation included but other physical effects, such as scatter and depth-dependent collimator effects were excluded due to the fact that the computing resources available were insufficient to generate data in a realistic time scale. Computation time is one of the most important considerations in assessing algorithms for routine clinical use. The recent installation of a large multi-processor computer system at Sheffield University (150 PC cluster) makes full simulation and reconstruction much more feasible for future work.

The scatter effect was not included in modelling because it is believed that scatter correction is best achieved outside reconstruction. Modelling scatter reliably is more difficult. Models which introduce scatter as a blurring function (i.e. treat it as part of the geometric response) cannot easily deal with the variation in scatter caused by different densities. However, other approaches to scatter correction include the measurement of one or more images of scatter at each projection and the use of this data to directly correct scatter in the projection image. If these work the projection data becomes scatter free and the problem is resolved. This seems a more principled approach than geometric modelling although the accuracy of such algorithms for SPECT needs to be more firmly established.

Modelling the geometric response of the collimator should be more straightforward, but there appear to be no examples of its use commercially. A better approach might be to try and model the image which would be produced by a gamma camera which had constant resolution with depth. Although it seems fairly clear how this might be done (smooth the scatter corrected projection data before reconstruction with a smoothing filter with a resolution equivalent to that of the gamma camera at an appropriate depth and then include the actual collimator geometry in the reconstruction) this has not been attempted as far as we are aware

7.1.3 Using phantom in validation studies

Although clinical investigations are important in checking that the image data is clinically useful they offer minimal insight into the reasons why artefacts appear. Acceptability or otherwise of such images is often subjective. Furthermore it is impossible to understand and validate the formation and compensation of artefacts due to one physical effect (such as attenuation) in the presence of many other effects (scatter and patient motion). The only way to attempt to understand the mechanisms by which artefacts are generated is through phantom studies. Physical phantoms are able to realistically generate data, which includes scatter and geometric effects, but commonly lack anatomical credibility. Software phantoms can hope to more closely mimic anatomy and, if enough computation effort is put in, can come close to generating realistic data. However, it may take much longer to generate the data than to prepare and scan a hardware phantom. However, because the physical effects, such as scatter and attenuation, can be isolated in software models they represent a key tool in understanding the origin of the artefacts that are seen in the images. Studies with simulated data are not a substitute for clinical studies, but the validation results of such a study can aid in the interpretation of the results.

In this work we have attempted to use a realistic software phantom to generate cardiac SPECT data. Given an anatomical phantom of sufficient sophistication and appropriate isotope uptake data there appears to be no fundamental reason why realistic image data cannot be generated by computer. We expect this approach to be used more widely as good anatomical models become widely available and adequate computing power becomes more widespread.

7.1.4 OSEM algorithm

The aim of image reconstruction is to replicate the data from which projections are generated. Iterative reconstruction algorithms generate projections from a current estimate, which is then compared to the measured projections. The difference between the estimated and measured projections, i.e. the "error", is then back-projected and used to update the current estimate. The process is iterated until some stopping criteria is met and usually many iterations have to be performed to obtain the final acceptable image. All physical effects can be incorporated in the model of the imaging system at the forward projection stage. The major disadvantages of the iterative algorithm are the slow convergence rate to an acceptable image and the high computational cost for a practical implementation. The slow convergence can be overcome by using a large number of iterations which leads to the resulting image becoming noisy. The computational cost was reduced by using the OSEM algorithm (an accelerated version of the EM algorithm) which is typically quite fast, requiring only a few iterations to produce an image acceptable to many users. However, the OSEM algorithm does not converge to the maximum likelihood solution, except for the case of noise-free data [119]. Practically, for noisy projection data, the final image with acceptable convergence (following a high number of iterations) has a very noisy appearance and is no use clinically. Clinically useful images can be achieved by stopping the iterative procedures long before the convergence is reached, or by applying post-filtering processing.

In the literature there are some clinical studies claiming that OSEM attenuation correction does not present significant improvement in the AC reconstructed image compared to FBP without AC. Others claim that the reconstructed image with AC could produce new artefacts [3], [4], [5]. The origin of these artefacts could be due to the deteriorated images after AC with a small number of iterations (computational time is greatly reduced) which can still acceptable to some users and provide useful clinical information. Despite this, some users decided to stop the OSEM algorithm earlier, even though it is not fully converged. Alternatively the number of iterations can be increased until it converges and the noise can be controlled after reconstruction.

Furthermore, these validation and evaluation experiments have explored the importance of the choice of the iteration stopping point, which is generally determined empirically for each individual application based on an acceptable level of noise. Mustafovic *et al*

2004 [145] also pointed out that the criteria for early stopping of the OSEM reconstruction before the image becomes too noisy can be difficult since different parts of the image converge at different rates, leading to non-uniformities in the final image.

7.1.5 Scaling factor

For an iterative reconstruction algorithm it is clear that the final image must match the original activity data. However, much image data, including projection data, is stored in integer form and this can lead to problems of rounding errors or overflow when such data is used. Image reconstruction algorithms may attempt to deal with some of these issues by use of internal scaling factors. As a consequence the final image is a scaled version of the underlying activity distribution. Although this may not be important for visual interpretation of the image it does potentially raise difficulties when comparing images. This is especially true when comparing images produced by different algorithms, for example FBP and OSEM. In chapter 4, we calculated experimentally scaling factors, which can be used to relate the amplitude of the reconstructed images to the amplitude of the original data. These scaling factors have been used throughout the work.

7.1.6 Misregistration issue

A key assumption is that the attenuation data and the emission data are in registration. Clearly if the data were misregistered, artefacts may be generated in the final reconstructed image. The new hybrid Hawkeye system achieves registration by collecting data on the same imaging system without moving the patient. However, patients may move within the period of data collection as well as between the collection of the emission data and the transmission data if these are collected serially. There is little data on the effects of misregistration on the quality of the images and it may be that this is a dominant effect. In Chapter 5 (section 5.8), data from a single simulation were used to investigate the magnitude of possible artefacts from patient movement. Clearly, more work needs to be done on this misregistration issue. The simulation done in this study suggests that misregistration of the order of 1 cm does produce significant errors. Recent study (2004) by Fricke *et al* [127] on 140 patients and phantom data acquired using Hawkeye hybrid imaging system and reconstructed by OSEM algorithm indicated that misalignment between SPECT emission data and attenuation map can lead to artefacts in the apical, septal, and anterior wall, which appears as a defect. These artefacts can cause overcorrection in the basal inferior and lateral segments. They also

suggest "the co registration of SPECT and the attenuation map needs to be verified for every patient, even when using integrated dual-modality imaging devices"

7.1.7 Gold standard model

Validation of image reconstruction invariably requires comparison with a 'gold standard'. In some cases this may be the underlying distribution of activity but such a comparison may not always be appropriate. Because of the limitations of any imaging system we know that the reconstructed image will not be perfect, even if all the conditions for correct reconstruction are met. Still the final image will be blurred. A better 'gold standard' might be an image which has been reconstructed under ideal conditions. In this thesis we generate data without attenuation being present and use this image as a 'gold standard' for images generated from data in which attenuation was included but which used a reconstruction algorithm which included attenuation correction. The reconstructed images (AC and NC) are then compared with the reference gold standard image. The comparison of reconstructed images with the gold standard was relatively straightforward because the gold standard images were free from attenuation effects (no noise, and no scatter effects were included).

We might reasonably argue that if the second algorithm can produce data equal to that in the first case then attenuation correction works. There are some complications to this approach since there are some free parameters in the reconstruction algorithms used, principally the number of iterations. Although in the above cases we could use the same number of iterations in both cases it may be that when attenuation effects are not present in the data and attenuation correction is not used convergence to the solution may be faster than in the case where attenuation is present. Equal numbers of iterations may not be equivalent. We have not solved this problem. Nevertheless we believe the approach is still useful. More pragmatically, problems with reconstruction of myocardial images are often expressed as decreases or increases in counts within the four walls of the left ventricle. Therefore, the relative counts in the four walls were used to assess accuracy of reconstruction.

7.1.8 Physical phantom and patient data

Some data from a physical phantom and a patient has also been included. In these cases, we do not have any 'gold standard'. We note that the images from the physical

phantom reconstruct reasonably well, even though this data contains scatter. The distribution of activity in the wall of the phantom heart should be uniform. We note that this is almost the case, especially with large numbers of iterations (beyond 16 iterations). On the other hand, low number of iterations produces images with non-uniform uptake. This illustrates the importance of when to stop the iterations and shows that stopping criteria remains an issue in algorithms used clinically. Despite this, AC appears to have worked well. Although the patient data is less easy to interpret since we have no knowledge of the true distribution of the tracer the AC corrected images do appear to be more uniform. Some uncorrected counts at inferior wall might be due to a real defect.

Despite the use of a relative semiquantitative analysis in chapter 6 (with no gold standard compared with the simulated data presented in chapter 5), our results using relative counts in region of interest in both AC and NC images showed that attenuation artefacts in AC images were corrected quite reasonably when compared with the NC images. Furthermore, the physical phantom and patient data, before and after applying AC were compared using counts density profiles. Both measured mean counts in LV walls and counts density profiles were used successfully as a useful quantitative approach to evaluate the efficacy of AC technique (using OSEM algorithm and transmission images obtained from CT system) for correcting attenuation artefacts in cardiac SPECT imaging.

It is always desirable to correct images for all errors so that accurate quantitative images may be produced. Realistically, this is never entirely possible because the reconstructed solution is not unique and only represents one of many solutions that are consistent with the projection dataset. Nonetheless, it is important for a research-oriented department to undertake simulation studies and physical experiments in order to fully understand the algorithms used and to be able to recognize their limitations. In this thesis, examples have been shown that indicate that significant improvement of attenuation artefacts is possible for imaging of the LV, based on results using absolute quantitation in a 3D simulation model and using relative quantitation in a physical phantom and patient data.

7.2. Conclusion

Based on the experiments carried out in this thesis the following conclusions can be drawn:

1. The validation results in this thesis demonstrate that OSEM reconstruction can produce more reliable and quantitatively more accurate results than FBP. Therefore, for the next few years there may be a replacement of FBP by OSEM iterative algorithms (or other versions of iterative reconstruction algorithms). In future, the majority of hospitals may shift image reconstruction from a conventional FBP algorithm to an iterative algorithm. This is mainly due to iterative algorithms allowing the incorporation of such factors as attenuation and scatter corrections. Kontaxakis [119] believed that "Iterative reconstruction techniques are becoming more and more popular, as they produce images of better contrast and signal-to-noise-ratio than conventional FBP".
2. Based on the validation experiments carried out on cardiac SPECT data obtained from simulation models (both uniform and non-uniform), it is concluded that OSEM algorithm can be reasonably reliable and robust in correcting attenuation artefacts (especially when taking only the attenuation artefacts into account and excluding other artefacts such as scatter and motion in modelling and correction).
3. One concern in this project was the attenuation artefact at the anterior wall, which was under-corrected (or overcorrected especially when there was a misregistration error between emission and transmission scans). This finding was also noted by Baily *et al*, [82] who reported that "if we accept the proposal that AC does work, we are then left with the question as to what is causing the confusing results, especially in the anterior wall and apex of the heart".
4. The nonuniformity additional artefacts (after applying AC) were qualitatively observed only when high number of iterations was used to reconstruct the simulated noiseless data with AC. In the case of noisy data, some artefacts were observed in the reconstructed image, but these were less significant (the FRMSE in all images were within 10%). The noise was simulated only in emission data (with only a single noise level), and the transmission models

were free from noise. However, when other levels of noise (from moderate to severe) in both emission and transmission model and scatter simulation, are incorporated in the reconstruction this probably leads to additional artefacts in the AC images.

5. According to the validation results of both patient data and the physical phantom, it was found that the attenuation artefacts were significantly corrected in the majority of cardiac walls with some artefacts were under-corrected in inferior wall (in patient data) and anterior wall (in physical phantom). The addition of scatter correction to AC would likely improve the results with physical phantom without altering the fundamental conclusion of this work. However, because the actual emission counts before reconstruction (gold standard) is not known, it is difficult to determine whether OSEM-AC corrects the counts to a level equivalent (higher or lower) to the reference level. Although, the OSEM produce images with improved counts after AC, still the lack of gold standard is the main disadvantage of the clinical study.
6. In general, this validation study indicates that OSEM algorithm is able to substantially correct attenuation artefacts of cardiac SPECT images using transmission-based attenuation map.
7. However, the issue of the clinical usefulness of AC remains as a matter of describing the glass as half empty or half full. Recently, Watson 2004 [137] believed that "The path to widespread clinical implementation of AC is not yet clear. Nevertheless, it is clear that AC can offer significant benefits to clinical SPECT imaging and should be further developed and integrated into standard practice".

In conclusion, despite the fact that, these validation results are only accurate and as relevant as the simulated models used to generate the SPECT data, still the results of this work strongly suggest that OSEM attenuation correction using data that simulates attenuation artefacts only can accurately correct for these artefacts when the correct number of iterations is selected. It also appears that there is no evidence from the simulated models that AC generates additional artefacts (after AC). If such artefacts exist quantitatively then they must arise either from early stopping of the OSEM algorithm or from other sources e.g. scatter or misregistration. The present study

revealed the improvement in cardiac SPECT studies and thus OSEM reconstruction algorithm is recommended for AC in clinical situations.

7.3. Future work

Accurate cardiac SPECT quantification could possibly be obtained when all attenuation, scatter, and motion corrections are applied to the reconstructed image accurately with no additional artefacts in the final corrected image. Therefore, for any future validation studies, a simulation which includes modelling of attenuation, scatter, motion, and noise (in both emission and transmission models) in all female and male models may lead to further improvement in accurate correction of SPECT cardiac images. Further work should focus on the validation of AC combined with scatter correction on clinical data. Bokulic *et al* [146] believed that, when AC is combined with scatter correction, it represents a significant advance in cardiac SPECT imaging and holds great promise for improved assessment of cardiac patient. A recent study by Khalil *et al* 2004 [147], concluded that the expected improvement when combining attenuation and scatter correction on the diagnostic accuracy of clinical cardiac SPECT images requires further study.

Further study also has to determine how the accuracy of AC depends on the quality of the attenuation map. Kashiwagi *et al* [139] claims that the low-quality transmission scan images resulting from low photon flux, and the algorithms that are used, can cause inaccurate corrections. The qualitative accuracy of the attenuation map depends on the transmission system used and the degree of misregistration of the transmission scan related to the emission scan. The misregistration can be at a maximum when the CT scan is acquired with much longer time in addition to the long acquisition time of SPECT scans. The possibility of body motion artefacts, especially for a patient who find it challenging to remain still through CT/SPECT examination remains a problem. Patient motion can be the most important obstacle to exact matching (co-registration) of the CT and SPECT images. One of the most significant recent developments in CT technology has been the emergence of a new generation of CT system, which called multi-slice CT (MSCT) system. In contrast to conventional single-slice CT (SSCT) scanner, in which the x-ray source illuminates a single row of detector elements, the

multi-slice system has multiple detectors of elements (4-rows of detectors). The advantage of this new MSCT system is the ability to do faster scanning by acquiring one slice in 0.13 second (30 slices in a total scan time of 3.9 seconds) [148] compared to 14 seconds per slice in SSCT [69]. These new MSCT systems (in the future more number of detectors will be involved, e.g. 32-rows of detectors) will reduce the likelihood of non-cardiac motion artefacts and thus contributed to CT/SPECT scans with minimum registration error. Therefore, the influence of the misregistration error on AC needs further investigation especially using the new generation of hybrid system (SPECT and fast MSCT).

In summary, it can be said that the OSEM algorithm has a clear advantage in correcting attenuation artefacts in cardiac SPECT data, and therefore is recommended to improve SPECT imaging quantitatively. Although, validation of AC using simulated data was applicable only to the situation modelled in this study, further validation studies will undoubtedly appear in the near future aiming for broader acceptance of the use of AC in myocardial SPECT imaging in routine clinical practice.

References

1. Wackers FJ: **Should SPET attenuation correction be more widely employed in routine clinical practice? Against.** *Eur J Nucl Med Mol Imaging* 2002, **29**(3):412-415.

2. Pretorius PH, Narayanan MV, Dahlberg ST, Leppo JA, King MA: **The influence of attenuation and scatter compensation on the apparent distribution of Tc-99m sestamibi in cardiac slices.** *J Nucl Cardiol* 2001, 8(3):356-364.

3. O'Connor MK, Kemp B, Anstett F, Christian P, Ficaro EP, Frey E, Jacobs M, Kritzman JN, Pooley RA, Wilk M: **A multicenter evaluation of commercial attenuation compensation techniques in cardiac SPECT using phantom models.** *J Nucl Cardiol* 2002, 9(4):361-376.

4. Corbett JR, Ficaro EP: **Clinical review of attenuation-corrected cardiac SPECT.** *J Nucl Cardiol* 1999, **6**(1 Pt 1):54-68.

5. Stowers SA, Umfrid R: **Supine-prone SPECT myocardial perfusion imaging: the poor man's attenuation compensation.** *J Nucl Cardiol* 2003, **10**(3):338.

6. Ficaro EP, Fessler JA, Shreve PD, Kritzman JN, Rose PA, Corbett JR: **Simultaneous transmission/emission myocardial perfusion tomography. Diagnostic accuracy of attenuation-corrected 99mTc-sestamibi single-photon emission computed tomography.** *Circulation* 1996, **93**(3):463-473.

7. Kluge R, Sattler B, Seese A, Knapp WH: **Attenuation correction by simultaneous emission-transmission myocardial single-photon emission tomography using a technetium-99m-labelled radiotracer: impact on diagnostic accuracy.** *Eur J Nucl Med* 1997, **24**(9):1107-1114.

8. Vidal R, Buvat I, Darcourt J, Migneco O, Desvignes P, Baudouy M, Bussiere F: **Impact of attenuation correction by simultaneous emission/transmission tomography on visual assessment of 201Tl myocardial perfusion images.** *J Nucl Med* 1999, **40**(8):1301-1309.

9. Hendel RC, Berman DS, Cullom SJ, Follansbee W, Heller GV, Kiat H, Groch MW, Mahmarian JJ: **Multicenter clinical trial to evaluate the efficacy of correction for photon attenuation and scatter in SPECT myocardial perfusion imaging.** *Circulation* 1999, **99**(21):2742-2749.

10. Banzo I, Pena FJ, Allende RH, Quirce R, Carril JM: **Prospective clinical comparison of non-corrected and attenuation- and scatter-corrected myocardial perfusion SPECT in patients with suspicion of coronary artery disease.** *Nucl Med Commun* 2003, **24**(9):995-1002.

11. Hendel RC, Kiat H, Follansbee WP, Heller GV, Cullom SJ, Berman DS: **Correction of photon attenuation in SPECT myocardial perfusion imaging: preliminary results of multicenter trial.** *J Nucl Med* 1996, **37**:176P.

12. Lee DS, So Y, Cheon GJ, Kim KM, Lee MM, Chung JK, Lee MC: **Limited incremental diagnostic values of attenuation-noncorrected gating and ungated attenuation correction to rest/stress myocardial perfusion SPECT in patients with an intermediate likelihood of coronary artery disease.** *J Nucl Med* 2000, **41**(5):852-859; discussion 860-852.

13. Aaronson P, Ward J, Winer C, Schulman S, Gill J: **The Cardiovascular System at a Clance,** 1 edn. Oxford: Blackwell science Ltd; 1999.

14. Strauss HW, Griffeth, L.K., Shahrokh, F.D., and Gropler, R.J.: **Cardiovascular System.** In: *Nuclear Medicine Technology and Techniques.* Edited by Bernier DR CP, and Langan JK, 4 edn. Missouri: Mosby; 1997: 323-354.

15. Tortora GJ, and Anagnostakos, N.P.: **Principles of Anatomy and Physiology,** 5 edn. New York: Harper & Row; 1987.

16. Higley B, Smith FW, Smith T, Gemmell HG, Das Gupta P, Gvozdanovic DV, Graham D, Hinge D, Davidson J, Lahiri A: **Technetium-99m-1,2-bis[bis(2-ethoxyethyl) phosphino]ethane: human biodistribution, dosimetry and safety of a new myocardial perfusion imaging agent.** *J Nucl Med* 1993, **34**(1):30-38.

17. Rosenthal MS, Cullom J, Hawkins W, Moore SC, Tsui BM, Yester M: **Quantitative SPECT imaging: a review and recommendations by the Focus Committee of the Society of Nuclear Medicine Computer and Instrumentation Council.** *J Nucl Med* 1995, **36**(8):1489-1513.

18. Jahns MJ: **The influence of penetrating radiation on collimator performance.** *Phys Med Biol* 1981, **26**(1):113-124.

19. Fleming JS, Alaamer AS: **Influence of collimator characteristics on quantification in SPECT.** *J Nucl Med* 1996, **37**(11):1832-1836.

20. Jaszczak RJ, Greer KL, Coleman RE: **SPECT using a specially designed cone beam collimator.** *J Nucl Med* 1988, **29**(8):1398-1405.

21. Gullberg GT, Tsui BM, Crawford CR, Ballard JG, Hagius JT: **Estimation of geometrical parameters and collimator evaluation for cone beam tomography.** *Med Phys* 1990, **17**(2):264-272.

22. Kimiaei S, Larsson SA, Jacobsson H: **Collimator design for improved spatial resolution in SPECT and planar scintigraphy.** *J Nucl Med* 1996, **37**(8):1417-1421.

23. Links JM: **General Electric-Healthcare.,** http://egems.gehealthcare.com/geCommunity/nmpet/education/nm_intro/collimator.jsp.

24. Links JM: **Multidetector single-photon emission tomography: are two (or three or four) heads really better than one?** *Eur J Nucl Med* 1993, **20**(5):440-447.

25. Groch MW, Erwin WD: **Single-photon emission computed tomography in the year 2001: instrumentation and quality control.** *J Nucl Med Technol* 2001, **29**(1):12-18.

26. Watson DD, Smith WH: **SPECT: current and future developments.** *J Nucl Biol Med* 1992, **36**(2 Suppl):108-112.

27. Garcia EV, Faber TL, Galt JR, Cooke CD, Folks RD: **Advances in nuclear emission PET and SPECT imaging.** *IEEE Eng Med Biol Mag* 2000, **19**(5):21-33.

28. Bacharach SL, Bax JJ, Case J, Delbeke D, Kurdziel KA, Martin WH, Patterson RE: **PET myocardial glucose metabolism and perfusion imaging: Part 1-Guidelines for data acquisition and patient preparation.** *J Nucl Cardiol* 2003, **10**(5):543-556.

29. Groch MW, Erwin WD: **SPECT in the year 2000: basic principles.** *J Nucl Med Technol* 2000, **28**(4):233-244.

30. Brooks RA, Di Chiro G: **Theory of image reconstruction in computed tomography.** *Radiology* 1975, **117**(3 Pt 1):561-572.

31. Larsson SA: **Gamma camera emission tomography. Development and properties of a multi-sectional emission computed tomography system.** *Acta Radiol Suppl* 1980, **363**:1-75.

32. Patton JA, Budinger TF: **Single Photon Emission Computed Tomography.** In: *Diagnostic Nuclear Medicine.* Edited by Sandler MP, Coleman RE, Patton JA, Wackers FJ, Gottschalk A, 4th edn. USA: Lippincott Williams & Wilkins; 2003: 43-59.

33. Tung CH, Gullberg GT: **A simulation of emission and transmission noise propagation in cardiac SPECT imaging with nonuniform attenuation correction.** *Med Phys* 1994, **21**(10):1565-1576.

34. Bruyant PP: **Analytic and iterative reconstruction algorithms in SPECT.** *J Nucl Med* 2002, **43**(10):1343-1358.

35. Tsui BM, Frey EC, LaCroix KJ, Lalush DS, McCartney WH, King MA, Gullberg GT: **Quantitative myocardial perfusion SPECT.** *J Nucl Cardiol* 1998, **5**(5):507-522.

36. Hudson HM, Larkin RS: **Accelerated image reconstruction using ordered subsets of projection data.** *IEEE Trans Med Imag* 1994, **MI-13**:601-609.

37. King MA, Tsui BM, Pan TS: **Attenuation compensation for cardiac single-photon emission computed tomographic imaging: Part 1. Impact of attenuation and methods of estimating attenuation maps.** *J Nucl Cardiol* 1995, **2**(6):513-524.

38. King MA, Tsui BM, Pan TS, Glick SJ, Soares EJ: **Attenuation compensation for cardiac single-photon emission computed tomographic imaging: Part 2. Attenuation compensation algorithms.** *J Nucl Cardiol* 1996, **3**(1):55-64.

39. DePuey EG, 3rd: **How to detect and avoid myocardial perfusion SPECT artifacts.** *J Nucl Med* 1994, **35**(4):699-702.

40. Galt JR, Cullom J, Garcia EV: **Attenuation and scatter compensation in myocardial perfusion SPECT.** *Semin Nucl Med* 1999, **29**(3):204-220.

41. Yester M: **Theory of Tomographic Image Reconstruction.** In: *Nuclear Medicine.* Edited by Henkin RE BM, . Dillehay GL,. Halama JR,. Karesh SM,. Wagner RH,. Zimmer AM,. USA: Mosby; 1996: 222-231.

42. Tsui B: **Quantitative SPECT.** In: *Nuclear Medicine.* Edited by Henkin RE BM, . Dillehay GL,. Halama JR,. Karesh SM,. Wagner RH,. Zimmer AM,. vol. 1. USA: Mosby; 1996: 260-278.

43. Chang L-T: **A method for attenuation correction in radionuclide computed tomography.** *IEEE Trans Nucl Sci* 1978, **25**:638-643.

44. Rajeevan N, Zubal IG, Ramsby SQ, Zoghbi SS, Seibyl J, Innis RB: **Significance of nonuniform attenuation correction in quantitative brain SPECT imaging.** *J Nucl Med* 1998, **39**(10):1719-1726.

45. Bailey DL: **Transmission scanning in emission tomography.** *Eur J Nucl Med* 1998, **25**(7):774-787.

46. Stone CD, McCormick JW, Gilland DR, Greer KL, Coleman RE, Jaszczak RJ: **Effect of registration errors between transmission and emission scans on a SPECT system using sequential scanning.** *J Nucl Med* 1998, **39**(2):365-373.

47. Ficaro EP, Fessler JA, Rogers WL, Schwaiger M: **Comparison of americium-241 and technetium-99m as transmission sources for attenuation correction of thallium-201 SPECT imaging of the heart.** *J Nucl Med* 1994, **35**(4):652-663.

48. Jaszczak RJ, Chang LT, Stein NA, Moore FE: **Whole-body single-photon emission computed tomography using dual, large-field-of-view scintillation cameras.** *Phys Med Biol* 1979, **24**(6):1123-1143.

49. Ljungberg M, Strand SE: **Attenuation correction in SPECT based on transmission studies and Monte Carlo simulations of build-up functions.** *J Nucl Med* 1990, **31**(4):493-500.

50. Bailey DL, Hutton BF, Walker PJ: **Improved SPECT using simultaneous emission and transmission tomography.** *J Nucl Med* 1987, **28**(5):844-851.

51. Frey EC, Tsui BM, Perry JR: **Simultaneous acquisition of emission and transmission data for improved thallium-201 cardiac SPECT imaging using a technetium-99m transmission source.** *J Nucl Med* 1992, **33**(12):2238-2245.

52. Manglos SH, Bassano DA, Thomas FD, Grossman ZD: **Imaging of the human torso using cone-beam transmission CT implemented on a rotating gamma camera.** *J Nucl Med* 1992, **33**(1):150-156.

53. Manglos SH, Bassano DA, Duxbury CE, Capone RB: **Attenuation maps for SPECT determined using cone beam transmission computed tomography.** *IEEE Trans Nucl Sci* 1990, **31**:600-608.

54. Tan P, Bailey DL, Meikle SR, Eberl S, Fulton RR, Hutton BF: **A scanning line source for simultaneous emission and transmission measurements in SPECT.** *J Nucl Med* 1993, **34**(10):1752-1760.

55. Tung CH, Gullberg GT, Zeng GL, et al.,: **Non-uniform attenuation correction using simultaneous transmission and emission converging tomography.** *IEEE Trans Nucl Sci* 1992, **39**:1134-1143.

56. Jaszczak RJ, Gilland DR, Hanson MW, Jang S, Greer KL, Coleman RE: **Fast transmission CT for determining attenuation maps using a collimated line source, rotatable air-copper-lead attenuators and fan-beam collimation.** *J Nucl Med* 1993, **34**(9):1577-1586.

57. Chang W, Loncaric S, Huang G, Sanpitak P: **Asymmetric fan transmission CT on SPECT systems.** *Phys Med Biol* 1995, **40**(5):913-928.

58. Cao Z, Tsui BM: **Performance characteristics of transmission imaging using a uniform sheet source with parallel-hole collimation.** *Med Phys* 1992, **19**(5):1205-1212.

59. Murase K, Tanada S, Inoue T, Sugawara Y, Hamamoto K: **Improvement of brain single photon emission tomography (SPET) using transmission data acquisition in a four-head SPET scanner.** *Eur J Nucl Med* 1993, **20**(1):32-38.

60. Hashimoto J, Ogawa K, Kubo A, Ichihara T, Motomura N, Takayama T, Iwanaga S, Mitamura H, Ogawa S: **Application of transmission scan-based attenuation compensation to scatter-corrected thallium-201 myocardial single-photon emission tomographic images.** *Eur J Nucl Med* 1998, **25**(2):120-127.

61. Ichihara T, Maeda H, Yamakado K, Motomura N, Matsumura K, Takeda K, Nakagawa T: **Quantitative analysis of scatter- and attenuation-compensated dynamic single-photon emission tomography for functional hepatic imaging with a receptor-binding radiopharmaceutical.** *Eur J Nucl Med* 1997, **24**(1):59-67.

62. Tsui BM, Gullberg GT, Edgerton ER, Ballard JG, Perry JR, McCartney WH, Berg J: **Correction of nonuniform attenuation in cardiac SPECT imaging.** *J Nucl Med* 1989, **30**(4):497-507.

63. Tan P, Bailey DL, Hutton BF, et al.,: **A moving line source for simultaneous transmission/emission SPECT.** *J Nucl Med* 1989, **30**:964.

64. Manglos SH, Bassano DA, Thomas FD: **Cone-beam transmission computed tomography for nonuniform attenuation compensation of SPECT images.** *J Nucl Med* 1991, **32**(9):1813-1820.

65. Celler A, Sitek A, Stoub E, Hawman P, Harrop R, Lyster D: **Multiple line source array for SPECT transmission scans: simulation, phantom and patient studies.** *J Nucl Med* 1998, **39**(12):2183-2189.

66. Manglos SH: **Truncation artifact suppression in cone-beam radionuclide transmission CT using maximum likelihood techniques: evaluation with human subjects.** *Phys Med Biol* 1992, **37**(3):549-562.

67. Lang TF, Hasegawa BH, Liew SC, Brown JK, Blankespoor SC, Reilly SM, Gingold EL, Cann CE: **Description of a prototype emission-transmission computed tomography imaging system.** *J Nucl Med* 1992, **33**(10):1881-1887.

68. Kalki K, Blankespoor SC, Brown JK, Hasegawa BH, Dae MW, Chin M, Stillson C: **Myocardial perfusion imaging with a combined x-ray CT and SPECT system.** *J Nucl Med* 1997, **38**(10):1535-1540.

69. Bocher M, Balan A, Krausz Y, Shrem Y, Lonn A, Wilk M, Chisin R: **Gamma camera-mounted anatomical X-ray tomography: technology, system characteristics and first images.** *Eur J Nucl Med* 2000, **27**(6):619-627.

70. von Schulthess GK, Pelc NJ: **Integrated-modality imaging: the best of both worlds.** *Acad Radiol* 2002, **9**(11):1241-1244.

71. Zaidi H, Hasegawa B: **Determination of the attenuation map in emission tomography.** *J Nucl Med* 2003, **44**(2):291-315.

72. Corbett JR, Kritzman JN, Ficaro EP: **Attenuation correction for single photon emission computed tomography myocardial perfusion imaging.** *Curr Cardiol Rep* 2004, **6**(1):32-40.

73. DePuey EG, Garcia EV: **Optimal specificity of thallium-201 SPECT through recognition of imaging artifacts.** *J Nucl Med* 1989, **30**(4):441-449.

74. Garcia EV, Cooke CD, Van Train KF, Folks R, Peifer J, DePuey EG, Maddahi J, Alazraki N, Galt J, Ezquerra N *et al*: **Technical aspects of myocardial SPECT imaging with technetium-99m sestamibi.** *Am J Cardiol* 1990, **66**(13):23E-31E.

75. DePuey EG, Rozanski A: **Using gated technetium-99m-sestamibi SPECT to characterize fixed myocardial defects as infarct or artifact.** *J Nucl Med* 1995, **36**(6):952-955.

76. Esquerre JP, Coca FJ, Martinez SJ, Guiraud RF: **Prone decubitus: a solution to inferior wall attenuation in thallium-201 myocardial tomography.** *J Nucl Med* 1989, **30**(3):398-401.

77. Bateman TM, Kolobrodov VV, Vasin AP, O'Keefe JH, Jr.: **Extended acquisition for minimizing attenuation artifact in SPECT cardiac perfusion imaging.** *J Nucl Med* 1994, **35**(4):625-627.

78. Cullom SJ, Case, J.A., Bateman, T.M.: **Attenuation Correction for Cardiac SPECT: Clinical and Developmental Challenges[Invited Commentary].** *J Nucl Med* 2000, **41**(5):860-862.

79. Ficaro EP, Fessler JA, Ackermann RJ, Rogers WL, Corbett JR, Schwaiger M: **Simultaneous transmission-emission thallium-201 cardiac SPECT: effect of attenuation correction on myocardial tracer distribution.** *J Nucl Med* 1995, **36**(6):921-931.

80. Prvulovich EM, Lonn AH, Bomanji JB, Jarritt PH, Ell PJ: **Effect of attenuation correction on myocardial thallium-201 distribution in patients with a low likelihood of coronary artery disease.** *Eur J Nucl Med* 1997, **24**(3):266-275.

81. Fanti S, Dondi M, Guidalotti PL, Fagioli G, Corbelli C, Monetti N: **Transmission-emission attenuation correction of myocardial SPECT.Impact of false positive rate in a population at low-risk of CAD [Scientif paper No.308](Proceedings of the 44th Annual Meeting).** *J Nucl Med* 1997:84P.

82. Bailey DL, Meikle SR: **Does attenuation correction work?** *J Nucl Med* 2000, **41**(5):960-961.

83. Corbett JR, Ficaro EP: **Attenuation corrected cardiac perfusion SPECT.** *Curr Opin Cardiol* 2000, **15**(5):330-336.

84. Chouraqui P, Livschitz S, Sharir T, Wainer N, Wilk M, Moalem I, Baron J: **Evaluation of an attenuation correction method for thallium-201 myocardial perfusion tomographic imaging of patients with low likelihood of coronary artery disease.** *J Nucl Cardiol* 1998, **5**(4):369-377.

85. Patton JA, Wilk M, Turkington TG, Balan A, Sandler MP: **Cardiac SPECT attenuation correction using an integrated x-ray CT/Dual-head scintillation camera system"[Scientific Paper, Proceedings of the 47th Annual Meeting].** *J Nucl Med* 2000, **41**(Supplement):22p.

86. Hendel RC, Corbett JR, Cullom SJ, DePuey EG, Garcia EV, Bateman TM: **The value and practice of attenuation correction for myocardial perfusion SPECT imaging:**

a joint position statement from the American Society of Nuclear Cardiology and the Society of Nuclear Medicine. *J Nucl Cardiol* 2002, 9(1):135-143.

87. Heller GV, Bateman TM, Johnson LL, Cullom SJ, Case JA, Galt JR, Garcia EV, Haddock K, Moutray KL, Poston C *et al.* **Clinical value of attenuation correction in stress-only Tc-99m sestamibi SPECT imaging.** *J Nucl Cardiol* 2004, **11**(3):273-281.

88. Wackers FJ: **Attenuation correction, or the emperor's new clothes?** *J Nucl Med* 1999, **40**(8):1310-1312.

89. Gallowitsch HJ, Unterweger O, Mikosch P, Kresnik E, Sykora J, Grimm G, Lind P: **Attenuation correction improves the detection of viable myocardium by thallium-201 cardiac tomography in patients with previous myocardial infarction and left ventricular dysfunction.** *Eur J Nucl Med* 1999, **26**(5):459-466.

90. Manglos SH, Thomas FD, Gagne GM, Hellwig BJ: **Phantom study of breast tissue attenuation in myocardial imaging.** *J Nucl Med* 1993, **34**(6):992-996.

91. Pitman AG, Kalff V, Van Every B, Risa B, Barnden LR, Kelly MJ: **Effect of mechanically simulated diaphragmatic respiratory motion on myocardial SPECT processed with and without attenuation correction.** *J Nucl Med* 2002, **43**(9):1259-1267.

92. Toma DM, White MP, Mann A, Phillips JM, Pelchat DA, Giri S, Ucros GR, Heller GV: **Influence of arm positioning on rest/stress technetium-99m labeled sestamibi tomographic myocardial perfusion imaging.** *J Nucl Cardiol* 1999, **6**(2):163-168.

93. Prvulovich EM, Jarritt PH, Lonn AH, Vorontsova E, Bomanji JB, Ell PJ: **Influence of arm positioning on tomographic thallium-201 myocardial perfusion imaging and the effect of attenuation correction.** *Eur J Nucl Med* 2000, **27**(9):1349-1355.

94. O'Connor MK, Bothun ED: **Effects of tomographic table attenuation on prone and supine cardiac imaging.** *J Nucl Med* 1995, **36**(6):1102-1106.

95. Tamaki N, Mukai T, Ishii Y, Fujita T, Yamamoto K, Minato K, Yonekura Y, Tamaki S, Kambara H, Kawai C *et al.* **Comparative study of thallium emission myocardial tomography with 180 degrees and 360 degrees data collection.** *J Nucl Med* 1982, **23**(8):661-666.

96. Coleman RE, Jaszczak RJ, Cobb FR: **Comparison of 180 degrees and 360 degrees data collection in thallium-20 1 imaging using single-photon emission computerized tomography (SPECT): concise communication.** *J Nucl Med* 1982, **23**(8):655-660.

97. Knesaurek K, King MA, Glick SJ, Penney BC: **Investigation of causes of geometric distortion in 180 degrees and 360 degrees angular sampling in SPECT.** *J Nucl Med* 1989, **30**(10):1666-1675.

98. LaCroix KJ, Tsui BM, Hasegawa BH: **A comparison of 180 degrees and 360 degrees acquisition for attenuation-compensated thallium-201 SPECT images.** *J Nucl Med* 1998, **39**(3):562-574.

99. Araujo LI, Jimenez-Hoyuela JM, McClellan JR, Lin E, Viggiano J, Alavi A: **Improved uniformity in tomographic myocardial perfusion imaging with attenuation correction and enhanced acquisition and processing.** *J Nucl Med* 2000, **41**(7):1139-1144.

100. Chen M, Peter J, Jaszczak RJ, Gilland DR, Bowsher JE, Torani MP, Metzler SD: **Observer Studies of Cardiac lesion Detectability With Triple-Head 360 Versus Dual-Head 180 SPECT Acquistion Using Simulated Projection Data.** *IEEE Trans Nucl Sci* 2002, **49**(3):655-660.

101. Zaidi H: **Relevance of accurate Monte Carlo modeling in nuclear medical imaging.** *Med Phys* 1999, **26**(4):574-608.

102. Zaidi H: **Monte Carlo techniques in diagnostic and theraputic nuclear medicine.** *IAEA-CN-96-65* 1996: .http://fresch.online.fr/Habib/www/pdf/IAEA02.pdf.

103. Segars WP, Lalush DS, Tsui B: **Modeling respiratory mechanics in the MCAT and spline-based MCAT phantoms.** *IEEE Trans Nucl Sci* 2001, 48:89-97.

104. Hollinger EF, Loncaric S, Yu DC, Ali A, Chang W: **Using fast sequential asymmetric fanbeam transmission CT for attenuation correction of cardiac SPECT imaging.** *J Nucl Med* 1998, **39**(8):1335-1344.

105. Tsui BMW, Segars WP, Lalush DS: **Effects of Upward Creep and Respiratory Motion in Myocardial SPECT.** *IEEE Trans Nucl Sci* 2000, **47**(3):1192-1195 http://www.bme.unc.edu/~wsegars/tsui_1199.pdf.

106. Buvat I, Castiglioni I: **Monte Carlo simulations in SPET and PET.** *Q J Nucl Med* 2002, **46**(1):48-61.

107. Zubal IG, Harrell CR, Smith EO, Rattner Z, Gindi G, Hoffer PB: **Computerized three-dimensional segmented human anatomy.** *Med Phys* 1994, **21**(2):299-302.

108. Krol A, Bowsher JE, Manglos SH, Feiglin DH, Tornai MP, Thomas FD: **An EM algorithm for estimating SPECT emission and transmission parameters from emissions data only.** *IEEE Trans Med Imaging* 2001, **20**(3):218-232.

109. Hutton BF, Hudson HM, Beekman FJ: **A clinical perspective of accelerated statistical reconstruction.** *Eur J Nucl Med* 1997, **24**(7):797-808.

110. Hutton BF: **An Introduction to Iterative Reconstruction.** *Alasbimn Journal* 2002, **5**(18):http://www2.alasbimnjournal.cl/alasbimn/CDA/sec_b/0,1206,SCID%1253D1455,1200.html.

111. Hendrik PP, Narayanan, M.V., Dahlberg, S.T., Leppo, J.A., and King, M.A.: **The influence of attenuation and scatter compensation on the apparent distribution of Tc-99m sestamibi in cardiac slices.** *J Nucl Cardiol* 2001, 8(3):356-364.

112. Bronnikov AV: **Numerical solution of the identification problem for the attenuated Radon transform.** *Inverse Problems* 1999, **15**:1315-1324.

113. Corbett JR, McGhie AI: **Physiologic Principles of Stress Myocardial Perfusion Imaging.** In: *Clinical SPECT Imaging.* Edited by Kramer EL, Sanger JJ. New York: Raven Press,Ltd.; 1995: 145-177.

114. Liew SC, Hasegawa BH, Brown JK, Lang TF: **Noise propagation in SPECT images reconstructed using an iterative maximum-likelihood algorithm.** *Phys Med Biol* 1993, **38**(12):1713-1726.

115. Gullberg GT, Morgan HT, Zeng GL, Christian PE, Di Bella VR, Tung. C-H, Maniawski PJ, Hsieh. Y-L, Datz FL: **The design and performance of a**

simultaneous transmission and emission tomography system. *IEEE Trans Nucl Sci* 1998, **45**(3):1676-1698.

116. Wallis JW, Miller TR: **Rapidly converging iterative reconstruction algorithms in single-photon emission computed tomography.** *J Nucl Med* 1993, **34**(10):1793-1800.

117. Hutton BF, Lau YH: **Application of distance-dependent resolution compensation and post-reconstruction filtering for myocardial SPECT.** *Phys Med Biol* 1998, **43**(6):1679-1693.

118. Hudson HM, Larkin RS: **Accelerated image reconstruction using ordered subsets of projection data.** *IEEE Trans Med Imag* 1994, **13**(4):601-609.

119. Kontaxakis G, Strauss LG, Thireou T, Ledesma-Carbayo MJ, Santos A, Pavlopoulos SA, Dimitrakopoulou-Strauss A: **Iterative image reconstruction for clinical PET using ordered subsets, median root prior, and a web-based interface.** *Mol Imaging Biol* 2002, 4(3):219-231.

120. Gutman F, Gardin I, Delahaye N, Rakotonirina H, Hitzel A, Manrique A, Le Guludec D, Vera P: **Optimisation of the OS-EM algorithm and comparison with FBP for image reconstruction on a dual-head camera: a phantom and a clinical 18F-FDG study.** *Eur J Nucl Med Mol Imaging* 2003, 30(11):1510-1519.

121. Vanhove C, Defrise M, Franken PR, Everaert H, Deconinck F, Bossuyt A: **Interest of the ordered subsets expectation maximization (OS-EM) algorithm in pinhole single-photon emission tomography reconstruction: a phantom study.** *Eur J Nucl Med* 2000, **27**(2):140-146.

122. Blocklet D, Seret A, Popa N, Schoutens A: **Maximum-likelihood reconstruction with ordered subsets in bone SPECT.** *J Nucl Med* 1999, **40**(12):1978-1984.

123. Townsend DW, Carney JP, Yap JT, Hall NC: **PET/CT today and tomorrow.** *J Nucl Med* 2004, **45 Suppl 1**:4S-14S.

124. Matsunari I, Boning G, Ziegler SI, Kosa I, Nekolla SG, Ficaro EP, Schwaiger M: **Effects of misalignment between transmission and emission scans on attenuation-corrected cardiac SPECT.** *J Nucl Med* 1998, **39**(3):411-416.

125. Delbeke D, Martin WH, Patton JA, Sandler MP: **Value of iterative reconstruction, attenuation correction, and image fusion in the interpretation of FDG PET images with an integrated dual-head coincidence camera and X-ray-based attenuation maps.** *Radiology* 2001, **218**(1):163-171.

126. El Fakhri G, Buvat I, Benali H, Todd-Pokropek A, Di Paola R: **Relative impact of scatter, collimator response, attenuation, and finite spatial resolution corrections in cardiac SPECT.** *J Nucl Med* 2000, **41**(8):1400-1408.

127. Fricke H, Fricke E, Weise R, Kammeier A, Lindner O, Burchert W: **A method to remove artifacts in attenuation-corrected myocardial perfusion SPECT Introduced by misalignment between emission scan and CT-derived attenuation maps.** *J Nucl Med* 2004, **45**(10):1619-1625.

128. Gullberg GT: **Innovative design concepts for transmission CT in attenuation-corrected SPECT imaging.** *J Nucl Med* 1998, **39**(8):1344-1347.

129. Meikle SR, Hutton BF, Bailey DL, Hooper PK, Fulham MJ: **Accelerated EM reconstruction in total-body PET: potential for improving tumour detectability.** *Phys Med Biol* 1994, **39**:1689-1704 http://www.iop.org/EJ/abstract/0031-9155/1639/1610/1012.

130. Anagnostopoulos C, Harbinson M, Kelion A, Kundley K, Loong CY, Notghi A, Reyes E, Tindale W, Underwood SR: **Procedure guidelines for radionuclide myocardial perfusion imaging.** *Heart* 2004, **90 Suppl 1**:i1-10.

131. McKiddie FL, Davidson FJ, Gemmell HG: **Reconstruction, Analysis, and Display of Myocardial Perfusion SPECT Images.** *new advances in Nuclear Cardiology* 2001, **2**(2):11-13 http://www.nanjournal.com/vol12_12/vol12_12_practicalguide.htm.

132. Prvulovich E: **How to Report Myocardial Perfusion.** *new advances in Nuclear Cardiology* 1999, **1**(1):9-11 http://www.nanjournal.com/vol11/vol_11practicalguide.htm.

133. Kiat H, Van Train K, Friedman J, Germano G, Silagan G, Wang F, Maddahi J, Prigent F, Berman D: **Quantitative Stress-Redistribution Thallium-201 SPECT Using Prone Imaging: Methodologic Development and Validation.** *J Nucl Med* 1992, **33**(8):1509-1515.

134. Schelbert HR, Beanlands R, Bengel F, Knuuti J, Dicarli M, Machac J, Patterson R: **PET myocardial perfusion and glucose metabolism imaging: Part 2-Guidelines for interpretation and reporting.** *J Nucl Cardiol* 2003, **10**(5):557-571.

135. Folks RD: **Interpretation and reporting of myocardial perfusion SPECT: a summary for technologists.** *J Nucl Med Technol* 2002, **30**(4):153-163; quiz 164.

136. Macey DJ, Giap HB: **Quantitative SPECT.** In: *Clinical SPECT Imaging.* Edited by Kramer EL, Sanger JJ. New York: Raven Press, Ltd.; 1995: 69-78.

137. Watson DD: **Is it time for SPECT attenuation correction?** *J Nucl Cardiol* 2004, **11**(3):239-241.

138. Narayanan MV, King MA, Pretorius PH, Dahlberg ST, Spencer F, Simon E, Ewald E, Healy E, MacNaught K, Leppo JA: **Human-observer receiver-operating-characteristic evaluation of attenuation, scatter, and resolution compensation strategies for (99m)Tc myocardial perfusion imaging.** *J Nucl Med* 2003, **44**(11):1725-1734.

139. Kashiwagi T, Yutani K, Fukuchi M, Naruse H, Iwasaki T, Yokozuka K, Inoue S, Kondo S: **Correction of nonuniform attenuation and image fusion in SPECT imaging by means of separate X-ray CT.** *Ann Nucl Med* 2002, **16**(4):255-261.

140. Song X, Frey EC, Wang WT, Du Y, Tsui BMW: **Validation and Evaluation of Model-Based Croostalk Compensation Method in Simultaneous 99mTc Stress and 201Tl Rest Myocardial Perfusion SPECT.** *IEEE Trans Nucl Sci* 2004, **51**(1):72-79.

141. El Fakhri G, Buvat I, Almeida P, Bendriem B, Todd-Pokropek A, Benali H: **Should scatter be corrected in both transmission and emission data for accurate quantitation in cardiac SPET?** *Eur J Nucl Med* 2000, **27**(9):1356-1364.

142. Xu XG, Chao TC, Bozkurt A: **VIP-Man: an image-based whole-body adult male model constructed from color photographs of the Visible Human Project for multi-particle Monte Carlo calculations.** *Health Phys* 2000, **78**(5):476-486.

143. Petoussi-Henss N, Zanki M, Fill U, Regulla D: **The GSF family of voxel phantoms.** *Phys Med Biol* 2002, **47**(1):89-106.

144. Zaidi H: **Scatter modelling and correction strategies in fully 3-D PET.** *Nucl Med Commun* 2001, **22**(11):1181-1184.

145. Mustafovic S, Thielemans K: **Object dependency of resolution in reconstruction algorithms with interiteration filtering applied to PET data.** *IEEE Trans Med Imaging* 2004, **23**(4):433-446.

146. Bokulic T, Vastenhouw B, De Jong HW, Van Dongen AJ, Van Rijk PP, Beekman FJ: **Monte Carlo-based down-scatter correction of SPECT attenuation maps.** *Eur J Nucl Med Mol Imaging* 2004, **31**(8):1173-1181.

147. Khalil ME, Brown EJ, Jr., Heller EN: **Does scatter correction of cardiac SPECT improve image quality in the presence of high extracardiac activity?** *J Nucl Cardiol* 2004, **11**(4):424-432.

148. Koepfli P, Hany TF, Wyss CA, Namdar M, Burger C, Konstantinidis AV, Berthold T, Von Schulthess GK, Kaufmann PA: **CT attenuation correction for myocardial perfusion quantification using a PET/CT hybrid scanner.** *J Nucl Med* 2004, **45**(4):537-542.

Appendix (A)

The C-based program used to create planar projection data ("fwdprj").

```
/*
 ============================================================================
 File:        fwdprj
 Author:      D C Barber Date:  12/4/96

 Program: fwdprj

  Usage: fwdprj {-s -r -p -c} {-a atten_image}  activity_image

 ============================================================================
 Public Routines:
 ============================================================================

 History:

 ============================================================================
*/

/* ========================== header files ========================== */

#include <stdio.h>

/* NM Header files: */
#include <math.h>
#include <link_interface.h>


/* ---------------------- print_usage_and_exit
---------------------------
 *
 *     Prints the command line options for the program and exits with an
 *     error code.
 *
 */

print_usage_and_exit ()
{
      /* Print message to stderr, and exit with `EXIT_USAGE_ERR' */
      /* exit code */
      /* See the `Error' module */
      err_user_exit ("Usage:Usage: fwdprj {-s -r -p} {-a atten_image}
activity_image", EXIT_USAGE_ERR);
}

/*---------------------------------- main
-----------------------------------
 */

main (argc, argv)
int argc;
char *argv[];
{

      IO_Command_Line *cl;     /* Command line handle */
      int num_args;
```

```
        /* check there is a current study */
        if (study_select_current() == -1)
              err_user_exit("fwdprj: No study current or failed to find
study",EXIT_CONFIG_ERR);


        /* Check command line for correct flags, parameters and arguments
*/
        /* See `Command Line' module */
        cl = cl_create (argc, argv, "am", "srpcn", 0, 2);
        if (cl == (IO_Command_Line *)NULL)
              /* If there are errors on the command line... */

              print_usage_and_exit ();


        fwdprj2D(cl);


        /* Dereference command line handle */
        cl_destroy (cl);
        return (0);
}


float bilint(r, s, p, cols, rows)
float r;
float s;
float **p;
int cols, rows;

{
        int nr,ns;
        int nru,nsu;
        float wr,ws;
        float va,vau;
        float res;


        nr=r;
        ns=s;


        if (nr < 0 || nr >= (cols-2) || ns < 0 || ns >= (rows-2))
              return (0.0);
        else
        {

              nru=nr+1;
              nsu=ns+1;
              wr=r-nr;
              ws=s-ns;


              va=p[ns][nr]+(p[ns][nru]-p[ns][nr])*wr;
              vau=p[nsu][nr]+(p[nsu][nru]-p[nsu][nr])*wr;

              res = va+(vau-va)*ws;
```

```
            return (res);
        }
}
```

```
void rotate(float **a, int rows, int cols, int proj, int projs, float
**b)
{
    int row, col;
    float twopi;
      float rowoff, coloff;
      float x,y,c,s;
      float xa,ya;

    twopi = atan(1.0)*8.0;

    rowoff = rows/2 - 0.5;
    coloff = cols/2 - 0.5;

    c = cos(-twopi*proj/projs);
    s = sin(-twopi*proj/projs);

    for (row = 0; row < rows; row++)
            for (col = 0; col < cols; col++)
            {
            x = (col - coloff);
            y = (row - rowoff);
            if ((x*x + y*y) <= cols*rows/4.0)
            {
                  xa = x*c + y*s;
                  ya = y*c - x*s;
                        b[row][col] = bilint(xa + coloff, ya + rowoff,
a, cols, rows);
            }
          else
                  b[row][col] = 0.0;
            }

}

void smooth(float *a, int cols)
{
    int col;

    for (col = 0;col < cols -1; col++)
            a[col] = (a[col] + a[col+1])/2.0;
    for (col = cols -1; col > 0; col--)
            a[col] = (a[col] + a[col-1])/2.0;
}

void pack(float *sn, float *snp, int cols, int pcols)
{
    int pcol, k;
    int r;

    r = cols/pcols;
```

```
for (pcol = 0; pcol < pcols; pcol++)
{
        snp[pcol] = 0.0;
        for (k = 0; k < r; k++)
              snp[pcol] += sn[pcol*r + k];
              snp[pcol] *= r;
    }
}


/*============================fwdprj=================================*/


fwdprj2D(cl)
IO_Command_Line *cl;
{
    float **a;
    float **aa;
    float **mu;
    float **mmu;
    float ***p;
    float *sn, *snp;
    int rows, cols, slices, projs;
    int row, col, slice, proj;
    float **b;
    float **u;
    float pix;
    int att;
    int i,j;
    int pcols;
    float utot, tot;
    int sm, r, s;
    float smax, norm;
     char string_scale[16];

sm = (int)numerical_parameter(cl, 'c',0.0);
norm = numerical_parameter(cl,'n',10000.0);
  att = flag(cl, 'a');



  if(att)
  {
        mu = load_float_image(cl, 1, &cols, &rows);
        pix = (float)512.0/cols;
        for (row = 0; row < rows; row++)
              for (col = 0; col < cols; col++)
                    mu[row][col] /= 10000.0;
        a = load_float_image(cl, 2, &cols, &rows);
}
else
{
        a = load_float_image(cl, 1, &cols, &rows);
        pix = (float)512.0/cols;
        mu = make_float_array_2d(cols, rows);
              for (row = 0; row < rows; row++)
                    for (col = 0; col < cols; col++)
                          mu[row][col] = 0.0;
```

```
  }
pcols = (int)numerical_parameter(cl, 'r', (float)cols);
projs = (int)numerical_parameter(cl, 'p', (float)pcols);
  slices = (int)numerical_parameter(cl, 's', (float)pcols);

b = make_float_array_2d(cols, rows);
u = make_float_array_2d(cols, rows);
aa = make_float_array_2d(cols, rows);
mmu = make_float_array_2d(cols, rows);
p = make_float_array_3d(pcols, slices, projs);
sn = make_float_array_1d(cols);
snp = make_float_array_1d(pcols);

for (proj = 0; proj < projs; proj++)
  {
        for (row = 0; row < rows; row++)
              for (col = 0; col < cols; col++)
              {
                    aa[row][col] = a[row][col];
                    mmu[row][col] = mu[row][col];
              }


        rotate(aa, rows, cols, proj, projs, b);
              rotate(mmu, rows, cols, proj, projs, u);

                    for (col = 0; col < cols; col++)
                    {
                    utot = 0.0;
                    for (row = 0; row < rows; row++)
                    {
                          utot += u[row][col]*pix;
                                u[row][col] = exp(-utot);
                    }
              }


                    for (col = 0; col < cols; col++)
                    {
                    tot = 0.0;
                    for (row = 0; row < rows; row++)
                                tot += b[row][col] * u[row][col];
                    sn[col] = tot;
                    }

                    for (s = 0; s < sm; s++)
                      smooth(sn, cols);

                    pack(sn, snp, cols, pcols);

              for (slice = 0; slice < slices; slice++)
                          for (col = 0; col < pcols; col++)
                          p[proj][slice][col] = snp[col];


}
```

```
smax = 0.0;
for (slice = 0; slice < slices; slice++)
      for (proj = 0; proj < projs; proj++)
            for (col = 0; col < pcols; col++)
                  if (smax < p[proj][slice][col])smax = p[proj]
[slice][col];

      smax = smax/norm;

    for (slice = 0; slice < slices; slice++)
          for (proj = 0; proj < projs; proj++)
                for (col = 0; col < pcols; col++)
                      p[proj][slice][col] /= smax;


    save_float_volume(p, pcols, slices, projs, 4);

      sprintf(string_scale, "%f", smax);
      put_kvp_image(cl, 0, "multiply by factor",string_scale);
      put_kvp_image(cl, 0, "process", "planar");
      put_kvp_image(cl, 0; "Image type", "4");
      put_kvp_image(cl, 0, "tomo start angle", "0");
      put_kvp_image(cl, 0, "tomo gantry direction", "clockwise");
      sprintf(string_scale, "%f", (float)pix*cols/pcols);
      put_kvp_image(cl, 0, "Pixel size (mm)",string_scale);
      put_kvp_image(cl, 0, "!scaling factor (mm/pixel)
[1]",string_scale);
      put_kvp_image(cl, 0, "!scaling factor (mm/pixel)
[2]",string_scale);
      put_kvp_image(cl, 0, "tomo orbit type", "1");
      put_kvp_image(cl, 0, "axial thickness", "1");
      put_kvp_image(cl, 0, "axial start", "0");
      put_kvp_image(cl, 0, "patient orientation", "head in");
      put_kvp_image(cl, 0, "patient rotation", "supine");
      sprintf(string_scale, "%d", projs);
      put_kvp_image(cl, 0, "!number of projections", string_scale);
      put_kvp_image(cl, 0, "number of detector heads", "1");
      put_kvp_image(cl, 0, "!direction of rotation", "CW");
      put_kvp_image(cl, 0, "start angle", "0");


    if (att == 0)
          return;


    p = make_float_array_3d(pcols, pcols, slices);
    a = make_float_array_2d(pcols, pcols);
    r = cols/pcols;

    for (row ='0; row < pcols; row++)
          for (col = 0; col < pcols; col++)
          {
                tot = 0.0;
                for (j = 0; j < r; j++)
                      for (i = 0; i < r; i++)
                      tot += mu[row*r + j][col*r + i];
```

```
            a[row][col] = tot*10000.0/(r*r);
      }

            for (slice = 0; slice < slices; slice++)
                  for (row = 0; row < pcols; row++)
                        for (col = 0; col < pcols; col++)
                              p[slice][row][col] = a[row][col];


      save_float_volume(p, pcols, pcols, slices, 5);

            put_kvp_image(cl, 0, "process", "axial");
            put_kvp_image(cl, 0, "Image type", "5");
            put_kvp_image(cl, 0, "tomo start angle", "0");
            put_kvp_image(cl, 0, "tomo gantry direction", "clockwise");
            sprintf(string_scale, "%f", (float)pix*cols/pcols);
            put_kvp_image(cl, 0, "Pixel size (mm)",string_scale);
            put_kvp_image(cl, 0, "!scaling factor (mm/pixel)
[1]",string_scale);
            put_kvp_image(cl, 0, "!scaling factor (mm/pixel)
[2]",string_scale);
            put_kvp_image(cl, 0, "tomo orbit type", "1");
            put_kvp_image(cl, 0, "axial thickness", "1");
            put_kvp_image(cl, 0, "axial start", "0");
            put_kvp_image(cl, 0, "patient orientation", "head in");
            put_kvp_image(cl, 0, "patient rotation", "supine");
            sprintf(string_scale, "%d", projs);
            put_kvp_image(cl, 0, "!number of projections", string_scale);
            put_kvp_image(cl, 0, "number of detector heads", "1");
            put_kvp_image(cl, 0, "!direction of rotation", "CW");
            put_kvp_image(cl, 0, "start angle", "0");
}
/*=======================end of fwdprj=================================*/
```

Appendix (B)

The Link program used for OSEM reconstruction without and with AC

```
#!/bin/csh
#
#########################################################################
# File:     OS-EM_ATT
# Author:   Ahmed Al-enezi
# Date:    18 April 2002
#
#
# Description: OSEM reconstruction with and without attenuation
#
# Arguments: The parmeter -a is used when attenuation included
#            The parameter -a should be followed by image number
#            The default number of iterations is 8
#            The default number of subsets is 1
#            The user can change the number of iteartion by
#            The parameter -i and followed by number of iteartions
#            The user can change the number of subsets by
#            The parameter -s and followed by number of subsets

#
# Exit status one of:
#
# Assumes:
#
# History:
#
#########################################################################
set im = 1
set at = "-"
#-----------------------------------------------
# set the prameter of number of iteartions -i
# default is 8 iterations
set ITS = 8
set a = `echo "-i" | com_arg $argv`
if ("$a" != "-")then
      set ITS = $a
      @ im = $im + 2

endif
#-----------------------------------------------
# set the prameter of number of subsets -s
# default is 1 subsets
set SUB = 1
set a = `echo "-s" | com_arg $argv`
if ("$a" != "-")then
      set SUB = $a
      @ im = $im + 2

endif
#-----------------------------------------------
# set the parametr of attenuation image included -a
set a = `echo "-a" | com_arg $argv`
if ("$a" != "-")then
      set at = $a
      @ im = $im + 2
endif


set im = `echo $argv[$im] | cut -c2-10`
```

```
set size = `filesize i$im`
set size = ($size)
set res = $size[1]
set proj = $size[3]
echo $res $proj
set dim1 = $size[2]
echo $dim1
#
set pix = `label_file -g "Pixel size (mm)" i$im`
set mbf = `label_file -g "multiply by factor" i$im`

scd
ls

echo $im
if_export -o IMAGE$im i$im
dos2unix IMAGE$im.HDR IMAGE$im.HDR
mv IMAGE$im.HDR temp
head -n 30 temp > IMAGE$im.HDR
echo "\!scaling factor (mm/pixel) [1]:= 4" >> IMAGE$im.HDR
echo "\!scaling factor (mm/pixel) [2]:= 4" >> IMAGE$im.HDR
echo "start angle:= 0" >> IMAGE$im.HDR
echo "patient orientation:= head in" >> IMAGE$im.HDR
echo "patient rotation:= supine" >> IMAGE$im.HDR
echo "\!direction of rotation:= CW" >> IMAGE$im.HDR
echo "number of detector heads:= 1" >> IMAGE$im.HDR
echo "\!number_of_projections:= 128" >> IMAGE$im.HDR
tail +31 temp >> IMAGE$im.HDR
ls -l

cat IMAGE$im.HDR

if ("$at" == "-")then
    echo "Iterative reconstruction with "$SUB" subsets "$ITS" iterations"

      ~/src/OSEM/r IMAGE$im.HDR  -OS:X$SUB -Iterations:$ITS
      if_convert IMAGE$im.r ;= xax
#     reverse_file $xax ;= rax
      copy_file $xax ;= rax
      label_file -p process -l "OSEM no AC($SUB subs & $ITS itrs) " i0
      label_file  -l "" i0
else
      set at = `echo $at | cut -c2-10`
      if_export -o IMAGE$at i$at
      dos2unix IMAGE$at.HDR IMAGE$at.HDR
      mv IMAGE$at.HDR temp
      head -n 30 temp > IMAGE$at.HDR
      echo "\!scaling factor (mm/pixel) [1]:= 4" >> IMAGE$at.HDR
    echo "\!scaling factor (mm/pixel) [2]:= 4" >> IMAGE$at.HDR
  echo "start angle:= 0" >> IMAGE$at.HDR
    echo "\!direction of rotation:= CW" >> IMAGE$at.HDR
    echo "number of detector heads:= 1" >> IMAGE$at.HDR
    echo "\!number_of_projections:= 128" >> IMAGE$at.HDR
    echo "patient orientation:= head in" >> IMAGE$at.HDR
    echo "patient rotation:= supine" >> IMAGE$at.HDR

    tail +31 temp >> IMAGE$at.HDR
echo "Iterative reconstruction with "$SUB" subsets "$ITS" iterations"
```

```
~/src/OSEM/r IMAGE$im.HDR -Attenuate:IMAGE$at.HDR -OS:X$SUB -Iterations:
$ITS
      if_convert IMAGE$im.r ;= xax
#     reverse_file $xax ;= rax
      copy_file $xax ;= rax
      label_file -p process -l "OSEM AC($SUB subs & $ITS itrs)" i0
      label_file  -l "" i0
endif

set oscale = `cat IMAGE$im.r | grep RPAH`
set oscale = `echo $oscale | cut -d= -f 2`
echo $oscale
#label_file -p "OSEM scale" -l $oscale i0
#-------------------------------------
#rm IMAGE$im.*
rm temp
#delete_file $ax
#delete_file $xax

cd ~
```

Appendix (C)

The program used for registration and interpolation of the phantom slices.

```
#!/bin/csh
#
##############################################################################
# File:    Reg_three_mod
# Author: Ahmed Alenezi
# Date:    01 May 2003
#
#
# Description: Registration multiple slices
#
# Arguments:
#
#
# Exit status one of:
#
# Assumes: #
# History:
##############################################################################
#
echo "The user should check the number of images included in this processing"
# un protect all images in the study

#protect_file -ui

echo -n "Enter the image number to start processing>"
set a = $<
echo -n "Enter the image number to end processing>"
set b = $<

set img1 = $a

while ($img1 <= $b)

        protect_file $img1

        @ img1 ++
end

#rh_tidy
show $a

make_roi -b
make_mask r0 ;= mask

protect_file $mask

#rh_tidy

#@ c = $b + 1

#set D = `CALC "D = 2;($c - $a)"`
#set C = 1
set im = $a
@ b = $b - 1

while ($im <= $b)
        @ in = $im + 1
        smooth_file -n 4 i$im ;= sim
        smooth_file -n 4 i$in ;= sin
        register -s 8 -a 10 -l 10 -f $mask $sin $sim i$im ;= reg
```

```
delete_file $reg
copy_file i$im ;= level0a
label_file -p "Image type" -l 5 i0
protect_file i0

apply_map -v 0.2 i$im ;= level1
apply_map -v 0.4 i$im ;= level2
apply_map -v 0.6 i$im ;= level3
apply_map -v 0.8 i$im ;= level4

register -s 8 -a 10 -l 10 -f $mask $sim $sin i$in ;= reg
delete_file $reg
apply_map -v 0.8 i$in ;= level
file_add -a 0.8 -b 0.2 $level1 $level
label_file -p "Image type" -l 5 i0
show
protect_file i0
delete_file $level

apply_map -v 0.6 i$in ;= level
file_add -a 0.6 -b 0.4 $level2 $level
label_file -p "Image type" -l 5 i0
show
protect_file i0
delete_file $level

        apply_map -v 0.4 i$in ;= level
        file_add -a 0.4 -b 0.6 $level3 $level
        label_file -p "Image type" -l 5 i0
        show
        protect_file i0
        delete_file $level

        apply_map -v 0.2 i$in ;= level
        file_add -a 0.2 -b 0.8 $level4 $level
        label_file -p "Image type" -l 5 i0
        show
        protect_file i0
        delete_file $level

        delete_file $level4
        delete_file $level3
        delete_file $level2
        delete_file $level1
        delete_file $sin
        delete_file $sim

        @ im++
end
copy_file $in ;= final
protect_file $final

#rh_tidy
```

Appendix (D)

The program used to simulate Poisson noise in projection data

```
/*
=============================================================================

  File:  poisson_noise.c
Author:         D C Barber Date:         26/02/01

        Program: poisson_noise


      */

      #include <stdio.h>
      #include <stddef.h>
      #include <stdlib.h>
      #include <math.h>


      #include <link_interface.h>

      float ***image(int dimslice,int dimrow,int dimcol)
      {
            float ***ppp;
            int row, slice;
            float *p;

            p=(float *)calloc((size_t)(dimslice*dimrow*dimcol),(size_t)sizeof(float));
            if(!p)
                  return(NULL);

      /* allocate pointer to whole buffer */

            ppp=(float ***)calloc((size_t)dimslice,(size_t)sizeof(float **));
            if(!ppp)
            {
                  return(NULL);
            }
      /* allocate pointers to slices */

            for (slice = 0; slice < dimslice; ++slice)
            {
                  ppp[slice] = (float **)calloc((size_t)dimrow,(size_t)sizeof(float
      *));
                  if(!ppp[slice])
                        return(NULL);

      /* allocate pointers to rows */

                  for (row = 0; row < dimrow; ++row)
                  {
                        ppp[slice][row] = p+row*dimcol+slice*dimrow*dimcol;
                        if(!ppp[slice][row])
                              return(NULL);
                  }
            }
            return(ppp);
      }


      free_image(ppp)
      float ***ppp;
      {
            float *p;
```

```
        p = ppp[0][0];
        free(p);
        free(ppp);
}


float uniform()
{
        return((float)rand()/RAND_MAX);
}

float normal()
{
        float r;
        float rd[2];
        float pi = 3.14159;
        float a,b;

        rd[0] = uniform();
        rd[1] = uniform();
        a=cos(2*pi*rd[1]);
        b=-2.0*log(rd[0]);
        return(a*sqrt(b));
}


float poisson(float num)
{
        float sd;
        int a;
        float r;
        int k;
        float z;
        float dum;
        float t;
/*
        Poisson generates a vector of n numbers with poisson
        distribution about a mean num. For counts above 50 use
        binomial approximation.
*/
        if(num > 50.)
        {
                sd=sqrt(num);
                r = normal();
                dum=sd*r+num;
                k=(int)(dum+0.5);
                k = (k<0)?0:k;
        }
        else
        {
                z=exp(-num);
                t=1.0;
                k=0;
                while (t > z)
                {
                        r = uniform();
                        t *= r;
                        k++;
                }
        }
        return((float)(k-1));

}
```

```
print_usage_and_exit ()
{
      /* Print message to stderr, and exit with `EXIT_USAGE_ERR' */
      /* exit code */
      /* See the `Error' module */
      err_user_exit ("Usage: poisson_noise", EXIT_USAGE_ERR);
}


void main(int argc, char *argv[])
{
      IO_Command_Line *cl;    /* Command line handle */
    float ***pic;
      float ***npic;
      int row, col;
      int cols, rows, slices;

      /* check there is a current study */
      if (study_select_current() == -1)
            err_user_exit("poisson: No study current or failed to find
study",EXIT_CONFIG_ERR);

      /* Check command line for correct flags, parameters and arguments */
      /* See `Command Line' module */
      cl = cl_create (argc, argv, "", "",0,1);
      if (cl == (IO_Command_Line *)NULL)
            /* If there are errors on the command line... */

            print_usage_and_exit ();

      pic = load_float_volume(cl, 1, &cols, &rows, &slices);


      npic = image(slices, cols, rows);
      for (row = 0; row < rows; row++)
            for (col = 0; col < cols; col++)
                  if (pic[0][row][col] > 0.0)
                        npic[0][row][col] = poisson(pic[0][row][col]);

/* gets the command line arguments into a behind the scenes form*/

      save_float_volume(npic,cols, rows, slices,0);

      copy_image_header(cl, 1);

      free_image(pic);
      free_image(npic);

}
```